

Christopher J. Wohl  
Douglas H. Berry *Editors*

# Contamination Mitigating Polymeric Coatings for Extreme Environments

**Editorial Board Members:**

- A. Abe, Yokohama, Kanagawa, Japan  
A.-C. Albertsson, Stockholm, Sweden  
G.W. Coates, Ithaca, NY, USA  
J. Genzer, Raleigh, NC, USA  
S. Kobayashi, Kyoto, Japan  
K.-S. Lee, Daejeon, South Korea  
L. Leibler, Paris, France  
T.E. Long, Blacksburg, VA, USA  
M. Möller, Aachen, Germany  
O. Okay, Istanbul, Turkey  
V. Percec, Philadelphia, PA, USA  
B.Z. Tang, Hong Kong, China  
E.M. Terentjev, Cambridge, UK  
P. Theato, Karlsruhe, Germany  
M.J. Vicent, Valencia, Spain  
B. Voit, Dresden, Germany  
U. Wiesner, Ithaca, NY, USA  
X. Zhang, Beijing, China

## **Aims and Scope**

The series *Advances in Polymer Science* presents critical reviews of the present and future trends in polymer and biopolymer science. It covers all areas of research in polymer and biopolymer science including chemistry, physical chemistry, physics, and material science.

The thematic volumes are addressed to scientists, whether at universities or in industry, who wish to keep abreast of the important advances in the covered topics.

*Advances in Polymer Science* enjoys a longstanding tradition and good reputation in its community. Each volume is dedicated to a current topic, and each review critically surveys one aspect of that topic, to place it within the context of the volume. The volumes typically summarize the significant developments of the last 5 to 10 years and discuss them critically, presenting selected examples, explaining and illustrating the important principles, and bringing together many important references of primary literature. On that basis, future research directions in the area can be discussed. *Advances in Polymer Science* volumes thus are important references for every polymer scientist, as well as for other scientists interested in polymer science - as an introduction to a neighboring field, or as a compilation of detailed information for the specialist.

Review articles for the individual volumes are invited by the volume editors. Single contributions can be specially commissioned.

Readership: Polymer scientists, or scientists in related fields interested in polymer and biopolymer science, at universities or in industry, graduate students.

More information about this series at <http://www.springer.com/series/12>

Christopher J. Wohl • Douglas H. Berry  
Editors

# Contamination Mitigating Polymeric Coatings for Extreme Environments

With contributions by

V. Andolina · R. Baier · M. Behroozi · D. H. Berry ·  
C. Blackburn · J.-D. Brassard · J. W. Connell ·  
R. Forsberg · A. F. Gross · S. Gruenke · F. Guerin ·  
M. Khudiakov · M. Kok · C. Laforte · E. Loth ·  
J. C. Meredith · A. Meyer · W. Ming · A. P. Nowak ·  
F. L. Palmieri · D. Raps · N. Rehfeld · M. Ricotta ·  
D. Rittschof · C. Ro · R. Robison · A. R. Rodriguez ·  
E. Sherman · D. Shin · F. Siraj · J. G. Smith Jr. · J. Sokhey ·  
L. Song · A. Stake · V. Stenzel · G. Tang · E. F. Tobin ·  
C. J. Wohl · S. S. Yang · H. Yildirim Erbil · Y. H. Yeong ·  
T. M. Young · J. Zhao · P. Zikmund

 Springer

*Editors*

Christopher J. Wohl  
NASA Langley Research Center  
Hampton, VA, USA

Douglas H. Berry  
The Boeing Company (Retired)  
Seattle, WA, USA

ISSN 0065-3195

Advances in Polymer Science

ISBN 978-3-030-45838-6

<https://doi.org/10.1007/978-3-030-45839-3>

ISSN 1436-5030 (electronic)

ISBN 978-3-030-45839-3 (eBook)

© Springer Nature Switzerland AG 2019

This work is subject to copyright. All rights are reserved by the Publisher, whether the whole or part of the material is concerned, specifically the rights of translation, reprinting, reuse of illustrations, recitation, broadcasting, reproduction on microfilms or in any other physical way, and transmission or information storage and retrieval, electronic adaptation, computer software, or by similar or dissimilar methodology now known or hereafter developed.

The use of general descriptive names, registered names, trademarks, service marks, etc. in this publication does not imply, even in the absence of a specific statement, that such names are exempt from the relevant protective laws and regulations and therefore free for general use.

The publisher, the authors, and the editors are safe to assume that the advice and information in this book are believed to be true and accurate at the date of publication. Neither the publisher nor the authors or the editors give a warranty, expressed or implied, with respect to the material contained herein or for any errors or omissions that may have been made. The publisher remains neutral with regard to jurisdictional claims in published maps and institutional affiliations.

This Springer imprint is published by the registered company Springer Nature Switzerland AG.  
The registered company address is: Gewerbestrasse 11, 6330 Cham, Switzerland

# Preface

This volume focuses on recent approaches and challenges toward the development of novel coatings for the prevention of contaminant adhesion in extreme terrestrial environments, such as those exemplified in aerospace, marine, and energy production applications. The volume should be of interest to chemists and material scientists in providing awareness of both the need for efficacy in mitigating contamination and for appropriate coating durability; to physicists in providing a better understanding of the interaction between the contaminant and the coated surface; and to engineers in describing the need for better scale-up tests between laboratory and field environments. The different chapters are not comprehensive reviews, but outline recent contributions toward understanding the adhesion mechanisms between the contaminant and the coating surface, approaches for coating formulation and development, and challenges in developing appropriate laboratory and scale-up tests to simulate the field environment.

This volume is divided into an Introduction and four parts:

- The Introduction, “Aerospace and Marine Environments as Design Spaces for Contamination-Mitigating Polymeric Coatings,” gives a more detailed overview of novel materials, test method advances, and durability issues discussed in the subsequent sections and chapters pertaining to ice and insect mitigation for aerospace coatings and biofouling mitigation for marine coatings. The chapter also includes an example showing the complexity of setting a laboratory benchmark for maximum ice adhesion strength.
- Part I, “Application of Biomimetics to Contamination-Mitigating Coatings,” contains a chapter on the evolution of animal and plant surface structures toward altering adhesion and how these structures and mechanisms might be applied to contaminant-reducing coatings.
- Part II focuses on “Ice Contamination-Mitigating Coatings” and consists of six chapters. The first chapter by Erbil and the last chapter by Zhao et al. provide reviews on liquid ad(ab)sorbing surfaces for anti-icing applications and antifogging/frost-resisting applications, respectively. The second through fourth

chapters by Yeong et al., Brassard et al., and Rehfeld et al. concentrate primarily on test development and secondarily on material development. The fifth chapter by Tang et al. focuses on the development of a polysiloxane-modified acrylic polyurethane. Rehfeld et al., Brassard et al., and Tang et al. also mention some of the important engineering tests that should be considered in the development of a durable coating.

- Part III, “Insect Contamination-Mitigation Coatings,” consists of five chapters. The first chapter by Smith et al. gives an overview of insect mitigation strategies over the years. The next chapter by Wohl et al. describes the mechanism of insect impact and residue expansion. The following two chapters by Kok et al. and Gross et al. describe both coating and test development. The final chapter by Gruenke discusses primarily requirements and test strategies for scale-up. The chapters by Gross et al. and Gruenke et al. also highlight some of the durability challenges that need to be addressed prior to implementation.
- Part IV focuses on “Biofouling-Mitigation Coatings” and consists of two chapters. In the first chapter, Rittschof reviews methods for incorporating antifouling agents into polymer coatings and describes an example that incorporates a biodegradable pharmacophore (chemical) that targets the fouling organism intermediate life cycle stages and so reduces the level of agent needed compared to one that targets the mature stage. The last chapter by Baier et al. concentrates on the mechanism and development of an abrasion-resistant, easy fouling-release, silicone-epoxy coating.

We would like to thank the authors who have participated in this volume for their insightful work. We hope the volume will be useful to chemists, material scientists, physicists, and engineers in pursuit of developing and implementing anti-contamination coatings.

Hampton, VA, USA  
Seattle, WA, USA

Christopher J. Wohl  
Douglas H. Berry

# Contents

<b>Aerospace and Marine Environments as Design Spaces for Contamination-Mitigating Polymeric Coatings . . . . .</b>	<b>1</b>
Douglas H. Berry and Christopher J. Wohl	
<b>Part I Application of Biomimetics to Contamination-Mitigating Coatings</b>	
<b>Influence of Topography on Adhesion and Bioadhesion . . . . .</b>	<b>19</b>
Donglee Shin and J. Carson Meredith	
<b>Part II Ice Contamination-Mitigating Coatings</b>	
<b>Use of Liquid Ad(ab)sorbing Surfaces for Anti-icing Applications . . . . .</b>	<b>53</b>
H. Yildirim Erbil	
<b>Ice Adhesion on Superhydrophobic Coatings in an Icing Wind Tunnel . . . . .</b>	<b>99</b>
Yong Han Yeong, Jack Sokhey, and Eric Loth	
<b>Icephobicity: Definition and Measurement Regarding Atmospheric Icing . . . . .</b>	<b>123</b>
Jean-Denis Brassard, Caroline Laforte, Frederic Guerin, and Caroline Blackburn	
<b>Development and Testing of Icephobic Materials: Lessons Learned from Fraunhofer IFAM . . . . .</b>	<b>145</b>
Nadine Rehfeld, Andrej Stake, and Volkmar Stenzel	
<b>Ice Release Coatings of High Durability for Aerospace Applications . . .</b>	<b>167</b>
Guangliang Tang, Yong Han Yeong, and Mikhail Khudiakov	
<b>Antifogging and Frost-Resisting Polymeric Surfaces . . . . .</b>	<b>185</b>
Jie Zhao, Lingjie Song, and Weihua Ming	



**Part III Insect Contamination-Mitigation Coatings**

**An Overview of Insect Residue Accretion and Mitigation Strategies on Aerodynamic Surfaces . . . . . 217**

J. G. Smith Jr., R. Robison, and E. Loth

**The Physics of Insect Impact and Residue Expansion . . . . . 235**

Christopher J. Wohl, Frank L. Palmieri, and John W. Connell

**Laboratory Investigation into Anti-contamination Coatings for Mitigating Insect Contamination with Application to Laminar Flow Technologies . . . . . 291**

Mariana Kok, Edmond F. Tobin, Pavel Zikmund, Dominik Raps, and Trevor M. Young

**Insect Abatement on Lubricious, Low Adhesion Polymer Coatings Measured with an Insect Impact Testing System . . . . . 315**

Adam F. Gross, Andrew P. Nowak, Elena Sherman, Christopher Ro, Sophia S. Yang, Maryam Behroozi, and April R. Rodriguez

**Requirements, Test Strategies, and Evaluation of Anti-Contamination and Easy-to-Clean Surfaces, and New Approaches for Development . . . 333**

Silke Gruenke

**Part IV Biofouling-Mitigation Coatings**

**Candy and Poisons: Fouling Management with Pharmacophore Coatings . . . . . 355**

Daniel Rittschof

**Unique Silicone-Epoxy Coatings for Both Fouling- and Drag-Resistance in Abrasive Environments . . . . . 367**

Robert Baier, Mark Ricotta, Vincent Andolina, Faraaz Siraj, Robert Forsberg, and Anne Meyer

**Index . . . . . 377**

# Aerospace and Marine Environments as Design Spaces for Contamination- Mitigating Polymeric Coatings



Douglas H. Berry and Christopher J. Wohl

**Abstract** Aerospace and marine environments are two of the most challenging arenas for durable coatings. This introductory chapter for the *Advances in Polymer Science* volume “Contamination-Mitigating Polymeric Coatings for Extreme Environments” gives an overview of materials and test method advances pertaining to ice and insect mitigation for aerospace coatings and biofouling mitigation for marine coatings. Each of these topics is then discussed in greater detail by subject matter experts in the following chapters. A common challenge in these arenas is the cost, complexity, and limited availability of field measurements, necessitating the need for laboratory-scale testing and the setting of benchmarks. An example is provided showing the complexity of setting a benchmark for maximum ice adhesion strength to anti-contamination coatings allowing passive ice removal by wind or vibration. Modeling ice as a cantilever beam on a coating surface in a wind stream indicates that the benchmark value is dependent on the assumed shape of the ice that needs to be removed.

**Keywords** Aerospace coatings · Biofouling-mitigation coatings · Biomimetics · Coating durability · Contamination-mitigating coatings · Frost-resisting coatings · Ice-mitigating coatings · Insect-mitigating coatings · Marine coatings

---

Douglas Berry performed this work after retirement from The Boeing Company.

D. H. Berry (✉)  
The Boeing Company, Seattle, WA, USA  
e-mail: [berrysok@comcast.net](mailto:berrysok@comcast.net)

C. J. Wohl (✉)  
NASA Langley Research Center, Hampton, VA, USA  
e-mail: [c.j.wohl@nasa.gov](mailto:c.j.wohl@nasa.gov)

## Contents

1	Introduction .....	2
2	Discussion .....	3
2.1	Part I: Application of Biomimetics to Contamination-Mitigating Coatings .....	3
2.2	Part II: Ice Contamination-Mitigating Coatings .....	3
2.3	Part III: Insect Contamination-Mitigation Coatings .....	9
2.4	Part IV: Biofouling-Mitigation Coatings .....	13
3	Concluding Comments .....	13
	References .....	14

## 1 Introduction

Prevention of contamination through polymeric coatings has been the subject of research and development in fields ranging from biomedical to industrial to transportation coatings. These coatings are designed to act passively so that no additional energy or mechanical input is required for them to perform their anti-contamination function. Drivers for the development and implementation of these coatings include improved safety and performance, and reduced cost through the reduction in mechanical complexity that is associated with active anti-contamination technologies. Additional improvements realized by the integration of these coatings should include extending the underlying structure and coating lifetime, reducing environmental impact, and enhancing appearance. This volume focuses on aerospace and marine operational environments that make the identification of successful contamination-mitigation coatings particularly challenging. Also discussed are other applications, such as those for wind turbines, power transmission, refrigeration, off-shore Arctic structures, automotive needs, and rooftops.

For aerospace applications, contamination by ice and insect residues is an area of concern. In-flight and on-ground icing introduce hazardous flight conditions, leading to aircraft failure that has resulted in loss of life [1]. Additionally, on-ground icing requires treatment of the airplane with glycol-based deicing and anti-icing fluids that limit the vehicle departure time before re-treatment is needed [2]. These fluids are environmentally hazardous, and the deicing/anti-icing process negatively impacts airport operations [3]. Insect residue prevention is also important, as future aircraft will be designed with greater aerodynamic efficiency that could be negated as a result of insect residue adhesion [4]. Besides having ice or insect mitigation functionality, these coatings must be durable. Extensive ultraviolet (UV) exposure; varying weather conditions; exposure to chemicals such as phosphate ester-based hydraulic fluid and cleaning solvents; rain erosion; and particulate erosion are all contributing factors creating a harsh environment in which a coating must persist for at least several years [5–7].

For marine applications, the diversity of contaminating species, even at a single location, as well as potential exposure to a variety of different marine environments, necessitates that the coatings be robust and effective against a variety of marine species and conditions. The mandate to remove tributyltin-containing coatings has exacerbated this issue and initially left a void in the market for available coatings [8].

Additionally, there is a need for better abrasion-resistant coatings for vessels exposed to frequent dockings or to ice floes [9]. Thus, both intrinsic resistance to contaminant accretion (accumulation) and adhesion and environmental durability are required for aerospace and marine contamination-mitigating coatings.

This *Advances in Polymer Science* volume “Contamination-Mitigating Polymeric Coatings for Extreme Environments” is organized as follows. The contribution [10] in Part I of this volume discusses how understanding gained from biological systems can be applied in the development of engineered surface coatings to mitigate contamination. Parts II–IV focus on the development of anti-contamination coatings to reduce ice [1, 5, 11–14], insects [4, 6, 7, 15, 16], and biofouling [8, 9], respectively. These Parts start with papers reviewing and discussing mechanisms and coating formulation approaches for the prevention or mitigation of the contaminant. This is followed by papers on approaches for test method development to measure the efficacy of the coatings. Each Part concludes with papers on industrial evaluations and engineering tests on the potential durability of the coating.

## 2 Discussion

### 2.1 *Part I: Application of Biomimetics to Contamination-Mitigating Coatings*

In this contribution, the evolution of animal and plant surface structures toward altering adhesion and overcoming contamination in nature is reviewed [10]. Physical principles for both wet and dry effects on adhesion are summarized, particularly how these effects are influenced by roughness and topology. Finally, current and potential applications of contaminant-reducing coatings, using biomimetic approaches, are described.

### 2.2 *Part II: Ice Contamination-Mitigating Coatings*

Numerous forms and types of ice formation are relevant to aerospace. On the ground or in flight, ice occurs from the condensation of moisture as frost onto a cold surface. In aviation, the moisture typically comes from super-cooled water droplets (SCWD). On the ground, ice formation occurs from super-cooled large droplets (SLD) of greater than 50- $\mu\text{m}$  diameter in the forms of freezing rain and drizzle. In flight, not only is SLD a concern up to an altitude of 3,660 m [17], but smaller SCWD, from 15 to 50  $\mu\text{m}$  in diameter, form rime, glaze, or mixed (rime/glaze) ice at altitudes up to 6,700 m [18]. The challenge in developing robust ice contamination-mitigating coatings and in specifying test conditions is demonstrated by referring to The Code of Federal Regulations Title 14 Part 25 Appendix C and Appendix O, which present characterizations of aircraft icing in-flight environments as functions of air

temperature, maximum liquid water content (LWC), and droplet mean effective diameter (MED), also known as mean volumetric diameter (MVD) [17, 18]. As discussed by various contributors to Part II of this volume, the mechanical properties of ice, ice accretion, and ice adhesion are influenced by a variety of these environmental parameters, in addition to ice type, ice structure, ice formation temperature, coating structure, and the test method itself [1, 11–13].

### 2.2.1 Material Development

Part II has several papers related to the development of surfaces for the mitigation of ice contamination through the prevention of ice accretion or by a reduction in ice adhesion [1, 11, 12, 14]. An overview of recent approaches is provided, including smooth low surface energy coatings, superhydrophobic coatings, and liquid-infused porous surfaces, where the coating surfaces were impregnated with perfluorinated silicone oil, hydrocarbon, or water [11]. The surfaces were evaluated using a variety of methods. These include determining the rate of frost creation from condensate formed by cooling the surface below  $0^{\circ}\text{C}$  in an atmosphere near room temperature, measuring the ice adhesion formed from water placed on the surface and then cooled below freezing (freezer ice), and a method developed in Erbil's laboratory that measures the amount of ice accreted after applying SCWD of unknown size at  $-1^{\circ}\text{C}$  with a liquid water content of about  $10.6\text{ g/m}^3$  onto a surface held at  $-2^{\circ}\text{C}$ . Another review focuses on polymeric structure approaches that form wet superhydrophilic, dry superhydrophobic, or zwitter-wettable surfaces with a goal of preventing fogging and, below  $0^{\circ}\text{C}$ , frosting [14]. The need for a small surface roughness lateral auto-correlation length in superhydrophobic coatings is evaluated by Yeong et al. [12]. They measure the adhesion of ice formed from the impingement of  $20\text{-}\mu\text{m}$ -diameter SCWD at an LWC of  $0.4\text{ g/m}^3$  and air speeds of 50 and 70 m/s in glaze ( $-5^{\circ}\text{C}$ ) and rime ( $-15^{\circ}\text{C}$ ) icing conditions. Tang et al. evaluate a novel polysiloxane-modified acrylic polyurethane, measuring adhesion using both freezer ice at  $-20^{\circ}\text{C}$  and ice formed from the impingement of freezing drizzle with an MVD of  $300\text{ }\mu\text{m}$  at  $-8^{\circ}\text{C}$  [5].

### 2.2.2 Test Method Development

Correlation between laboratory-scale testing and operational environment testing has not been confidently established. Although the expense and limited availability of so-called real world test methods, such as those in an icing wind tunnel and flight test campaigns for aerospace applications, are impractical for the routine screening of materials, these remain the best methods for assessing the true efficacy of contamination-mitigation approaches. In an effort to bridge the gap between the laboratory and the operational environment, an array of test methods has been developed, and a group of such test methods is reviewed in this volume. A concentration on ice accretion and adhesion test method development, with the need to

conduct the tests under very stable conditions, minimizing test device fluctuations, is provided in the contributions by Brassard et al. [1] and Rehfield et al. [13]. The paper by Erbil reviews coating development approaches, stresses the need for well-defined ice accretion tests, and suggests using a modification of his method that is described in Sect. 2.2.1 [11]. Brassard et al. stress the need for well-defined ice adhesion tests [1]. Their paper focuses on the centrifuge ice adhesion test (CAT), which uses 300- $\mu\text{m}$  MVD freezing drizzle that has been developed at their facility, Anti-Icing Materials International Laboratory (AMIL). To help reduce variability in their laboratory evaluation, bare aluminum reference samples were simultaneously iced with the test formulations that were coated on the same reference aluminum. Since small variations in the ice could not be eliminated, an adhesion reduction factor (ARF), defined as the ratio of average ice adhesion on the reference bare aluminum to the average ice adhesion on the coated aluminum, was utilized to further reduce variability, and this has allowed them to give comparative values for the 345 samples they have tested since 2003. While CAT uses freezing drizzle, they suggest that CAT should be considered as a screening test which should be followed by ice adhesion and accretion tests that more closely simulate actual icing conditions. They use an offshore Arctic structure as an example [1]. The myriad of ice mitigation tests that have been developed at Fraunhofer IFAM over the past decade is described in the contribution by Rehfield et al., and the tests they determined to be most useful and economical in their material evaluations of ice accretion and the adhesion of clear freezer ice and rime ice formation are discussed [13]. Their contribution stresses the importance of doing a series of laboratory-scale tests involving the accretion and accumulation of ice, followed by larger-scale wind tunnel testing, which simulates relevant icing scenarios experienced in field use, for coatings intended for applications such as aerospace, wind turbines, and automotive. Ultimately, field tests that then determine the significance and correlation of the artificial icing test results with the application should then be conducted [13]. They also recommend, as do several authors in Part II of this volume [1, 5, 11, 12, 14], performing surface characterizations, such as contact angle, surface energy, water sliding angle, contact angle hysteresis, and roughness, to better understand relationships between surface properties and icephobicity.

### 2.2.3 Adhesion Benchmark for Ice Removal

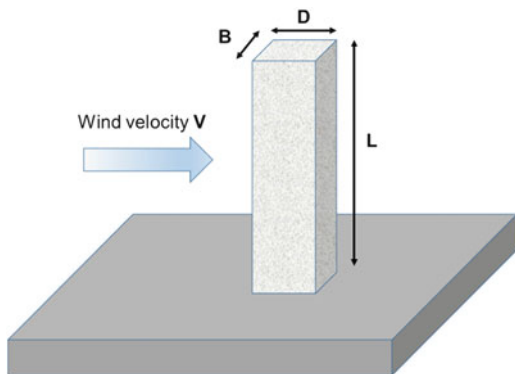
Because many researchers are limited to laboratory-scale investigations and do not have access to larger-scale simulations, such as wind tunnels, and in-service performance, such as flight tests, various benchmarks have been proposed for surfaces which allow passive ice removal. A review by Kreder et al. [19], citing prior work [20–22], suggested that ice adhesion below  $\sim 20$  kPa could be considered a benchmark for surfaces which might allow passive ice removal by factors such as wind or vibration. In their paper [20], Susoff et al. used Al 6082-T6 (EN AW-6082) as the reference bare aluminum and tested candidate coatings in a modified  $0^\circ$  cone shear test. For their testing, a test block containing deionized water was frozen overnight

between the test surface and an outer surface, called a mold, in a freezer at a temperature of less than  $-25^{\circ}\text{C}$ . Since the test block warmed during transfer between the freezer and the tester, testing was then performed at  $-14^{\circ}\text{C}$  with the bare aluminum reference producing an ice adhesion shear strength of  $1,594 \pm 72$  kPa. Kreder et al. [19] applied an ARF of 100, recommended by Beisswinger et al. as the minimum value needed for ice self-shedding [21], to the bare aluminum reference data of Susoff to help determine the suggested benchmark of  $\sim 20$  kPa. However, Beisswinger et al. had used CAT with freezing drizzle formed from deionized water at  $-8^{\circ}\text{C}$  in conjunction with ice accumulation data to produce their estimate of  $\text{ARF} = 100$  [21]. Using 6061-T6 aluminum, they found an ice adhesion shear strength of about 600 kPa for the bare reference and reported that a coating with an ice adhesion shear strength of about 6 kPa would reduce ice mass accumulation by 90% [1, 23, 24]. Additionally, a contribution in this volume estimates that an ice adhesion shear strength of 6 kPa is a good benchmark for ice self-shedding under the effect of gravitational force [1].

Kreder et al. [19] also referenced the work of Dou et al. [22] when suggesting that  $\sim 20$  kPa be considered a benchmark for surfaces allowing passive ice removal by wind. In that work, a polyurethane coating containing a hydrophilic dimethylolpropionic acid component that formed an aqueous lubricating layer at subzero environments was developed [22]. It was applied by spin coating onto an Al 6061 substrate and thermally cured at  $110^{\circ}\text{C}$ . For determining ice adhesion, bottomless cuvettes in close contact with the coating surface were filled with deionized water and held at  $-15^{\circ}\text{C}$  for 5 h to form freezer ice. The shear strength of ice adhesion was then determined using a force transducer. The best performing coating produced an ice adhesion shear strength of  $27.0 \pm 6.2$  kPa. This coating was then prepared with ice attached using the previously described preparation and tested in a wind tunnel, where a 12 m/s wind speed was determined to be sufficient to detach and remove the ice [22].

However, by performing a cantilever beam analysis with a uniform load, similar to that performed by Brassard et al. for self-shedding ice by gravity [1], there appeared to be some other factor involved that allowed for the ice in the experiments described by Dou et al. [22] to be removed at a low wind speed. In this first-order analysis with an ice column of height  $L$ , depth  $D$ , and breadth  $B$ , as illustrated in Fig. 1, it is assumed that the substrate supporting the ice column was rigid. The wind shedding stress ( $S$ ) in Eq. (1) is evaluated using the maximum bending moment ( $M$ ), the centroid ( $c$ ), and moment of inertia ( $I$ ) of the ice column [25].  $M$  is determined using the distributed applied force ( $F$ ) from the wind, as given in Eq. (2).  $F$ , as given in Eq. (3), is a function of the density of air ( $\rho$ ), wind velocity ( $V$ ), the drag coefficient ( $C_D$ ), and the area of ice perpendicular to the wind. The values for  $c$  and  $I$  depend on the ice column dimensions and are determined by Eqs. (4) and (5), respectively. Substitution of Eqs. (2)–(5) into Eq. (1) produces the final form for the stress at the base of the ice column, Eq. (6).

**Fig. 1** Dimension and orientation of ice column related to wind velocity



$$S = \frac{Mc}{I} \quad (1)$$

$$M = \frac{1}{2}FL \quad (2)$$

$$F = \frac{C_D \rho V^2 LB}{2} \quad (3)$$

$$c = \frac{D}{2} \quad (4)$$

$$I = \frac{BL^3}{12} \quad (5)$$

$$S = \frac{3C_D \rho V^2 L^2}{2D^2} \quad (6)$$

The value for  $C_D$  depends on the Reynolds (Re) number, which is a measure of the ratio of kinetic to viscous wind energy (Eq. 7):

$$\text{Re} = \frac{\rho VD}{\mu} \quad (7)$$

where  $\mu$  is the viscosity of air at the test temperature.

Parameters used and results from the calculation of  $S$  are given in Table 1. The size of the ice column formed by the cuvette was not mentioned in the work of Dou et al. [22], but was based on supplementary material provided in a previous publication by researchers who work in the same facility [28]. The ice column was 30 mm high, and had a base of 100 mm<sup>2</sup>, equating to a base that was 10 mm broad and 10 mm deep.  $C_D$  for a rectangular rod with square cross-section and aspect ratio ( $L/B$ ) of 3 could not be found. However, the value of  $C_D$  for an infinitely long rectangular rod with sharp corners is 2.05 when  $\text{Re} > 1,000$  [26] and with slightly



**Table 1** Dou et al. [22] ice column dimensions, wind tunnel conditions, and results for analysis of ice adhesion shear stress

Ice column height, $L$	30 mm [28]
Ice column breadth (perpendicular to wind flow), $B$	10 mm [28]
Ice column depth (parallel to wind flow), $D$	10 mm [28]
Wind tunnel wind velocity, $V$	12 m/s [22]
Wind tunnel temperature	$-15^{\circ}\text{C}$ [22]
Air density at $-15^{\circ}\text{C}$ , $\rho$	$1.369 \text{ kg/m}^3$ [35]
Air viscosity at $-15^{\circ}\text{C}$ , $\mu$	$1.648 \times 10^{-5} \text{ Pa}\cdot\text{s}$ [35]
Reynolds number, $\text{Re}$	9,980
Drag coefficient, $C_D$ (for $L/B = 3.0$ )	2.05 [26] <sup>a</sup>
Drag coefficient, $C_D$ (for $L/B = 1.0$ )	1.05 [26] <sup>b</sup>
Predicted shear stress (for $L/B = 3.0$ )	5.5 kPa <sup>a</sup>
Predicted shear stress (for $L/B = 1.0$ )	0.31 kPa <sup>b</sup>

<sup>a</sup>Value for an infinitely long rod<sup>b</sup>Value for a cube

rounded corners (radius of curvature,  $r/D = 0.021$ ) is 1.95 at  $\text{Re} \approx 18,000$  [27].  $C_D$  for a cube with sharp corners is 1.05 when  $\text{Re} > 1,000$  [26].

Substitution of the values from Table 1 with  $C_D$  for an infinitely long rod into Eq. (6) yields a shear stress produced on the ice column of 5.5 kPa. This suggests that some additional unknown mechanism was assisting in removal of the ice. Perhaps more importantly, Eq. (6) implies that the stress applied by wind shear increases as  $(VL/D)^2$ . Experiments should be performed to determine whether ice can be removed from a coating with larger base ice dimensions, particularly  $D$ , using airflow at several different velocities, before setting a benchmark value for passive ice removal. For example, if the block of ice is a cube with all dimensions equal to either 30 mm or 10 mm,  $C_D$  is 1.05 for  $\text{Re} > 1,000$  [26] and the stress  $S$  generated by a 12 m/s airflow on the ice column predicted by Eq. (6) is only 0.31 kPa, over 17 times lower than that predicted for the ice column that was 30 mm high with 10-mm length on each side of the base. The adhesion benchmark below which ice could passively shed from aircraft wings during take-off may be even lower. It has been suggested that wings are subjected to a maximum shear stress of 0.1 kPa at take-off speed, typically about 70 m/s [29].

From this discussion, it appears that the adhesion benchmark below which ice can passively shed is probably not a single value but depends on intended use, including the allowable size and shape of the ice, and test configuration parameters. Beyond this, the physical properties of the ice (type of ice, density, crystallinity, etc.), environmental conditions (temperature, rate of deposition, etc.) will influence the adhesion benchmark. The ice adhesion shear stress strength value needed for commercial aerospace applications may be quite low, even in-flight, where speeds may be up to 250 m/s, due to the low form factor of ice that is acceptable. Additionally, FAA 20-73, H 1.1.4 currently states that credit may not be taken for the contribution from an ice mitigation coating during approval of the overall ice protection system, since preserving its effective use is difficult to control [30]. This

suggests that the ice accretion mitigation properties of the coating, such as time to delay the freezing of SLD and small SCWD, as well as ice adhesion mitigation, must be considered. For at least initial aerospace applications, hybrid systems incorporating thermal or mechanical energy with the ice mitigation coating, as suggested in Refs. [5, 13], should be considered.

#### **2.2.4 Durability**

Ultimately, the use of an ice mitigating coating depends on the economic and safety benefits gained, versus the cost of application, maintenance, reparability, and loss of in-service time. The latter is especially important in commercial aviation. Besides the durability of the coating toward repeated icing/deicing cycles, Rehfeld et al. [13] mention several tests, and Tang et al. [5] describe in detail some of the important engineering tests that should be considered in the development of a durable coating for commercial aerospace applications. These include tests for wet and dry adhesion to the underlying coating and resistance to UV exposure, rain erosion, particulate erosion, and aircraft fluids, including hydraulic fluid, jet fuel, and deicing fluids. Brassard et al. [1] provide a more general outline of durability considerations using the previously stated example of an offshore Arctic structure.

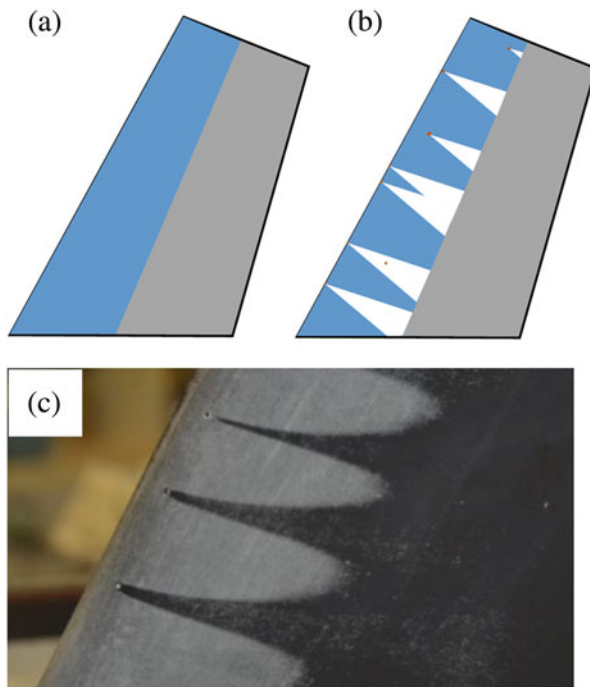
### ***2.3 Part III: Insect Contamination-Mitigation Coatings***

Unlike ice, insect residue adhesion is not considered a significant concern for current commercial aircraft; rather, it will play a significant role for future commercial aircraft designs where laminar airflow will be utilized extensively for increased fuel efficiency. The potential benefit that aircraft wings designed to enable natural laminar flow (NLF) have on drag reduction, and therefore improved fuel efficiency, is discussed in Part III of this volume by Smith et al. [4]. Beyond wing leading edges, airflow over other aircraft surfaces is influenced by the presence of insect residues. Other conceptual designs, such as boundary layer ingestion [31], may further increase requirements to reduce surface contaminant adhesion, regardless of what that contaminant is. Once a contaminant adheres to a surface of sufficient height to disrupt airflow, a turbulence wedge develops behind it (Fig. 2). This wedge results in a change in airflow properties over a much greater area than the region of the initial contaminant, further highlighting the need to develop contaminant adhesion-resistant surfaces.

#### **2.3.1 Material Development**

The genesis of materials with intrinsic insect residue adhesion-mitigating properties has largely been achieved through empirical observations of insect residue retention

**Fig. 2** (a) Laminar flow over a nominal 50% chord length shown in *blue*. (b) Premature transition to turbulent flow (shown in *white*) develops once a contaminant of sufficient height to disrupt the airflow adheres to the surface. (c) Transition dots show the turbulent wedge development (*dark area* is turbulent flow)



and the correlation of insect impact studies with surface properties. In Part III, an overview of the processes involved in an insect impact event is provided [15]. In this paper, the behavior of the insect residues at the moment of impact and during initial residue expansion is related to water droplets impacting a solid surface. For water droplet impact, the magnitude and nature of surface roughness play a dominant role in expansion. At later stages of the impact event, surface energy begins to influence the behavior of the expanded insect hemolymph, this behavior having important implications for how readily the retained insect residues can be removed.

Other contributions to Part III of this volume consider a series of materials with average roughness values ( $R_a$ ) that range from smooth ( $R_a < 0.1 \mu\text{m}$ ) to rough ( $R_a > 1 \mu\text{m}$ ) [7, 16]. Likewise, advancing water contact angle values indicate that the evaluated surfaces ranged from hydrophilic to superhydrophobic. The conclusions drawn from these studies are somewhat contradictory, in part due to how the post-impact sample surfaces were characterized. Research toward the development of a block-copolymer system with fluorinated and hygroscopic blocks has also been included as a novel materials approach [6]. These coatings were smooth and mildly hydrophobic and were designed to retain a significant hydration layer (potentially imparting a lubricious surface that will naturally be replenished as a result of exposure to humid environments), which would act as an interface between the impacting insect residues and the actual coating surface.

### 2.3.2 Testing Methodology

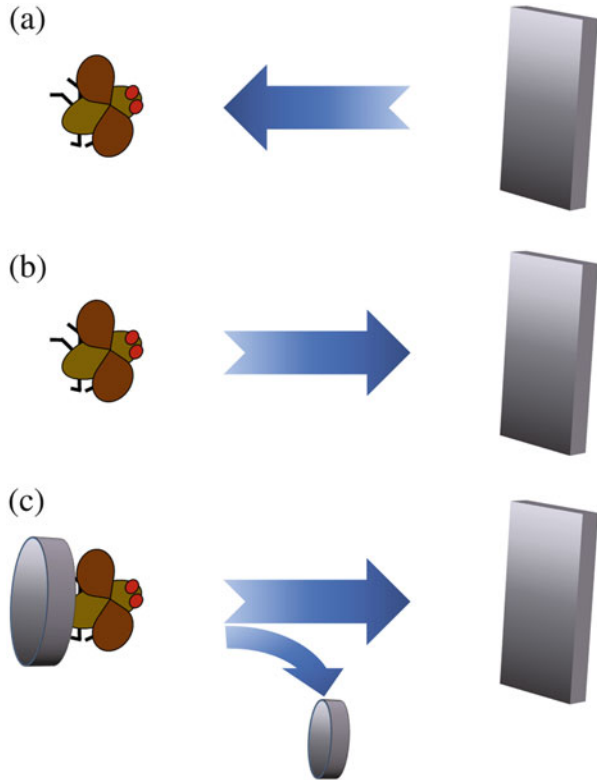
One of the best methods to evaluate a coating material's ability to mitigate insect residue adhesion in an operational environment is to perform flight testing. The nature of the tests, as well as the results, are discussed in Part III by Smith et al. [4]. These studies have indicated that a majority of insect impacts will occur during the take-off and approach and landing phases of a flight profile. Forces high enough to induce insect rupture occurred during taxiing for particularly soft insects, though this constituted a relatively small portion of the insect population that the aircraft encountered. The most significant result from flight testing has been that surface properties influence the number and magnitude of insect residues left behind.

Cost, the inherent complexity involved in testing in uncontrolled environmental conditions, and the limited applicability of flight test results, arising from the fact that different insects populate different geographic regions, all contribute to the majority of evaluation experiments being conducted in laboratory settings. In a laboratory setting, the insect being evaluated, the impact speed, and other test conditions can be controlled to reduce experimental complexity. Often, researchers will draw correlations between laboratory and operational conditions, though it is widely recognized that a true evaluation of any approach will require flight testing for validation.

There are two distinct phases involved in laboratory-based insect impact studies: the impact event and evaluation of the impacted surface. Although a myriad of different approaches can be envisioned for how to recreate an insect impact event, most studies fall into one of three categories: the propulsion of a surface toward an insect, the propulsion of an insect using a sabot to accelerate the insect, or the direct introduction of the insect into an air stream (Fig. 3) [32–34]. In Part III of this volume, the work of Gross et al. [6], Gruenke [7], and Wohl et al. [15] involved the direct introduction of an insect into an air stream, while Kok et al. [16] utilized both this approach and the sabot-style impact test. One potential benefit of the use of a sabot is that the stresses imparted on the insect during acceleration are reduced. However, this method also increases test configuration complexity. Gradual acceleration of an insect can overcome the challenge of utilizing a sabot. However, this requires a greater insect impact instrument footprint, and may increase the spread in insect impact location. For all of these approaches, the insect must be alive, to better emulate an impact event in an actual operational environment, although insect incapacitation is permitted. The nature of the insect hemolymph begins to change immediately after the insect has died, and this would change its interaction with an impacted surface.

The characterization of surface changes after an insect impact event has occurred has been approached by several methodologies. Due to the brittle nature of the accreted insect residues, direct mechanical testing, akin to some methodologies to assess ice adhesion strength, cannot be performed. Therefore, many researchers assess the efficacy of a surface by determining the amount of insect residues accreted and then draw comparisons with reference surfaces. This is the approach of Gross et al. [6], Wohl et al. [15], and Kok et al. [16]. Methods to qualitatively assess bond

**Fig. 3** Insect impact studies have been performed using propulsion of the substrate (a), propulsion of the insect (b), and propulsion of the insect supported by a sabot that leaves the insect trajectory prior to impact (c)



strength and cleanability are also described [7]. These two approaches, reduction in insect residue accretion and cleanability, may yield different results. For example, cleanability testing indicating that surfaces with minimal residue accretion can exhibit tenacious residue retention.

### 2.3.3 Durability

Identical to the durability assessment of coatings developed for ice mitigation described in Sect. 2.2.4, coatings developed for insect residue mitigation will be required to meet or exceed requirements based on environmental exposure, substrate adhesion, and mechanical robustness. The durability assessment of materials developed for insect residue mitigation is described in Part III [6, 7]. For any material developed for insect residue mitigation, durability and a determination of how environmental exposure changes the insect residue accretion properties are critical for integration into an operational environment.

## **2.4 Part IV: Biofouling-Mitigation Coatings**

Biofouling occurs in environments where water wets surfaces, including marine systems, roofs, pipes, and heat exchangers. Part IV of this volume has two contributions discussing the development of biofouling-mitigation coatings, with emphasis on applications to marine biofouling as the design space. A position paper is provided describing a holistic approach involving coating development strategies based on the life cycles of biofouling micro and macro organisms; business models; regulatory frameworks; and health, safety, and environmental concerns [8]. In this work, Rittschof describes how targeting the metamorphosis or transformation of a macro-organism biofoulant, such as a barnacle, from its larval to juvenile stage leads to a more environmentally benign approach with decreased use of less toxic chemicals than the common approach of using long-lived, broad spectrum biocides such as tributyltin-containing coatings. Also discussed is how this concept can be used to disrupt the transduction cascade in microbes undergoing metamorphosis from individual organisms to a complex, interdependent consortium. After describing the above mechanisms, Rittschof reviews methods for incorporating an anti-fouling agent into a polymer coating, and describes an example of marine biofouling mitigation that incorporates a biodegradable pharmacophore (chemical) that targets micro- and macro-organism intermediate life cycle stages [8].

The paper by Baier et al. concentrates on the mechanism and development of an abrasion-resistant, easy fouling-release, silicone-epoxy coating [9]. The methyl silicone-based fraction of this material is continuously refreshed with minimum wear at the environmental interface, while the epoxy component provides toughness and adhesion to the coating substrate. This paper describes the physicochemical characterization and comparative engineering performance test methods for abrasion resistance and drag reduction used to evaluate the coating, and also comments on the ability of the coating to reduce drag. Suggested applications where improved durability from abrasion resistance is needed include ships operating in ice fields or those that have frequent dockings, as well as large water intake grates and turbine encasement seals present in power plant facilities.

## **3 Concluding Comments**

This volume provides perspectives on the approaches, mechanisms, test methods, durability considerations, and environmental concerns for contamination-mitigating coatings and polymers, particularly for use in the more extreme aerospace and marine environments. By juxtaposing ice, insect, and marine mitigation coatings, researchers and users may more easily identify threads of similarity that might assist in future developments and potential applications.

There are almost always multiple aspects in assessing the contaminant-mitigating properties of a coating. For ice mitigation, low adhesion and ice accretion prevention

are both important; for insect mitigation, low adhesion and residue cleanability are both important; and for marine biofouling, low adhesion and an ability to kill the organism during some point in its life cycle are important. More collaborative work is needed in defining “best practices” and benchmarks, and in providing correlations between different tests to evaluate coatings for adhesion and accretion mitigation in each of these contamination-mitigation areas. Recognition is needed that there may not be a universal benchmark and unique correlations in each area, but rather that benchmarks and correlations may depend on the type of coating approach, such as smooth hydrophobic, superhydrophobic, or liquid-infused porous surfaces. The benchmark or correlations may also be specific to the application, such as on-ground aircraft, in-flight aircraft, or off-shore Arctic structure ice mitigation.

**Acknowledgments** Many of the contributions in this volume originate from presentations given at the 38th and 39th Annual Adhesion Society Meetings, held in 2015 and 2016 in Savannah, GA and San Antonio, TX, respectively, in sessions on Natural Phenomena: Antifouling in Marine and Aerospace Environment. The authors would like to acknowledge the encouragement of the Adhesion Society in publishing these contributions in *Advances in Polymer Science*.

## References

1. Brassard J-D, Laforte C, Guerin F, Blackburn C (2017) Icephobicity: definition and measurement regarding atmospheric icing. *Adv Polym Sci*. [https://doi.org/10.1007/12\\_2017\\_36](https://doi.org/10.1007/12_2017_36)
2. FAA (2017) FAA holdover time guidelines winter 2017–2018
3. Vasilyeva A (2009) Aircraft deicing operations. Final project report for 1.231/16.781/ESD.224, Airport Systems Planning & Design, Massachusetts Institute of Technology, [http://ardent.mit.edu/airports/ASP\\_exercises/2009%20reports/Aircraft%20Deicing%20Vasilyeva.pdf](http://ardent.mit.edu/airports/ASP_exercises/2009%20reports/Aircraft%20Deicing%20Vasilyeva.pdf). Accessed 20 Oct 2017
4. Smith Jr JG, Robinson R, Loth E (2018) An overview of insect residue accretion and mitigation strategies on aerodynamic surfaces. *Adv Polym Sci*. [https://doi.org/10.1007/12\\_2018\\_44](https://doi.org/10.1007/12_2018_44)
5. Tang G, Yeong YH, Khudiakov M (2017) Ice release coatings of high durability for aerospace applications. *Adv Polym Sci*. [https://doi.org/10.1007/12\\_2017\\_39](https://doi.org/10.1007/12_2017_39)
6. Gross AF, Nowak AP, Sherman E, Ro C, Yang SS, Behrooz M, Rodriguez AR (2017) Insect abatement on lubricious, low adhesion polymer coatings measured with an insect impact testing system. *Adv Polm Sci*. [https://doi.org/10.1007/12\\_2017\\_35](https://doi.org/10.1007/12_2017_35)
7. Gruenke S (2017) Requirements, test strategies and evaluation of anti-contamination and easy-to-clean surfaces and new approaches for development. *Adv Polm Sci*. [https://doi.org/10.1007/12\\_2017\\_38](https://doi.org/10.1007/12_2017_38)
8. Rittschof D (2017) Candy and poisons: fouling management with pharmacophore coatings. *Adv Polm Sci*. [https://doi.org/10.1007/12\\_2017\\_34](https://doi.org/10.1007/12_2017_34)
9. Baier R, Ricotta M, Andolina V, Siraj F, Forsberg R, Meyer A (2017) Unique silicone-epoxy coatings for both fouling- and drag-resistance in abrasive environments. *Adv Polm Sci* [https://doi.org/10.1007/12\\_2017\\_33](https://doi.org/10.1007/12_2017_33)
10. Shin D, Meredith JC (2017) Influence of topography on adhesion and bioadhesion. *Adv Polm Sci*. [https://doi.org/10.1007/12\\_2017\\_40](https://doi.org/10.1007/12_2017_40)
11. Erbil HY (2017) Use of liquid ad(ab)sorbing surfaces for anti-icing applications. *Adv Polm Sci*. [https://doi.org/10.1007/12\\_2017\\_41](https://doi.org/10.1007/12_2017_41)
12. Yeong YH, Sokhey J, Loth E (2017) Ice adhesion on Superhydrophobic coatings in an icing wind tunnel. *Adv Polm Sci*. [https://doi.org/10.1007/12\\_2017\\_32](https://doi.org/10.1007/12_2017_32)

13. Rehfeld N, Stake A, Stenzel V (2017) Development and testing of Icephobic materials: lessons learned from Fraunhofer IFAM. *Adv Polm Sci.* [https://doi.org/10.1007/12\\_2017\\_37](https://doi.org/10.1007/12_2017_37)
14. Zhao J, Song, L, Ming W (2017) Antifogging and frost-resisting polymeric surfaces. *Adv Polm Sci.* [https://doi.org/10.1007/12\\_2017\\_42](https://doi.org/10.1007/12_2017_42)
15. Wohl CJ, Palmieri FL, Connell JW (2017) The physics of insect impact and residue expansion. *Adv Polm Sci.* [https://doi.org/10.1007/12\\_2018\\_45](https://doi.org/10.1007/12_2018_45)
16. Kok M, Tobin EF, Zikmund P, Raps D, Young TM (2017) Laboratory investigation into anti-contamination coatings for mitigating insect contamination with application to laminar flow technologies. *Adv Polm Sci.* [https://doi.org/10.1007/12\\_2017\\_31](https://doi.org/10.1007/12_2017_31)
17. Electronic Code of Federal Regulations (2018) Title 14 chapter 1 subchapter C part 25 appendix C part I-atmospheric icing conditions (2018) [https://www.ecfr.gov/cgi-bin/text-idx?SID=86b29698088452b8675ee7c9ee789759&mc=true&node=ap14.1.25\\_11801.c&rgn=div9](https://www.ecfr.gov/cgi-bin/text-idx?SID=86b29698088452b8675ee7c9ee789759&mc=true&node=ap14.1.25_11801.c&rgn=div9). Accessed 7 Jan 2018
18. Electronic Code of Federal Regulations (2018) Title 14 chapter 1 subchapter C part 25 appendix O – supercooled large drop icing conditions (2018). [https://www.ecfr.gov/cgi-bin/text-idx?SID=aa82b4ebee20d2fa7b1587e7905fcb54&mc=true&node=ap14.1.25\\_11801.o&rgn=div9](https://www.ecfr.gov/cgi-bin/text-idx?SID=aa82b4ebee20d2fa7b1587e7905fcb54&mc=true&node=ap14.1.25_11801.o&rgn=div9) Accessed 7 Jan 2018
19. Kreder MJ, Alvarenga J, Kim P, Aizenberg J (2016) Design of anti-icing surfaces: smooth, textured or slippery? *Nat Rev Mater* 1:15003
20. Susoff M, Siegmann K, Pfaffenroth C, Hirayama M (2013) Evaluation of icephobic coatings - screening of different coatings and influence of roughness. *Appl Surf Sci* 282:870–879
21. Beisswenger A, Guy F, Laforte C (2010) Advances in ice adherence and accumulation reduction testing at The Anti-Icing Materials International Laboratory (AMIL). Future Deicing Technologies, Berlin. <http://www.uqac.ca/amil/en/publications/presentations/2009-2011/icephobic%20SAE%202010.pdf>. Accessed 23 Oct 2017
22. Dou R, Chen J, Zhang Y, Wang X, Cui D, Song Y, Jiang L, Wang J (2014) Anti-icing coating with an aqueous lubricating layer. *ACS Appl Mater Interfaces* 2014(6):6998–7003
23. Beisswenger, A, Laforte, C (2008) Advances in ice adherence and accumulation reduction testing at the Anti-Icing Materials International Laboratory (AMIL). SAE G-12 fluids subcommittee meeting Warsaw, May 2008. <http://www.uqac.ca/amil/en/publications/presentations/2007-2008/icephobic%202008-Ab-01%20warsaw.pdf>. Accessed 23 Oct 2017
24. Laforte C, Blackburn C, Perron J (2015) A review of icephobic coating performances over the last decade. SAE technical paper 2015-01-2149, 2015. <https://doi.org/10.4271/2015-01-2149>
25. D&T Online (2017) Calculating forces in beams. [http://wiki.dtonline.org/index.php/Calculating\\_Forces\\_in\\_Beams](http://wiki.dtonline.org/index.php/Calculating_Forces_in_Beams). Accessed 30 Oct 2017
26. Middle East Technical University (2017) ME 410 experiment 6: characteristics of an Airfoil, Fig. 2. <http://www.me.metu.edu.tr/courses/me410/exp6/exp6.html>. Accessed 31 Oct 2017
27. Scruton C, Rogers EWE (1971) II. Wind effects on buildings and other structures. *Philos Trans R Soc Lond A* 269:353–383
28. Chen J, Liu J, He M, Li K, Cui D, Zhang Q, Zeng X, Zhang Y, Wang J, Song Y (2012) Superhydrophobic surfaces cannot reduce ice adhesion. *Appl Phys Lett* 101:111603
29. Boluk Y (1996) Adhesion of freezing precipitates to aircraft surfaces. *Transports Canada publication TP 12860E*, Transports Canada, Montreal
30. Cabler SJM (2006) Advisory circular: aircraft ice protection. FAA 20-73A. Accessed 16 Aug 2006
31. Uranga A, Drelay A, Greitzerz EM, Titchenerx NA, Lieu MK, Siu NM, Huangk AC, Gatlin GM, Hannonyy JA (2014) Preliminary experimental assessment of the boundary layer ingestion benefit for the D8 aircraft. In: Proceedings of 52nd AIAA aerospace sciences meeting, National Harbor, MD, 13–17 Jan 2014
32. Kok M, Tobin EF, Zikmund P, Raps D, Young TM (2014) Laboratory testing of insect contamination with application to laminar flow technologies, part I: variables affecting insect impact dynamics. *Aerosp Sci Technol* 39:605–613



33. Wohl CJ, Smith Jr JG, Penner RK, Lorenzi TM, Lovell CS, Siochi EJ (2013) Evaluation of commercially available materials to mitigate insect residue adhesion on wing leading edge surfaces. *Prog Org Coat* 76:42–50
34. Krishnan KG, Milionis A, Tetteh F, Loth E (2017) Fruit fly impact on an aerodynamic surface: types of outcomes and residue components. *Aerosp Sci Technol* 69:181–192
35. Microelectronics Heat Transfer Laboratory (1997) Fluid properties calculator. University of Waterloo, Waterloo. <http://www.mhfl.uwaterloo.ca/old/onlinetools/airprop/airprop.html>. Accessed 24 Oct 2017

**Part I**  
**Application of Biomimetics to**  
**Contamination-Mitigating Coatings**

# Influence of Topography on Adhesion and Bioadhesion



Donglee Shin and J. Carson Meredith

**Abstract** Nature, through evolution, has developed many different structured adhesive systems to create strong and reliable adhesion on various substrates, including those with rough or smooth surfaces under dry and wet conditions. However, the details of the adhesive interactions of structured or roughened surfaces are just beginning to be resolved. This chapter examines the physical principles of dry and wet adhesion of structured surfaces from simple to complex geometries. A particular emphasis is placed on bioadhesive systems that achieve an impressive level of control over adhesion via fascinating structural features such as fibrils and spines. The influence of surface morphology and roughness on adhesion is also covered. Recent studies show that the attachment abilities of bioadhesive systems are dramatically reduced below a critical roughness. Based on this and other principles borrowed from nature, strategies can be pursued to create anti-adhesive surfaces via manipulating the surface topography of the substrate.

**Keywords** Adhesion • Bioadhesion • Contact mechanics • Surface morphology • Surface topography

## Contents

1	Introduction .....	21
2	Physical Principles of Adhesion .....	24
2.1	Wet Adhesion .....	28
3	Influence of Surface Geometry on Bioadhesion .....	31
3.1	Functional Morphology of Bioadhesive Surfaces .....	32

---

D. Shin and J. C. Meredith (✉)

School of Chemical & Biomolecular Engineering, Renewable Biomaterials Institute, Georgia Institute of Technology, Atlanta, GA, USA

e-mail: [carson.meredith@chbe.gatech.edu](mailto:carson.meredith@chbe.gatech.edu)

3.2 Bioadhesion on Rough Surfaces .....	38
4 Anti-adhesive Surfaces .....	40
5 Conclusion .....	43
References .....	43

## List of Abbreviations

$A$	Hamaker constant
$a$	Contact area
$b$	Slip length
$C$	Coefficient in the atom-atom pair potential
$D$	Separation distance
$D_0$	Cutoff separation distance
$D_w$	Separation distance (wet adhesion models)
$d$	Interplanar separation
$F$	External loading force
$F_{\text{DMT}}$	Pull-off force (DMT model)
$F_{\text{JKR}}$	Pull-off force (JKR model)
$H_w$	Meniscus height
$h_l$	Thickness of liquid film
$K$	Elastic modulus
$k_1$	Proportionality factor (Rabinovich's model)
$l_a$	Azimuthal radius
$N$	Total number of liquid bridges
$p_1, p_2$	Number of atoms in unit volume
$p(z)$	Peak height distribution function
$R$	Radius of sphere
$R_c$	Contact radius
$R_{\text{LS}}$	Radius of sphere (Rumpf's model, Rabinovich's model)
$R_p$	Mean peak radius
$R_S$	Radius of sphere (JKR model, DMT model)
$R_w$	Radius of sphere (wet adhesion models)
$r$	Radius of small hemispherical asperities (Rumpf's, Rabinovich's models)
$r_m$	Meridional radius
rms	Root-mean-square
$W_{12}$	Work of adhesion
$x$	Ratio between the contact radius and half of the cutoff separation distance
$\gamma, \gamma_l$	Surface tension
$\eta$	Viscosity of liquid
$\theta, \theta_l$	Contact angle
$\lambda$	Peak-to-peak distance
$\phi$	Filling angle
$\Omega$	Meniscus area
$\Delta P$	Laplace pressure
$f^*$	Correction factor to account for the effect of a partial slip boundary

## 1 Introduction

This chapter introduces the fundamentals of adhesion relevant to other chapters by discussing the causes and prevention of accumulated insect residues and ice on aircraft and biofouling constituents on marine surfaces. Using natural and man-made examples, this contribution aims to review the effects of microscale and nanoscale topography on adhesion, caused by the potential role of topography in future solutions to the problems of residue accumulation. Nanostructured surfaces have been studied widely because of the fascinating functions they enable, such as anti-wetting [1], anti-icing [2], water droplet harvesting [3] and mobilization [4], photonic color [5], turbulent fluid drag reduction [6], and glueless adhesion [7]. Although man-made approaches for these functions exist, each of these functions is also naturally occurring. The surface structures of animals and plants have evolved in many instances to confer specific functionalities that improve survival or reproduction. For example, lotus leaves possess a superhydrophobic (water-repellent) surface attributed to a hierarchical structure containing both micrometer- and nanometer-scale features [8, 9] (Fig. 1a, b), and this function improves the efficiency of photosynthesis by facilitating self-cleaning mechanisms. The micro-patterned structures of hydrophobic and hydrophilic regions on the back of desert beetles promote water condensation to collect water droplets from humid air [10] (Fig. 1c, d). Some butterflies use structural colors, created by controlling the transport of light via photonic nanostructures, to produce vivid and bright wing colors with low energy consumption [11] (Fig. 1e, f). The aligned riblet structures on shark skin reduce the drag experienced by fast-swimming sharks in turbulent flow [12] (Fig. 1g, h).

Many plants and animals have evolutionarily optimized surface structures that create strong and functional adhesion for locomotion or transportation. For example, the multi-branched structure of gecko foot hairs creates exceptionally strong adhesion to enable climbing on both smooth and rough surfaces without an adhesive secretion [13]. The hairy structures (200–500 nm long and 15 nm thick) on the gecko setae (30–130  $\mu\text{m}$  long) allow the foot pads to create contact area sufficient to sustain the gecko's body weight, even on vertical walls. Tree frogs can adhere strongly to wet and rough surfaces. The adhesive pads of tree frogs have hexagonal cells (approximately 10  $\mu\text{m}$  in diameter) separated by deep channels (1  $\mu\text{m}$  wide) filled with a mucus secretion. The microstructured channels are the paths for distributing mucus over the whole contact area between the adhesive pad and a contact surface, and the channels also work to drain water, enabling attachment on water-coated surfaces [14]. Insects have both hairy and smooth adhesive pads whose adhesion is mediated by thin layers of adhesive secretions [15]. The tip radius of structures on the hairy adhesive pad are a size roughly ranging from 1 to 10  $\mu\text{m}$ , and these can attach at multiple points to create a large contact area on a rough surface [15, 16], similar to the action of the gecko setae. The smooth adhesive pad, which is a "pillow-like" soft structure that consists of branching fibrils and the outer cuticle layer [17], can also adapt to surface roughness features to create large

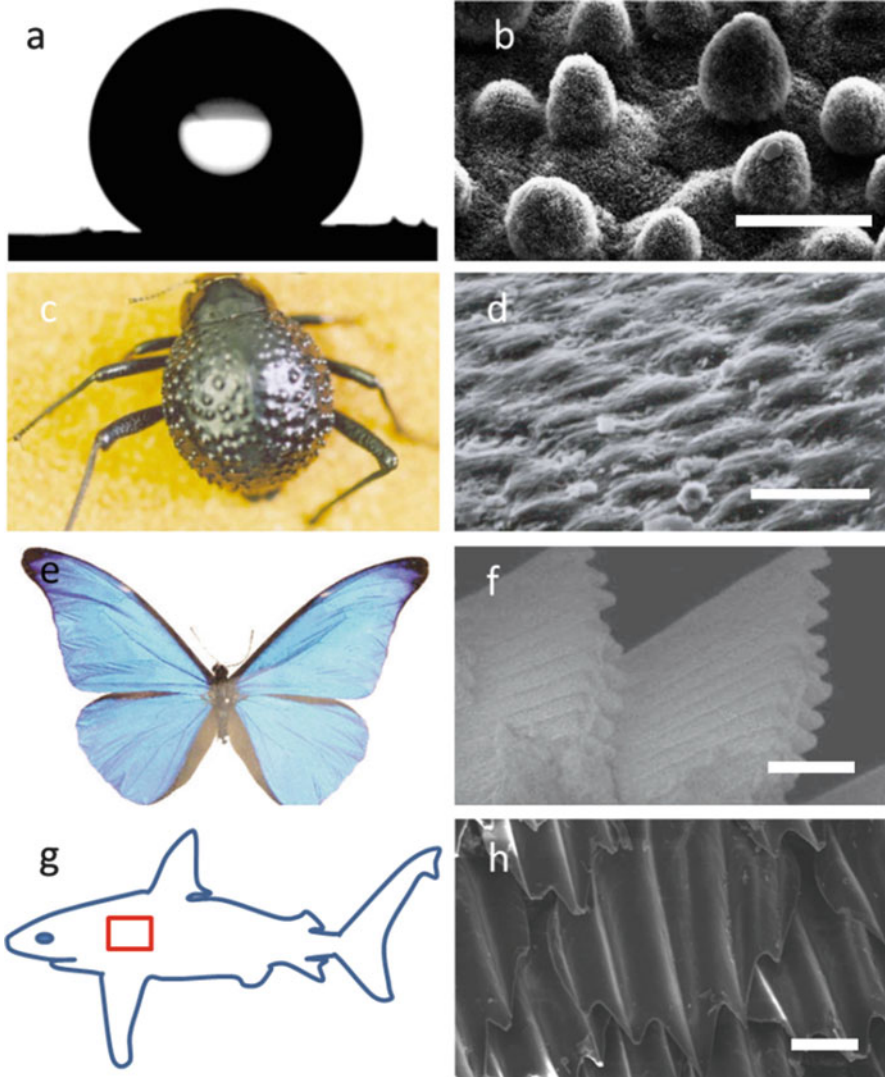


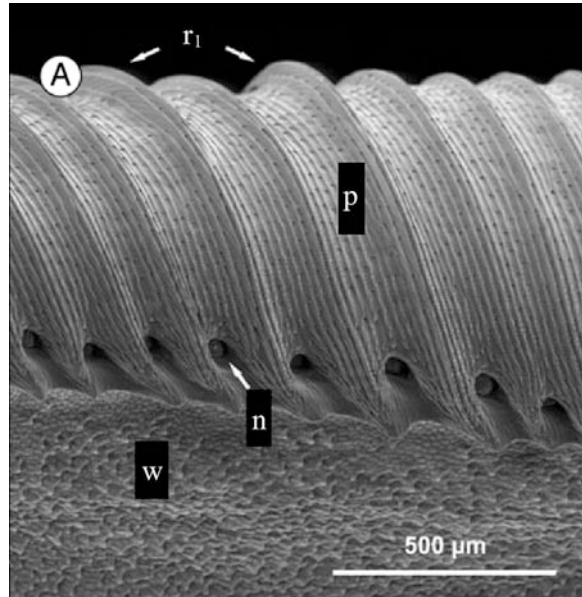
**Fig. 1** (a) Water droplet on a lotus leaf  $CA = 152^\circ$ . (Reproduced with permission from Hao et al. [8].) (b) Scanning electron microscopy (SEM) image of the lotus leaf. (Reproduced with permission from Barthlott et al. [9].) (c, d) Photograph and SEM image of the water-harvesting surface of the desert beetle. (Reproduced with permission from Parker et al. [10].) (e, f) Photograph and SEM image of distinctive iridescent blue color of the wings of *Morpho* butterfly. (Reproduced with permission from Parker et al. [11].) (g, h) Cartoon and SEM image of the scale structure of shark skin. (Reproduced with permission from Luo et al. [12].) Scale bars = 20  $\mu\text{m}$  (b), 10  $\mu\text{m}$  (d), 400 nm (f), and 50  $\mu\text{m}$  (h)

contact areas for strong adhesion. Pollens from different plant species display a remarkable variety of ornamentations with unique size, shape, and density on their exine (shell) surface. When pollens interact with a structured flower stigma, their surface features cause pressure-sensitive adhesion mediated by mechanical interlocking [18]. Pollen grains exhibiting structural ornamentations have been shown to adhere strongly to the stigma surfaces within the same botanical family [19], which is thought to facilitate reproduction.

In addition to these examples of natural adhesive structures, examples exist in nature of anti-adhesive and slippery surfaces as well. A prominent example is the pitcher plant *Nepenthes alata*, which possesses both anti-adhesive cuticular wax surfaces [20] and a slippery peristome consisting of grooved structures that are continuously wetted by water in humid environments [21]. Whereas the waxy cuticle reduces normal adhesion forces of insects such as ants, the wetted peristome presents a lubricated low-shear interface, on which insects slide into the pitcher where they are digested. The lubricant infusion of *Nepenthes* has inspired the engineering of synthetic lubricant-infused surfaces that promote sliding and resist attachment of particles, ice, and other contaminants [22, 23]. Another example of anti-adhesive structures is the riblets of shark skin (Fig. 1h), which have been mimicked by surface wrinkling to produce biofouling resistance [24].

Numerous researchers have studied the adhesion mechanisms of simple geometries, such as plane-plane, sphere-sphere, cone-cone, sphere-plane, sphere-cylinder, and cone-plane over the past several decades [25–31]. Based on this background knowledge, studies of the influence of geometry on adhesion have more recently expanded to treat surfaces with complex fine features. The investigation of bioadhesion, such as in the examples mentioned above, has been an important part of an emerging understanding of the effects of microscale and nanoscale topography on adhesion. Herein, we discuss the basic physical principles of adhesion with simple geometric models as the adhesion of complex structured surfaces is also based on the same physical principles. These include van der Waals (vdW), capillary, and viscous forces (Sect. 2). Then we discuss how different surface geometries (hairy, smooth, and echinate) affect adhesive mechanisms and focus on the dependence of bioadhesion on substrate structure (Sect. 3). We also review recent efforts to produce anti-adhesive surfaces based on surface topography designed from natural adhesive phenomena (Sect. 4). Because of the primary importance of wet adhesion – adhesion between solids that is mediated by liquids – in the problems of aircraft and marine surface bioadhesion, this review focuses in particular on the static and dynamic contributions of capillary forces to adhesion. As a result, we do not consider in detail the contributions of dynamics in deformable bodies on solid adhesion, such as the role of shear forces in soft solid–solid adhesion. However, these are significant in many soft biological adhesion systems, and there are excellent recent reviews available on this topic [32–34]. By examining adhesion fundamentals as well as examples taken from natural systems, we hope to motivate thoughts about how aircraft or marine surface features could be designed to prevent or mitigate adhesion of contaminants (Fig. 2).

**Fig. 2** SEM image of pitcher plant *N. alata* peristome surface (p), showing the first- ( $r_1$ ) and second-order radial ridges, extrafloral nectaries (n), and waxy inner wall surface (w). Reproduced with permission from Bauer et al. [21]



## 2 Physical Principles of Adhesion

A practical question that this volume seeks to address is how aircraft and marine surfaces can be designed to minimize adhesion in extreme environments. It is important to begin by defining the concepts. Adhesion refers to the energy or work required to separate two surfaces that are already in contact. Although events that occur during the impact of insects with aircraft are important in determining the contact area, and are discussed in detail elsewhere in this volume [35], we consider adhesion here to be the resistance to surface separation after contact is established. A separate, but related topic is that of surface friction, which displays itself in perceived properties of surface slipperiness. Slippery surfaces often also exhibit low adhesion, but strictly speaking they are not always correlated. Friction relates to the lateral forces occurring when contacting surfaces are moved parallel to one another (shearing), whereas adhesion relates to the movement of surfaces away (normal direction) from one another. The fascinating behavior of slippery surfaces in nature has been the subject of recent work, such as the lubricated surfaces of the pitcher plant [23, 36], and this behavior can undermine initial adhesive contact by promoting sliding.

Animals and plants utilize transitory (nonpermanent) adhesive force for transport and locomotion [37, 38], and this temporary adhesion is strongly affected by the topography of the adhesive surface. Adhesive mechanisms related to transitory bioadhesion can be classified roughly into two categories: (1) dry adhesion based on intermolecular forces and (2) wet adhesion based on liquid-mediated static and



dynamic capillary forces. These mechanisms are also operative in synthetic adhesives in manmade materials, such as pressure-sensitive adhesives [39], latex paints [40], ink toner, and powder coatings [41]. In this section we discuss the physical principles of both dry and wet adhesive mechanisms with representative simple geometry models.

These adhesion fundamentals relate to the problem of biological residue accumulation in extreme environments in a number of ways. After insect impact on aircraft, the adhesion of hemolymph is expected to be governed initially by a combination of capillary static and dynamic forces that resist removal from the surface. As hemolymph gels and solidifies, adhesion becomes dominated by dry adhesive forces that are likely controlled by vdW and specific noncovalent interactions with the aircraft surfaces. Adhesion of other solid contaminants on aircraft (including ice) surfaces varies between these dry and wet mechanisms depending on the presence of a wetting fluid that may form capillary bridges between the solid surfaces. Of course, it is expected that adhesion of biological fluids or solids, including those of living animals such as diatoms, mussels, or barnacles, on marine underwater surfaces may involve vdW forces, specific interactions, covalent bonding, and capillarity, as well as mechanical contributions from shearing and viscoelasticity.

In general, the adhesive force of neutral surfaces in a ‘dry’ atmosphere, such as nitrogen or vacuum, is comprised of vdW interactions, and hydrogen, covalent, or metallic bonds [42]. The energy of vdW interactions is normally much smaller than covalent or hydrogen bonds. However, the vdW interaction plays a prominent role in determining the attractive force magnitude of surfaces and colloids because the vdW interaction has a longer range (0.2–10 nm) than the other inter- or intramolecular bonding (covalent, hydrogen, and metallic bonding) scales (normally 0.1–0.2 nm) [43]. Even though there is no universal model that accounts for the influence of all contributions (e.g., elastic moduli, surface energy, temperature, relative humidity, and Hamaker constant) on vdW interactions, the following adhesion models for simple geometry help us to understand the physical principles of dry adhesion. Common classical models to estimate the adhesion force between two elastic spheres (or sphere and planar surfaces) originated from Hertzian theory [44]. In 1882 Heinrich Hertz developed a model for the contact area ( $a$ ) of two elastic spheres (of radii  $R_1$  and  $R_2$  with elastic moduli  $K$ ) with external loading force ( $F$ ) [43]:

$$a = \left( \frac{FR}{K} \right)^{1/3}, \quad (1)$$

where  $R = R_1R_2/(R_1 + R_2)$ .

In Hertzian theory, the intermolecular attraction between contact surfaces was ignored, so the contact area is apparently zero when there is no (or negative) external load. In 1971, Johnson, Kendall, and Roberts (JKR) developed a theory to estimate the adhesion between two solid surfaces [45]. They observed that the experimentally measured contact areas were larger than values estimated by Hertz

theory, and they confirmed that the solid surfaces still adhered under zero or small negative external loading force. They proposed that the surface interaction affects both deformed shape and overall loading force, which is represented by the sum of the external loading force and adhesion of the surfaces. The deformed contact area was derived as follows [46]:

$$a^3 = \frac{R}{K} \left( F + 3\pi W_{12}R + \left( 6\pi W_{12}RF + (3\pi W_{12}R)^2 \right)^{1/2} \right), \quad (2)$$

where  $F$  is external load and  $W_{12}$  is work of adhesion, which is the work done in separating a unit area of the interface. For a sphere (radius of sphere,  $R_s = R_1$ ) on a flat surface ( $R_2 = \infty$ ), the adhesion or pull-off force can be derived as [47]

$$F_{\text{JKR}} = \frac{3}{2} \pi R_s W_{12}. \quad (3)$$

Unlike the JKR case, Derjaguin, Muller, and Toporov (DMT) assumed that the shape of the contacting surfaces is not affected by surface intermolecular interactions [48]. Therefore, the deformed contact area could be derived as [46]

$$a^3 = \frac{R}{K} (F + 2\pi W_{12}R), \quad (4)$$

and adhesion or pull-off force of a sphere on a flat surface can be derived as [47]

$$F_{\text{DMT}} = 2\pi R_s W_{12}. \quad (5)$$

The JKR and DMT models consider the deformation of the contact area, but neither model accounts for the influence of separation distance on adhesion. When the contact surfaces have roughness or geometrical features, the assumption of complete contact is no longer valid and the separation distance of the surfaces must be considered [49]. The separation distance is the most significant factor defining adhesive force magnitude in the nonretarded region (separation distance less than 5 nm) [43]. Therefore, the adhesion models for rough or structured surfaces often use the Hamaker approach as a starting point. Hamaker proposed that the adhesion between particles and surfaces can be estimated by the integration of the vdW pair potential between all atoms in one body and all atoms in the other body [25]. In his study, the vdW interaction between a sphere and a flat surface was derived as

$$F_{\text{vdw}} = -\frac{A_{132}}{24R_c} \left( \frac{2}{x} - \frac{1}{x^2} - \frac{2}{x+1} - \frac{1}{(x+1)^2} \right), \quad (6)$$

where  $A_{132}$  is the material-dependent nonretarded Hamaker constant, which represents the magnitude of interaction of the two interacting bodies (1 and 2) consisting of atoms with induced dipoles across a medium (3). The Hamaker constant can be determined by [43]

$$A = \pi^2 C p_1 p_2, \quad (7)$$

where  $p_1$  and  $p_2$  are the number of atoms in a unit volume of the two bodies (1 and 2), and  $C$  is the coefficient in the atom-atom pair potential. The  $x$  in (6) represents the ratio between the contact radius ( $R_c$ ) and half of the cutoff separation distance ( $D_0$ ), which is the predicted separation distance of contacting surfaces. (Some references approximate the cutoff distance at around 0.3–0.4 nm [49, 50], but others evaluate it as 0.165 nm [13, 43].) Equation (6) can be simplified to (8) in the limit of  $x \ll 1$  [43]:

$$F_{\text{vdw}} = \frac{A_{132} R_c}{6D^2}, \quad (8)$$

where  $D$  is separation distance.

It is well-known that the surface pattern and roughness reduce the adhesion between surfaces or a spherical particle and a planar surface [51, 52]. Rumpf's model is a common and simple model based on Hamaker's approach to consider the effect of nanoscale surface roughness on adhesion [53]. This model estimates the adhesion between a large spherical particle (radius  $R_{\text{LS}}$ ) and a flat surface covered with small hemispherical asperities (radius  $r$ ), and normal alignment of the center of the particle and asperity is assumed (Fig. 3a). Rumpf's model consists of two terms as shown in the following formula [53]:

$$F_{\text{Rumpf}} = \frac{A_{132}}{6D_0^2} \left[ \frac{rR_{\text{LS}}}{r + R_{\text{LS}}} + \frac{R_{\text{LS}}}{\left(1 + \frac{r}{D_0}\right)^2} \right], \quad (9)$$

where  $D_0$  is the cutoff distance. The first term represents the adhesion between the particle and hemispherical asperity in contact. The second term represents the “noncontact” attractive interaction between the particle and flat surface where

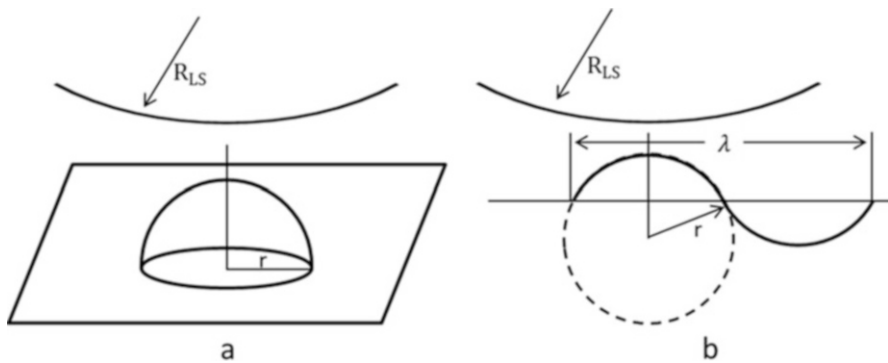


**Fig. 3** Schematic illustration of the geometry proposed by: (a) Rumpf et al. [53]; (b) Rabinovich et al. [50]

separation distance is the radius of the hemispherical asperities. Rabinovich et al. found that Rumpf's model is not accurate in real systems with low roughness surface as it requires the center of a small hemisphere to be at the surface as shown in Fig. 3a [50]. In many real systems the center is located below the surface, and multiple surface asperities have contact with the large spherical particle. They proposed the approximation of this case with root-mean-square (rms) roughness and peak-to-peak distance ( $\lambda$ ) (Fig. 3b) as shown in the following [50]:

$$F_{\text{Rabin.}} = \frac{A_{132}R_{\text{LS}}}{6D_0^2} \left[ \frac{1}{1 + \left(\frac{32R_{\text{LS}}k_1\text{rms}}{\lambda^2}\right)} + \frac{1}{\left(1 + \frac{k_1\text{rms}}{D_0}\right)^2} \right], \quad (10)$$

where  $k_1$  is a proportionality factor determined to be 1.817. In conventional adhesion and bioadhesion, surfaces can display surface roughness with a wide variety of structures and shapes, but the previous dry adhesion models are limited because of assumptions made about the shape or distribution of asperities. Recent dry adhesion models represent attempts to account for the interaction of complex contact shapes [16, 54], asymmetric structures [55], multiple contacts [56], and mechanical interlocking [57].

## 2.1 Wet Adhesion

In practical industrial and natural applications, wet adhesion is common. Strong wet adhesion driven by water condensation or by the presence of thin liquid lubricant on the contact surfaces is a critical issue in operation of fine-scale devices, including atomic force microscopy, magnetic storage devices, and fuel injectors [58]. For locomotion of animals, liquid secretions can create a larger contact area on a rough surface, compared to a dry surface because of strong capillary forces [59]. The mediating liquid can increase contact between the adhesive pad and a rough surface by filling the gaps between the pad and the surface. This is a topic of relevance to surface contamination in aerospace and marine applications, including biofouling, insect residue adhesion during hemolymph curing, and in-flight icing. The wet adhesion force can be split into two main components, capillary (meniscus) and viscous forces [60], as shown in (11):

$$F_{\text{Wet adhesion}} = F_{\text{Capillary force}} + F_{\text{Viscous force}}. \quad (11)$$

The vdW interaction may dominate wet adhesion in the case of very thin films (less than 10 nm), but its contribution is in most cases smaller than the capillary or viscous force. These forces are likely to be important in insect residues adhesion post-impact, that is, to prevent the residues from being driven off the surface by drag forces. The contribution of these primary components to wet adhesion can be

determined by considering the meniscus curvatures, dynamics, and viscosity of liquid films [58].

The capillary force is caused by a liquid meniscus (bridge) between two separated surfaces, and the curvature of the liquid meniscus is characterized by two radii, the azimuthal radius ( $l_a$ ) and the meridional radius ( $r_m$ ), shown in Fig. 4. The total capillary force between a sphere (radius,  $R_w$ ) and a flat surface is defined as the summation of the surface tension and Laplace pressure contributions as shown in the following equation for a symmetric contact angle [58, 61]:

$$F_{\text{Capillary force}} = \Delta P \Omega + 2\pi R_w \gamma \sin \phi \sin(\phi + \theta), \tag{12}$$

where  $\Omega$  is the meniscus area,  $\phi$  is the filling angle,  $\theta$  is the contact angle,  $\gamma$  is the surface tension of the liquid, and  $\Delta P$  is Laplace pressure, estimated by the Young–Laplace equation:

$$\Delta P = \gamma \left( \frac{1}{l_a} - \frac{1}{r_m} \right). \tag{13}$$

The Young–Laplace equation describes the capillary pressure difference between two static phases. The surface tension and Laplace pressure forces explain the static contribution of the capillary liquid bridges to wet adhesion, but neither expression has dynamic terms. The contribution of hydrodynamic response can be estimated by a viscous force model, often called “Stefan adhesion” [60]. The viscous term of wet adhesion is a significant component of the wet adhesion mediated by highly viscous liquid capillary bridges, but it can also dominate for liquids of modest viscosity at high shear rate [62]. The viscous force acting on a sphere and a flat surface connected by a capillary bridge (Fig. 4) can be approximated by (14) [58]:

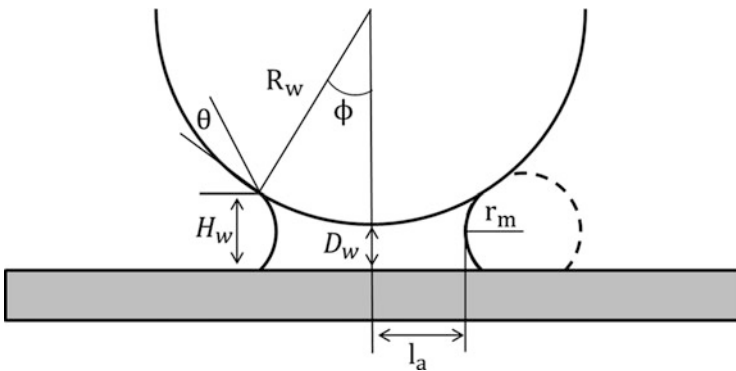


**Fig. 4** Schematic of a meniscus bridge present at the interface between a sphere and a plane surface

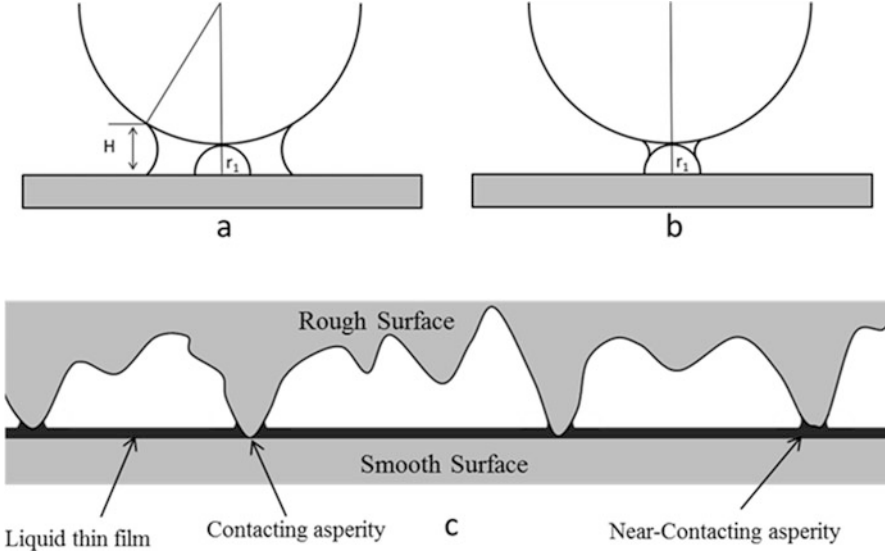


**Fig. 5** Schematic of a liquid meniscus when: (a)  $H > r_1$ ; (b)  $H < r_1$ . (c) Schematic for a rough surface in contact with a flat surface coated by a thin liquid film

$$F_{\text{Viscous force}} = 6\pi\eta R_w^2 \left[ 1 - \frac{D_w}{H_w} \right]^2 \frac{1}{D_w} \frac{dD_w}{dt}, \quad (14)$$

where  $\eta$  is the viscosity,  $D_w$  is the distance between a sphere and a flat surface,  $R_w$  is the radius of the spheres,  $H_w$  is the meniscus height, and  $dD_w/dt$  is the separation rate. The total wet adhesion between a sphere and a flat surface can be estimated by the summation of (12) and (14).

The previous capillary (12) and viscous (14) force models are commonly used to estimate wet adhesion of a sphere and planar surface for simplicity, but the models fail to estimate accurately the wet adhesion for rough and patterned surfaces [63]. The topographical effect on capillary force is strongly dependent on the height of the liquid meniscus (the thickness of liquid) as shown in Fig. 5. When the meniscus height is greater than the hemispherical asperity as shown in Fig. 5a ( $H > r_1$ ), the contact line and the curvatures of the meniscus are determined by the larger separation distance  $H$ . The previous (12) (sphere and flat surface model) is still valid as long as the increased separation distance is accounted for. However, when meniscus height is smaller than the hemispherical asperity (Fig. 5b), the wet adhesion model between two spheres (a large sphere and a small hemisphere) should be considered. The capillary force for interaction between two spheres was studied by Willett et al. [64] and Rabinovich et al. [65]. For multiple asperity contacts, Bhushan proposed a capillary force model of a randomly rough surface in contact with a smooth surface with a continuous liquid film as shown in Fig. 5c [66]. Both contacting and near-contacting asperities have a liquid meniscus, peak

radii (of the asperities) are assumed constant, and peak heights are assumed to follow a Gaussian distribution. By the summation of the wet adhesion on the asperities, the total wet adhesion of the surface is given as

$$F_{\text{Capillary force}} = 2\pi R_p \gamma_l (1 + \cos \theta_l) N \int_{d-h_l}^{\infty} p(z) dz, \quad (15)$$

where  $N$  is the total number of liquid bridges,  $R_p$  is the mean peak radius,  $\gamma_l$  is the liquid surface tension,  $\theta_l$  is the contact angle of the liquid in contact with the rough surface,  $d$  is the interplanar separation [62],  $h_l$  is the thickness of liquid film, and  $p(z)$  is the peak height distribution function.

The viscous force acting between a sphere and a flat surface is generated by hydrodynamic drainage of liquid in the gap separating the surfaces. The surface topography affects the viscous force magnitude by creating slip or partial slip boundary conditions [67]. Remarkable hydrodynamic force reduction has been observed in capillaries on nanostructured surfaces [68, 69], such as structured superhydrophobic surfaces. The reduction is commonly explained by the slip boundary of liquid on trapped air pockets [70]. The classical viscous model (14) originates from Reynolds' lubrication theory with nonslip boundary conditions. Vinogradova initially proposed using a multiplying factor ( $f^*$ ) to correct for the effect of a partial slip boundary, assuming creeping flow and the same slip length  $b$  for both surfaces [71]:

$$f^* = \frac{D_w}{3b} \left[ \left( 1 + \frac{D_w}{3b} \right) \ln \left( 1 + \frac{6b}{D_w} \right) - 1 \right]. \quad (16)$$

In practice, it is still challenging to estimate precisely the effective slip length because it is dependent on multiple factors, such as wettability, surface structure, and rheological properties of the liquid. However, recent studies have made meaningful progress in understanding the influence of diverse surface structures on boundary conditions of the viscous force model [72, 73].

### 3 Influence of Surface Geometry on Bioadhesion

The evolutionarily-adapted surfaces of animals and plants show how nature utilizes structure for functional adhesion. For example, the adhesive pads of animals support body weight on varying surfaces, such as smooth or rough, hydrophilic or hydrophobic, and clean or contaminated [74]. The structured adhesive pads and/or secretions both function critically to create strong but reversible adhesion for locomotion [38]. Plants also use structural surfaces and bioadhesives. For example, pollen grains use complex surface asperities and an adhesive liquid coating to facilitate transfer from anthers to pollinators, and from pollinators to stigmas [18, 75, 76]. In this section we discuss adhesive functional morphology in nature,

focusing on geckos, insects, tree frogs, and pollens. We also introduce experimental studies of the influence of structure on dry and wet adhesion, including the complex interactions of structure with surface roughness. It is hoped that lessons based on the evolved designs of nature can be applied to the prevention of adhesion in the extreme environments of aerospace and marine surfaces.

### ***3.1 Functional Morphology of Bioadhesive Surfaces***

#### **3.1.1 Fibrillar Structure**

It has been suggested that the adhesion of fibrillar structures on rough surfaces can be stronger than smooth surfaces [47] because fibrils with small effective elastic modulus can adapt to rough surfaces to increase contact area. Fine-scale hairs, with tip size less than the opposing surface roughness, can adapt to surface features, producing low strains on the hairs, increasing the fibrils total contact area [77]. In addition, it is well-known that the detachment of multifibrillar contacts requires more work than required to hold continuous contact [78], because the stored energy in a peeling fibril is not available for the detachment of the next fibril [47]. Therefore, many animals, from tiny mites to geckos and some mammals, take advantage of fibrillar adhesive pads to achieve strong adhesion on both smooth and rough surfaces.

In nature, the bioadhesive mechanism of hairy surfaces can be classified as dry or wet adhesion. Using a scaling analysis from mites to geckos, Gorb discussed the dependence of contact density on body mass [38]. He suggested that heavier animals, such as geckos and spiders, rely more on dry adhesion, and these animals tend to have compactly packed small fibrillar ends to create large peeling lines for strong adhesion [79]. However, recent studies claim that the total pad area of fibrillar systems is a main contributor to strong dry adhesion, not the high density of the fibrillar ends [80, 81].

Autumn et al. claimed that molecular vdW interactions are the dominant attractive force for gecko adhesion, as gecko adhesion was not affected by the hydrophobicity of the surface [13, 82]. Most gecko feet have hierarchical fibrillar structures consisting of lamellae, setae, branches, and spatulae [83], as shown in Fig. 6a–c. The second level of the hierarchy, consisting of the fibrillar ‘setae’ (ST in Fig. 6b), is typically 30–130  $\mu\text{m}$  long and 5–10  $\mu\text{m}$  in diameter, and the density is about 14,000 setae/ $\text{mm}^2$ . In many species these setae are split into multiple branches (BR in Fig. 6b, c) which are 20–30  $\mu\text{m}$  long and 1–2  $\mu\text{m}$  wide. Most setae terminate into 100–1,000 spatulae (SP in Fig. 6c) with a diameter of 0.1–0.2  $\mu\text{m}$  [83]. To create strong adhesion, the fibrillar structures should be mechanically soft to achieve a large number of contacting hairs with low strains. However, if the hairs are too soft, they are intricately entangled, and adhesion is reduced significantly. The hierarchical structure is a solution to this problem. Hierarchical structures, such as lamellae and setae, provide the mechanical stability



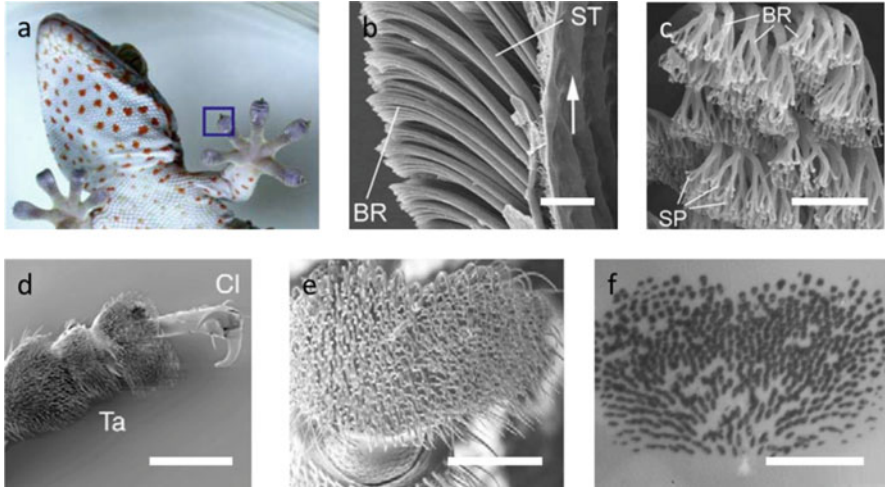


**Fig. 6** (a–c) The hierarchical structure of *Gekko gekko* adhesive pads: (a) photograph of gecko toe; (b, c) scanning electron microscopy (SEM) images of branch (BR), seta (ST), and spatula (SP) in the adhesive pad of geckos. (Reproduced with permission from Gao et al. [84].) (d–f) The adhesive pad structure of a male dock beetle (*G. viridula*): (d, e) SEM images of the adhesive pad (Cl: claws; Ta: tarsal segments); (f) visualized contact area of the beetle adhesive pad with glass via epi-illumination. (Reproduced with permission from Bullock et al. [85].) Scale bars = 20  $\mu\text{m}$  (b), 5  $\mu\text{m}$  (c), 250  $\mu\text{m}$  (d), 100  $\mu\text{m}$  (e), and 100  $\mu\text{m}$  (f)

attributed to relatively high modulus and thick diameter structures, whereas lower level hierarchy, such as branches and spatulae, provide compliance and adaptability to roughness [38, 86]. Another significant feature of gecko adhesion is the asymmetrical structure (slope) of the setae. When setae are attached on a surface, they are not vertical but tilted with respect to the surface, and that is the reason why the pull-off force of a single seta is strongly dependent on orientation [13]. It was observed that adhesion of a single seta was enhanced by more than an order of magnitude when the pulling angle was reduced from 90° to 30° [38, 87]. This result indicates that the asymmetrical structure of the setae plays a significant role in achieving reversible adhesion, which can be easily switched between attachment and detachment for locomotion.

Insects with fibrillar adhesive pads, such as reduviid bugs, flies, and beetles, utilize liquid adhesive secretions to increase attachment force [59]. Unlike geckos, the insects don't have complex hierarchical structures, and the setae of most insects end in a single and relatively large spatula (the areas of terminal contact of beetles and flies are larger than 1  $\mu\text{m}^2$ ) as shown in Fig. 6d–f. To increase the contact area of the large spatulae on a rough surface, insects fill the gap between the spatula and surface with a liquid adhesive secretion. It was observed that the adhesion of insect pads was reduced significantly by organic solvent washing [88], and insufficient adhesive forces were recorded when beetles were tested on a liquid-absorbing nanoporous substrate [89]. Those studies show that the force magnitude of overall

adhesion relies strongly on the capillary adhesion of the liquid bridges. In addition, the fibrillar structure allows multiple liquid bridges, which can produce a stronger total capillary force than a single liquid bridge with equal total liquid volume [90].

The contact geometries strongly affect the adhesive functions of the fibrillar adhesive pad [16, 91]. Mushroom- and spatula-shaped elements are commonly observed contact geometries in nature and are strongly related to the duration of adhesion [92]. Spatula-shaped elements require a shear force to generate adhesion, and these terminal elements are useful for short-term dynamic adhesion during fast locomotion because the contact can be easily detached by peeling within a few milliseconds. By contrast, the mushroom-shaped terminal elements are more suitable for creating long-term adhesion. These elements do not require external applied shear forces, and a relatively higher pull-off force is required to rupture the contact.

### 3.1.2 Smooth Structure

Smooth adhesive pads are observed from diverse animals such as ants, bees, stick insects, grasshoppers, tree frogs, and arboreal possums [93]. As mentioned before, unlike fibrillary adhesive systems, continuous surfaces cannot make a large number of contacts that adapt to the geometry of a rough surface. Thus, animals with smooth adhesive pads have developed strategies to overcome this limitation. One adaptation is the soft mechanical properties of the smooth adhesive pads, which have high deformability to adapt a larger contact area on rough surfaces. For example, the reported effective elastic modulus of the adhesive pad of tree frogs is in the range of 4–25 kPa [94], and it is one of the softest biological structures. Smooth pads have an ultrastructure consisting of cuticular rods (insects) [17] or hexagonal epithelial cells (tree frogs) [14], and the fine structures of the pads allow close contact with low strain on rough surfaces. All known smooth adhesive pads utilize thin liquid films, such as watery mucus of tree frogs, multi-phase adhesive secretion of insects, and sweat of arboreal possums, to fill the gap between the pads and substrates, and this liquid film helps to create a large contact area on rough surfaces.

Tree frogs are well-known heavy body mass amphibians that utilize smooth adhesive pads. The details of the adhesive mechanism still remain elusive, but it was found that the physical properties and surface structures of the smooth adhesive pad have a critical role in attachment on vertical and overhanging surfaces [95]. These adhesive pads (Fig. 7a) consist of regular hexagonal epithelial cells (10–15  $\mu\text{m}$ ) (Fig. 7b) separated by watery mucus-filled channels (1  $\mu\text{m}$  wide). Each cell consists of densely-packed nanopillars (Fig. 7c) that are 300–400 nm in diameter with a concave end [96]. The thin intervening watery mucus layer between the pad and surface forms an essential part of wet adhesion. The capillary force generated by a liquid bridge around the edge of the pad, and the viscous force generated over the whole contact area, strongly contribute to the adhesion of tree frogs [96]. The channel structure on the pad surface works to distribute fluid across

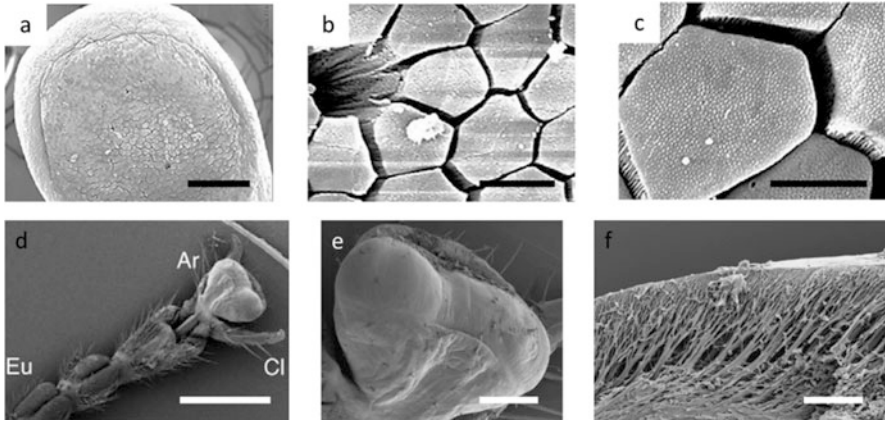


**Fig. 7** (a–c) Scanning electron microscopy (SEM) images of tree frog (*Litoria caerulea*) adhesive pad: (a) toe pad; (b) hexagonal epithelial cell; (c) densely packed nanopillars. (Reproduced with permission from Scholz et al. [96].) (d–f) SEM images of Indian stick insect (*C. morosus*) adhesive pad: (d) front view of tarsal segments (CL, claws; Eu, euplantulae; Ar, arolium); (e) the distal adhesive pad (reproduced with permission from Bullock et al. [85]); (f) cross-section view of the distal adhesive pad within the smooth cuticle layer (branching fibrils oriented almost perpendicular to the contact surface) (reproduced with permission from Dirks et al. [17]). Scale bars = 100  $\mu\text{m}$  (a), 10  $\mu\text{m}$  (b), 5  $\mu\text{m}$  (c), 1,000  $\mu\text{m}$  (d), 200  $\mu\text{m}$  (e), and 20  $\mu\text{m}$  (f)

the pad, similar to, for example, a tire tread, which allows for rapid drainage of liquid. The structured adhesive pad maintains an extremely thin liquid film for strong wet adhesion in air, and allows for the close contact of the pad with the surface under wet conditions [14]. Recently, the smooth pad morphology of torrent frogs, which are able to climb a vertical surface covered by flowing water, have been under investigation [97, 98]. It is proposed that the straight channels between elongated cells can accelerate drainage rate of excess fluid underneath the pad.

Many insects with smooth adhesive pads also utilize wet adhesion of the adhesive secretion as do the insects with fibrillar pads. The smooth pads (Fig. 7d) of the insects are a “pillow-like” soft structure (Fig. 7e) that consist of branching fibrils (Fig. 7f) oriented perpendicular to the surface within an outer cuticle layer [17]. This internal fibrous structure helps to increase adaptability to surface roughness, and it can be used to facilitate manipulation of the pad contact area via proximal pulling by the insects. It is not well-understood how the presence of a continuous liquid film between a smooth pad and substrate can create strong static attachment ability on a vertical surface. Dirks et al. suggested that the two-phase emulsion structure of the pad secretion could prevent insects from slipping [99]. The hydrophobic droplets dispersed in a watery continuous phase could impart viscous and non-Newtonian (shear thinning) properties to the secretion for maximizing dynamic wet adhesion. Simple wet adhesion models, considering the contribution of the capillary and viscous forces, are often used to explain insect adhesion. However, for a more accurate representation, models should be expanded

to include the contribution of both the pad mechanical properties and viscous properties of the liquid adhesive. One recent study shows that the elastic deformation of the adhesive pad likely dominates the mechanical response when the adhesive secretions of animal are confined between elastic solids [33], and the authors utilize a fracture mechanics approach to estimate the adhesive mechanism of insects with the smooth adhesive pad.

### 3.1.3 Echinate Structure

Echinate structures normally have a limited contact area on hard and smooth surfaces because the adhesive force relies on the interaction between a few contacting tips of spines and a hard surface [100]. However, when the substrate is a soft or a fibrillar/hairy surface, the spiny structures can create unexpectedly strong adhesion by penetrating the surface and/or creating mechanical interlocking [18]. Adhesion associated with penetration is much harder to explain with simple models of dry or wet adhesion, and fibrillar or smooth structures, so the details of the comprehensive mechanism still remain elusive.

Strong and tailored adhesion based on surface topography has a significant role in the active locomotion of animals, but it is also essential for the passive transport of plant pollens and seeds. Pollens are one example to show how the size and shape of nanoscale features can be utilized for adhering selectively to specific surfaces [19]. The surface of some flowering pollens consists of a structured exine, which interacts with pollinators and stigmas, and the exine is often covered by a viscous liquid coating, pollenkitt [101]. It is known that the adhesion of pollens to the stigma of the same species or family is often much stronger than to another species, suggesting a physically-specific adhesion [102, 103]. For instance, the adhesive force magnitude of pollens from Asteraceae (sunflower) and Oleaceae (olive) families on stigma from Asteraceae was directly measured by AFM. The results showed that the echinate (spiny) structure of sunflower pollens strongly affects the adhesive mechanism of the pollen–stigma interaction on Asteraceae but not Oleaceae [18].

The sunflower pollen particle (Fig. 8a) has a spherical core body ( $30 \pm 4 \mu\text{m}$  in diameter) with 1.5–2  $\mu\text{m}$ -long spines, as shown in Fig. 8d. Structurally-derived load-dependent adhesion was attributed to the interlocking between the conical spines on the pollen surface and the stigma's receptive papillae (Fig. 8a). Previously, it was reported that the main contribution of the selective pollen–stigma interaction was dry adhesion (vdW interaction), as no significant difference of force magnitude was observed when the viscous liquid (pollenkitt) on the pollen surfaces was washed by organic solvents [19]. However, it is hard to generalize this observation because different species of pollen carry different amounts of pollenkitt. The contribution of the wet adhesive force attributed to pollenkitt seems to be comparable to the contribution of dry adhesion when pollens are coated with a sufficient amount (more than 30 wt% of innate pollens) of pollenkitt [76]. Moreover, it was shown that adhesion between unpurified pollens (coated

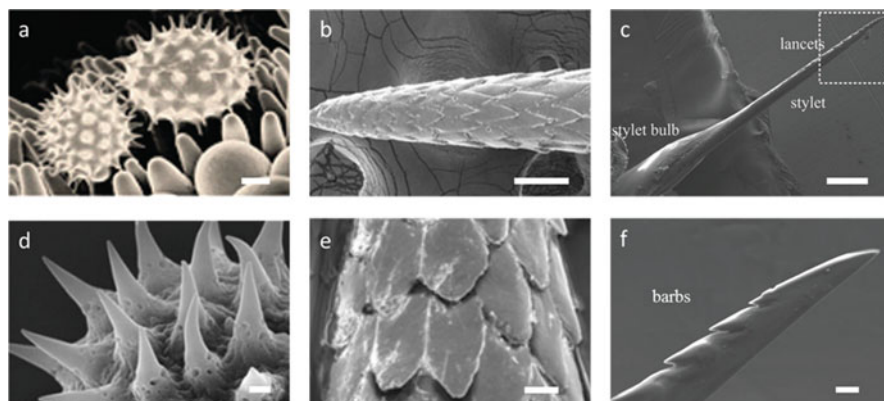


**Fig. 8** Scanning electron microscopy (SEM) images of sunflower (*Helianthus annuus*) pollen on the stigma (a) and spiny structures on the sunflower pollen (d). (Reproduced from Lin et al. [18] with permission from Royal Society of Chemistry.) SEM images of the tip of a North American porcupine quill (b) and microstructures (barbs) on the tip (e). (Reproduced with permission from Cho et al. [104].) SEM images of stinger of honeybee (*Apis cerana cerana*) (c) and the tip of stinger and barbs near tip (f). (Reproduced with permission from Ling et al. [105].) Scale bars = 5  $\mu\text{m}$  (a), 100  $\mu\text{m}$  (b), 200  $\mu\text{m}$  (c), 500 nm (d), 20  $\mu\text{m}$  (e), and 10  $\mu\text{m}$  (f)

with pollenkitt) and stigma-mimetic polymer surfaces had more than doubled adhesive magnitude when compared to purified pollens. In addition, the selective interaction between pollens and stigmas from the same botanical families was also observed when liquid pollenkitt wetted the surfaces [18].

In nature, many animals and plants utilize spiny features to protect themselves from natural predators, and these features can produce adhesion by penetration into tissue. North American porcupines utilize micro-structured barbs (Fig. 8b, e) on the tip of their specialized quills [104]. The conical shape of the tip is covered by a layer of backward-facing micro-structured barbs, which are 100–120  $\mu\text{m}$  long and 35–45  $\mu\text{m}$  wide (Fig. 8e). Compared with barbless quills, structured quills required 54% less loading force to penetrate into tissue, but required about four times larger pull-out force to be detached from the tissue surface. This suggests that the high-stress concentration near the barbs reduces the required force to deform the tissue around the tip of the quill, and the enhanced adhesion is attributed to the mechanical interlocking between barbs and tissue [104]. Micro-structured barbs (Fig. 8c, f) are also observed from the stingers of honeybees and paper wasps [106]. Different shapes of barbs are observed from those two animals, and the shape and size of the barbs strongly affect the penetration, extraction and the repeatable usage of their stingers. Similar mechanical interlocking adhesion on tissue surfaces is also observed in spiny-headed worms, such as *Pomphorhynchus laevis* [107]. This endoparasitic worm utilizes a barbed proboscis, which is swollen after embedding into the soft tissue of its host, to create strong adhesion.

### 3.2 Bioadhesion on Rough Surfaces

It is well-known that surface roughness reduces adhesion between relatively dry surfaces because the actual contact area is strongly affected by the surface topography [51, 52]. To achieve close contact on a rough surface, two different types of adhesive pads, which are smooth and fibrillar in structure, are utilized by animals, as discussed in Sect. 3.1. However, the roughness adaptability efficiency of adhesive pads can differ significantly. For example, when the scale of the surface asperity of a rough surface is smaller than the dimensions of the spatulae of the fibrillar system, only partial contact formation between the spatula and the surface is achieved [77]. Additional energy (loading energy) is required to achieve a close contact between a smooth pad and rough surface because the deformation of the pad surface is needed, and the required energy becomes maximized at an intermediate level of surface roughness [108]. Therefore, the attachment ability of adhesive pads is strongly dependent on surface roughness as shown in Fig. 9, and attachment ability is dramatically reduced near a particular scale of roughness, called the critical roughness [77, 109, 110].

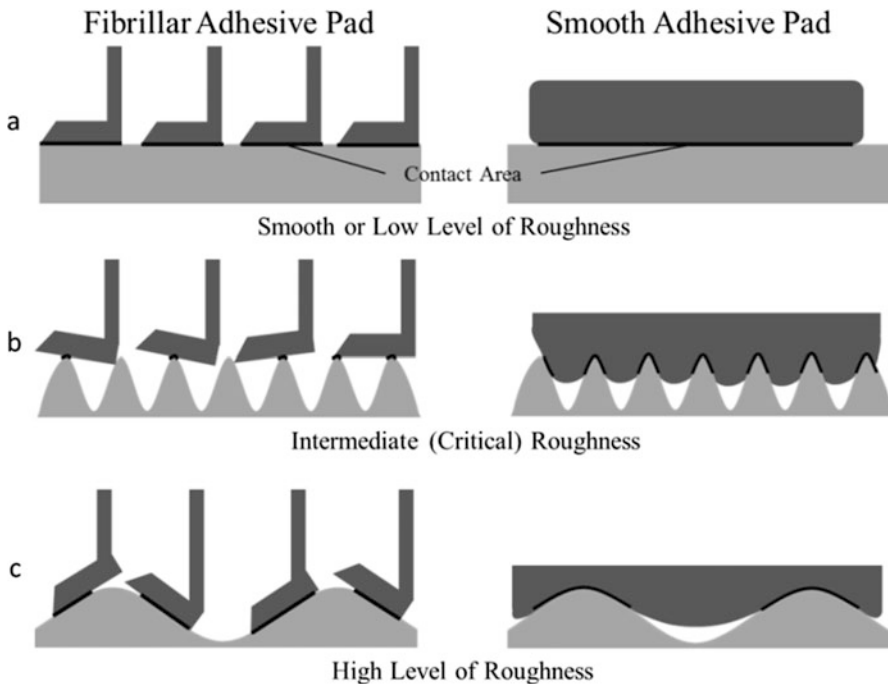


**Fig. 9** Diagram explaining the influence of surface roughness on the roughness adaptability of fibrillar and smooth adhesive systems. (a) Large contact area on a smooth surface. (b) Partial contact formation on surface with critical roughness. (c) Roughness adaptability on a surface with a high roughness

When fibrillar adhesive structure is utilized by animals such as geckos, spiders, flies, and beetles to generate strong adhesion on rough surfaces, the dimension of the fibrils is a crucial factor for creating surface adaptability. For example, the length of adhesive hairs should be sufficient to deform around large asperities and thin enough to accommodate fine-scale surface roughness [111]. In a previous study, the attachment ability of a single hair (seta) was investigated to study the influence of surface roughness on gecko adhesion [77]. The pull-off force of a single hair was measured as a function of the surface root mean square (RMS) roughness from 20 to 1,100 nm. The relationship between adhesion and RMS roughness resembled an inverted parabola, with a distinctive minimum between 100 and 300 nm RMS roughness. The diameter of a single spatula of the gecko’s adhesive pad is about 200 nm, and the surface adaptability of both a single spatula and the gecko itself was not efficient when surface roughness was close to the spatular dimension.

In experiments on the adhesion of other animals utilizing the fibrillar system, such as flies [112], beetles [111], and spiders [109], the critical roughness was investigated for substrates with an asperity size in the range 0.3–1  $\mu\text{m}$ . According to previous studies, the spatula dimensions of geckos (0.2  $\mu\text{m}$ ) and spiders (0.7  $\mu\text{m}$ ) are smaller than those of flies (1.8  $\mu\text{m}$ ) and beetles (6  $\mu\text{m}$ ). As shown in Fig. 10a, there is a greater reduction of adhesion forces when substrate roughness is below the critical roughness for animals utilizing larger contact-forming elements [109]. Conversely, the fibrillar systems with smaller spatulae create relatively stronger adhesion than the larger spatulae on a surface with roughness below the critical value.

The geometrical scale of surface morphology in nature varies by seven to nine orders of magnitude, and the attachment organs of many animals, such as nanoscale

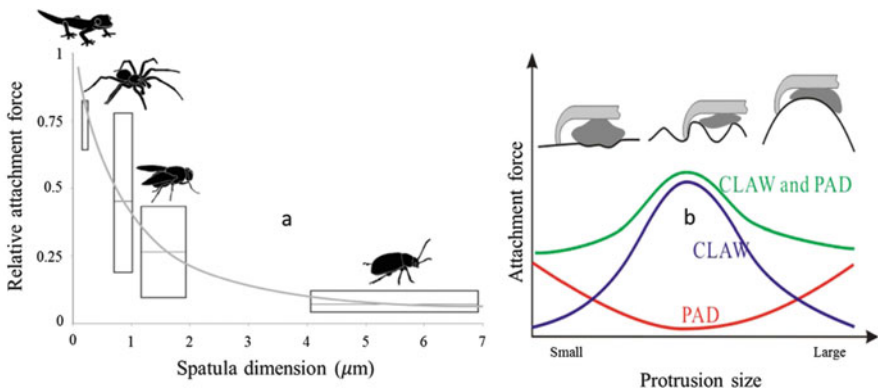


**Fig. 10** (a) Comparison of force reduction on the intermediate level of rough surface (surface asperity size, 0.3  $\mu\text{m}$ ) as a function of spatula dimension. The attachment forces are normalized to the measured force on smooth surface. (Reproduced with permission from Wolff et al. [109].) (b) Diagram explaining the contribution of adhesive pad and claw on the wide range of protrusion size. (Reproduced with permission from Song et al. [108])

spatulae and macroscopic claws, have been optimized to generate adhesion on a wide range of surface asperities [108]. Many insects utilize rigid claws to create strong mechanical interlocking on microscopic surface irregularities when they stand or move on rough surfaces [108, 110, 111]. They are able to take advantage of the surface irregularities and use them as anchorage when the surface roughness is larger or compatible to the size of their claw tips.

In a previous study, the detachment forces of dock beetles, *Gastrophysa viridula* (with fibrillar adhesive pads and intact claws) and the same beetles without claws (adhesive pads only) were investigated as a function of surface roughness [111]. On smooth substrates (roughness, 0.01–1  $\mu\text{m}$ ), clawless beetles produced nearly the same magnitude of adhesion as intact beetles, but intact beetles produced a significantly larger force on larger scale roughness (12–30  $\mu\text{m}$ ) than clawless beetles. Theoretically, the maximum attachment ability of the beetle's fibrillar pad should be achieved on the smoothest substrates (roughness = 0.01  $\mu\text{m}$ ), but the intact beetles generated much stronger adhesion on the substrates with larger scale roughness (>5  $\mu\text{m}$ ). This force enhancement indicates that claws become more efficient at adhesion than pads when the surface roughness is close to the dimension of the claw tip, a diameter of 2.6  $\mu\text{m}$ . The attachment ability of locusts (smooth adhesive pads with claws) also showed a similar response to surface roughness changes [110]. The measured attachment ability of the locust (critical roughness 1  $\mu\text{m}$ ) on rough surfaces (roughness > 5  $\mu\text{m}$ ) was stronger than on smooth surfaces, indicating that the contribution of the claws became significant when the surface roughness was greater than 5  $\mu\text{m}$ . However, a recent study showed that the attachment ability of claws decreases when the surface asperity is much larger than the size of claw tips (Fig. 10b) [108]. Thus, the synergistic effect between claws and adhesive pads may generate stronger adhesion on various surface roughnesses than the sum of claws and adhesive pads alone.

## 4 Anti-adhesive Surfaces

In this section we discuss how substrate surface topography of substrates can be manipulated to reduce bioadhesion. Several strategies for creating anti-adhesive or slippery surfaces via surface topography have been proposed: (1) reducing the real contact area by controlling surface topography [20, 110, 111, 113], (2) contamination of the adhesive pad by fracturing of highly fragile surfaces [114–117], (3) absorbing the adhesive secretions into structured substrates [89], and (4) infusing a lubricating liquid that becomes locked in place by special structures [36]. Strategies (1)–(3) are examples of reduced adhesion (defined as energy required to separate two surfaces by pulling normal to one another) and (4) is an example of a slippery surface (low shear resistance or low friction lateral to the surface) that still retains adhesive characteristics (normal forces).

It is well-known that surface topography strongly affects the real contact area between surfaces. Even though animals have adapted features to adhere to



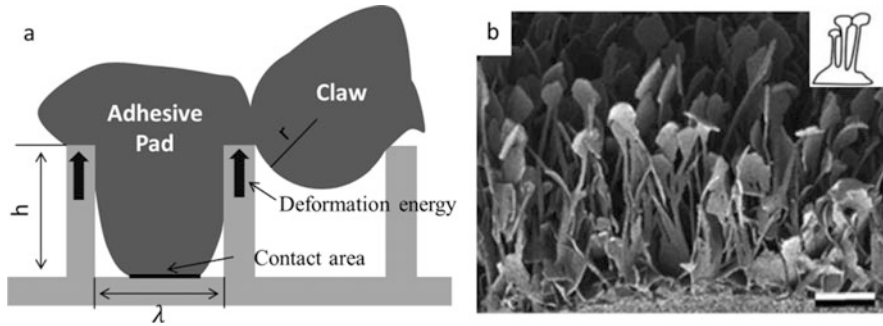


**Fig. 11** (a) Diagram explaining the adhesive model of an adhesive pad and a claw with mathematical simplicity as a flat surface with walls of negligible thickness and height ( $h$ ) which are spaced at a distance ( $\lambda$ ). (b) Cryo-SEM microscopy image of the slippery zone wax coverage of *N. alata* (upper and lower wax layers connected by thin stalk). Scale bar = 1  $\mu\text{m}$ . (Reproduced with permission from Gorb et al. [117])

structured surfaces, there is an opportunity to minimize adhesion by decreasing the feature size to achieve roughness below a critical value, a concept described in Sect. 3.2 [77, 109, 110]. In a previous study, the adhesion and deformation energy of adhesive pads and claws (with tip radius  $r$ ) on a structured surface were modeled, as shown in Fig. 11a [20]. Interestingly, the results showed a finite range of wall sizes ( $h$ ) and spacings ( $\lambda$ ) where the required deformation energy to achieve a close contact is comparable to the adhesion energy. This indicates that, in theory, low adhesion surfaces, to which it is difficult for insect pads and claws to remain attached, can be designed by controlling surface topography. However, animals have different sizes and shapes of adhesive pads and claws, and the critical roughness required for each adhesive system varies according to this structural diversity. For example, the critical roughness of the locust (arithmetic mean roughness  $R_a = 1.0\text{--}2.0\ \mu\text{m}$ ) is one or two orders of magnitude higher than for the beetle ( $R_a = 0.01\text{--}0.13\ \mu\text{m}$ ) [110, 111]. Recent studies show that the design of hierarchical surface roughness consisting of small scale critical roughness ( $R_a = 0.01\text{--}0.13\ \mu\text{m}$ ) distributed on features with larger scale critical roughness ( $R_a = 1.0\text{--}2.0\ \mu\text{m}$ ) can be used to create anti-adhesive surfaces for both locusts and beetles [113, 118]. This idea has been extended to the development of icephobic [23, 119, 120] and insect mitigation coatings [121, 122]. It has been proposed that ice adhesion on multi-textured surfaces may be reduced because of trapped air bubbles as well as delayed ice nucleation [122]. The regular raised riblets of biofouling-resistant shark skin have led to bioinspired pillar/ridge [123] and ‘wrinkled’ [24] surface structures that resist adherence of biofouling organisms. In addition to shark skin, the microtextured surfaces of mussels and crabs are known to resist adhesion of biofouling organisms, a topic that has been reviewed extensively [124–126]. Based on the aforementioned bioadhesion studies, future research in optimizing surface topography is warranted.

Insects utilize adhesive pads and claws to generate strong adhesion, and the contribution of the claws of insects can be eliminated by adding submicron surface morphology, as the dimension of many of insect claws is on the micron scale or larger. However, it is challenging to design a universal surface roughness to reduce the functionality of the insects' adhesive pads because, as previously mentioned, each adhesive pad has a different critical roughness. A solution to overcome this challenge, suggested by Gorb et al., is to reduce insect adhesion by 'structural contamination' [115]. If the surface asperities of a substrate can be designed to break off under the loading of the animal body mass, the pieces may remain adhered to the insect adhesive pad and undermine the effectiveness of those features on enhancing adhesion. This strategy is inspired by the surface structure of the anti-adhesive zone in a carnivorous plant (*Nepenthes*). In previous studies of insect locomotion on the slippery zone, insects with smooth or fibrillar adhesive pads were unable to move, or moved only very slowly, because of reduced contact area caused by surface contamination attributed to the bilayer wax structure [114, 116]. The surface of the anti-adhesion zone is covered with upper and lower wax layers, and the platelet shape of the upper layer is connected to the lower layer with thin and long stalks, as shown in Fig. 11b [117]. There are three expected topographical effects that could lead to the reduction of insect adhesion: (1) the perpendicular orientation of the upper platelets reduces the contact area of the insect [20], (2) the long and thin stalk can break off during locomotion [127], contaminating the adhesive pads [114], and (3) the mechanical interlocking function of the claw cannot function because of the platelet's small dimension and their fragile and brittle nature [116]. In a recent study, the bilayer wax surfaces showed much better anti-adhesive functionality than substrates with roughness similar to the single lower wax layer [116]. This result indicates that the combination of the sacrificial structural features, mimicking the contaminated pads, and critical roughness strategies can improve anti-adhesive functionality.

Insects utilize a liquid secretion to increase the effective contact area on a rough surface. A loss of adhesive function of the insect foot pad was observed when the liquid secretion on the pad was washed with organic solvent [128]. Physical models and previous experiments also suggested that excessive volumes of the adhesive secretion reduce attachment ability because of hydrodynamic lubrication [59, 88]. These studies indicated that the attachment ability of liquid-based bioadhesive systems can be reduced or eliminated if the structure of substrates can increase or reduce the volume of the liquid secretion between the pad and substrate. For example, the adhesion of ladybird beetles on a nanoporous substrate was measured [89], and a significant drop of the attachment ability was observed on the nanoporous substrate compared to the adhesion on a smooth substrate. The authors claimed that the beetle secretion was absorbed by the porous substrate, causing reduced adhesion. To work effectively, the absorption rate of the structure must be faster than the production and delivery rate of the liquid secretion. Alternatively, to increase the liquid volume between the adhesive pad and rough substrate, a surface coated with a lubricating liquid was suggested [129–131]. However, the liquid coating on the surface might easily flow away by low shear forces or

even gravitational force. Recently, inspired by the continuously-wetted textured ridges of the peristome of *N. alata*, synthetic liquid-infused porous surfaces (SLIPS) were developed to create a stable lubricant film and impart slipperiness to interfaces [22, 36]. Key factors in retaining the infused lubrication fluid were the nanometer- and micrometer-scale porous and textured structures of the substrate. The attachment ability of the carpenter ant was tested on the SLIPS wall (perpendicular to gravity), which showed reliable low-friction functionality [36], causing the insects to slide and fail to attach. SLIPS structures have also been shown to impart icephobic characteristics to interfaces [22]. Interestingly, SLIPS have been shown to have exceptional biofouling resistant properties as well [132].

## 5 Conclusion

In this chapter we have summarized the physical principles of roughness and surface feature effects on adhesion, starting with simple geometries (such as spherical and planar surfaces) and expanding to consider complex surface morphologies. Both dry and wet adhesive mechanisms have been considered. Although there are no universal, simple models that capture all adhesive mechanisms, surface topography has been recognized as the most critical factor in determining adhesive properties. The evolutionarily-adapted surface structures of animals and plants show how surface topography can be utilized to create functionalized adhesive properties. The bioadhesive mechanisms of many of these structured surfaces have been investigated in order to mimic their adhesive functionality. Based on these investigations, diverse applications, such as surfaces for water-repellency, oil-water separation, and water purification, as well as anti-icing, anti-corrosion, and anti-bacterial surfaces, have been proposed or developed [23, 36, 133–136]. Further studies of structural effects may suggest designs for anti-adhesive and anti-icing surfaces for eliminating the detrimental impacts of aerodynamic residues, such as insects and ice, on transportation industries and other contamination-mitigating surfaces for extreme environments.

## References

1. Shirtcliffe NJ, McHale G, Atherton S, Newton MI (2010) An introduction to superhydrophobicity. *Adv Colloid Interf Sci* 161:124–138. <https://doi.org/10.1016/j.cis.2009.11.001>
2. Lv J, Song Y, Jiang L, Wang J (2014) Bioinspired strategies for anti-icing. *ACS Nano* 8:3152–3169. <https://doi.org/10.1021/nn406522n>
3. Lee A, Moon MW, Lim H et al (2012) Water harvest via dewing. *Langmuir* 28:10183–10191. <https://doi.org/10.1021/la3013987>
4. Park K-C, Kim P, Grinthal A et al (2016) Condensation on slippery asymmetric bumps. *Nature* 531:78–82. <https://doi.org/10.1038/nature16956>

5. Gu ZZ, Uetsuka H, Takahashi K et al (2003) Structural color and the lotus effect. *Angew Chem Int Ed* 42:894–897. <https://doi.org/10.1002/anie.200390235>
6. Bechert DW, Bruse M, Hage W et al (1997) Experiments on drag-reducing surfaces and their optimization with an adjustable geometry. *J Fluid Mech* 338:59–87. <https://doi.org/10.1017/S0022112096004673>
7. Geim AK, Dubonos SV, Grigorieva IV et al (2003) Microfabricated adhesive mimicking gecko foot-hair. *Nat Mater* 2:461–463. <https://doi.org/10.1038/nmat917>
8. Hao P, Yao Z, Zhang X (2011) Study of dynamic hydrophobicity of micro-structured hydrophobic surfaces and lotus leaves. *Sci China Phys Mech Astron* 54:675–682. <https://doi.org/10.1007/s11433-011-4269-1>
9. Barthlott W, Neinhuis C (1997) Purity of the sacred lotus, or escape from contamination in biological surfaces. *Planta* 202:1–8. <https://doi.org/10.1007/s004250050096>
10. Parker AR, Lawrence CR (2001) Water capture by a desert beetle. *Nature* 414:33–34. <https://doi.org/10.1038/35102108>
11. Parker AR, Townley HE (2007) Biomimetics of photonic nanostructures. *Nat Nanotechnol* 2:347–353. <https://doi.org/10.1038/nnano.2007.152>
12. Luo Y, Liu Y, Anderson J et al (2015) Improvement of water-repellent and hydrodynamic drag reduction properties on bioinspired surface and exploring sharkskin effect mechanism. *Appl Phys A Mater Sci Process* 120:369–377. <https://doi.org/10.1007/s00339-015-9198-9>
13. Autumn K, Liang YA, Hsieh ST et al (2000) Adhesive force of a single gecko foot-hair. *Nature* 405:681–685
14. Federle W, Barnes WJP, Baumgartner W et al (2006) Wet but not slippery: boundary friction in tree frog adhesive toe pads. *J R Soc Interface* 3:689–697. <https://doi.org/10.1098/rsif.2006.0135>
15. Varenberg M, Pugno NM, Gorb SN (2010) Spatulate structures in biological fibrillar adhesion. *Soft Matter* 6:3269. <https://doi.org/10.1039/c003207g>
16. Spolenak R, Gorb S, Gao H, Arzt E (2005) Effects of contact shape on the scaling of biological attachments. *Proc R Soc A Math Phys Eng Sci* 461:305–319. <https://doi.org/10.1098/rspa.2004.1326>
17. Dirks JH, Li M, Kabla A, Federle W (2012) In vivo dynamics of the internal fibrous structure in smooth adhesive pads of insects. *Acta Biomater* 8:2730–2736. <https://doi.org/10.1016/j.actbio.2012.04.008>
18. Lin H, Qu Z, Meredith JC (2016) Pressure sensitive microparticle adhesion through biomimicry of the pollen-stigma interaction. *Soft Matter* 12:2965–2975. <https://doi.org/10.1039/C5SM02845K>
19. Edlund AF, Swanson R, Preuss D (2004) Pollen and stigma structure and function: the role of diversity in pollination. *Plant Cell* 16:S84–S97. <https://doi.org/10.1105/tpc.015800>
20. Scholz I, Bückins M, Dolge L et al (2010) Slippery surfaces of pitcher plants: nepenthes wax crystals minimize insect attachment via microscopic surface roughness. *J Exp Biol* 213:1115–1125. <https://doi.org/10.1242/jeb.035618>
21. Bauer U, Federle W (2009) The insect-trapping rim of nepenthes pitchers: surface structure and function. *Plant Signal Behav* 4:1019–1023. <https://doi.org/10.4161/psb.4.11.9664>
22. Kim P, Wong TS, Alvarenga J et al (2012) Liquid-infused nanostructured surfaces with extreme anti-ice and anti-frost performance. *ACS Nano* 6:6569–6577. <https://doi.org/10.1021/nm302310q>
23. Kreder MJ, Alvarenga J, Kim P, Aizenberg J (2016) Design of anti-icing surfaces: smooth, textured or slippery? *Nat Rev Mater* 1:15003. <https://doi.org/10.1038/natrevmats.2015.3>
24. Efimenko K, Finlay J, Callow ME et al (2009) Development and testing of hierarchically wrinkled coatings for marine antifouling. *ACS Appl Mater Interfaces* 1:1031–1040. <https://doi.org/10.1021/am9000562>
25. Hamaker HC (1937) The London—van der Waals attraction between spherical particles. *Physica* 4:1058–1072

26. Butt H-J, Kappl M (2009) Normal capillary forces. *Adv Colloid Interf Sci* 146:48–60. <https://doi.org/10.1016/j.cis.2008.10.002>
27. Mehrotra VP, Sastry KVS (1980) Pendular bond strength between unequal-sized spherical particles. *Powder Technol* 25:203–214. [https://doi.org/10.1016/0032-5910\(80\)87031-8](https://doi.org/10.1016/0032-5910(80)87031-8)
28. Gu Y, Li D (1999) The van der Waals interaction between a spherical particle and a cylinder. *J Colloid Interface Sci* 217:60–69. <https://doi.org/10.1006/jcis.1999.6349>
29. Hartmann U (1991) Van der Waals interactions between sharp probes and flat sample surfaces. *Phys Rev B* 43:2404–2407. <https://doi.org/10.1103/PhysRevB.43.2404>
30. Tselishchev YG, Val'tsifer VA (2003) Influence of the type of contact between particles joined by a liquid bridge on the capillary cohesive forces. *Colloid J* 65:385–389. <https://doi.org/10.1023/A:1024275327145>
31. Tadmor R (2001) The London-van der Waals interaction energy between objects of various geometries. *J Phys Condens Matter* 13:L195–L202. <https://doi.org/10.1088/0953-8984/13/9/101>
32. Majumder A, Sharma A, Ghatak A (2010) Bioinspired adhesion and adhesives: controlling adhesion by micro-nano structuring of soft surfaces. In: Chakraborty S (ed) *Microfluid. Microfabr.* Springer, New York, pp 283–307. [https://doi.org/10.1007/978-1-4419-1543-6\\_7](https://doi.org/10.1007/978-1-4419-1543-6_7)
33. Labonte D, Federle W (2015) Rate-dependence of “wet” biological adhesives and the function of the pad secretion in insects. *Soft Matter* 11:8661–8673. <https://doi.org/10.1039/C5SM01496D>
34. Jagota A, Hui CY (2011) Adhesion, friction, and compliance of biomimetic and bioinspired structured interfaces. *Mater Sci Eng R Rep* 72:253–292. <https://doi.org/10.1016/j.mser.2011.08.001>
35. Wohl CJ, Smith JG, Palmieri FL, Connell JW (2017) The physics of insect impact and residue expansion. *Adv Polym Sci* (in press)
36. Wong T-S, Kang SH, Tang SKY et al (2011) Bioinspired self-repairing slippery surfaces with pressure-stable omniphobicity. *Nature* 477:443–447. <https://doi.org/10.1038/nature10447>
37. Gorb SN (2008) Biological attachment devices: exploring nature’s diversity for biomimetics. *Philos Transact A Math Phys Eng Sci* 366:1557–1574. <https://doi.org/10.1098/rsta.2007.2172>
38. Gorb SN (2011) Biological fibrillar adhesives: functional principles and biomimetic applications. In: *Handb Adhes Technol*, pp 1409–1436. [https://doi.org/10.1007/978-3-642-01169-6\\_54](https://doi.org/10.1007/978-3-642-01169-6_54)
39. Derks D, Lindner A, Creton C, Bonn D (2003) Cohesive failure of thin layers of soft model adhesives under tension. *J Appl Phys* 93:1557–1566. <https://doi.org/10.1063/1.1533095>
40. Croll S (2002) DLVO theory applied to TiO<sub>2</sub> pigments and other materials in latex paints. *Prog Org Coat* 44:131–146. [https://doi.org/10.1016/S0300-9440\(01\)00261-2](https://doi.org/10.1016/S0300-9440(01)00261-2)
41. Lin L (2003) Mechanisms of pigment dispersion. *Pigm Resin Technol* 32:78–88. <https://doi.org/10.1108/03699420310464784>
42. Leite FL, Bueno CC, Da Róz AL et al (2012) Theoretical models for surface forces and adhesion and their measurement using atomic force microscopy. *Int J Mol Sci* 13(10):12773–12856. <https://doi.org/10.3390/ijms131012773>
43. Israelachvili JN (2010) *Intermolecular and surface forces*, 3rd edn. Academic Press, Cambridge, p 710. <https://doi.org/10.1016/B978-0-12-375182-9.10025-9>
44. Hertz H (1896) *Miscellaneous papers*. Macmillan, London
45. Johnson KL, Kendall K, Roberts AD (1971) Surface energy and the contact of elastic solids. *Proc R Soc A Math Phys Eng Sci* 324:301–313. <https://doi.org/10.1098/rspa.1971.0141>
46. Grierson DS, Flater EE, Carpick RW (2005) Accounting for the JKR-DMT transition in adhesion and friction measurements with atomic force microscopy. *J Adhes Sci Technol* 19:291–311. <https://doi.org/10.1163/1568561054352685>
47. Kamperman M, Kroner E, Del Campo A et al (2010) Functional adhesive surfaces with “Gecko” effect: the concept of contact splitting. *Adv Eng Mater* 12:335–348. <https://doi.org/10.1002/adem.201000104>

48. Derjaguin BV, Muller VM, Toporov YP (1975) Effect of contact deformations on the adhesion of particles. *J Colloid Interface Sci* 53:314–326. [https://doi.org/10.1016/0021-9797\(75\)90018-1](https://doi.org/10.1016/0021-9797(75)90018-1)
49. Götzinger M, Peukert W (2004) Particle adhesion force distributions on rough surfaces. *Langmuir* 20:5298–5303. <https://doi.org/10.1021/la049914f>
50. Rabinovich YI, Adler JJ, Ata A et al (2000) Adhesion between nanoscale rough surfaces. *J Colloid Interface Sci* 232:10–16. <https://doi.org/10.1006/jcis.2000.7167>
51. Fuller KNG, Tabor D (1975) The effect of surface roughness on the adhesion of elastic solids. *Proc R Soc A Math Phys Eng Sci* 345:327–342. <https://doi.org/10.1098/rspa.1975.0138>
52. Persson BNJ, Tosatti E (2001) The effect of surface roughness on the adhesion of elastic solids. *J Chem Phys* 115:5597–5610. <https://doi.org/10.1063/1.1398300>
53. Rumpf H (1974) Die Wissenschaft des agglomerierens. *Chem Ing Tech* 46:1–11. <https://doi.org/10.1002/cite.330460102>
54. Gao H, Yao H (2004) Shape insensitive optimal adhesion of nanoscale fibrillar structures. *Proc Natl Acad Sci U S A* 101:7851–7856. <https://doi.org/10.1073/pnas.0400757101>
55. Eichenlaub S, Kumar G, Beaudoin S (2006) A modeling approach to describe the adhesion of rough, asymmetric particles to surfaces. *J Colloid Interface Sci* 299:656–664. <https://doi.org/10.1016/j.jcis.2006.03.010>
56. Prokopovich P, Starov V (2011) Adhesion models: from single to multiple asperity contacts. *Adv Colloid Interf Sci* 168:210–222. <https://doi.org/10.1016/j.cis.2011.03.004>
57. Yu J, Chary S, Das S et al (2012) Friction and adhesion of gecko-inspired PDMS flaps on rough surfaces. *Langmuir* 28:11527–11534. <https://doi.org/10.1021/la301783q>
58. Cai S, Bhushan B (2007) Meniscus and viscous forces during normal separation of liquid-mediated contacts. *Nanotechnology* 18:465704. <https://doi.org/10.1088/0957-4484/18/46/465704>
59. Dirks JH, Federle W (2011) Fluid-based adhesion in insects – principles and challenges. *Soft Matter* 7:11047. <https://doi.org/10.1039/c1sm06269g>
60. Dirks JH (2014) Physical principles of fluid-mediated insect attachment-shouldn't insects slip? *Beilstein J Nanotechnol* 5:1160–1166. <https://doi.org/10.3762/bjnano.5.127>
61. Orr FM, Scriven LE, Rivas AP (1975) Pendular rings between solids: meniscus properties and capillary force. *J Fluid Mech* 67:723. <https://doi.org/10.1017/S0022112075000572>
62. Matthewson MJ (1988) Adhesion of spheres by thin liquid films. *Philos Mag A* 57:207–216. <https://doi.org/10.1080/01418618808204510>
63. Ata A, Rabinovich Y, Singh R (2002) Role of surface roughness in capillary adhesion. *J Adhes Sci Technol* 4243:37–41. <https://doi.org/10.1163/156856102760067145>
64. Willett CD, Adams MJ, Johnson SA, Seville JPK (2000) Capillary bridges between two spherical bodies. *Langmuir* 16:9396–9405. <https://doi.org/10.1021/la000657y>
65. Rabinovich YI, Esayanur MS, Moudgil BM (2005) Capillary forces between two spheres with a fixed volume liquid bridge: theory and experiment. *Langmuir* 21:10992–10997. <https://doi.org/10.1021/la0517639>
66. Bhushan B (2003) Adhesion and stiction: mechanisms, measurement techniques, and methods for reduction. *J Vac Sci Technol B Microelectron Nanom Struct* 21:2262. <https://doi.org/10.1116/1.1627336>
67. Lee T, Charrault E, Neto C (2014) Interfacial slip on rough, patterned and soft surfaces: a review of experiments and simulations. *Adv Colloid Interf Sci* 210:21–38. <https://doi.org/10.1016/j.cis.2014.02.015>
68. Mongruel A, Chastel T, Asmolov ES, Vinogradova OI (2013) Effective hydrodynamic boundary conditions for microtextured surfaces. *Phys Rev E Stat Nonlinear Soft Matter Phys* 87:1–4. <https://doi.org/10.1103/PhysRevE.87.011002>
69. Kunert C, Harting J, Vinogradova OI (2010) Random-roughness hydrodynamic boundary conditions. *Phys Rev Lett* 105:2–5. <https://doi.org/10.1103/PhysRevLett.105.016001>

70. Maali A, Pan Y, Bhushan B, Charlaix E (2012) Hydrodynamic drag-force measurement and slip length on microstructured surfaces. *Phys Rev E Stat Nonlinear Soft Matter Phys* 85:1–5. <https://doi.org/10.1103/PhysRevE.85.066310>
71. Vinogradova OI (1995) Drainage of a thin liquid film confined between hydrophobic surfaces. *Langmuir* 11:2213–2220. <https://doi.org/10.1021/la00006a059>
72. Pilkington GA, Gupta R, Fréchet J (2016) Scaling hydrodynamic boundary conditions of microstructured surfaces in the thin channel limit. *Langmuir* 32:2360–2368. <https://doi.org/10.1021/acs.langmuir.5b04134>
73. Nizkaya TV, Dubov AL, Mourran A, Vinogradova OI (2016) Probing effective slippage on superhydrophobic surfaces by atomic force microscopy. *Soft Matter* 12:6910–6917. <https://doi.org/10.1039/C6SM01074A>
74. Creton C, Gorb SN (2007) Sticky feet: from animals to materials. *MRS Bull* 32:466–472
75. Pacini E, Hesse M (2005) Pollenkitt - its composition, forms and functions. *Flora Morphol Distrib Funct Ecol Plants* 200:399–415. <https://doi.org/10.1016/j.flora.2005.02.006>
76. Lin H, Gomez I, Meredith JC (2013) Pollenkitt wetting mechanism enables species-specific tunable pollen adhesion. *Langmuir* 29:3012–3023
77. Huber G, Gorb SN, Hosoda N et al (2007) Influence of surface roughness on gecko adhesion. *Acta Biomater* 3:607–610. <https://doi.org/10.1016/j.actbio.2007.01.007>
78. Lake GJ, Thomas AG (1967) The strength of highly elastic materials. *Proc R Soc A Math Phys Eng Sci* 300:108–119. <https://doi.org/10.1098/rspa.1967.0160>
79. Arzt E, Gorb S, Spolenak R (2003) From micro to nano contacts in biological attachment devices. *Proc Natl Acad Sci U S A* 100:10603–10606. <https://doi.org/10.1073/pnas.1534701100>
80. Peattie AM, Full RJ (2007) Phylogenetic analysis of the scaling of wet and dry biological fibrillar adhesives. *Proc Natl Acad Sci* 104:18595–18600. <https://doi.org/10.1073/pnas.0707591104>
81. Labonte D, Clemente CJ, Dittrich A et al (2016) Extreme positive allometry of animal adhesive pads and the size limits of adhesion-based climbing. *Proc Natl Acad Sci* 113:201519459. <https://doi.org/10.1073/pnas.1519459113>
82. Autumn K, Sitti M, Liang YA et al (2002) Evidence for van der Waals adhesion in gecko setae. *Proc Natl Acad Sci U S A* 99:12252–12256. <https://doi.org/10.1073/pnas.192252799>
83. Bhushan B, Sayer RA (2007) Gecko feet: natural attachment systems for smart adhesion. In: *Appl Scanning Probe Methods VII*, pp 41–76. <https://doi.org/10.1007/11785705>
84. Gao H, Wang X, Yao H et al (2005) Mechanics of hierarchical adhesion structures of geckos. *Mech Mater* 37:275–285. <https://doi.org/10.1016/j.mechmat.2004.03.008>
85. Bullock JMR, Drechsler P, Federle W (2008) Comparison of smooth and hairy attachment pads in insects: friction, adhesion and mechanisms for direction-dependence. *J Exp Biol* 211:3333–3343. <https://doi.org/10.1242/jeb.020941>
86. Autumn K, Majidi C, Groff RE et al (2006) Effective elastic modulus of isolated gecko setal arrays. *J Exp Biol* 209:3558–3568. <https://doi.org/10.1242/jeb.02469>
87. Tian Y, Pesika N, Zeng H et al (2006) Adhesion and friction in gecko toe attachment and detachment. *Proc Natl Acad Sci U S A* 103:19320–19325. <https://doi.org/10.1073/pnas.0608841103>
88. Drechsler P, Federle W (2006) Biomechanics of smooth adhesive pads in insects: influence of tarsal secretion on attachment performance. *J Comp Physiol A Neuroethol Sens Neural Behav Physiol* 192:1213–1222. <https://doi.org/10.1007/s00359-006-0150-5>
89. Gorb EV, Hosoda N, Miksch C, Gorb SN (2010) Slippery pores: anti-adhesive effect of nanoporous substrates on the beetle attachment system. *J R Soc Interface* 7:1571–1579. <https://doi.org/10.1098/rsif.2010.0081>
90. De Souza EJ, Brinkmann M, Mohrdieck C, Arzt E (2008) Enhancement of capillary forces by multiple liquid bridges. *Langmuir* 24:8813–8820. <https://doi.org/10.1021/la8005376>
91. Su Y, Ji B, Huang Y, Hwang K (2007) Effects of contact shape on biological wet adhesion. *J Mater Sci* 42:8885–8893. <https://doi.org/10.1007/s10853-007-1759-7>

92. Gorb S, Varenberg M (2007) Mushroom-shaped geometry of contact elements in biological adhesive systems. *J Adhes Sci Technol* 21:1175–1183. <https://doi.org/10.1163/156856107782328317>
93. Barnes WJP (2007) Functional morphology and design constraints of smooth adhesive pads. *MRS Bull* 32:479–485. <https://doi.org/10.1557/mrs2007.81>
94. Barnes WJP, Goodwyn PJP, Nokhbatolfoghahai M, Gorb SN (2011) Elastic modulus of tree frog adhesive toe pads. *J Comp Physiol A Neuroethol Sens Neural Behav Physiol* 197:969–978. <https://doi.org/10.1007/s00359-011-0658-1>
95. Barnes WJP, Oines C, Smith JM (2006) Whole animal measurements of shear and adhesive forces in adult tree frogs: insights into underlying mechanisms of adhesion obtained from studying the effects of size and scale. *J Comp Physiol A Neuroethol Sens Neural Behav Physiol* 192:1179–1191. <https://doi.org/10.1007/s00359-006-0146-1>
96. Scholz I, Barnes WJP, Smith JM, Baumgartner W (2009) Ultrastructure and physical properties of an adhesive surface, the toe pad epithelium of the tree frog, *Litoria Caerulea* white. *J Exp Biol* 212:155–162. <https://doi.org/10.1242/jeb.019232>
97. Iturri J, Xue L, Kappl M et al (2015) Torrent frog-inspired adhesives: attachment to flooded surfaces. *Adv Funct Mater* 25:1499–1505. <https://doi.org/10.1002/adfm.201403751>
98. Endlein T, Barnes WJP, Samuel DS et al (2013) Sticking under wet conditions: the remarkable attachment abilities of the torrent frog, *Staurois Guttatus*. *PLoS One* 8(9):e73810. <https://doi.org/10.1371/journal.pone.0073810>
99. Dirks J-H, Clemente CJ, Federle W (2010) Insect tricks: two-phasic foot pad secretion prevents slipping. *J R Soc Interface* 7:587–593. <https://doi.org/10.1098/rsif.2009.0308>
100. Thio BJR, Lee JH, Meredith JC (2009) Characterization of ragweed pollen adhesion to polyamides and polystyrene using atomic force microscopy. *Environ Sci Technol* 43:4308–4313
101. Lin H, Lizarraga L, Bottomley LA, Meredith JC (2015) Effect of water absorption on pollen adhesion. *J Colloid Interface Sci* 442:133–139. <https://doi.org/10.1016/j.jcis.2014.11.065>
102. Zinkl GM, Zwiebel BI, Grier DG, Preuss D (1999) Pollen-stigma adhesion in *Arabidopsis*: a species-specific interaction mediated by lipophilic molecules in the pollen exine. *Development* 126:5431–5440
103. Luu DT, Passelègue E, Dumas C, Heizmann P (1998) Pollen-stigma capture is not species discriminant within the Brassicaceae Family. *C R Acad Sci III* 321:747–755. [https://doi.org/10.1016/S0764-4469\(98\)80015-2](https://doi.org/10.1016/S0764-4469(98)80015-2)
104. Cho WK, Ankrum JA, Guo D et al (2012) Microstructured barbs on the north American porcupine quill enable easy tissue penetration and difficult removal. *Proc Natl Acad Sci U S A* 109:21289–21294. <https://doi.org/10.1073/pnas.1216441109>
105. Ling J, Jiang L, Chen K et al (2016) Insertion and pull behavior of worker honeybee stinger. *J Bionic Eng* 13:303–311. [https://doi.org/10.1016/S1672-6529\(16\)60303-7](https://doi.org/10.1016/S1672-6529(16)60303-7)
106. Zhao Z-L, Zhao H-P, Ma G-J et al (2015) Structures, properties, and functions of the stings of honey bees and paper wasps: a comparative study. *Biol Open* 4:921–928. <https://doi.org/10.1242/bio.012195>
107. Yang SY, O’Cearbhaill ED, Sisk GC et al (2013) A bioinspired swellable microneedle adhesive for mechanical interlocking with tissue. *Nat Commun* 4:1702. <https://doi.org/10.1038/ncomms2715>
108. Song Y, Dai Z, Wang Z et al (2016) The synergy between the insect-inspired claws and adhesive pads increases the attachment ability on various rough surfaces. *Sci Rep* 6:26219. <https://doi.org/10.1038/srep26219>
109. Wolff JO, Gorb SN (2012) Surface roughness effects on attachment ability of the spider *Philodromus Dispar* (Araneae, Philodromidae). *J Exp Biol* 215:179–184. <https://doi.org/10.1242/jeb.061507>
110. Wang L, Johannesson CM, Zhou Q (2015) Effect of surface roughness on attachment ability of locust *Locusta migratoria manilensis*. *Wear* 332:694–701. <https://doi.org/10.1016/j.wear.2015.02.036>



111. Bullock JMR, Federle W (2011) The effect of surface roughness on claw and adhesive hair performance in the dock beetle *Gastrophysa viridula*. *Insect Sci* 18:298–304. <https://doi.org/10.1111/j.1744-7917.2010.01369.x>
112. Peressadko AG, Gorb SN (2004) Surface profile and friction force generated by insects. In: *First Int Ind Conf Bionik 2004*, pp 257–261
113. Prüm B, Florian Bohn H, Seidel R et al (2013) Plant surfaces with cuticular folds and their replicas: influence of microstructuring and surface chemistry on the attachment of a leaf beetle. *Acta Biomater* 9:6360–6368. <https://doi.org/10.1016/j.actbio.2013.01.030>
114. Gaume L, Perret P, Gorb E et al (2004) How do plant waxes cause flies to slide? Experimental tests of wax-based trapping mechanisms in three pitfall carnivorous plants. *Arthropod Struct Dev* 33:103–111. <https://doi.org/10.1016/j.asd.2003.11.005>
115. Gorb E, Haas K, Henrich A et al (2005) Composite structure of the crystalline epicuticular wax layer of the slippery zone in the pitchers of the carnivorous plant *Nepenthes alata* and its effect on insect attachment. *J Exp Biol* 208:4651–4662. <https://doi.org/10.1242/jeb.01939>
116. Gorb EV, Purtov J, Gorb SN (2014) Adhesion force measurements on the two wax layers of the waxy zone in *Nepenthes alata* pitchers. *Sci Rep* 4:5154. <https://doi.org/10.1038/srep05154>
117. Gorb EV, Baum MJ, Gorb SN (2013) Development and regeneration ability of the wax coverage in *Nepenthes alata* pitchers: a cryo-SEM approach. *Sci Rep* 3:3078. <https://doi.org/10.1038/srep03078>
118. Eichler-Volf A, Kovalev A, Wedeking T et al (2016) Bioinspired monolithic polymer microsphere arrays as generically anti-adhesive surfaces. *Bioinspir Biomim* 11:25002. <https://doi.org/10.1088/1748-3190/11/2/025002>
119. Varanasi KK, Deng T, Smith JD et al (2010) Frost formation and ice adhesion on superhydrophobic surfaces. *Appl Phys Lett* 97:234102. <https://doi.org/10.1063/1.3524513>
120. Schutzius TM, Jung S, Maitra T et al (2015) Physics of icing and rational design of surfaces with extraordinary icephobicity. *Langmuir* 31:4807–4821. <https://doi.org/10.1021/la502586a>
121. Wohl CJ, Smith JG, Penner RK et al (2013) Evaluation of commercially available materials to mitigate insect residue adhesion on wing leading edge surfaces. *Prog Org Coat* 76:42–50. <https://doi.org/10.1016/j.porgcoat.2012.08.009>
122. Krishnan KG, Milonias A, Loth E et al (2017) Influence of hydrophobic and superhydrophobic surfaces on reducing aerodynamic insect residues. *Appl Surf Sci* 392:723–731. <https://doi.org/10.1016/j.apsusc.2016.09.096>
123. Carman ML, Estes TG, Feinberg AW et al (2006) Engineered antifouling microtopographies - correlating wettability with cell attachment. *Biofouling* 22:11–21. <https://doi.org/10.1080/08927010500484854>
124. Genzer J, Efimenko K (2006) Recent developments in superhydrophobic surfaces and their relevance to marine fouling: a review. *Biofouling* 22:339–360. <https://doi.org/10.1080/08927010600980223>
125. Scardino AJ, de Nys R (2011) Mini review: biomimetic models and bioinspired surfaces for fouling control. *Biofouling* 27:73–86. <https://doi.org/10.1080/08927014.2010.536837>
126. Magin CM, Cooper SP, Brennan AB (2010) Non-toxic antifouling strategies. *Mater Today* 13:36–44. [https://doi.org/10.1016/S1369-7021\(10\)70058-4](https://doi.org/10.1016/S1369-7021(10)70058-4)
127. Borodich FM, Gorb EV, Gorb SN (2010) Fracture behaviour of plant epicuticular wax crystals and its role in preventing insect attachment: a theoretical approach. *Appl Phys A Mater Sci Process* 100:63–71. <https://doi.org/10.1007/s00339-010-5794-x>
128. Edwards JS, Tarkanian M (1970) The adhesive pads of Heteroptera: a re-examination. *Proc R Entomol Soc Lond A Gen Entomol* 45:1–5
129. Bauer U, Federle W, Seidel H et al (2015) How to catch more prey with less effective traps: explaining the evolution of temporarily inactive traps in carnivorous pitcher plants. *Proc Biol Sci* 282:20142675. <https://doi.org/10.1098/rspb.2014.2675>

130. Bauer U, Bohn HF, Federle W (2008) Harmless nectar source or deadly trap: nepenthes pitchers are activated by rain, condensation and nectar. *Proc Biol Sci* 275:259–265. <https://doi.org/10.1098/rspb.2007.1402>
131. Bohn HF, Federle W (2004) Insect aquaplaning: nepenthes pitcher plants capture prey with the peristome, a fully wettable water-lubricated anisotropic surface. *Proc Natl Acad Sci U S A* 101:14138–14143. <https://doi.org/10.1073/pnas.0405885101>
132. Epstein AK, Wong T-S, Belisle RA et al (2012) Liquid-infused structured surfaces with exceptional anti-biofouling performance. *Proc Natl Acad Sci U S A* 109:13182–13187. <https://doi.org/10.1073/pnas.1201973109>
133. Darmanin T, Guittard F (2013) Recent advances in the potential applications of bioinspired superhydrophobic materials. *R Soc Chem* 0:1–3. <https://doi.org/10.1039/C4TA02071E>
134. Sun X, Damle VG, Liu S, Rykaczewski K (2015) Bioinspired stimuli-responsive and antifreeze-secreting anti-icing coatings. *Adv Mater Interfaces* 2:25–27. <https://doi.org/10.1002/admi.201400479>
135. Bhushan B (2012) Bioinspired structured surfaces. *Langmuir* 28:1698–1714. <https://doi.org/10.1021/la2043729>
136. Ivanova EP, Hasan J, Webb HK et al (2013) Bactericidal activity of black silicon. *Nat Commun* 4:2838. <https://doi.org/10.1038/ncomms3838>

**Part II**  
**Ice Contamination-Mitigating Coatings**

# Use of Liquid Ad(ab)sorbing Surfaces for Anti-icing Applications



H. Yildirim Erbil

**Abstract** Aizenberg and co-workers developed slippery liquid-infused porous surfaces (SLIPS) where a textured solid was infused with an immiscible perfluorinated lubricant with low surface free energy to create a smooth liquid over layer. The lubricant was selected to minimize ice nucleation and ice adhesion strength. Many slippery surfaces using various lubricating fluids (perfluorinated, silicone oil, hydrocarbon, and water) have been produced in the last 5 years. As the possible interactions between the lubricant and the patterned or porous solid structure would be adsorption or absorption in scientific terms, in this work the terminology commonly used to describe these systems, “infuse (or impregnate),” is replaced by defining these materials as “liquid ad(ab)sorbing surfaces” (LAAS) instead. In this review, initial discussion is on two main conditions to form ice on surfaces, that is, ice formation from impinging supercooled droplets and frost formation from atmospheric humidity. This is followed by a summary of the synthesis and properties of flat low surface energy and superhydrophobic anti-icing surfaces, the basic reference surfaces used in passive anti-icing. Then the synthesis and anti-icing performances of LAAS are reviewed in three subtopics, depending on the lubricant used in their preparation such as fluorinated lubricants, silicone liquids, and hydrophilic liquids. The factors affecting ice adhesion strength are discussed and the importance of ice accretion experiments is highlighted. The need for standardization of both measurements is stressed in order to compare the results reported from different laboratories. Finally, some promising approaches are recommended for future research such as the use of LAAS in combination with traditional anti-icing and deicing techniques, superhydrophobic surfaces, or Joule heating systems to decrease the amount of electrical energy supplied.

---

H. Yildirim Erbil (✉)

Department of Chemical Engineering, Gebze Technical University, Gebze, Kocaeli, Turkey  
e-mail: [yerbil@gtu.edu.tr](mailto:yerbil@gtu.edu.tr)

**Keywords** Anti-icing • Drop freezing time • Ice accretion • Ice adhesion • Icephobic • Liquid-impregnated surfaces • LIS • Slippery liquid-infused porous surfaces • SLIPS

## Contents

1	Introduction .....	54
2	Ice Formation from Impinging Super-Cooled Droplets .....	56
3	Frost Formation from Atmospheric Humidity .....	58
4	Types and Properties of Anti-icing Surfaces .....	59
	4.1 Flat Anti-icing Surfaces with Low Surface Free Energy .....	59
	4.2 Superhydrophobic Anti-Icing Surfaces .....	61
5	Slippery Liquid Ad(ab)sorbing Surfaces .....	62
	5.1 Surfaces Formed with Fluorinated Lubricants .....	63
	5.2 Surfaces Formed with Silicone Liquids .....	76
	5.3 Surfaces Formed with Hydrophilic Liquids .....	80
6	Factors Affecting Ice Adhesion Strength and Its Standardization .....	87
7	Standardization of Ice Accretion Experiments .....	89
8	Concluding Remarks and Perspective .....	90
	References .....	92

## 1 Introduction

Passive anti-icing methods [1, 2] are very important in everyday life and also in industry, because icing on surfaces causes the breakdown of many systems, such as aircraft [3], wind turbines [4–6], power lines [7], offshore platforms [8], photovoltaic devices [9], cars, trains, and ships, which results in large economic and human losses. In general, methods to prevent ice accretion or to remove ice after it forms on a surface can be classified into two main categories: active and passive. In “active” anti-icing systems, which are currently widely used, thermal, mechanical, or pneumatic energy is supplied from beneath or outside of a surface to decrease ice accretion or remove ice after it has been deposited. Active methods include mechanical scraping and applying de-icing fluids. However, many of these methods are time- and energy-consuming, expensive because of the high energy requirements, and entail a risk of faulty applications, which can damage the existing infrastructure [1, 2, 6, 10–12].

To develop “passive” anti-icing methods, where no external energy is supplied, intensive research efforts have been made to synthesize and understand surfaces with icephobic (ice-repellent) properties to prevent ice from adhering to them or to allow ice to be easily delaminated afterward by natural airflows or solar radiation. Many extensive reviews have been published on these subjects [1–7, 13–16]. Unfortunately, passive methods have found few industrial applications because of their limited success in rapidly shedding impacting supercooled water droplets or condensing water droplets from the atmosphere, preventing ice nucleation, and minimizing ice adhesion with enough longevity and durability, especially in sub-zero environments with high humidity. Currently, no known surface coating can

completely prevent ice or snow from accumulating on a surface [1, 2, 9, 14], and the complex nature of icing creates many challenges in synthesizing icephobic coatings. Some details of the strategies to develop passive icephobic surfaces that can reduce the amount of accreted ice, delay the freezing time of impacting droplets, and reduce the ice adhesion strength on a surface are examined in Sects. 2–7. Problems also occur with the standardization of anti-icing tests, as described in Sects. 2, 3, 6, and 7, partly because of the complexity of these measurements and partly because of large differences in the test systems built and used by the various groups working on icephobic surfaces throughout the world [1, 2, 14, 17].

Historically, smooth surfaces were thought to be the best candidates on which to minimize ice adhesion. Smooth polydimethylsiloxane (PDMS) copolymers [18] or polytetrafluoroethylene (PTFE) [19] surfaces with low surface energy have been used for this purpose since the 1970s. However, mechanical weakness of these surfaces was a major concern. Repeated icing-shear removal cycles and freeze-thaw cycles on these surfaces were shown to increase the ice adhesion strength significantly and cause damage to them. This subject is discussed in Sect. 4.1.

Synthetic superhydrophobic surfaces (SHSs) were first developed in the 1990s. They exhibit water contact angles greater than  $150^\circ$ , and water droplets roll off readily from these surfaces at a tilt angle of less than  $10^\circ$  at room temperature conditions [20, 21]. They can be formed when extensive micro- and/or nanoscale roughness on a hydrophobic material is created or a previously micro/nano-structured surface is coated with a hydrophobic material with a low surface energy [1, 2, 14, 20, 21]. Starting in 2009, SHSs were proposed to prevent ice formation by means of rapidly sliding or bouncing water droplets off before they freeze [22–35]. However, it was later shown that superhydrophobicity, by itself, is not useful in anti-icing applications as this property is lost, especially in high humidity and sub-zero conditions. Moisture condenses inside the rough structure of an SHS over time under high humidity conditions, and cold water droplets grow and coalesce rapidly to form an ice layer on this surface [9, 13, 14, 23, 36–43]. Ice adhesion strength increases when ice penetrates into the texture of an SHS and superhydrophobicity can be destroyed in de-icing/icing cycles. This subject is discussed in Sect. 4.2.

Inspired by the insect-eating *Nepenthes* pitcher plants, a method for creating slippery liquid-infused porous surfaces (SLIPS) was developed in 2011 by Aizenberg and co-workers [44]. In this method, a textured solid is infused with an immiscible lubricant with low surface free energy to create a smooth liquid overlayer. The lubricant is selected to minimize ice nucleation, ice accretion, and ice adhesion strength, and to impart other useful properties. Many slippery surfaces similar to SLIPS using various lubricating fluids were produced for anti-icing applications after 2012, and are described as “liquid-impregnated surfaces” (LISs) in some papers [45–65]. The manufacture, properties, and successes of LISs on anti-icing tests are discussed in detail in Sect. 5.

However, a problem exists with the terminology of using the words “to infuse” in SLIPS according to current scientific terminology. In general, “to infuse a liquid” means to pour in (or imbibe) gradually a liquid into a specific volume, but it is

unclear how this liquid is kept in this volume without being drained or evaporated for a definite time suitable for a practical application. If a porous structure such as a sponge is used for the specific three-dimensional (3D) material to be infused with the lubricant (similar to the original SLIPS publication [44]), then the possible interactions between the lubricant and the porous structure would be adsorption or absorption. Instead of the word “infusion,” the well-known scientific terms “absorption” [66, 67] and “adsorption” [68] can both be used analogous to their use in liquid/sponge studies. The quantity of liquid absorption inside a 3D structure per mass of solid, or the amount of liquid adsorption on the surface of the pores of a 3D structure, can be reported when absorption and/or adsorption terminology is used. Unfortunately, these quantities were not given in most of the SLIPS or LIS synthesis papers and anti-icing characterization reports. The use of “liquid ad(ab)sorbing surfaces” (LAASs), instead of “liquid-infused surfaces” or LISs, is a better description of such systems in current scientific terminology.

In summary, this review focuses mostly on the synthesis and properties of LAASs and also highlights the importance of laboratory-scale ice accretion tests. Because LAASs have not yet been tested extensively in icing wind tunnels, no dynamic anti-icing results are presented. The content of this review is different from recent reviews that broadly describe the subject of designing smooth, textured, and slippery anti-icing surfaces [1] and compare the results of low surface energy and LISs [16].

## 2 Ice Formation from Impinging Super-Cooled Droplets

Icing problems on surfaces arise from the solidification of supercooled water droplets on substrates. If no supercooled water droplets are present in an outdoor medium, accumulations (for example, from when snow (ice crystals), sleet (frozen ice pellets), and hail (balls or irregular lumps of ice) precipitate onto surfaces) do not pose important safety risks for transportation craft such as ships and aircraft. Without melting and refreezing, the snow, sleet, or hail can easily be removed from the surface through air motion [69]. Conversely, the formation of glaze and hard and soft rime from supercooled droplets is a very important problem in industry and daily life. Supercooled water droplets are in a metastable state and solidify in an irreversible process when impacting a surface, usually with heterogeneous nucleation at the water–solid interface, because the protrusions on the substrate reduce the activation energy to form crystal nuclei in the droplet, which grow irreversibly into ice [70]. “Freezing rain” comprises large drops of liquid water, with diameters ranging from 70  $\mu\text{m}$  to a few millimeters, that fall when surface temperatures are below freezing. Freezing rain is made entirely of liquid droplets that become supercooled when passing through a freezing layer of air, and then freeze upon impact with any surface. It forms “glaze” (wet ice) when it accumulates on the surfaces at temperatures below zero. Glaze is a transparent, clear, dense, and hard ice with a density of 800–900  $\text{kg/m}^3$  [69, 71]. Its density is less than that of pure ice,

which has a density of  $917 \text{ kg/m}^3$ . Glaze formation on surfaces adversely and strongly affects aircraft, ships, transmission lines, and many other types of infrastructure.

When small supercooled water droplets ( $5\text{--}20 \text{ }\mu\text{m}$ ) accrete on surfaces at high wind velocities and air temperatures between  $-2$  and  $-8^\circ\text{C}$ , “rime” (dry ice) forms on these surfaces. “Ice accretion” is a kind of crystal growth process occurring when supercooled droplets and snow crystals make contact with each other, leading to the freezing of the liquid droplets onto the surface of the crystals. There are two types of rime, “hard” and “soft.” Hard rime is less transparent than glaze because of the air trapped in it and has a density of  $600\text{--}900 \text{ kg/m}^3$ . Soft rime is feathery, milky, crystalline, and granular, with a white/opaque color and a density less than  $600 \text{ kg/m}^3$  [69]. The size and temperature of supercooled droplets, substrate surface temperature, wind speed, impact velocity of droplet, and liquid water content per unit volume of air are the most important parameters designating the type of icing. In general, the increase in drop size, wind speed, impact velocity, liquid water content per unit volume of air, and decrease in droplet temperature result in an increase in ice density up to  $900\text{--}917 \text{ kg/m}^3$  [72].

The ice accretion mechanism is explained as follows: Supercooled droplets do not freeze instantly when they impact a surface. Only part of the droplets freeze, and the remaining liquid flows onto the substrate as a film and forms a larger icing ridge when completely frozen. This frost layer changes the surface properties of the original solid, because any hydrophobic surface exhibits hydrophilicity after being coated with a thin frost layer. On the other hand, the ice accretion rate depends on the removal of the latent heat released during freezing by local heat transfer on the surface because of convective cooling and evaporative cooling. In some cases, a thin water condensate film forms on the surface when the relative humidity (RH) of the air is high. Once the super-saturation conditions are achieved, frost formation is unavoidable on all surfaces [36].

The determination of ice accretion in mass per unit area on test surfaces is an important parameter in evaluating the anti-icing performance of a surface [6, 10–12, 23, 26, 65, 69, 73–83]. The minimization (or complete prevention) of ice accretion on a sample surface is the most significant test for the success of an anti-icing coating [17]. Unfortunately, only a few papers have reported ice accretion results on surfaces [65, 69, 73–76, 78, 79, 81]. Only photographs have been given in most of these publications to compare the relative ice or snow accumulation on different surfaces under different test conditions [10, 23, 26, 77, 80, 83]. This is probably because of the high cost of the laboratory setups used for ice accretion tests which has hampered some researchers carrying out these experiments. However, the lack of ice accretion results on test surfaces causes confusion and also the false evaluation of the success of the synthesized anti-icing surfaces. Unfortunately, no ice accretion result of any large area slippery LAAS has been reported in mass/area units in any publication except for the results reported by Ozbay et al. [65]. Most of the papers on LAAS have presented icing delay times or ice adhesion strength values after ice formation [44–64]. Standardization of ice accretion experiments is required for better comparison of the results obtained from different laboratories [17, 84, 85]. This subject is discussed in Sect. 7.



### 3 Frost Formation from Atmospheric Humidity

Ice can accumulate on surfaces through either homogeneous or heterogeneous nucleation mechanisms from the vapor phase. In the “homogeneous nucleation” mechanism, a crystallite, which is a germ of ice, is formed by the continuous movement of molecules caused by thermal fluctuations in the liquid during cooling. However, most of the crystallites thus formed then dissolve back into the liquid. A large enough crystallite size is required to form the critical nucleus, which can turn rapidly into ice. In reality, the homogeneous nucleation process is difficult to take place and may take a long time because of the energy barrier caused by the surface tension of the surrounding liquid preventing favorable interactions between molecules to form the crystalline arrangement of ice [72].

“Heterogeneous nucleation” of ice on surfaces, however, can readily occur when a seed such as another ice crystal, solid particle, dust, or solid surface is in contact with a supercooled droplet. These roughness asperities already present or formed by the seed on a substrate reduce the barrier of the activation energy. Ice formation with heterogeneous nucleation happens in two subsequent phases. In the first phase, the liquid solidifies in the form of a dendritic structure accompanied by the release of latent heat. Only part of the supercooled liquid freezes in the order of milliseconds, that is, just enough to warm up the mixture of solid as latent heat is released. After the first phase, the remaining liquid freezes isothermally at the melting temperature if further heat is conducted away from the mixture in the order of seconds [70]. Nucleation from the vapor phase via desublimation or liquid condensation [86, 87] followed by freezing leads to formation of frost, which consists of sparse dendritic crystal structures that become denser with time. The supplied large surface area and confinement because of the presence of microstructures increase the rate of droplet condensation on SHSs, especially in high RH conditions [1, 14]. When moisture condenses inside the rough structure of a SHS under high humidity conditions, water droplets coalesce rapidly to form an ice layer on the surface [13, 23, 36–43]. Surfaces with dense nanoscale topography result in a better resistance toward condensation-induced wetting with longer freezing times [29, 88, 89]. This may be because of the same mechanisms responsible for the delayed ice nucleation of sessile droplets on hydrophobic nanostructures [22, 90]. Thus, it is important to measure properly the freeze delay time of droplets [14, 22, 27, 29, 30, 32, 42, 43, 91–96].

Drop freezing time measurements are usually carried out by visual inspection of the color of the droplet. Initially, all the water droplets are transparent on the surfaces. After a time, water droplets lose their transparency and become translucent/white upon freezing. However, there are many problems with the determination of drop freezing times. The temperature of the liquid water droplets should be precisely measured and monitored by using thin thermocouple probes. It should be taken into account that the temperature of the droplets takes a finite amount of time to reach the temperature of the cold climatic chamber and thus measurement conditions are usually non-equilibrium. When pure water is used in these

experiments, poor reproducibility is generally obtained because the start of freezing depends on the spontaneous formation of the first ice nucleus and the time of this process is mostly stochastic. Some researchers have used tap water with a dilute salt content instead of pure water to obtain repeatable icing time measurement values [17, 91] and some others vibrate the thermocouple wire to disturb the droplet and initiate spontaneous icing. The temperature and RH in the chamber should be precisely controlled as well as the initial temperature of the droplet (the temperature of water in the syringe) and this data should be reported in order to achieve reasonable comparisons between independent ice delay times. When Peltier elements are used to cool the surface in a room environment for droplet icing time tests, the results are far from those obtained in natural outdoor icing conditions where no temperature gradient is present between the drop–air interface and air. In addition, the temperature difference between the drop/solid (Peltier stage) interface and drop–air interface is sometimes much larger than in natural conditions, where all the materials are closer to thermal equilibrium. Thus such Peltier stage drop cooling time results are not reliable for comparison with the results obtained in a closed chamber or outdoor conditions.

There were some drop freezing time reports for the slippery LAAS, and the long drop freeze times and low surface coverage by frost were attributed to a reduction in the number of potential nucleation sites [48]. For example, only 20% of the surface of a lubricant absorbed surface was covered by frost in 80 min under frosting conditions, which is approximately four times better than a SHS [45, 97].

## 4 Types and Properties of Anti-icing Surfaces

Classifying anti-icing (or icephobic) surfaces according to their various properties is possible, as can be seen in many review articles [1, 2, 5–9, 14, 16]. In these reviews, icephobic surfaces are classified according to different approaches, including material surface properties, delaying droplet freezing time, preventing frost formation, lowering the ice adhesion strength, and by mechanism used to obtain icephobicity. However, here we classify them into three main categories according to their synthesis methods: (1) flat anti-icing surfaces with low surface free energy, (2) superhydrophobic anti-icing surfaces, and (3) slippery LAAS. Only a summary is given in the text for the first two items in Sects. 4.1 and 4.2, respectively (and only some important references are cited), as the main objective is to discuss the slippery LAAS, which is done in Sect. 5.

### 4.1 Flat Anti-icing Surfaces with Low Surface Free Energy

In early anti-icing studies, smooth surfaces with low surface free energy (less than  $30 \text{ mJ/m}^2$ ) were used to minimize both the ice accretion and its adhesion to a

surface. However, only limited success was achieved in decreasing ice adhesion and it seems unlikely that ice accretion minimization was achieved [18, 19, 98–100]. It has been suggested that smooth surfaces minimize heterogeneous nucleation of ice [70]. In practice, smooth anti-icing surfaces were successful in reducing ice adhesion strength in the laboratory when surfaces with low surface free energies were used. However, only limited success was achieved in industrial applications because of their poor ice accretion performances in outdoor conditions and also because of their low mechanical durability [18, 19].

Meuler et al. [100] derived a relationship between the equilibrium and receding contact angles of water on a surface and the ice adhesion strength of the surface. Hydrogen bonding, polar, van der Waals forces, and electrostatic interactions are the main physical mechanisms responsible for ice adhesion onto a surface [9, 14]. Contact angles and wettability of a surface are dependent on molecular interactions [101]. Correspondingly, the wettability of a surface was proposed to be an important parameter in choosing the type of coating material to reduce the ice adhesion strength on a surface [17, 19, 73, 74, 100, 102–104]. Flat fluoropolymers which give very high water contact angles up to  $120^\circ$  were tested as anti-icing surfaces [19, 28, 35, 74, 99, 105]. Yang et al. [74], who used smooth fluoropolymer surfaces in their studies, reported that these could significantly reduce ice adhesion strength, but did not show any important effect in reducing ice accretion on them at  $-8^\circ\text{C}$ . Silicone-containing polymers, which also gave high water contact angles, were tested for anti-icing applications because of their low surface free energy and low glass transition temperature,  $T_g$ , giving flexible chains. However, until recently, only limited success was obtained because of the low mechanical resistance of silicone polymers [18, 28, 106–108].

In 2015, cross-linked PDMS gels with good mechanical properties were synthesized and resulted in very low ice adhesion strength down to 5 kPa [109, 110]. It is well-known that low work of adhesion, low shear modulus (obtained by soft materials), and high thickness leads to lower ice adhesion strength [108]. Based on these observations, trimethylterminated-PDMS, vinyl-PDMS, and hydride-PDMS were used to obtain a PDMS gel giving ultra-low ice adhesion strength [109]. Similarly, Golovin et al. fabricated a series of different icephobic gels using PDMS, polyurethane (PU) rubbers, fluorinated PU polyols, and perfluoropolyethers after embedding these elastomeric samples with either silicone, Krytox, vegetable oil, cod liver oil, or safflower oil to enable interfacial slippage. Interfacial slippage was reported to make the biggest impact on the ice adhesion strength of the low cross-link density elastomer samples and resulted in ultra-low ice adhesion strength of as low as 0.2 kPa [110].

Fluorosilicone block copolymer coatings were also tried in order to diminish the ice adhesion strength by the application of the synergistic effects of water and oil-repellent properties of fluorides and silicones [111–113]. Some success on the reduction of ice adhesion was obtained because of the decrease of the interaction between ice and the copolymer surface where the fluorine-containing chains were enriched because of the formation of microphase separation of the block copolymers on the surface [112].

## 4.2 *Superhydrophobic Anti-Icing Surfaces*

It was hypothesized that artificial SHSs which were prepared by the combination of low surface energy materials and enhanced surface roughness [1, 2, 14, 20, 21] would be successful in anti-icing applications by repelling impinging water droplets and eliminating their presence on a surface before they can freeze. In addition, it was expected that ice adhesion strength would be reduced after icing occurs because of the formation of only a small solid-ice interfacial area [1, 2, 10, 14, 23–34].

Conversely, many researchers reported that the use of SHSs were not successful for anti-icing applications [9, 13, 14, 22, 36–43]. There are various reasons for this result: superhydrophobicity is lost, especially in high humidity and sub-zero conditions, or can be destroyed afterward under the de-icing/icing cycles, and ice adhesion strength increases when ice penetrates into the surface texture. As predicted by classical nucleation theory, condensed water droplets nucleate and grow randomly within hydrophobic microscale structures [36, 114]. The rate of condensation on SHSs increases because of the presence of the larger surface area and microstructure confinement. Consequently, the growing water droplets are trapped in the Wenzel state and prevented from being completely removed by external forces [36, 114–116]. When ice accretion occurs on an SHS, it usually damages the surface microstructures during icing and deicing cycles and the ice adhesion strength has been found to be very high in a humid atmosphere [38, 39]. It was later found that surfaces with dense nanoscale topography offer promising condensation-induced wetting resistance, and condensing droplets on nanostructured SHSs experience longer freezing times [29, 88, 89, 117]. This may be because of the same mechanisms responsible for the delayed ice nucleation of sessile droplets on hydrophobic nanostructures [22, 90].

The expectation of the repulsion of impinging water droplets and eliminating their presence on a surface before they can freeze has not been validated. The motion of droplets is affected by the initial droplet volumes, viscous dissipation, size, and structural hierarchy of surface features [1]. Droplet bouncing can occur when the impacting liquid maintains enough energy to depart the surface, but if a droplet strikes the surface with high velocity with sufficient kinetic energy, then it may displace the air pockets present on the SHS and imbibe into the rough structure. The superhydrophobic property is then lost and the increased contact area of the droplet with the underlying solid improves heat transfer, leading to rapid heterogeneous ice nucleation [1, 118]. The resultant decrease in temperature results in an increase of the viscosity of supercooled droplets, thus increasing contact time and reducing bouncing ability [119]. In summary, the use of SHS for anti-icing applications has not been successful, especially in humid conditions, contrary to initial expectations [1, 2, 9, 13, 14, 22, 36–43].

## 5 Slippery Liquid Ad(ab)sorbing Surfaces

Aizenberg and co-workers developed SLIPS in 2011 using perfluorinated liquids as the lubricant and reported their icephobic properties in terms of the extent of the mobility of a previously frozen water drop on them under outdoor conditions of  $-4^{\circ}\text{C}$  and 45% RH [44]. Stone has described SLIPS as “wet icephobic” surfaces as shown in Fig. 1 [46].

In one of their works, an ordered epoxy resin-based nanostructured surface was prepared from silicon masters through the replica molding method with dimensions of  $\sim 300$  nm diameter,  $5\ \mu\text{m}$  height, and  $2\ \mu\text{m}$  pitch length between the centers of the protrusions [44]. The epoxy replicas were initially hydrophobized with heptadecafluoro-1,1,2,2-tetrahydrodecyltrichloro-silane. Fluorinert FC-70 (perfluorotri-*n*-pentylamine) lubricating fluid, with low surface free energy ( $17.1 \pm 0.3$  mN/m), was added dropwise onto this structured solid to form a smooth over-coated layer with the fluid spreading spontaneously onto the whole patterned substrate through capillary wicking. The thickness of the over-coated layer was controlled by the fluid volume and this was added only until it spread across the tops of the surface features. Half of the Fluorinert FC-70 lubricant which was infiltrated into the epoxy resin-based nanostructured surface evaporated in 5 days (complete evaporation took place in approximately 10 days) [44]. In this publication, no anti-icing tests were carried out. Only the high mobility of previously formed ice drops on this LAAS sample placed on an inclined plane was shown in a movie and compared to the mobility of ice drops formed on the uncoated epoxy resin-based nanostructured SHS at outdoor conditions of  $-4^{\circ}\text{C}$  and 45% RH [44].

The study of Aizenberg and co-workers inspired other scientists in the anti-icing field and many slippery surfaces were produced to investigate the efficacy of this approach for reducing ice adhesion strength. Similar to the original LAAS article [44], various lubricating fluids based on fluorinated, silicone, and hydrophilic liquids were used in these studies, and the surfaces were termed LIS in some papers [45–65]. The synthesis and anti-icing properties of such surfaces were the partial subject of four recent reviews [1, 2, 14, 16]. Two of these reviews comprise a very

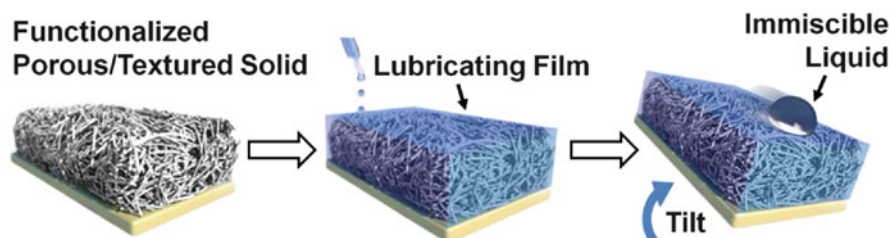


**Fig. 1** Preparation of an LAAS (SLIPS) by infiltrating a functionalized porous/textured solid with a low surface energy, chemically inert liquid to form a smooth lubricating film on the surface of the substrate. (Reproduced with permission from Stone [46]. Copyright (2012) American Chemical Society)

broad range of the subject of designing smooth, textured, and slippery icephobic surfaces and their comparison [1, 2]. Another one presented a comprehensive review of the physics of ice formation on surfaces and mechanisms of anti-icing [14]. The last one compared the anti-icing performances of low surface free energy and LAAS [16]. Anti-icing results of LAAS were only partially given and discussed in all the above-mentioned reviews. The focus in this review is only on the performance of slippery icephobic LAAS and examines the synthesis–anti-icing property relationship of these LAAS according to the type of lubricant used in their manufacture in three separate sections below. The anti-icing properties of LAAS described in this section are summarized in Table 1 by substrate and lubricant types along with the subsection number in which they are discussed.

## ***5.1 Surfaces Formed with Fluorinated Lubricants***

### **5.1.1 Krytox 100 Lubricant on Hydrophobized Highly Textured Polypyrrole Electrodeposited on Aluminum**

In another study, Aizenberg and co-workers prepared LAAS-coated aluminum surfaces by oxidative electrodeposition of highly textured polypyrrole (PPy) with a thickness of 3–4  $\mu\text{m}$  on aluminum substrates, post-hydrophobization of this surface by a fluorosilane (tridecafluoro-1,1,2,2-tetrahydrooctyl trichlorosilane), and then infiltration of a perfluorinated lubricant (Krytox 100-DuPont, which is a fluorocarbon ether polymer of polyhexafluoropropylene oxide) with low-viscosity (7 cSt at 20°C) and low freezing point (below  $-70^\circ\text{C}$ ) properties [45]. Krytox 100 was added dropwise onto the porous hydrophobic surface which was held vertically to remove excess lubricant until no macroscopic movement of lubricant on the surface was evident. The thickness of the lubricating layer was calculated to be 8–10  $\mu\text{m}$  based on the measured weight change, substrate size, and density of the lubricating liquid. Water droplets were formed by condensation in a humid medium (60% RH) on Krytox-coated Al surfaces and froze during the cooling cycle from room temperature to  $-10^\circ\text{C}$  at a rate of  $5^\circ\text{C}/\text{min}$ . The authors reported that the frozen droplets were able to slide down with a tilt angle of  $75^\circ$  from horizontal and left the LAAS during the defrost cycle from  $-10$  to  $25^\circ\text{C}$  at a rate of  $10^\circ\text{C}/\text{min}$  [45]. For conditions, such as  $-2^\circ\text{C}$ , 60% RH, a frost-free surface could be obtained on the LAAS-Al surfaces for 100 min. Unfortunately, the LAAS-Al surface eventually accumulated ice after a prolonged exposure to cold temperatures ( $< -10^\circ\text{C}$  at 60% RH). The ice formed on the LAAS-Al surface was somewhat different than the ice formed on a bare Al surface. The ice on the LAAS-Al surface tended to form large and isolated patches and these large ice patches slid off the surface immediately upon heating and melting of the ice at the interface during the defrost cycle, leaving the surface clean, as seen in Fig. 2.

It was proposed that the LAAS-Al surface more easily shed the melted water drops or ice sheets because the infiltrated lubricant did not freeze and this surface

**Table 1** Anti-icing properties of LAAS which were reported in publications described in Sect. 5 according to their substrate and lubricant types

Substrate (template)	Lubricant	Ice adhesion test	Icing time test	Ice accretion test	Ref No	Section
Hydrophobized epoxy resin-based nanostructured surface	Fluorinert FC-70 (perfluorotri- <i>n</i> -pentylamine)	–	–	–	[44]	5
Hydrophobized highly textured polypyrrole electrodeposited on Al	Krytox 100 (fluorocarbon ether polyhexafluoropropylene oxide)	+	+	–	[45]	5.1.1
Square silicon microposts obtained by lithography coated with hydrophobized nanograss	Krytox-1506 (fluorocarbon ether polyhexafluoropropylene oxide)	–	–	–	[47]	5.1.2
Alumina nanoparticle coated Cu foil, silicone nanowires, square silicon microposts obtained by lithography	Krytox-1506 (fluorocarbon ether polyhexafluoropropylene oxide)	–	+	–	[53]	5.1.3
Boehmite (aluminum oxy-hydroxide) nanostructured DSC pans after hydrophobized	Krytox GPL 101 (fluorocarbon ether polyhexafluoropropylene oxide)	–	+	–	[48]	5.1.4
Boehmite (aluminum oxy-hydroxide) nanostructured surface on aluminum	Krytox GPL 100 (fluorocarbon ether polyhexafluoropropylene oxide)	+	–	–	[49]	5.1.5
Hydrophobized inverse colloidal silica monolayer template	A- Krytox 100 (fluorocarbon ether polymers of polyhexafluoropropylene oxide)	+	–	–	[50]	5.1.6
	B- Krytox 103					
	C- Olive Oil					
Nanoparticle suspension of cellulose lauroyl ester coating	(Fomblin Y) perfluoroether lubricant	–	+	–	[59]	5.1.7
Polydimethylsilicone (PDMS) layer containing Fe <sub>3</sub> O <sub>4</sub> nanoparticles	Krytox 100 (fluorocarbon ether polyhexafluoropropylene oxide)	+	+	+	[61]	5.1.8
Heptadecafluorodecyl trimethoxysilane microstructured silicone rubber	A- Krytox GPL 103 (fluorocarbon ether polyhexafluoropropylene oxide)	+	+	+	[62]	5.1.9
	B- Perfluoropolyether					

(continued)

**Table 1** (continued)

Substrate (template)	Lubricant	Ice adhesion test	Icing time test	Ice accretion test	Ref No	Section
A- Hydrophobic PP sheet	A- Fluorinert FC-70	+	+	+	[65]	5.1.10
	B- Polyalphaolefin					5.3.6
	C- Silicone oil					
B- Hydrophilic cellulose-based filter paper	D- Decamethylcyclopenta siloxane					
	E- Water					
	F- Ethylene glycol					
	G- Formamide					
H- Glycerine/water						
Suspension of hydrophobized SiO <sub>2</sub> nanoparticles and PMMA in THF solvent was spray coated	Fluorinert FC-70 (perfluorotri- <i>n</i> -pentylamine)	–	–	–	[120]	5.1.11
Perfluorododecylated graphene nanoribbon film	Heptacosafuoro-tributylamine	–	–	–	[121]	5.1.12
Carbon nanofibers dispersed in a fluoroacrylic copolymer and spray coated	A- Krytox (fluorocarbon ether polymers of polyhexafluoropropylene oxide)	–	+	+	[122]	5.1.13
	B- Silicone oil					
Square silicon microposts obtained by lithography coated with hydrophobized nanoglass	A- Silicone oil	–	–	–	[51]	5.2.1
	B- Ionic liquid (1-butyl-3-methylimidazolium bis-trifluoromethyl-sulfonyl imide)					
Hydrophobized lithographically patterned square silicon micropost array	A- Silicone oil	+	–	–	[52]	5.2.2
	B- Tetramethyl tetraphenyl trisiloxane					
Synthesized PDMS coating mixed with nano-SiO <sub>2</sub> and cured	Silicone oil	+	+	+	[56]	5.2.3
Butyl methacrylate-lauryl methacrylate copolymer organogel	Silicone oil	–	–	–	[55]	5.2.4
Cross-linked PDMS	Paraffin	+	–	–	[63]	5.2.5
Cross-linked PDMS	Aliphatic, aromatic hydrocarbons, silanes and siloxanes	+	–	–	[64]	5.2.6

(continued)



**Table 1** (continued)

Substrate (template)	Lubricant	Ice adhesion test	Icing time test	Ice accretion test	Ref No	Section
Cross-linked poly(acrylic acid) grafted inside pores of patterned silicon wafer obtained by photolithography	Water	+	–	–	[54]	5.3.1
PU obtained from dimethylol propionic acid, isocyanates, and $\gamma$ -butyrolactone	Water	+	–	–	[57]	5.3.2
Hyaluronic acid and dopamine copolymer coating	Water	+	–	–	[58]	5.3.3
Superhydrophilic polyelectrolyte brush coatings	Water	+	–	–	[123]	5.3.4
Nylon 66 membrane coated by Hydrobead superhydrophobic coating	Propylene glycol	–	+	+	[71]	5.3.5
Water on PEG and PDMS blends	Water	+	–	–	[124]	5.3.7

(+) means the property was measured and (–) means not measured

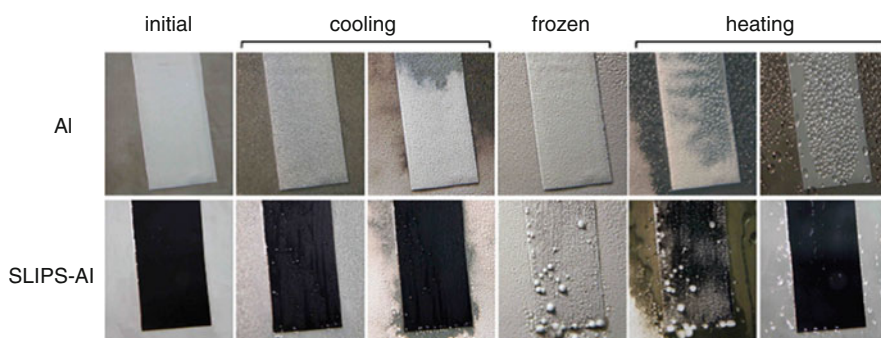


**Fig. 2** Images of ice formation on LAAS-Al and on bare Al surfaces by freezing ( $-10^{\circ}\text{C}$ ) in high humidity condition (60% RH) and subsequent deicing by heating. The morphology of accumulated ice on LAAS-Al was significantly different from that on bare Al. Condensation/freezing cycle: from room temperature to  $-10^{\circ}\text{C}$  at  $5^{\circ}\text{C}/\text{min}$ . Melting (defrost) cycle: from  $-10$  to  $25^{\circ}\text{C}$  at  $10^{\circ}\text{C}/\text{min}$ . Ice formed mostly around the edges of LAAS-Al by bridging from the surrounding aluminum substrate, whereas it formed uniformly all over the aluminum substrate. The samples were mounted with  $75^{\circ}$  tilt angle, and the widths of the substrates were approximately 3 cm. (Reproduced with permission from Kim et al. [45]. Copyright (2012) American Chemical Society)

had a low contact angle hysteresis value of  $2 \pm 1^\circ$  in comparison with the  $41 \pm 4^\circ$  of the bare Al surface. Contact angle hysteresis is the difference between advancing and receding contact angles and is generally a measurement of the surface roughness and chemical heterogeneity of a surface [101, 125]. The shedding of water or ice droplets was attributed to the lack of roughness and chemical heterogeneity on the lubricant surface [45]. This is possible only if the top of the protrusions in the lubricant are below the lubricant surface level because the pinning of a water drop to the exposed surface defects is the main reason for high contact angle hysteresis, and only a defect-free, molecularly flat liquid interface can be achieved by forming a lubricating film that overcoats the solid support.

In that paper, ice adhesion strength tests performed in a closed chamber by attaching the LAAS-Al and bare Al samples to a temperature-controlled aluminum plate using thermally conductive tape, placing the fluoroalkyl-silanized cylindrical glass columns on the substrate, and then filling the columns with 150  $\mu\text{L}$  of fresh deionized water [45]. These glass columns were made by cutting Pasteur pipettes with a well-polished end and had a contact area of around 24  $\text{mm}^2$  with the substrate. The humidity in the chamber was decreased below 3% RH to avoid frost formation. Then the temperature of the substrate was lowered at a rate of  $2^\circ\text{C}/\text{min}$  down to  $-20^\circ\text{C}$  (or below) to ensure freezing. The temperature was raised to  $-10^\circ\text{C}$  at a rate of  $2^\circ\text{C}/\text{min}$  after ice formation and the samples were allowed to equilibrate for 30 min. Later, the applied force was measured using a tensiometer with a maximum force of 50 N by either pulling or pushing the sample columns at a contact point less than 1 mm above the surface of the substrate, at the same time maintaining the temperature at  $-10^\circ\text{C}$ . The force gauge was moved forward and backward at a precise rate of 0.5 mm/s for the bare Al and all other surface-treated Al samples and 0.1 mm/s for SLIPS-Al because of the large difference in the ice adhesion value. Average ice adhesion strengths of the samples were measured to be 15.6 kPa on LAAS-Al and 1,359 kPa on bare Al. Only adhesive failure (no cohesive failure) of ice was seen on any sample during the experiments [45].

The Aizenberg group attributed the main effect of LAAS to minimization of contact angle hysteresis as well as contact line pinning with the use of lubricant [44–46]. If the lubricant has a freezing point much below the temperature to be used in anti-icing applications, then only a minimum contact line pinning can occur on this liquid layer with the condensing or impinging water (supercooled or not) droplet. In general, the three-phase contact line of a droplet on a surface pins at the surface defects of solid substrates and the contact angle hysteresis is typically large on rough surfaces and small on smooth surfaces. The smaller the contact angle hysteresis, the smaller the force tangent to the surface needed to move the drop. Thus, the ease of sliding drops on a surface is an important parameter to affect icephobicity, and LAAS is successful in this respect. However, the durability of the lubricant on the porous solid layer is a very important factor that was not reported by Kim et al. [45]. Additionally, the lubricant must be kept in the supporting matrix and must cover the top of the protrusions for all of its service life for anti-icing applications, otherwise the droplet would pin at the ridges on the surface and contact angle hysteresis would increase rapidly. High cost and environmental

constraints of the perfluorinated lubricants used in the LAAS synthesis are additional adverse considerations.

### **5.1.2 Krytox-1506 Lubricant on Silicon Microposts Coated with Hydrophobized Nanograss**

Varanasi and co-workers raised the criticism concerning the longevity of the lubricant film and its possible depletion through evaporation. Similarly, entrainment with the droplets being shed was not thoroughly addressed in the first LAAS publications [51, 53]. They reported that the main weakness of an LAAS made of perfluorinated lubricants was their durability on the porous substrate, which is limited by how long this lubricant stays in the patterned surfaces or porous matrix without evaporating or leaking [47, 51, 53]. Another issue they found was the “cloaking effect” which was the spreading of the lubricant over the water droplets forming on the lubricant infiltrated surfaces. This cloaking (or encapsulation) of water droplets by the lubricant can cause the progressive loss of the lubricant through entrainment in the water droplets as they are shed from the surface [47].

The authors formed patterned square silicon microposts 10  $\mu\text{m}$  high, 10  $\mu\text{m}$  wide, and 10  $\mu\text{m}$  edge to-edge, spacing via photolithography. A nano-grass texture consisting of sharp spikes with a height of 200 nm and a characteristic spacing of 100 nm was also introduced by etching the silicon microposts in a plasma of  $\text{O}_2$  and  $\text{SF}_6$ . The microposts were then further hydrophobized after cleaning the samples with piranha solution to allow lubricant to adhere stably to the surface in the presence of water. It was shown that condensed water droplets on the Krytox-1506 lubricant-filled surfaces cannot be evaporated, even under high superheat conditions, suggesting that cloaking occurred strongly during drop condensation. In summary, the useful lifetime of an LAAS is affected by lubricant drainage, miscibility of water with the lubricant, and cloaking of lubricant with water droplets, and, if enough lubricant loss occurs, water droplets on the lubricant surface are pinned to the solid texture at the post tops and the positive effect of the lubricant surface is eliminated as shown in Fig. 3 [47].

As previously mentioned, the patterned texture should be completely submerged in the lubricant to achieve low contact angle hysteresis and this complete submergence can be achieved temporarily by depositing excess lubricant. Complete submergence is possible only if the lubricant completely wets the texture with a zero contact angle on the flat substrate [51]. Otherwise, the excess lubricant drains away by gravity and other drag forces and the lubricant–air interface contacts the textured solid, thereby exposing the solid to the air. Varanasi and co-workers used silicone oil and an ionic liquid (1-butyl-3-methylimidazolium bis-trifluoromethylsulfonyl imide) as the lubricants in their LAAS samples with a solid texture of square silicon microposts obtained by lithography coated with hydrophobized nano-grass, and concluded that meeting such a full wetting requirement is very difficult in practice and restricts the choice of lubricants [51].

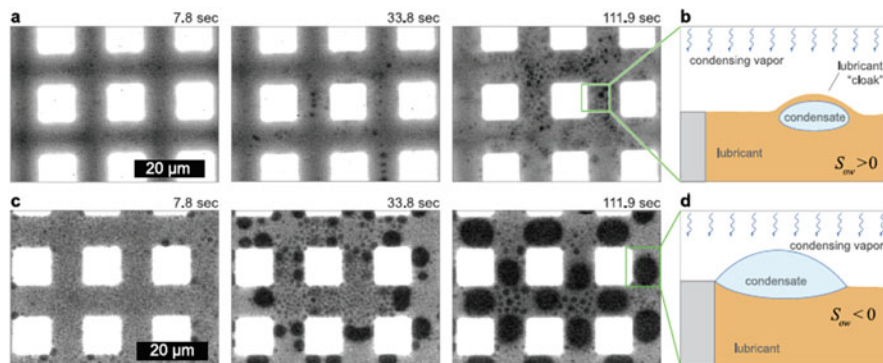


**Fig. 3** (a) ESEM image sequence of condensation on a micropost surface impregnated with perfluorinated lubricant that has a positive spreading coefficient on water ( $S_{ow} > 0$ ). Condensation is inhibited as the lubricant cloaks the condensed droplets. (b) Illustration of cloaked condensate droplet depicting the thin film of condensate that spreads on the droplet. (c) ESEM image sequence of condensation on micropost surface impregnated with ionic liquid that has a negative spreading coefficient with water ( $S_{ow} < 0$ ). (d) Illustration of unclanked condensate droplet. (Reproduced with permission from Anand et al. [47]. Copyright (2012) American Chemical Society)

### 5.1.3 Krytox 100 Lubricant on Hydrophobized Inverse Colloidal Silica

In another publication by the Varanasi group, the condensation frost formation conditions on nanostructured and microstructured SHSs with and without the use of a perfluorinated lubricant layer were investigated [53]. A dip-coating procedure was applied which avoided the formation of a temporary excess of Krytox-1506 lubricant film on their LAAS. The lubricant film was formed on three different substrates made of alumina nanoparticle-coated Cu foil, silicone nanowires, and square silicon microposts obtained by lithography. Horizontally located samples on a thermoelectric cooler were cooled from about 20 to  $-10^{\circ}\text{C}$  in a room environment of  $22^{\circ}\text{C}$  and an RH of 25–30%, and the condensation frosting process was imaged using a light microscope. In parallel experiments, frosting of droplets was also monitored with an environmental scanning electron microscope (ESEM) and with Cryo-FIB/SEM systems. The gradual draining of the lubricant from the drop's wetting ridge and from the neighboring microposts by capillary attraction onto frozen drops was observed to be accompanied by the growth of dendritic structures. It was determined that the lubricant was nearly completely drained from the wetting ridge within 3–18 s and the majority of the perfluorinated lubricant migrated from the wetting ridge and the substrate's texture to the frozen drop's surface. The authors applied defrosting and found that the underlying nanostructure was clearly visible after the second frosting-defrosting cycle, indicating that nearly all the lubricant oil was depleted and the anti-icing and self-healing characteristics of the surface were lost [53]. They concluded that the perfluorinated lubricant is likely to be depleted from any LAAS in any practical anti-frosting applications and recommended the

use of external lubricant reservoirs that allow the replenishment of the lubricant for the sustained performance of such LIS surfaces [53].

#### **5.1.4 Krytox GPL 10 Lubricant on Boehmite Nanostructured DSC Pans After Hydrophobization**

Aizenberg and co-workers investigated the effects of surface modification on the heterogeneous nucleation of supercooled water on various surfaces using a differential scanning calorimeter (DSC) [48]. They tested hydrophilic (untreated aluminum), hydrophobic, hydrophobized superhydrophobic, and Krytox GPL 101-coated (LAAS) aluminum DSC pans. The nucleation temperatures were reported to be in the order of hydrophilic ( $-25.1^{\circ}\text{C}$ ) < Krytox GPL 101 coated (LAAS) ( $-24.8^{\circ}\text{C}$ ) < textured hydrophobic ( $-23.3^{\circ}\text{C}$ ) < textured hydrophobized superhydrophobic ( $-22.0^{\circ}\text{C}$ ) pans. No deterioration and lowering of performance were seen even after 150 freeze–thaw cycles. The authors commented that the use of lubricant on the pan surface provided an ultrasMOOTH and chemically homogeneous interface to eliminate possible nucleation sites [48].

#### **5.1.5 Krytox GPL 100 Lubricant on Boehmite Nanostructured Surface Formed on Aluminum**

Environmental shear stresses from continuous exposure of air flows or other foreign fluids against capillary forces holding the lubricant on the LAAS was investigated by Aizenberg and co-workers as a function of the length scale of the underlying porous solids [49]. The authors used sandblasting and boehmite (aluminum oxy-hydroxide) nanostructure formation as methods to create directly microscale and nanoscale textures, respectively, on an Al substrate. They then hydrophobized the substrate with a fluorinated coating. Krytox GPL 100 was used as the lubricant. Centrifugal force using a spin coater was applied to simulate high shear conditions on LAAS samples and it was determined that thinning of the lubricant layer led to exposure of the underlying solid on flat surfaces, as only a very small capillary force is present to hold the lubricant once subjected to various spinning rates between 100 and 10,000 rpm. Microtextured substrates retained more lubricant than nanotextured substrates after subjecting them to a high spinning rate. Their performance as SLIPS, however, was worse than that of the nanotextured surface, indicating that the robustness of SLIPS is not directly correlated to the retention of the lubricant alone. LAAS coatings gave low ice adhesion strengths ( $\approx 10$  kPa) before shearing that were two orders of magnitude lower than that of bare stainless steel ( $\approx 700$  kPa) and Teflon ( $\approx 240$  kPa) [49].

### 5.1.6 Krytox 100, Krytox 103 and Olive Oil Lubricants on Hydrophobized Inverse Colloidal Silica Monolayer

In another publication, Aizenberg group reported that the stability of LAAS could be improved by employing a closed-cell architecture of the substrate using an inverse colloidal monolayer template to design transparent, nano-porous LAAS structures [50]. A multi-step and complex procedure was used for this purpose. A styrene and acrylic acid copolymer latex was synthesized by a surfactant-free emulsion polymerization. This latex was diluted by water and ethanol to give a colloidal dispersion of water/ethanol (with a solid content of 2.5%). After spreading and drying the colloidal dispersion, a close packed colloidal monolayer was obtained which uniformly covered the substrate. A mixture of tetraethylorthosilicate, hydrochloric acid, and ethanol was then spin coated onto the colloidal covered monolayer located on the substrate. Polymeric colloids were removed by combustion at 500°C to obtain an inverse structure composed of silica. The final inverse coating was cleaned in acid piranha and plasma-treated with oxygen plasma for 10 min and coated with (1*H*,1*H*,2*H*,2*H*H-tridecafluorooctyl-trichlorosilane) by vapor-phase deposition. Krytox 100 and olive oil were used as test lubricants and their uniform coverage on the surface was achieved by removing the excess lubricant by vertical placement of the substrates. More viscous Krytox 103 was also used when the minimization of the lubricant evaporation was required. They reported that lubricants could be firmly locked in the structures and the lubricant-poured layers demonstrated good stability of more than 9 months of vertical storage [50]. Ice adhesion was measured at -40°C using a custom ice adhesion setup adapted from the literature [45, 100] for different glass substrates and LAAS samples, but no details of the ice adhesion measurement were given. Ice adhesion to hydrophilic glass was reported to be  $1,318 \pm 63$  kPa, to fluorinated glass  $743 \pm 334$  kPa, to a superhydrophobic fluorinated inverse monolayer structure  $387 \pm 204$  kPa, and to the LAAS  $10 \pm 7$  kPa. However, no information was provided in this publication on the effect of time and the number of freezing-defrosting cycles on the ice adhesion strength or how the lubricant could be kept on these pores for such a long time without evaporation and draining out when placed vertically [50].

### 5.1.7 Fomblin Y Lubricant on Nanoparticle Suspension of Cellulose Lauroyl Ester Coating

Chen et al. [59] synthesized cellulose lauroyl ester from cellulose and obtained its nanoparticle suspension, prepared via nano-precipitation in a non-solvent. Glass slides were dip coated with solution in toluene to give a thin transparent layer which was used as an adhesion layer between the target surface and the subsequent nanoporous film. Then the nanoporous cellulose lauroyl ester films were coated by spraying the nanoparticle-containing suspension in ethanol onto the previously

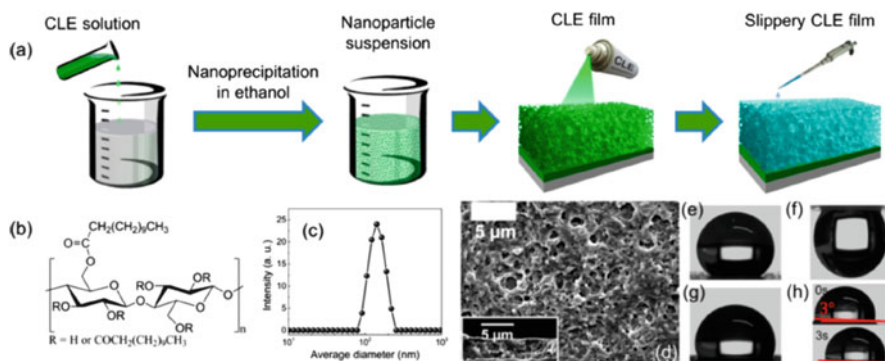


**Fig. 4** (a) Schematic illustration of the fabrication process of slippery cellulose lauroyl ester (CLE) surfaces. (b) Schematic representation of the chemical structure of CLE. (c) Dynamic light scattering (DLS) curve of CLE nanoparticles. (d) Scanning electron microscope (SEM) images of the nanoporous CLE film. The *inset* shows the side profile of the film. (e) Photograph of a 5- $\mu$ L water drop on the nanoporous CLE film. (f) Shape of the drop on the nanoporous CLE film when it was turned upside down. (g) Photograph of a 5- $\mu$ L water drop on the slippery CLE film after the infusion of perfluoropolyether into the nanoporous CLE film. (h) Sliding of a 5- $\mu$ L water drop on the slippery CLE film. (Reproduced with permission from Chan et al. [59]. Copyright (2014) American Chemical Society)

coated surfaces. After the evaporation of ethanol, the final dry porous layer was infiltrated with a perfluoroether lubricant (Fomblin Y) to give a transparent slippery surface. This LAAS layer delayed the ice formation (ice formation took place after 40 min at  $-10^{\circ}\text{C}$ ) and the surface coverage of the drops on the LAAS film was less than that on the nanoporous film as shown in Fig. 4 [59].

### 5.1.8 Krytox 100 Lubricant on PDMS Layer Containing $\text{Fe}_3\text{O}_4$ Nanoparticles

Yin et al. synthesized a PDMS layer containing  $\text{Fe}_3\text{O}_4$  nanoparticles which was infused by perfluorinated lubricant (Krytox 100) to form an LAAS [61]. The main objective was to afford a high efficiency photothermal effect under near-infrared irradiation for rapidly melting the accumulated ice by the addition of  $\text{Fe}_3\text{O}_4$  nanoparticles into the PDMS layer. Initially, an assembly of polystyrene microspheres was coated onto the substrate. Then  $\text{Fe}_3\text{O}_4$  nanoparticle solution was added to the mixture of PDMS prepolymer and curing agent, and the mixture was spread on the polystyrene colloidal crystals template to fill the void spaces among colloidal particles. It was then cured in an oven at  $70^{\circ}\text{C}$  for 3 h. The  $\text{Fe}_3\text{O}_4$ -PDMS film elastomer was carefully peeled off from the mold after curing and polystyrene (PS) microspheres were dissolved by immersing PDMS composite elastomer in toluene for approximately 4–6 h. Later, the porous PDMS film was fluorinated by using trichloro(perfluorooctyl)silane and Krytox 100 was infiltrated into fluorinated

substrate by a wetting apparatus, where the excess lubricant was removed by drying with tissue paper. The slippery lubricant was locked in the porous structures and formed a defect-free interface with efficient water repellency to impede water vapor condensation and reduced the ice adhesion strength down to 150 kPa at  $-15^{\circ}\text{C}$ . A procedure similar to the method given in [45] was used for the anti-icing tests. Ice accretion tests were also carried out in an icing instrument where 5- $\mu\text{L}$  droplets were sprayed onto the samples for 120 min via an array of micro-syringe needles under  $-5^{\circ}\text{C}$  air temperature and the impact height of the droplets was set at about 10 cm. Only photographs of the samples were given. The laser-induced photothermal burning to enhance the ice removal capability of the accumulated ice was also tested [61]. The integration of LAAS and thermogenesis into a single surface was proposed to be a novel icephobic and deicing strategy to maximize the efficiency of external energy. The photothermal defrost and deicing tests were investigated in a  $<-5^{\circ}\text{C}$  and  $\text{RH} \approx 70\%$  environment, where a near-IR laser (808 nm, 1 W) was shone onto the samples. It was found that the ice melting ability depends on both the laser light density and the concentration of  $\text{Fe}_3\text{O}_4$  nanoparticles in the coatings. Although original, the authors accepted that this multi-step procedure was at its conceptual stage and very complex [61]. In addition, the use of a near-IR laser for deicing large areas does not seem to be a feasible method.

### **5.1.9 Krytox GPL 103 Lubricant on Heptadecafluorodecyl Trimethoxysilane Microstructured Silicone Rubber**

A one-step electrospray method coupled with phase separation was applied to prepare heptadecafluorodecyl trimethoxysilane fluorinated and hierarchically microstructured high temperature vulcanized silicone rubber substrates which were infiltrated with two perfluorinated lubricants (Krytox GPL 103 and a perfluoropolyether) to form an LAAS [62]. Lubricant retention behavior, contact angle hysteresis, ease of frost formation, delay time for ice formation, simulated rainfall tests, and ice adhesion strength were investigated on these LAAS. The authors reported that when the lubricant covers the surface completely, it can reduce the heterogeneous nucleation and frost propagation velocity. The ice adhesion strengths of these LAAS were found to be one to two orders of magnitude lower than on the conventional surfaces. However, ice adhesion strengths increased from  $\approx 40$  kPa to  $\approx 1,000$  kPa with increasing lubricant loss during the frosting/defrosting cycles [62].

### **5.1.10 Variety of Hydrophobic and Hydrophilic Lubricants on Hydrophobic Polypropylene (PP) and Hydrophilic Filter Paper**

Ozbay et al. pointed out that the ice accretion performances of LAAS have not been reported previously as a function of the type of lubricants used [65]. They tested Fluorinert FC-70, polyalphaolefin, silicone oil, and decamethylcyclopentasiloxane as hydrophobic lubricants and water, ethylene glycol, formamide, and



water–glycerine mixtures as hydrophilic lubricants. These lubricants were impregnated into hydrophobic PP and hydrophilic cellulose-based filter paper surfaces [65]. The ice accretion, drop freezing delay time, and ice adhesion strength properties of these surfaces were examined. After equilibrium in a chamber at  $-10^{\circ}\text{C}$  and  $58 \pm 3\%$  RH,  $24\text{-}\mu\text{L}$  water droplets were injected onto test surfaces by a motorized syringe. Tap water was used instead of ultrapure water to prevent the unexpectedly rapid freezing of the droplets caused by the instability of the supercooled pure water. Drop freezing times were recorded when a droplet became translucent and reported as the average of ten measurements.

For the ice adhesion tests,  $50\text{-}\mu\text{L}$  water droplets were placed on the test surface at room conditions, and the samples were kept in a deep freezer at  $-30^{\circ}\text{C}$  for 15 min. After freezing of the drop, the sample was moved to a climatic chamber at  $-10^{\circ}\text{C}$  and  $58 \pm 3\%$  RH where a tensiometer and micrometric-controlled 2D plaser was previously located and cooled. The force required to detach each frozen water drop on the sample was measured by propelling the probe of an analogue force transducer horizontally into the side of the frozen water drop at a constant velocity of roughly  $0.25\text{ mm/s}$  using a manually controlled 2D plaser. The probe was located less than 1 mm above the substrate surface to minimize torque on the ice. The value of applied maximum force at the break moment of the ice drop was recorded. An indirect method was applied to filter paper impregnated surfaces: Frozen  $50\text{-}\mu\text{L}$  droplets were formed in the deep freezer at  $-30^{\circ}\text{C}$  and then placed onto the hydrophilic liquid swollen filter paper in the climatic chamber and kept there for 15 min to maintain ice adhesion with the substrate. The same dynamometer force test was then applied again. The details of the ice accretion measurements are given in Sect. 7 [65]. Results are given in Table 2 with some conventional reference surfaces such as aluminum, copper, PP, and PTFE. As seen in Table 2, the best results for the ice accretion tests at  $-2^{\circ}\text{C}$  and  $56\text{--}83\%$  RH were obtained by using hydrophilic lubricants (especially a water–glycerine mixture) rather than hydrophobic lubricants.

**Table 2** Ice accretion values with standard deviation, and ice adhesion values with standard deviation on some substrates [65]

Substrate sample	Ice accretion ( $\text{g/m}^2$ )	Ice adhesion (kPa)
Copper plate	$1,006 \pm 49$	$1,217 \pm 34$
Aluminum plate	$880 \pm 30$	$731 \pm 53$
PTFE sheet	$742 \pm 33$	$268 \pm 13$
Silicone oil impregnated filter paper	$901 \pm 15$	$133 \pm 9$
Water impregnated filter paper	$815 \pm 20$	–
Fluorinert FC-70 impregnated filter paper	$498 \pm 17$	$16 \pm 3$
Water–glycerine mixture (85 wt% glycerine) impregnated filter paper	$266 \pm 14$	$16 \pm 3$

### 5.1.11 Fluorinert FC-70 Lubricant on Hydrophobized SiO<sub>2</sub> Nanoparticles in PMMA

Xiong and coworkers fabricated an SHS by spraying a suspension consisting of hydrophobized SiO<sub>2</sub> nanoparticles and poly(methyl methacrylate) (PMMA) in THF solvent onto substrates. An LAAS was formed by infusing the perfluoro-tripentylamine (Fluorinert FC-70) lubricant onto the SHS. A water droplet could slide on this prepared LAAS, even at  $-20^{\circ}\text{C}$  [120].

### 5.1.12 Heptacosafuorotributylamine Lubricant on Graphene Nanoribbon Film

Tour and coworkers developed both passive and active anti-icing coatings by using a perfluorododecylated graphene nanoribbon film [121]. Multi-walled carbon nanotubes, 1,2-dimethoxyethane, liquid Na/K alloy, and 1-iodoperfluorododecane were used to prepare the substrate material, which was dispersed in chloroform by bath ultrasonication, sprayed onto polyimide films (Kapton, DuPont) and glass slides, and then heated to  $90^{\circ}\text{C}$  on a hot plate. This superhydrophobic coating prevented freezing of incoming ice-cold water down to  $-14^{\circ}\text{C}$ . When the heptacosafuorotributylamine lubricant was added onto this surface, an LAAS was formed which improved the film's deicing performance and energy efficiency. Ice quickly started to mobilize by gravity when the ice at the interface was melted by Joule heating, as seen in Fig. 5 [121]. Only photographs were supplied where ice is still left on the lubricated surface after de-icing. Before the infiltration of the lubricant, the application of  $\sim 12\text{ V}$  was enough to keep the film at  $-14^{\circ}\text{C}$  when the ambient temperature was  $-32^{\circ}\text{C}$ , and if a higher voltage ( $\sim 40\text{ V}$ ) was applied, the film temperature could be kept at  $30^{\circ}\text{C}$ , even though the environmental temperature was  $-32^{\circ}\text{C}$ . After the addition of the lubricant, the deicing process proceeded faster

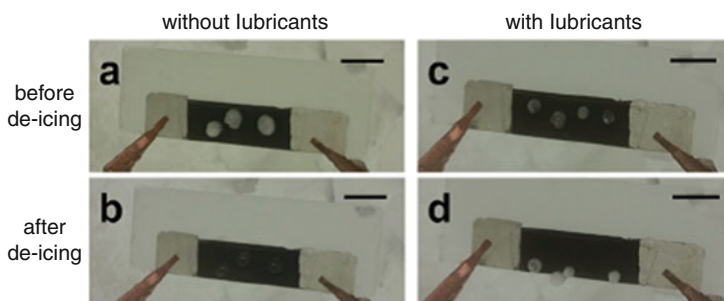


**Fig. 5** Photographs of the film without lubricating liquid: (a) before and (b) after active deicing by resistive heating. Photographs of the film with lubricating liquid: (c) before and (d) after active deicing by resistive heating. All the *scale bars* are 1 cm. (Reproduced with permission from Chang et al. [121]. Copyright (2016) American Chemical Society)

and saved more energy with the entire piece of ice falling off by gravity at  $-32^{\circ}\text{C}$ . The coating became icephobic again when the film was electrically heated at a power density of  $0.3\text{ W/cm}^2$  or kept above  $50^{\circ}\text{C}$  on a hot plate for 10 min [121].

### **5.1.13 Krytox and Silicone Oil Lubricants on Carbon Nanofibers Dispersed in Fluoroacrylic Copolymer**

Megaridis and co-workers investigated the behavior of electrically conducting superhydrophobic and LAAS coatings infiltrated by fluorinated lubricant (Krytox) and silicone oil for frosting/defrosting cycles by Joule heating for several hours [122]. The coatings were deposited by spraying carbon nanofibers dispersed in a fluoroacrylic copolymer dispersion in water (Capstone ST-100, DuPont). Fluoroacrylic copolymer was a low surface-energy hydrophobic material and the carbon nanofibers provided hierarchical microstructure-nanostructures and also electrical conductivity. The thermal properties of the lubricant were found to play little to no importance once a thick layer of frost formed on the sample surface at  $-7.5^{\circ}\text{C}$  and 80% RH conditions because of the strong thermal resistance of the thick (millimeter-scale) frost layer. Both frost coverage and frost weight increase were measured. When periodic thermal defrosting was applied, the dominance of the thermal resistance of the thick frost layers formed over prolonged periods was overcome. The pulse heating approach showed an energy savings of 20–30% over the method where the frost deposited over long periods was melted by applying heating once [122].

## **5.2 Surfaces Formed with Silicone Liquids**

Instead of perfluorinated oil lubricant, other suitable liquids such as silicone oils were also applied as lubricant on LAAS [51, 52, 55, 56, 60, 63, 64, 108–110, 122, 126].

### **5.2.1 Silicone Oil or Ionic Liquid on Silicon Microposts Coated with Hydrophobized Nanograss**

In 2013, Varanasi and co-workers prepared textured substrates consisting of a lithographically patterned silicon micropost array which was coated with octadecyltrichlorosilane and finally dip coated with silicone oil as the lubricant to obtain LAAS [51]. Silicone oil has a zero contact angle on the flat hydrophobic substrate and spreads completely; thus the silicone lubricant film encapsulating the solid texture was stable and no textures emerged from the lubricant film. However, the water droplets on this LAAS caused cloaking of the silicone oil by

encapsulating the water droplets on the surface, and silicone oil losses occurred during the shedding of water droplets. No anti-icing tests were carried out in this work [51].

### **5.2.2 Silicone Oil and Tetramethyl Tetraphenyl Trisiloxane on Hydrophobized Silicon Microposts**

In another study, Varanasi and co-workers used silicon microposts fabricated by photolithography, consisting of periodic silicon 10  $\mu\text{m}$  square microposts with inter-post spacings of 5, 10, 25, and 50  $\mu\text{m}$  and coated with octadecyltrichlorosilane through liquid deposition [52]. These substrates were then dip coated with two silicone lubricants, silicone oil and tetramethyl tetraphenyl trisiloxane (DC704-Dow Corning), which have positive and negative spreading coefficients on the flat octadecyltrichlorosilane-coated surfaces, respectively. The ice adhesion strength of the highest-texture density LAAS was found to be about four to five times smaller than that of a smooth surface coated with octadecyltrichlorosilane. Silicone oil, which can cover the post tops during drop freezing, resulted in low ice adhesion strengths, much better than the tetramethyl tetraphenyl trisiloxane lubricant which allows the exposure of post tops. It is known that lubricant losses occur between the textures because of water droplet cloaking together with evaporation to air and mechanical body forces. When the quantity of the lubricant decreased by any one of these mechanisms and the formed ice was able to be in complete contact with the post tops of the surface, then a relation with the corresponding ice adhesion strength and the surface texture was observed. Ice adhesion strength on the LAAS was found to decrease with increasing texture density [52].

### **5.2.3 Silicone Oil on Cross-Linked and Nano-SiO<sub>2</sub>-Containing PDMS Coating**

Zhu et al. prepared silicone-oil-infused PDMS coatings for anti-icing applications [56]. The authors suggested that PDMS has a very large free-volume at ambient temperature, which would act as a void to accommodate the infused silicone oil. They synthesized a two-part curable PDMS resin by using cyclotetrasiloxane, methylidisiloxane, and divinylidisiloxane components and mixed them with nano-SiO<sub>2</sub> to produce a nanoscale surface roughness. The mixed silicone resin was coated onto an aluminum plate or a Teflon disk using a spin-coater to produce a smooth surface. The coated samples were kept in an air chamber overnight to remove any residual small molecules and then cured using a pre-determined temperature sequence (30 min at 25°C, 45 min at 75°C, and 135 min at 150°C). Ice formation time and ice accretion was tested by using droplets with a volume of 15  $\mu\text{L}$  to simulate freezing rain. However, no ice mass increase was reported. When 20–40-wt% silicone oil was impregnated into LAAS, the ice adhesion tensile

strength was only about 5% of the value for the bare aluminum surface, and the ice adhesion shear strength decreased from 1,200 to 40 kPa [56].

#### **5.2.4 Silicone Oil on Thin Acrylic Organogel Coatings Formed on Various Substrates**

Jiang and co-workers fabricated organogel-based silicone oil-infused surfaces by applying free radical copolymerization of butyl methacrylate and lauryl methacrylate monomers on various substrates, including silicon wafers, microstructured silicon posts, aluminum, copper, and iron [55]. Initially the substrates were incubated in methanol containing 3-(trimethoxysilyl) propyl methacrylate to generate an alkene-terminated surface before polymerization, and later an organogel film with a thickness of about 30 nm was formed on the substrate. This thin film not only absorbed silicone oil but also held it in the cross-linked network with increased thickness to about 110 nm. The authors reported that a water droplet of 8 mg could easily slide off a swollen organogel-modified silicon wafer with sliding angle of 5° and no sliding was observed on the organogel-modified silicon wafer without absorbing oil. The critical sliding angle increased with increasing viscosity of absorbed silicone oil and the easy-sliding property of the water droplets on these organogel-modified surfaces exhibited good self-cleaning. This was demonstrated with the use of sand dust (5–170 μm) as the material to be cleaned on the samples where the tilt angle of the plates was 10°. The authors also explored the influence of surface microstructure on droplet sliding ability using a series of regular arrays of square silicon microposts which were then modified with the organogel film and swollen with low viscosity silicone oil. They found that the critical sliding angles of the water droplets increased with the increase in spacing between the silicon microposts, showing that nanoscale roughness was favorable to obtain easier sliding whereas microscale roughness was not good for easy sliding. However, no anti-icing tests were reported for any of these LAAS samples [55].

#### **5.2.5 Liquid Paraffin Oil on Cross-Linked PDMS Coating**

In another study, Jiang and co-workers developed an anti-icing coating by swelling cross-linked PDMS networks (Sylgard 184, Dow Corning) with warm liquid paraffin [63]. The polymer network absorbed and held the paraffin that was not removed during the shed off the accreted ice. Cured PDMS was cut into square pieces and immersed into a warm paraffin bath for at least 7 h. Then the swollen PDMS pieces were cooled and excess paraffin on the surface was removed. A liquid layer was formed on the surface of prepared LAAS by diffusion from inside after it was kept overnight. The ice adhesion strength of the samples was tested by an XY motion stage with force transducer using a probe velocity of 0.5 mm/s. In order to prepare the ice columns, 1 mL ultrapure water was syringed into a glass cuvette (10 × 10 × 25 mm) on the organogel sample surface when the cooling stage

reached a desired temperature. Ice columns were kept at the same temperature for 5 h to ensure full contact between the ice and the substrate. A nitrogen gas flow with a low flow rate was utilized to purge the environment continuously in an effort to avoid water vapor frosting onto the substrate. The contact area between the ice and the substrate was  $1 \text{ cm}^2$ . The shear forces of nine samples were measured for each temperature. Ice adhesion strength remained in the range of  $1.7 \pm 1.2$  to  $5.8 \pm 1.8 \text{ kPa}$  between  $-20$  and  $-60^\circ\text{C}$ . The ice adhesion strength on the sample that was measured at  $-30^\circ\text{C}$  showed very little increase after 35 cycles of icing/ deicing. In addition, the service lifetimes of the samples were long, and ice adhesion remained less than  $10 \text{ kPa}$ , even after exposing the samples to sunlight for 100 days at ambient environment [63].

### 5.2.6 Silicone Oils, Aliphatic, Aromatic Hydrocarbons and Silanes on Transparent Organogel PDMS Coating

Hozumi and coworkers pointed out that coatings that can autonomously provide functional liquids (lubricating, anti-freezing, etc.) at the topmost surface under specific conditions can be a solution for passive anti-icing [64]. They prepared novel self-lubricating transparent organogels that are capable of spontaneously releasing liquids from inner gel matrices to their outer surfaces when triggered by a change in the surrounding temperature (syneresis). Cross-linked PDMS (Sylgard 184 silicone elastomer) was prepared in the presence of several liquids such as aliphatic and aromatic hydrocarbons, silanes, and siloxanes. For specific swelling liquids, a liquid layer was continuously formed on the topmost of the PDMS gel surfaces because of syneresis. Although the weight of the gel samples continued to decrease gradually, they exhibited good long-lasting syneresis behavior in the case of silicone oils, even after being left in air for 3 months. An ice adhesion test was performed by freezing water (15 mL) at  $-15^\circ\text{C}$  in the freezer for 6 h in a PP tube (diameter 24 mm, height 55 mm) placed on top of the sample. A home-made ice adhesion strength tester was used, which was equipped with a Peltier cooling stage. The ice adhesion strength was measured by pushing the ice pillar with a stainless pole with a load cell. A thermoresponsive syneresis-organogel synthesized with the addition of 25% TSF437 (polymethylphenylsiloxane) showed a very small adhesion force (ca.  $0.4 \text{ kPa}$ ) between the ice and the organogel surface (no peak of maximum sharing force was observed during the experiment). It was claimed that this value is far smaller than that of any anti-icing LAASs reported so far (ca.  $15 \text{ kPa}$ ). An ice pillar which formed on the organogel could slide off a slightly inclined surface, even at  $-15^\circ\text{C}$  [64]. However, there was no report on the performance of these swelled gels after freezing/defrosting cycles. In addition, there was no report on the ice adhesion strength increase with the decrease of the organic liquid content in the PDMS gel.

### 5.2.7 Various Lubricating Liquids on Cross-Linked PDMS Coatings

Cross-linked PDMS gels with good mechanical properties have resulted in very low ice adhesion strength down to 5 kPa in recent studies [108–110, 126]. Trimethyl terminated-PDMS, vinyl-PDMS, and hydride-PDMS were used to obtain a PDMS gel giving ultra-low ice adhesion strength [109]. Similarly, Golovin et al. fabricated a series of different icephobic gels using PDMS, PU rubbers, fluorinated PU polyols, and perfluoropolyethers. These elastomeric samples were impregnated with either silicone, Krytox, vegetable oil, cod liver oil, or safflower oil to enable interfacial slippage with ice and produced ultra-low ice adhesion strength values of 9–0.2 kPa [110]. Yeong et al. obtained an oil-infused PDMS elastomer by replicating microtextures from a laser-irradiated aluminum substrate. They showed that an infusion of silicone oils with viscosity at 100 cSt at levels below 8 wt% in the PDMS solution was sufficient to reduce the ice shear strength from 115 kPa to an average of 38 kPa [126].

### 5.3 Surfaces Formed with Hydrophilic Liquids

Inspired by ice skating, water and other hydrophilic liquids were used as lubricants to prepare new LIS for anti-icing applications [54, 57, 58, 65]. It is well-known that a liquid-like water film forms on the ice surface and this film substantially decreases the adhesion strength between the skate blades and ice, enabling the skaters to move on the ice surface easily [127]. Ikeda-Fukazawa et al. have proposed that the water molecules at the liquid film surface are different than water molecules in the bulk [128]. The molecular layers at the surface adopt a more amorphous reconstruction in response to the reduced number of chemical bonds holding the surface water molecules in place. Atoms in the outermost surface vibrate with greater amplitude as a function of temperature than atoms in the interior lattice, and surface melting is attributed to the interaction of the vibrational motion of the surface water molecules with the interior bulk water molecules [128].

#### 5.3.1 Water on Cross-Linked Hygroscopic Poly(Acrylic Acid) Layer Grafted on Patterned Silicon Wafer Surfaces

Jiang and coworkers suggested using this liquid-like water layer as a self-lubricating liquid in a novel LAAS and fabricated an anti-icing coating with a liquid water layer [54]. For this purpose, cross-linked hygroscopic poly(acrylic acid) was grafted inside the micropores of photolithographically patterned silicon wafer surfaces. Silicon patterns were treated with a piranha solution, 3-(methacryloxy propyl-trimethoxy silane) was attached on the hydroxylated silicon wafers, and then cross-linked poly(acrylic acid) was grafted onto the silanized

surface by free radical polymerization. The hygroscopic polymer network inside the micropores deliquesced and swelled because of water absorption or condensation at low temperatures. After enough water was absorbed, the water swollen polymer network inside the micropores bulged out of the micropores and merged together because of molecular attractions between the water molecules, forming a self-lubricating liquid water layer as seen in Fig. 6. The setup for measuring the ice adhesion shear strength consisted of an XY motion stage, a force transducer, a home built cooling stage, and water-filled cuvettes that were frozen onto the test surfaces. The cooling stage with the cuvettes atop of it was placed in a closed box, which was purged with nitrogen gas to minimize the frost formation outside the cuvettes. The test was carried out after the pure water in the cuvette was kept at  $-15^{\circ}\text{C}$  for 5 h, which ensured that the water froze completely. The probe of the force transducer was then pushed to the ice columns at a speed of 0.5 mm/s and the peak force required to detach each ice column was measured. Ice adhesion on this water-swollen polymer network surface was measured as  $55 \pm 15$  kPa. The authors measured the ice adhesion on SHSs obtained by treating micropore arrayed silicon wafer surfaces with heptadecafluoro-1,1,2,2-tetradecyl-trimethoxysilane as  $1192 \pm 195$  kPa. A narrow ice column formed by freezing water on these surfaces was blown off by a strong breeze generated in a wind tunnel. Ice adhesion strength remained almost the same ( $67 \pm 8$  kPa) as the temperature was lowered from  $-15$  to  $-25^{\circ}\text{C}$ , but it increased sharply and reached  $1156 \pm 152$  kPa around  $-30^{\circ}\text{C}$ , indicating the disappearance of the self-lubricating liquid-like water layer by phase transition to ice [54].

### 5.3.2 Water on Hydrophilic PU Surfaces

Later, Jiang and co-workers replaced the micropatterned silicon wafer template with a PU coating for a mechanically robust anti-icing coating with an aqueous lubricating layer [57]. However, the synthesis of the coating was multi-step and complex: a hydrophilic component, dimethylol propionic acid, of the PU was obtained from the reaction of toluene 2,4-diisocyanate and poly(neopentyl glycol adipate). Neopentyl glycol and triethylamine were reacted to obtain the PU anionomer which was dispersed in water. Chain extension was achieved by reacting with isophorone diamine. Finally, mixtures of PU, hexamethylene diisocyanate curing agent, and  $\gamma$ -butyrolactone were spin-coated on the substrate, and then this film was thermally cured at  $110^{\circ}\text{C}$  for 11 h to fabricate the anti-icing coating. Hydrophilic pendant groups were introduced into the PU coating structure to absorb water in humid environments, forming a lubricating water layer on the surface even at subzero environments. This coating was applied to various substrates such as metals, metal alloys, ceramics, and polymers, and the ice adhesion strength on these surfaces was found to be around  $25 \pm 4$  kPa. The aqueous lubricating layer was experimentally determined to exist down to as low as  $-53^{\circ}\text{C}$ . A thin ice column, three times higher than wide, formed on this surface can be blown off by a strong breeze in a wind tunnel [57].



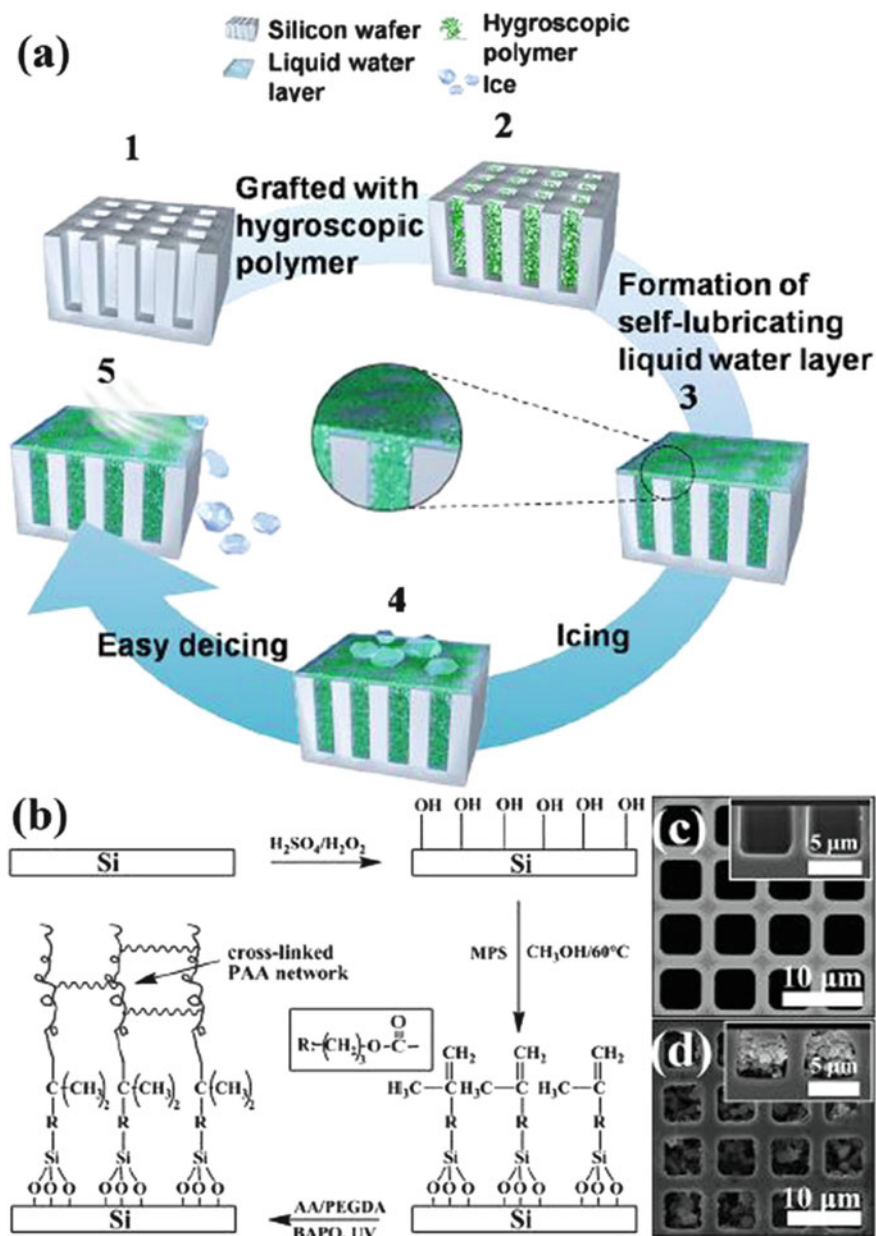


**Fig. 6** (a) Schematic illustration of the preparation of the self-lubricating liquid water layer surface. (1) Fabrication of micropore arrayed silicon wafer surfaces via a photolithographic process. (2) Grafting the micropore arrayed silicon wafer surfaces with cross-linked hygroscopic polymers. (3) Self-lubricating liquid water layer forms on micropore arrayed silicon wafer surfaces when condensation or deliquesce occurs. *Inset* is the magnified image of self-lubricating liquid water layer. (4) Ice formation atop of the self-lubricating liquid water layer. (5) Ice shed off with a

### 5.3.3 Water on a Hydrophilic Coating Formed from Hyaluronic Acid and Dopamine

Wang and coworkers used hyaluronic acid and dopamine to synthesize an anti-icing coating with an aqueous lubricating layer on the top of the surface [58]. Hyaluronic acid contains carboxyl and hydroxyl groups and has moisture-retention ability, whereas dopamine can adhere onto most organic and inorganic surfaces because of its nonselective adhesive property.

Dopamine was coupled to the carboxyl groups of hyaluronic acid by soaking in a catalyst containing phosphate-buffered saline solution for 10 h. The copolymer was applied onto metal, alumina, ceramic, and polymer surfaces. Water is absorbed onto the surface when the temperature is lowered, allowing the polymer to swell at the surface. A minimum ice adhesion strength value of 61 kPa was measured when the copolymer film thickness was 20 nm. Further increase of the film thickness of the anti-ice coating had an adverse effect and resulted in stronger ice adhesion to the surface [58].

### 5.3.4 Water on Superhydrophilic Polyelectrolyte Brush Coatings

Chernyy et al. investigated the possible use of superhydrophilic polyelectrolyte brush coatings for anti-icing applications and reported that they exhibit better anti-icing properties at  $-10^{\circ}\text{C}$  compared to partially hydrophobic brushes such as PMMA and surfactant exchanged polyelectrolyte brushes [123]. Ionizable groups were introduced to incorporate 13 mono-, bi-, and trivalent ions by ion exchange. All polyelectrolyte coatings demonstrated significant reduction in ice adhesion by 20–80% at  $-10^{\circ}\text{C}$  from 370 kPa down to 100 kPa, depending on ion type. Ice adhesion was reduced by approximately 40% at  $-18^{\circ}\text{C}$  from 560 kPa down to 320 kPa when  $\text{Li}^+$  ions were used [123].

### 5.3.5 Propylene Glycol on a Bilayer Coating Made of Nylon 66 Membrane and Hydrobead Superhydrophobic Layers

Ryckaczewski and co-workers drew inspiration from a poison dart frog that secretes mucus from its dermis to remain hydrated on its epidermis (skin) to develop a bilayer anti-icing coating that prevents accumulation of frost, rime, and glaze forms



**Fig. 6** (continued) wind action. **(b)** Preparation process of the micropore arrayed silicon wafer surface impregnated with cross-linked poly(acrylic acid) (PAA). Top view SEM images of representative micropore-arrayed silicon wafer surface: **(c)** before and **(d)** after being grafted with cross-linked hygroscopic polymers. *Insets* are the fracture-view SEM images of **(c)** and **(d)**. (Reproduced with permission from Chen et al. [54]. Copyright (2013) American Chemical Society)

of ice by responding to its presence with secretion of antifreeze liquid from the so-called “dermis” layer [71]. In practice, the “dermis” layer was a nylon 66 membrane (0.45  $\mu\text{m}$  pore size, 47 mm diameter) impregnated with propylene glycol antifreeze and the “epidermis” layer was a superhydrophobic layer formed on the nylon layer by spraying the commercial “Hydrobead” superhydrophobic water repellent coating to a thickness of 20–100  $\mu\text{m}$ . This bilayer coating consisted of a porous superhydrophobic “Hydrobead” layer at the top and a nylon layer that was infused with propylene glycol antifreeze that allowed the wicking of antifreeze through it to the upper layer. The outer superhydrophobic layer served as a barrier between the antifreeze and environment to shed large sessile drops, whereas the antifreeze present in the nylon layer responded to ice formation by wicking up of the stored propylene glycol. When condensation frosting or droplet impact occurred on the upper surface, water diffused downward through the pores of the superhydrophobic layer and this process initiated the wicking of propylene glycol upward after the water contact.

The addition of the propylene glycol antifreeze dramatically improved the performance of the surface in freezing rain conditions and slowed both the icing-onset time and complete icing time over the surface by about 1,000–2,000% (i.e., 30–60 min vs <3 min) as compared to samples not impregnated with propylene glycol (PG). For the condensation frosting experiments, addition of the Hydrobead epidermis slowed both the icing onset and complete icing over of the surface by about 133% compared to Nylon + PG (additional 20–40 min) and by at least 1,600% compared to all other samples (i.e., 80 min vs <5 min). Only a thin frost-like layer formed on this surface instead of the large ice crystals that formed on others. Moreover, icing onset during the misting experiments was delayed by the presence of the antifreeze by about 600% (i.e., 30 min vs <5 min) on both the antifreeze infused coatings when compared to the rest of the samples [71].

In another study, Rykaczewski and co-workers investigated the formation of frost-delaying areas by using the formation of macroscopic drops of propylene glycol and salt-saturated water on a surface [129]. It was previously shown that an individual salt-saturated water microdroplet can form a region of inhibited condensation and condensation frosting (RIC) in its surrounding area. This can occur because salt-saturated water is hygroscopic and has a water vapor pressure at its surface lower than the water saturation pressure at the substrate [130].

Rykaczewski and co-workers reported that the absolute RIC size can remain essentially unchanged for several hours for macroscopic drops of propylene glycol and salt-saturated water. Additionally, frost formation can be completely inhibited between microscopic and macroscopic arrays of propylene glycol and salt-saturated water drops when the spacing is smaller than twice the radius of the RIC, as seen in Fig. 7, where  $R_0$  is the radius of propylene glycol containing drops and  $S$  is the separation distance between the drop centers. The authors demonstrated that complete frosting can be delayed 1.6–10 times longer than with films of the liquids with equivalent volume by characterizing the condensation frosting dynamics around

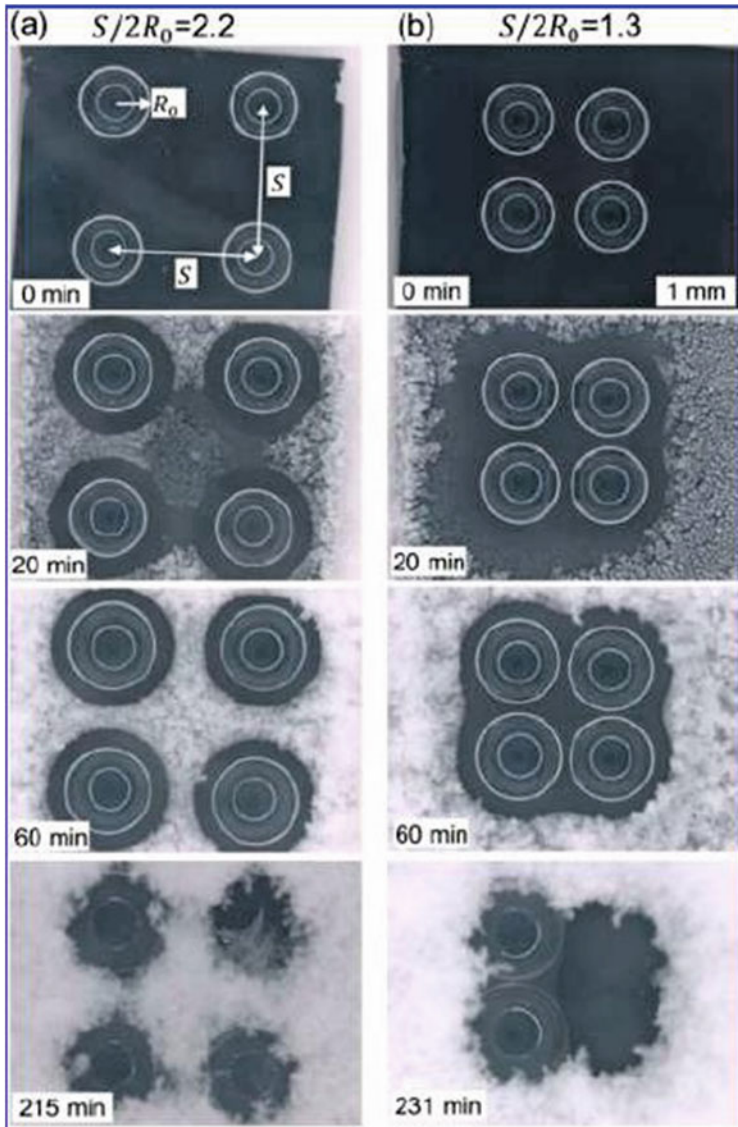


**Fig. 7** Images of condensation frosting around four 2- $\mu$ L propylene glycol drops with (a) sparse separation of  $S/2R_0 \approx 2.2$  and (b) dense separation of  $S/2R_0 \approx 1.3$ . (Reproduced with permission from Sun et al. [129]. Copyright (2015) American Chemical Society)

various hygroscopic drop arrays [129]. However, a method for the formation of such propylene glycol and salt-saturated water droplets with which to obtain the precise droplet locations to cover the large area required for practical applications still needs to be developed.

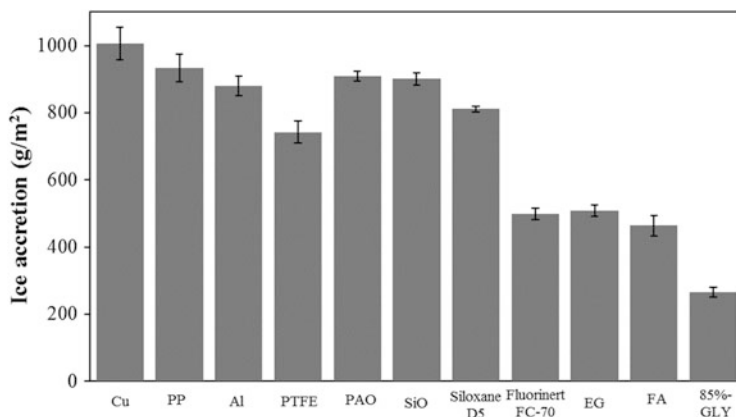


**Fig. 8** Ice accretion values on various reference and solvent impregnated filter paper surfaces at  $-2^{\circ}\text{C}$ . Four reference solid surfaces are copper (Cu), PP, aluminum (Al), and PTFE. The solvents used to form seven solvent impregnated filter paper surfaces are polyalphaolefin (PAO), silicone oil (SiO), decamethylcyclopentasiloxane (Siloxane D5), Fluorinert FC-70, ethylene glycol (EG), formamide (FA), and water–glycerine mixture containing 85 wt% glycerine (85%-GLY). (Reprinted with permission from Ozbay et al. [65]. Copyright (2015) American Chemical Society)

### 5.3.6 Aqueous Glycerine Solution on Filter Paper

As discussed in Sect. 5.1.10, Ozbay et al. studied what type of lubricants were efficient after impregnation in filter paper regarding ice accretion, drop freezing delay time, and ice adhesion strength by performing experiments at  $-2^{\circ}\text{C}$  and 56–83% RH [65]. Ice accretion test results were found to be unsatisfactory when hydrophobic lubricants such as polyalphaolefin, decamethylcyclopentasiloxane, silicone oil, and Fluorinert FC-70 were used after infusion in filter paper. However, when hydrophilic lubricants such as water, ethylene glycol, formamide, and water–glycerine mixtures were used for the same purpose, some good results for the ice accretion tests were obtained as shown in Fig. 8. The lowest ice accretion and ice adhesion values were obtained when aqueous glycerine solution containing 85 wt% glycerine was impregnated in hydrophilic filter paper. The details of ice accretion measurement are given in Sect. 7.

### 5.3.7 Water on Poly(Ethylene Glycol) and PDMS Blends

In recent work, Chen et al. designed self-lubricating icephobic coatings by blending PDMS with poly(ethylene glycol) (PEG) amphiphilic copolymers into a polymer matrix, which resulted in low ice adhesion strength values of about 50 kPa [124]. The authors proposed that an increased water depletion layer thickness at the interface weakens the van der Waals' interactions between the ice and the polymeric substrate for the smooth hydrophobic surfaces, whereas the PEG

component of the amphiphilic copolymer is capable of forming strong hydrogen bonds with water molecules. Consequently, the surface hydrogen-bonded water molecules do not freeze, even at substantial levels of subcooling.

## 6 Factors Affecting Ice Adhesion Strength and Its Standardization

The two most popular methods for measuring ice adhesion consist of freezing a thin column of ice and shearing it from a surface using a dynamometer force probe [18], or removing ice with the shear or tensile forces experienced during centrifugation [131]. In general, area-normalized ice adhesion strength depends on the methods of measurement because a fundamental aspect in measuring ice adhesion is the stress distribution at the ice–substrate interface upon loading. The shear stress should be evenly distributed on the interface, but it is very difficult to obtain this condition in practical ice adhesion tests and sometimes tensile strength is measured instead of shear strength [132]. Sometimes the “centrifuge ice adhesion test” method is applied, where the force required to separate the accreted ice from the coating is measured (e.g., adhesive failure). The test involves simultaneously icing bare reference and freshly coated aluminum samples using supercooled precipitation and then performing the centrifuge test on the samples one at a time. The ice adhesion shear stress is calculated from the ice detachment rotation speed. Stresses between 0.5 and 800 kPa have been measured [133].

In many instances, ice adhesion measurements can be normalized with respect to untreated control substrates such as aluminum. However, the variations in the surface properties produced by surface finish or preparation can affect the results. Furthermore, when the drop size, spray speed, and liquid water content per unit volume of air increase under sub-zero temperature conditions during ice accretion measurements, the ice density increases and the adhesive strength of accreted glaze on a surface increases because of the formation of larger contact areas of the glaze particles with the surface [14, 133].

As discussed in Sect. 4.1, the ice adhesion strength of smooth surfaces decreases as the surface free energy decreases [17–19]. There is an inverse relationship between the water contact angle and the ice adhesion strength of flat surfaces, which corresponds to a direct relationship between the total surface free energy and the ice adhesion strength [17, 19, 31, 57, 74, 79, 100, 131]. Ice adhesion strength values of some of the common materials have been reported to decrease in the following order: Cu ( $1217 \pm 34$ ) > stainless steel (SS) ( $1010 \pm 41$ ) > Al ( $731 \pm 53$ ) > PP ( $640 \pm 36$ ) > styrene butadiene rubber ( $412 \pm 26$ ) > PTFE ( $268 \pm 13$ ) all in kPa units [17]. However, these values are far larger than the ~20 kPa value which has been proposed to be the benchmark for surfaces that allow passive ice removal by factors such as wind, gravity, or vibration [1, 2, 6, 14,

57]. Much lower ice adhesion strength values have also been proposed as criteria for ice removal [133].

Slippery LAAS have been reported to reduce ice adhesion significantly down to  $\sim 0.5\text{--}10$  kPa [45, 49, 50, 52, 54, 56–58, 61–65, 123, 124, 126]. The dependence of ice adhesion on the lubricant level was investigated and it was found that ice adhesion increased significantly as excess lubricant above the posts was depleted [52]. Closely spaced posts were better able to keep the lubricant inside and may have contributed to decreased ice adhesion because of the increased Laplace pressure, which would allow maintenance of a smoother substrate–ice interface [49]. Very low ice adhesion strengths were reported when PDMS networks were used with silicone oil lubricants and liquid paraffin [56, 63]. When water was used as an aqueous lubricant layer, these surfaces were capable of suppressing ice nucleation through molecular confinement, although hydrophilic surfaces generally possess high ice adhesion [54, 57, 58, 123]. A very low ice adhesion value of  $\sim 25$  kPa at temperatures down to  $-53^\circ\text{C}$ , even after 30 icing–deicing cycles, was reported [57].

The standardization of ice adhesion strength tests is required. First of all, some researchers use cylindrical hydrophobized glass columns (Pasteur pipette), some used square prism glass or plastic columns, and some use spherical cap water drops of various volumes to obtain adhered ice on a sample surface. If columns are used, then the ends of these columns must be very uniform and well-polished to ensure complete adhesion through the interfacial contact area and prevent the leakage of water to form a thin (or thick) film on the sample.

In some experiments, only Peltier or other cooling instruments were used to cool the samples underneath in room conditions. Others used specific closed chambers and sometimes deep freezers. The temperature and duration of the water freezing process varied considerably with temperatures ranging between  $-10$  and  $-30^\circ\text{C}$  and cooling times from 15 min to 8 h. Some researchers passed  $\text{N}_2$  gas through the test chamber and others use a predefined procedure to control the RH and cooling rate in the chamber. For example: “The humidity in the chamber is decreased below 3% RH in order to avoid frost formation and the temperature of the substrate is lowered at a rate of  $2^\circ\text{C}/\text{min}$  until ice forms on it, at a substrate temperature of  $-20^\circ\text{C}$  or below to ensure freezing. The temperature is then raised to  $-10^\circ\text{C}$  at a rate of  $2^\circ\text{C}/\text{min}$  after ice formation and the samples are allowed to equilibrate for 30 min” [45]. It is better if the freezing experiments are carried out in a deep freezer which is set to a specific cold temperature, because the types of ice crystals are different depending on the applied temperature. A temperature of  $-10^\circ\text{C}$  is a good choice for ice formation to be used in ice adhesion tests because, if high ice adhesion values are measured at  $-10^\circ\text{C}$ , there is no need to investigate the sample surface for colder conditions. In addition, this standardization helps to compare the ice adhesion results from different laboratories.

The force application location during the adhesion test is also important. The sample columns must be either pulled or pushed using a tensiometer at a contact point less than 1 mm above the surface of the substrate, at the same time maintaining a specified temperature. However, the temperature during the

tensiometer application is not usually reported in many publications and only the ice formation temperature is given. This test temperature can be standardized as  $-5$  or  $-10^{\circ}\text{C}$  or both. The location of the tensiometer is important to discriminate the shear force from tensile and tearing forces. If some ice remains on the surface it indicates the presence of cohesive failure of ice and the experiments should be repeated. The rate of the forward or backward movement of the force gauge ( $0.4\text{--}0.6$  mm/s) should be controlled precisely to obtain repeatable test results.

Another problem is the measurement of real contact area after adhesive failure. Usually only plan area is considered for the ice adhesion strength calculations. If an area increase occurs because of a high surface roughness present on the sample surface, then this factor should be considered in the shear strength calculations. Although it is a difficult process to calculate the real interfacial area, simple optical microscopy investigation can be applied immediately after the adhesive failure to both sample and ice surfaces to ascertain the failure mode.

## 7 Standardization of Ice Accretion Experiments

The standardization of ice accretion experiments is required for better comparison of the results obtained from different laboratories [17, 113, 134]. Some researchers have performed ice accretion experiments on LAAS [56, 61, 62, 65, 71, 122] although only one publication reported the ice accretion results of large area slippery LAASs in mass/area units [65]. Correspondingly, in most of the anti-icing studies, only a few papers reported ice accretion results on sample surfaces in mass/area units [17, 65, 69, 73–76, 78, 79]. Providing images of samples after ice accretion is not a feasible way to evaluate the ice accretion on samples; this can help for only simple comparisons [10, 21, 24, 77, 80, 84].

In the ice accretion experiments, which are carried out in closed chambers by spraying the cold water droplets with a spray gun [17, 33, 65, 74], the inlet and outlet temperatures of water droplets, the mean particle size, and total quantity of the sprayed droplets during the test are very important parameters, which are usually overlooked. The control of the initial and final temperature, initial and final RH of air, and its change rate during spraying water droplets in the chamber are also very important. The shape, inclination angle, and initial and final temperatures of the substrates must also be precisely controlled and should be reported. The mass increase on the samples should be immediately determined in a proper way (gravimetrically or volumetrically), preventing mass losses of accreted glaze or rime because of melting on the samples during measurement.

As an example of ice accretion experiments, we performed these tests in a climatic chamber (Mettert CTC-256) at a constant temperature of  $-2^{\circ}\text{C}$  [17, 65]. Representative photographs of the experimental system were given in the supplementary material files of these publications. As it was not possible to control the RH in this environmental chamber below  $+10^{\circ}\text{C}$ , a procedure was developed to obtain a roughly constant RH in this chamber. Initially, the



temperature of the chamber was set to  $+10^{\circ}\text{C}$  and RH 50% and then the RH setting was turned off and the temperature of the chamber was set to cool down to  $-2^{\circ}\text{C}$ ; the RH value in the chamber became constant at around  $56 \pm 3\%$  at  $-2^{\circ}\text{C}$  after 45 min for all the experiments. A previously weighed test sample was placed in the chamber. The distance between the spray gun and the substrate was approximately 18 cm. The inclination angle between substrate and spray gun was  $90^{\circ}$ .

After equilibrium, supercooled water droplets at a temperature of around  $-1^{\circ}\text{C}$  were sprayed through a metallic spray gun that used compressed air. Pure water which was sprayed onto the sample was previously placed in the chamber in a graduated cylinder and connected to the air spray gun with a plastic tube. This graduated cylinder was heated externally by a long plastic pipe connected to a Lauda circulator which was placed out of the chamber where the temperature of a 50% aqueous propylene glycol circulation solution was kept constant at  $1.2^{\circ}\text{C}$ . The external heating tubing was isolated externally with glass fiber layers to maintain a constant temperature within the chamber. The heat balance in the environmental chamber at  $-2^{\circ}\text{C}$  resulted in a supercooled water temperature of  $-1^{\circ}\text{C}$  in the graduated cylinder before the spraying started (there was a temperature probe in the graduated cylinder). Around 30 mL of water was sprayed for 10 min at a rate of 0.05 mL/s by the application of  $17 \text{ m}^3/\text{h}$  air velocity to the air gun which was adjusted by using a flow meter. Supercooled water was sucked by the spray gun through a PU hose from the graduated cylinder. The RH of the chamber gradually increased from 56% to 83% during this spraying period. After spraying, the sample was removed from the chamber rapidly and the mass increase on the sample produced by the ice accretion was determined by a nearby balance in less than 15 s. Meanwhile, the volume of the remaining supercooled water in the graduated cylinder was determined and the mass increase on the samples was normalized for a constant amount of 30 mL supercooled water spray to obtain comparable ice accretion results on different test samples. The area of sample coated with ice was measured and ice accretion results were reported in  $\text{g}/\text{m}^2$  units [17, 65]. Improvements to this ice accretion system would be to develop a method for measuring size distribution of the supercooled droplets and also to decrease the temperature of the test chamber from  $-2$  to  $-10^{\circ}\text{C}$ .

## 8 Concluding Remarks and Perspective

Ice accumulation on surfaces is an important problem in aerospace, wind turbines, marine applications, power transmission, cell phone communications, building infrastructure, refrigeration, and other industries. It is well-known that presently no single surface has shown the ability to remove impacting and condensing water droplets rapidly, minimize ice nucleation, and reduce ice adhesion with high durability and longevity, although progress has been made, especially in the last decade. We have examined the anti-icing performances of LAAS in comparison with other proposed surfaces such as smooth and SHSs in this review. It is well-

known that SHSs have mostly failed in icephobic applications because of issues of condensation frosting at high relative humidities at below 0°C conditions and also weak mechanical resistance during ice removal. They may, however, be used in heat exchangers in some controlled environments [1].

In many publications it is reported that the use of LAAS incorporating fluorinated or silicone lubricating layers for anti-icing surfaces have limitations because the loss of lubricants present in them is high because of the evaporation, drainage, and cloaking of the lubricant when water droplets condense on them. Short lifetimes of these lubricants on an LAAS during the anti-icing service period are the major problem. There are also environmental pollution and cost issues which may hamper the use of some proposed lubricants for large scale applications. When the performances of fluorinated and silicone lubricants are compared, silicone lubricants are better because of their longer lifetimes, lower cost, and lower environmental constraints.

On the other hand, the use of LAAS incorporating water and other hydrophilic lubricating layers on hygroscopic polymers in anti-icing applications seem to be more promising because replenishment of the aqueous lubricant by atmospheric moisture allows their long term usage. However, some important anti-icing properties such as ice accretion mass per unit area and drop freezing times have not been reported for these surfaces, and need to be tested both in laboratory and outdoor conditions. A hydrophilic water–glycerine mixture-impregnated filter paper surface exhibited good ice accretion properties, outperforming fluorinated or silicone lubricants [65], indicating the need for suitable solid supports to hold such anti-freeze liquids on intended surfaces for the long durations required in some industrial applications. In addition, most of the antifreeze solutions are environmentally harmful and this may restrict their industrial scope.

Future research into a continuous supply of a cheap and environmentally favorable hydrophilic lubricant from a liquid reservoir onto a textured support is necessary for the sustained performance of LAAS coatings. Another option may be to use LAAS and SHSs in combination with traditional anti-icing and deicing techniques [71]. The superhydrophobic layer covers the matrix layer to prevent the rapid evaporation or leakage of the lubricant and, if the porosity of the superhydrophobic layer can be adequately controlled, the infusion of the lubricant beneath the matrix through the top layer improves the icephobicity and increases the service time of the coating. However, much research may be required to create such a successful matrix-coating pair. Another promising option is the combination of Joule heating with LAAS to decrease the required energy and expenses [121].

There are many types of ice adhesion measurements which are reported in the literature and this causes confusion when comparing the results. There is a need for the standardization of ice adhesion experiments and some suggestions are made in this review. In addition, the importance of the determination of the ice accretion in mass per area units on test surfaces is mostly overlooked in most of the publications, probably because of the high cost of the laboratory setups used for such tests. An example of a relatively inexpensive laboratory setup was given in this review.

The standardization of ice accretion experiments is also required for better comparison of results obtained from different laboratories in the future.

Lastly, another problem is the sole reporting of ice adhesion strength results of the tested anti-icing surfaces in most of the scientific publications. This is generally insufficient to evaluate the practical usage of the coating and it is better if the journal editors and reviewers ask for the simultaneous reporting of the results of ice adhesion, ice accretion, icing delay times, and effect of freezing/defrosting cycles on these properties.

**Acknowledgment** This work was supported by the Scientific and Technological Research Council of Turkey (TUBITAK) under the project “Synthesis and characterization of anti-icing coatings made of porous polymer/impregnated liquid pair” (Project No: 112T813).

## References

1. Kreder MJ, Alvarenga J, Kim P, Aizenberg J (2016) Design of anti-icing surfaces: smooth, textured or slippery? *Nat Rev Mater* 1:15003
2. Lv J, Song Y, Jiang L, Wang J (2014) Bio-inspired strategies for anti-icing. *ACS Nano* 8:3152–3169
3. Marwitz J, Politovich M, Bernstein B, Ralph F, Neiman P, Ashenden R, Bresch J (1997) Meteorological conditions associated with the ATR72 aircraft accident near Roselawn, Indiana, on 31 October 1994. *Bull Am Meteorol Soc* 78:41–52
4. Makkonen L, Laakso T, Marjaniemi M, Finstad KJ (2001) Modeling and prevention of ice accretion on wind turbines. *Wind Eng* 25:3–21
5. Dalili N, Edrissy A, Cariveau R (2009) A review of surface engineering issues critical to wind turbine performance. *Renew Sust Energ Rev* 13:428–438
6. Parent O, Ilincă A (2011) Anti-icing and de-icing techniques for wind turbines: critical review. *Cold Reg Sci Technol* 65:88–96
7. Laforte JL, Allaire MA, Laflamme J (1998) State-of-the-art on power line de-icing. *Atmos Res* 46:143–158
8. Ryerson CC (2011) Ice protection of offshore platforms. *Cold Reg Sci Technol* 65:97–110
9. Fillion RM, Riahi AR, Edrissy A (2014) A review of icing prevention in photovoltaic devices by surface engineering. *Renew Sust Energ Rev* 32:797–809
10. Antonini C, Innocenti M, Horn T, Marengo M, Amirfazli A (2011) Understanding the effect of superhydrophobic coatings on energy reduction in anti-icing systems. *Cold Reg Sci Technol* 67:58–67
11. Mohseni M, Amirfazli A (2013) A novel electro-thermal anti-icing system for fiber-reinforced polymer composite airfoils. *Cold Reg Sci Technol* 87:47–58
12. Muthumani A, Fay L, Akin M, Wang S, Gong J, Shi X (2014) Correlating lab and field tests for evaluation of deicing and anti-icing chemicals: a review of potential approaches. *Cold Reg Sci Technol* 97:21–32
13. Meuler AJ, McKinley GH, Cohen RE (2010) Exploiting topographical texture to impart icephobicity. *ACS Nano* 4:7048–7052
14. Schutzius TM, Jung S, Maitra T, Eberle P, Antonini C, Stamatopoulos C, Poulidakos D (2015) Physics of icing and rational design of surfaces with extraordinary icephobicity. *Langmuir* 31:4807–4821
15. Darmanin T, Guittard F (2014) Recent advances in the potential applications of bioinspired superhydrophobic materials. *J Mater Chem A* 2:16319–16359

16. Liu B, Zhang K, Tao C, Zhao Y, Li X, Zhu K, Yuan X (2016) Strategies for anti-icing: low surface energy or liquid infused? *RSC Adv* 6:70251–70260
17. Ozbay S, Erbil HY (2016) Ice accretion by spraying supercooled droplets is not dependent on wettability and surface free energy of substrates. *Colloids Surf A Physicochem Eng Asp* 504:210–218
18. Jellinek HHG, Kachi H, Kittaka S, Lee M, Yokota R (1978) Ice releasing block-copolymer coatings. *Colloid Polym Sci* 256:544–551
19. Saito H, Takai K, Yamauchi G (1997) Water and ice-repellent coatings. *Surf Coat Int* 80:168–171
20. Roach P, Shirtcliffe NJ, Newton MI (2008) Progress in superhydrophobic surface development. *Soft Matter* 4:224–240
21. Erbil HY, Demirel AL, Avci Y, Mert O (2003) Transformation of a simple plastic into a superhydrophobic surface. *Science* 299:1377–1380
22. Jung S, Dorrestijn M, Raps D, Das A, Megaridis CM, Poulikakos D (2011) Are superhydrophobic surfaces best for icephobicity? *Langmuir* 27:3059–3066
23. Cao L, Jones AK, Sikka VK, Wu J, Gao D (2009) Anti-icing superhydrophobic coatings. *Langmuir* 25:12444–12448
24. Kulinich SA, Farzaneh M (2009) Ice adhesion on super-hydrophobic surfaces. *Appl Surf Sci* 255:8153–8157
25. Kulinich SA, Farzaneh M (2009) How wetting hysteresis influences ice adhesion strength on superhydrophobic surfaces. *Langmuir* 25:8854–8856
26. Wang F, Li C, Lv Y, Lv F, Du Y (2010) Ice accretion on superhydrophobic aluminum surfaces under low-temperature conditions. *Cold Reg Sci Technol* 62:29–33
27. He M, Wang J, Li H, Song Y (2011) Superhydrophobic surfaces to condensed micro-droplets at temperatures below the freezing point retard ice/frost formation. *Soft Matter* 7:3993–4000
28. Menini R, Ghalmi Z, Farzaneh M (2011) Highly resistant icephobic coatings on aluminum alloys. *Cold Reg Sci Technol* 65:65–69
29. Guo P, Zheng Y, Wen M, Song C, Lin Y, Jiang L (2012) Icephobic/anti-icing properties of micro/nanostructured surfaces. *Adv Mater* 24:2642–2648
30. Ruan M, Li W, Wang B, Deng B, Ma F, Yu Z (2013) Preparation and anti-icing behavior of superhydrophobic surfaces on aluminum alloy substrates. *Langmuir* 29:8482–8491
31. Boinovich LB, Emelyanenko AM (2013) Anti-icing potential of superhydrophobic coatings. *Mendeleev Commun* 23:3–10
32. Arianpour F, Farzaneh M, Kulinich SA (2013) Hydrophobic and ice-retarding properties of doped silicone rubber coatings. *Appl Surf Sci* 265:546–552
33. Bharathidasan T, Kumar SV, Bobji MS, Chakradhar RPS, Basu BJ (2014) Effect of wettability and surface roughness on ice-adhesion strength of hydrophilic, hydrophobic and superhydrophobic surfaces. *Appl Surf Sci* 314:241–250
34. Davis A, Yeong YH, Steele A, Bayer IS, Loth E (2014) Superhydrophobic nanocomposite surface topography and ice adhesion. *ACS Appl Mater Interfaces* 6:9272–9279
35. Ozbay S, Erbil HY (2015) Superhydrophobic and oleophobic surfaces obtained by graft copolymerization of perfluoroalkyl ethyl acrylate onto SBR rubber. *Colloids Surf A Physicochem Eng Asp* 481:537–546
36. Varanasi KK, Deng T, Smith JD, Hsu M, Bhate N (2010) Frost formation and ice adhesion on superhydrophobic surfaces. *Appl Phys Lett* 97:234102
37. He M, Li H, Wang J, Song Y (2011) Superhydrophobic surface at low surface temperature. *Appl Phys Lett* 98:093118
38. Farhadi S, Farzaneh M, Kulinich SA (2011) Anti-icing performance of superhydrophobic surfaces. *Appl Surf Sci* 257:6264–6269
39. Kulinich SA, Farhadi S, Nose K, Du XW (2011) Superhydrophobic surfaces: are they really ice-repellent? *Langmuir* 27:25–29
40. Chen J, Liu J, He M, Li K, Cui D, Zhang Q, Zeng X, Zhang Y, Wang J, Song Y (2012) Superhydrophobic surfaces cannot reduce ice adhesion. *Appl Phys Lett* 101:111603

41. Nosonovsky M, Hejazi V (2012) Why superhydrophobic surfaces are not always icephobic. *ACS Nano* 6:8488–8491
42. Oberli L, Caruso D, Hall C, Fabretto M, Murphy PJ, Evans D (2014) Condensation and freezing of droplets on superhydrophobic surfaces. *Adv Colloid Interf Sci* 210:47–57
43. Wang H, He G, Tian Q (2012) Effects of nano-fluorocarbon coating on icing. *Appl Surf Sci* 258:7219–7224
44. Wong TS, Kang SH, Tang SKY, Smythe EJ, Hatton BD, Grinthal A, Aizenberg J (2011) Bioinspired self-repairing slippery surfaces with pressure-stable omniphobicity. *Nature* 477:443–447
45. Kim P, Wong TS, Alvarenga J, Kreder MJ, Adorno-Martinez WE, Aizenberg J (2012) Liquid-infused nanostructured surfaces with extreme anti-ice and anti-frost performance. *ACS Nano* 6:6569–6577
46. Stone HA (2012) Ice-phobic surfaces that are wet. *ACS Nano* 6:6536–6540
47. Anand S, Paxson AT, Dhiman R, Smith JD, Varanasi KK (2012) Enhanced condensation on lubricant-impregnated nanotextured surfaces. *ACS Nano* 6:10122–10129
48. Wilson PW, Lu W, Xu H, Kim P, Kreder MJ, Alvarenga J, Aizenberg J (2013) Inhibition of ice nucleation by slippery liquid-infused porous surfaces (SLIPS). *Phys Chem Chem Phys* 15:581–585
49. Kim P, Kreder MJ, Alvarenga J, Aizenberg J (2013) Hierarchical or not? Effect of the length scale and hierarchy of the surface roughness on omniphobicity of lubricant-infused substrates. *Nano Lett* 13:1793–1799
50. Vogel N, Belisle RA, Hatton B, Wong TS, Aizenberg J (2013) Transparency and damage tolerance of patternable omniphobic lubricated surfaces based on inverse colloidal monolayers. *Nat Commun* 4:2176–2185
51. Smith JD, Dhiman R, Anand S, Reza-Garduno E, Cohen RE, McKinley GH, Varanasi KK (2013) Droplet mobility on lubricant-impregnated surfaces. *Soft Matter* 9:1772–1780
52. Subramanyam SB, Rykaczewski K, Varanasi KK (2013) Ice adhesion on lubricant-impregnated textured surfaces. *Langmuir* 29:13414–13418
53. Rykaczewski K, Anand S, Subramanyam SB, Varanasi KK (2013) Mechanism of frost formation on lubricant-impregnated surfaces. *Langmuir* 29:5230–5238
54. Chen J, Dou R, Cui D, Zhang Q, Zhang Y, Xu F, Zhou X, Wang J, Song Y, Jiang L (2013) Robust prototypical anti-icing coatings with a self-lubricating liquid water layer between ice and substrate. *ACS Appl Mater Interfaces* 5:4026–4030
55. Liu H, Zhang P, Liu M, Wang S, Jiang L (2013) Organogel-based thin films for self-cleaning on various surfaces. *Adv Mater* 25:4477–4481
56. Zhu L, Xue J, Wang Y, Chen Q, Ding J, Wang Q (2013) Ice-phobic coatings based on silicon-oil-infused polydimethylsiloxane. *ACS Appl Mater Interfaces* 5:4053–4062
57. Dou R, Chen J, Zhang Y, Wang X, Cui D, Song Y, Jiang L, Wang J (2014) Anti-icing coating with an aqueous lubricating layer. *ACS Appl Mater Interfaces* 6:6998–7003
58. Chen J, Luo Z, Fan Q, Lv J, Wang J (2014) Anti-ice coating inspired by ice skating. *Small* 10:4693–4699
59. Chen L, Geissler A, Bonaccorso E, Zhang K (2014) Transparent slippery surfaces made with sustainable porous cellulose lauroyl ester films. *ACS Appl Mater Interfaces* 6:6969–6976
60. Eifert A, Paulssen D, Varanakkottu SN, Baier T, Hardt S (2014) Simple fabrication of robust water-repellent surfaces with low contact-angle hysteresis based on impregnation. *Adv Mater Interfaces* 1:1300138
61. Yin X, Zhang Y, Wang D, Liu Z, Liu Y, Pei X, Yu B, Zhou F (2015) Integration of self-lubrication and near-infrared photothermogenesis for excellent anti-icing/deicing performance. *Adv Funct Mater* 25:4237–4245
62. Liu Q, Yang Y, Huang M, Zhou Y, Liu Y, Liang X (2015) Durability of a lubricant-infused electro-spray silicon rubber surface as an anti-icing coating. *Appl Surf Sci* 346:68–76
63. Wang Y, Yao X, Chen J, He Z, Liu J, Li Q, Wang J, Jiang L (2015) Organogel as durable anti-icing coatings. *Sci China Mater* 58:559–564

64. Urata C, Dunderdale GJ, England MW, Hozumi A (2015) Self-lubricating organogels (SLUGs) with exceptional syneresis-induced anti-sticking properties against viscous emulsions and ices. *J Mater Chem A* 3:12626–12630
65. Ozbay S, Yuceel C, Erbil HY (2015) Improved icephobic properties on surfaces with a hydrophilic lubricating liquid. *ACS Appl Mater Interfaces* 7:22067–22077
66. Liu Y, Ma J, Wu T, Wang X, Huang G, Liu Y, Qiu H, Li Y, Wang W, Gao J (2013) Cost-effective reduced graphene oxide-coated polyurethane sponge as a highly efficient and reusable oil-absorbent. *ACS Appl Mater Interfaces* 5:10018–10026
67. Wu Y, Yi N, Huang L, Zhang T, Fang S, Chang H, Li N, Oh J, Lee JA, Kozlov M, Chipara AC, Terrones H, Xiao P, Long G, Huang Y, Zhang F, Zhang L, Lepro X, Haines C, Lima MD, Lopez NP, Rajukumar LP, Elias AL, Feng S, Kim SJ, Narayanan NT, Ajayan PM, Terrones M, Aliev A, Chu P, Zhang Z, Baughman RH, Chen Y (2015) Three-dimensionally bonded spongy graphene material with super compressive elasticity and near-zero Poisson's ratio. *Nat Commun* 6:6141
68. Tai MH, Tan BYL, Juay J, Sun DD, Leckie JO (2015) Self-assembled superhydrophobic electrospun carbon-silica nano-fiber sponge for selective removal and recovery of oils and organic solvents. *Chem Eur J* 21:5395–5402
69. Tattelman P (1982) An objective method for measuring surface ice accretion. *J Appl Meteorol* 21:599–612
70. Sastry S (2005) Ins and outs of ice nucleation. *Nature* 438:746–747
71. Sun X, Damle VG, Liu S, Rykaczewski K (2015) Bioinspired stimuli-responsive and antifreeze-secreting anti-icing coatings. *Adv Mater Interfaces* 2:1400479
72. Macklin WC (1961) The density and structure of ice formed by accretion. *Q J R Meteorol Soc* 88:30–50
73. Yin L, Xia Q, Xue J, Yang S, Wang Q, Chen Q (2010) In situ investigation of ice formation on surfaces with representative wettability. *Appl Surf Sci* 256:6764–6769
74. Yang SQ, Xia Q, Zhu L, Xue J, Wang QJ, Chen QM (2011) Research on the icephobic properties of fluoropolymer-based materials. *Appl Surf Sci* 257:4956–4962
75. Peng C, Xing S, Yuan Z, Xiao J, Wang C, Zeng J (2012) Preparation and anti-icing of superhydrophobic PVDF coating on a wind turbine blade. *Appl Surf Sci* 259:764–768
76. Yuan Z, Bin J, Wang X, Liu Q, Zhao D, Chen H, Jiang H (2012) Preparation and anti-icing property of a lotus-leaf-like superhydrophobic low-density polyethylene coating with low sliding angle. *Polym Eng Sci* 52:2310–2315
77. Li H, Zhao Y, Yuan X (2013) Facile preparation of superhydrophobic coating by spraying a fluorinated acrylic random copolymer micelle solution. *Soft Matter* 9:1005–1009
78. Jiang X, Zou D, Kong XZ, Zhu X, Zhang Z (2014) Styrene-butyl acrylate copolymers latexes prepared with different functional monomers and their application as anti-icing coatings. *J Polym Res* 21:473–478
79. He Y, Jiang C, Hu P, Yang R, Tian W, Yuan W (2015) Reducing ice accumulation and adhesion by using a flexible micro-rod film. *Cold Reg Sci Technol* 118:57–63
80. Mangini D, Antonini C, Marengo M, Amirfazli A (2015) Runback ice formation mechanism on hydrophilic and superhydrophobic surfaces. *Cold Reg Sci Technol* 109:53–60
81. Pureskiy N, Chanda J, Stoychev G, Synytska A, Ionov L (2015) Anti-icing superhydrophobic surfaces based on core-shell fossil particles. *Adv Mater Interfaces* 2:1500124
82. Zuo Z, Liao R, Guo C, Yuan Y, Zhao X, Zhuang A, Zhang Y (2015) Fabrication and anti-icing property of coral-like superhydrophobic aluminum surface. *Appl Surf Sci* 331:132–139
83. Saleema N, Farzaneh M, Paynter RW, Sarkar DK (2011) Prevention of ice accretion on aluminum surfaces by enhancing their hydrophobic properties. *J Adhes Sci Technol* 25:27–40
84. Fang G, Amirfazli A (2014) Understanding the anti-icing behavior of superhydrophobic surfaces. *Surf Innov* 2:94–102

85. Erbil HY (2016) Improvement of lubricant-infused surfaces for anti-icing applications. *Surf Innov* 4:214–217
86. Ucar IO, Erbil HY (2012) Use of diffusion controlled drop evaporation equations for dropwise condensation during dew formation and effect of neighboring droplets. *Colloids Surf A Physicochem Eng Asp* 411:60–68
87. Ucar IO, Erbil HY (2012) Dropwise condensation rate of water breath figures on polymer surfaces having similar surface free energies. *Appl Surf Sci* 259:515–523
88. Zhang Q, He M, Zeng X, Li K, Cui D, Chen J, Wang J, Song Y, Lei Jiang L (2012) Condensation mode determines the freezing of condensed water on solid surfaces. *Soft Matter* 8:8285–8288
89. Wen M, Wang L, Zhang M, Jiang L, Zheng Y (2014) Antifogging and icing-delay properties of composite micro- and nanostructured surfaces. *ACS Appl Mater Interfaces* 6:3963–3968
90. Eberle P, Tiwari MK, Maitra T, Poulikakos D (2014) Rational nanostructuring of surfaces for extraordinary icephobicity. *Nanoscale* 6:4874–4882
91. Tourkine P, Merrer ML, Quéré D (2009) Delayed freezing on water repellent materials. *Langmuir* 25:7214–7216
92. He M, Wang J, Li H, Jin X, Wang J, Liu B, Song Y (2010) Super-hydrophobic film retards frost formation. *Soft Matter* 6:2396–2399
93. Huang Y, Hu M, Yi S, Liu X, Li H, Huang C, Luo Y, Li Y (2012) Preparation and characterization of silica/fluorinated acrylate copolymers hybrid films and the investigation of their icephobicity. *Thin Solid Films* 520:5644–5651
94. Li K, Xu S, Shi W, He M, Li H, Li S, Zhou X, Wang J, Song Y (2012) Investigating the effects of solid surfaces on ice nucleation. *Langmuir* 28:10749–10754
95. Boinovich L, Emelyanenko AM, Korolev VV, Pashinin AS (2014) Effect of wettability on sessile drop freezing: when superhydrophobicity stimulates an extreme freezing delay. *Langmuir* 30:1659–1668
96. Hao P, Lv C, Zhang X (2014) Freezing of sessile water droplets on surfaces with various roughness and wettability. *Appl Phys Lett* 104:161609
97. Chen X, Ma R, Zhou H, Zhou X, Che L, Yao S, Wang Z (2013) Activating the microscale edge effect in a hierarchical surface for frosting suppression and defrosting promotion. *Sci Rep* 3:2515
98. Landy M, Freiberger A (1967) Studies of ice adhesion. *J Colloid Interface Sci* 25:231–244
99. Bascom WD, Cottington RL, Singleterry CR (1969) Ice adhesion to hydrophilic and hydrophobic surfaces. *J Adhes* 1:246–263
100. Meuler AJ, Smith JD, Varanasi KK, Mabry JM, McKinley GH, Cohen RE (2010) Relationships between water wettability and ice adhesion. *ACS Appl Mater Interfaces* 2:3100–3110
101. Erbil HY (2006) *Surface chemistry of solid and liquid interfaces*. Blackwell Publishing, Oxford
102. Menini R, Farzaneh M (2009) Elaboration of Al<sub>2</sub>O<sub>3</sub>/PTFE icephobic coatings for protecting aluminum surfaces. *Surf Coat Technol* 203:1941–1946
103. Petrenko VF, Peng S (2003) Reduction of ice adhesion to metal by using self-assembling monolayers (SAMs). *Can J Phys* 81:387–393
104. Zou M, Beckford S, Wie R, Ellis C, Hatton G, Miller MA (2011) Effects of surface roughness and energy on ice adhesion strength. *Appl Surf Sci* 257:3786–3792
105. Sojoudi H, McKinley GH, Gleason KK (2015) Linker-free grafting of fluorinated polymeric cross-linked network bilayers for durable reduction of ice adhesion. *Mater Horiz* 2:91–99
106. Menini R, Farzaneh M (2011) Advanced icephobic coatings. *J Adhes Sci Technol* 25:971–992
107. Frankenstein S, Tuthill AM (2002) Ice adhesion to locks and dams: past work; future directions? *J Cold Reg Eng* 16:83–96
108. Wang C, Fuller T, Zhang W, Wynne KJ (2014) Thickness dependence of ice removal stress for a polydimethylsiloxane nanocomposite: Sylgard 184. *Langmuir* 30:12819–12826

109. Beemer DL, Wang W, Kota AK (2016) Durable gels with ultra-low adhesion to ice. *J Mater Chem A* 4:18253–18258
110. Golovin K, Kobaku SP, Lee DH, DiLoreto ET, Mabry JM, Tuteja A (2016) Designing durable icephobic surfaces. *Sci Adv* 2:e1501496
111. Fu QT, Wu XH, Kumar D, Ho JWC, Kanhere PD, Srikanth N, Liu EJ, Wilson P, Chen Z (2014) Development of sol-gel icephobic coatings: effect of surface roughness and surface energy. *ACS Appl Mater Interfaces* 6:20685–20692
112. Li XH, Zhao YH, Li H, Yuan XY (2014) Preparation and icephobic properties of polymethyltrifluoropropylsiloxane–polyacrylate block copolymers. *Appl Surf Sci* 316:222–231
113. Zhang KQ, Cai JZ, Li XH, Li H, Zhao YH, Yuan XY (2015) Balance of polyacrylate–fluorosilicone block copolymers as icephobic coatings. *Chin J Polym Sci* 33:153–162
114. Narhe RD, Beysens DA (2004) Nucleation and growth on a superhydrophobic grooved surface. *Phys Rev Lett* 93:076103
115. Wier KA, McCarthy TJ (2006) Condensation on ultrahydrophobic surfaces and its effect on droplet mobility: ultrahydrophobic surfaces are not always water repellent. *Langmuir* 22:2433–2436
116. Varanasi KK, Hsu M, Bhate N, Yang W, Deng T (2009) Spatial control in the heterogeneous nucleation of water. *Appl Phys Lett* 95:094101
117. Zhang Y, Yu X, Wu H, Wu J (2012) Facile fabrication of superhydrophobic nanostructures on aluminum foils with controlled-condensation and delayed-icing effects. *Appl Surf Sci* 258:8253–8257
118. Attinger D, Frankiewicz C, Betz AR, Schutzius TM, Ganguly R, Das A, Kim CJ, Megaridis CM (2014) Surface engineering for phase change heat transfer: a review. *MRS Energy Sustain* 1:E4
119. Maitra T, Antonini C, Tiwari MK, Mularczyk A, Imeri Z, Schoch P, Poulikakos D (2014) Supercooled water drops impacting superhydrophobic texture. *Langmuir* 30:10855–10865
120. Wang N, Xiong D, Lu Y, Pan S, Wang K, Deng Y, Shi Y (2016) Design and fabrication of the lyophobic slippery surface and its application in anti-icing. *J Phys Chem C* 120:11054–11059
121. Wang T, Zheng Y, Raji ARO, Li Y, Sikkema WKA, Tour JM (2016) Passive anti-icing and active deicing films. *ACS Appl Mater Interfaces* 8:14169–14173
122. Elsharkawy M, Tortorella D, Kapatral S, Megaridis CM (2016) Combating frosting with Joule-heated liquid-infused superhydrophobic coatings. *Langmuir* 32:4278–4288
123. Chernyy S, Jäm M, Shimizu K, Swerin A, Pedersen SU, Daasbjerg K, Makkonen L, Claesson P, Iruthayaraj J (2014) Superhydrophilic polyelectrolyte brush layers with imparted anti-icing properties: effect of counter ions. *ACS Appl Mater Interfaces* 6:6487–6496
124. Chen D, Gelenter MD, Hong M, Cohen RE, McKinley GH (2017) Icephobic surfaces induced by interfacial nonfrozen water. *ACS Appl Mater Interfaces* 9:4202–4214
125. Erbil HY (2014) The debate on the dependence of apparent contact angles on drop contact area or three-phase contact line: a review. *Surf Sci Rep* 69:325–365
126. Yeong YH, Wang C, Wynne KJ, Gupta MC (2016) Oil-infused superhydrophobic silicone material for low ice adhesion with long-term infusion stability. *ACS Appl Mater Interfaces* 8:32050–32059
127. Rosenberg R (2005) Why is ice slippery? *Phys Today* 58:50–55
128. Ikeda-Fukazawa T, Kawamura K (2004) Molecular-dynamics studies of surface of ice. *J Chem Phys* 120:1395–1406
129. Sun X, Damle VG, Uppal A, Linder R, Chandrashekar S, Mohan AR, Rykaczewski K (2015) Inhibition of condensation frosting by arrays of hygroscopic antifreeze drops. *Langmuir* 31:13743–13752
130. Guadarrama-Cetina J, Mongruel A, González-García Y, Beysens D (2015) Frost formation with salt. *Europhys Lett* 110:56002
131. Dotan A, Dodiuk H, Laforte C, Kenig S (2009) The relationship between water wetting and ice adhesion. *J Adhes Sci Technol* 23:1907–1915



132. Makkonen L (2012) Ice adhesion-theory, measurements and countermeasures. *J Adhes Sci Technol* 26:413–445
133. Laforte C, Blackburn C, Perron J (2015) A review of icephobic coating performances over the last decade. *SAE Technical Paper* 2015-01-2149
134. Mishchenko L, Hatton B, Bahadur V, Taylor JA, Krupenkin T, Aizenberg J (2010) Design of ice-free nanostructured surfaces based on repulsion of impacting water droplets. *ACS Nano* 4:7699–7707

# Ice Adhesion on Superhydrophobic Coatings in an Icing Wind Tunnel



Yong Han Yeong, Jack Sokhey, and Eric Loth

**Abstract** Researchers have recently focused on superhydrophobic coatings as an ice-mitigation tool. These surfaces have a high degree of water-repellency and were shown in previous low-speed droplet studies to reduce surface ice adhesion strength. However, there has been little research regarding testing in aerospace icing conditions, that is, high-speed super-cooled droplet impact ( $>50$  m/s) on a cold substrate in an environment where the air temperature is below freezing. A detailed set of experiments was conducted in an icing wind tunnel to measure the ice adhesion strength of various superhydrophobic coatings by subjecting the surfaces to a super-cooled icing cloud consisting of  $20\ \mu\text{m}$  droplets at a constant liquid water content (LWC) of  $0.4\ \text{g/m}^3$ . Test conditions included air speeds of 50 and 70 m/s and in glaze ( $-5^\circ\text{C}$ ) and rime ice regimes ( $-15^\circ\text{C}$ ). The accreted ice was then removed by pressurized nitrogen in the tensile direction in an ice adhesion test. The pressure required for ice removal and the fraction of ice remaining were combined into an overall adhesion parameter (AP). Results showed that the present superhydrophobic coatings generally resulted in increased ice APs relative to the baseline titanium surface. The strongest indicator of ice adhesion performance for these coatings was found to be the surface roughness lateral auto-correlation length. Only superhydrophobic coatings with length-scales less than  $40\ \mu\text{m}$  reduced the ice AP. When compared to previous results, it can be seen that increased droplet impact speeds tended to increase the ice adhesion strength on the superhydrophobic coatings. This was because of the increased droplet impact Bernoulli and hammer

---

Y. H. Yeong (✉) and E. Loth  
Department of Mechanical and Aerospace Engineering, University of Virginia, Charlottesville,  
VA, USA  
e-mail: [yyeong@virginia.edu](mailto:yyeong@virginia.edu); [loth@virginia.edu](mailto:loth@virginia.edu)

J. Sokhey  
Rolls-Royce North America, Indianapolis, IN, USA

pressures which exceeded the resistive capillary pressure of the surface features induced by large surface lateral auto-correlation lengths.

**Keywords** Ice adhesion • Superhydrophobic coating

## Contents

1	Introduction .....	100
2	Experimental Methods .....	102
2.1	Tested Coatings .....	104
2.2	Ice Fracture Data Analysis .....	107
3	Results and Discussion .....	110
4	Conclusions .....	118
	References .....	119

## 1 Introduction

The occurrence of icing creates undesirable effects on the performance of aircraft exterior surfaces and jet engines. Ice accretion typically occurs when an aircraft encounters a cloud consisting of super-cooled water droplets. These droplets impact the surfaces to form ice, which can lead to a complete stall on an aircraft with devastating consequences [1]. In addition, as shown in Fig. 1, ice accretion can occur on aircraft engine fan blades, compressor blades, and static guide vanes [2]. This can result in compressor damage caused by the impact and shedding of ice from these components [3]. Compressor damage can potentially cause engine operation anomalies such as non-recoverable or repeated surge, stall, rollback, or flameout, which eventually lead to engine power or thrust loss [3]. Current ice mitigation methods are active de-icing technologies that require external energy. These include installing pneumatically controlled rubber boots on turboprop aircraft to shed any ice that forms at the leading edge of the wing. Electro-thermal de-icing systems are typically used on leading edges of wings on turbofan aircrafts and also at inlets of jet engines. In certain aircraft variants, hot bleed air from aircraft engines is used. However, challenges still exist with these active de-icing technologies. Operation of the pneumatic de-icing boot is effective only after a certain amount of ice has built up on the boot, and electro-thermal systems require a continuous supply of energy, which often reduces the operating efficiency of the aircraft or jet engine [4, 5].

Superhydrophobic coatings have shown promise in reducing both ice accumulation and adhesion on a test surface [6, 7]. With anti-wetting properties, such as contact angles (CAs) greater than  $150^\circ$  and roll-off angles (ROAs) less than  $10^\circ$ , the hypothesis is that water droplets are repelled from a superhydrophobic surface before ice nucleation can occur [8]. These surfaces have the potential to be an attractive, passive alternative to the more expensive active de-icing technologies currently used on aircraft and jet engines. Numerous investigations that exposed superhydrophobic coatings to icing conditions showed that, although ice accretion

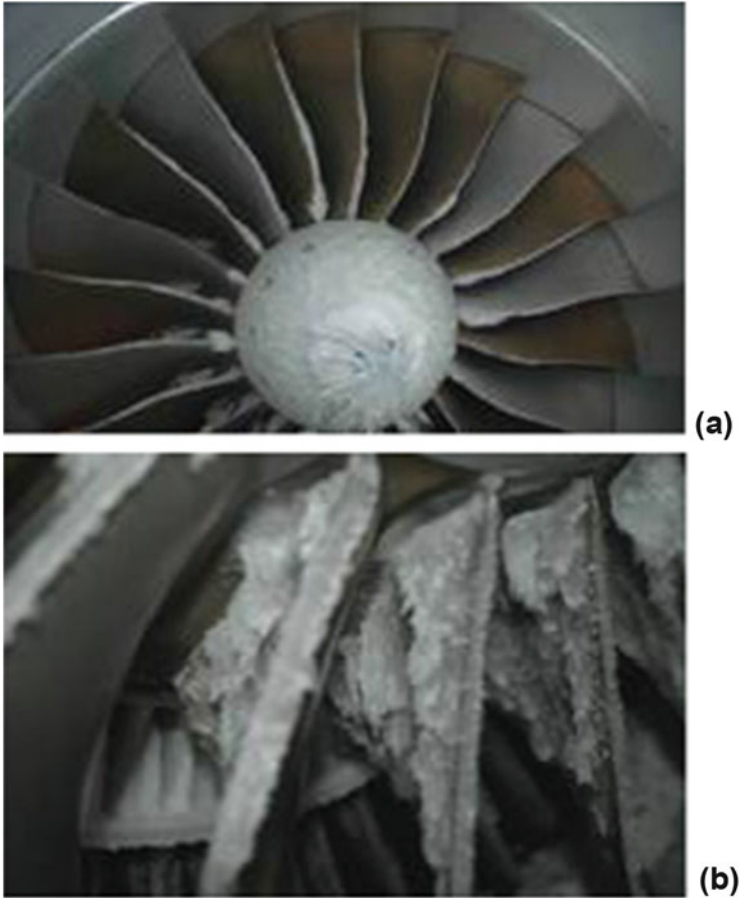


**Fig. 1** Icing in aircraft turbofan engine. (a) Ice accretion on the inlet fan blades. (b) Close-up view of icing on the outlet guide vanes [2]

could be delayed on the surface, it would eventually occur after an extended period of time [9–17]. For example, in a study by Jung et al. [9] super-cooled droplets were allowed to impinge a superhydrophobic surface, which was found to delay droplet freezing for 100 s, relative to the onset of super-cooled drop impact, after which ice accretion would occur.

Hence, the use of superhydrophobic surfaces as an ice mitigation tool has recently shifted from the prevention of ice accretion to the reduction of ice adhesion strength. This is especially relevant for aircraft and jet engine surfaces. Aerodynamic or centrifugal forces can potentially overcome the ice adhesion strength of the surface and release it from the superhydrophobic surface. Current ice adhesion strength studies on superhydrophobic surfaces were conducted either in environments that do not resemble realistic aerospace icing conditions [15, 18–22], or at low super-cooled droplet impact speeds ( $\leq 10$  m/s) [7, 17, 23–26]. For example, Chen

et al. [20] placed water-filled cuvettes on the tested surfaces and placed them on a cooling stage to be frozen. Similarly, Yang et al. [15] used a zero degree cone test in which a cylinder was coated with superhydrophobic materials and submerged in water to be frozen. Reports such as that from Kulinich et al. [23] exposed superhydrophobic surfaces to impact with super-cooled droplets in a freezing environment but the droplet impact speeds were limited to 10 m/s. Although these ice accretion methods do result in ice build-up on the test surface and provide insight for ice adhesion in other applications, they do not simulate the high-speed super-cooled droplet impact condition that is prevalent in aircraft in-flight icing conditions.

The goal of this study was to conduct an experimental investigation of ice adhesion strength on superhydrophobic surfaces in environmental conditions typical of aircraft in-flight icing. Testing was accomplished by accreting ice on superhydrophobic coatings in a cloud of super-cooled droplets in an icing wind tunnel at high air speeds (50 and 70 m/s) in both glaze ( $-5^{\circ}\text{C}$ ) and rime ice regimes ( $-15^{\circ}\text{C}$ ) at a constant LWC of  $0.4\text{ g/m}^3$ . The accreted ice was then removed from the surface in situ using pressurized nitrogen in a tensile direction in accordance with a test method specified by Andrews and Lockington [27]. This results in a Mode 1 ice fracture. In fracture mechanics, Mode 1 refers to a fracture in an opening, tensile direction whereas Modes 2 and 3 represent in-plane and out-of-plane shear modes, respectively [28]. The factors that control ice adhesion strength on superhydrophobic surfaces at high droplet impact speeds were then investigated by deriving ice fracture energies and defining new ice APs that combine ice fracture pressures and residual ice fraction. The relationships between the wettability and texture of a superhydrophobic surface to ice adhesion strength were also studied in detail.

## 2 Experimental Methods

The ice adhesion experiment was performed in an icing wind tunnel located at Cranfield University, UK with a test cross-section size of  $0.7 \times 0.7\text{ m}$  and a maximum air speed of 100 m/s [29]. It is driven by a diesel engine-powered fan and is composed of two floors. The test section area is located on the first floor and the fan drives the air flow to the second floor return duct and heat exchangers. A spray rake is located upstream of the test section and equipped with 6 rows of spray nozzles for a maximum placement of 99 nozzles for icing cloud generation. Upon calibration, these nozzles are capable of generating a super-cooled icing cloud with droplets of diameters ranging from 16 to  $300\text{ }\mu\text{m}$ , at LWCs ranging from 0.05 to  $3\text{ g/m}^3$ . The facility can be operated at total temperatures as low as  $-25^{\circ}\text{C}$ . An image of the icing wind tunnel test section and downstream area is shown in Fig. 2.

The superhydrophobic coatings were on the surface of 30 mm diameter aluminum sample discs with a 4-mm hole at the center of the disc. A shot-peened disc made of titanium alloy Ti-6Al-4V was used as a control surface. The designation 6Al-4V refers to the inclusion of 6% aluminum and 4% vanadium in the alloy, by weight.

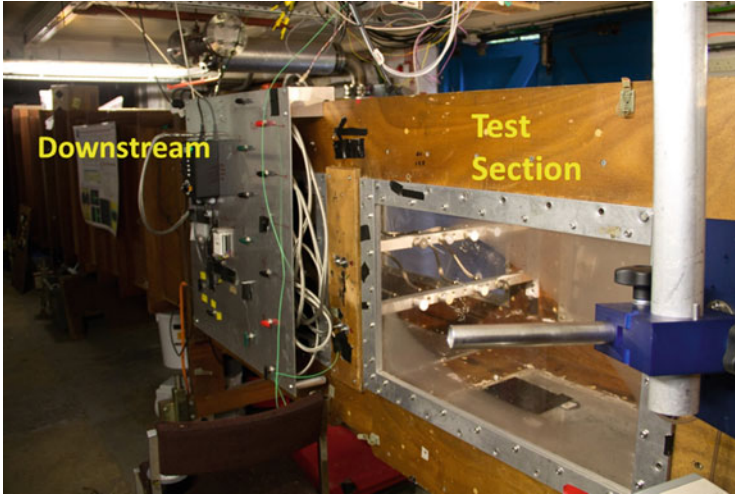


**Fig. 2** Cranfield University icing wind tunnel facility

Ti-6Al-4V is a common material used in aircraft engines and shot-peening refers to a process whereby the titanium alloy surface has a compressive surface stress applied by impacting glass beads. This is a procedure commonly conducted on aircraft engine blades to improve their fatigue strength [30]. The coated disc was attached to an aluminum cylinder called the “boss” using hot-melt adhesive (Adhesive #224, Lenderink Technologies, USA) at 120°C. It should be noted that this temperature is approximately the curing temperature of the coatings during fabrication. Therefore, the hot melt temperature was not expected to alter the properties of the coating. The boss with the disc was connected to a horizontal bar fixture installed within the test section. The boss was machined to include an internal channel with dimensions matching the size of the disc hole. To prevent super-cooled droplets from entering the hole in the disc, a 50  $\mu\text{m}$  thick, 6 mm diameter polytetrafluoroethylene (PTFE) disc called the “defect” is placed over the disc hole. This “defect” is held in position by vacuum pressure. A picture of the set-up of the boss with the substrate disc is shown in Fig. 3a.

As shown in Fig. 3b, fixtures consisting of two horizontal bars were installed within the test section of the wind tunnel. These horizontal bars allowed the installation of eight bosses with their respectively attached coated discs and are positioned at 90° so that they would be directly exposed to the incoming airflow. Internal channels were machined within the bars, which connect to the bosses and to the holes of the discs. This provides an air path from outside the wind tunnel to the sample discs. The purpose of this air path is twofold: (1) to provide vacuum pressure to hold the “defect” disc in place and (2) to provide pressurized nitrogen

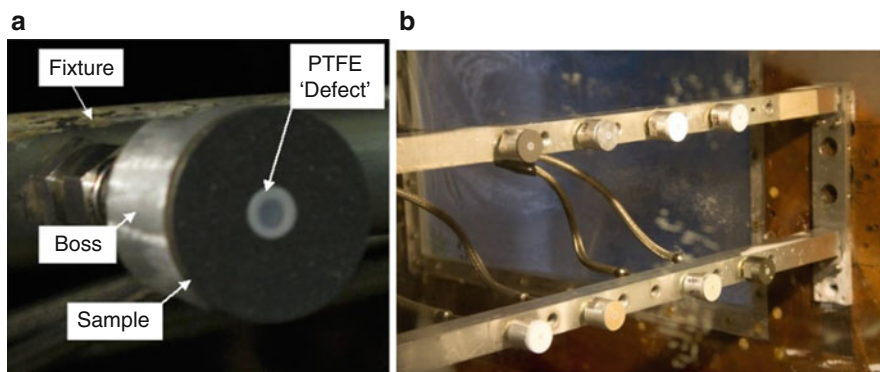


**Fig. 3** (a) Installation of a coated sampled disc and “boss” on a horizontal fixture bar. Note the placement of PTFE “defect” on the disc held in position by vacuum pressure. (b) The attachment of horizontal bars in the wind tunnel test section to position and expose the eight samples in the direction of air flow for ice accretion

from a tank outside of the wind tunnel to the samples after ice has accreted on the discs and “defect.” This pressure is applied at a rate of 6 bar/s until the point of fracture and release of ice from the sample discs. The role of the “defect” disc is to provide an initiation of ice fracture. The fracture pressure for each coating was measured with a high frequency pressure transducer. This method of measurement for ice adhesion on a surface was designed and implemented by Andrews and Lockington [27, 31] to provide ice adhesion values with good repeatability. The Andrews and Lockington test method has been adapted as described to enable in situ testing in an icing wind tunnel.

The coatings were exposed to two different temperatures:  $-15$  and  $-5^{\circ}\text{C}$ . Air speeds of 50 and 70 m/s were used at each test temperature. For all the combinations of air speeds and temperatures, the icing cloud droplet size of  $20\ \mu\text{m}$  and a  $\text{LWC} = 0.4\ \text{g/m}^3$  were kept constant, representing a case-limiting freezing fog condition. The ice on the sample discs was allowed to accrete to a thickness of 15 mm (specified by Andrews and Lockington [27]), before the process of ice removal by nitrogen pressurization was initiated. The time required for ice to accrete to this thickness was approximately 30 min. Ice accretion and removal was repeated three times for each coating so that the repeatability of the ice fracture could be determined.

## 2.1 Tested Coatings

Superhydrophobic coatings fabricated by spray deposition techniques have gained prominence as they are simple and cost effective. Therefore, these coatings are potentially suitable for large-scale aerospace applications. The superhydrophobic

coatings tested in this experiment included a commercially available coating (*Hydrobead*) along with two nanocomposite coatings of different formulations (*SH* coating series and *Pdip* coating), which were developed at the Fluids Research and Innovation Laboratory at University of Virginia. All the coatings were applied on the sample discs with an air-atomizing spray gun and heat treated to give dual scale (micro and nano) textured high water-repellency coatings. Based on abrasion and water spray impact tests, these coatings were found to be more durable when compared to other coatings fabricated via photolithography techniques [32–34]. These coatings are discussed in more detail in the following paragraphs.

The *SH* nanocomposite coating consists of silicon dioxide nanoparticles (3 wt% of slurry), an aerospace-grade polyurethane component (24–25 wt% of slurry) for increased durability, a low-surface energy fluoropolymer (3–5 wt% of slurry) and solvents (58–66 wt% of slurry). These components were mixed together with a combination of vortex and sonication techniques and then spray-cast on substrates in a controlled fashion by using a motorized platform, during which the spray gun was held stationary [34]. By changing the weight percentages of the involved chemical components and spray deposition parameters (height and spray pressure), two different coatings of two different coating arithmetic roughness values ( $S_a$ ) were produced: an  $S_a$  of a 1- $\mu\text{m}$  coating (*SH-1*) and an  $S_a$  of a 3- $\mu\text{m}$  coating (*SH-3*). The details on the coating fabrication process can be found in Davis et al. [35]. Figure 4 shows scanning electron microscope (SEM) images of an *SH* coating at different magnifications. It could be observed that the surface consisted of irregular and hierarchical features at different length scales. Higher magnification shown in Fig. 4b revealed the presence of the sub-micron silicon dioxide nanoparticles.

The *Pdip* coating is also a nanocomposite coating but contains *Plasti Dip*<sup>®</sup>, a commercially available rubber polymer by Plasti Dip International USA as well as *Aerosil*<sup>®</sup>, which is a product consisting of hydrophobically modified fumed silica (HMFS) nanoparticles manufactured by Evonik Industries. These two products (~15% *Plasti Dip* and ~5 wt% HMFS in slurry) are dispersed into a low-surface energy fluoropolymer (~13 wt% in slurry) with a combination of toluene and

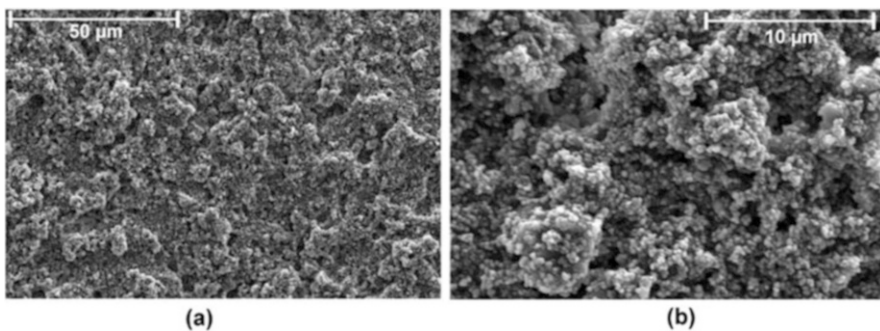


**Fig. 4** Scanning electron microscope (SEM) images of an *SH* coating. (a) Magnification of 1,000 $\times$ . (b) Magnification of 5,000 $\times$



acetone solvents (~65 wt% in slurry) to form a nanocomposite slurry before being spray coated on the substrates and allowed to air-dry for 8 h.

The *Hydrobead* coating is a two-part mixture and was fabricated by spraying it on substrates. This is a process and formulation said by the company to result in a thicker and more durable superhydrophobic coating. In addition, a *Hydrobead* enhancer was sprayed on top of the original coating to improve the superhydrophobic effect.

The wettability performances of the above superhydrophobic coatings were measured with a Ramé-Hart goniometer (model 290). All dynamic CA [RCA (receding contact angle), CAH (contact angle hysteresis), and ROA] were measured using the tilting method. It was discovered that all coatings had high CA of  $> 150^\circ$  and extremely low ROA of  $< 2^\circ$ . This showed that all the coatings were extremely water-repellent. However, even though all the coatings were superhydrophobic, their surface roughness and surface texture characteristics were measured to be different. Laser confocal microscope measurements revealed differences in surface height parameters such as average roughness ( $S_a$ ), and the surface spatial parameter of autocorrelation length ( $S_{al}$ ). As previous studies have reported the significance of surface texture characteristics on ice adhesion performance, each of the coatings used in this experiment were labeled separately, even if the coatings were fabricated using a single specific formulation. This resulted in four different variations of the *Hydrobead* coating (labeled a–d) and two different variations of the SH-1 coating (labeled a and b). The averaged values of the CA, ROA,  $S_a$ , and  $S_{al}$  parameters of the coatings prior to wind tunnel testing are listed in Table 1. The wettability and topology characteristics of the coatings were measured again after the test and reported in Table 2.

**Table 1** Averaged wettability, surface roughness, and texture measurements of the tested superhydrophobic coating and control surface prior to ice adhesion tests

Coating	CA ( $^\circ$ )	ROA ( $^\circ$ )	RCA ( $^\circ$ )	$S_a$ ( $\mu\text{m}$ )	$S_{al}$ ( $\mu\text{m}$ )
Hydrobead-a	160.1	0.3	158.0	2.0	34.8
Hydrobead-b	157.5	0.2	158.3	3.4	25.2
Hydrobead-c	160.3	0.4	161.4	3.9	31.5
Hydrobead-d	164.7	0.2	159.3	3.2	28.6
SH-1 a	167.4	1.9	149.9	2.0	77.5
SH-1 b	165.5	1.7	149.4	2.4	78.0
SH-3	162.3	1.0	156.1	2.9	39.4
Pdip	155.2	0.9	154.1	6.9	55.7
Control (Ti-64)	94.6	Pinned	N/A	2.1	70.6

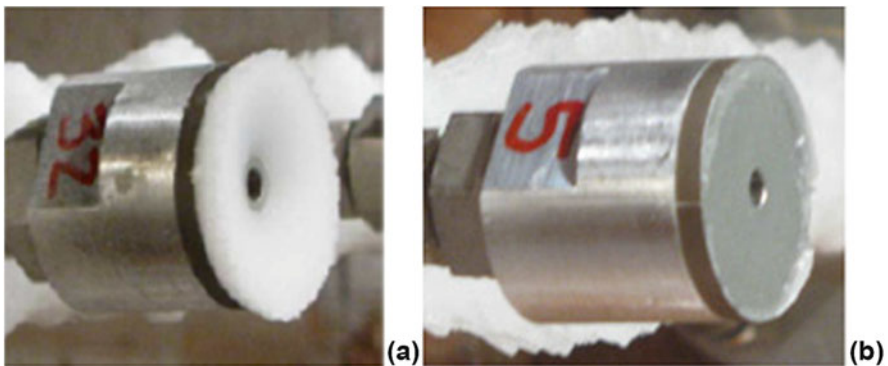
**Table 2** Averaged wettability, surface roughness and, texture measurements of the tested superhydrophobic coatings and control surfaces after ice adhesion tests

Coating	CA (°)	ROA (°)	RCA (°)	$S_a$ ( $\mu\text{m}$ )	$S_{al}$ ( $\mu\text{m}$ )
Hydrobead-a	152.3	20.6	104.3	1.8	42.6
Hydrobead-b	126.6	Pinned	64.1	2.4	44.7
Hydrobead-c	156.8	12.1	121.4	2.0	29.1
Hydrobead-d	134.7	Pinned	66.7	2.6	25.9
SH-1 a	128.9	Pinned	68.6	2.0	109.1
SH-1 b	92.8	62.7	54.4	1.7	57.4
SH-3	120.3	Pinned	48.1	2.3	41.4
Pdip	155.2	Pinned	58.9	4.1	71.7
Control (Ti-64)	94.6	Pinned	N/A	2.1	70.6

## 2.2 Ice Fracture Data Analysis

The process of ice fracture by pressurized nitrogen can result in a cohesive or an adhesive fracture. Full cohesive fracture refers to a failure within the ice structure, resulting in ice remaining (adhering) on the test surface. This is shown in Fig. 5a. Conversely, a 100% adhesive fracture denotes an ice-surface interfacial failure (Fig. 5b) in which a complete removal of ice from the substrate surface occurs. The event of a mixed-mode fracture, which is a combination of cohesive and adhesive failures, could also occur. This condition leaves a partial amount of ice on the substrate surface.

The cohesive ( $2\tau$ ) and adhesive ( $\omega$ ) ice fracture energies were derived by Andrews and Stevenson [31] and are expressed in (1) and (2), respectively:

**Fig. 5** (a) Ice cohesive fracture. (b) Ice adhesive fracture

$$2\tau = \frac{P_c^2 c}{E f_1} \quad (1)$$

$$\omega = \frac{P_c^2 c}{E f_2} \quad (2)$$

where  $c$  is the radius of the “defect,”  $E$  is the Young’s modulus of ice (taken as  $8.5 \text{ GN/m}^2$  at temperatures above  $-20^\circ\text{C}$ ) and  $P_c$  is the critical nitrogen pressure required for ice fracture [30]. The constants  $f_1$  and  $f_2$  are geometric functions defined as

$$f_1 = \frac{1}{1 - \nu^2} \left\{ \frac{3}{32} \left[ \left( \frac{c}{h} \right)^3 + \left( \frac{c}{h} \right) \frac{4}{1 - \nu} \right] + \frac{1}{\pi} \right\}^{-1} \quad (3)$$

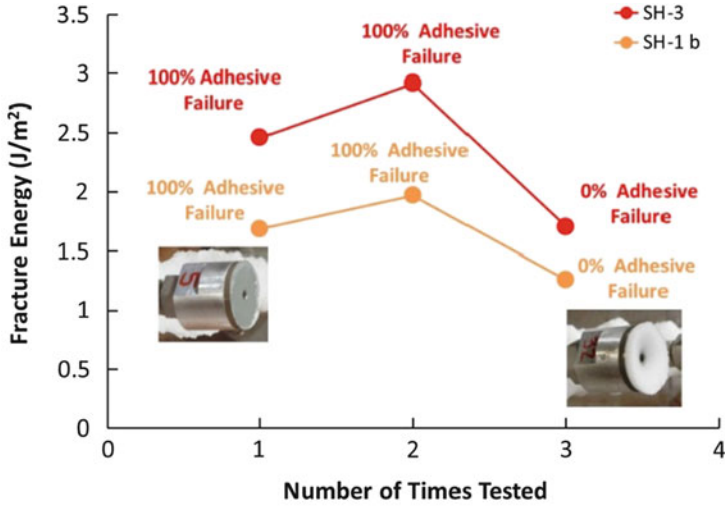
$$f_2 = \frac{1}{1 - \nu^2} \left\{ \frac{3}{32} \left[ \left( \frac{c}{h} \right)^3 + \left( \frac{c}{h} \right) \frac{4}{1 - \nu} \right] + \frac{2}{\pi} \right\}^{-1} \quad (4)$$

where  $h$  is the height of ice accretion and  $\nu$  is the Poisson’s ratio for ice (taken as 0.35). The ice fracture energy could then be determined by quantifying the area of adhesive and cohesive fractures of the substrate surface and multiplying them by their respective energies. This is expressed in (5) as

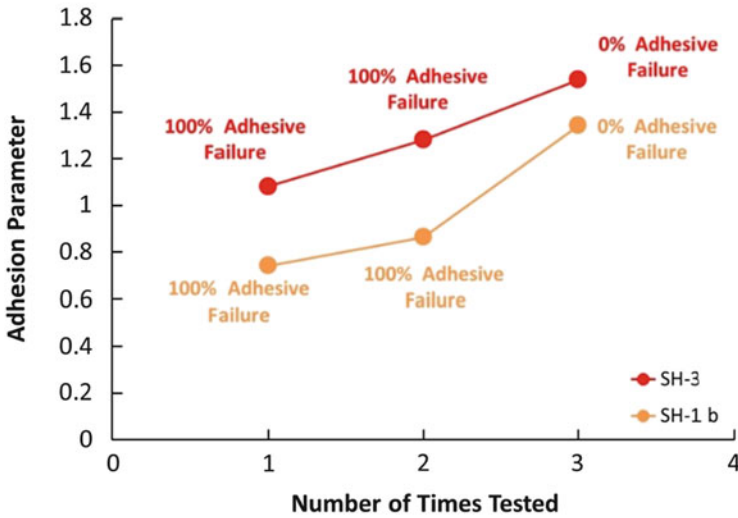
$$\begin{aligned} \text{Fracture Energy} \left( \frac{J}{m^2} \right) &= \left( \frac{100 - \% \text{Area Ice Released}}{100} \times 2\tau \right) \\ &+ \left( \frac{\% \text{Area Ice Released}}{100} \times \omega \right) \end{aligned} \quad (5)$$

The ice fracture energies recorded in the experiment were found to vary strongly with the percentage of adhesive failure (amount of ice adhered on the surface after the event of ice removal). For example, as shown in Fig. 6a, where the fracture energies of SH-3 and SH-1 b coatings are plotted as a function of the number of tests, the fracture energies increased with complete adhesive failures (complete removal of ice from surface) for the first two tests. However, during the third test, the ice fracture energies were dramatically reduced with a 0% adhesive failure (full adhesion of ice on the surface). This indicates that the fracture energies were dependent on the percentage of ice removal from the surface. As the coatings were repeatedly tested, degradation of coatings occurred. This degradation resulted in an increase in ice adhesion and fracture energies of the coatings to the point where the ice-surface interfacial bond is so strong that a cohesive fracture of the ice occurs before adhesive failure (third test in Fig. 6). Therefore, if one were to include the fracture energy from the third test for averaging, the ice adhesion property of this coating would be misrepresented because this fracture energy reduction was associated with an increase in residual ice. As such, it was determined that it would be ideal to define an ice AP which integrates both the fracture energy (which is ideally minimized) and the fraction of remaining ice (which is also ideally minimized).

To integrate these effects and to ensure that the adhesion performance of ice to the coatings is consistently evaluated, an ice AP is introduced and defined herein as



(a)



(b)

**Fig. 6** The introduction of an ice AP to reflect increasing ice adhesion strength of coatings during testing and to ensure evaluation consistency of the adhesion values. (a) Ice fracture energies which increased during the first two tests but decreased for the third test accompanied by a fully cohesive failure. (b) Conversion of the ice fracture energy to an ice AP to reflect an approximately linear increase in ice adhesion strength

$$AP = (1 - \beta) \frac{FE_{\text{coating}}}{FE_{\text{ref, avg}}} + \beta \frac{\left( \frac{\% \text{ Ice Remaining}_{\text{coating}}}{\% \text{ Ice Remaining}_{\text{ref, avg}}} \right)}{\left( \frac{\% \text{ Ice Remaining}_{\text{ref, avg}}}{\% \text{ Ice Remaining}_{\text{ref, avg}}} \right)} \quad (6)$$

In this expression,  $FE_{\text{coating}}$  refers to the fracture energy of the tested coating,  $FE_{\text{ref, avg}}$  to the averaged fracture energy of the control surface (Ti-64 shot peened), and  $\beta$  to a weightage parameter selected based on preliminary sensitivity tests to be 0.5. More importantly, the area percentage of ice remaining on the test surface of the coating and the averaged percentage of ice remaining on the control surface is included in (6) as well. Therefore, AP is a non-dimensional number that describes the ice adhesion performance of a coating as compared to that for a control surface by taking the adhesive failures and desired performance metrics into consideration. It should be noted that the derivation of AP was empirical and based on strategic modeling of the parameters within (6) to express an increase in ice adhesion strength of the coatings during the test. It should also be noted that the initial lower ice fracture energy could be from coating delamination, induced by the force of ice removal in the tensile direction. Future studies should include an in-depth investigation of coating delamination effect on ice adhesion strength.

Fracture energies of the coatings shown in Fig. 6a were converted to APs as shown in Fig. 6b. Results showed that by selecting  $\beta$  to be 0.5, the AP for the third test increased and exceeded the values recorded for the first and second test. This resulted in an approximately linear trend line for performance degradation, and this overall trend was generally consistent for other coatings. These coatings refer to coatings with increasing ice adhesion strength followed by a sudden decrease in the third test, as shown in Fig. 6. Therefore,  $\beta$  was set to be 0.5 for all results shown herein. The fracture energy (cohesive fracture) in the third test shown in Fig. 6a was lower than the fully adhesive fracture energies in the first two tests because of inconsistent surface physical properties of the coatings, which were continuously degraded during testing. Previous work has shown that ice fracture energy is highly dependent on the ice grain size [29]. In addition to air speed and LWC, ice grain sizes are also dependent on the surface physical properties of a substrate material [29]. We hypothesize that the decrease in fracture energy in the third test was caused by changes in ice grain size brought on by degraded surface structures.

### 3 Results and Discussion

Figure 7 shows the regimes of ice formation on the sample disc at different temperatures. At  $-5^{\circ}\text{C}$  the super-cooled droplets would impact the coating but not immediately freeze because of warmer temperatures. Driven by the incoming airflow and low freezing fraction, the droplets would rather “flow” outward and freeze in motion, forming a flat and large ice shape with a transparent appearance and

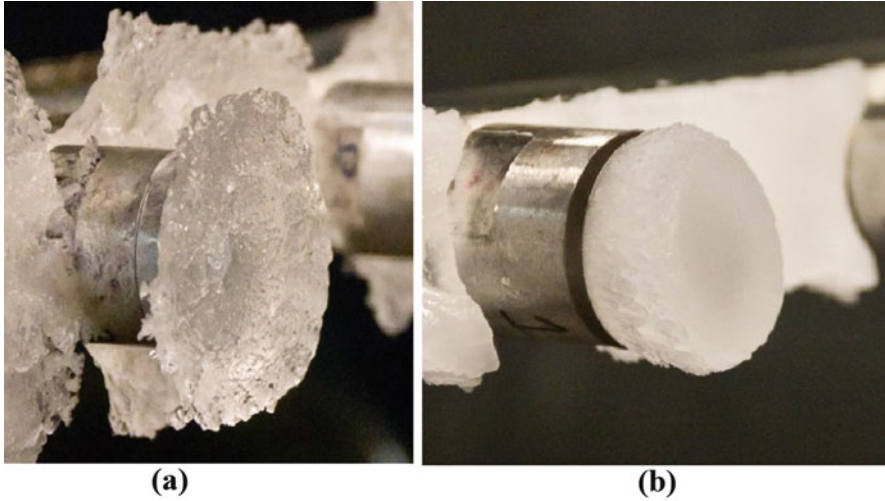


**Fig. 7** Accretion of ice on the sample discs at different test temperatures. (a) Glaze ice ( $-5^{\circ}\text{C}$ ). (b) Rime ice ( $-15^{\circ}\text{C}$ )

rough texture. This is called the glaze ice regime and is shown in Fig. 7a. At the colder temperatures of  $-15^{\circ}\text{C}$ , incoming super-cooled droplets instantaneously freeze upon impacting the coating and accrete in a shape similar to a cylinder with a milky white appearance (from entrapped air). This is called the rime regime, is of high freezing fraction (close to 1), and is shown in Fig. 7b. The freezing fraction is defined as the mass fraction of super-cooled water that converts to ice upon impact on a surface. The difference in these ice regimes was only observed when air temperatures were varied; air speed did not alter the shape or appearance of the ice structure.

An analysis of the data acquired in the icing wind tunnel test revealed a wide range of ice adhesion strengths for the superhydrophobic surfaces. For example the *Pdip* coating and the SH-3 coatings recorded an ice AP that was consistently higher than the Ti-64 shot-peened control surface. The ice AP of the *Hydrobead* coatings was slightly lower than that of the control surface. An investigation was conducted to examine the relationship between the coating surface wettability and ice AP as surface wettability characteristics have been reported in numerous publications to influence the ice adhesion strength. For example, Kulinich and Farzaneh reported that the ice adhesion strength on superhydrophobic coatings was reduced with the decrease of the CAH [25]. CAH is the difference between the ACA and RCA of the surface. These angles are created between the liquid-solid interface of a drop at the leading edge and trailing edge, respectively, as it starts to roll on the superhydrophobic surface from a dormant position. A low CAH value would indicate a high degree of drop mobility on a superhydrophobic surface and may also signify a Cassie wetting state [36], where a drop is suspended on the tips of the surface micro- and nano-surface texture with a layer of air trapped within the spaces

between the asperities. In an icing event, the reduced area of contact between the ice and the surface was theorized to reduce its adhesion strength.

Meuler et al. [12] recently reported an inverse relationship between the coating RCA and ice adhesion strength, that is, an increase of ice adhesion strength at low RCA values [37]. This is because RCAs quantify the spread of a liquid on a coating; a low RCA value indicates that the drop is prone to wet a surface. This finding was examined with data obtained in this experiment. To make this comparison, it was important to consider the degradation of wettability performance during the test. It can be observed from Tables 1 and 2 that the coatings have generally degraded in terms of wettability performance after ice adhesion testing, with averaged RCA values measured at less than  $60^\circ$  on certain coatings. This coating degradation was caused by high-speed droplet impact and the process of ice fracture. An example of surface feature degradation of a coating is shown in Fig. 8 for the Hydrobead-b coating via laser confocal mapping. A significant portion of the surface features was removed as a result of the test. In comparison, previous testing of these coatings at low speed-conditions ( $\sim 5$  m/s) showed little degradation [38]. It should be noted that coating Hydrobead-d degraded to the point where a majority of the coating was stripped from the substrate disc after being tested at the condition of 70 m/s airspeed. This coating was therefore not included in the remaining tests. In addition, coating Hydrobead-c was not tested for the test condition of 70 m/s,  $-15^\circ\text{C}$  air temperature (Fig. 10b) because of limited resources during testing.

Figure 9 shows the relationship of AP of the superhydrophobic coatings with the averaged RCA. Although Fig. 9a may suggest that this relationship is still true for the present aerospace conditions, Fig. 9b suggests that the effect of RCA on AP is not consistent. Analysis of the results also revealed that, for all test conditions, the AP of the surfaces did not significantly correlate with the CA, ROA, and CAH of the coatings. This can be inferred from Table 1, where all the coatings contained high CA and low ROA values yet displayed a wide range of ice APs as shown in Fig. 9. This lack of correlation for the present conditions does not agree with Meuler et al. [12] findings for static freezing conditions. The disagreement with literature is

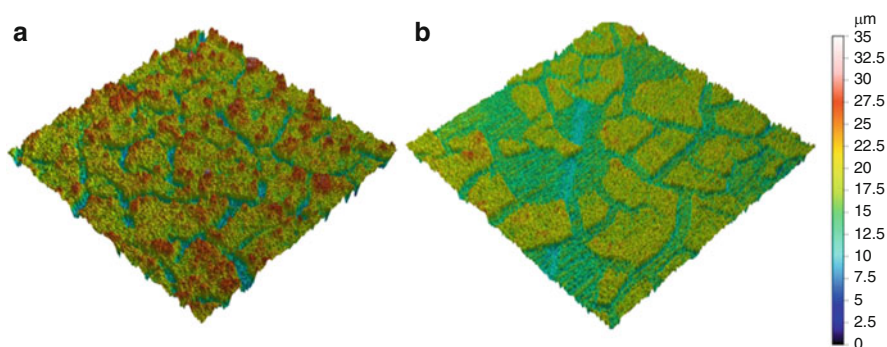


**Fig. 8** Laser confocal 3D mapping showing the degradation of surface features of a Hydrobead-b coating after testing. (a) Prior to test. (b) After completion of test

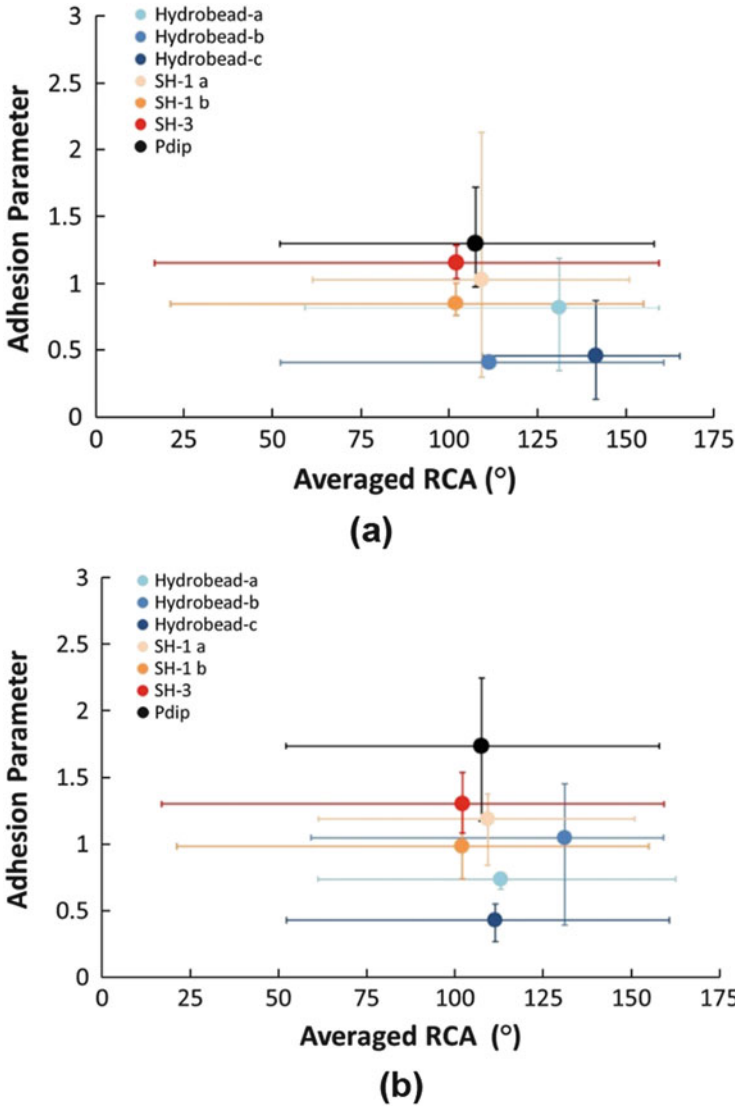


**Fig. 9** Absence of correlation between superhydrophobic coating averaged RCA and AP. Results shown were obtained at a temperature of  $-15^{\circ}\text{C}$  and airspeeds of: (a) 50 m/s; (b) 70 m/s

hypothesized to be caused by different ice accretion mechanisms. In previous tests, most experiments accreted ice on superhydrophobic surfaces by positioning water on the test surface, simultaneously reducing the air temperature to allow for freezing [15, 18–22]. In this testing method, the coating could potentially remain in a Cassie–Baxter wetting state when undergoing freezing, which significantly reduces the ice adhesion strength of the coating. However, this method of ice accretion does not resemble the ice formation mechanisms in aerospace in-flight icing conditions,



that is, high-speed super-cooled droplet impact on a freezing surface. Such high velocity, super-cooled droplets can penetrate into the asperities of a superhydrophobic coating (which achieve reduced wettability through surface roughness via the nano-composite topography). Such penetration can cause an increase in ice adhesion strength because of the increased interlocking surface area. Ice adhesion strength tests of superhydrophobic coatings formed by super-cooled droplet impact were previously conducted but at speeds of less than 10 m/s, lower than the impact speeds reported herein and thus not representative of aerospace flight conditions [7, 17, 23–26].

The above hypothesis suggests that the surface topography of the superhydrophobic surface may have an influence on its ice adhesion strength, especially at higher droplet impact speeds. Previous publications have studied and reported the influence of roughness heights on the effectiveness of ice-release on superhydrophobic coatings [19, 25]. However, in this current experiment, an evaluation of the relationship between ice adhesion and coating arithmetic roughness [ $S_a$  defined in (7)] revealed no significant correlations:

$$S_a = \iint_A |z(x, y)| dx dy \quad (7)$$

However, an examination of the surface autocorrelation length ( $S_{al}$ ) yielded correlations with the AP.  $S_{al}$  is a roughness parameter that describes the spatial relationship between surface features. This is defined in (8) as

$$S_{al} = \underset{t_x t_y \in R}{MIN} \sqrt{t_x^2 + t_y^2} \text{ where } R = \{(t_x, t_y) : ACF(t_x, t_y) \leq 0.2\} \quad (8)$$

where  $t_x$  and  $t_y$  are the autocorrelation functions (ACFs) in the x and y directions. The ACF is a measure of how similar the textures are at given distances from the original location. It is obtained by mathematically multiplying together two surfaces separated by a relative lateral displacement to yield functions which quantify the degree of overlap. If the ACF is near unity for a given amount of lateral shift, the texture is similar along that direction. On the other hand, if ACF is close to zero, the surfaces are different and bear no similarity to the original measurement location [39]. The autocorrelation length ( $S_{al}$ ) specified in (8) is the spatial distance which has the fastest decay in ACF to a value of 0.2. Hence, this parameter provides a quantification of feature wavelengths on a surface. A high  $S_{al}$  indicates that the textures on a surface are further apart (high wavelengths) compared to a low  $S_{al}$  which signifies features that are located closer together. Figure 10 shows 3D confocal mapping for two *SH* coatings of different surface textures. It could be observed that, even though both coatings had almost identical roughness  $S_a$ , the lateral autocorrelation length values,  $S_{al}$ , were different. The coating (Fig. 10a) with a lower  $S_{al}$  had visible surface features that were denser and spaced closer together compared to the coating in Fig. 10b of high  $S_{al}$  where features were sparser and spaced further apart.

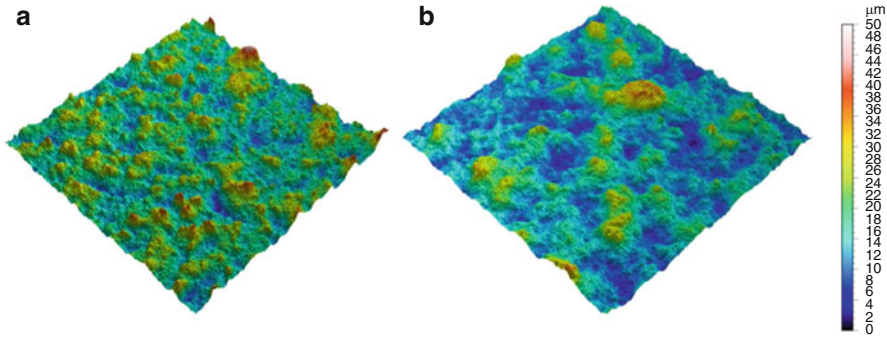


**Fig. 10** Laser confocal 3D mapping of two *SH* surfaces with similar averaged roughness ( $S_a$ ) but different surface autocorrelation length ( $S_{al}$ ). (a)  $S_a = 3.9 \mu\text{m}$ ,  $S_{al} = 42.9 \mu\text{m}$ . (b)  $S_a = 3.8 \mu\text{m}$ ,  $S_{al} = 67.9 \mu\text{m}$

Figure 11 shows the correlation of  $S_{al}$  and AP for superhydrophobic coatings tested at a temperature of  $-5^\circ\text{C}$  (glaze ice regime) and at airspeeds of 50 and 70 m/s. Similar to averaged RCA plotted in Fig. 9, the averaged  $S_{al}$  is evaluated over  $S_{al}$ s measured before and after the experiments. A reasonable correlation between  $S_{al}$  and AP can be seen, that is, increasing  $S_{al}$  of the surface generally leads to an increase in ice adhesion strength. A coefficient of determination ( $R^2$ ) of the data linear fit was also provided in Fig. 11 to quantify the prediction and variation of the data.

This correlation may be attributed to the local impact fluid dynamics. The droplets travel at high speeds and, upon impact on the superhydrophobic coating, exert a water hammer and Bernoulli pressure on the surface texture [40–42]. If these pressures are greater than the capillary pressure of the surface textures, the water droplets penetrate into the surface asperities, triggering a transition from a Cassie wetting state to a Wenzel wetting state before freezing [43]. This causes an increase in the ice adhesion strength because the ice has a larger surface area to adhere to. The control of capillary pressure of the surface texture is therefore crucial toward maintaining a strong resistance against droplet penetration. This capillary pressure is a strong function of spatial distances between surface features [42, 44, 45]. In a study conducted by Extrand [44], reducing the spatial distance of posts by two orders of magnitude was found to result in an increase of capillary pressure by the same amount. The present superhydrophobic surfaces with high  $S_{al}$  were found to record stronger ice APs compared to superhydrophobic coatings with a lower  $S_{al}$  because high  $S_{al}$  surfaces contain features that are spaced further apart that allow for easier droplet penetration and freezing. As shown in Fig. 12, this result also holds true for data acquired at  $-15^\circ\text{C}$  (rime ice regime). To quantify the maximum feature spacing  $D_{max}$  for resisting droplet penetration, one could equate the analytical solution of feature capillary pressure with the wetting pressures of hammer and Bernoulli pressure, as derived by Deng et al. [40] for a structured micro-textured surface. The wetting pressure, derived by Deng based on an estimate of  $P_{wh}$  given by Engel [46], is shown in (9), where  $\rho$  refers to water density,  $C$  the speed of sound in water, and  $V$  the droplet impact speed:

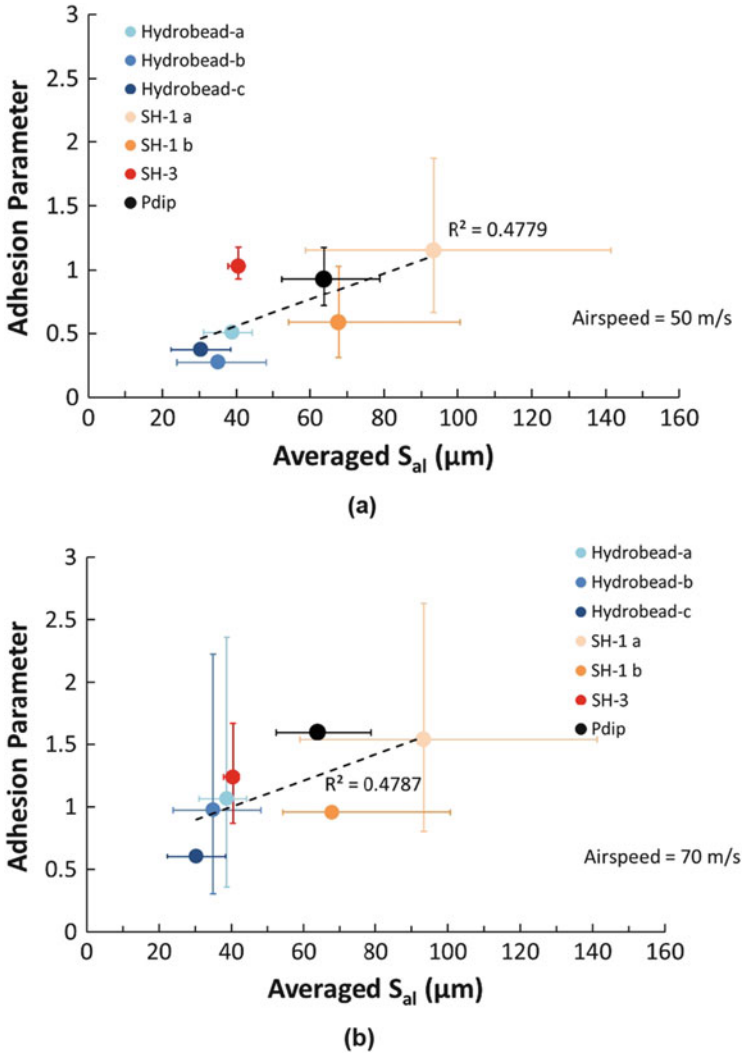


**Fig. 11** Relationship between coating averaged  $S_{al}$  and AP. Results shown were obtained at a temperature of  $-5^{\circ}\text{C}$  (glace ice regime) and airspeeds of: (a) 50 m/s; (b) 70 m/s

$$P_{\text{wetting}} = P_{WH} + P_B = \rho V \left( \frac{2C + 5V}{10} \right) \quad (9)$$

The calculation of  $D_{\text{max}}$  is shown in (10), where  $\gamma_{LV}$  refers to water surface tension and  $\theta_A$  the advancing CA of the surface:

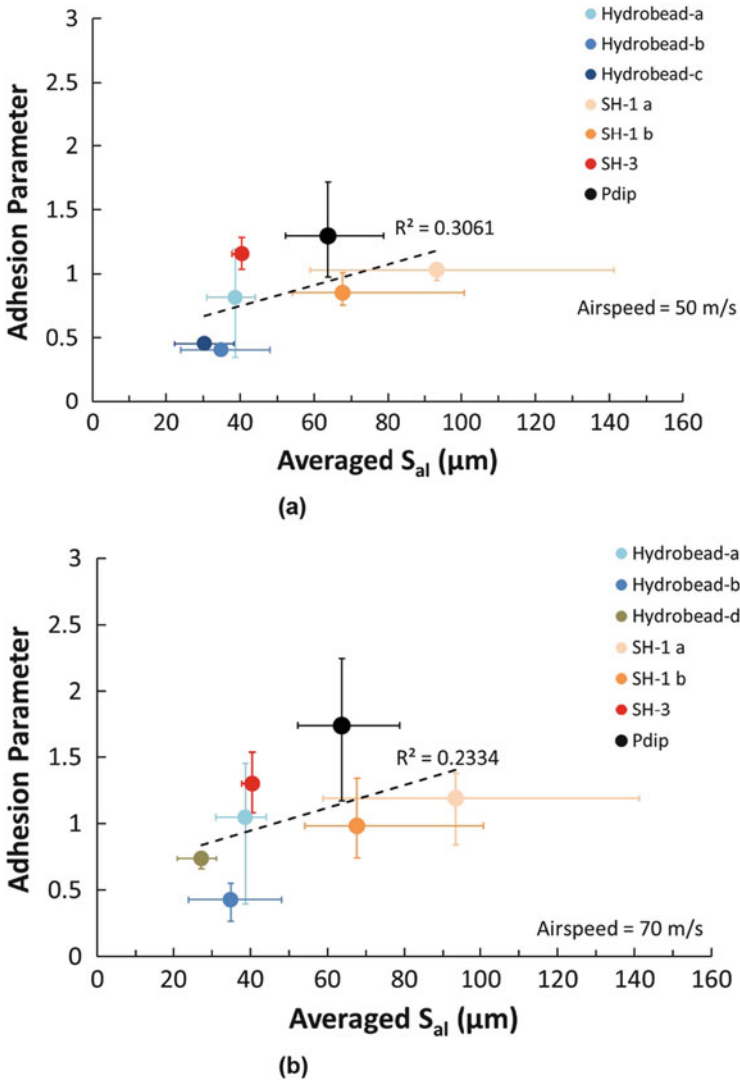


Fig. 12 Relationship between coating averaged  $S_{al}$  and AP. Results shown were obtained at a temperature of  $-15^\circ\text{C}$  (rime ice regime) and airspeeds of: (a) 50 m/s; (b) 70 m/s

$$D_{\max} = \frac{-2\sqrt{2} \gamma_{LV} \cos \theta_A}{P_{\text{wetting}}} \tag{10}$$

Based on (10), for a water droplet impact speed of 50 m/s and a surface advancing angle of  $150^\circ$  (which is indicative of a superhydrophobic surface), a maximum feature spacing  $D_{\max}$  of approximately 10 nm is required to resist the penetration of the water droplet into the surface asperities. Although this

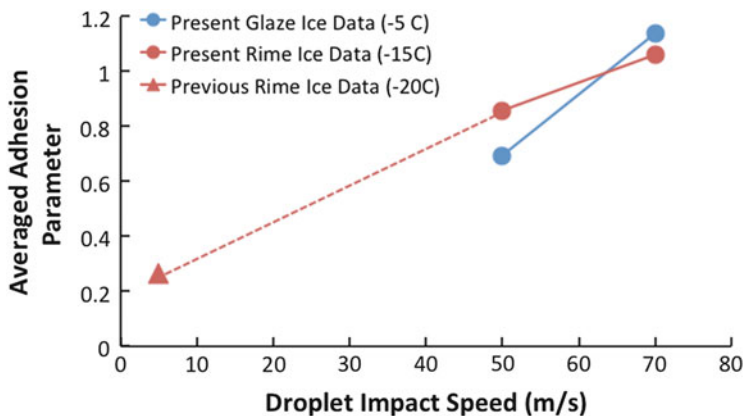


Fig. 13 Effect of super-cooled droplet impact speeds on AP of superhydrophobic coatings

calculation is simplified for structured and not for irregular surface features (as used in this experiment), it is clear that the spacing of the surface features of coatings tested in this experiment was too large to resist water droplet penetration.

The relationship between the droplet impact speed and ice adhesion of the superhydrophobic coatings is further examined in Fig. 13. The APs of all the tested coatings in the present experiment for each test condition were averaged and plotted. In addition, averaged AP of superhydrophobic surfaces from a previous study at low droplet impact speeds (5 m/s) was included [38]. This previous study was conducted using the same test method as the present experiment; the impact of icing cloud consisting of 20- $\mu\text{m}$  droplets on substrate discs for rime ice accretion ( $-20^\circ\text{C}$ ), followed by removal of ice using pressurized air. The results suggest that AP for these surfaces tends to increase with droplet impact speed. As previously shown, this is because increased droplet impact speeds increase the wetting pressures (9) and hence result in increased likelihood of droplet penetration. This shows that the effectiveness of superhydrophobic surfaces in reducing ice adhesion strength under super-cooled droplet impact icing conditions is not primarily dependent on the detailed surface wettability (CA, CAH, ROA, and RCA) but rather is more dependent on the surface texture characteristics such as  $S_{\text{al}}$  and droplet impact speeds.

## 4 Conclusions

Icing wind tunnel tests of a set of superhydrophobic coatings were conducted at air speeds of 50 and 70 m/s and at air temperatures of  $-5$  and  $-15^\circ\text{C}$  under a constant icing cloud of 20  $\mu\text{m}$  super-cooled droplets and LWC of  $0.4 \text{ g/m}^3$ . The coatings were evaluated in terms of the ice AP, defined herein to combine the performance metrics of fracture energy and residual ice fraction. Results showed that there were no strong relationships between coating wettability parameters (CA, CAH, RCA,

and ROA) and ice AP. This indicates that adjusting the coating water-repellency of superhydrophobic surfaces does not generally ensure low ice adhesion properties for aerospace applications. Results showed instead that the surface spatial roughness parameter of auto-correlation length controlled the magnitude of ice adhesion strength on the superhydrophobic coating. In particular, coatings with low autocorrelation lengths have surface features that are spaced closer together and hence contain a higher capillary pressure which resist droplet penetration and can maintain a Cassie–Baxter wetting state to give lower ice adhesion strength. In addition, it was found that increased droplet impact speeds tend to increase the ice AP of a superhydrophobic coating. This is attributed to higher Bernoulli and water hammer pressures on the superhydrophobic surface that causes the drops to penetrate the asperities of the coating and hence increase the ice adhesion strength. The results obtained in this experiment highlighted the importance of high-speed droplet impact testing at freezing conditions when evaluating superhydrophobic ice adhesion performance in an aerospace icing condition.

## References

1. Kinnersley S, Roelen A (2007) The contribution of design to accidents. *Saf Sci* 45:31–60
2. Sokhey J (2014) Images of ice accretion in aircraft engines. Personal communication
3. Hempe D (2004) Turbojet, turboprop, and turbofan engine induction system icing and ice ingestion. Federal Aviation Administration AC, Washington, pp 20–147
4. Render P, Jenkinson L (1996) Investigation into ice detection parameters for turboprop aircraft. *J Aircr* 33:125–130
5. Shires G, Munns G (1958) The icing of compressor blades, and their protection by surface heating. Aeronautical Research Council, London. Technical Report 3041
6. Cao L, Jones AK, Sikka VK, Wu J, Gao D (2009) Anti-icing superhydrophobic coatings. *Langmuir* 25:12444–12448
7. Kulinich S, Farzaneh M (2009) Ice adhesion on super-hydrophobic surfaces. *Appl Surf Sci* 255:8153–8157
8. Mishchenko L, Hatton B, Bahadur V, Taylor JA, Krupenkin T, Aizenberg J (2010) Design of ice-free nanostructured surfaces based on repulsion of impacting water droplets. *ACS Nano* 4:7699–7707
9. Jung S, Dorrestijn M, Raps D, Das A, Megaridis CM, Poulikakos D (2011) Are superhydrophobic surfaces best for icephobicity? *Langmuir* 27:3059–3066
10. Wang F, Li C, Lv Y, Lv F, Du Y (2010) Ice accretion on superhydrophobic aluminum surfaces under low-temperature conditions. *Cold Reg Sci Technol* 62:29–33
11. Tourkine P, Le Merrer M, Quéré D (2009) Delayed freezing on water repellent materials. *Langmuir* 25:7214–7216
12. Meuler AJ, McKinley GH, Cohen RE (2010) Exploiting topographical texture to impart icephobicity. *ACS Nano* 4:7048–7052
13. Sarshar MA, Swartz C, Hunter S, Simpson J, Choi C (2013) Effects of contact angle hysteresis on ice adhesion and growth on superhydrophobic surfaces under dynamic flow conditions. *Colloid Polym Sci* 291:427–435
14. He M, Wang J, Li H, Song Y (2011) Super-hydrophobic surfaces to condensed micro-droplets at temperatures below the freezing point retard ice/frost formation. *Soft Matter* 7:3993–4000
15. Yang S, Xia Q, Zhu L, Xue J, Wang Q, Chen Q (2011) Research on the icephobic properties of fluoropolymer-based materials. *Appl Surf Sci* 257:4956–4962

16. Jung S, Tiwari MK, Doan NV, Poulikakos D (2012) Mechanism of supercooled droplet freezing on surfaces. *Nat Commun* 3:615
17. Kulinich S, Farhadi S, Nose K, Du X (2010) Superhydrophobic surfaces: are they really ice-repellent? *Langmuir* 27:25–29
18. Ge L, Ding G, Wang H, Yao J, Cheng P, Wang Y (2013) Anti-icing property of superhydrophobic octadecyltrichlorosilane film and its ice adhesion strength. *J Nanomater* 2013:3
19. Susoff M, Siegmann K, Pfaffenroth C, Hirayama M (2013) Evaluation of icephobic coatings—screening of different coatings and influence of roughness. *Appl Surf Sci* 282:870–879
20. Chen J, Liu J, He M, Li K, Cui D, Zhang Q, Zeng X, Zhang Y, Wang J, Song Y (2012) Superhydrophobic surfaces cannot reduce ice adhesion. *Appl Phys Lett* 101:111603
21. Wang Y, Xue J, Wang Q, Chen Q, Ding J (2013) Verification of icephobic/anti-icing properties of a superhydrophobic surface. *Appl Mater Sci* 5:3370–3381
22. Varanasi KK, Deng T, Smith JD, Hsu M, Bhate N (2010) Frost formation and ice adhesion on superhydrophobic surfaces. *Appl Phys Lett* 97:234102
23. Kulinich S, Farzaneh M (2011) On ice-releasing properties of rough hydrophobic coatings. *Cold Reg Sci Technol* 65:60–64
24. Jafari R, Menini R, Farzaneh M (2010) Superhydrophobic and icephobic surfaces prepared by RF-sputtered polytetrafluoroethylene coatings. *Appl Surf Sci* 257:1540–1543
25. Kulinich S, Farzaneh M (2009) How wetting hysteresis influences ice adhesion strength on superhydrophobic surfaces. *Langmuir* 25:8854–8856
26. Farhadi S, Farzaneh M, Kulinich S (2011) Anti-icing performance of superhydrophobic surfaces. *Appl Surf Sci* 257:6264–6269
27. Andrews E, Lockington N (1983) The cohesive and adhesive strength of ice. *J Mater Sci* 18:1455–1465
28. Anderson TL, Anderson T (2005) *Fracture mechanics: fundamentals and applications*. CRC Press, Boca Raton
29. Pervier M (2012) *Mechanics of ice detachment applied to turbomachinery*. Dissertation. Cranfield University, Cranfield
30. Namjoshi S, Jain V, Mall S (2002) Effects of shot-peening on fretting-fatigue behavior of Ti-6Al-4V. *J Eng Mater Tech* 124:222–228
31. Andrews E, Stevenson A (1978) Fracture energy of epoxy resin under plane strain conditions. *J Mater Sci* 13:1680–1688
32. Steele A, Bayer I, Loth E (2012) Adhesion strength and superhydrophobicity of polyurethane/organoclay nanocomposite coatings. *J Appl Polym Sci* 125:E445–E452
33. Davis A, Yeong YH, Steele A, Loth E, Bayer IS (2014) Spray impact resistance of a superhydrophobic nanocomposite coating. *AIChE J* 60:3025–3032
34. Yeong YH, Davis A, Steele A, Loth E, Bayer IS (2014) Spray deposition effects on superhydrophobicity and durability of nano-coatings. *Surf Sci* 2:70
35. Davis A, Yeong YH, Steele A, Bayer IS, Loth E (2014) Superhydrophobic nanocomposite surface topography and ice adhesion. *ACS Appl Mater Inter* 6(12):9272
36. Cassie A, Baxter S (1944) Wettability of porous surfaces. *Trans Faraday Soc* 40:546–551
37. Meuler AJ, Smith JD, Varanasi KK, Mabry JM, McKinley GH, Cohen RE (2010) Relationships between water wettability and ice adhesion. *ACS Appl Mater Inter* 2:3100–3110
38. Yeong YH, Milionis A, Loth E, Sokhey J, Lambourne A (2015) Atmospheric ice adhesion on water-repellent coatings: wetting and surface topology effects. *Langmuir* 31:13107–13116
39. Michigan Metrology (2014) 3D parameters-spatial parameters. [http://www.michmet.com/3d\\_s\\_spatial\\_parameters\\_sal.htm](http://www.michmet.com/3d_s_spatial_parameters_sal.htm). Accessed Mar 28 2014
40. Deng T, Varanasi KK, Hsu M, Bhate N, Keimel C, Stein J, Blohm M (2009) Nonwetting of impinging droplets on textured surfaces. *Appl Phys Lett* 94:133109
41. Field J (1999) ELSI conference: invited lecture: liquid impact: theory, experiment, applications. *Wear* 233:1–12

42. Varanasi KK, Deng T, Hsu M, Bhate N (2009) Hierarchical superhydrophobic surfaces resist water droplet impact. Paper presented at the 2009 NSTI Nanotechnology Conference and Expo, May 3–7, 2009, Houston, Texas, USA
43. Wenzel RN (1936) Resistance of solid surfaces to wetting by water. *Ind Eng Chem* 28: 988–994
44. Extrand C (2006) Designing for optimum liquid repellency. *Langmuir* 22:1711–1714
45. Fortin G, Perron J (2012) Ice adhesion models to predict shear stress at shedding. *J Adhes Sci Technol* 26:523–553
46. Engel OG (1955) *J Res Natl Bur Stand* 54:281



# Icephobicity: Definition and Measurement Regarding Atmospheric Icing



Jean-Denis Brassard, Caroline Laforte, Frederic Guerin,  
and Caroline Blackburn

**Abstract** Atmospheric ice that adheres to structures and accumulates is a critical issue in numerous northern areas. Even if different de-icing methods exist, they consume a great deal of energy or necessitate elaborate infrastructures. However, using coatings with icephobic properties could be the “miracle” solution. This chapter proposes a complete definition of icephobicity in line with the ice adhesion test methods used. The general way to assess this property is described using a holistic approach, the first step of which is a screening test campaign with many different candidate coatings evaluated in terms of their adhesion reduction factor (ARF). The relevance of this factor is also discussed. Further tests are recommended, after the better candidate coatings are identified, in an extensive test campaign performed under simulated icing and outdoor conditions prevailing in the real environment of the targeted application. Finally, a specific example of a test campaign in which the icephobic coatings are exposed to Arctic offshore conditions is presented.

**Keywords** Atmospheric icing • Coating • Ice • Ice accumulation • Ice adhesion • Icephobic

## Contents

1	Introduction .....	124
2	Passive Anti-Icing Methods .....	125
3	Icephobicity .....	126
4	Evaluation .....	126
	4.1 Ice Adhesion Measurement .....	126
	4.2 Screening Evaluation Test and Adhesion Reduction Factor (ARF) .....	129

---

J.-D. Brassard, C. Laforte, F. Guerin, and C. Blackburn (✉)  
Anti-Icing Materials International Laboratory, Université du Québec à Chicoutimi,  
Chicoutimi, QC, Canada  
e-mail: [claforte@uqac.ca](mailto:claforte@uqac.ca)

4.3	Establishing a Test Campaign to Evaluate the Icephobic Properties/Efficiency of a Coating or Surface Treatment .....	136
4.4	Example of Extended Test Campaign: Icephobic Coating for Arctic Offshore Environments .....	138
5	Conclusions .....	140
	References .....	141

## 1 Introduction

Atmospheric ice adhering to structures causes numerous problems in telecommunications, electrical distribution, road, marine, and aviation transportation networks. The need for reliable transportation in the most severe icing conditions highlights the importance of ice adhesion studies. It is well known that ice accumulation on aircraft causes loss of lift, increase in drag, faults in gauge readings, and greater risk of stalling and potentially fatal crashes. Table 1 presents a selection of ten fatal aircraft crashes caused by icing over the past five decades [1–10].

Although the requirements for the deployment of de-icing and anti-icing fluids are tightly regulated and well documented, these fluids are useless if they are not used properly, or if they fail to accomplish their work [11]. Consequently, efforts to improve the efficiency of de-icing and anti-icing methods are still a very active field

**Table 1** Selected fatal aircraft crashes caused by icing over the past five decades

Ref	Flight name	Date	Fatalities/ survivors	Causes
[1]	Surgut Aeroflot Antonov	Jan. 22, 1971	14/0	Icing caused by bleed air valves being closed
[2]	Turkish Airlines Flight 301	Jan. 26, 1974	66/7	Atmospheric icing, loss of control
[3]	Air Florida Flight 90	Jan. 13, 1982	78/5	Faulty engine gauge readings caused by atmospheric icing and pilot error
[4]	Arrow Air Flight 1285	Dec. 12, 1985	256/0	Icing conditions, weight and reference speed miscalculation
[5]	Air Ontario Flight 1363	Mar. 10, 1989	24/45	Icing, improper de-icing procedures, pilot error
[6]	USAir Flight 405	Mar. 22, 1992	27/24	Icing, improper de-icing procedures, pilot error
[7]	American Eagle Flight 4184	Oct. 31, 1994	68/0	Freezing rain
[8]	China Eastern Airlines Flight 5210	Nov. 21, 2004	55/0	Ice accumulation, no de-icing done before take-off
[9]	Colgan Air Flight 3407	Feb. 9, 2009	50/4	Inadequate procedures for airspeed selection and management during approaches in icing conditions.
[10]	Air France Flight 447	Jun. 1, 2009	228/0	Obstruction of pitot probes by ice crystals during flight

of multidisciplinary research. Many efficient de-icing methods have been developed, although they consume a great deal of energy and/or necessitate elaborate infrastructures and maintenance [12]. At present, various methods have been proposed to remove or even prevent and mitigate the formation of ice on structures and vehicles. These techniques are categorized into three main groups: thermal, chemical, and mechanical.

Thermal methods are the most used in both automotive and aerospace applications, where the iced elements have relatively small areas. The most common methods use thermal heating elements and fluids applied at a high temperature, for example, by means of hot air jets, hot water, or steam, and liquids that lower the melting point and melt ice, when required, or even prevent ice formation. Today, these methods are commonly used for de-icing and anti-icing aircraft protection before take-off. The most common chemical methods use commercial fluids, aqueous propylene and ethylene glycol solutions, which reduce the freezing point of water, thereby preventing the formation of ice. Likewise, other liquids and solids that lower the melting point are also commonly used for de-icing airport runways and taxiways [13–16]. Mechanical methods using pneumatic boots, electro-expulsive sheaths, and piezoelectric cells have also been developed. They are all based on the same principle – they deform the ice enough to break the adhesive bond with the interface [17].

## 2 Passive Anti-Icing Methods

Passive methods do not require energy other than from natural forces, such as gravity, wind, or surface tension, to induce ice detachment or mitigate its formation. Passive methods include surface treatments, normally paints and coatings that have been developed specifically by the industries and academia to decrease the accumulation and/or adhesion of ice [12]. Ideally, icephobic materials would be solid, durable, easy to apply, inexpensive, and efficient in a wide range of icing conditions – the “miracle” solution.

Today, protective materials applied to ice-exposed surfaces appear to be an interesting solution to prevent ice build-up. Since the early 1960s, several research projects attempting to identify those materials have been published [18]. Over the last decade, the development of efficient icephobic coatings and investigations of their effects have multiplied [19–22]. Many materials have been developed using polymers and, more recently, nanotechnology-based research involving the “lotus effect” has been carried out [23–25]. A mixture of micro- and nano-scale roughness and a hydrophobic material induces a superficial superhydrophobic effect with air entrapment, which lowers the contact angle of ice with the solid [26–29]. The latter has been partially validated under specific testing conditions. Moreover, with the development of superhydrophobic coatings, researchers have begun to combine these coatings with existing de-icing methods in order to improve their efficiency [30, 31].

Despite the considerable number of studies on icephobic materials, knowledge regarding the widely anticipated anti-adhesion properties is still lacking and sometimes controversial. It follows that no material has yet been identified as efficient enough to ensure full and safe protection against ice accumulation.

### 3 Icephobicity

The term icephobic has been chosen by analogy with the word hydrophobic introduced in the seventeenth century. The adjective hydrophobic describes a substance having only slight or no affinity with water from a chemistry point of view. Concretely, this no-chemical affinity induces a weak electrostatic bonding of water with a surface and the difference between water and surface energies results in the formation of water droplets that are more spherical on a hydrophobic surface.

However, in the case of icephobic surface materials, the water is either in a supercooled or solid state, leading to two other factors – mechanical adhesion and ice accumulation. Therefore, theoretically, an icephobic surface should:

- Reduce the adhesion of ice on a substrate
- Prevent ice from accumulating on a surface

Moreover, the hydrophobicity of a surface can be easily assessed by simple methods, such as determining the contact angle of water drops. In the case of icephobicity, determination of effectiveness requires assessment of both ice adhesion reduction and accumulation prevention. So what is an effective icephobic material? Knowing that the perfect one has not yet been developed, effectiveness must first be determined through targeted applications – energy, transportation, atmospheric, and environmental – in consideration of the economic conditions.

## 4 Evaluation

### 4.1 Ice Adhesion Measurement

Obviously, ice adhesion properties have been evaluated on many solid materials showing icephobic properties [32]. In most studies, so-called icephobic products are selected according to their hydrophobic properties in terms of water-repulsion abilities [33–35]. The most common and older hypothesis is that any product having poor chemical affinity with water should also have weak ice adhesion [18, 36]. However, this theory is not unanimous among researchers.

A great number of techniques have been developed to measure ice adhesion strength [37]. Adhesion measurement methods can be classified in two main groups. In the first group, the ice deposit adhering to a substrate is confined when a load is applied. The ice deposit is surrounded by boundaries, being sandwiched

between two substrates or partly restricted because of the apparatus design. The adhesive strength is the shear force at ice detachment divided by its apparent contact area with the surface. This group includes most of the adhesion tests reported in the literature presented in Fig. 1 [18, 38–40].

For example, in the Cold Regions Research and Engineering Lab (CRREL) method [38] (Fig. 1a), a bare or coated 25.4 mm diameter cylinder is made to freeze in a mold filled with water to form a 2.54 mm thick ice deposit sandwiched between the cylinder and the mold. Once frozen, an axial force is applied to the cylinder with the mold held at its base, which causes the adhesive interactions between the ice and cylinder to fail in shear. In the method reported by Jellinek [39] (Fig. 1b), ice deposits are sandwiched between two disks which are loaded to shear ice. Test variants involve tensile and compressive loads applied on disks. In the method reported by Landy and Freiburger [18] (Fig. 1c), the ice is formed from distilled water and frozen in a circular container placed on the candidate substrate; once frozen, the ice deposit is sheared by pulling up the container. As opposed to the aforementioned methods, where ice samples are formed from refrigerated water, the tests reported by Druetz et al. [40] (Fig. 1d) were specifically developed for use with atmospheric ice grown from supercooled droplets. Because of its higher solidification rate, ice grown from supercooled droplets has, in general, a smaller grain size than those of refrigerated or cold box ice. In that test, a cylindrical ice

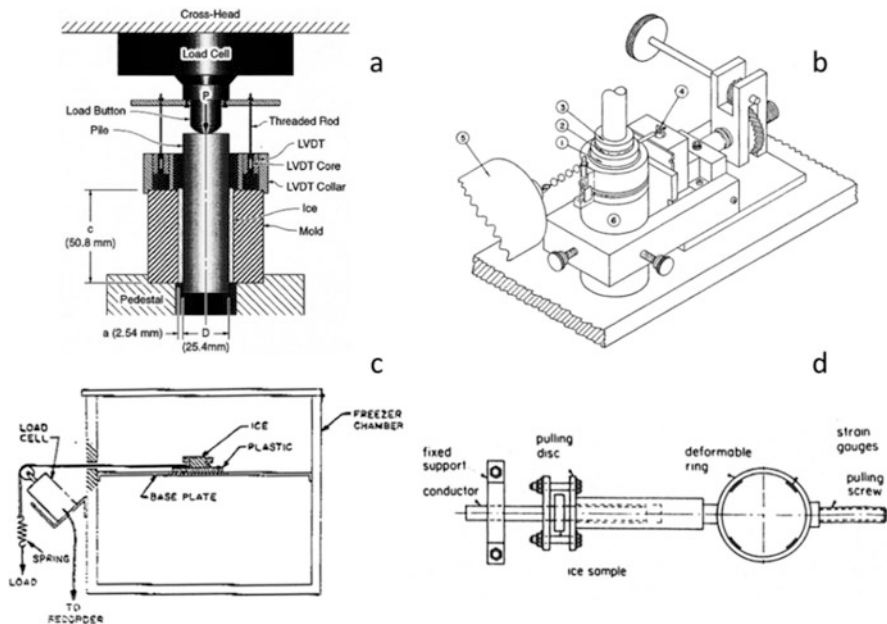


**Fig. 1** Examples of confined ice-adhesion measurement methods. (a)  $0^\circ$  cone test of U.S. Army: ERDC-CRREL [38]. (b) Test setup of Jellinek [39]. (c) Test setup of Landy and Freiburger [18]. (d) Test setup of Druetz et al. [40]. Reproduced with permission

deposit is accreted to a bare or coated cylinder and an axial force is directly applied to the tubular piece of ice by means of a flat disk.

In the second group of adhesion measurement methods, the ice deposits are non-confined. This group comprises tests in which ice samples are detached by bending small iced beams (Fig. 2a) [41], deforming an iced plate using piezoelectric cells (Fig. 2b) [42], or submitting the setup to centrifugal force [43, 44].

In the first two test methods of this second group (Fig. 2), the ice deposits are strained via the substrate, the load then not being directly exerted on the ice. However, in centrifuge tests, as described below, the load is applied directly to the ice. Adhesion tests with non-confined ice samples are not used as often as tests with confined ice samples. Nevertheless, non-confined ice deposits are more representative of those accreted on structures during natural icing events.

Commonly, ice adhesion stress values, as determined in all methods, vary considerably, ranging from 0 to 2 MPa [45]. The latter value corresponds to the cohesive shear fracture energy of ice [46]. These large variations are caused by many differences, such as the way ice is formed, atmospheric or refrigerated in a cold box, as well as the substrate characteristics.

Essentially, the mechanical properties of ice adhesion depend on several parameters, which can be divided into three main groups: (1) *icing conditions* including droplet median volumetric diameter (MVD), impact speed, and water-air surface tension, (2) *coating properties* including mean spacing of profile irregularities, average roughness, and contact angle, and (3) *parameters related to the temperature and depending on both icing and substrate*, including liquid-like layer (LLL) thickness and recalescence time, and thermal conductivity of the substrate.

Following these parameters, an analytical model has been developed and validated with experimental observations [47]. This analytical model shows that the LLL between the ice crystal and the substrate could be a useful approach to understanding the physical mechanisms acting on the ice adhesion phenomenon. It also reveals that the icing parameters are the most important factors in ice adhesion. However, in nature, icing conditions are diverse and cannot be controlled. One possible way to lower ice adhesion is to increase the LLL thickness, which can be done by changing the surface profile in order to increase the thermal isolation of

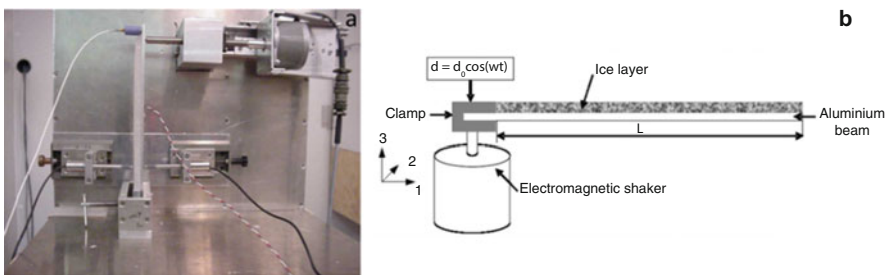


**Fig. 2** Examples of non-confined ice adhesion measurements methods. (a) Blackburn et al. [41]. (b) Javan-Mashmool et al. [42]. Reproduced with permission

the substrate and also decrease ice-substrate friction. The model also demonstrates that using a very low thermal conductivity material could help to increase the LLL thickness, and thus lower ice adhesion. Although the model can predict the behavior of the ice adhesion shedding stress, some other parameters, such as thermal conductivity of the substrate and recalescence time, should be measured experimentally to refine it. Finally, many parameters are interrelated, and the relations between them should be resolved to simplify the equation for the modeling of low-adhering surfaces.

## **4.2 Screening Evaluation Test and Adhesion Reduction Factor (ARF)**

Obtaining reliable and precise ice adhesion values is a challenge. Some tests can produce highly variable results, with up to 300% variation. Consequently, it is difficult to compare different icephobic material candidates in order to choose the best for further research and development.

To overcome these limitations, accreted ice in the form of freezing precipitation under highly controlled conditions is required. Small ice coupons for a more homogenous ice would also improve repeatability. Any test would also be comparative, where the ice adhesion, or reduction thereof, would be evaluated on coated and uncoated surfaces simultaneously iced, as small variations in the ice cannot be entirely eliminated.

The ice Centrifuge Adhesion Test (CAT) is a good example of a screening test method meeting these requirements. This method has already been described in the literature [20, 43, 46–48] and consists of a two-step procedure by which test blades with one extremity either bare or coated with a test sample are iced on a stand in a cold room (Fig. 3a–c). They are then rotated in a centrifuge until they shed their ice deposits. The centrifuge apparatus (Fig. 3d) is installed in the same cold room but separated by removable panels.

The extremities of the nine aluminum blades are iced simultaneously at different temperatures under freezing drizzle with demineralized water droplets of 300  $\mu\text{m}$  MVD. The MVD is measured using the oil slide technique, in accordance with the SAE aerospace informational report AIR4906 [49]. Ice coupons are around 1,100  $\text{mm}^2$  in area and  $7 \pm 1$  mm in thickness. The icing period is constant at 30 min and yields  $5.5 \pm 0.5$  g of ice. A minimum of 60 min between the end of icing and the centrifuge test is necessary for the ice coupons to cool to  $-10^\circ\text{C}$ . The ice coupons are then individually tested in the CAT apparatus.

The CAT apparatus consists of a centrifuge (Fig. 3d), in which the balanced aluminum blade iced at one extremity is spun at an acceleration rate of around 300 rpm/s for between 0 and 30 s, until the ice is detached by centrifugal force. That acceleration creates a strain rate of about  $10^{-6}/\text{s}$ . An accelerometer device is set on the centrifuge vat to detect instantly when the ice detaches. The rotation speed at the

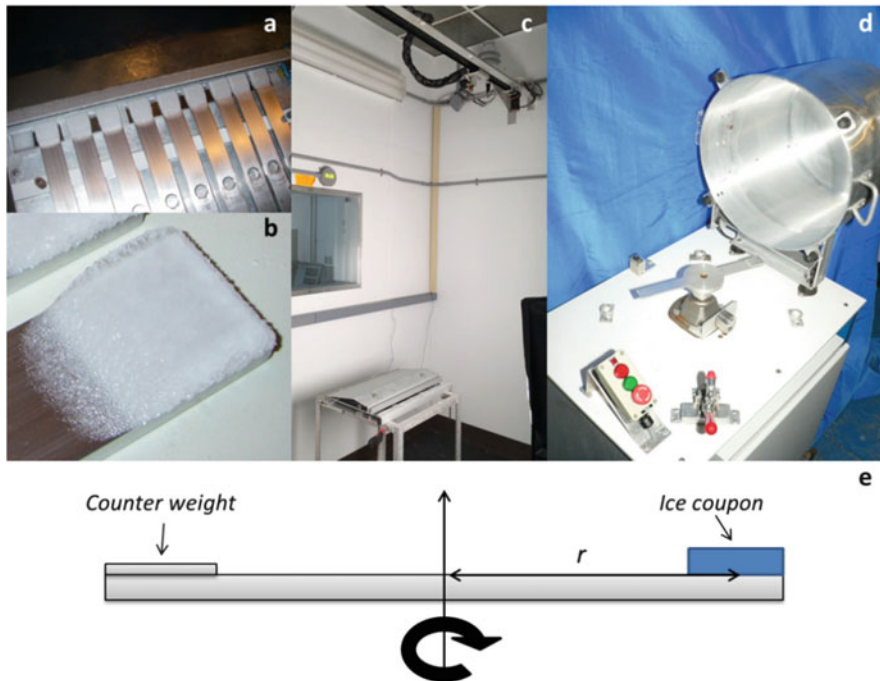


**Fig. 3** CAT setup. (a) Icing stand with nine iced blades in climatic chamber. (b) Ice coupon on aluminum blade. (c) Climatic chamber icing setup with the stand. (d) AMIL’s CAT apparatus. (e) 2D view of an iced and balanced aluminum blade

time of ice detachment is determined by a sharp increase in vibration signals. The ice adhesion corresponds to the centrifugal shear stress exerted at the position of the ice sample as it detaches. The adhesive shear stress,  $\tau$ , is calculated using (1), where  $F$  is the centrifugal force (N),  $m_{ice}$  the mass of the ice samples (kg),  $\omega$  the angular velocity (rad/s),  $r$  the radius of the beam at mid-length ice coupon position ( $m$ ) (Fig. 3e), and  $A$  the surface area of the iced interface ( $m^2$ ):

$$\tau = \frac{F}{A} = \frac{m_{ice}\omega^2 r}{A} \tag{1}$$

The ARF was first introduced in 2003 by the Anti-Icing Materials International Laboratory (AMIL) to normalize ice adhesion reduction values between the different existing methods by incorporating a reference material comparison. The ARF is calculated using (2):

$$ARF = \frac{AVG \text{ Ice Adhesion on Reference Bare Al}}{AVG \text{ Ice Adhesion on Coating}} \tag{2}$$

The ice adhesion reduction performance of coatings is evaluated using the following criteria:



- $ARF > 1$ : ice adhesion reduction, icephobic effect, the higher the value, the more icephobic the coating
- $ARF < 1$ : an increase in adhesion on the candidate coating with respect to the bare Al

Since 2003, 345 different coatings have been evaluated with CAT tests performed under similar icing and experimental conditions, that is, freezing drizzle at  $-8^{\circ}\text{C}$  and centrifuge testing at  $-10^{\circ}\text{C}$ . Figure 4 shows the range of the ARF results, including freshly applied solid coatings, viscous greases, embedded polymeric coupons, and surface treatments. Every coating is compared with an Al 6061 T6 reference blade. This reference blade has an average roughness of  $0.8\ \mu\text{m}$  and shows a water contact angle (WCA) of  $\sim 75^{\circ}$ . The average bulk shear stress measure is about  $0.51\ \text{MPa} \pm 7\%$  [46]. Note that the standard deviation of ARFs is  $\pm 15\%$  (based on six icing test repeats). Figure 4 shows those ARF results, classified by the year of the test.

Overall, the performance of tested coatings over the years is similar within a wide range of ARF values, from 0.5 to 1,000, corresponding to stresses from about 0.8 to 0.0005 MPa, respectively. Most of the candidate coatings (67%) reduce ice adhesion, compared to bare Al, by a factor between 1 and 5. Only 23% of the solid coatings demonstrated significant adherence reduction effects with ARFs above 10. While grease-based materials have been found to be the most efficient because of the mechanical anchorage of ice being inhibited by the viscous nature of the coatings, the fact that they are non-permanent limits their use in practice. Indeed,

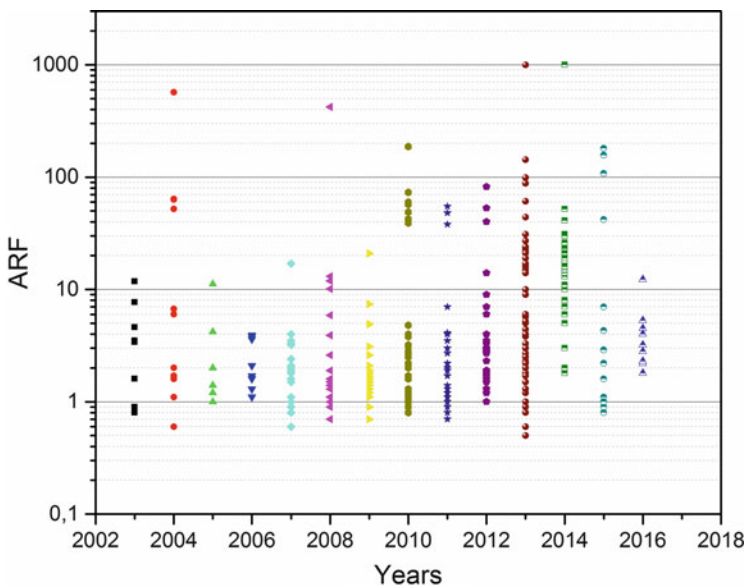


Fig. 4 ARFs from AMIL CAT tests (compared to Al, hard rime ice,  $-10^{\circ}\text{C}$ )

their efficiency is affected by wear, which needs to be adequately assessed before use.

Since 2005, ice adhesion results have been expressed in terms of ARF by many other research groups, although nearly every group has different definitions or experimental protocols. Therefore, ARF should only be used with respect to a number of criteria. ARF should be used to compare an icephobic material to its reference substrate iced under the same precipitation conditions or, if this is not possible, to repeat the measurement with the reference substrate at each test and/or specify the frequency of reference measurements during the test campaign. The soundness of ARF results rests on the fact that intrinsic experimental variations are attenuated by the use of reference controls. Table 2 presents 13 results from research groups that are working in the field of icephobic coatings and using the ARF to describe their coatings' effectiveness in reducing ice adhesion [21, 50–61].

It shows details about their studied coatings: WCA and reference substrate, ice adhesion measurement methods used, test temperatures, and types of ice, when cited in the references. Results with three types of ice are presented: (1) cocktail ice, or water frozen in a mold, (2) atmospheric ice (Atm), or ice obtained from supercooled droplet precipitations, and (3) impact ice, which is ice obtained in an icing wind tunnel simulating in-cloud icing with supercooled droplets less than 20  $\mu\text{m}$  in diameter. The last three columns show the ice adhesion stresses on the coatings, the reference substrate (when they are cited in the references), and the calculated ARF.

Most of the above studies propose new hydrophobic and superhydrophobic coatings using different types of ice adhesion tests. ARF results vary from 2.4 to 100. The ARFs were calculated according to their reference substrates, which were evaluated in the same icing conditions. Using the ARFs yields normalized results, which allows the comparison of results from different methods.

However, at which value of ARF is the coating considered to have efficient icephobicity? This value can be evaluated by calculating the ice thickness needed for it to self-shed only under the effect of the gravitational force. Figure 5a shows a stationary iced cylinder. The quantity of ice increases linearly and horizontally with time. This inspired a simple model of atmospheric ice accumulation in which the mass increases linearly on a flat surface (Fig. 5b, c), with perfect contact between the ice and the solid surface.

Stress ( $S$ ) is evaluated using the inertia value of the beam ( $I$ ), its centroid ( $c$ ), and the force ( $F$ ) caused by gravity, which is a function of the density of ice ( $\rho$ ), taken to be  $0.9 \text{ g/cm}^3$ , the thickness of ice ( $E$ ), the length of ice ( $L$ ), the width ( $D$ ), and the gravitational acceleration ( $g$ ), taken to be  $9.81 \text{ m/s}^2$ . Stress is calculated using (3–8):

$$S = \frac{Mc}{I} \quad (3)$$

**Table 2** Survey of different ice adhesion values cited in the literature

Ref	Coating (WCA°)	Ref. substrate	Ice adhesion method	$\tau_{\text{coating}}$ (MPa $\pm$ SD)	$\tau_{\text{substrate}}$ (MPa $\pm$ SD)	ARF
[21]	PDMS type coating	Al	0° Cone test -14°C Cocktail ice	0.015	1.5808	100
[50]	Nanostructured etching sili- con + octadecylsilane (168°)	Silicon	Pull test -15°C Cocktail ice	n.m.	n.m.	15 <sup>a</sup>
[51]	Smooth silicone rubber (105°)	Al	0° Cone test -20°C Cocktail ice	1.072	0.024	43.2
[52]	Superhydrophobic Zn and silicone (155°)	Steel	CAT -10°C Atm. ice	0.617 $\pm$ 0.004	0.098 $\pm$ 0.012	6.3
[53]	Phase change materials based on organophosphorus	Al	Double lap shear test CAT -10°C Atm. ice	0.400 $\pm$ 0.050 n.m.	0.005 n.m.	80 <sup>b</sup> 39
[54]	Polycarbonate ultrahydrophobic coating (160°)	Polycarbonate and Al	CAT -15°C In cloud icing	0.074 $\pm$ 20%	0.129 $\pm$ 20%	18.3 <sup>c</sup>
[55]	Anodized Al with plasma coated hexamethyldisiloxane (158°)	Al	CAT -15°C Impact ice	0.350 $\pm$ 0.025	0.100 $\pm$ 0.009	3.5
[56]	Epoxy containing aromatic diamines	Al	Adverse Env. Rotor test -8, -12, -16°C Impact ice	n.m.	n.m.	-2
[57]	Fluoropolymer with Ag particles (153°)	Al	CAT -15°C Impact ice	n.m.	n.m.	5.7

(continued)

Table 2 (continued)

Ref	Coating (WCA°)	Ref. substrate	Ice adhesion method	$\tau_{\text{coating}}$ (MPa $\pm$ SD)	$\tau_{\text{substrate}}$ (MPa $\pm$ SD)	ARF
[58]	Zn-Al Bayer (Nano micro) stearic acid (167°)	Al	CAT -10°C Cocktail ice	n.m	n.m	8
[59]	Stainless steel 316 meshes (102°)	Steel	Push test -15°C Cocktail ice	0.048 $\pm$ 0.015	0.682 $\pm$ 0.046	14.2
[60]	Anodized Al + PTFE (~150°)	Al	CAT -10°C Impact ice	0.209	0.500	2.4
[61]	Silicone + alumina Np (~150°)	Al	CAT -10°C Impact ice	~0.065 $\pm$ 0.018	0.317 $\pm$ 0.025 <sup>d</sup>	5 <sup>e</sup>

<sup>a</sup>The authors did not describe it as an ARF

<sup>b</sup>Calculated with values; No ARF specified

<sup>c</sup>As compared to Al

<sup>d</sup>Reference not repeated at each test

<sup>e</sup>After one test. ARF reduced to 1.4 after four tests

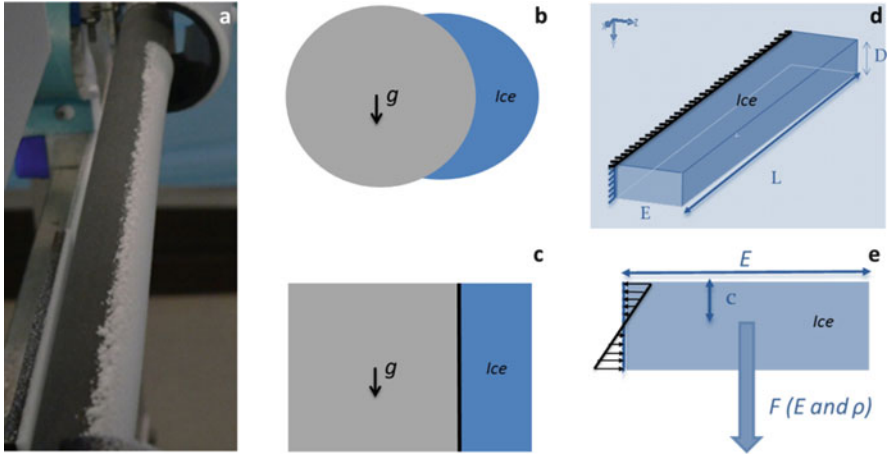


**Fig. 5** Ice accumulation over a stationary collector. (a) Iced cylinder. (b, c) Simplified model from cylinder to rectangular prism of ice accretion. (d, e) Rectangular prism model showing dimensional and mechanical parameters. Adapted from Brassard [62]

$$M = \frac{1}{2}FE \tag{4}$$

$$F = \rhoELDg \tag{5}$$

$$c = \frac{D}{2} \tag{6}$$

$$I = \frac{LD^3}{12} \tag{7}$$

$$S = \frac{3\rho E^2g}{D} \tag{8}$$

Based on (8), stress is calculated as a function of the accreted ice thicknesses. Stress is also proportional to the density and inversely proportional to the width ( $D$ ) of ice. For the calculation,  $D$  is taken as 5 cm. Stress is converted to ARF using (2) in which ice adhesion on an aluminum substrate is specified to be 0.6 MPa. Results are reported in Fig. 6. The resulting curve is the relation between the self-shedding ARF values, depending on its thickness. As expected, coatings with higher ARFs should self-shed at lower thicknesses [62].

It can be predicted from Fig. 6 that to have an efficient icephobic coating that self-sheds, a targeted ARF value of about 100 is needed (compared to Al substrate). As an example, for a coating having an ARF of 100, where the ice adhesion is reduced by 99%, the accreted ice should never grow more than 83 mm because it self-sheds when reaching this thickness. In addition, at this value of ARF, compared to Al bare substrate, the allowed weight of ice before self-shedding is 90% less, so

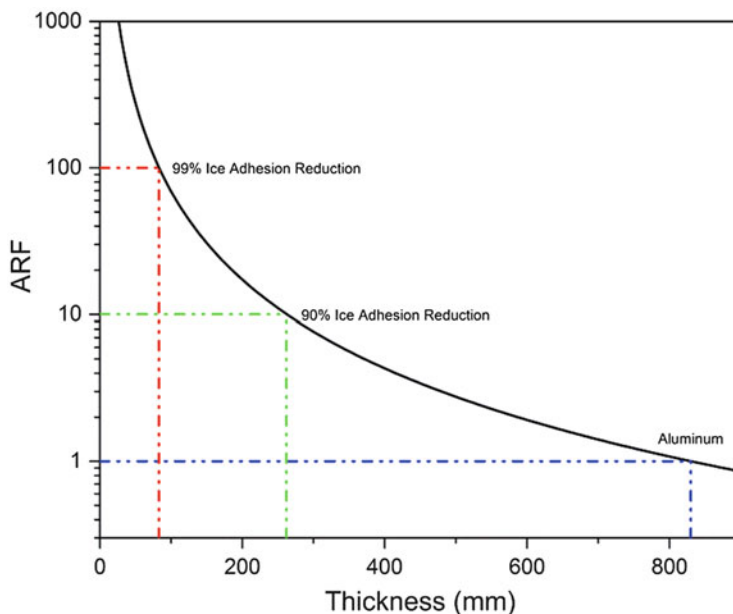


**Fig. 6** ARF causing ice self-shedding according to accreted ice thickness for a hypothetical case: hard rime  $0.9 \text{ g/cm}^3$ , adhesion stress on aluminum is assumed to be  $0.6 \text{ MPa}$  at  $-10^\circ\text{C}$ . Adapted from Brassard [62]

the iced structure is then less stressed. This result has also been demonstrated experimentally in previous research [48].

### ***4.3 Establishing a Test Campaign to Evaluate the Icephobic Properties/Efficiency of a Coating or Surface Treatment***

After establishing the better icephobic candidate coating with a screening test method such as CAT, further and expanded properties must be considered. Actually, an efficient icephobic coating must not only reduce the adhesion and accumulation of ice, it must also be efficient under the targeted application conditions of temperatures, icing, and harsh environment, such as those encountered in actual environments in service use.

The chart presented in Fig. 7 summarizes the main properties that could be taken in consideration for establishing a test campaign to evaluate an icephobic protective surface material.

Obviously, depending on the icephobic application, it can be subjected to different frozen hydrometeors, which do not interact in the same way with the coating. Then, the density of the ice deposit may vary. For example, ice from

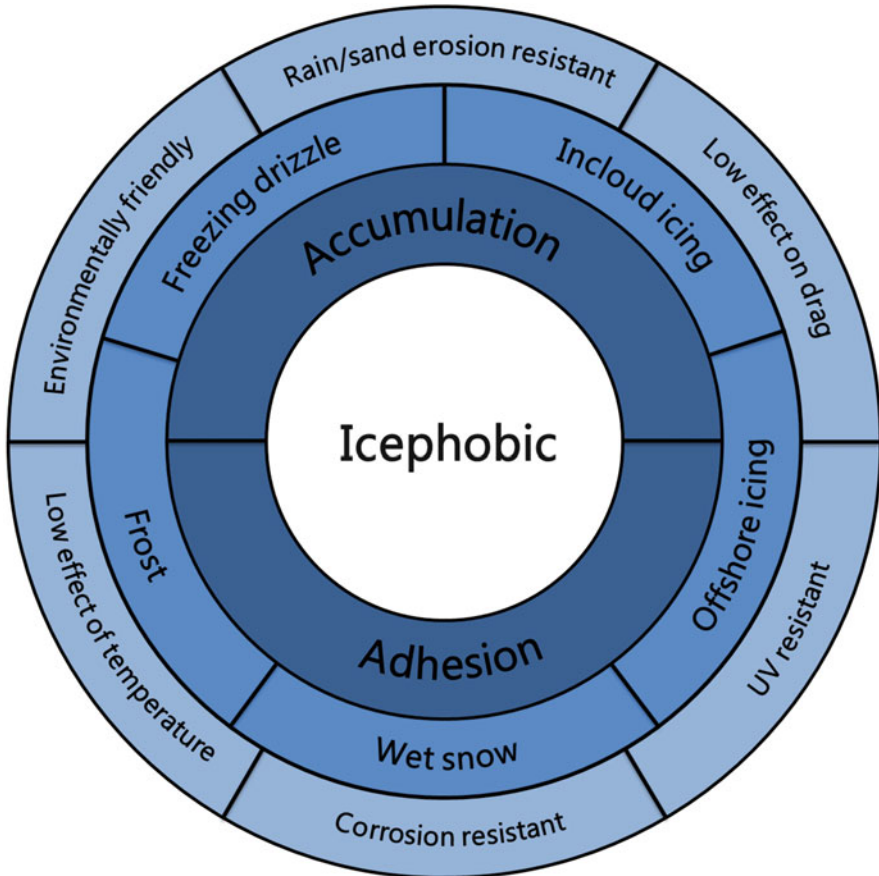


Fig. 7 Icephobic property overview

freezing drizzle has a higher density than frost, and therefore different adhesion properties with the surface material. Moreover, icephobic materials are used under environmental conditions; in some cases they must resist ultraviolet radiation (UV), corrosion, rain, and sand erosion at very low or high temperatures, and be environmentally friendly.

As there is no standard for the evaluation of icephobic coatings, in line with common applications, that is, aircraft, ground transportation, energy production, or buildings, several tests must be performed to evaluate their true efficiency. The first part of the testing should consider ice adhesion. In the second part, the coating is put through ice accumulation tests, always depending on its expected use. Finally, the effect of external conditions, such as temperature, UV, corrosion, rain and/or sand erosion, must be taken into account. However, various other tests could be added to this non-exhaustive list, as needed, based on the targeted application. In Sect. 4.4, an example of an extended test campaign is described for the application of an icephobic coating to Arctic offshore applications.

#### 4.4 *Example of Extended Test Campaign: Icephobic Coating for Arctic Offshore Environments*

A complete test campaign has been proposed to evaluate a series of different coatings to reduce ice adhesion and accumulation under Arctic offshore conditions. The selected coating could be applied to an oil rig, for example. As a first step, all the freshly applied coatings are characterized at room temperature according to thickness, WCA, and surface roughness, and optical photographs are taken. Thus, the effects of degradation is well-assessed and monitored. As a second step, all the coatings should go through the CAT in fresh-water freezing drizzle conditions at  $-10^{\circ}\text{C}$  (ARF CAT). All the coatings having substantial ARF results should then be selected for further analysis under more specific testing conditions. Afterward, the CAT can be repeated at least five times (CAT rep. 5) to ensure the stability of the candidate coating to repetitive icing/de-icing cycles. After each icing/de-icing cycle, the characterization step is repeated.

The coatings should also be tested under simulated offshore icing conditions. Plates and cylinders simulating various vertical surfaces and cables on an offshore structure should first be evaluated under white cap spray (WCS), involving droplets spraying from the tops of waves and blown by wind, and then be evaluated under interaction spray (IS) resulting from waves colliding with a structure. The ice ARF and the ice accumulation reduction factor (% red.) are assessed for these specific conditions. Figure 8 illustrates such a procedure in the AMIL climatic chamber using plates and cylinders iced in laboratory-simulated WCS conditions at different water salinities and temperatures [63], with controlled MVD droplets. Under these

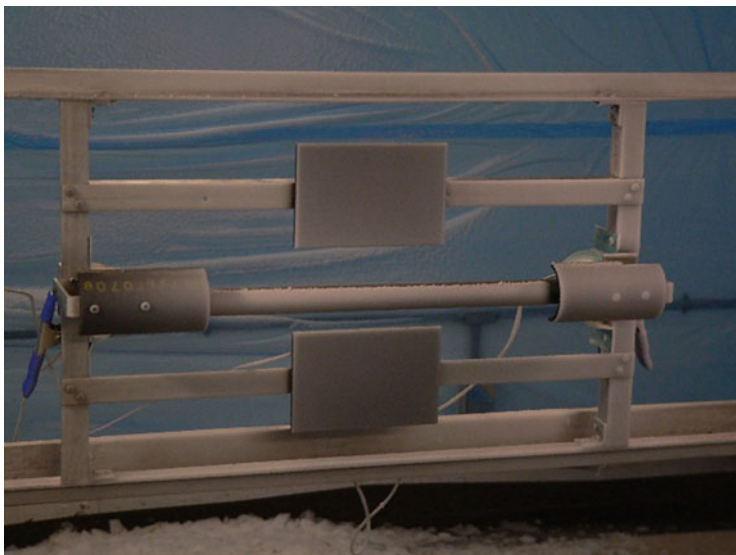


**Fig. 8** AMIL laboratory-simulated accumulation of WCS on cylindrical and steel plate collectors



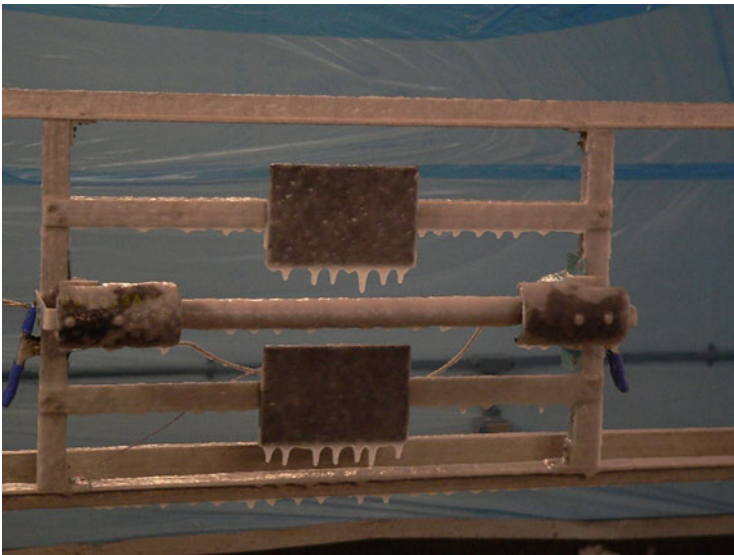
conditions, samples can also be iced and tested in the centrifuge to measure ice adhesion.

Figure 9 shows an example of ice accumulation under simulated IS with saline water.

In some cases, the candidate material could be tested under extreme cold temperatures, below  $-30^{\circ}\text{C}$ , and after freeze-thaw cycles (ARF Cold). Likewise, the effect of long-term exposure to sunlight (UV radiation) on the efficiency of the candidate coating can be assessed by exposing it to accelerated weathering, such as specified in ASTM D4587 [64] followed by a recharacterization step, and then CAT testing again (ARF UV).

The stability of the candidate coating could be evaluated under rain and sand erosions and under corrosive environments. Finally, experiments should be carried out to evaluate its environmental impact. In order to simplify, the latter four test results can be ranked following a 1–5 scale, 1 corresponding to poor characteristics and 5 to perfect characteristics.

All the results can be presented in the form of a radar chart, as shown in Fig. 10. This type of chart is useful to compare different coatings subjected to the same conditions, and helpful to select the most promising one, as the larger the area, the better the coating.



**Fig. 9** AMIL laboratory-simulated accumulation of an IS on plates and cylinders

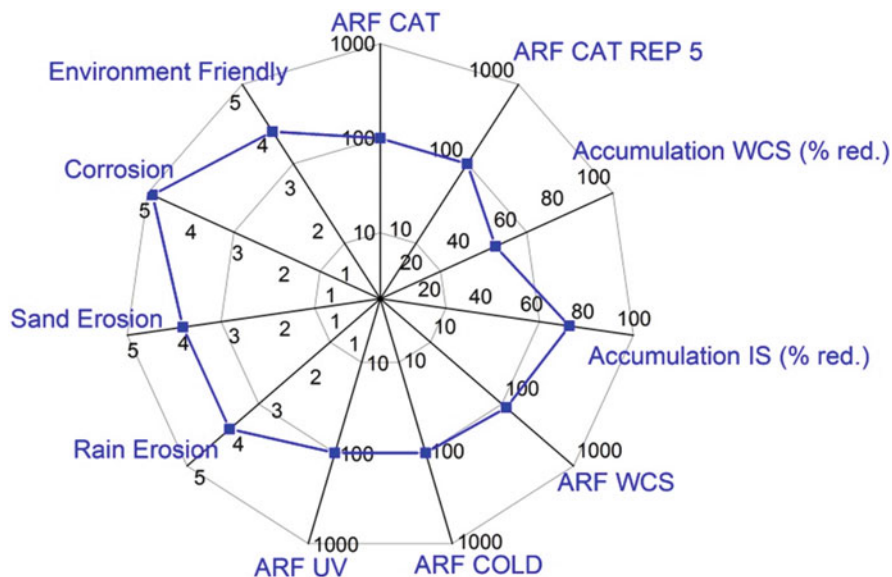


**Fig. 10** Radar chart efficiency result of a hypothetical icephobic coating under offshore conditions

## 5 Conclusions

The aim of this chapter is to propose a definition of icephobicity expressed in terms of ARF measured under general testing conditions. It appears that an ARF of 100 is a good target value, indicating that the coating has a considerable degree of efficiency. Moreover, the coating's efficiency needs to be assessed under the most specific icing conditions representative of harsh environments prevailing in the field. Therefore, the icephobic coating's efficiency is more than a simple measurement of ice adhesion; indeed, many more aspects need to be considered, these being related to targeted applications, considering first the security factor in terms of efficacy, safety, and durability and then the economic point of view of their implementation. Is it worth applying a protective coating to lower the ice adhesion by a factor of 3 on an offshore structure? It depends on the level of safety needed and the cost. For example, is it worth applying this coating to a vertical surface already designed to withstand the ice load and then de-iced using mechanical methods at the same price, with the same durability? Yes, making the de-icing easier may be worth the cost. However, the perfect icephobic coating does not exist, and no simple answer can be proposed. Finally, for each different field of application, a material standard specification would be very useful to help further develop efficient icephobic materials.

## References

1. Aviation Safety (1971) Surgut aeroflot antonov. <http://aviation-safety.net/database/record.php?id=19710122-0>. Accessed 30 Sept 2016
2. Aviation Safety (1974) Turkish airlines flight 301. <http://aviation-safety.net/database/record.php?id=19740126-0>. Accessed 30 Sept 2016
3. National Transportation Safety Board (1982) Aircraft accident report: Air Florida flight 90. Washington
4. Aviation Safety (1985) Arrow air flight 1285. <http://aviation-safety.net/database/record.php?id=19851212-0>. Accessed 30 Sept 2016
5. Moshansky VP (1992) Commission of inquiry into the air Ontario crash at Dryden, Ontario (Canada). <http://epe.lac-bac.gc.ca/100/200/301/pc0-bcp/commissions-ef/moshansky1992-eng/moshansky1992-eng.htm>. Accessed 30 Sept 2016
6. National Transportation Safety Board (1992) Aircraft accident report: USAIR flight 405. Washington
7. National Transportation Safety Board (1994) Aircraft accident report: American Eagle flight 4184. Washington
8. Aviation Safety (2004) China eastern airlines flight 5210. <http://aviation-safety.net/database/record.php?id=20041121-0>. Accessed 30 Sept 2016
9. National Transportation Safety Board (2009) Aircraft accident report: Colgan Air flight 3407. Washington
10. Aviation Safety (2009) Air France flight 447. <https://aviation-safety.net/database/record.php?id=20090601-0>. Accessed 31 Jan 2017
11. Transports Canada (2005) Guidelines for aircraft ground icing operations. Ottawa
12. Laforde J-L, Allaire M-A, Laflamme J (1998) State-of-the-art on power line de-icing. *Atmos Res* 46(1):143–158. [https://doi.org/10.1016/S0169-8095\(97\)00057-4](https://doi.org/10.1016/S0169-8095(97)00057-4)
13. SAE AMS1424 (2016) Deicing/anti-icing fluid, aircraft, SAE Type I. SAE International, Warrendale
14. SAE AMS1428 (2017) Fluid aircraft deicing/anti-icing, non Newtonian (Pseudoplastic), SAE Types II, Type III and Type IV. SAE International, Warrendale
15. SAE AMS1431 (2012) Compound, solid runway and taxiway deicing/anti-icing. SAE International, Warrendale
16. SAE AMS1435 (2012) Fluid, generic, deicing/anti-icing runways and taxiways. SAE International, Warrendale
17. Goraj Z (2004) An overview of the deicing and antiicing. Paper presented at the 24th international congress of the aeronautical sciences, Yokohama
18. Landy M, Freiburger A (1967) Studies of ice adhesion: ice adhesion to plastics. *J Colloid Interf Sci* 25(2):231–244
19. Tarquini S, Antonini C, Amirfazli A, Marengo M, Palacios J (2014) Investigation of ice shedding properties of superhydrophobic coatings on helicopter blades. *Cold Reg Sci Technol* 100:50–58. <https://doi.org/10.1016/j.coldregions.2013.12.009>
20. Laforde C, Blackburn C, Perron J, Aubert R (2014) Icephobic coating evaluation for aerospace application. Paper presented at the 55th AIAA/ASME/ASCE/AHS/SC structures, structural dynamics, and materials conference, National Harbor
21. Susoff M, Siegmann K, Pfaffenroth C, Hirayama M (2013) Evaluation of icephobic coatings—screening of different coatings and influence of roughness. *Appl Surf Sci* 282:870–879. <https://doi.org/10.1016/j.apsusc.2013.06.073>
22. Makkonen L (2012) Ice adhesion – theory, measurements and countermeasures. *J Adhes Sci Technol* 26(4–5):413–445. <https://doi.org/10.1163/016942411x574583>
23. Kreder MJ, Alvarenga J, Kim P, Aizenberg J (2016) Design of anti-icing surfaces: smooth, textured or slippery? *Nat Rev Mater* 1:15003

24. Schutzius TM, Jung S, Maitra T, Eberle P, Antonini C, Stamatopoulos C, Poulikakos D (2014) Physics of icing and rational design of surfaces with extraordinary icephobicity. *Langmuir* 31 (17):4807–4821
25. Sojoudi H, Wang M, Boscher N, McKinley G, Gleason K (2016) Durable and scalable icephobic surfaces: similarities and distinctions from superhydrophobic surfaces. *Soft Matter* 12(7):1938–1963
26. He Y, Jiang C, Cao X, Chen J, Tian W, Yuan W (2014) Reducing ice adhesion by hierarchical micro-nano-pillars. *Appl Surf Sci* 305:589–595. <https://doi.org/10.1016/j.apsusc.2014.03.139>
27. Xiao J, Chaudhuri S (2012) Design of anti-icing coatings using supercooled droplets as nano-to-microscale probes. *Langmuir* 28(9):4434–4446. <https://doi.org/10.1021/la2034565>
28. Jung S, Dorrestijn M, Raps D, Das A, Megaridis CM, Poulikakos D (2011) Are superhydrophobic surfaces best for icephobicity? *Langmuir* 27(6):3059–3066. <https://doi.org/10.1021/la104762g>
29. Zheng L, Li Z, Bourdo S, Khedir KR, Asar MP, Ryerson CC, Biris AS (2011) Exceptional superhydrophobicity and low velocity impact icephobicity of acetone-functionalized carbon nanotube films. *Langmuir* 27(16):9936–9943. <https://doi.org/10.1021/la201548k>
30. Parent O, Ilinca A (2011) Anti-icing and de-icing techniques for wind turbines: critical review. *Cold Reg Sci Technol* 65(1):88–96. <https://doi.org/10.1016/j.coldregions.2010.01.005>
31. Antonini C, Innocenti M, Horn T, Marengo M, Amirfazli A (2011) Understanding the effect of superhydrophobic coatings on energy reduction in anti-icing systems. *Cold Reg Sci Technol* 67(1–2):58–67. <https://doi.org/10.1016/j.coldregions.2011.02.006>
32. Baum B, Thoma LA, Holley WH (1996) Development of conductor deicing systems. Electric Power Research Institute, Palo Alto, p 133
33. Andersson L-O, Golander C-G, Persson S (1994) Ice adhesion to rubber materials. *J Adhes Sci Technol* 8(2):117–132. <https://doi.org/10.1163/156856194X00104>
34. Crutch VK, Hartley RA (1992) Adhesion of ice to coatings and the performance of ice release coatings. *J Coating Technol* 64(815):41–53
35. Yoshida M, Ohichi T, Konno K, Gocho M (1991) Adhesion of ice to various materials. Paper presented at the cold regions technology conference, Japan
36. Lliboutry L (1964) *Traite de glaciologie*. Masson, Paris
37. Schulz M, Sinapius M (2015) Evaluation of different ice adhesion tests for mechanical deicing systems. Paper presented at the international conference on icing of aircraft, engines, and structures, Prague
38. Haehnel RB (2002) Evaluation of coatings for icing control at hydraulic structures. *Ice Eng* 33:4
39. Jellinek HG (1959) Adhesive properties of ice. *J Coll Sci* 14(3):268–280
40. Druetz J, Phan LC, Laforte J-L, Nguyen DD (1979) The adhesion of glaze and rime on aluminium electrical conductors. *Trans CSME* 5(4):215–220
41. Blackburn C, Laforte C, Laforte J-L (2000) Apparatus for measuring the adhesion force of a thin ice sheet on a substrate. Paper presented at the 9th international workshop on atmospheric icing on structures, Chester, England
42. Javan-Mashmool M, Volat C, Farzaneh M (2006) A new method for measuring ice adhesion strength at an ice-substrate interface. *Hydrol Process* 20(4):645–655
43. Laforte C, Beisswenger A (2005) Icephobic material centrifuge adhesion test. Paper presented at the 11th international workshop on atmospheric icing on structures, Montreal
44. Stallabrass JR, Price RD (1963) On the adhesion of ice to various materials, National Research Laboratories. *Can Aeronaut Space J* 9:199–204
45. Raraty LE, Tabor D (1958) The adhesion and strength properties of ice. *Proc Soc Math Phys Sci* 245(1241):184–201. <https://doi.org/10.1098/rspa.1958.0076>
46. Fortin G, Beisswenger A, Perron J (2010) Centrifuge adhesion test to evaluate icephobic coatings. Paper presented at the 2nd AIAA atmospheric and space environments conference, Toronto

47. Guerin F, Laforte C, Farinas M-I, Perron J (2016) Analytical model based on experimental data of centrifuge ice adhesion tests with different substrates. *Cold Reg Sci Technol* 121:93–99. <https://doi.org/10.1016/j.coldregions.2015.10.011>
48. Laforte C, Blackburn C, Perron J (2015) A review of icephobic coating performances over the last decade. Paper presented at the conference on icing of aircraft, engines, and structures, Prague, Czech Republic, June 22–25
49. SAE AIR4096 (1995) Droplet size instrumentation used in icing facilities. SAE International, Warrendale
50. Bengaluru Subramanyam S, Kondrashov V, Rhe J, Varanasi KK (2016) Low ice adhesion on nano-textured superhydrophobic surfaces under supersaturated conditions. *ACS Appl Mater Inter* 8(20):12583–12587
51. Bharathidasan T, Kumar V, Bobji M, Chakradhar R, Basu BJ (2014) Effect of wettability and surface roughness on ice-adhesion strength of hydrophilic, hydrophobic and superhydrophobic surfaces. *Appl Surf Sci* 314:241–250
52. Brassard JD, Sarkar DK, Perron J, Audibert-Hayet A, Melot D (2015) Nano-micro structured superhydrophobic zinc coating on steel for prevention of corrosion and ice adhesion. *J Colloid Interface Sci* 447:240–247. <https://doi.org/10.1016/j.jcis.2014.11.076>
53. Dixon B, Walsh A, Gall B, Goodwin M (2011) Novel phase change material icephobic coating for ice mitigation in marine environments. In: Proceedings of the 12th general assembly of IAMU, Gydnia
54. Dodiuk H, Kenig S, Dotan A (2012) Do self-cleaning surfaces repel ice? *J Adhes Sci Technol* 26(4–5):701–714
55. Foroughi Mobarakeh L, Jafari R, Farzaneh M (2013) The ice repellency of plasma polymerized hexamethyldisiloxane coating. *Appl Surf Sci* 284:459–463. <https://doi.org/10.1016/j.apsusc.2013.07.119>
56. Smith JG, Wohl CJ, Kreeger RE, Palacios J, Knuth T, Hadley KR (2016) Effect of molecular flexibility upon ice adhesion shear strength. Paper presented at the 39th annual adhesion society meeting, San Antonio
57. Kulinich SA, Farzaneh M (2009) Ice adhesion on super-hydrophobic surfaces. *Appl Surf Sci* 255(18):8153–8157
58. Li W, Zhang X, Yang J, Miao F (2013) In situ growth of superhydrophobic and icephobic films with micro/nanoscale hierarchical structures on the aluminum substrate. *J Coll Inter Sci* 410:165–171. <https://doi.org/10.1016/j.jcis.2013.07.063>
59. Ling EJY, Uong V, Renault-Crispo J-S, Kietzig A-M, Servio P (2016) Reducing ice adhesion on nonsmooth metallic surfaces: wettability and topography effects. *ACS Appl Mater Inter* 8(13):8789–8800
60. Menini R, Farzaneh M (2009) Elaboration of Al<sub>2</sub>O<sub>3</sub>/PTFE icephobic coatings for protecting aluminium surfaces. *Surf Coat Technol* 203:1941–1946
61. Momen G, Jafari R, Farzaneh M (2015) Ice repellency behaviour of superhydrophobic surfaces: effects of atmospheric icing conditions and surface roughness. *Appl Surf Sci* 349:211–218. <https://doi.org/10.1016/j.apsusc.2015.04.180>
62. Brassard JD (2016) Revtements nanostructurs pour la protection des mtaux dans les environnements marins – Nanostructured coatings for the protection of metal in marine environments. Dissertation, Universit du Qubec à Chicoutimi, Chicoutimi
63. ASTM D1141-98 (2013) Standard practice for the preparation of substitute ocean water. ASTM International, West Conshohocken
64. ASTM D4587-11 (2011) Standard practice for fluorescent UV-condensation exposures of paint and related coatings. ASTM International, West Conshohocken

# Development and Testing of Icephobic Materials: Lessons Learned from Fraunhofer IFAM



Nadine Rehfeld, Andrej Stake, and Volkmar Stenzel

**Abstract** The effective development of icephobic coatings requires test scenarios that simulate relevant icing conditions in the desired application field. Because of a lack of available standardized tests, developers rely on comparative tests, comparing results with pre-defined benchmark systems. In this context, tests need to be conducted under very stable conditions without allowance for fluctuation. This guarantees a development process with stepwise material improvement. Fraunhofer IFAM in Germany began working on icephobic materials over 10 years ago, seeking to develop not only the materials but also adequate test methods. This chapter describes the development process and results of these activities, as well as proposals to improve efficiency further in the future development of icephobic materials.

**Keywords** Ice adhesion test • Ice formation test • Icephobic coatings • Icing wind tunnel • Surface characterization

## Contents

1	Introduction .....	146
2	Materials and Testing Approaches .....	146
3	Ice Formation Tests .....	147
3.1	Results of Ice Formation Tests .....	149
3.2	Significance of Ice Formation Tests .....	152
4	Ice Adhesion Tests .....	154
4.1	Results of Ice Adhesion Tests .....	156
4.2	Significance of Ice Adhesion Tests .....	157

5	Ice Wind Tunnel Tests .....	158
5.1	Results of Ice Wind Tunnel Tests .....	159
5.2	Conclusions for Ice Wind Tunnel Tests .....	160
6	Surface Characterizations .....	161
6.1	Methods for Surface and Material Characterizations .....	161
6.2	Correlations: Surface Properties Vs Icephobicity .....	162
7	Conclusions .....	164
	References .....	165

## 1 Introduction

In recent decades, many research groups have worked to develop icephobic coatings and methods for adequately testing icephobic materials [e.g. 1–4]. These developments have been accompanied by investigations into correlations between specific surface characteristics and icephobic behavior [5–9]. More than 10 years ago, Fraunhofer IFAM started to develop icephobic coatings, despite the absence of standardized ice-related test methods and guidelines or requirements for icephobic materials. These coatings are relevant to all application fields, including not only means of transportation (aircraft, ships, trains, and cars) but also wind turbines, buildings, and heat exchanger systems.

Specific tests have also been developed at Fraunhofer IFAM over the past 10 years to characterize these icephobic coatings. These include ice chamber tests to assess ice formation, ice adhesion tests, and ice wind tunnel tests. In all cases, the tests address the demands of relevant application fields to simulate icing environments as close as possible to the predominant natural conditions. Furthermore, comprehensive surface characterization of icephobic materials was concurrently conducted to improve the understanding of correlations between surface parameters and icephobic effects. However, the complexity of icing mechanisms as well as interacting surface characteristics do not allow for the definition of general design rules for icephobic surfaces. Additionally, developers face challenges, such as reduced durability, that limit coating efficacy and the need for multi-functional material approaches.

This chapter addresses primary test designs developed by Fraunhofer IFAM for the evaluation of icephobic materials. Results of these successive development processes are described, and the subsequent conclusions are discussed.

## 2 Materials and Testing Approaches

Fraunhofer IFAM is involved in different national and international research and development projects related to icephobic materials and technologies. Over the years a comprehensive data set has been derived, allowing for the assessment of correlations and the significance of tests. Major outcomes of these studies are presented in the following sections. Coating types involved (though not specified

in detail) are polyurethane (PUR)-based – fluorine and/or silicone modified, sol-gel coatings, plasma coatings, polysilazane, temporary waxes and lubricants (also modified with freezing point depressors), ceramic coatings, particle-modified materials, and slippery liquid-infused porous surface approaches.

The evaluation of icephobic materials requires test methods that assess the specific function of the surface (e.g., accelerated water run-off, reduced ice formation, minimized ice adhesion). Additionally, test conditions need to be defined that discriminate between different surfaces as well as reflect relevant icing scenarios for the envisaged application field. Field tests need to be conducted to draw conclusions about the significance of artificial ice test results in realistic applications. Figure 1 shows an example of a flow chart for material screenings at Fraunhofer IFAM; tests are marked by rectangles and decision gates by diamonds. All aspects of this flow chart may be adapted to relevant technical requirements of the targeted application field and to customer specifications. Test methods are described in Sect. 3, encompassing different ice formation types and ice adhesion tests.

### 3 Ice Formation Tests

To start the characterization process of icephobic coatings, Fraunhofer IFAM developed the Icing Chamber about 10 years ago (Fig. 2). Preliminary tests showed that even minor fluctuations in temperature and wind speed led to significant deviations in ice formation results. This test device was therefore designed to create very stable icing conditions and to allow for an easy and fast evaluation of newly developed coatings against predefined benchmarks. The selection of benchmark coatings is dependent on the relevant application field and customer requirements. Unless otherwise stated in this chapter, benchmark coating refers to an unmodified PUR coating as used on external aircraft surfaces.

Two standard test scenarios have been defined, allowing for comparative studies of coatings under ice rain and rime ice conditions. Depending on the coating approach under development, the relevant test regime is used.

For coatings that improve water run-off and consequently reduce ice formation under wet conditions, the ice rain test is selected. Coatings are evaluated under freezing conditions (temperature  $-5^{\circ}\text{C}$ , wind speed 11.5 m/s, rain duration 5 s). Reference photographs rank the coatings from Ice Grade Level 0 for “no ice at all” to Ice Grade Level 5 for “severe ice formation over complete surface” (shown in Fig. 3). This test simulates formation of clear ice, which is, according to SAE ARP 5624, defined as transparent ice that is conformal to the substrate upon which it forms. However, pictures in Fig. 3 indicate that droplets occur, as surface characteristics have significant influence in this initial formation phase. This test allows an easy and fast evaluation and is used as a standard evaluation test at Fraunhofer IFAM for the development of icephobic coating materials.



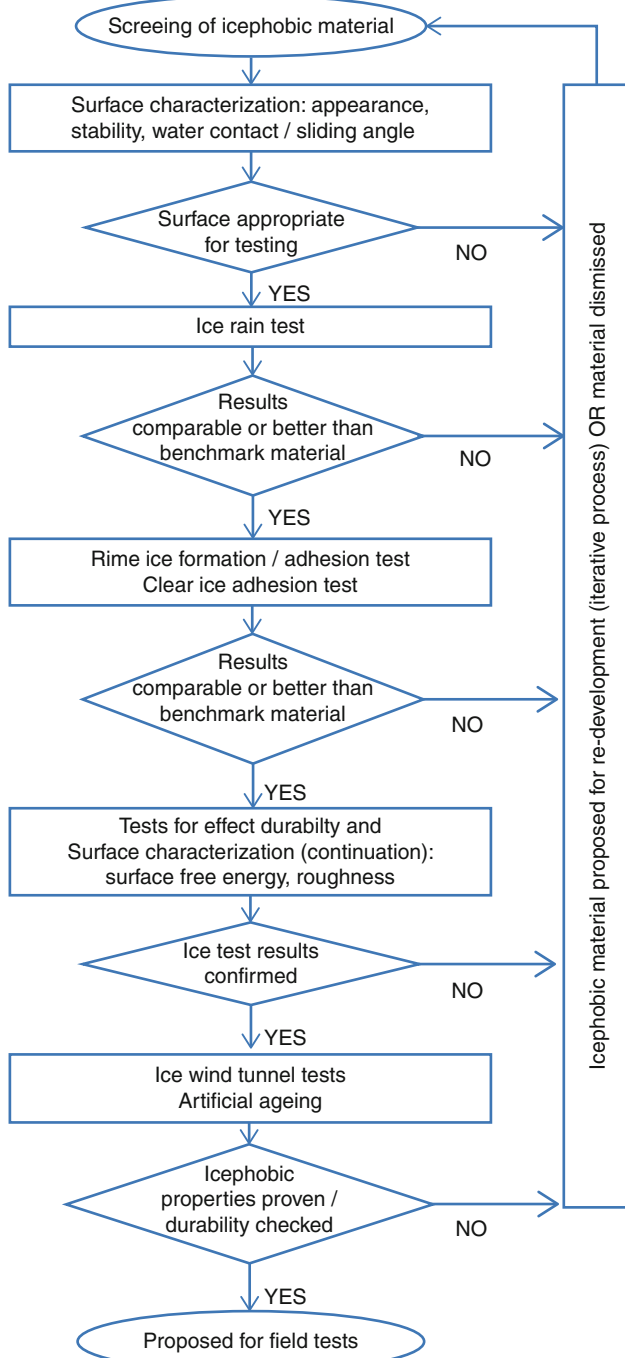
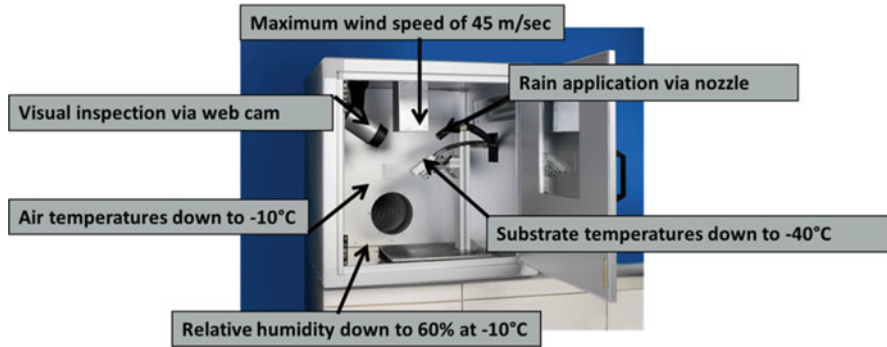


Fig. 1 Example of a flow chart for the assessment of icephobic materials



**Fig. 2** Fraunhofer IFAM Ice Chamber. Published with kind permission of © Fraunhofer IFAM 2016. All rights reserved







For coatings designed to reduce the formation of frost (or rime ice), a second standard test scenario has been defined for the Fraunhofer IFAM Ice Chamber in Fig. 2. In this test, the temperature of the substrate is at a sub-zero level ( $-2^{\circ}\text{C}$ ), whereas the surrounding air is at  $+2^{\circ}\text{C}$  with a relative humidity of 88%. These test conditions lead to significant rime ice formation on unmodified surfaces. The thickness of ice layers is determined after a predefined time by using a conventional film thickness measurement gauge (Fig. 4 left). Generally, the best test results (greatest reduced ice formation) are achieved by coatings with so-called active ingredients, such as chemical freezing point depressors or sequences of anti-freeze proteins.

Additionally, rime ice adhesion is evaluated by using a mar resistance tester modified by Fraunhofer IFAM (Fig. 4 right). An ice scraper is mounted on this device and moved over the test surface with a force varied by stepwise adjustment of the tension in the embedded spring. The force at which ice can be removed completely is measured and converted into ice adhesion strength categories. Icephobic coatings can potentially be assessed against a benchmark coating to check the ice adhesion reduction.

Both tests deliver results that can be compared with a pre-defined benchmark surface. As previously stated, the selection of a benchmark is dependent on customer specifications and the targeted application field. The main drawback of these tests is that results do not provide a full view of icing behavior under realistic conditions. They should therefore only be considered as initial ice-related laboratory tests to be used in successive coating development.

### 3.1 Results of Ice Formation Tests

The Fraunhofer IFAM Ice Chamber (Fig. 2) has been used for many years to evaluate the formation of different ice types on surfaces. The tests have

		
<b>0 = Ice-free after test-run</b>	<b>1 = Nearly ice-free</b> (Only a few, relatively small water droplets on the surface)	<b>2 = Isolated ice droplets</b> (Small to medium sized droplets – most part of surface ice free)
		
<b>3 = Moderate ice formation</b> (Ice droplets relatively evenly distributed but also ice free areas)	<b>4 = Enhanced ice formation</b> (Most of the surface is covered by ice)	<b>5 = Extensive and (nearly) complete ice coverage</b>

**Fig. 3** Reference pictures with increasing ice formation levels on different surfaces during Fraunhofer IFAM ice rain test. Published with kind permission of © Fraunhofer IFAM 2016. All rights reserved

demonstrated their reliability and are important tools for coating developers. For instance, the Fraunhofer ice rain test has been used since 2008 for internal coating developments, market surveys of commercially available materials, and test series for external partners. Figures 5 and 6 show the range of results that have been



**Fig. 4** Rime ice test in Fraunhofer IFAM Ice Chamber: thickness measurement with film thickness gauge (*left*) and adhesion measurement with modified mar resistance tester (*right*). Published with kind permission of © Fraunhofer IFAM 2016. All rights reserved

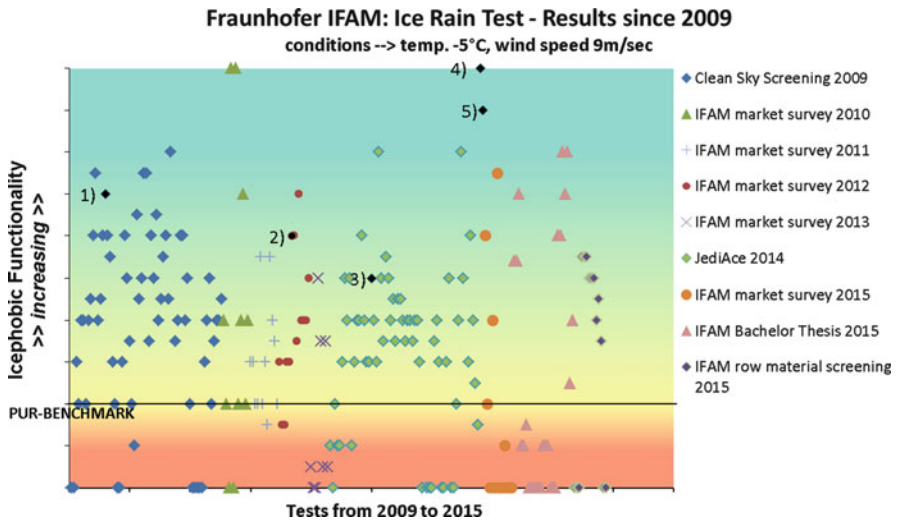


**Fig. 5** Results of Fraunhofer IFAM ice rain test over a period of 7 years. (Numbers correspond to coatings tested in the field or in wind tunnel and are further explained in Sect. 3.2.) Published with kind permission of © Fraunhofer IFAM 2016. All rights reserved

derived from different test series in recent years with the Fraunhofer IFAM ice rain test and rime ice test. As previously stated, an unmodified PUR coating is used as a benchmark surface, and results are evaluated against this benchmark. The better the material can prevent ice formation compared to the benchmark, the higher its “Icephobic Functionality” ranking, as depicted by the y-axes of the graphs in Figs. 5 and 6.

Test results of the ice rain and rime ice tests serve as initial evaluation criteria regarding icephobic properties at Fraunhofer IFAM (see also Fig. 1).

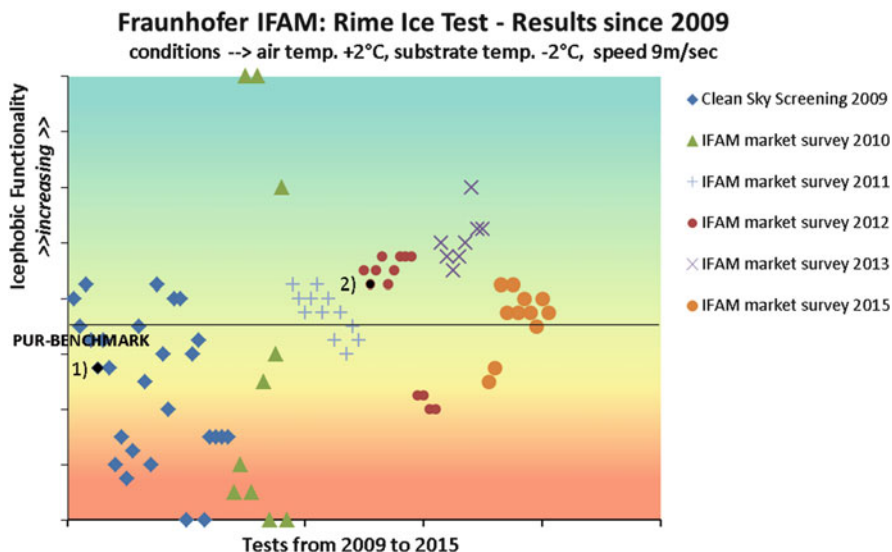


**Fig. 6** Results of Fraunhofer IFAM rime ice test over a period of 7 years. (Numbers correspond to coatings tested in the field and are further explained in Sect. 3.2.) Published with kind permission of © Fraunhofer IFAM 2016. All rights reserved

### 3.2 Significance of Ice Formation Tests

Laboratory-based ice tests do not fully reflect icing conditions in the relevant technical application. This can lead to the risk of misinterpretation and overestimation of the observed ice reduction capabilities. The coatings and consequent results listed below illustrate these challenges and correspond to numbered data points in Fig. 5 (ice rain tests compared to field or ice wind tunnel tests):

1. Performed well in ice rain laboratory test and had proven effectiveness and durability in the field for 2 years on static parts
2. By contrast, this coating performed well in ice rain laboratory test but showed no favorable icephobic properties on aerodynamic parts in the field
3. Ice wind tunnel tests: significant leading edge ice reduction could be demonstrated for this material
4. and 5. Ice wind tunnel tests: no demonstrated icephobic effects at leading edges but significant runback ice reduction

Not all coatings (1–5) are presented in all of the following figures in this chapter because all laboratory-based tests were not carried out for every coating. In summary, ice formation tests at Fraunhofer IFAM can give initial indications of icephobic material properties. However, harsher icing conditions, different ice formation processes, and durability are not covered with these tests.

Factors influencing different ice formation processes can be considered by comparing results of Fraunhofer IFAM ice rain tests with rime ice tests, as shown in Fig. 7. In general, there is no correlation though it may appear that coating materials tested in both test regimes show good performance under ice rain conditions but poor performance under rime ice conditions (and vice versa).

The variation in results can be explained by differences in surface characteristics and their effects on icephobicity. For liquid water in the form of ice rain, surfaces with a minimum of water/surface interactions and good water run-off behavior are beneficial, and this is often achieved by coatings following the Cassie–Baxter regime (Fig. 8) with a certain surface roughness. In contrast, rime ice is formed from water molecules in the gaseous phase. Here the increased surface area of rough surfaces may result in even greater ice formation, and the topography may also result in mechanical anchoring of ice crystals in the surface structure.

Based on these results, it appears that the development of *THE ONE* icephobic coating is highly unlikely. Of interest may be the upper rightmost data point in

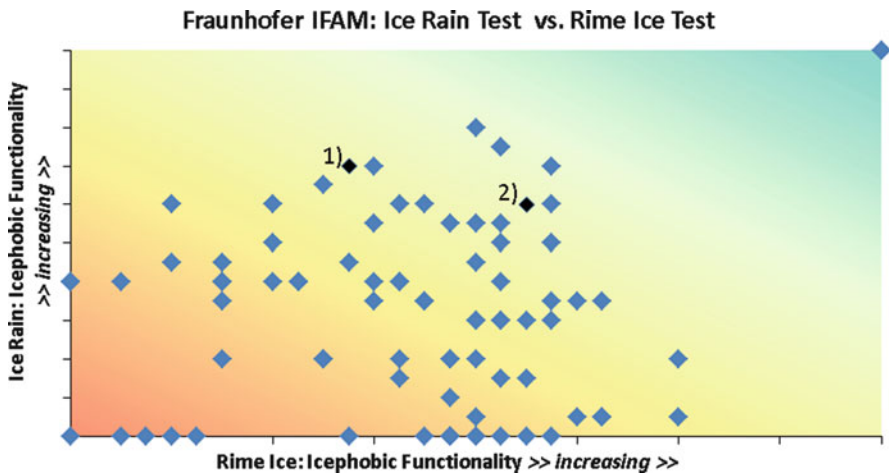


Fig. 7 Comparison of two ice formation test results derived at Fraunhofer IFAM. (Numbers correspond to coatings tested in the field and are further explained in Sect. 3.2.) Published with kind permission of © Fraunhofer IFAM 2016. All rights reserved



Fig. 8 Schematic representation of the two different cases of wetting on rough surfaces: (a) the Wenzel-regime; (b) the Cassie–Baxter regime. From Stenzel et al. [10]. Published with kind permission of © Fraunhofer IFAM 2016. All rights reserved

Fig. 7 with excellent performance in ice rain as well as rime ice tests; this coating is temporarily acting and heavily filled with freezing point depressors that prevent all ice formation under the test conditions.

## 4 Ice Adhesion Tests

A further essential property of icephobic materials is the reduction in the adhesive strength of ice to the surface. This allows for better de-icing performance, meaning that the ice removal from surfaces requires less force or can even be achieved by wind forces or gravity. To evaluate ice adhesion to surfaces, different test methods have been described in the literature – for example [4, 11–14]. At Fraunhofer IFAM, various ice adhesion tests have been assessed over a period of about 5 years, including lap shear, rotational shear, rotating arm, and pendulum tests as shown in Fig. 9 and the ice scraper test, as shown in Fig. 4 *right*.

In the initial phases of test development, challenges arose because of handling problems of iced test objects, undesired temperature fluctuations, and cohesive instead of adhesive failures. These problems led to relatively high standard deviations of test results, often making discrimination between different coatings difficult. Furthermore, requisite time and testing costs were in many cases far too high compared to the utility of the result.

The most suitable test methods, as determined by Fraunhofer IFAM, appeared to be the ice scraper test after rime ice accretion in the IFAM Ice Chamber (Fig. 4 *right*) and the pendulum test for clear ice adhesion (Fig. 9 *lower right*). These methods provided the most reliable results with standard deviations lower than 10% and a reasonable cost/benefit relationship. Other ice adhesion tests are not described further in this chapter because of difficulties in reproducibility of results. However, customer requirements may result in the use of these tests.

The ice scraper test assesses rime ice adhesion and is described in Sect. 3. The pendulum test assesses the adhesion of clear ice to surfaces. Ice cubes that are 30 mm long, 15 mm wide, and 18 mm high are prepared in a freezer at  $-15^{\circ}\text{C}$  and placed on a preconditioned test substrate (surface temperature  $+4^{\circ}\text{C}$ ) to allow the formation of a thin water film at the interface. This assembly is directly put in a cooling unit to allow freezing to the surface. Prepared test samples are then placed in the pre-cooled specimen holder of the pendulum device, shown in Fig. 9 *lower right*. After fixing the sample and covering the ice with a shield, the pendulum is released and hits the shielded ice. The impact leads to the removal of the ice from the test surface, and the subsequent pendulum amplitude correlates to the force that was needed to remove the shielded ice. If ice is completely removed from the surface (adhesive failure), comparative ice adhesion data can be obtained by measuring the degree of pendulum amplitude after ice removal. The measuring range of pendulum amplitudes is defined by the maximum amplitude at which no ice adhesion occurs and the pendulum is only slowed by the weight of the ice cubes. The minimum amplitude is that at which cohesive failure of the ice occurs. In this

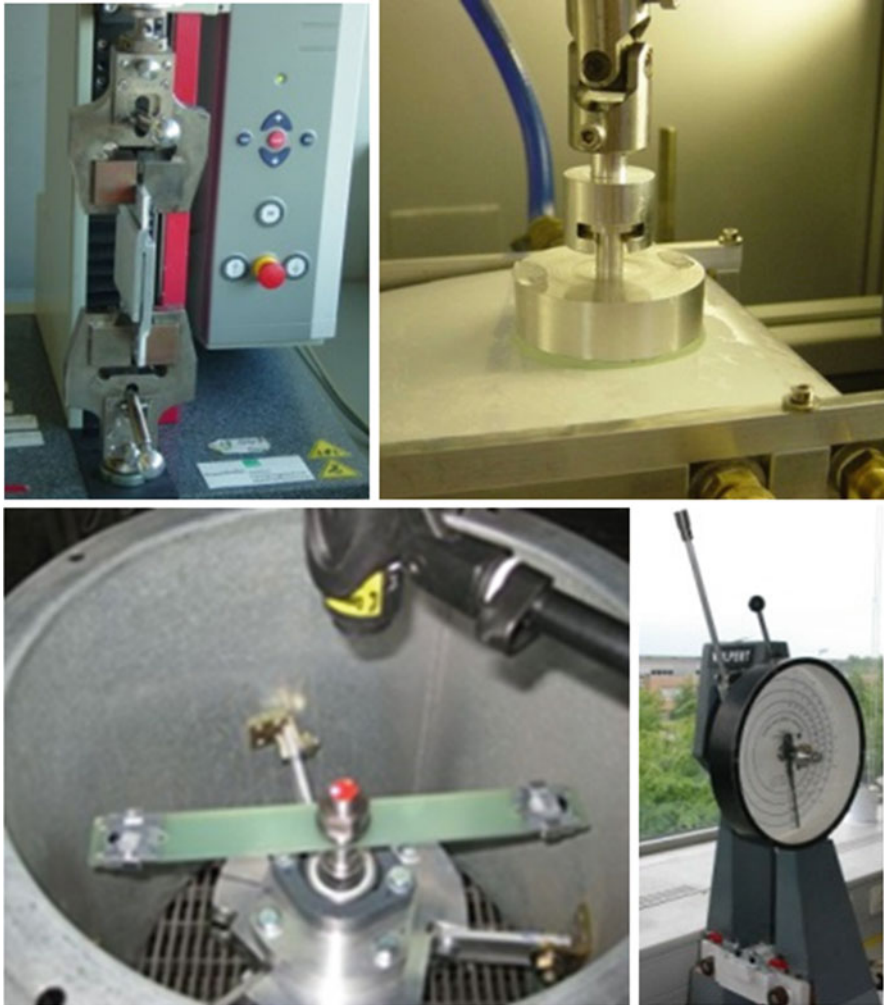


**Fig. 9** Examples of ice adhesion test devices, evaluated at Fraunhofer IFAM: (*upper left*) lap shear test; (*upper right*) rotational shear test; (*lower left*) rotating arm test; (*lower right*) pendulum test. Published with kind permission of © Fraunhofer IFAM 2016. All rights reserved

predefined range the result of this test are converted into ice adhesion strength categories and compared with results from different test surfaces. In the case of ice residues remaining on a substrate after pendulum impact, this is expressed as cohesive failure without any further quantification (further explanations are given in Sect. 4.1).

The previously described tests have one main drawback; clear ice is artificially attached to a surface and therefore doesn't represent a realistic ice formation



process. Further ice adhesion test developments are ongoing in the ice wind tunnel test facility, described in Sect. 5.

### 4.1 Results of Ice Adhesion Tests

Summaries of rime ice adhesion tests using a modified mar resistance tester and clear ice adhesion tests using a modified pendulum test are shown in Figs. 10 and 11, respectively. To interpret these findings and compare the performance of different materials, the results are classified into various “ice adhesion categories,” ranging from “zero ice adhesion” as the minimum value to “cohesion of ice weaker than ice adhesion to substrate” as the maximum value. The category “very low ice adhesion” refers to ice adhesion in the range 0–21% of maximum measurable ice adhesion for the relevant test. “Low ice adhesion” refers to 22–55%. “Moderate ice adhesion” covers adhesion values 56–89% within the measureable range of values. “Strong ice adhesion” refers to 90–100%. Results for clear ice adhesion are displayed as a mean of individual data points from a minimum of six test runs, including the resulting standard deviations (Fig. 10). Rime ice adhesion values are shown as single measurements because tests are being conducted in duplicate and deviations cannot generally be observed (Fig. 11). In both cases, results in the “strong ice adhesion” category reflect cohesive failure of ice with ice residues left on the surface after test completion.

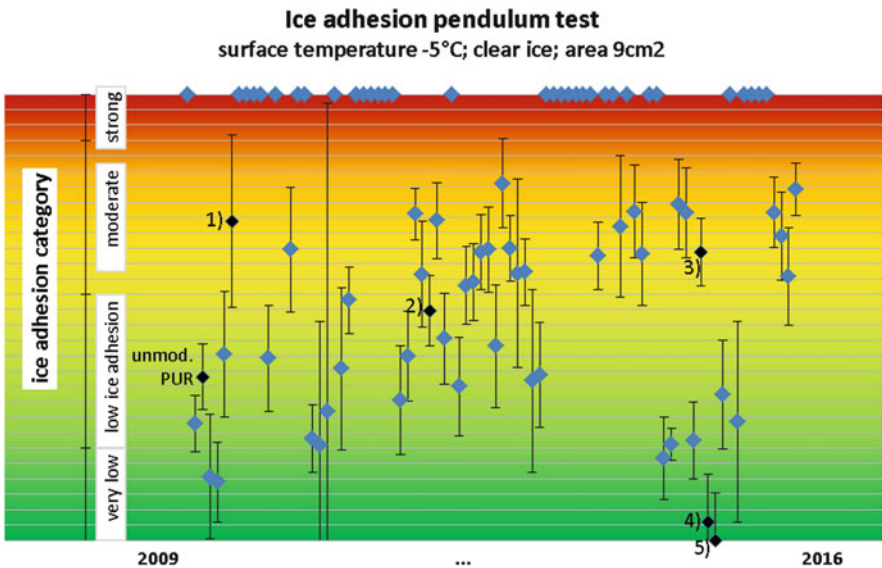
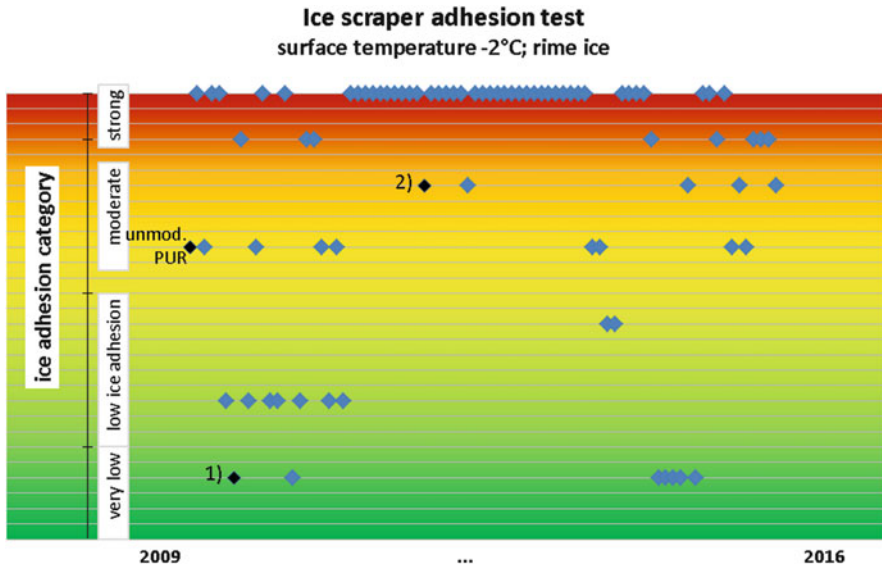


Fig. 10 Results of Fraunhofer IFAM pendulum test, assessing clear ice adhesion. (Numbers correspond to coatings tested in the field or in wind tunnel and are further explained in Sect. 3.2.) Published with kind permission of © Fraunhofer IFAM 2016. All rights reserved



**Fig. 11** Results of Fraunhofer IFAM ice scraper test, assessing rime ice adhesion. (Numbers correspond to coatings tested in the field and are further explained in Sect. 3.2.) Published with kind permission of © Fraunhofer IFAM 2016. All rights reserved

Tests for ice adhesion showed that coatings are available with the potential to reduce ice adhesion significantly. It should, however, be remembered that the ice formation processes used in the adhesion tests are not fully comparable to realistic conditions.

### 4.2 Significance of Ice Adhesion Tests

Ice adhesion is influenced by various factors, including environmental temperature, ice formation processes, ice type, and method of ice removal. This leads to significant deviation in results and a risk of data misinterpretation. An example is presented in Fig. 12, where results of the Fraunhofer IFAM pendulum test for clear ice adhesion and the ice scraper test for rime ice adhesion are compared. Coatings were observed to have strong adhesion to rime ice but low adhesion to clear ice and vice versa. This can also be seen by comparing ice adhesion test results of different research groups carried out in other projects, for example, JediAce [15].

The results show that ice-related laboratory tests reflect only a very narrow view into the icing performance of the tested material. Developers should keep this in mind during the coating formulation process and should also conduct more

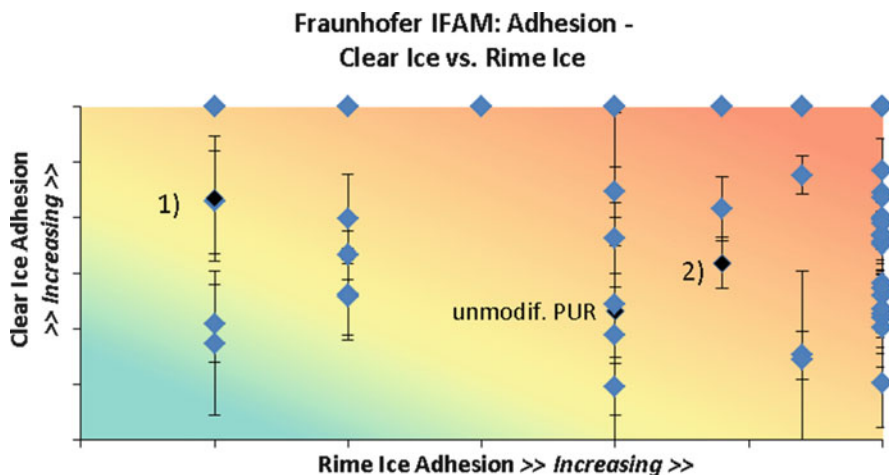


**Fig. 12** Comparison of two ice adhesion test results, derived at Fraunhofer IFAM. (Numbers correspond to coatings tested in the field and are further explained in Sect. 3.2.) Published with kind permission of © Fraunhofer IFAM 2016. All rights reserved

complex tests such as in an icing wind tunnel under close-to-real conditions. Ice wind tunnel tests at Fraunhofer IFAM are described in Sect. 5.

## 5 Ice Wind Tunnel Tests

Ice wind tunnel tests allow more complex evaluations of icephobic materials and ice protection systems. The ice wind tunnel test facility at Fraunhofer IFAM is a closed-loop tunnel with a cooling unit and water injection system that creates characteristic environments for icing by supercooled water droplets (Fig. 13). The maximum speed is 95 m/s, relevant, for example, to aircraft applications. The wind tunnel can be cooled down to temperatures of  $-30^{\circ}\text{C}$ , and liquid water content (LWC) and mean volume diameter (MVD) are adjustable to the desired conditions. The current standard range of the tunnel for LWC is  $0.5\text{--}3.0\text{ g/m}^3$  and for MVD  $15\text{--}45\text{ }\mu\text{m}$ . This test facility has been characterized against SAE ARP 5905 (Calibration and Acceptance of Icing Wind Tunnels) [16], and tests have been conducted to evaluate the performance of icephobic coatings, ice sensors, and different heating technologies [15, 17].

Generally, the more complex the test design for icephobic properties, the more icing processes and correlations can be taken into account. Ice wind tunnel tests are therefore an important tool to evaluate these complex scenarios.



**Fig. 13** Ice Wind Tunnel test facility of Fraunhofer IFAM. Published with kind permission of © Fraunhofer IFAM 2016. All rights reserved

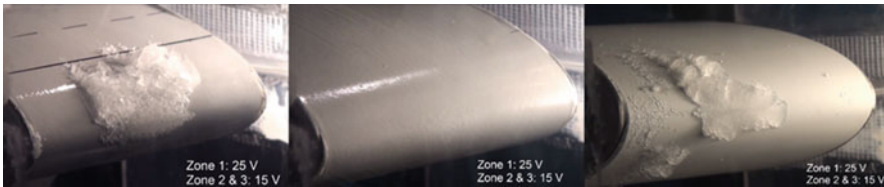


**Fig. 14** Ice formation at leading edges of an aerodynamic profile with heating elements: (*left*) unmodified PUR reference coating; (*center*) elastomeric icephobic coating; (*right*) superhydrophobic coating [17]. Published with kind permission of © Fraunhofer IFAM 2016. All rights reserved

## 5.1 Results of Ice Wind Tunnel Tests

Ice wind tunnel tests allow for the assessment of anti-icing and de-icing technologies under dynamic icing conditions that are relevant to industries such as aerospace, automotive, and wind energy. Icing mechanisms are very dynamic because of impacting water droplets, and various ice formation types can be investigated, including surface icing caused by supercooled water droplets and runback ice formation. This means that ice wind tunnel tests cover a wider range of icing scenarios than other testing methods previously mentioned that are relevant to many applications. It is therefore advisable to use such facilities during the complex development processes prior to testing on real components, including aircraft wings and rotor blades.

Tests in the Fraunhofer IFAM ice wind tunnel have primarily evaluated ice protection systems consisting of electrothermal heating devices and icephobic coatings. Tests are typically conducted at a temperature of  $-15^{\circ}\text{C}$ , wind speed of  $95\text{ m/s}$ , LWC  $0.35\text{ g/m}^3$ , and MVD  $\sim 40\text{ }\mu\text{m}$ . Heating power consumption was also assessed as the voltage at which no ice can form on relevant aerodynamic profiles [18].

Wind tunnel tests on heated leading edges of aerodynamic profiles showed the following results:

- Unmodified state-of-the-art PUR coatings (similar to the benchmark coating in Figs. 5 and 6) were used as reference materials (see Fig. 14 left). Minor defects on the surface (caused by scratches, impurities, etc.) served as ice nucleation points and led to nearly instant ice formation in the ice wind tunnel. After ice accretion reached a certain magnitude, shear forces removed the ice at the surface, and the ice formation process started again (cycling icing). Heating power was stepwise reduced to the point where ice could no longer be removed.
- Chemical additives were introduced into a second elastomeric coating to reduce surface/water interactions (see Fig. 14 center). During the tests, small ice fragments formed directly at the stagnation point of the aerodynamic profile. By closer investigation of this ice formation, it became apparent that this ice did not stick to the surface but was held in place by the occurring aerodynamic forces. Upon reaching a certain volume of ice, it was again removed from the leading edge by wind forces. Compared to the reference model (Fig. 14 left), the ice build-up was significantly reduced and heating power was minimal.
- The third material tested was a particle-modified organic coating with superhydrophobic properties (Fig. 14 right). The rough topography of the surface led to the Cassie–Baxter regime and therefore further minimization of water/surface interactions. However, the aerodynamic factor involving the retention of impacting water droplets at the leading edge was also observed in this test. As a result, the benefit of such rough surfaces in terms of icephobicity could not be found for leading edge zones, and performance was comparable to that of the reference material. This can be explained by the ice formation process of impacting water droplets that overcome the Cassie–Baxter regime and infiltrate the surface topography. The conclusion can therefore be drawn that superhydrophobic surfaces are not necessarily icephobic.

Results for these superhydrophobic coatings were not as favorable as expected at the leading edge. However, in the prevention of runback ice formation in unheated areas of the aerodynamic profiles, the application of such coatings proved to be advantageous. Ice wind tunnel tests have shown that in well-defined coated areas, runback ice can be prevented, even with the heating power reduced by more than 50% [18].

## 5.2 Conclusions for Ice Wind Tunnel Tests

As demonstrated by ice wind tunnel test results, the performance of icephobic materials is dependent on ice formation type (impacting water droplets vs running water droplets). A combination of surface characteristics is needed to achieve icephobic properties and further parameters have been widely discussed elsewhere – for example [7, 15]. Results of these studies clearly show that, for material

developers, the pre-definition of relevant icing conditions and expected ice formation types are important in order to develop tailor-made materials.

## 6 Surface Characterizations

When conducting tests for icephobic properties, the coating evaluation should also be accompanied by surface characterization methods to improve the understanding of the relationship between surface properties and icephobicity. Water contact angle, surface free energy, water sliding angle, and contact angle hysteresis are widely discussed parameters for such evaluation processes [1, 19–22]. However, correlations with icephobic properties are in many cases not clear, and data sets are limited. Furthermore, they are dependent on the ice formation processes in the relevant application field.

Surface roughness is also known to play a key role in water/surface interactions. Depending on topography (and surface chemistry), different wetting regimes can be determined, as shown in Fig. 8. One may imagine that in determining icephobic characteristics of a surface, the Cassie–Baxter regime is preferable because water is only in contact with a very limited area of the surface, resulting in fast water run-off and low ice adhesion [10]. However, this model does not consider dynamic factors, as impacting water droplets are highly likely to show a different behavior compared to carefully settled water droplets in an analytical laboratory.

### 6.1 *Methods for Surface and Material Characterizations*

To evaluate water contact angle, surface free energy, water sliding angle, and contact angle hysteresis, test devices are on the market worldwide, and Fraunhofer IFAM uses a contact angle goniometer DSA100S (Kruess, Germany) for this evaluation. Furthermore, surface roughness can be measured using tactile methods such as a mechanical roughness gauge, contact profilometry, and atomic force microscopy (AFM), as well as optical methods, such as laser confocal microscopy and optical profilometry. The method to be used depends on the roughness scale and the coating type that the developer wishes to assess.

Further parameters that have been discussed in relation to icephobicity are those of coating thickness and elastomeric properties, especially with regard to erosion-resistant materials [22–24]. The influence of these properties certainly depends on the coating type and the specific icing conditions that the developer is investigating. When a coating developer meets an end user, the durability of laboratory-derived icephobic effects often comes into question. Coatings on an aircraft wing or a rotor blade of a wind turbine need to show sufficient performance over a certain period of time in order to justify the increased costs and efforts that might be linked to the use of such icephobic coatings. Various standardized tests are available for the artificial

aging of coating materials, including fluorescent ultraviolet (QUV)- and xenon arc-based weathering tests, rain and grit erosion tests, thermal cycling, etc. These aging processes can be combined with ice-related tests to gain an understanding of the durability of coating icephobicity. However, no exact prognosis can be given about the coating behavior in the field, especially because of additional various environmental parameters requiring multi-functional approaches (e.g., anti-contamination, erosion resistance). Despite the importance of these aspects for the assessment of coating materials, a deeper discussion thereof extends beyond the scope of this chapter. The current situation in most cases is that field tests are required in order to gain experience with newly developed materials.

## 6.2 Correlations: Surface Properties Vs Icephobicity

After presenting the primary results of Fraunhofer IFAM laboratory-based tests and ice wind tunnel tests in this chapter, it is worth comparing results with surface characteristics. This may allow for the observation of correlations between surface properties and icephobicity and/or the identification of deficiencies in the fundamental understanding of ice formation processes. The most commonly used surface characterization technique is the water contact angle, which defines surfaces as hydrophilic ( $10\text{--}89^\circ$ ), hydrophobic ( $90\text{--}149^\circ$ ), or superhydrophobic (greater than  $150^\circ$ ). In theory, a greater water contact angle, and therefore fewer interactions between water molecules and the surface, should result in reduced ice formation and adhesion. As mentioned in Sect. 5, dynamic ice formation processes (e.g.,

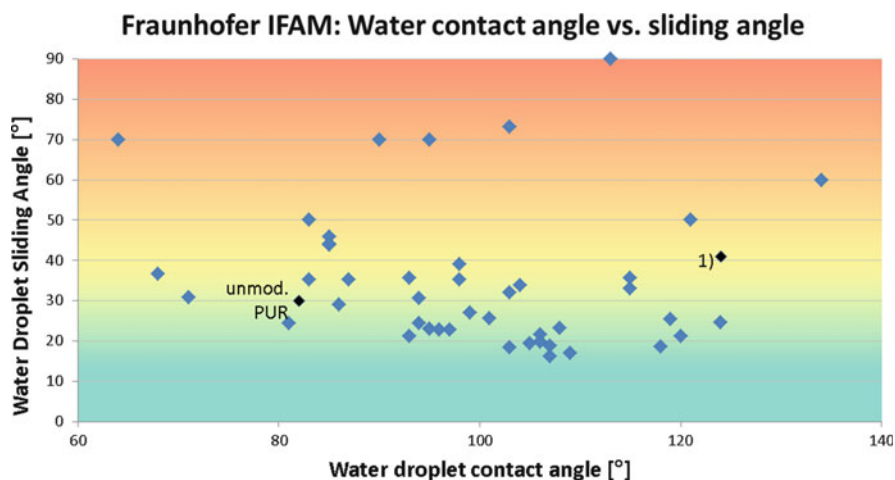


**Fig. 15** Comparison of results of water contact angle and water sliding angle for different surfaces. (Number corresponds to coating tested in the field and is further explained in Sect. 3.2.) Published with kind permission of © Fraunhofer IFAM 2016. All rights reserved

impacting water droplets) hinder this theory in practice. Especially for rough surfaces, it appeared to be important not only to assess the water contact angle but also the water droplet sliding angle, or the angle at which a well-defined water droplet starts to move when the underlying surface is tilted. Figure 15 shows that surfaces with high water contact angles ( $>90^\circ$ ) do not necessarily show low water droplet sliding angles ( $<20^\circ$ ), which should be associated with improved water run-off and reduced ice formation.

It may happen that, although materials show high water contact angles ( $>130^\circ$ ), water droplets still stick quite well to the surface (sliding angle  $\geq 60^\circ$ ), the so-called

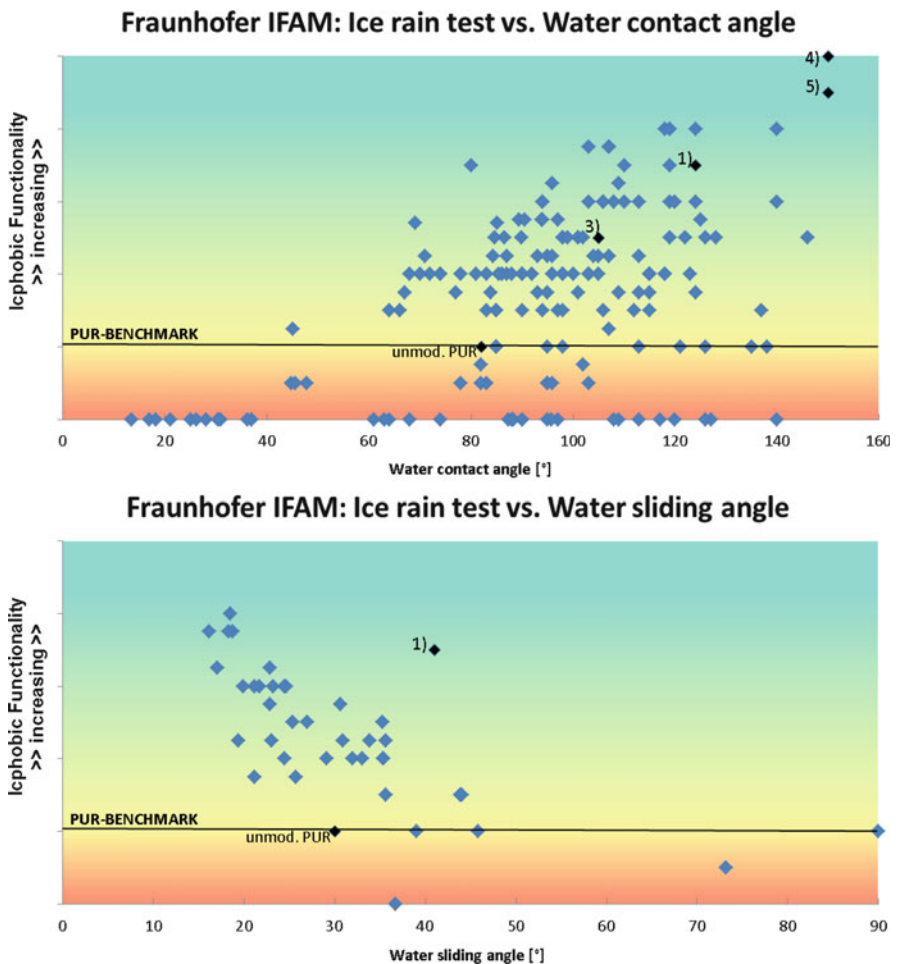


**Fig. 16** Comparison of results for Fraunhofer IFAM ice rain test vs water contact angle (*top*) and water sliding angle (*bottom*). (Numbers correspond to coatings tested in the field or in wind tunnel and are further explained in Sect. 3.2.) Published with kind permission of © Fraunhofer IFAM 2016. All rights reserved



“rose petal effect.” This is mainly caused by mechanical interlocking in rough surfaces, but further variables may also play a role. Additional evidence of the phenomenon is presented in the results of ice formation in Fraunhofer IFAM ice rain tests, summarized in Fig. 16.

A comparison of results of the Fraunhofer IFAM ice rain test vs water contact angle shows that high water contact angles (hydrophobic properties) are not always directly linked to good performance under ice rain conditions. On the other hand, surfaces with low water contact angles ( $<60^\circ$ ) show consistently poor performance in this test.

Surfaces with water contact angles around  $140^\circ$  showed varying results. They vary from very poor icephobic performance and completely ice-covered surfaces to very good performance with no ice at all after the test. This is a strong indication that additional parameters have a significant influence on icephobic properties. Comparison of results of Fraunhofer IFAM ice rain test with water sliding angle showed clearer trends, as decreased water sliding angles correlated to improved ice formation reduction in ice rain test. This can be explained by the test design of the ice rain test as test samples are placed in the Fraunhofer IFAM Ice Chamber (Fig. 2) at an angle of  $45^\circ$ , and water droplets are applied by using moderate wind speeds (11.5 m/s) under freezing conditions (temperature  $-5^\circ\text{C}$ ). Surfaces with more efficient water run-off (low sliding angle) were less ice covered than surfaces with slower water run-off. It is important to note again that all described observations display only a narrow window of ice formation processes and changing the test designs may lead to different findings. This is also discussed in [15].

Further variables that were considered include surface free energy (polar and disperse components), contact angle hysteresis, and surface roughness properties. Surface roughness appeared to be a significant parameter because of its influence on surface free energy and related properties. Correlation assessments related to surface roughness using  $R_a$  (arithmetic average of the measured roughness profile) showed no meaningful results (data not shown here). This value seems to reflect insufficiently the complexity of surface roughness parameters. At this point, no single general conclusion relating surface characteristics and icephobicity can be presented because of the complexity of ice formation processes. It is therefore advisable to focus research efforts more specifically on evaluating relevant ice formation types in order to support future material developments and raise the efficiency of evaluation processes.

## 7 Conclusions

This chapter summarizes the experiences of Fraunhofer IFAM in developing and testing icephobic materials. Different test designs have been described, including ice formation tests, ice adhesion tests, ice wind tunnel tests, and surface characterization methods. The results of about 8 years of testing history have demonstrated possible correlations between material properties and icephobicity, which can be

used to determine the main objectives for future material development projects and lead to further investigation. Within the framework of this chapter, important steps for the future in terms of the development of icephobic materials were addressed. Additional challenges need to be taken into consideration when starting or proceeding with material development:

- Limited durability of icephobic effects
- Need for a multi-functional approach, including erosion (e.g., rain and grit) resistance and anti-contamination (depending on application field)

With regards to ice-related testing, there is a wide range of test designs that take into account the different ice formation types. Results showed that, depending on ice formation type, various surface characteristics are required to achieve icephobic properties. Therefore, it is important to define the relevant icing scenarios in the desired application field. Material developers should avoid quick and broad interpretation of ice test results and should not universally consider hydrophobic surfaces as icephobic surfaces without multiple tests under various conditions. In addition, the exchange of experiences with other working groups can aid in the understanding of the main parameters for different ice formation processes and improve the efficiency of development processes.

**Acknowledgements** The authors would like to thank all colleagues at Fraunhofer IFAM working on ice-related topics and supporting activities in the development of icephobic materials. Special thanks go to Ms. Catherine Yokan for support in editing. Furthermore, the results of mainly two previous publicly funded R&D projects have been used in this chapter: Clean Sky SFWA and JediAce. Partners of these projects are thanked for their support. Both projects have received funding from the European Commission under grant agreement numbers CSJU-GAM-SFWA-2008-001 and 314335, respectively. Finally, the Fraunhofer Gesellschaft e.V. is thanked for supporting research on ice-related topics, including preparation of this chapter.

## References

1. Anderson DN, Reich AD (1997) Tests of the performance of coatings for low ice adhesion. NASA technical memorandum. <http://gltrs.grc.nasa.gov/reports/1997/TM-107399.pdf>. Accessed 1 Nov 2016
2. Laforte C, Beisswenger A (2002) Icephobic material centrifuge adhesion test. Contribution to IWAIS. <http://www.uqac.ca/amil/fr/documentation/articles/IW53-CAT.pdf>. Accessed 1 Nov 2016
3. Yeong Y, Loth E, Sokhey J, Lambourne A (2015) Ice adhesion performance of superhydrophobic coatings in aerospace icing conditions. SAE technical paper 2015-01-2120. <https://doi.org/10.4271/2015-01-2120>
4. Schulz M, Sinapius M (2015) Evaluation of different ice adhesion tests for mechanical deicing systems. SAE technical paper 2015-01-2135. <https://doi.org/10.4271/2015-01-2135>
5. Kulinich SA, Farhadi S, Nose K, Du XW (2011) Superhydrophobic surfaces: are they really ice-repellent? *Langmuir* 27(1):25–29
6. Chuppina SV (2007) Anti-icing gradient organosilicate coatings. *Glas Phys Chem* 33 (5):502–509

7. Hyugaji T, Kimura S, Endo H, Hasegawa M (2015) Runback water behavior on hydro-phobic/philic surfaces of circular cylinder placed in flow field. SAE technical paper 2015-01-2158. <https://doi.org/10.4271/2015-01-2158>
8. Dyer JM, Storey BD, Hoke JL, Jacobi AM, Georgiadis JG (2000) An experimental investigation of the effect of hydrophobicity on the rate of frost growth in laminar channel flows. ASHRAE Winter Meeting, Dallas. ISSN 0001-2505
9. Susoff M, Siegmann K, Pfaffenroth C, Hirayama M (2013) Evaluation of icephobic coatings – screening of different coatings and influence of roughness. *Appl Surf Sci* 282:870–879
10. Stenzel V, Rehfeld N (2011) Functional coatings. Vincentz, Hannover. ISBN 9783866308565
11. Blackburn C, Laforte C, Laforte JL (2000) Apparatus for measuring the adhesion force of a thin ice sheet on a substrate. In: Ninth international workshop of atmospheric icing of structures, Chester UK, 5–8 June 2000
12. Kraj AG, Bibeau EL (2010) Measurement method and results of ice adhesion force on the curved surface of a wind turbine. *Renew Energy* 35:741–746
13. Javan-Mashmool M, Volat C, Farzaneh M (2006) A new method for measuring ice adhesion strength at an ice-substrate interface. *Hydrol Process* 20:645–655
14. Laforte C, Blackburn C, Perron J (2015) A review of icephobic coating performances over the last decades. SAE technical paper 2015-01-2149. <https://doi.org/10.4271/2015-01-2149>
15. Rehfeld N, Berton B, Morita K, Kimura S (2016) A way forward to design efficient wing ice protection systems. In: Proceedings of greener aviation conference, Brussels
16. SAE Aerospace (2009) Aerospace recommended practice ARP 5905: calibration and acceptance of icing wind tunnels. Issued 2003-09, Reaffirmed 2009-12
17. Rehfeld N, Berton B, Diaz F, Tanaka T, Morita K, Kimura S (2016) JediAce: Japanese-European de-icing aircraft collaborative exploration. In: Conference book aerodays 2015, London
18. Berton B, Rehfeld N, Kimura S (2016) Evaluation of functional coatings to reduce contamination of aircraft leading edges. In: Proceedings of 2016 annual meeting of the adhesion society, San Antonio, 21–24 Feb 2016
19. Meuler AJ, Smith JD, Varanasi KK, Mabry JM, McKinley GH, Cohen RE (2010) Relationships between water wettability and ice adhesion. *ACS Appl Mater Interfaces* 2(11):3100–3110
20. Kulinich SA, Farzaneh M (2009) Ice adhesion on super-hydrophobic surfaces. *Appl Surf Sci* 255:8153–8157
21. Zou M, Beckford S, Wei R, Ellis C, Hatton G, Miller MA (2011) Effects of surface roughness and energy on ice adhesion strength. *Appl Surf Sci* 257:3786–3792
22. Arianpoir F, Farzaneh M, Kulinich SA (2013) Hydrophobic and ice-retarding properties of doped silicone rubber coatings. *Appl Surf Sci* 265:546–552
23. Andersson LO, Golander CG, Persson S (1994) Ice adhesion to rubber surfaces. *J Adhesion Sci Technol* 8(2):117–132
24. Tobin EF, Young TM, Raps D (2012) Evaluation and correlation of inter-laboratory results from a rain erosion test campaign. Presented at the 28th international congress of the aeronautical science ICAS, Brisbane, 23–28 Sept 2012

# Ice Release Coatings of High Durability for Aerospace Applications



Guangliang Tang, Yong Han Yeong, and Mikhail Khudiakov

**Abstract** Current in-flight aircraft anti-icing and de-icing systems rely on active methods such as heat for ice mitigation, which tends to reduce the operating efficiency of the aircraft. Significant research is currently ongoing to develop anti-icing coatings for passive ice removal from aircraft surfaces. Although significant coating advances have been achieved in reducing ice adhesion and accretion, the majority of the developed prototypes cannot survive the harsh operating environments of an aircraft. Therefore, the goal of this work was to develop a coating with significant ice adhesion reduction and of sufficiently high durability to withstand typical aerospace operating conditions (with the exception of conditions at the wing leading edge areas). Low ice adhesion topcoats and clear coats have been developed based on qualified exterior aerospace coatings, and ice adhesion tests showed a decrease of up to 95% in the ice adhesion strength as compared to control coatings. These coatings are also as durable as current polyurethane aerospace topcoats. For example, the coatings did not sustain any damage for up to 30 min in a rain erosion test conducted at typical rain impact speeds to approximate real flight conditions. In addition, ice adhesion tests performed on degraded coatings (1,700 h of QUV Accelerated Weathering Test, UVB-313 nm lamp) showed that the ice release properties were retained.

**Keywords** Aerospace • Coating • Durability • Durable • Ice adhesion • Ice release

## Contents

1	Introduction .....	168
2	Experimental Methods .....	170
2.1	Coating Fabrication and Characterization .....	170

---

G. Tang, Y. H. Yeong, and M. Khudiakov (✉)  
PPG Aerospace Research and Technology Center, Burbank, CA, USA  
e-mail: [mikhail.khudiakov@ppg.com](mailto:mikhail.khudiakov@ppg.com)

2.2 Durability Tests .....	171
2.3 Ice Adhesion Test .....	174
3 Results and Discussion .....	175
4 Conclusions .....	181
References .....	182

## 1 Introduction

Ice accretion is very common on the leading edge of airplane wings, pitot tubes, fan blades, and internal components of aircraft engines, possibly resulting in a stall or loss of thrust. Current ice protection approaches can be broadly classified into two categories – anti-icing and de-icing. Anti-icing solutions are designed to prevent completely the accretion of ice whereas de-icing methods target the removal of ice after it has formed [1]. The approaches can be further classified as active (electrical, thermal, mechanical, chemical, and biochemical) and passive (design, water runoff, wetting, and adhesion reduction). Ice release coatings fall into the category of passive de-icing solutions. Although they do not fully prevent the accretion of ice, the adhesion of ice to the coating surface is drastically reduced, which allows its easy removal from the surface upon exertion of external forces, such as aerodynamic and centrifugal forces. Therefore, ice release coatings could be either deployed on certain components of the aircraft as a completely passive ice mitigation approach or used in combination with active de-icing systems (e.g., electrical heating, electro-mechanical). These hybrid systems can reduce the amount of energy required for active anti- and de-icing processes [2].

The role of low coating surface energy in reducing ice adhesion strength is well understood and extensive effort has been devoted to the design of hydrophobic materials with low ice adhesion or reduced ice accretion properties [3–9]. Most of these efforts focused on the incorporation of fluorinated additives into the coatings to induce hydrophobicity. Extreme anti-wetting coatings or superhydrophobic coatings were recently invented and shown to be a potentially attractive method to delay the event of icing and to reduce ice adhesion strength [10–14]. Inspired by the lotus leaf, superhydrophobic coatings rely on micro- or nano-sized surface features on materials with low surface energy to induce a wetting state whereby drops are suspended on the tips of the surface features. This results in a high water droplet contact angle and a low roll-off angle. The above wetting state is conducive toward low-energy ice release properties because of the minimal contact area between the ice and the surface. However, studies have shown that the superhydrophobic effect could be lost under certain aerospace icing or weather conditions, resulting in more ice adhering to the surface compared to control surfaces [15, 16]. In addition, nearly all superhydrophobic coatings are not mechanically robust enough to withstand the harsh operating conditions of an aircraft [14, 17, 18].

Other strategies for achieving low ice adhesion properties include altering the elasticity of the coating material through the incorporation of silicone functionality

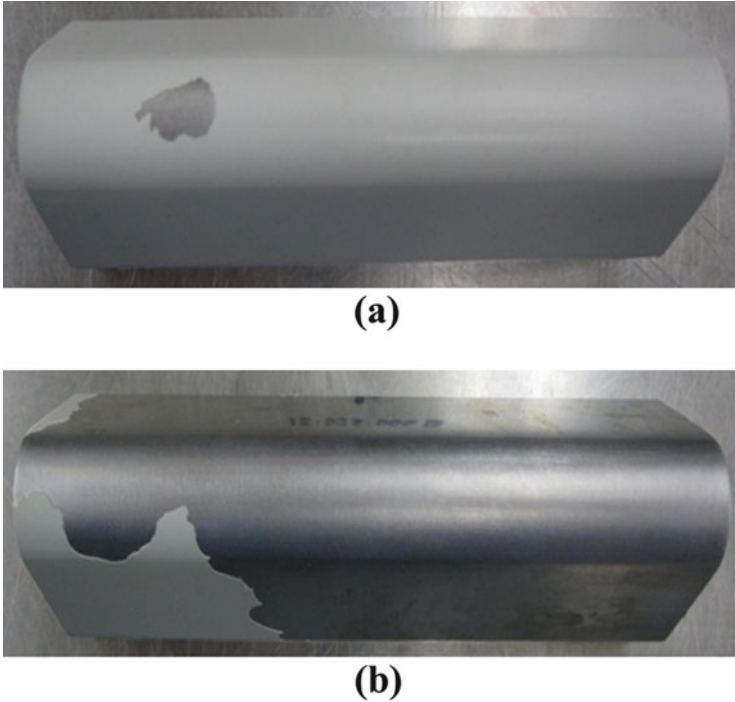


**Fig. 1** Rain erosion airfoils coated with a low ice adhesion silicone coating after exposure to high-speed impact of rain drops for a duration of: (a) 5 min; (b) 30 min (Whirling Arm Rain Erosion)

and with oil infusion to lubricate the surface [19–23]. An elastic material can cause a concentrated area of strain at the ice-coating interface when placed under stress for enhanced ice release [19]. Surface lubrication introduces slippage between the ice-coating interface to reduce the ice adhesion strength [21, 22]. In previous studies performed by other researchers, both of these methods (elasticity and lubrication) have been shown to result in significant ice adhesion strength reduction [19–23]. However, they are not durable enough for application on an aircraft. In a PPG Aerospace rain erosion test, delamination of a silicone coating started after a 5-min exposure to the impact of water droplets (1–4 mm size distribution) at speeds of 172 m/s. The silicone coating was almost completely eroded from the test airfoil after a 30-min exposure, as shown in Fig. 1.

In the case of oil-infused coatings where the surface is saturated with a layer of lubricant, external forces exerted on the surface by moving air or liquid can displace and deplete the lubricants. In addition, the lubricants can also evaporate under high temperature conditions [24, 25]. These results show that although the above-mentioned techniques to create low ice adhesion coatings appear to be promising, their lack of durability has prevented the implementation of these methods for practical applications. It is especially true for aerospace applications where a

typical exterior coating needs to be extremely durable to withstand a variety of operating and environment stresses.

Consequently, our goal was to develop a low ice adhesion coating system with a significant reduction in the ice release force (minimum of 75% compared to a polyurethane topcoat control) and with durability equivalent to current polyurethane aerospace topcoats. The ice release force of the developed coatings was measured using a “static” ice adhesion test developed internally by PPG. The durability tests that were performed reflect the harsh environment to which aerospace coatings are exposed. A typical inter-continental flight cruises at an altitude of 10,000–11,000 m and at an air speed of 250 m/s with an outside temperature as low as  $-60^{\circ}\text{C}$  [26]. The pressure differences between cabin and outside air at this altitude, combined with the flexing of wings from air turbulence, requires an aerospace coating to be flexible at freezing temperatures [26]. Therefore our developed coatings were evaluated using a low temperature flexibility test according to ASTM standards. In addition, an aerospace coating must maintain adhesion to the airframe when in contact with water, which frequently occurs because of extreme condensation when the aircraft descends for landing [26]. Wet immersion cross-hatch adhesion tests were performed to verify this property. Other important durability tests include ultraviolet radiation (QUV Accelerated Weathering Test, UVB-313 lamp) and hydraulic fluid exposure as an aircraft is subjected to UV radiation and aggressive fluids such as Skydrol, respectively. Finally, aircraft coatings can erode when subjected to rain droplet impact at flight speeds and therefore the developed ice release coatings were tested in a whirling arm rain erosion test conducted internally at PPG Aerospace. It should be noted that the coatings developed in this work were not intended for leading edge applications, which generally require much more stringent and harsher rain erosion testing (AMS-C-82321, for example).

## 2 Experimental Methods

### 2.1 Coating Fabrication and Characterization

The developed ice release coatings were based on qualified exterior aerospace coatings technology with conventional mix ratios, application methods (spray, roll, brush, dip), and ambient cure. These qualified coatings are based on polyurethane chemistry, which is known for its durability under a wide range of conditions (e.g., weather, chemical, low temperature, corrosion, and fluids). However, the polyurethane chemical structure is of high surface energy, which results in a strong adhesion of ice because of hydrogen bonding.

For that reason, improvements were made to the polyurethane coating formulations to reduce surface energy at the same time maintaining their strong durability characteristics. The end product is a smooth coating composition comprised of (1) a curing agent of isocyanate functional groups, (2) a film-forming polymer of

functional groups reactive with the isocyanate groups listed in (1), (3) an acrylic polymer containing pendant functional groups reactive with the isocyanate groups and polysiloxane side chains, and (4) a polysiloxane different from the film-forming polymer (2) and acrylic polymer (3) [27]. Two types of ice release coatings were developed based on this concept: a pigmented topcoat and a clear coat. It should be noted that commercial PPG aerospace exterior coatings were used as control coatings in the experiment. These coatings are composed based on previously listed chemical components of (1) and (2) whereas the ice release topcoats and clear coats are comprised of components (3) and (4), in addition to (1) and (2). The wetting characteristics and surface energy of the fabricated coatings were measured using a contact angle goniometer (Kruss DSA 100) with a 2.0- $\mu\text{L}$  water droplet. Methylene iodide and water (2.0  $\mu\text{L}$  each) were used to determine the surface energy of the coating using the Owens, Wendt, Rabel, and Kaelble (OWRK) method. The dispersion and polar surface tension values used in this measurement for water was 21.8 and 51 mN/m, respectively. For methylene iodide the dispersion surface tension was 49.5 mN/m and the polar surface tension was 1.3 mN/m. The measurements were conducted three times for each coating and the contact angle and surface energy values obtained were averaged. In addition, the gloss levels of the coatings were measured using a BYK-Gardner Haze-Gloss meter in accordance with ASTM D523, Standard Test Method for Specular Gloss at incident beam angles of 20° and 60°.

## 2.2 Durability Tests

The fabricated ice release coating prototypes were subjected to a series of durability tests based on specifications from aircraft manufacturers and according to ASTM standards to measure their resistance toward typical stresses encountered during flight. These were cross-hatch tests under dry and wet conditions (ASTM D3359.B) to determine coating-to-substrate bond strength, low temperature flexibility test (ASTM D522.B), pencil hardness test (ASTM D3363), hydraulic fluid (Skydrol) resistance test (ASTM D3363), QUV-B exposure test (fluorescent light exposure test using a UVB-313 lamp according to ASTM G154 standard), and a high-speed rain erosion test conducted internally at PPG Aerospace using a whirling arm rain erosion test setup. These methods are listed in Table 1 and described in detail below. All tests, unless otherwise noted, were performed using clad aluminum 2024-T3 alloy panels. Before the application of ice release prototypes, the panels were cleaned, lightly abraded using a Scotch-Brite pad, rinsed with solvent, treated with a thin layer of an adhesion promoter (thickness of <1  $\mu\text{m}$ ) such as Desogel™ EAP-9, and coated with an epoxy primer such as Desoprime™ CF/CA7502 (for pigmented ice release topcoat testing) at a thickness of 12–25  $\mu\text{m}$  or with an epoxy primer and a base coat such as



**Table 1** Results of the aerospace coating durability tests for the control topcoat, ice release topcoat, and ice release clear coat

Durability test (standard)	Control topcoat	Ice release topcoat	Ice release clear coat
Cross hatch dry adhesion <i>ASTM D3359.B</i>	5B	5B	5B
Cross hatch wet adhesion <i>ASTM D3359.B</i>	5B	5B	5B
Low temperature flexibility <i>ASTM D522.B</i>	1 in.	1 in.	1 in.
Pencil hardness <i>ASTM D3363</i>	2H–3H	2H–3H	2H–3H
Skydrol resistance 54°C, 24 h ( <i>ASTM D3363</i> )	HB	HB	HB
Ice adhesion reduction after QUV-B exposure for 1,700 h	N/A	67%	N/A

Note that the control topcoat is a PPG aerospace commercial exterior coating

Desothane™ CA8000 (for ice release clear coat testing). The base coats are typically coated at a thickness of 25–50 µm. The samples were allowed to cure for 7 days under ambient conditions before testing.

### 2.2.1 Cross-Hatch Adhesion Test (Dry and Wet)

The cross-hatch adhesion test was conducted in accordance with the ASTM D3359 standard, method B. A cross-hatch pattern was scribed through the coating down to the substrate. A strip of 1 in. wide masking tape such as 3M 250 or equivalent was applied. The tape was pressed down using two passes of a 4.5-pound rubber roller and then removed in one abrupt motion perpendicular to the panel. The coating-substrate adhesion was rated by a visual examination of the paint at the cross-hatch area using the rating system provided by the ASTM standard. Dry adhesion refers to testing on fully cured coating systems whereas wet adhesion refers to testing on fully cured coating systems after immersion in 60°C water for 24 h. The immersed samples were wiped with a paper towel and allowed to dry for 5 min before the test was conducted.

### 2.2.2 Low Temperature Flexibility Test

The test was conducted in accordance with the ASTM D522 standard, Method B. Coated panels and the Mandrel Tester were subjected to a temperature of –54°C for 2 h. When at this temperature, the coated panels were placed over a mandrel jig with a radius of approximately 5 cm (2 in.) with the uncoated side in contact with the jig and with at least 5 cm overhang on either side. Using a steady pressure of fingers, the panel was bent around the cylindrical mandrel at a uniform velocity until the opposite ends of the panel are parallel to each other. This procedure was performed in approximately one second. The panel was removed and visually examined immediately after the test for any cracking or loss of adhesion and the results were compared with a polyurethane aerospace control coating.

### 2.2.3 Pencil Hardness Test

This test was conducted in accordance with the ASTM D3363 standard. The coating hardness was determined relative to a standard set of pencil leads by scratching the leads across the coating film at 45° for an approximately 6.35 cm (2.5 in.) stroke. The process was repeated with multiple pencil lead types as listed in the ASTM standard until one that could not scratch the film was identified. The number of this lead was recorded as the hardness.

### 2.2.4 Hydraulic Fluid Resistance Test

Coated panels were immersed in a hydraulic fluid (i.e., Skydrol LD-4 from Solutia Inc.) at a temperature of 54°C for 24 h. The panels were removed for the determination of coating pencil hardness in accordance with the ASTM D3363 standard described above.

### 2.2.5 QUV-B Exposure Test

QUV-B exposure test was selected because of its aggressive radiation characteristics and conducted according to ASTM G154 standard with a UVB-313 lamp. The coating was applied to both sides of aluminum panels and was allowed to cure at room temperature for 14 days. The coated panels were then subjected to a standard QUV-B exposure cycle alternating between 8 h of ultraviolet irradiation (0.68 W/m<sup>2</sup>) at 60°C and 100% relative humidity at 45°C without ultraviolet irradiation for 4 h (ASTM G154). After ~1,700 h of exposure on one side of the panel, the panels were turned over to expose the other side for another ~1,700 h to ensure equal QUV-B exposure on both sides of the panels.

### 2.2.6 High-Speed Rain Erosion

The rain erosion test was conducted using a whirling arm rain erosion test setup built internally by PPG Aerospace. The coatings were applied to cover completely the leading edges of two airfoils and mounted at the tips of a whirling arm. The arm was rotated to reach a tip velocity of 172 m/s. Water drops (1–4 mm) were released at a rate of 25–100 mm/h to impact the coating. Two separate tests were conducted at two different durations: 5 min and 30 min. After the tests, the coating was visually inspected and its condition compared to results from current aerospace polyurethane topcoats used as controls.

### 2.3 Ice Adhesion Test

An ice adhesion test setup was designed and fabricated according to the test method used and described in a document published by the US Army Corps of Engineers, Engineer Research and Development Center (document number ERDC/CRREL TR-06-11). The adhesion test was based on “static” ice accretion, whereby a volume of water was placed in contact with the coating and subjected to freezing temperatures for ice accretion.

The procedure was as follows. A  $10.2 \times 12.7$  cm ( $4 \times 5$  in.) aluminum alloy test panel was coated on both sides with the desired coating(s). After the appropriate cure time,  $2.54 \times 10.16$  cm ( $1 \times 4$  in.) strips were cut from the test panel and taped in place in the center of a test fixture (pictures of the test fixture and the taped test panel are shown in Fig. 2a, b, respectively). The taping of the panels onto the fixture provides a 1 in.-deep cavity that could be filled with deionized water to be frozen at

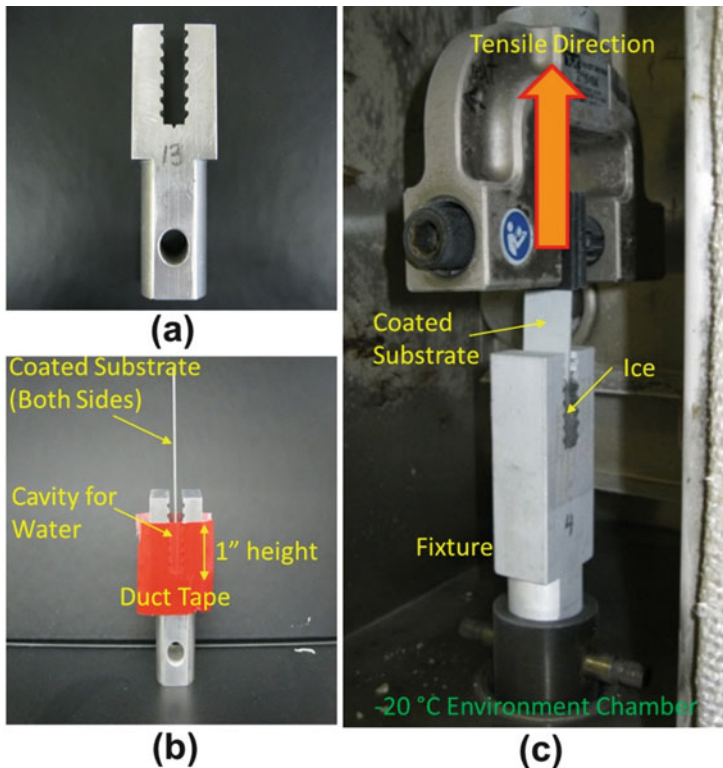


**Fig. 2** The ice adhesion test setup: (a) test fixture; (b) taping of the coated substrate on the test fixture for water accumulation and ice accretion; (c) the tensile test method to release the coated substrate from the accreted ice

$-20^{\circ}\text{C}$  overnight. The test fixture was then transferred to a tensile tester (INSTRON 5567) installed within an environmental chamber with the temperature also set at  $-20^{\circ}\text{C}$ . The test fixture was mounted on the chamber floor on one end and attached to the tensile tester jaw on the other (Fig. 2c). The duct tape was then removed and the temperature of the setup was allowed to equilibrate for 5 min before the tensile tester jaw was extended upward at a rate of 50 cm/min to release the coated substrate from the ice. The maximum force that was required to release the ice was recorded as the shear force. The ice shear stress could then be calculated based on this force. To account for variances in the ice shear stress, the test was repeated five times to obtain an average shear stress.

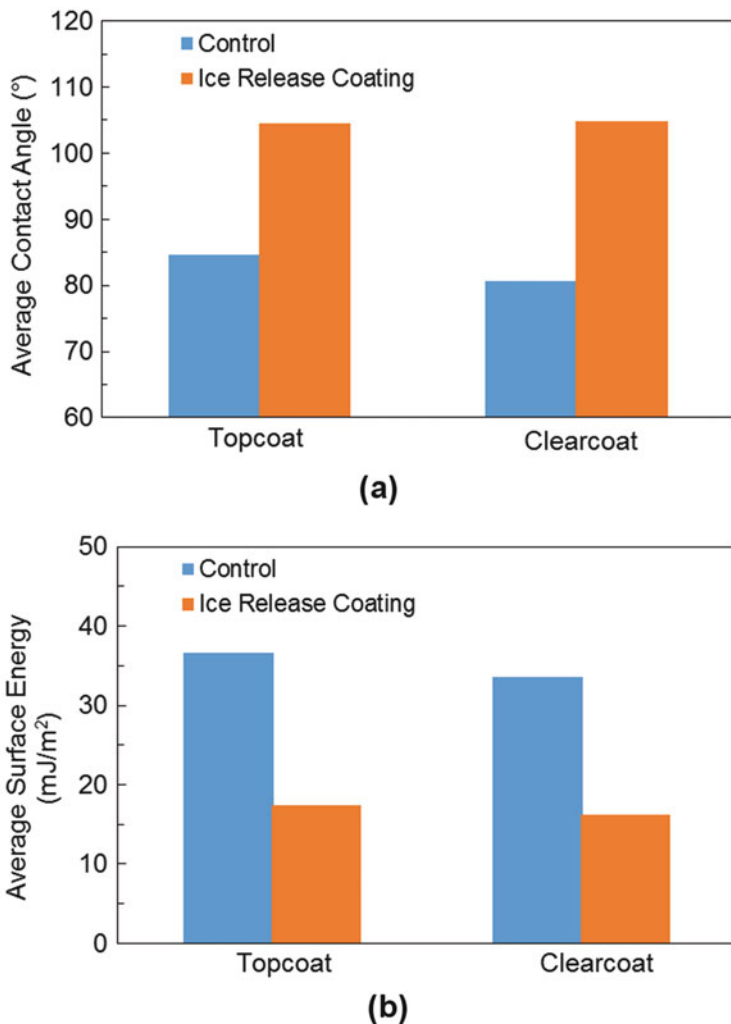
### 3 Results and Discussion

Figure 3 shows the wetting and surface energy characteristics of the ice release topcoat and clear coat. Contact angle measurements (Fig. 3a) revealed that the contact angle for the ice release topcoat was  $104.5 \pm 0.5^{\circ}$ . In comparison, a control topcoat, which was not formulated for ice release properties, had a contact angle of  $84.6 \pm 0.5^{\circ}$ . A similar increase was observed for the ice release clear coat. Surface energy measurements further confirmed the increase in hydrophobicity. Surface energy, defined as the work required to form a unit of the surface [28], provides a representation of attraction between surface and liquid molecules, and is described in the classical Young's equation in (1):

$$\gamma_{sg} = \gamma_{sl} + \gamma_{lg} \cos \theta \quad (1)$$

where  $\gamma$  refers to the surface tension and  $\theta$  to the contact angle. The combination of subscripts represents the interfaces with  $s$  referring to the coating surface,  $l$  to the liquid, and  $g$  to the gas (air). Therefore,  $\gamma_{sg}$  is the coating surface energy. Equation (1) shows that an increase in contact angle results in a decrease in surface energy. As shown in Fig. 3b, where direct surface energy measurements of the coating are reported, the ice release topcoat had a surface energy of  $17.5 \text{ mJ/m}^2$ , compared to a control topcoat measurement of  $36.7 \text{ mJ/m}^2$ . A similar decrease in surface energy for ice release clear coat coating was observed. This result confirmed that the efforts in reducing surface energy and increasing hydrophobicity of a polyurethane topcoat and clear coat systems were successful.

Results from gloss measurements of the ice release topcoat and clear coats are reported in Fig. 4. Gloss is a parameter that quantifies the amount of light reflection from a surface and describes the level of surface shininess. High gloss is desirable for exterior aerospace coatings as it is visually attractive. It could be observed that a high gloss for both ice release basecoat and clear coat was achieved, with gloss units above 80 for a  $20^{\circ}$  beam illumination and above 90 for a  $60^{\circ}$  beam



**Fig. 3** Wetting and surface energy characteristics of the developed ice release topcoat and clear coat as compared to the control topcoat and clear coats: (a) average contact angle; (b) average surface energy

illumination. The values are very similar to the gloss levels of control coatings (conventional polyurethane topcoats and clear coats).

The ice adhesion test using the setup described in Sect. 2.3 can result in two possible modes of ice fracture – ice adhesive fracture and ice cohesive fracture. A fully ice adhesive fracture is an adhesive failure condition between the ice and coating interface resulting in complete ice removal. The ice fracture load curves record the tensile force that was exerted on the panels as a function of panel displacement to remove the panel from the accreted ice. Figure 5a shows the ice

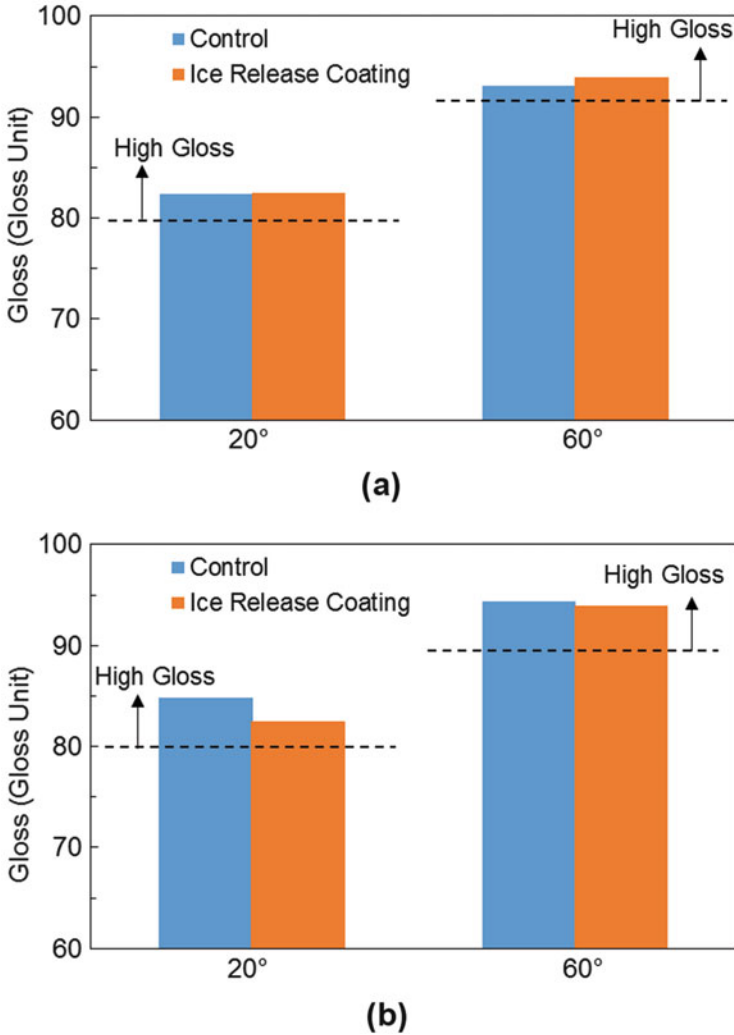


**Fig. 4** Gloss measurements for the control and ice release coatings: (a) topcoat; (b) clear coat. Results show similarly high gloss levels for the ice release coatings as compared to the control coatings

fracture load curve for a control topcoat. It could be observed that the tensile force gradually increased before abruptly decreasing at a panel displacement of 1 mm. This was the first instance of ice partial fracture, occurring at a location away from the ice-coating interface. However, a combination of opposing forces such as friction forces and partial ice-coating bond contributed to the continued, gradual rise of the tensile force, until the panel was completely removed from the ice, as indicated by the dot at the maximum point of the curve. This trend indicated an ice

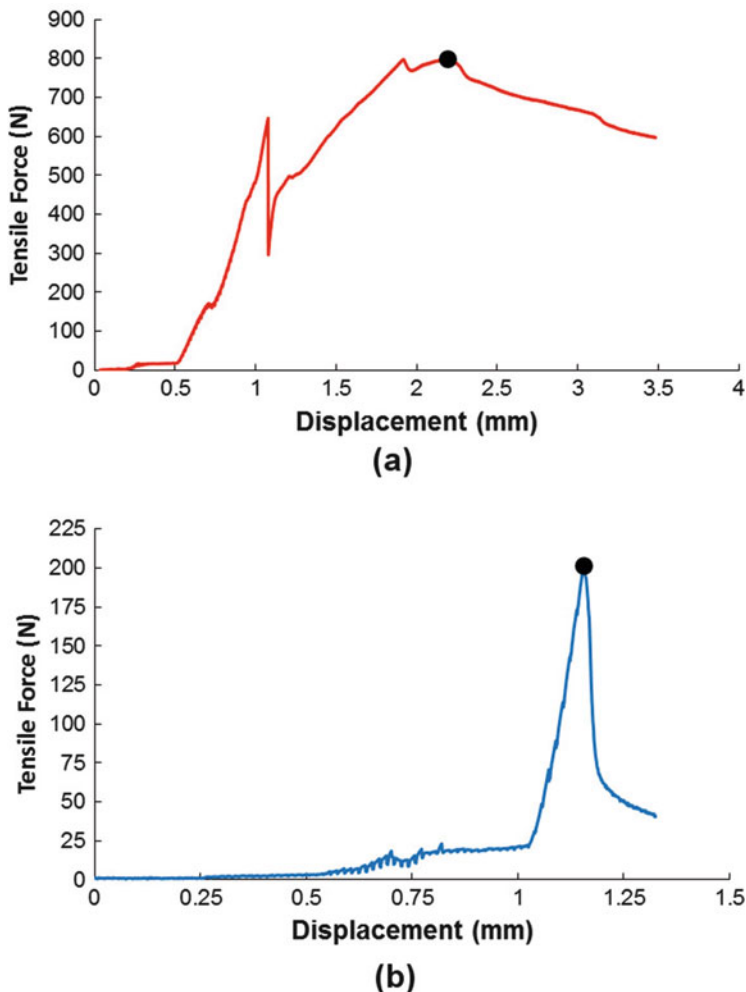


**Fig. 5** Sample ice fracture load curves for the internal PPG ice adhesion test showing: (a) cohesive ice fracture of a control topcoat; (b) adhesive ice fracture of an ice release topcoat. The dots on the curve indicate the maximum tensile force that was required to: (a) partially; (b) completely release ice from the substrate

cohesive fracture mode, and signified in general a high ice adhesion strength. On the other hand, as shown in Fig. 5b, the tensile force for an ice release topcoat rapidly increased to a peak before a sudden drop in load. The peak of the curve represented the point where ice was completely removed from the coating to result in a full ice adhesive fracture mode. It could be observed that the maximum force for a full adhesive fracture (Fig. 5b) was lower than the maximum force of a cohesive fracture (Fig. 5a). Figure 6 shows the comparison of ice shear stresses

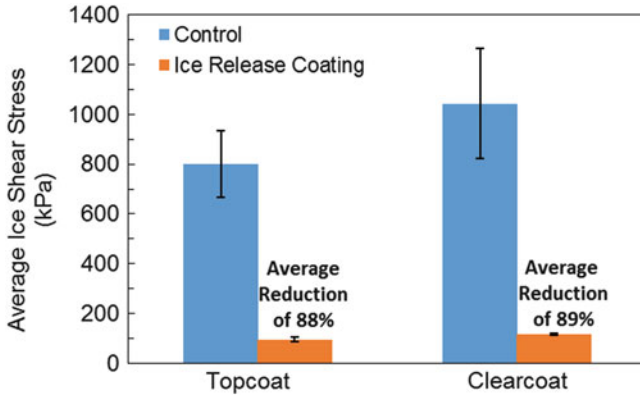


**Fig. 6** Ice shear stresses of the ice release topcoat and clear coat as compared to control coatings

of the ice release topcoat and clear coat with their respective control coatings. Significant reductions in shear stress were recorded for both the topcoat (average reduction of 88%) and clear coat (average reduction of 89%) with some measurements indicating as much as 95% reduction.

The results from Fig. 6 were obtained from a “static” ice accretion condition conducted internally. A study was performed to validate these test results by comparing them with data obtained from a well-established ice adhesion test – the Centrifuge Adhesion Test (CAT) developed by the Anti-Icing Materials International Laboratory (AMIL) at the University of Quebec, Chicoutimi. The CAT test is an unconfined droplet icing test and involves exposing test beams with coatings to a freezing drizzle with droplet mean volumetric diameter (MVD) of approximately 200  $\mu\text{m}$  for an ice accretion of 1 cm. The beams are then attached to a centrifuge and rotated at a controlled acceleration rate of 300 rpm/s until the point of ice detachment [29]. This test has been used by various research organizations to investigate and measure ice adhesion on substrates and coatings [30–32]. As shown in Fig. 7, the ice shear stress of different prototype ice release coatings was measured with the AMIL CAT test and compared with the shear stress values determined with the PPG internal test. With the exception of coating 6, the results demonstrated approximately 90% correlation between performance trends from our internal ice adhesion tests and the CAT tests. The ice adhesion performance of the developed prototypes was therefore validated.

Table 1 summarizes the results of the durability tests that were conducted on the ice release topcoat and clear coat. Durability tests were also performed on the control coatings (commercial PPG aerospace exterior topcoats and clear coats) and are included in Table 1. The hardness of the coatings was rated at 2H–3H pencil hardness, which signified a robust performance. Minimal coating degradation to HB pencil hardness was observed after exposure to Skydrol. A 5B rating was achieved for dry and wet adhesion tests and the coatings also demonstrated good



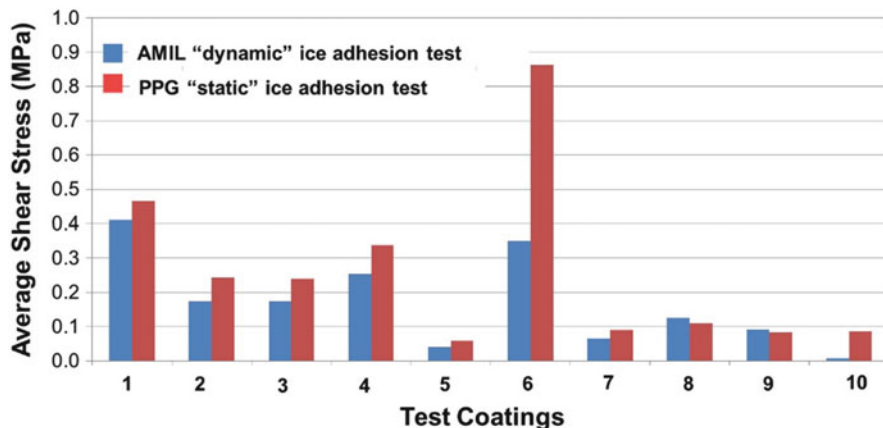
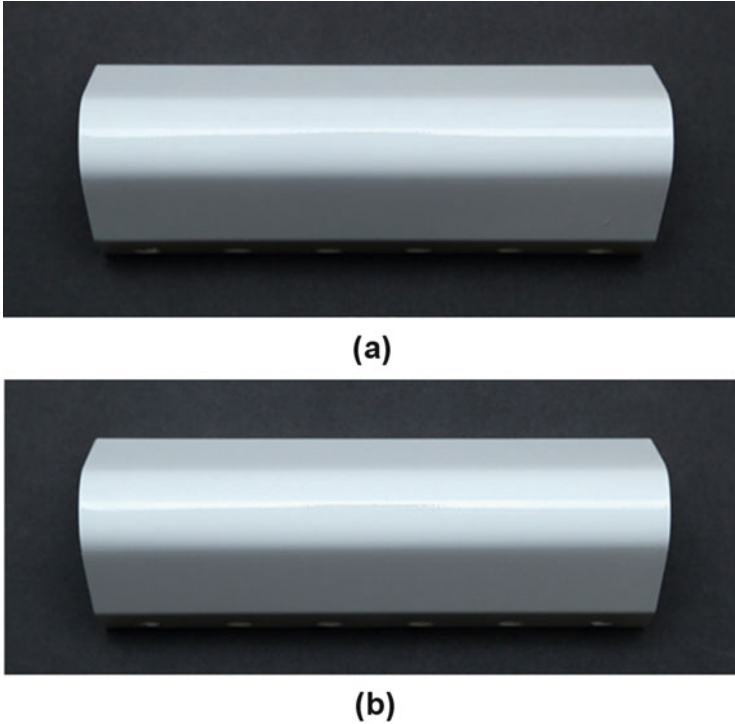


Fig. 7 Comparison of average ice shear stresses of different test coatings fabricated for a different study measured using an unconfined droplet ice adhesion test performed at AMIL (blue bars) and an internal PPG "static" ice adhesion test (red bars). With the exception of coating 6, results from the two separate tests showed approximately 90% correlation

low temperature flexibility at 1 in. mandrel radius of curvature values. The results of these durability tests for the ice release coatings were essentially the same as those for the commercial coatings. This showed that the developed ice release coatings were as durable as current commercial PPG aerospace exterior coatings. An additional ice adhesion test was conducted on the ice release topcoat which had been exposed to QUV-B light (QUV Accelerated Weathering Test, UVB-313 lamp) for an extended period of time. Results showed that although the ice adhesion strength increased, it was still ~67% lower compared to a fresh control coating. Most importantly, as shown in Fig. 8, the ice release prototypes did not visually degrade even after being exposed to the impact of rain-sized droplets at flight speeds for up to 30 min in the whirling arm rain erosion test. It should be noted that the same result was achieved by the commercial PPG aerospace exterior coating. This finding demonstrated that the developed ice release coatings can potentially withstand the harsh conditions of aircraft flight operation, with the exception of operating conditions at the wing leading edge.

PPG is currently collaborating with various commercial airframe and engine manufacturers to validate the coatings' efficiency for a variety of applications, including hybrid de-icing systems. More extensive durability tests are being performed to confirm the prototypes' performance after prolonged exposure to UV light, deicing fluids, hydraulic fluids, jet fuel, and water. Finally, additional testing is planned to evaluate ice adhesion strength under conditions more accurately replicating icing clouds (Advanced Environment Rotor Test Stand, AERTS facility at the Pennsylvania State University).



**Fig. 8** Rain erosion airfoils coated with the ice release topcoat after exposure to high-speed impact of rain drops for a duration of: (a) 5 min; (b) 30 min (Whirling Arm Rain Erosion). No coating degradation was observed, which is similar to results obtained for commercial PPG aerospace polyurethane coatings (control coatings)

## 4 Conclusions

Smooth and robust ice release topcoats and clear coats have been developed by PPG Aerospace based on qualified exterior polyurethane coating technology. The ice release coatings have decreased surface energy, as demonstrated by an increase in the water contact angles to above  $100^\circ$ , at the same time maintaining high gloss appearance. The coatings also show good resistance to a variety of stresses as demonstrated by the results of durability tests conducted based on ASTM standards, that is, cross-hatch dry and wet adhesion test, low temperature flexibility test, Skydrol resistance test, and QUV-B exposure test. In addition, no degradation of the ice release coatings was visually detected, even after impact of rain-sized droplets at flight speeds for 30 min. The achieved durability characteristics of the ice release prototypes are similar to the characteristics of commercial PPG aerospace exterior coatings not designed to be applied on leading edges of an aircraft wing. “Static” ice adhesion tests showed significant reduction in ice adhesion strength

compared to control coatings. An average reduction of approximately 88 and 89% was achieved for ice release topcoats and clear coats, respectively. Based on a comparative study of ice adhesion values of test coatings conducted for a different study, an approximately 90% correlation was demonstrated between “static” (internal PPG testing) and unconfined droplet ice accretion conditions (AMIL CAT testing). The ice release properties of the coatings were therefore validated.

**Acknowledgements** The authors acknowledge Ed Rakiewicz, Mike Mayo, Michael Zalich, Scott Moravek, and Emily Chunderlik of PPG Coatings Innovation Center, Allison Park, PA for their contributions to this work.

## References

1. Thomas SK, Cassoni RP, MacArthur CD (1996) Aircraft anti-icing and de-icing techniques and modeling. *J Aircr* 33:841–854
2. Antonini C, Innocenti M, Horn T, Marengo M, Amirfazli A (2011) Understanding the effect of superhydrophobic coatings on energy reduction in anti-icing systems. *Cold Reg Sci Technol* 67:58–67
3. Itagaki K (1983) Adhesion of ice to polymers and other surfaces. *Physicochemical aspects of polymer surfaces*. Springer, Berlin, pp 241–252
4. Itagaki K (1983) The implications of surface energy in ice adhesion. *J Adhes* 16:41–48
5. Murase H, Nanishi K, Kogure H, Fujibayashi T, Tamura K, Haruta N (1994) Interactions between heterogeneous surfaces of polymers and water. *J Appl Polym Sci* 54:2051–2062
6. Ahlborn G, Poehlmann H (1976) Development of a hydrophobic substance to mitigate pavement ice adhesion. *Environmental protection technology series EPA-600/2-76-242*
7. Bascom W, Cottingham R, Singletery C (1969) Ice adhesion to hydrophilic and hydrophobic surfaces. *J Adhes* 1:246–263
8. Zou M, Beckford S, Wei R, Ellis C, Hatton G, Miller M (2011) Effects of surface roughness and energy on ice adhesion strength. *Appl Surf Sci* 257:3786–3792
9. Yang S, Xia Q, Zhu L, Xue J, Wang Q, Chen Q (2011) Research on the icephobic properties of fluoropolymer-based materials. *Appl Surf Sci* 257:4956–4962
10. Cao L, Jones AK, Sikka VK, Wu J, Gao D (2009) Anti-icing superhydrophobic coatings. *Langmuir* 25:12444–12448
11. Wang F, Li C, Lv Y, Lv F, Du Y (2010) Ice accretion on superhydrophobic aluminum surfaces under low-temperature conditions. *Cold Reg Sci Technol* 62:29–33
12. Kulinich S, Farzaneh M (2009) How wetting hysteresis influences ice adhesion strength on superhydrophobic surfaces. *Langmuir* 25:8854–8856
13. Kulinich S, Farzaneh M (2009) Ice adhesion on super-hydrophobic surfaces. *Appl Surf Sci* 255:8153–8157
14. Kulinich S, Farhadi S, Nose K, Du X (2010) Superhydrophobic surfaces: are they really ice-repellent? *Langmuir* 27:25–29
15. Yeong YH, Milionis A, Loth E, Sokhey J, Lambourne A (2015) Atmospheric ice adhesion on water-repellent coatings: wetting and surface topology effects. *Langmuir* 31:13107–13116
16. Yeong YH, Loth E, Sokhey J, Lambourne A (2015) Ice adhesion performance of superhydrophobic coatings in aerospace icing conditions. *SAE technical paper 2015-01-2120*
17. Davis A, Yeong YH, Steele A, Loth E, Bayer IS (2014) Spray impact resistance of a superhydrophobic nanocomposite coating. *AIChE J* 60:3025–3032
18. Wang S, Jiang Y (2015) The durability of superhydrophobic films. *Appl Surf Sci* 357:1647–1657

19. Wang C, Fuller T, Zhang W, Wynne KJ (2014) Thickness dependence of ice removal stress for a polydimethylsiloxane nanocomposite: Sylgard 184. *Langmuir* 30:12819–12826
20. Dou R, Chen J, Zhang Y, Wang X, Cui D, Song Y, Jiang L, Wang J (2014) Anti-icing coating with an aqueous lubricating layer. *ACS Appl Mater Inter* 6:6998–7003
21. Golovin K, Kobaku SP, Lee DH, DiLoreto ET, Mabry JM, Tuteja A (2016) Designing durable icephobic surfaces. *Sci Adv* 2:e1501496
22. Wong T, Kang SH, Tang SK, Smythe EJ, Hatton BD, Grinthal A, Aizenberg J (2011) Bioinspired self-repairing slippery surfaces with pressure-stable omniphobicity. *Nature* 477:443–447
23. Zhu L, Xue J, Wang Y, Chen Q, Ding J, Wang Q (2013) Ice-phobic coatings based on silicon-oil-infused polydimethylsiloxane. *ACS Appl Mater Interfaces* 5:4053–4062
24. Kreder MJ, Alvarenga J, Kim P, Aizenberg J (2016) Design of anti-icing surfaces: smooth, textured or slippery? *Nat Rev Mater* 1:15003
25. Howell C, Vu TL, Johnson CP, Hou X, Ahanotu O, Alvarenga J, Leslie DC, Uzun O, Waterhouse A, Kim P (2015) Stability of surface-immobilized lubricant interfaces under flow. *Chem Mater* 27:1792–1800
26. Blackford R (1997) Aerospace coatings and the environment: some problems and constraints. *Surf Coat Int* 80:564–567
27. Tang G, Moravek SJ, Rakiewicz EF, Schwartzmiller DJ, Zalich M, Connelly BA, Roper T (2015) Method of mitigating ice buildup on a substrate. US Patent 9,090,797, 2015
28. Orowan E (1970) Surface energy and surface tension in solids and liquids. *Proc R Soc Lond A Math Phys Eng Sci R Soc* 316:473–491
29. Laforte C, Beisswenger A (2005) Icephobic material centrifuge adhesion test. In: Proceedings of the 11th international workshop on atmospheric icing of structures, IWAIS, Montreal QC, Canada, pp 12–16
30. Laforte C, Blackburn C, Perron J (2015) A review of icephobic coating performances over the last decade. SAE technical paper 2015-01-2149
31. Menini R, Ghalmi Z, Farzaneh M (2011) Highly resistant icephobic coatings on aluminum alloys. *Cold Reg Sci Technol* 65:65–69
32. Tarquini S, Antonini C, Amirfazli A, Marengo M, Palacios J (2014) Investigation of ice shedding properties of superhydrophobic coatings on helicopter blades. *Cold Reg Sci Technol* 100:50–58

# Antifogging and Frost-Resisting Polymeric Surfaces



Jie Zhao, Lingjie Song, and Weihua Ming

**Abstract** Fogging/frosting can significantly reduce clarity of a transparent substrate, resulting in not only inconvenience but also potential danger in daily life. There has therefore been great demand for effective antifogging/frost-resisting surfaces to maintain visibility and transparency in high-humidity environments in a variety of applications. Although tremendous efforts have been made to prepare inorganic antifogging surfaces, the primary focus of this review is on *polymeric* antifogging/frost-resisting surfaces, as polymer-based antifogging/frost-resisting surfaces hold great promise for large-scale preparation via easily implementable techniques and, subsequently, find more practical applications. In this chapter, recent progress is reviewed in the design, preparation, and typical properties of various antifogging/frost-resisting polymeric surfaces.

**Keywords** Antifogging • Frost-resisting • Functional coating • Hydrophilicity • Hydrophobicity • Layer-by-layer assembly • Semi-interpenetrating polymer network (SIPN)

---

J. Zhao

Department of Chemistry and Biochemistry, Georgia Southern University, Statesboro, GA, USA

Key Laboratory of Bionic Engineering of Ministry of Education, Jilin University, Changchun, China

L. Song

Department of Chemistry and Biochemistry, Georgia Southern University, Statesboro, GA, USA

State Key Laboratory of Polymer Physics and Chemistry, Changchun Institute of Applied Chemistry, Chinese Academy of Sciences, Changchun, China

W. Ming (✉)

Department of Chemistry and Biochemistry, Georgia Southern University, Statesboro, GA, USA

e-mail: [wming@georgiasouthern.edu](mailto:wming@georgiasouthern.edu)

## Contents

1	Introduction .....	186
2	Various Strategies to Develop Antifogging Polymeric Surfaces .....	187
2.1	Superhydrophilic Antifogging Polymeric Surfaces .....	188
2.2	Superhydrophobic Antifogging Polymeric Surfaces .....	197
2.3	Water-Absorbing Antifogging and Frost-Resisting Polymeric Surfaces .....	199
3	Multifunctional Antifogging Coatings .....	205
3.1	Dual-Functional Antifogging/Easy-Cleaning Coating .....	205
3.2	Dual-Functional Antifogging/Antimicrobial Coating .....	208
3.3	Dual-Functional Antifogging/Self-Healing Coating .....	209
4	Conclusions and Outlook .....	211
	References .....	212

## 1 Introduction

Caused by the condensation of light-scattering microscopic water droplets under various environmental conditions, fogging of a transparent surface creates complications in both daily life and many technological applications relying on maximizing light transmission, such as greenhouse windows [1], solar energy arrays [2, 3], analytical and medical instruments [4, 5], windshields, eyeglasses/goggles, and bathroom mirrors. Fog occurs when water vapor condenses onto a cold surface to form discrete, light-scattering water droplets. Surface wettability has been considered as a primary factor regarding whether a surface has the capability to prevent fog formation and maintain high clarity. Many approaches have been developed to alleviate fogging, mainly via manipulating surface wettability ranging from superhydrophilicity [6–20] to superhydrophobicity [21, 22]. As an effective strategy, superhydrophilic surfaces with water contact angles smaller than  $5^\circ$  have been developed to create fog-free surfaces, primarily because of their ability to reduce significantly light scattering related to the formation of water droplets on the surfaces by only allowing water to condense in a thin-film-like form. However, generally complicated procedures are required to fabricate the surface texture needed to obtain surface superhydrophilicity [23, 24]; a superhydrophilic  $\text{TiO}_2$  coating is an exception but it needs to be activated by UV illumination [25]. Moreover, these superhydrophilic surfaces would likely fail to resist frost formation because an ice layer would still form out of the thin water layer under the right conditions (for instance, at a sufficiently low temperature). On the other hand, superhydrophobic surfaces with special mosquito-eye-like topography [21] have been examined as potential antifogging candidates because of their excellent water-repellent and self-cleaning properties that originate from the combination of nano-scale surface roughness and low surface energy. However, it is still technically very challenging to fabricate the intricate biomimetic surface morphology [21, 26] for these surfaces. In addition, a superhydrophobic coating is generally opaque, further limiting its application as an antifogging surface.

A new antifogging strategy has recently been reported [27–33]. An effective antifogging surface does not have to rely on superhydrophilicity or superhydrophobicity; instead, excellent antifogging/frost-resisting properties originate from the water-absorbing capability of a judiciously designed polymeric system (See Sect. 2.3), leading to a fog-/frost-free surface even under aggressive fogging/frosting conditions.

In this review, primary emphasis is put on antifogging and frost-resisting, *polymeric* coatings because polymer-based surfaces have great potential for large-scale preparation via easily implementable techniques, which may subsequently find more practical applications. We give an overview of the different strategies to obtain antifogging polymeric surfaces and recent development in antifogging applications. The chapter concludes with an outlook on further development of antifogging/frost-resisting polymeric surfaces.

## 2 Various Strategies to Develop Antifogging Polymeric Surfaces

There have been three major approaches in preparing antifogging surfaces, including (1) wet, superhydrophilic surface, (2) dry, superhydrophobic surface, and (3) zwitterable-wetting, water-absorbing surface. Their typical features are summarized in Table 1, and a few examples from each approach are highlighted in this review. Again, the focus is primarily on polymeric surfaces.

**Table 1** Main strategies to prepare antifogging polymeric surfaces

Approach	1	2	3
Surface characteristics	Superhydrophilic	Superhydrophobic	Zwitter-wettable
Antifogging mechanism	Water spreading as thin film	Jumping-droplet condensation (nanoscale structure helpful)	Rapid water-absorbing
Polymer involved	Yes	Possible, but challenging	Yes
Ease of preparation	Moderately complicated	(Moderately) complicated	Straightforward
Scale-up preparation	Possible, but challenging	Possible, but challenging	Highly possible
Other remarks	May not be frost-resisting; likely structurally vulnerable	Structurally vulnerable because of surface nanotexture	Not surface-structured; mechanical property easily tunable
Typical references	[6, 9–11, 19, 20, 38–41]	[21, 47, 50]	[27–30, 32]

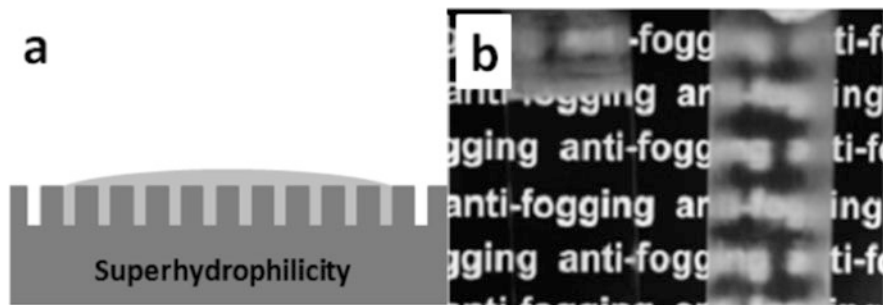


**Fig. 1** (a) Thin water film on a roughened, superhydrophilic surface with water filling in the surface cavity. (b) Comparison of the fogging behavior of a bare glass slide (*right*) with a slide partially coated (*left*) with a superhydrophilic film. Reproduced with permission from Cebeci et al. [6]

## 2.1 Superhydrophilic Antifogging Polymeric Surfaces

It has been generally accepted that a superhydrophilic surface with a water contact angle smaller than  $5^\circ$  can effectively inhibit fog formation by preventing light-scattering water droplets from forming on a surface. In spite of the inevitable water vapor condensation at the surface, the formed droplet in this case would immediately spread over the surface, leading to a thin-film-like sheet and thus avoiding the reduction of light transmission (Fig. 1).

The contact angle (CA) of a liquid on an ideal, atomically smooth solid surface is indicative of the solid's surface wettability, and is commonly expressed in the Young equation [34]:

$$\cos \theta = \frac{\gamma_{SV} - \gamma_{SL}}{\gamma_{LV}} \quad (1)$$

where  $\gamma_{SV}$ ,  $\gamma_{SL}$ , and  $\gamma_{LV}$  refer to the interfacial energy with S, L, and V as solid, liquid, and gas (vapor), respectively. Ideally, the Young equation gives the equilibrium CA, which can be approximated by an experimentally measured static CA. With respect to the water CA (WCA), a solid surface is conventionally categorized as hydrophilic when WCA is smaller than  $90^\circ$ , and as hydrophobic when WCA is greater than  $90^\circ$  [35, 36]. For a common polymer surface, the typical WCA is in the range of  $30\text{--}120^\circ$ . In the case of a very hydrophilic polymer, the WCA may approach  $5^\circ$  or smaller; however, the polymer tends to be water-soluble, thus rendering it useless as a coating.

For a common polymer surface to become superhydrophilic ( $\text{WCA} < 5^\circ$ ), the surface roughness plays an important role. When the surface roughness is low to moderate, there is intimate contact between the liquid and the solid surface (Fig. 1a), and the wetting is in the Wenzel regime [37]:

$$\cos \theta_w = r \cos \theta_0 \quad (2)$$



where  $\theta_0$  and  $\theta_w$  are the intrinsic CA (on the smooth surface) and the apparent CA on the roughened surface, respectively, and  $r$  is the roughness factor, that is, the ratio of the real surface area over the projected area so that  $r$  is always greater than 1. Equation (2) predicts that both hydrophobicity and hydrophilicity are amplified by the increasing surface roughness. For a solid surface with WCA  $< 90^\circ$ , an increasing surface roughness would lead to a decreasing apparent CA, eventually less than  $5^\circ$  (reaching the superhydrophilic state). Roughening a smooth surface represents a practical way to obtain a superhydrophilic surface. On the other hand, for the superhydrophilic surface to be used as an antifogging surface, the surface texture creating the roughness must remain at a size scale that does not scatter light to maintain the film clarity. Therefore, the two factors, a proper surface roughness and high-surface-energy chemistry (to reduce the intrinsic WCA), are required to obtain superhydrophilic surfaces [23, 24] with good antifogging performance.

### 2.1.1 Multilayer Antifogging Polymeric Coating from Layer-by-Layer Assembly

The layer-by-layer (LbL) assembly technique has been used extensively to fabricate thin films with molecular level control over film thickness and chemical composition. LbL assembly holds some advantages in developing an antifogging coating: (1) LbL deposition can be applied to a wide range of materials even with complex structures and (2) by changing the number of LbL deposition cycles the film thickness can be easily controlled, allowing for the maximum light transmittance. To render an LbL-assembled coating superhydrophilic, the surface needs to be roughened via, for instance, the use of nanoparticles [9, 38, 39], in combination with high-surface-energy chemical modification if necessary. The driving force for LbL film fabrication includes, primarily, electrostatic and hydrogen-bonding interactions. The LbL assemblies based on electrostatic interaction normally involve oppositely charged polyelectrolytes (PE), including polycations and polyanions, and often charged nanoparticles. Other interactions, such as hydrogen-bonding in particular, also play an additional role [40].

Cebeci et al. [6] reported a nanoporosity-driven superhydrophilic film from the LbL assembly involving PEs including poly(allylamine hydrochloride) (PAH), poly(sodium 4-styrene sulfonate) (PSS), and poly(acrylic acid) (PAA), as well as silica nanoparticles. Prior to the assembly of the nanoparticle-containing multilayers, bilayers consisting of alternating layers of PAH and sulfonated polystyrene (SPS) or PAA were assembled on the surface to promote better adhesion to the glass substrate. The colloidal silica nanoparticles were then alternately assembled with PAH to complete the thin film fabrication. They reported that the assembly conditions (solution pH and nanoparticle concentration) and the nanoparticle size strongly influenced the porous structure of the film. The atomic force microscopy (AFM) image (Fig. 2a, b) of a 12-bilayer film revealed the porous structure typically observed from all optimized multilayers. The typical peak-to-valley

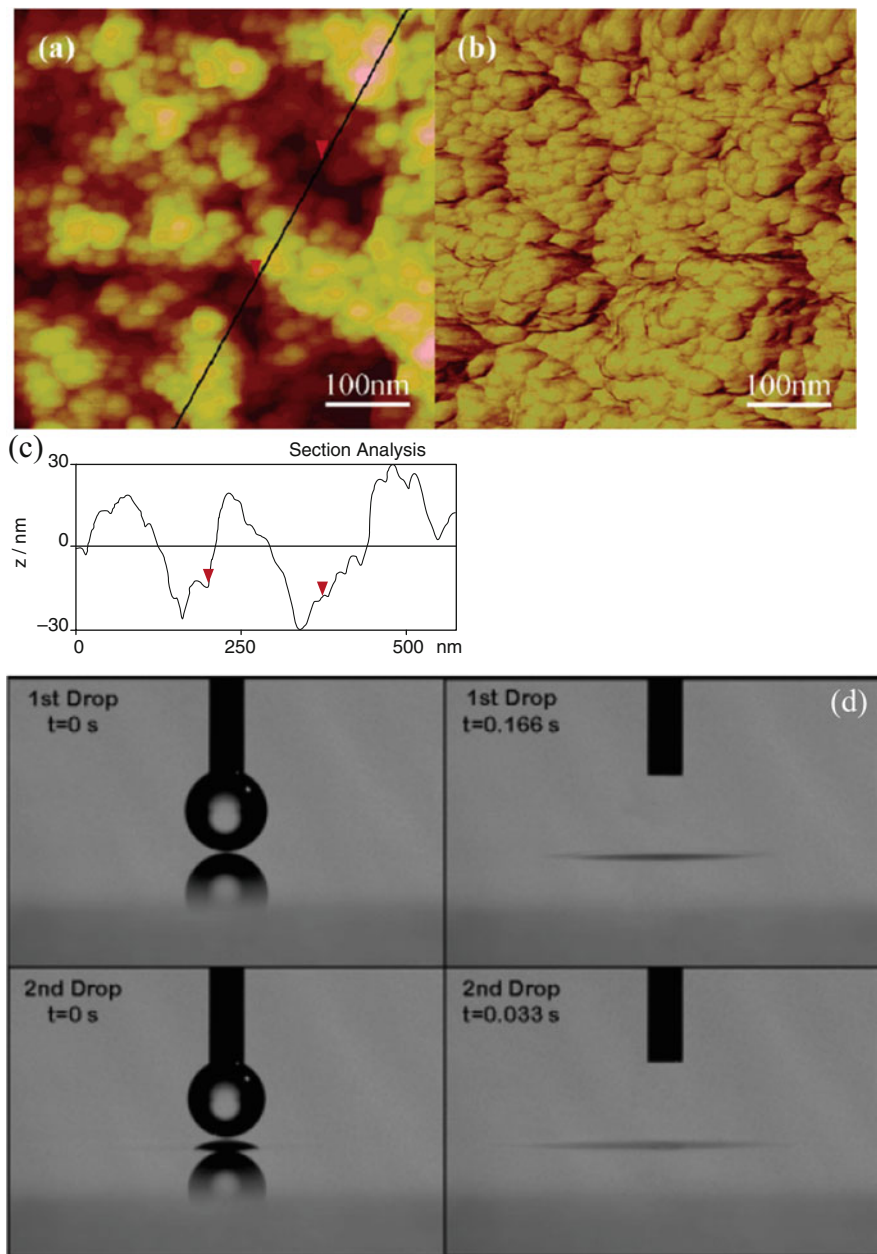


**Fig. 2** AFM tapping mode. (a) Height image of a polyelectrolyte multilayer film prepared from PAH/SiO<sub>2</sub> with PAH/SPS adhesion layers: (7 nm nanoparticles in a 0.03 wt% solution). (b) Phase image and (c) an AFM cross-section of the line shown in image (a). (d) Still images from video CA measurements for a first and second drop (0.5  $\mu$ L) of water on a superhydrophilic surface. Reproduced with permission from Cebeci et al. [6]

distance of 40–60 nm (Fig. 2c) was ascribed to nanoparticle aggregates. The excellent antifogging property was a direct consequence of the superhydrophilic wetting characteristics of the LbL film ( $WCA < 5^\circ$  within 0.5 s or less), as shown in Fig. 2.

Long-lasting antifogging coatings [10] were prepared based on a molecular-level blending of polysaccharides with multilayers containing chitosan (CHI) and carboxymethyl cellulose (CMC) via an LbL assembly process. To improve the mechanical durability of the coating, the substrate was first modified via self-assembly of epoxy-functionalized silane molecules. Environmental scanning electron microscopy (ESEM) was used to confirm that the excellent antifogging property of the polysaccharide-containing multilayer film was associated with the formation of a thin water sheet (Fig. 3C–E), as opposed to discrete, light-scattering water droplets observed in a fogging film (Fig. 3A, B). A permanent antifogging coating was generated through the unique water-absorbing property of polysaccharides [10], with a practical example, an antifogging goggle, given in Fig. 3F.

### 2.1.2 Hydrophilic Antifogging Polymeric Coatings Other than LbL Assembly

The LbL assembly has been found to be very effective in the preparation of superhydrophilic antifogging polymeric coatings. However, because of the multiple cycles of deposition of polyelectrolytes and nanoparticles where applicable, the LbL assembly is still a rather tedious procedure. Simpler procedures have therefore been sought to obtain antifogging coatings.

Chevallier et al. [14] employed a spin-coating process to prepare a polymeric antifogging coating with a bilayer configuration that allowed water to spread uniformly on the surface. As shown in Fig. 4, a glass substrate was first activated by plasma treatment to produce amino groups on the surface, which are also used as anchoring points for covalent grafting of the polymer layer. The antifogging coating was then created by the successive spin coating of poly(ethylene-maleic anhydride) (PEMA) and poly(vinyl alcohol) (PVA) layers. The PEMA layer, as an intermediate layer, acted as an interface through covalent reactions of the anhydride groups with both the amino groups on the glass substrate and the hydroxyl groups in PVA (forming multiple cross-linking sites), thus ensuring long-term stability of the coating. The PVA layer, because of its hydrophilicity, rendered the coating highly antifogging. Adding subsequent layers of PEMA/PVA could further improve the antifogging property of the coating [14].

With a similar strategy, Chang et al. [15] developed a water-resistant antifogging hard coating for plastic substrates, which has a special hydrophilic/hydrophobic bilayer structure. An organic-inorganic hybrid layer, comprising acrylic-functionalized silica nanoparticles and a cross-linker, dipentaerythritol hexaacrylate (DPHA), was first deposited on the substrate via UV curing. This bottom layer acted as a mechanical support and a hydrophobic barrier against water penetration. The top layer was also prepared via UV curing of a mixture of DPHA

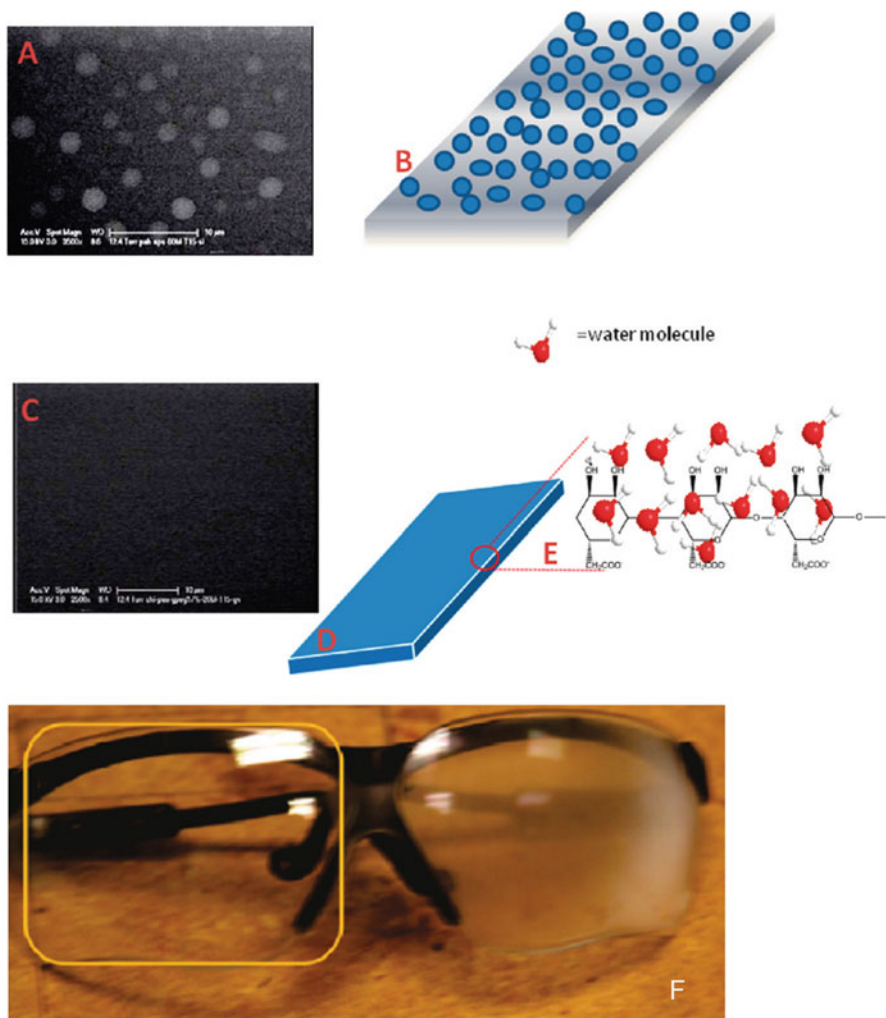


**Fig. 3** Scheme illustrating antifogging and fogging mechanisms on different polyelectrolyte films. (a) ESEM image of water droplets formed on a fogging PAH/SPS film. (b) Simple cartoon of water droplets on the PAH/SPS film. (c) ESEM image of CHI/CMC 20-bilayer antifogging coating after exposure to 90% humidity. (d) Simple cartoon showing a water film forming on the antifogging film. (e) Water molecules interacting with dense polar groups on polysaccharide. (f) Photo image of a 20-bilayer CHI/CMC coating on the right-eye lens of a safety goggle as indicated by the yellow line (the left-eye lens was not coated). Reproduced with permission from Nuraje et al. [10]

and a macromonomer, which was made from 2-hydroxyethyl methacrylate, isophorone diisocyanate, and a surfactant Tween-20. The interlayer adhesion was enhanced by the presence of DHPA in both layers (partially cross-linked for the bottom layer). The presence of Tween-20, with an optimal content of 10 wt%, rendered the as-prepared bilayer coating superhydrophilic and antifogging. The

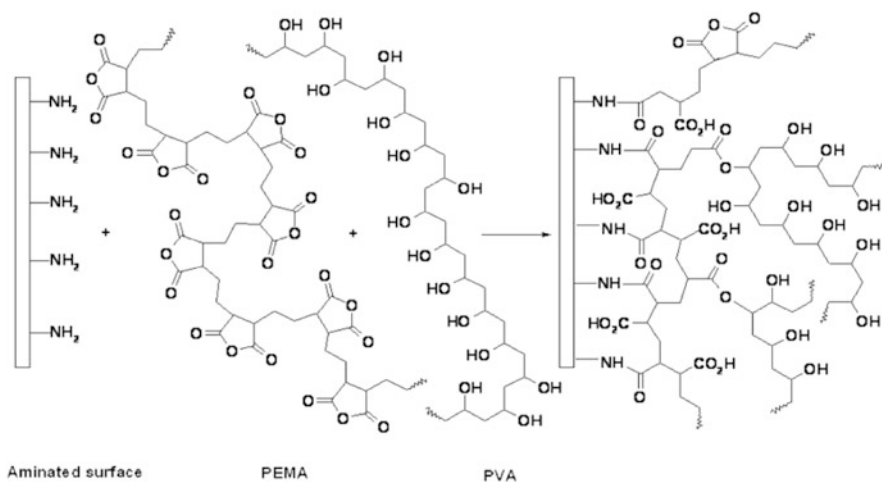


**Fig. 4** Bilayer antifogging polymer coating based on PEMA and PVA. Reproduced with permission from Chevallier et al. [14]

coating maintained its stability and antifogging property after being soaked in water for 7 days at 25°C.

Using a novel catalyst-induced cross-linking (CIC) technique, Nam et al. [41] developed surface-confined and cross-linked antifogging thin films at room temperature, mediated by ring-opening metathesis polymerization. As illustrated in Fig. 5, various poly(ethylene glycol)-based (PEG-based) prepolymers with pendent polymerizable norbornene (NB) groups were deposited on the allyl-modified substrate surface by spin coating, followed by exposure of the substrate to a solution consisting of Grubbs' catalyst to induce cross-linking of the polymer film. The hydrophilic/hydrophobic balance of the coating can be tailored by the selection of appropriate macro-cross-linkers, and the cross-linking density and swellability can also be controlled by varying the catalyst concentration and reaction time. The cross-linked coatings with NB contents of 5 and 9 mol% were the most hydrophilic ( $WCA < 20^\circ$ ) and demonstrated the best antifogging properties. In addition, the cross-linking density played an important role in the antifogging performance: a more densely cross-linked network resulted in a shorter period of antifogging performance and a loosely cross-linked coating remained fog-free because of a greater water pickup ability [41].

### 2.1.3 Polymer/Inorganic Nanocomposite Antifogging Coating

Apart from polyelectrolyte/nanosilica combinations via the LbL strategy, other inorganic particles such as clay have also been employed to obtain antifogging coatings. England et al. [19] first modified clay with aminopropyl triethoxysilane (AMP), leading to AMP-clay, then spin-coated an aqueous dispersion of AMP-clay

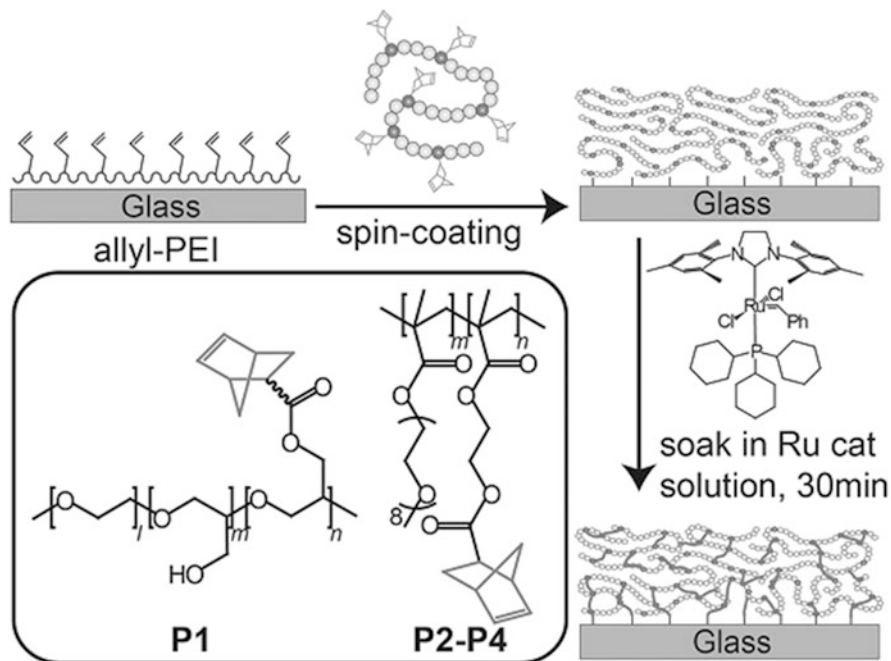


**Fig. 5** Schematic of the CIC process to obtain antifogging films with structure of macro-cross-linkers **P1** (PEO-g-NB with 5 mol% NB groups) and **P2-P4** (POEGMA-g-NB with 9, 20, and 35 mol% NB groups), respectively. Reproduced with permission from Nam et al. [41]

and poly(vinyl pyrrolidone) (PVP) onto various substrates. Subsequent drying at 100 °C led to the evaporation of water and promoted noncovalent interaction between AMP-clay and PVP, resulting in a superhydrophilic antifogging coating. The antifogging performance (Fig. 6) of the PVP/AMP-clay coating appeared to be strongly dependent on the film thickness rather than on the inherent surface hydrophilicity of the coating. The water-absorbing ability by the film was considered to be the vital factor for antifogging, and the critical thickness for effective antifogging was determined to be 12 nm [19], below which a thinner film could not prevent the formation of water droplets upon vapor condensation. An additional feature of this antifogging coating is its self-healing capability (discussed in Sect. 3.3) in the case of surface damage, because of the recovery of the noncovalent interaction upon exposure to ambient moisture.

#### 2.1.4 Surface-Initiated Hydrophilic Polymer Brush

Surface-initiated polymerization (also called “grafting from”) from initiators chemically bound to a solid surface is a useful alternative for growing a layer of polymer brushes with controlled functionality, density, and thickness. Controlled radical

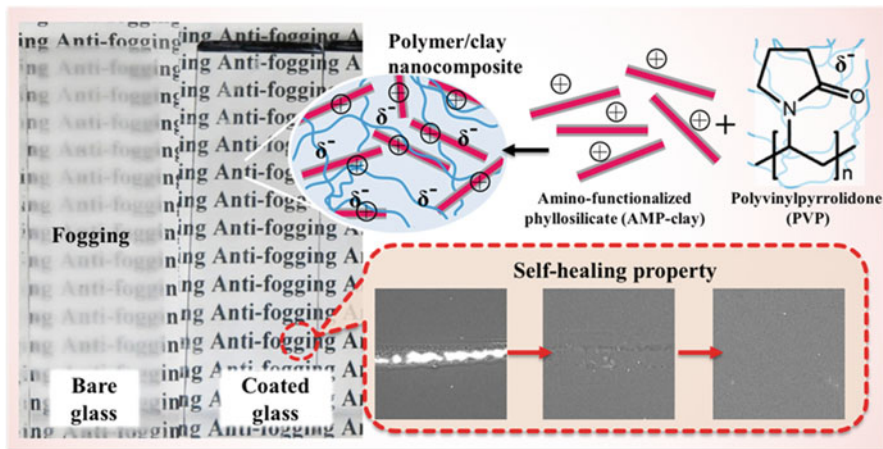
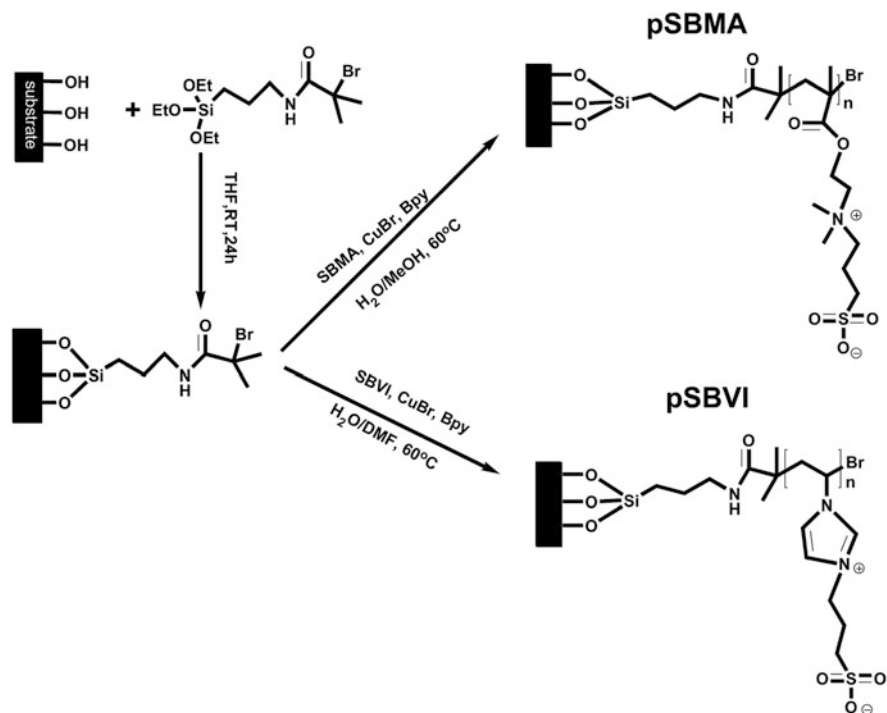


Fig. 6 Schematic illustration of antifogging/self-healing properties of PVP/AMP-clay coating. Reproduced with permission from England et al. [19]

polymerizations, notably atom transfer radical polymerization (ATRP), are highly desired to obtain polymer brushes, mostly because of their tolerance to a wide range of functional monomers and less stringent experimental conditions. Ezzat and Huang [20] synthesized a zwitterionic polymer brush coating with significant antifogging and frost-resisting properties via surface-initiated ATRP of poly (sulfobetaine methacrylate) (PSBMA) and poly(sulfobetaine vinylimidazole) (PSBVI), as illustrated in Fig. 7. The surface hydrophilicity was critically dependent on the polymer brush thickness: only brushes thinner than 50 nm were superhydrophilic ( $WCA < 5^\circ$ ) and, thus, effectively antifogging, whereas a thicker brush (100 nm) was still hydrophilic ( $WCA \sim 15^\circ$ ) but could not prevent fog formation. Various substrates modified by the zwitterionic polymer brush maintained high optical clarity under both hot and cold fogging conditions; no considerable difference in antifogging performance was observed between the two zwitterionic polymer brushes.

### 2.1.5 Plasma-Assisted Processes

Plasma-assisted processes are very efficient in creating superhydrophilic surfaces by quickly altering surface chemistry and increasing surface roughness of various substrates. For instance, plasma treatments with Ar-O<sub>2</sub> feeds have been used on optometric lenses to oxidize, and in turn hydrophilize, the carbon chains already present in the substrate [42]. However, the surface hydrophilicity may diminish over time after treatment, as the highly hydrophilic surfaces are intrinsically unstable in air and surface organization would likely occur to reduce the solid/air interfacial energy, leading to the increase of surface hydrophobicity (thus, WCA).



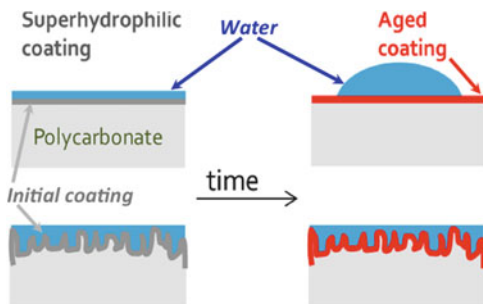
**Fig. 7** Schematic illustration of the synthesis procedure of PSBMA and PSBVI polymer brushes via surface-initiated ATRP polymerization. Reproduced with permission from Ezzat et al. [20]

As a result, the antifogging performance is significantly reduced shortly after treatment [43], especially at elevated temperatures.

To overcome this limitation, De Mundo et al. [18] prepared a superhydrophilic surface based on coupling silicon-based coatings with a nanotextured polymer surface in a two-step plasma process. First, a nanoscale texture was created on a polycarbonate substrate using a self-masked plasma etching process. Once etched with O<sub>2</sub> plasma, the nanotextured sample was subjected to plasma deposition from a feed containing hexamethyldisiloxane (HMDSO) as monomer to obtain a silicon-based coating on the polycarbonate film. The result showed that the deposition of the silicon-based coating on the flat substrates allows a continuous variation of wettability from hydrophobic to superhydrophilic, caused by a continuous reduction of carbon-containing groups. On the other hand, by depositing these different coatings on nanotextured substrates, the surface wettability behavior is changed consistently, as well as the condensation phenomenon in terms of microdroplet/liquid film appearance. More importantly, the superhydrophilic property, because of the nanotexture, is quite durable, despite a gradual decrease of surface energy. As shown in Fig. 8, this stable superhydrophilic behavior can be explained by wetting in the Wenzel regime. The nanotexture counterbalances the aging effect because it hides the variation in the surface chemistry, maintaining its superhydrophilicity.



**Fig. 8** Simplified scheme showing how surface texture ensures a durable superhydrophilic performance by hiding the chemical variations (surface energy decrease) suffered by the coating. Reproduced with permission from Di Mundo et al. [18]



Tahk et al. [12] presented a simple method to fabricate a polymeric optical sheet with antifogging property via two consecutive steps: (1) photo cross-linking of a UV-curable polyurethane acrylate (PUA) resin and (2) reactive ion etching. During photopolymerization, the cured PUA film was divided into two domains of randomly distributed macromers and oligomers because of a relatively short exposure time of 20 s at ambient conditions. Using the macromer domain as an etch-mask, dry etching was subsequently carried out to remove the oligomer domain, leaving a nanoturf surface with tunable roughness. The etching depth, as well as the surface roughness, increased with etching time, leading to a disordered, randomly distributed network of nanoturf surface. Notably, the nanoturf surface of the PUA sheet etched for 120 s exhibited superhydrophilicity ( $WCA < 5^\circ$ ), rendering the surface antifogging in a humid environment.

Superhydrophilic and highly hydrophilic antifogging coatings are effective in preventing fog formation under conventional conditions because of their ability to reduce significantly light scattering by only allowing water to condense in a thin-film-like form. However, in more aggressive environments, such as very cold conditions, superhydrophilic antifogging coatings may fail to resist frost formation because ice would still form from the thin water layer under certain conditions. In addition, the superhydrophilic property can be easily contaminated in the presence of an oily substance in the environment, likely leading to gradual reduction in the antifogging performance with time.

## 2.2 Superhydrophobic Antifogging Polymeric Surfaces

Superhydrophobic surfaces, especially for those in the Cassie–Baxter wetting regime ( $WCA > 150^\circ$  and low CA hysteresis), are attractive as antifogging coatings because, in many cases, water droplets can easily roll off these surfaces (Fig. 9a). The Cassie–Baxter wetting regime can be described as follows [44, 45]:

$$\cos \theta_{CB} = f \cos \theta_0 + f - 1 \quad (3)$$

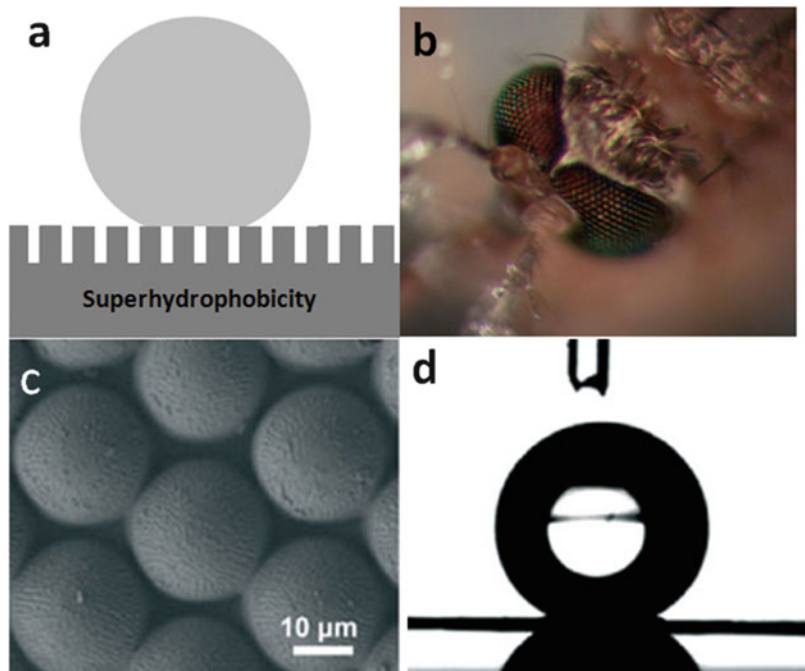


**Fig. 9** (a) Water droplet on a roughened, superhydrophobic surface with air trapped in the surface cavities. (b) Optical image of an antifogging mosquito eye in a fogging test chamber. (c) SEM image of PDMS micro-hemispheres mimicking the microstructure of the mosquito compound eye. (d) Spherical water droplet on the artificial compound-eye surface. Reproduced with permission from Gao et al. [21]

where  $\theta_{CB}$  is the apparent CA in the Cassie–Baxter regime and  $f$  is the liquid/solid contact area fraction. Equation (3) depicts a simplified scenario in which the liquid/solid contact area is flat. The smaller the  $f$  value the greater the  $\theta_{CB}$  value and the more liquid repellent the surface becomes.

Most superhydrophobic surfaces, even in the Cassie–Baxter regime, fail to exhibit antifogging behavior. For example, the well-known self-cleaning lotus leaf easily becomes wetted under suitable condensation conditions, because the micro-scale fog droplets can easily be trapped in the interspaces among micropapillae [46]. Only those superhydrophobic surfaces with a surface structure of dimensions smaller than the size of a water microdroplet (preventing the smallest possible droplet from sticking to the structured surface) may possess dry antifogging properties. Cicada wings covered with unique nanocones were reported to maintain the self-cleaning function [47] via the jumping-droplet condensation mechanism [47–49], which may make a surface antifogging. However, this type of superhydrophobic surface is not necessarily entirely fog-free. Only on a nanocone-textured surface with dimensions less than 100 nm (sharp cone tips < 20 nm) was excellent antifogging ability (water departure of droplets smaller than 2  $\mu\text{m}$ ) achieved [50]; however, the fabrication of this nanocone surface is complex.

Gao et al. [21] found that the compound eye of the mosquito *Culex pipiens* can maintain clear vision in a humid habitat because of its unique superhydrophobic property. The unique property is attributed to the smart design of delicate microstructures and nanostructures: hexagonally non-close-packed nipples (Fig. 9b) at the nanoscale prevent microscale fog drops from condensing onto the ommatidia surface [21]. An artificial analogue with hierarchical microstructure/nanostructure was developed on the basis of the combination of polydimethylsiloxane (PDMS) hemispheres, silica particles, and a low surface energy perfluoroalkyl silane layer (Fig. 9c). However, the artificial counterpart is much less effective in antifogging than the mosquito eye because it is far from easy to prepare the perfectly organized compound-eye-like structure; this strategy is also not easily carried out on a large scale. Furthermore, a superhydrophobic surface is generally opaque, which would limit its use as an antifogging coating when film transparency is required.

Recent studies have shown that a hierarchically structured surface, because of its large surface area and increased nucleation site density for condensing droplets, may induce frost formation at an even faster rate than a smooth surface of the same material under high humidity conditions. As a consequence, frost can build up within the topographical features of the superhydrophobic surface, potentially increasing the amount of energy required to remove the frost layer [51].

### 2.3 Water-Absorbing Antifogging and Frost-Resisting Polymeric Surfaces

Different from the superhydrophilic/superhydrophobic antifogging strategies discussed above, recent work by several researchers has demonstrated that effective antifogging surfaces can also be realized by carefully balancing the hydrophilicity and hydrophobicity of a coating [27–33]. These surfaces show WCAs in the range of, typically, 40–110°, higher than a superhydrophilic surface but significantly lower than a superhydrophobic surface, which implies that these surfaces can neither spread water microdroplets in a thin-film-like form nor cause the droplet to roll off the surface easily.

When moist water vapor starts to condense on a solid surface, microscale water (fog) or ice (frost) droplets (Fig. 10a) may form during the first few seconds of contact. Antifogging behavior at this initial stage is extremely important, as subsequent fogging or frosting may be much less severe or even diminish because the

**Fig. 10** (a) Condensed water droplet on a hydrophobic surface. (b) Humid water vapor contacts with a water-absorbing surface



subject has adapted to the environmental temperature and humidity after a certain time [27]. If a coating can rapidly imbibe water molecules from the vapor into the bulk of the coating (Fig. 10b), the microscale water/ice droplet may not form at all, even though the initial WCA on the surface may be in a modest range (say, 40–110°). Thus no fogging or frosting on the coating surface is observed. Once absorbed inside the coating, water molecules may exist in the nonfreezing state because of their strong hydrogen-bonding interaction with the polymer, thus avoiding the formation of a large, light-scattering water or ice domain. On the other hand, the existence of the hydrophobic moiety in the coating plays an important role in helping to maintain the film stability and integrity, avoiding over-swelling of the polymer coating.

### 2.3.1 Water-Absorbing Antifogging/Frost-Resisting Polymeric Surfaces via LbL Assembly

Lee et al. [29] first developed polymeric surfaces based on the LbL assembly of PVA and PAA, followed by thermal treatment to induce cross-linking between PVA and PAA via esterification (Fig. 11a). An additional step of functionalizing the PVA/PAA multilayer film with poly(ethylene glycol) methyl ether led to

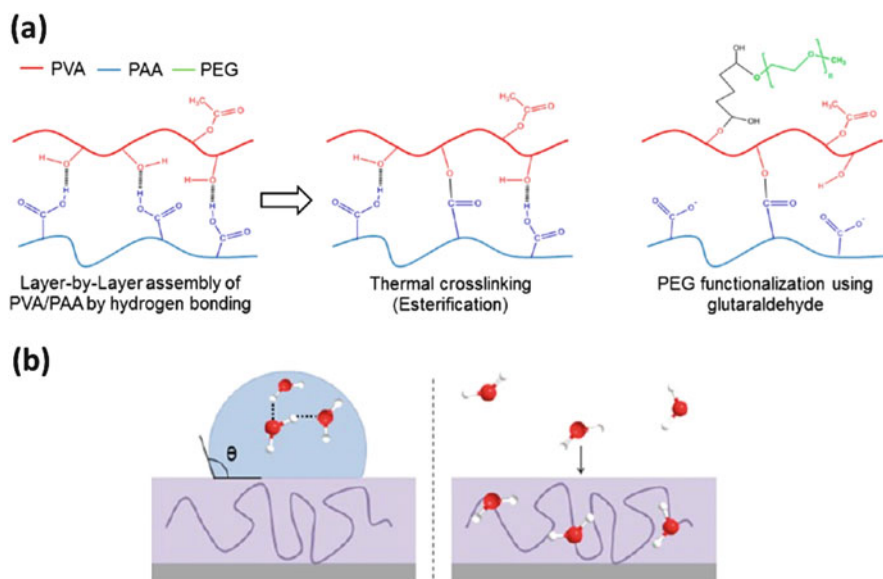


**Fig. 11** (a) Preparation of antifogging coating including reacting a thermally stabilized PVA/PAA multilayer film with PEG segments. (b) Schematic illustration of the zwitter-wettability. Reproduced with permission from Lee et al. [29]

significantly enhanced antifogging property, and frost-resisting behavior in particular. They coined the term “zwitter-wettability” to describe the unique wetting characteristics of this surface: a surface that has the ability to absorb molecular water rapidly from the environment, simultaneously appearing hydrophobic when probed with water droplets (Fig. 11b). Indeed, the initial WCA on the zwitter-wettable surface was about  $110^\circ$ , followed by continuous decay over a period of 600 s, indicating water was gradually imbibed into the coating. Although the PVA/PAA multilayer coating already showed good antifogging property, the addition of the PEG segment to the film provided an additional capacity to absorb nonfreezing water, which was critical in leading to excellent frost-resisting behavior [29].

To help sustain the surface hydrophobicity of a zwitter-wettable coating, Lee et al. [30] further developed a nanostructured LbL-assembled film consisting of a hydrophilic reservoir of chitosan (CHI)/carboxymethyl cellulose (CMC) multilayers, which was capped with three bilayers of hydrophobic CHI/Nafion. The hydrophobically capped multilayer was evidently zwitter-wettable, with a stable WCA of  $105^\circ$  (Fig. 12b), whereas the WCA on the hydrophilic CHI/CMC multilayer was  $20^\circ$  (Fig. 12a). In the meantime, the thin hydrophobic capping layer allowed water vapor to diffuse rapidly into the underlying hydrophilic reservoir rather than nucleating drops of liquid water on the surface [30], thus maintaining an excellent antifogging/frost-resisting property. A potential advantage of the zwitter-

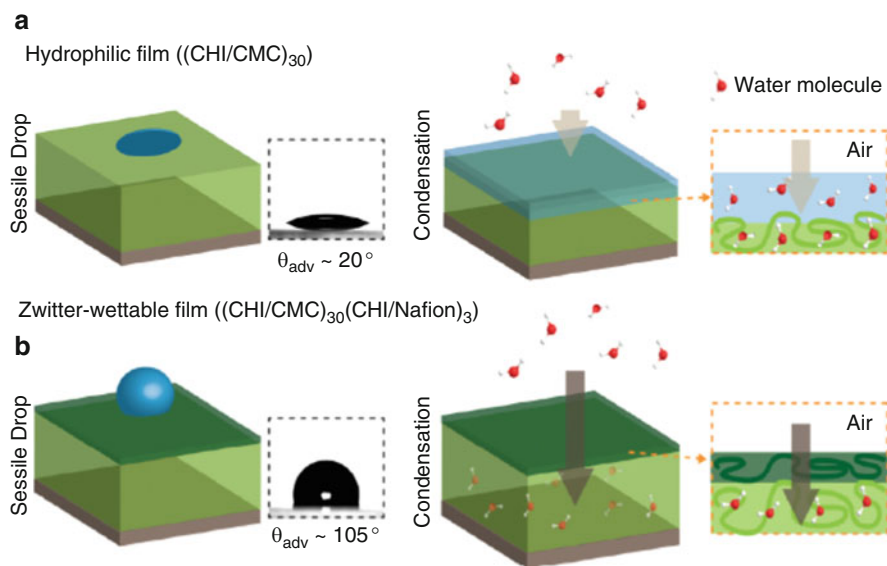


**Fig. 12** Schematic representation of (a) a hydrophilic film with added sessile drop and during condensation and (b) a zwitter-wettable film with added sessile drop and during condensation. Reproduced with permission from Lee et al. [30]

wettable antifogging coating is that removal of possible organic contaminants would be easier, compared to a typical hydrophilic antifogging coating, because of the weak retention forces offered by the hydrophobic capping layer [30].

### 2.3.2 Antifogging/Frost-Resisting Coating Based on Semi-Interpenetrated Polymer Network (SIPN) Containing Copolymers with Balanced Hydrophobicity/Hydrophilicity

Antifogging behavior at the initial stage is critical, because subsequent fogging may diminish as the surface coating adapts to the environmental temperature and humidity. With this understanding, we recently developed an effective antifogging/frost-resisting coating [27] on the basis of a semi-interpenetrating polymer network (SIPN) comprising a linear, binary acrylic random copolymer poly(2-(dimethylamino)ethyl methacrylate-*co*-methyl methacrylate) [poly(DMAEMA-*co*-MMA)] and a cross-linked network formed from ethylene glycol dimethacrylate (EGDMA). The molar ratio between the MMA and DMAEMA units was varied to tailor the hydrophilic/hydrophobic balance of the copolymer, which would enable water to diffuse through the coating, yet the polymer did not dissolve in water. In the meantime, the presence of the polymerized EGDMA network (the optimal EGDMA content was 0.5%) would prevent the copolymer from being overly swollen by water, thus ensuring coating stability. A SIPN coating with 70% DMAEMA in poly(DMAEMA-*co*-MMA) demonstrated excellent antifogging/frost-resisting properties (Fig. 13a); in contrast, the coating with less DMAEMA (60%) did not completely prevent the formation of fog/frost (still much better than the control glass and a hydrophobically modified glass).

The basal diameter change of a water sessile droplet (initial WCA:  $\sim 60^\circ$ ) on various coatings (Fig. 13b) was examined. Practically, no change in the diameter was observed for a perfluoroalkyl silane (Rf-Si)-modified glass and the control glass. In contrast, the diameter increased on all four copolymer-based SIPN coatings:  $\sim 12\%$  for Copolymer-70 and  $18\%$  for Copolymer-80, respectively, and smaller increase for the other two coatings with lower DMAEMA contents over the 600-s period. This observation further suggests that water had diffused into the copolymer coating, causing the expansion of the droplet contact area with the polymer surface, and the more DMAEMA segments in the coating the more significant the water diffusion became. This remarkable water-absorbing capability, coupled with the coating stability produced by the cross-linked EGDMA network, contributed to the excellent antifogging/frost-resisting properties of Copolymer-70.

When molecular water in moist air started to condense on the antifogging surface, the water molecules were immediately and rapidly absorbed into the hydrophilic segments of the copolymer, not allowing micro-droplets to form on the coating surface (fogging or frosting) [27], as schematically illustrated in Fig. 14. Once inside the copolymer coating, water molecules could exist in the nonfreezing state because of strong binding with the polymer via hydrogen bonding, avoiding formation of a large light-scattering water domain.

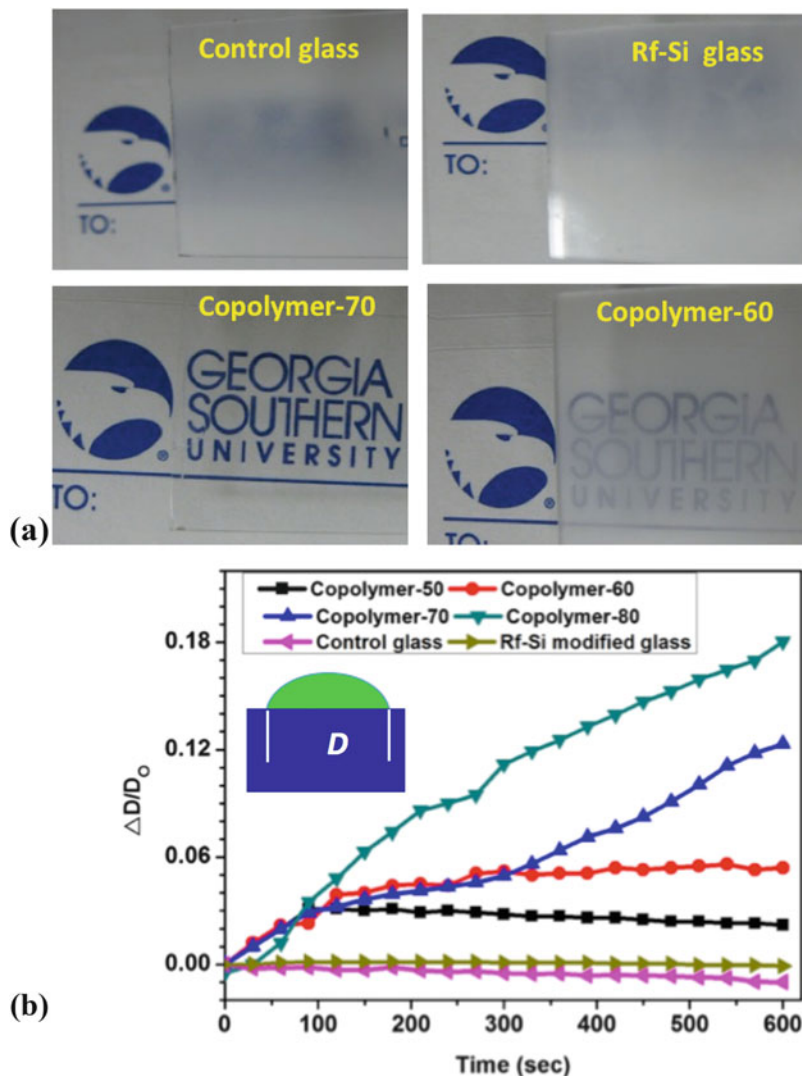


**Fig. 13** (a) Fogging test results for various samples, first stored at  $-20^{\circ}\text{C}$  for 30 min and then exposed to ambient lab conditions for 5 s. Copolymers-70 and -60 refer to the SIPN coating with the DMAEMA molar content in the copolymer of 70% and 60%, respectively. (b) Basal diameter change of a water sessile droplet on various samples over the 600-s period, as expressed as  $\Delta D/D_0$  where  $\Delta D = D - D_0$ , and  $D_0$  and  $D$  are the initial basal diameter (time zero) and the basal diameter at different times, respectively, of the wetted area by the water droplet. Reproduced with permission from Zhao et al. [27]

Despite the excellent frost-resisting property of the above SIPN coating, its antifogging performance became poor when exposed to hot moist air because of the lower critical solution temperature (LCST) associated with the DMAEMA

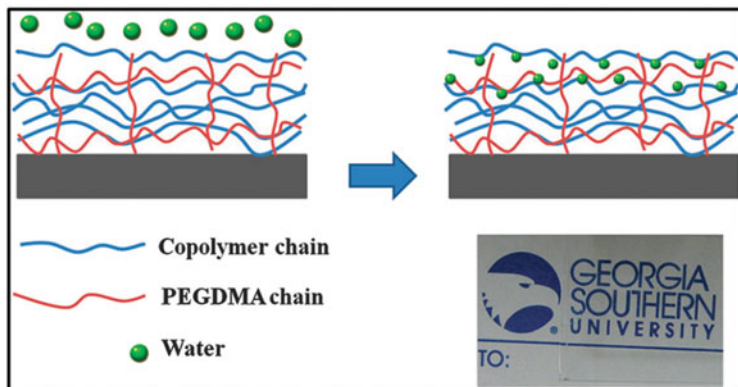


**Fig. 14** Schematic illustration of antifogging mechanism of the SIPN coating comprising a random copolymer with balanced hydrophobicity/hydrophilicity. Reproduced with permission from Zhao et al. [27]

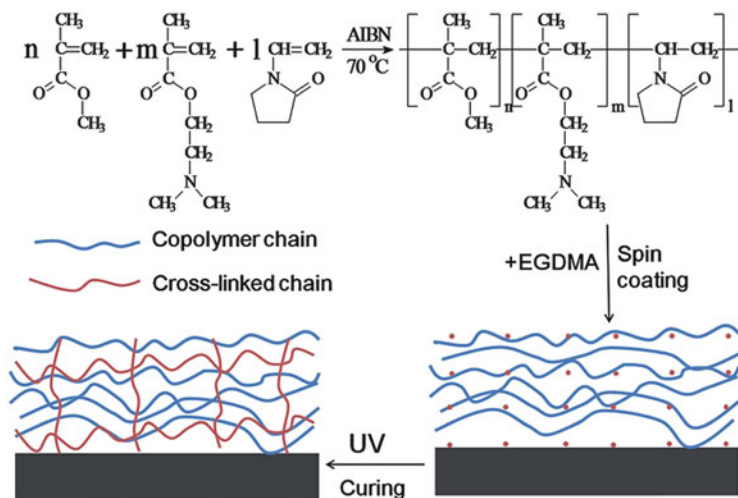


**Fig. 15** Synthesis of a random terpolymer poly(DMAEMA-*co*-NVP-*co*-MMA), and the subsequent preparation of an SIPN coating on the basis of the terpolymer. Reproduced with permission from Zhao et al. [28]

segments. To eliminate the LCST, DMAEMA was partially replaced with another hydrophilic monomer, *N*-vinylpyrrolidone (NVP), to obtain a random terpolymer, poly(DMAEMA-*co*-NVP-*co*-MMA), at the same time maintaining the desirable hydrophobic/hydrophilic balance in the terpolymer [28]. Indeed, the terpolymer-based SIPN coating (Fig. 15), with the optimal DMAEMA/NVP/MMA molar ratio of 40/30/30 (initial WCA:  $\sim 60^\circ$ ), demonstrated excellent antifogging/frost-resisting properties against both hot and cold moist air. To guarantee excellent



antifogging/frost-resisting performance for the SIPN coating, the coating has to be sufficiently thick (~500 nm) to be capable of absorbing, rapidly and fully, water molecules from the surrounding into the coating. It is interesting to note that, for a 920 nm thick coating, the coating thickness increased by 36% relative to the initial thickness after it was exposed to ambient conditions (~20°C, 50% RH), following storage at -20°C for 30 min, suggesting the coating had taken up a substantial amount of water [28]. Furthermore, after about 150 s at ambient conditions, the coating had almost recovered to its original thickness, suggesting that this type of antifogging/frost-resisting coating would be effective for a long time. The terpolymer-based coating indeed remained fog-free over a test period of 6 months [28].

### 3 Multifunctional Antifogging Coatings

Apart from antifogging/frost-resisting functions, various polymeric coatings have also demonstrated other functional properties, such as easy-cleaning [7, 8, 17, 52, 53], antimicrobial [11, 54, 55], self-healing [19, 31, 32, 56], and anti-reflection properties [6, 9, 12, 16, 38, 39], to name just a few. The multifunctionality of these polymeric coatings renders them particularly useful in a variety of potential applications.

#### 3.1 Dual-Functional Antifogging/Easy-Cleaning Coating

Howarter et al. [7, 8] successfully developed easy-cleaning and anti-fogging surfaces via stimuli-responsive polymer brushes. As shown in Fig. 16, an isocyanate-containing silane was first bonded to a silica substrate, followed by surface grafting with a PEG oligomer end-capped with a perfluoroalkyl group (f-PEG). This brush-like surface displayed a response associated with a “low surface energy” material upon exposure to oil and, at the same time, a “high surface energy” response upon exposure to water, which would trigger surface reorganization to expose the hydrophilic PEG segments. As a result, the surface has been shown to be simultaneously hydrophilic and moderately oleophobic, which may have the potential for use as a promising coating for both easy-cleaning and antifogging purposes.

Wang et al. [52] designed and synthesized a Y-shaped amphiphilic fluorinated monomer (Fig. 17A), containing both a perfluoroalkyl and a PEG side chain, and further prepared a block copolymer with 2-(*N,N*-dimethylamino)ethyl methacrylate (DMAEMA) by reversible addition–fragmentation chain transfer polymerization. The surfaces of the block copolymer simultaneously exhibited excellent antifogging and oil-repellent properties (Fig. 17C). They also found that antifogging performance for the random copolymers between the two monomers was not as good as their block copolymer counterparts [52].

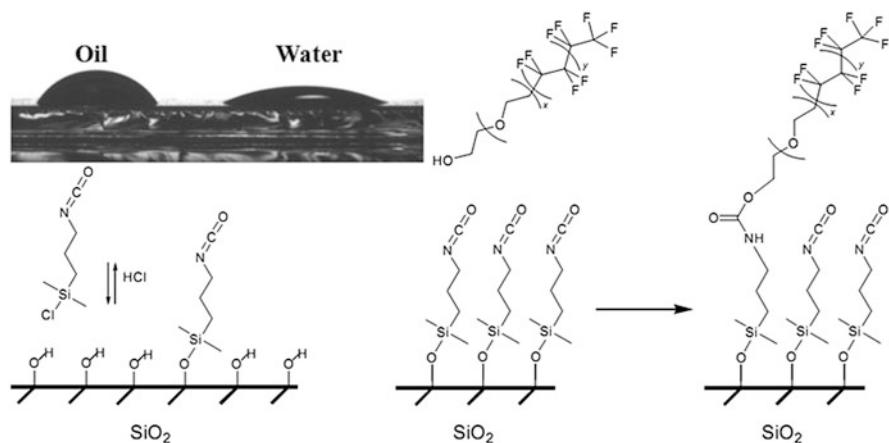


**Fig. 16** A two-step procedure to a prepare oleophobic/hydrophilic surface. Isocyanate-functionalized silane monolayer was formed on the silica surface, followed by grafting of f-PEG oligomer. The inset shows two droplets: oil (left) and water (right) on the surface; there was no time delay between exposing the surface to the liquid and taking the photo. Reproduced with permission from Howarter et al. [7]

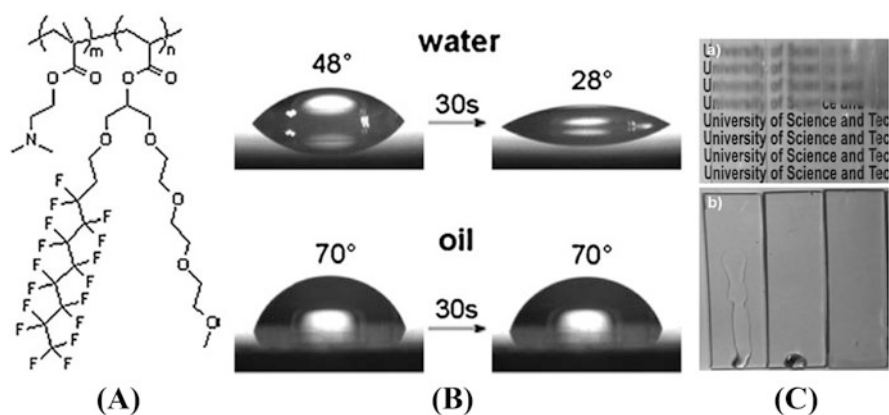
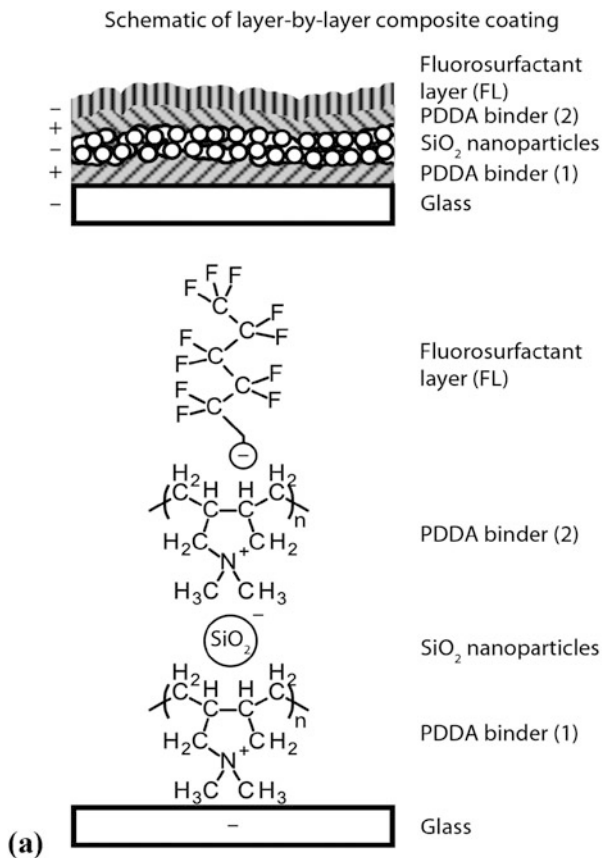


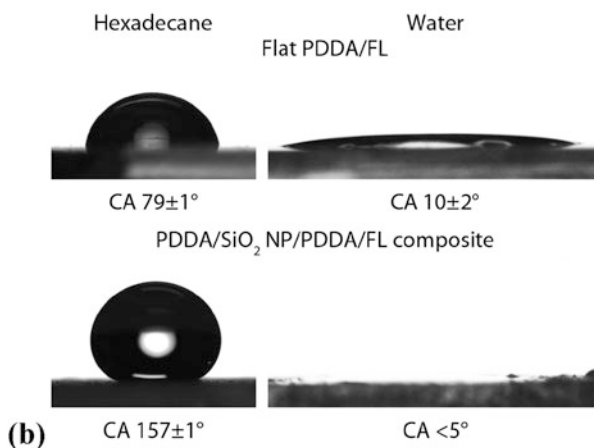
**Fig. 17** Schematic (A) and surface wettability (B) of a block copolymer containing a Y-shape monomer (the oil was hexadecane). (C) Fogging behavior (a) and oil-repency (b) of three films: (from left to right) PDMAEMA homopolymer, block copolymers with 5 and 10 units of the Y-shape monomer. Reproduced with permission from Wang et al. [52]

Via layer-by-layer assembly, Brown and Bhushan [53] developed a durable, superoleophobic/superhydrophilic coating, involving the use of polyelectrolyte binder poly(diallyldimethylammonium chloride) (PDDA),  $\text{SiO}_2$  nanoparticles, and a fluorosurfactant (Fig. 18a). The complex between PDDA and the fluorosurfactant contributed to oil repellency, at the same time being hydrophilic, which was further enhanced via surface roughening by incorporating  $\text{SiO}_2$

**Fig. 18 (a)** Superoleophobic/superhydrophilic, multilayer composite coating. **(b)** Both oleophobicity and hydrophilicity were enhanced via the addition of silica nanoparticles. Reproduced with permission from Brown et al. [53]



Liquids on flat and layer-by-layer composite coatings



nanoparticles (Fig. 18b). The as-prepared coating was also antifogging because of its superhydrophilicity, and may also be desirable for oil-water separation applications.

### 3.2 Dual-Functional Antifogging/Antimicrobial Coating

For medical procedures, such as laparoscopy and endoscopy [4, 5], lens fogging is a common problem and may lead to sudden loss of vision for operator, potentially provoking complications. Therefore, there is great need for more effective, permanent antifogging coatings for medical devices. Furthermore, antifogging coating which are also antimicrobial may help reduce, and even eliminate, potential pathogenic infection. There have been very few studies on coatings that are both antifogging and antimicrobial, one based on a superhydrophilic polymer-SiO<sub>2</sub> nanocomposite [11] and the other on a UV-cured coating [54]; however, the combined antifogging and antimicrobial performance still needs major improvement.

A polymeric coating was recently developed with both antifogging and antimicrobial performances on the basis of an SIPN coating of partially quaternized poly(DMAEMA-co-MMA) and a polymerized EGDMA network [55], as schematically illustrated in Fig. 19. This approach was built upon the recent strategy by Zhao et al.

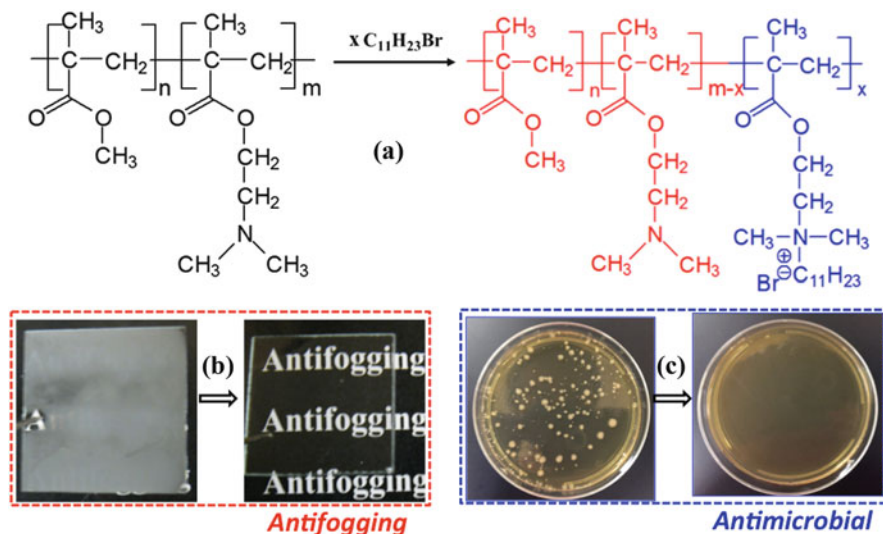


**Fig. 19** (a) Synthesis of partially quaternized poly(DMAEMA-co-MMA) random copolymer, which was subsequently used to prepare dual-functional SIPN coating. Reproduced with permission from Zhao et al. [55]. The coating demonstrated (b) excellent antifogging and (c) excellent antimicrobial properties

[27] of preparing an antifogging coating from poly(DMAEMA-*co*-MMA)-based SIPN. The excellent antifogging behavior of the smooth coating was mainly attributed to the hydrophilic/hydrophobic balance of the partially quaternized copolymer. Covalent incorporation of up to 7 mol% hydrophobic quaternary ammonium compound (QAC) did not significantly affect the overall water-absorbing ability of the SIPN coating (the initial WCA on the surface did increase to 70–80°), thus maintaining its excellent antifogging property (even against hot moist air). Meanwhile, the covalently bonded, hydrophobic QAC (5 mol% in the copolymer) rendered the coating strongly antimicrobial, as demonstrated by total kill against both Gram-positive *Staphylococcus epidermidis* and Gram-negative *Escherichia coli*. The antimicrobial action of the SIPN coating was based on contact killing [55], without leaching of bactericidal species, as revealed by a zone of inhibition test. This type of dual-functional coating may find unique applications where both antimicrobial and antifogging properties are desired.

### 3.3 Dual-Functional Antifogging/Self-Healing Coating

Various antifogging surfaces on the basis of hygroscopicity have been developed. However, the soft nature of polymeric coatings makes them susceptible to damage, potentially leading to quick deterioration of the antifogging property [56]. The self-healing function has been a hallmark of living tissues, and has inspired numerous recent efforts in obtaining artificial self-healing materials to extend their lifespan, at the same time maintaining their different functions. It is therefore desirable to integrate self-healing capability into antifogging polymeric coatings to ensure long-term effectiveness and coating durability.

Zhang and He [31] successfully constructed a self-healing antifogging thin film on the basis of partially cross-linked PVA and PAA via a one-step procedure. By tailoring the molar ratio of hydroxyl groups (in excess) in PVA to carboxylic groups in PAA, the cross-linked polymer coating presented an excellent antifogging property, which was mainly attributed to the hydrophilicity and hygroscopicity of the film. Meanwhile, the coating also possessed intrinsic self-healing characteristics toward damage caused by external forces, primarily because of the presence of abundant free hydroxyl groups at the scratched interfaces to reform H-bonds across the interfaces and sufficient chain mobility for the reformation of H-bonds (Fig. 20).

Wang et al. [56] recently developed a healable, highly transparent antifogging and frost-resisting polymeric coating via the LbL assembly of polyethylenimine (PEI) and a blend of hyaluronic acid and PAA (HA-PAA). Because of the remarkable water-absorbing capability, the (PEI/HA-PAA)\*50 coatings showed excellent antifogging properties even under aggressive conditions.

The coating (PEI/HA-PAA)\*50, with 50 bilayers, also exhibited significant self-healing performance. As shown in Fig. 21a, the scratched sample became translucent with an obviously decreased light transmission (~42%). After a 6-h exposure to 65% relative humidity (RH) at room temperature, the scratches on the film

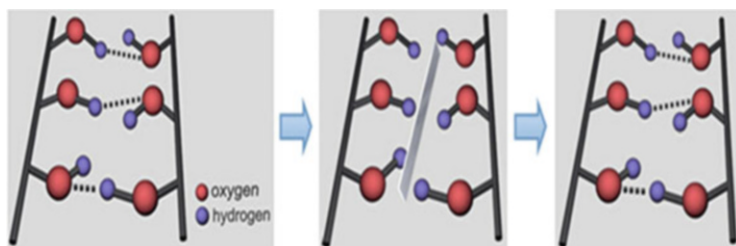


**Fig. 20** Schematic illustration of the self-healing procedure. Reproduced with permission from Zhang et al. [31]

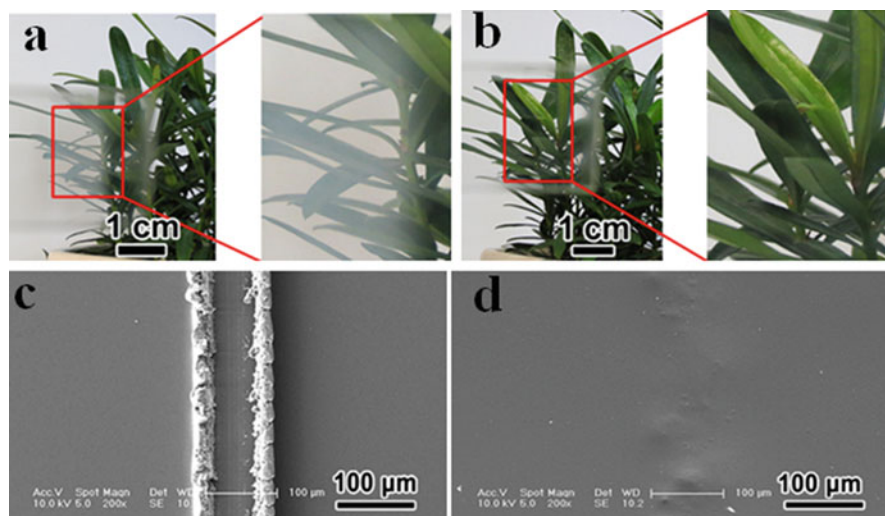


**Fig. 21** Digital images of a (PEI/HA-PAA)\*50 coating on a glass substrate that heals scratches. (a) Scratched coating. (b) Scratched coating after exposure to ~65% RH for 6 h. (c, d) SEM images of a (PEI/HA-PAA)\*50 coating with a cut about 55  $\mu\text{m}$  wide (c) before and (d) after being healed. Reproduced with permission from Wang et al. [56]

completely disappeared (Fig. 21b). SEM images confirmed the capability of the coating to “repair” the scratch upon exposure to moisture (Fig. 21c, d). The reversibility of the electrostatic and hydrogen bonding interactions, as well as the high mobility of PEI, HA, and PAA polyelectrolytes upon exposure to water, endowed the (PEI/HA-PAA)\*50 coating with the ability to heal damage repeatedly, restoring its original transparency and antifogging and frost-resisting properties.

Li et al. [32] further developed self-healing, antifogging films via a convenient dip-coating technique from a solution of hydrogen-bonded PVA and Nafion complexes. The as-prepared PVA-Nafion films were then soaked in an aqueous NaOH solution to induce the formation of PVA crystallites, which acted as physical cross-links and significantly improved the stability of PVA-Nafion antifogging films in

water. The antifogging/frost-resisting properties of the coating originated from the water-absorbing PVA, whereas the reversible hydrogen-binding interactions between PVA and Nafion and the high mobility of the polymer chains triggered by water gave the PVA-Nafion film self-healing ability [32].

## 4 Conclusions and Outlook

Significant progress has been made over the past two decades regarding the preparation of antifogging *polymeric* surfaces. We have briefly reviewed different strategies leading to antifogging polymeric surfaces, including superhydrophilic surfaces, superhydrophobic surfaces, water-absorbing coatings with balanced hydrophobicity/hydrophilicity, as well as several examples of antifogging surfaces with, simultaneously, other interesting functions. Among these, the “wet,” superhydrophilic antifogging coatings have been most extensively investigated. However, several challenges still remain, such as possible poor frost-resisting performance, easy contamination by oily substances, as well as long-term effectiveness and durability, especially in high-humidity environments. The “dry,” superhydrophobic antifogging surface supposedly has its advantage over its “wet” counterparts, but the surface has to be nanotextured to demonstrate good antifogging ability. The fabrication of a dry antifogging surface still remains a major technical challenge, and mechanical robustness and long-term effectiveness is not easy to achieve because of its roughened surface structure. The water-absorbing coatings with balanced hydrophobicity/hydrophilicity represent a different opportunity in obtaining excellent antifogging performance and frost-resisting property in particular. The coating properties, such as mechanical and thermal properties, may be readily tuned by altering the polymer composition to meet different application requirements and the coating preparation may be easily scaled up. As no surface roughening is required, water-absorbing antifogging coatings may be much more advantageous in terms of their mechanical robustness and long-term durability compared to both superhydrophilic and superhydrophobic antifogging surfaces. On the other hand, a delicate balance is needed between the water-absorbing capability and the cross-linking density of the coating to achieve optimal antifogging/frost-resisting performance, which may not be an easy task. There is therefore still great demand for new technologies for production of high-performance antifogging/frost-resisting polymer coatings that are durable, long-term effective, and easy to prepare and scale-up for a variety of applications.

**Acknowledgements** Financial support for this research from USDA/NIFA (Award No.: 2011-67022-30229) is gratefully acknowledged.

## References

1. Briscoe BJ, Galvin KP (1991) The effect of surface fog on the transmittance of light. *Sol Energy* 46:191
2. Raut HK, Dinachali SS, Loke YC, Ganesan R, AnsahAntwi KK, Góra A, Khoo EH, Ganesh VA, Saifullah MS, Ramakrishna S (2015) Multiscale ommatidial arrays with broadband and omnidirectional antireflection and antifogging properties by sacrificial layer mediated nanoimprinting. *ACS Nano* 9:1305
3. Zhang XT, Sato O, Taguchi M, Einaga Y, Murakami T, Fujishima A (2005) Self-cleaning particle coating with antireflection properties. *Chem Mater* 17:696
4. Ohdaira T, Nagai H, Kayano S, Kazuhito H (2007) Antifogging effects of a socket-type device with the superhydrophilic, titanium dioxide-coated glass for the laparoscope. *Surg Endosc* 21:333
5. Knauth A, Weiss M, Dave M, Frotzler A, Haas A (2012) Comparison of antifog methods in endoscopy: what really helps. *Anaesthesist* 61:1036
6. Cebeci FC, Wu Z, Zhai L, Cohen RE, Rubner MF (2006) Nanoporosity-driven superhydrophilicity: a means to create multifunctional antifogging coatings. *Langmuir* 22:2856
7. Howarter JA, Youngblood JP (2007) Self-cleaning and anti-fog surfaces via stimuli-responsive polymer brushes. *Adv Mater* 19:3838
8. Howarter JA, Youngblood JP (2008) Self-cleaning and next generation anti-fog surfaces and coatings. *Macromol Rapid Commun* 29:455
9. Zhang L, Li Y, Sun J, Shen J (2008) Mechanically stable antireflection and antifogging coatings fabricated by the layer-by-layer deposition process and postcalcination. *Langmuir* 24:10851
10. Nuraje N, Asmatulu R, Cohen RE, Rubner MF (2011) Durable antifog films from layer-by-layer molecularly blended hydrophilic polysaccharides. *Langmuir* 27:782
11. Dong H, Ye P, Zhong M, Pietrasik J, Drumright R, Matyjaszewski K (2010) Superhydrophilic surfaces via polymer-SiO<sub>2</sub> nanocomposites. *Langmuir* 26:15567
12. Tahk D, Kim T-I, Yoon H, Choi M, Shin K, Suh KY (2010) Fabrication of antireflection and antifogging polymer sheet by partial photopolymerization and dry etching. *Langmuir* 26:2240
13. Howarter JA, Genson KL, Youghblood JP (2011) Wetting behavior of oleophobic polymer coatings synthesized from fluorosurfactant-macromers. *ACS Appl Mater Interfaces* 3:2022
14. Chevallier P, Turgeon SP, Sarra-Bournet C, Turcotte RL, Laroche GT (2011) Characterization of multilayer anti-fog coatings. *ACS Appl Mater Interfaces* 3:750
15. Chang C, Huang F, Chang H, Don T, Chen C, Cheng L (2012) Preparation of water-resistant antifog hard coatings on plastic substrate. *Langmuir* 28:17193
16. Li J, Zhu J, Gao X (2014) Bio-inspired high-performance antireflection and antifogging polymer films. *Small* 10:2578
17. Brown PS, Atkinson ODLA, Badyal JPS (2014) Ultrafast oleophobic-hydrophilic switching surfaces for antifogging, self-cleaning, and oil-water separation. *ACS Appl Mater Interfaces* 6:7504
18. Di Mundo R, Agostino RD, Palumbo F (2014) Long-lasting antifog plasma modification of transparent plastics. *ACS Appl Mater Interfaces* 6:17059
19. England MW, Urata C, Dunderdale GJ, Hozumi A (2016) Anti-fogging/self-healing properties of clay-containing transparent nanocomposite thin films. *ACS Appl Mater Interfaces* 8:4318
20. Ezzat M, Huang CJ (2016) Zwitterionic polymer brush coatings with excellent anti-fog and anti-frost properties. *RSC Adv* 6:61695
21. Gao X, Yan X, Yao X, Xu L, Zhang K, Zhang J, Yang B, Jiang L (2007) The dry-style antifogging properties of mosquito compound eyes and artificial analogues prepared by soft lithography. *Adv Mater* 19:2213
22. Liu K, Yao X, Jiang L (2010) Recent developments in bio-inspired special wettability. *Chem Soc Rev* 39:3240



23. Drelich J, Chibowski E, Meng DD, Terpilowski K (2011) Hydrophilic and superhydrophilic surfaces and materials. *Soft Matter* 7:9804
24. Drelich J, Chibowski E (2010) Superhydrophilic and superwetting surfaces: definition and mechanisms of control. *Langmuir* 26:18621
25. Wang R, Hashimoto K, Fujishima A, Chikuni M, Kojima E, Kitamura A, Shimohigoshi M, Watanabe T (1997) Light-induced amphiphilic surfaces. *Nature* 388:431
26. Sun Z, Liao T, Liu K, Jiang L, Kim JH, Dou SX (2014) Fly-eye inspired superhydrophobic anti-fogging inorganic nanostructures. *Small* 10:3001
27. Zhao J, Meyer A, Ma L, Ming W (2013) Acrylic coatings with surprising antifogging and frost-resisting properties. *Chem Commun* 49:11764
28. Zhao J, Meyer A, Ma L, Wang X, Ming W (2015) Terpolymer-based SIPN coating with excellent antifogging and frost-resisting properties. *RSC Adv* 5:102560
29. Lee H, Alcaraz ML, Rubner MF, Cohen RE (2013) Zwitter wettability and antifogging coatings with frost-resisting capabilities. *ACS Nano* 7:2172
30. Lee H, Gilbert JB, Angile FE, Yang R, Lee D, Rubner MF, Cohen RE (2015) Design and fabrication of zwitter-wettable nanostructured films. *ACS Appl Mater Interfaces* 7:1004
31. Zhang X, He J (2015) Hydrogen-bonding-supported self-healing antifogging thin films. *Sci Rep* 5:9227
32. Li Y, Fang X, Wang Y, Ma B, Sun J (2016) Highly transparent and water-enabled healable antifogging and frost-resisting films based on poly(vinyl alcohol)-nafion complexes. *Chem Mater* 28:6975
33. Shibraen MHMA, Yagoub H, Zhang X, Xu J, Yang S (2016) Anti-fogging and anti-frosting behaviors of layer-by-layer assembled cellulose derivative thin film. *Appl Surf Sci* 370:1
34. Young T (1805) An essay on the cohesion of fluids. *Philos Trans R Soc Lond* 95:65
35. Balkenede AR, van de Boogaard H, Scholten M, Willard NP (1998) Evaluation of different approaches to assess the surface tension of low-energy solids by means of contact angle measurements. *Langmuir* 14:5907
36. Blossey R (2003) Self-cleaning surfaces-virtual realities. *Nat Mater* 2:301
37. Wenzel RN (1936) Resistance of solid surfaces to wetting by water. *Ind Eng Chem* 28:988
38. Zhang L, Qiao Z, Zheng M, Huo Q, Sun J (2010) Rapid and substrate-independent layer-by-layer fabrication of antireflection- and antifogging-integrated coatings. *J Mater Chem* 20:6125
39. Xu L, He J (2012) Antifogging and antireflection coatings fabricated by integrating solid and mesoporous silica nanoparticles without any post- treatments. *ACS Appl Mater Interfaces* 4:3293
40. Guo Y, Geng W, Sun J (2009) Layer-by-layer deposition of polyelectrolyte-polyelectrolyte complexes for multilayer film fabrication. *Langmuir* 25:1004
41. Nam E, Wong EHH, Tan S, Fu Q, Blencowe A, Qiao GG (2017) Antifogging surface facilitated by nanoscale coatings with controllable hydrophobicity and cross-linking density. *Macromol Mater Eng* 302:160019
42. Grosu G, Andrzejewski L, Veilleux G, Ross GG (2004) Relation between the size of fog droplets and their contact angles with CR39 surfaces. *J Phys D Appl Phys* 37:3350
43. Patel P, Choi CK, Meng DD (2010) Superhydrophilic surfaces for antifogging and antifouling microfluidic devices. *J Assoc Lab Autom* 15:114
44. Cassie ABD, Baxter S (1944) Wettability of porous surfaces. *Trans Faraday Soc* 40:546
45. Cassie ABD (1948) Contact angles. *Discuss Faraday Soc* 3:11
46. Cheng YT, Rodak DE (2005) Is the lotus leaf superhydrophobic? *Appl Phys Lett* 86:144101
47. Wisdom KM, Watson JA, Qu X, Liu F, Watson GS, Chen C-H (2013) Self-cleaning of superhydrophobic surfaces by self-propelled jumping condensate. *Proc Natl Acad Sci U S A* 110:7992
48. Boreyko JB, Chen C-H (2009) Self-propelled dropwise condensate on superhydrophobic surfaces. *Phys Rev Lett* 103:184501

49. Miljkovic N, Enright R, Nam Y, Lopez K, Dou N, Sack J, Wang EN (2013) Jumping-droplet-enhanced condensation on scalable superhydrophobic nanostructured surfaces. *Nano Lett* 13:179
50. Mouterde T, Lehoucq G, Xavier S, Checcon A, Black CT, Rahman A, Midavaine T, Clanet C, Quéré D (2017) Antifogging abilities of model nanotextures. *Nat Mater* 16:658
51. Kim P, Wong T-S, Alvarenga J, Kreder MJ, Adorno-Martinez WE, Aizenberg J (2012) Liquid-infused nanostructured surfaces with extreme anti-ice and anti-frost performance. *ACS Nano* 6:6569
52. Wang Y, Dong Q, Wang Y, Wang H, Li G, Bai R (2010) Investigation on RAFT polymerization of a Y-shaped amphiphilic fluorinated monomer and anti-fog and oil-repellent properties of the polymers. *Macromol Rapid Commun* 31:1816
53. Brown PS, Bhushan B (2015) Mechanically durable, superoleophobic coatings prepared by layer-by-layer technique for anti-smudge and oil-water separation. *Sci Rep* 5:8701
54. Tang R, Muhammad A, Yang J, Nie J (2014) Preparation of antifog and antibacterial coatings by photopolymerization. *Polym Adv Technol* 25:651
55. Zhao J, Ma L, Millians W, Wu T, Ming W (2016) Dual-functional antifogging/antimicrobial polymer coating. *ACS Appl Mater Interfaces* 8:8737
56. Wang Y, Li T, Li S, Sun J (2015) Antifogging and frost-resisting polyelectrolyte coatings capable of healing scratches and restoring transparency. *Chem Mater* 27:8058

**Part III**  
**Insect Contamination-Mitigation**  
**Coatings**

# An Overview of Insect Residue Accretion and Mitigation Strategies on Aerodynamic Surfaces



J. G. Smith Jr., R. Robison, and E. Loth

**Abstract** Research in the utilization of laminar flow technologies on aircraft to improve fuel efficiency (and hence be more environmentally friendly) has been ongoing since the conclusion of World War II. A persistent issue with regard to the maintenance of laminar flow, however, is insect residue accretion. The residues are recurrent, distributed randomly across the surface, and have the potential to exceed heights that can result in a premature transition to turbulent flow. Numerous approaches have been explored over the decades, with success being seen in a research setting. In general, implementation of these approaches in the commercial sector has not been realized. These approaches are briefly discussed herein, along with a general description of the relevant insect characteristics and a discussion of why the reduction of insect accretion on aircraft is such a challenging problem.

**Keywords** Insect · Laminar flow · Mitigation · Physiology

## Contents

1	Introduction .....	218
2	Insects in the Aircraft Flight Path .....	222
3	Insect Physiology .....	222
4	Mitigation Approaches .....	224
4.1	Natural Erosion .....	225
4.2	Disposable Covers .....	226
4.3	Scrapers .....	226
4.4	Fluid Surfaces .....	227

---

J. G. Smith Jr. (✉)  
NASA Langley Research Center, Hampton, VA, USA  
e-mail: [joseph.g.smith@nasa.gov](mailto:joseph.g.smith@nasa.gov)

R. Robison and E. Loth  
Mechanical and Aerospace Engineering, University of Virginia, Charlottesville, VA, USA

4.5	Liquid Discharge Systems .....	227
4.6	Deflectors .....	227
4.7	Coatings .....	228
4.8	Elastic Surfaces .....	229
5	Summary .....	229
	References .....	229

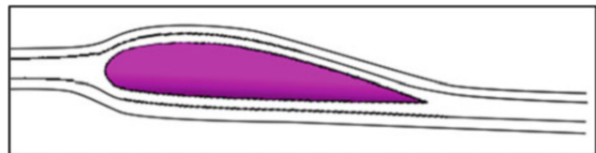
## Abbreviations

AEROMUCO	AERODynamic Surfaces by advanced MULTifunctional Coatings
HLFC	Hybrid laminar flow control
LEFT	Leading edge flight test
LF	Laminar flow
NLF	Natural laminar flow
WWII	World War II

## 1 Introduction

The cost of aviation fuel (i.e., U.S. Gulf Coast Kerosene-Type Jet Fuel) has varied over the past three decades from a low of approximately \$0.30 per gallon in December 1998 to a high of \$3.89 per gallon in July 2008 [1]. During the 3-year period from 2011 to 2014, the average cost was \$2.92 per gallon [2]. However, the falling cost of crude oil has led to a significant decrease in the average price per gallon of aviation fuel, to \$1.55 as of March 20, 2017 [1]. Based on historical data the low cost of aviation fuel, though, will not last indefinitely. Therefore, technologies to improve fuel efficiency remain relevant and have been under investigation for a number of decades. One technology that has been under investigation since the end of World War II (WWII) involves the incorporation of laminar flow (LF) on aircraft. As shown in Fig. 1, LF is defined as the smooth, uninterrupted flow of air over the contour of wings, fuselage, or other parts of an aircraft in flight [3, 4]. It is most often found at the front of a streamlined body, forming a boundary layer, which is described as the region between the surface where the flow has zero velocity to some distance above the surface where air flows at the same velocity as the freestream velocity. If this boundary layer flows in parallel layers, with no energy

**Fig. 1** Laminar flow (LF) across wing. Image: Wikimedia Commons



transfer between layers, the flow is laminar. Laminar flow can be maintained either (1) passively, through natural laminar flow (NLF) induced by airfoil shape; (2) actively, utilizing perforations on the airfoil surface that can introduce suction (LF control); or (3) by hybrid laminar flow control (HLFC) through a combination of these two approaches. Joslin provides a review of LF technologies from the 1930s through the 1990s [3, 4].

As suggested by several studies, the benefit of LF is realized during the cruise portion of the flight profile for long-range subsonic aircraft, where the potential fuel savings can range from 5 to 25% [5]. These projections were based upon a completely smooth surface (i.e., no biological or material imperfections) and varied in the amount of fuel saved depending on the type and amount of LF technologies (i.e., NLF, HLFC, and LFC) employed on the vehicle [5]. In current commercial aircraft, LF technologies are used only in select areas: (1) NLF on the Boeing 787 nacelles [6] and (2) Boeing 737 Max winglets [7] and (3) HLFC on the Boeing 787-9 vertical fin [8]. However, LF in these examples is limited to the front of the structure, since the fit between component parts is not sufficient for maintaining LF over the entire area.

An essential requirement for LF maintenance is that the aircraft surface be smooth. Factors that can disturb LF include adverse pressure gradients, surface roughness/imperfections, heat, and acoustic energy [3, 4]. The disturbance of LF can lead to turbulent flow resulting in increased drag and, consequently, increased fuel consumption. This chapter focuses on surface imperfections, especially those on the wing leading edge, potentially leading to the disruption of LF. The critical height of a particular surface imperfection causing LF transition to turbulent flow depends on a myriad of variables, including the airfoil type and Reynolds number, and can be as small as several microns [3, 4].

Surface imperfections resulting from material issues can be addressed during the fabrication and maintenance of the aircraft. However, significant challenges exist in generating economical and durable LF structures, especially leading edges, and in developing efficient repair techniques, both of which are outside the scope of this review. Biological surface imperfections; namely, residues resulting from impacting insects on the wing leading edge, are not easily addressed, since these are recurrent and randomly scattered across the surface. These residues can potentially be of sufficient height to cause LF disruption across the wing. Examples of insect residue accretion are provided for three different flight tests. Figure 2 depicts 22 residues that were obtained during the Jetstar C-140 Leading Edge Flight Test (LEFT) experiment on September 10, 1985, from Boston, Massachusetts, to Pittsburgh, Pennsylvania [9, 10]. Examination of the unprotected NLF glove that was flown on a Boeing 757 test flight during the late 1980s showed the accumulation of seven insect residues near the attachment line [3, 11]. The part of the flight profile when these residues were accreted on the wing was not determined in either flight experiment.

On an uncoated aluminum panel (Fig. 3) that was flown on the right wing of the Boeing 757 ecoDemonstrator during early Spring of 2015 in Shreveport, Louisiana, a total of 255 insect residues were obtained [12]. As with previous flight tests, when the insect residues were accrued during the flight profile is unknown.

**Fig. 2** Insect residue accretion location with residue heights in inches. Reproduced from Maddalon et al. [10]

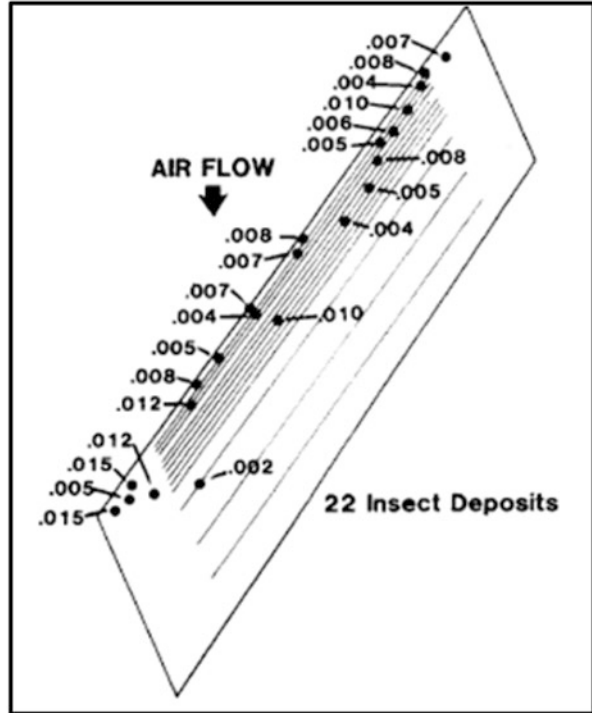


**Fig. 3** Insect residue accretion location on uncoated aluminum panel



Coleman has reviewed details of the relationship between airflow, insect strike location, and the resultant insect residue height [13]. Based on this report and others, it has been shown that a majority of the insect residues accrete on the wing leading edge during the taxi, take-off, and climb, and approach and landing phases of the flight profile. During taxi it was estimated that approximately 54% of the insect residues were accumulated, with an additional approximately 46% accreted during take-off and climb [13, 14]. Insect residues obtained during climb were further broken down to 33% being accreted during climb to approximately 305 m with an additional 13% accreted as the aircraft ascended to 1,525 m. Typically, the location of the residues would be within 15–20% of the stagnation point on the wing leading edge, with the greatest height found around the stagnation point [13–15]. For insect residues accreted past 20% of the stagnation point, Coleman concluded that the surface was “aerodynamically smooth” [16]. An important point to keep in mind concerning accreted insect residues within this 20% area of the stagnation point on the wing surface is that not all of the insect residues would be of sufficient height (i.e., critical residue height) to disrupt LF. Wind tunnel test results suggested that up to 30% of insect residues would be of sufficient height to disrupt LF, in agreement with flight tests results [14]. Once the insect residue critical height is attained, LF transition results in increased drag and, hence, leads to increased fuel consumption, as has been documented [3]. The amount of increased fuel burn would depend on the aircraft, the severity of the LF degradation, and a host of other factors present at the time. For conventional aircraft, this represents a modest increase in fuel consumption, since the vehicles are not designed with LF in mind. However, future aircraft designs employing LF technologies will rely more on the maintenance of LF across wing surfaces to achieve the reductions in fuel consumption.

Using the results of insect residues obtained on coated and uncoated aluminum panels flown on a 2015 flight test on the Boeing 757 ecoDemonstrator, a systems analysis study suggested that one coating composition had the potential to reduce the LF knockdown factor by 10–20%. A broader evaluation determined that by employing this coating a ~1.2% drag reduction recovery could be attained. For a single-aisle aircraft incorporating an NLF wing design, this translates into a potential total drag reduction of ~3.3% [17].

An enhanced systems analysis study looked at the effect of insect residues accreted in the wing leading edge area upon both fuel efficiency and economic benefit for a 150-seat aircraft designed with forward swept NLF wings [18]. For pristine clean wings, the improvement in fuel efficiency was determined to be 9.2% for long hauls and this result was comparable to prior studies [5]. Since no insect residue mitigation technologies were employed, it was assumed that the wings would be cleaned periodically during overnight hours (10 p.m. to 6 a.m.) when the vehicle was not operated. Following this approach, the benefit of the NLF technology would gradually diminish with time until the vehicle was cleaned so as to restore performance. This restorative approach would be governed by the economic benefit (if any) derived at the time that would depend upon the fuel price, rapidity of insect residues of critical height accreted, interval between wing cleanings, and the cost of cleaning (personnel and supplies). It was estimated that the fuel efficiency



improvement would decrease by approximately 50% (to 4.4%) for an accretion of around 400 insect residues of critical height.

## 2 Insects in the Aircraft Flight Path

To better understand the adhesion issue once insects impact the aircraft surface and leave residues, one must step back and look at the insect, its physiology, and its residence in the flight envelope. Research determining insect aerial population density and distribution, as well as the atmospheric conditions present at the time the insects were collected, was conducted in the late 1920s and early 1930s [19–21]. This study was performed in southern Louisiana, with the results documented in several publications [3, 13, 22–24]. A total of 22,580 insect specimens were collected during the course of the study, at elevations between 61 and 1,524 m, with the order Diptera constituting the largest percentage of these collected insects [19]. The order Diptera refers to an insect with one pair of wings; the order includes true flies, mosquitoes, and gnats [25]. Another study found that the aerial populations were mostly “small or light-bodied” insects with “relatively large wing surface compared with body mass” with the most common insects being of the orders Diptera, Aphididae, and Hymenoptera [21]. Overall the studies revealed that most insects were light (<10 mg) and small (<25 mm in length), occupying altitudes <152 m. The aerial concentration was greatest at ground level, decreasing with height. In addition, the greatest insect populations were prevalent during atmospheric conditions of light winds (2.6–5.1 m/s), high humidity, and temperatures ranging from 21 to 29°C. However, a correlation with the atmospheric conditions and insect population density could not be made [13]. These atmospheric conditions can be found sometime during the year around many of the world’s airports, thereby placing aircraft surfaces at a constant risk for insect strikes during the aforementioned portions of the flight profile. Knowing that an aircraft employing LF technologies would be sensitive to such natural imperfections (i.e., insect residue accretion), research has been ongoing since the conclusion of WWII to develop a technology to mitigate insect residue adhesion [3, 13].

## 3 Insect Physiology

Why does an impacting insect adhere to the vehicle surface? The answer to this question requires an understanding of insect physiology with respect to wound healing. An insect consists primarily of an exoskeleton and hemolymph (i.e., blood), with the latter accounting for up to 40% of the insect’s body volume [26]. Hemolymph is contained within an open circulatory loop inside the insect, unlike the closed one present in vertebrates. In general, hemolymph is a slightly acidic complex mixture containing various quantities of proteins, lipids, free amino

acids, trehalose (an abundant sugar), inorganic compounds, proenzymes, and hemocytes (the common name for various cells present in the hemolymph) and having a specific gravity slightly greater than one [26–31]. Depending upon the different life stages of the insect and the insect type, these fluid characteristics can vary.

The insect residue accretion process begins with an insect present in the flight path of the aircraft impacting the vehicle surface (e.g., wing leading edge surface), with sufficient velocity (i.e., rupture velocity) to burst its exoskeleton. Results from wind tunnel experiments have indicated that the rupture velocity for various insects ranged from 10 to 20 m/s, with a mean value of  $10.8 \pm 1.7$  m/s being determined in the natural environment [13]. Due to similarities in the resultant residue size found on aircraft in service impacted with insects, the fruit fly (*Drosophila melanogaster*) is the typical insect of choice in laboratory and wind tunnel testing [13]. The rupture velocity for a fruit fly has been reported to be approximately 13.9 m/s [22].

Upon rupture of the insect exoskeleton, the released hemolymph has a consistency similar to that of water, thus allowing it to spread downstream from the impact location over the surface as a result of the impact force and aerodynamic shear. Even though the insect is no longer alive, a number of components present in the hemolymph initiate a complex series of intrinsic/innate biological reactions, immediately resulting in an increase in hemolymph viscosity, along with the formation of a network of fibrils (i.e., a scaffold) to aid in the wound-healing process (i.e., coagulation) [32]. This coagulation process involves several hemolymph components that include phenoloxidase and hemocytes. Phenoloxidase is created due to the cleavage of prophenoloxidase (an inactive enzyme) by a serine protease, once an injury (e.g., as a result of the impact event) occurs. This activated enzyme then participates in the deposition of melanin (a phenolic biopolymer) at the wound site (i.e., the aircraft surface) via melanogenesis [33–35]. Two chemical reactions involving phenoloxidase have been reported: the orthohydroxylation of phenols to catechols, with the subsequent oxidation of the catechols to o-quinones [36]. Strong cytotoxic materials such as reactive oxygen species and other intermediates are reportedly formed at this time as well [37, 38]. A normal wound-healing event is rapid; resulting in the initial formation of a soft gelatinous mass. Chemical and biological reactions continue in this soft mass via melanization, forming a hard mass that is confined to the injured area [39]. In the case of the insect impacting a wing leading edge, the released hemolymph components become activated all at once as the insect residue (i.e., hemolymph and insect exoskeleton parts) spreads across the wing surface, rapidly coagulating upon contact with the environment [39]. The fluid is extremely sticky; it adheres to a myriad of surfaces including glass, plastic, and metal [31, 35, 39, 40]. The height of the solidified hemolymph, and potentially entrapped insect exoskeleton parts, can exceed the critical height on an LF wing so as to induce localized boundary layer transitions. The insect (i.e., invertebrate) coagulation process is markedly different from that present in vertebrates. The process is not fully understood to date, even though it has been studied for more than a century. Further details concerning this healing process can be found in three review articles on the subject [41–43].

From wind tunnel tests performed at the University of Virginia with flightless fruit flies, three distinct types of insect residue were found to be accreted upon the surface, depending upon the impact angle. These were (1) hemolymph, (2) red residue from eye pigments, and (3) exoskeleton parts entrapped within the hemolymph [24, 44, 45]. Residues containing exoskeleton parts and hemolymph were primarily observed to occur for impact angles ranging from 70 to 90° (normal to the surface), while hemolymph was the primary residue for impact angles occurring at  $\leq 40^\circ$  (i.e., glancing). At intermediate impact angles, both hemolymph and the red residue were most common, with occasional exoskeleton parts being incorporated in the residue. Since exoskeleton parts within the residue can result in heights in the order of 500–1,000  $\mu\text{m}$  or more, the area near the stagnation point is the region where heights tended to be largest.

## 4 Mitigation Approaches

Regarding the subject of this chapter, the “Holy Grail” in the maintenance of LF throughout the entire aircraft flight profile is “zero insect residues” adhered to the vehicle surface. To attain this goal, research regarding this insect residue adhesion problem commenced shortly after the end of WWII [13]. Initially, natural environmental exposure (i.e., cold conditions leading to embrittlement, wind shear, flying through clouds) of the residues was thought to be sufficient to remove the residues from the surface; however, this removal was time- and airspeed-dependent [3, 10, 13, 23, 46, 47]. So as to obtain a more reliable approach, numerous strategies involving sacrificial coatings, various mechanical devices such as scrapers and deflectors, and physical and soluble coverings were explored. In many instances, these strategies provided good results for the take-off and climb portions of the flight profile. However, they either were not operated or were not present during the approach and landing phases, leading to the potential accumulation of insect residues that would necessitate removal prior to the following flight. From a commercial operational viewpoint, these strategies were not practical for various reasons, including mechanical complexity and/or increased weight. Thus, an approach that is active during the entire flight profile and does not have to be reapplied or activated by the crew to be beneficial was desirable. To implement such an approach, research into non-sacrificial coatings was initiated in the 1970s. While considerable progress has been made in understanding the problem and reducing residue numbers, a non-sacrificial coating is still (in the authors’ opinion) far from attaining “zero insect residue accretion”.

As seen in Fig. 4, many of the approaches can trace their roots back to the onset of research in the various concepts, with periods of active research in the area followed by periods during which the results were evaluated and scientific understanding progressed due to additional information gleaned from the prior work. A brief description of these various approaches is discussed below. The intent of the authors is not to go into detail, since an adequate description of each approach can be found

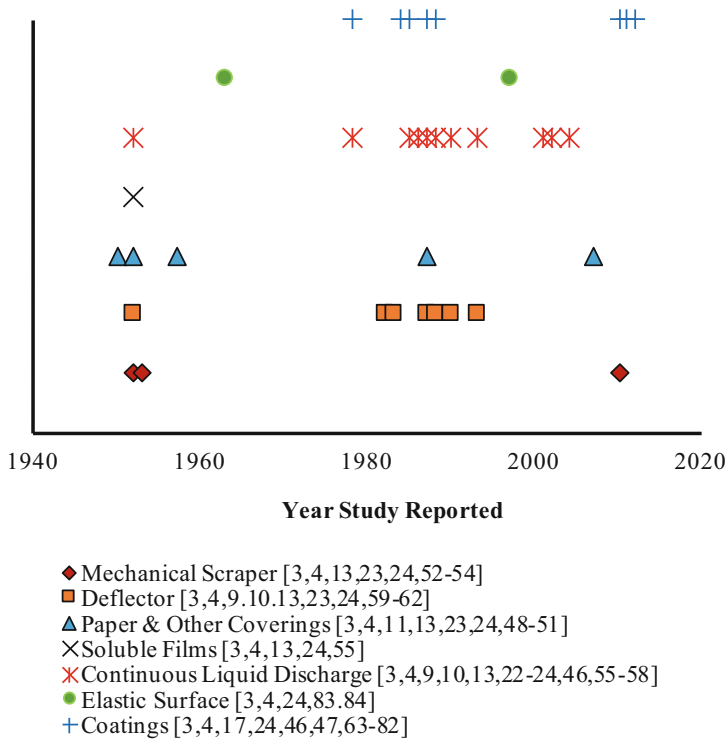


**Fig. 4** Insect residue mitigation approaches 1945–2015

in publications by Coleman [13], Joslin [3, 4], and Kok [24] (and the references contained within), as well as others.

### 4.1 Natural Erosion

An example of natural erosion was reported for a series of flight tests simulating airline service flights that evaluated LF leading edge technologies utilizing a Jetstar C-140 (i.e., LEFT). Observations from these tests indicated that insect residues that had accreted on the test article surface eroded away after time and that surfaces were naturally washed as the aircraft traversed through cloud cover [10]. In addition, earlier investigators reported that a combination of airspeed and low temperatures at altitude could erode accreted insect residues [13].

However, this process cannot guarantee the removal of insect residues sufficient for the maintenance of LF. For example, insect residues accreted upon take-off and climb [at a speed of 180 knots (93 m/s)] on the wing leading edge of the Jetstar at NASA Dryden (now Armstrong) Flight Research Center resulted in premature transition at cruise, as determined from pitot probe data [46, 47]. Cruise conditions

were (1) an altitude of 11,600 m, (2) speed of Mach 0.7, and (3) an airplane lift coefficient,  $C_L$ , of 0.3 [45, 46]. Post-flight inspection found that the insect residues were still present [46, 47]. These contradictory results suggest that natural erosion processes are insufficient as a reliable mitigation approach.

## 4.2 *Disposable Covers*

Paper or fabric covers attached to the wing leading edge just after the stagnation point have been flown successfully for >200 h on aircraft evaluating LF technologies [3, 11, 23, 48–50]. This concept, though, was beneficial only upon take-off, as the coverings were released from the vehicle once cruising altitude was attained, as detailed by Head et al. [51]. Cover removal was achieved using either a tear strip or by stalling the aircraft. However, the release process was not always successful, as found during three test flights of a Boeing 757 to protect an NLF glove [3, 11]. The first two flights were unsuccessful at cover removal, requiring roller coaster type maneuvers to eventually remove the cover. Covers based on vinyl copolymers sprayed on the wing surface were investigated in the laboratory [13, 23]. Removal from the surface via peeling by the airflow was proposed once the cover was torn at the leading edge.

## 4.3 *Scrapers*

Mechanical devices such as fine wires, felt pads, and scrapers (types include those by Armstrong-Whitworth and by Handley Page) have been evaluated on flight tests [13, 23, 52, 53]. The fine wire worked well on metal surfaces and removed roughness in two or three passes. On other surfaces (e.g., painted, plastic), the upper portions of the insect residues were removed but the remaining portions that were estimated to exceed the critical height were crushed. Replacement of the wires with felt pads and flowing water was successful. This device could potentially be used during times of the flight profile when insects were encountered. However, issues with drag when the device was not in use were not addressed [13, 23]. In addition, the quantity of water required to refill the reservoir after each flight would present a problem in terms of both weight and expense. The Handley Page Scraper relied upon dry felt pads to clean the surface [13, 23]. The device was not tested, but was proposed to be jettisoned at the wing tip after one pass across the surface, thus eliminating the drag problem. A mechanical device employing felt pads to clean the wing surface has been used recently on gliders [54].

#### ***4.4 Fluid Surfaces***

Liquid-based sacrificial coatings/surfaces to prevent the accumulation of insect residues have been evaluated in a wind tunnel setting [13, 55]. Materials that were evaluated included glycerine, blends of glycerine and gelatin, and silicone fluids. These fluids reportedly trapped an impacting insect on this temporary surface that could then be removed by washing with water. Drawbacks to this approach were that (1) it could only be used on the take-off and climb phase of the flight profile and (2) it was successful only if the aircraft surface was adequately covered by the sacrificial material; otherwise insect residues adhered to the surface.

#### ***4.5 Liquid Discharge Systems***

A modification of the fluid surface approach involved the release of liquids (e.g., water, detergents, deicing fluids, enzymes, surfactants) through orifices on the wing surface [9, 10, 13, 22, 23, 46, 55–58]. This modification was as successful as the approach outlined in Sect. 4.4., but suffered the same issues as those mentioned in Sect. 4.4., plus system weight. Attempts, by the reapplication of fluid, to remove insect residues that had already adhered to the surface proved unsuccessful.

#### ***4.6 Deflectors***

An approach based on deflectors was evaluated in both wind tunnel and flight tests [13, 23, 59]. The deflector was envisioned to allow insects to impact this extended sacrificial surface during times when insects would be encountered, with the deflector being pulled back toward the vehicle leaving a clean wing leading edge at cruise altitudes. An early version involved a curved plate extended through an opening in the wing leading edge. This, along with several subsequent variants, was successful at protecting the upper wing, but suffered from several issues including breaks in the wing surface once the deflector was retracted, resulting in ridges that could be potentially as bad as the accreted residue. A related concept is the Krueger Flap [9, 10, 60, 61]. The primary use of this flap is as a high lift device for large aircraft during take-off and climb; the flap would subsequently be retracted and stowed against the lower wing. The mitigation of insect residues on the wing leading edge was seen as a secondary benefit that was realized after flap stowage. While LF across the upper wing surface could be attained, LF across the lower wing was a concern due to difficulties surrounding the tight tolerances required for flap stowage during the cruise portion of the flight profile. Regarding insect residue mitigation, the device was evaluated in wind tunnel tests and on the Jetstar C-140 LEFT and Boeing 757 HLFC flight experiments [9, 10, 60, 61]. Recently, it was tested on the left

wing of the Boeing 757 ecoDemonstrator flights conducted in Shreveport, Louisiana, during the spring of 2015 [62].

## 4.7 Coatings

Many of the approaches discussed thus far were able to mitigate the accretion of insect residues during the take-off and climb phase of the flight profile. Insect residues acquired during the approach and landing phases would be an issue for subsequent flights unless the surfaces were cleaned once the vehicle was at the airport gate. This is not conducive to the operation of commercial airlines, where time would be needed to perform such a task; thus, there is a need for an approach that is active during all phases of the flight profile. Coatings were seen as being able to fulfill this requirement. As mentioned previously, the “Holy Grail” here would be the accretion of “zero insect residues”. Early flight tests conducted from NASA Dryden (now Armstrong) Flight Research Center to airports in California, Texas, and Florida during 1977 evaluated four coatings (Teflon<sup>®</sup> and commercial off-the-shelf materials used to repel rain on aircraft) plus an aluminum control on the wing leading edge [46, 47]. Insect residues accreted on these surfaces on a majority of the flights. However, the residues were noted to be easier to wipe off the low surface energy Teflon<sup>®</sup> coating. A subsequent university study evaluated surface energy and surface roughness effects for a wide range of coatings that were attached to the overhead rack of a vehicle driven in coastal Virginia during the summer of 1984 [63–66]. From that study, surface roughness was determined to have had a minimal effect on residue adhesion. Recent coating studies were performed under the Boeing 757 ecoDemonstrator [17, 67–74] and AEROMUCO (AERodynamic Surfaces by advanced MUltifunctional Coatings) [24, 75–81] projects in the United States and Europe, respectively. Numerous coating compositions were evaluated in wind tunnel tests. Several coating compositions developed by NASA were flown on the right wing of the Boeing 757 ecoDemonstrator in the late spring of 2015 in Shreveport, Louisiana [12]. Results compared with those for the uncoated aluminum panels indicated that surface energy and surface roughness (as induced by fillers) were important for reducing the numbers of insect residues. The best performing material saw an approximately 40% reduction in the number of residues. The difference in results between the flight test and the earlier road test, presumably, is due to the speeds attained by the two vehicles. As previously stated, a systems analysis study suggested that one coating composition from the ecoDemonstrator flight test had the potential to reduce the LF knockdown factor by 10–20% [17]. A broader evaluation estimated that a ~1.2% drag reduction recovery could be achieved, which would translate into a potential total drag reduction of ~3.3% for a single-aisle aircraft incorporating an NLF wing design [17]. Other material parameters besides surface energy and roughness could influence residue adhesion on the coatings; however, the identification of such parameters remains elusive at this time due to limitations in scientific knowledge.

## 4.8 Elastic Surfaces

In the 1960s, the concept of using an elastic surface to prevent insect residue on aircraft was evaluated [82]. It was anticipated that insects impacting this surface would recoil off the surface due to the elastic nature of the material acting as a spring. Various rubber thicknesses and compositions were flight-tested. On visual observation there were traces of dried hemolymph and, occasionally, insect exoskeleton parts. While this surface was promising, rain and hail were concerns, since they could result in damage to the flexible surface. A combination of the coating and elastic approaches was performed in university research during the late 1980s [83]. Coated panels, having either no backing or a foam rubber backing, were impacted with fruit flies using an insect delivery device, and reductions in residue height were revealed in the latter compared with the former.

## 5 Summary

As seen from this brief synopsis, research in mitigating insect residue accretion upon aircraft surfaces, specifically wing leading edges, for the maintenance of LF is quite old, spanning decades. Essentially no new concepts have been brought forth, with several concepts dating back to the conclusion of WWII. These early concepts and the following modifications over the years have demonstrated some level of success in research settings. However, acceptance in the commercial sector has not been achieved due to a number of factors, including the complexity of the concept and the ability to guarantee “zero insect residue accretion” on the surface. One technology – the Krueger flap – is an exception; however, the mitigation of insect residues is a secondary benefit of the technology. As fuel burn and environmental concerns justify the incorporation of LF technologies on aircraft, the mitigation of insect residues will become ever more important. It is anticipated that an ultimate solution will be achieved. This may come about by a combination of several concepts, as well as by a greater scientific understanding of the insect residue accretion process.

## References

1. US Energy Information Administration (2017) U.S. Gulf Coast kerosene-type jet fuel spot price FOB, US\$ per gallon. <http://www.indexmundi.com/commodities/?commodity=jet-fuel>. Accessed 20 Mar 2017
2. Industrial Equipment News (2017) Lower fuel costs improving airlines profits. <http://www.ien.com/operations/news/20852560/lower-fuel-costs-improving-airlines-profits>. Accessed 18 Feb 2017
3. Joslin R (1998) Overview of laminar flow control. National Aeronautics and Space Administration, NASA/TP-1998-208705
4. Joslin R (1998) Aircraft laminar flow control. *Annu Rev Fluid Mech* 30:1–29



5. Kirchner ME (1987) Laminar flow: challenge and potential. In: Hefner JF, Sabo FE (Compilers) Research in natural laminar flow and laminar-flow control part 1. NASA CP-2487, pp 25–45
6. Boeing (2017) 787 Dreamliner by design: superior technology. <http://www.boeing.com/commercial/787/by-design/#/superior-tech>. Accessed 20 June 2017
7. Boeing (2017) 737 Max at winglet. <http://www.boeing.com/commercial/737max/737-max-winglets/>. Accessed 20 June 2017
8. Boeing (2013) Welcome to the family: meet the 787-9. <http://www.boeing.com/commercial/787/frontiers-787-9-october-2013/>. Accessed 20 June 2017
9. Wagner RD, Fischer MC (1983) Developments in the NASA transport aircraft laminar flow program. AIAA 1983-90 presented at AIAA 21st aerospace sciences meeting, Reno, 10–13 Jan 1983
10. Maddalon DV, Fisher DF, Jennett LA, Fischer, MC (1987) Simulated airline service experience with laminar flow control leading edge systems. In: Hefner JF, Sabo FE (Compilers) Research in natural laminar flow and laminar-flow control part 1. NASA CP-2487, pp 195–218
11. Runyan LJ, Bielak GW, Behbehani R, Chen AW, Rozendaal RA (1987) 757 NLF glove flight test results. In: Hefner JF, Sabo FE (Compilers) Research in natural laminar flow and laminar-flow control part 3. NASA CP-2487, pp 795–818
12. NASA media advisory 15-022 (2017) NASA, Boeing ecoDemonstrator 757 plane come to Shreveport for bug research. <https://www.nasa.gov/langley/nasa-boeing-ecodemonstrator-757-plane-come-to-shreveport-for-bug-research>. Accessed 20 Mar 2017
13. Coleman WS (1961) Roughness due to insects. In: Lachman GV (ed) Boundary layer and flow control: its principles and applications, vol 2. Pergamon Press, Oxford, pp 682–747
14. Maresh JL, Bragg MB (1984) The role of airfoil geometry in minimizing the effect of insect contamination of laminar flow sections. AIAA 84-2170 presented at AIAA 2nd applied aerodynamics conference, Seattle, 21–23 Aug 1984
15. Atkins PB (1951) Wing leading edge contamination by insects. Note 17
16. Coleman WS (1959) The characteristics of roughness from insects as observed for two-dimensional, incompressible flow past airfoils. *J Aerosp Sci* 25:264–280
17. Lin JC, Whalen EA, Eppink JL, Siochi EJ, Alexander MG, Andino MY (2016) Innovative flow control concepts for drag reduction. AIAA 2016-0864 presented at AIAA SciTech Forum, 54th AIAA aerospace sciences meeting, San Diego, 4–8 Jan 2016
18. Wicke K, Linke F, Gollnick V, Kruse M (2016) Insect contamination impact on operational and economic effectiveness of natural laminar flow aircraft. *J Aircr* 53:158–167
19. Glick PA (1939) The distribution of insects, spiders, and mites in the air. *US Dept Agric Tech Bull No.* 673
20. Hardy AC, Milne PS (1938) Studies in the distribution of insects by aerial currents – experiments in aerial tow-netting from kites. *J Anim Ecol* 7:199–229
21. Freeman JA (1945) Studies in the distribution of insects by aerial currents – the insect population of the air from ground level to 300 feet. *J Anim Ecol* 14:128–154
22. Young T, Humphreys B (2004) Liquid anti-contamination systems for hybrid laminar control flow aircraft: a review of critical issues and important experimental results. *J Aerosp Eng* 218:267–277
23. Lachman GV (1960) Aspects of insect contamination in relation to laminar flow aircraft. A.R. C. Technical Report C.P. No. 484
24. Kok M, Smith Jr JG, Wohl CJ, Siochi EJ, Young TM (2015) Critical considerations in the mitigation of insect residue contamination on aircraft surfaces – a review. *Prog Aerosp Sci* 75:1–14
25. Meyer JR (2013) General entomology. North Carolina State University <http://www.cals.ncsu.edu/course/ent425/index.html>. Accessed 20 Mar 2017
26. Wyatt GR, Pan ML (1978) Insect plasma proteins. *Annu Rev Biochem* 47:779–817
27. Wyatt GR, Loughheed TC, Wyatt SS (1956) The chemistry of insect hemolymph-organic components of the hemolymph of the silkworm, *Bombyx Mori*, and two other species. *J Gen Physiol* 39:853–868

28. Wyatt GR, Kalf GF (1957) The chemistry of insect hemolymph II. Trehalose and other carbohydrates. *J Gen Physiol* 40:833–847
29. Nation JL (2001) *Insect physiology and biochemistry*. CRC Press, Taylor and Francis Group, Boca Raton
30. Theopold U, Schmidt O, Soderhall K, Dushay MS (2004) Coagulation in arthropods: defense, wound closure and healing – review. *Trends Immunol* 25:289–294
31. Evans PD, Wigglesworth VB (1990) *Advances in insect physiology*, vol 22. Academic Press, London
32. Scherfer C, Karlsson C, Loseva O, Bidla G, Goto A, Havemann J, Dushay M, Theopold U (2004) Isolation and characterization of hemolymph clotting factors in *Drosophila Melanogaster* by a pullout method. *Curr Biol* 14:625–629
33. De Gregorio E, Han SJ, Lee WJ, Baek MJ, Osaki T, Kawabata SI, Lee BL, Iwanaga S, Lemaitre B, Brey PT (2002) An immune responsive serpin regulates the melanization cascade in *Drosophila*. *Dev Cell* 3:581–592
34. Sugumaran M, Duggaraju R, Generozova F, Ito S (1999) Insect melanogenesis. 11. Inability of *Manduca phenoloxidase* to act on 5,6-dihydroxyindole-2-carboxylic acid. *Pigment Cell Res* 12:118–125
35. Sugumaran M, Nellaiappan K (2000) Characterization of a new phenoloxidase inhibitor from the cuticle of *Manduca sexta*. *Biochem Biophys Res Commun* 268:379–383
36. Duckworth HW, Coleman JE (1970) Physicochemical and kinetic properties of mushroom tyrosinase. *J Biol Chem* 245:1613–1625
37. Nappi AJ, Ottaviani E (2000) Cytotoxicity and cytotoxic molecules in invertebrates. *BioEssays* 22:469–480
38. Cerenius L, Soderhall K (2004) The prophenoloxidase-activating systems in invertebrates. *Immunol Rev* 198:116–126
39. Gregoire CH (1953) Blood coagulation in arthropods. 111. Reactions of insect hemolymph to coagulation inhibitors of vertebrate blood. *Biol Bull* 104:372–393
40. Mandato CA, Diehl-Jones WL, Downer RGH (1996) Insect hemocyte adhesion in vitro – inhibition by apolipophorin I and an artificial substrate. *J Insect Physiol* 42:143–148
41. Theopold U, Li D, Fabbri M, Scherfer C, Schmidt O (2002) The coagulation of insect hemolymph. *Cell Mol Life Sci* 59:363–372
42. Sugumaran M (2002) Comparative biochemistry of eumelanogenesis and the protective roles of phenoloxidase and melanin in insects. *Pigment Cell Res* 15:2–9
43. Dushay MS (2009) Insect hemolymph clotting. *Cell Mol Life Sci* 66:2643–2650
44. Krishnan K, Milionis A, Tetteh F, Starr M, Loth E (2015) Fruit fly impact outcomes and residue components on an aerodynamic surface. AIAA 2015-1279 presented at AIAA SciTech, 53rd AIAA aerospace sciences meeting, Kissimmee, 5–9 Jan 2015
45. Krishnan K, Robison R, Tetteh E, Loth E, Farrell T, Crouch J, Berry D (2016) Characterization of insect residue on an aerodynamic leading edge. AIAA 2016-3445 presented at AIAA AVIATION Forum, 8th AIAA atmospheric and space environments conference, Washington, 13–17 June 2016
46. Peterson JB Jr, Fisher DF (1978) Flight investigation of insect contamination and its alleviation. In: *Proceedings of the CTOL transport technology conference*, Hampton, NASA CP 2036, Part I, 28 Feb–3 Mar 1978, pp 357–373
47. Fisher DF, Peterson JB Jr (1978) Flight experience on the need and use of inflight leading edge washing for a laminar flow airfoil. AIAA 1978-1512 presented at AIAA aircraft systems and technology meeting, Los Angeles, 21–23 Aug 1978
48. Smith F, Higton DJ (1950) Flight tests on king cobra FZ440 to investigate the practical requirements for the achievement of low profile drag coefficients on a low drag aerofoil. R&M No. 2375, HMSO, London
49. Gray WE, Davies H (1952) Note on the maintenance of laminar flow wings. R&M 2485. British Aeronautical Research Council (ARC)

50. Groth EE, Carmichael BH, Whites RC, Pfenninger W (1957) Low drag boundary layer suction experiments in flight on the wing glove of a F94-A airplane – Phase II: suction through 69 slots. NAI-57-318 (BLC-94) (Contract AF-33(616-3108)). Northrop Aircraft
51. Head MR, Johnson D, Coxon M (1955) Flight experiments on boundary-layer control for low drag. R. & M. No. 3025. British ARC
52. Beech G, Nicholas WM (1953) A mechanical type of scraper for dealing with insect contamination of aircraft wings. Armstrong Whitworth Report No WT 53/18
53. Anon (1953) Note on the Blackburn and general aircraft wind-tunnel tests of the A.W.A. fly scraper. Report to the Boundary Layer Control Committee, B.L.C.C. Paper No. B 0142, MOS, London
54. DG Group (2017) A bug cleaner with “garage”. <http://www.dg-flugzeugbau.de/en/library/a-bug-cleaner>. Accessed 20 Mar 2017
55. Coleman WS (1952) Wind tunnel experiments on the prevention of insect contamination by means of soluble films and by liquids discharged over the surface. Report to the Boundary Layer Control Committee, BLCC Note 39. MOS, London
56. Croom CC, Holmes BJ (1986) Insect contamination protection for laminar flow surfaces. In: Langley symposium on aerodynamics, vol 1, pp 539–556
57. Croom CC, Holmes BJ (1985) Flight evaluation of an insect contamination protection for laminar flow wings. SAE Paper 850860 presented at the general aviation aircraft meeting and exposition, Wichita, 16–19 Apr 1985
58. O'Donoghue D, Young TM, Pembroke JT, O'Dwyer TF (2002) An investigation of surfactant and enzyme formulations for the alleviation of insect contamination on hybrid laminar flow control (HLFC) surfaces. *Aerosp Sci Technol* 6:19–29
59. Coleman WS (1952) Development of a mechanical device for the protection of wings against insect contamination. Report to the Boundary Layer Control Committee, BLCC Note 34. MOS, London; Blackburn and General Aircraft Ltd. Note WT 128
60. Tamigniaux TLB, Stark SE, Brune GW (1987) An experimental investigation of the insect shielding effectiveness of a Kreuger flap/wing airfoil configuration. AIAA 1987-2615 presented at 5th applied aerodynamics conference, fluid dynamics and co-located conferences, Monterey, 17–19 Aug 1987
61. Pearce WE (1982) Evaluation of laminar flow control systems concepts for subsonic commercial transport aircraft. National Aeronautics and Space Administration, NASA CR 159252
62. Backgrounder: the Boeing ecode demonstrator Dent Prog (2017) [http://www.boeing.com/resources/boeingdotcom/principles/environment/pdf/Backgrounder\\_ecoDemonstrator.PDF](http://www.boeing.com/resources/boeingdotcom/principles/environment/pdf/Backgrounder_ecoDemonstrator.PDF). Accessed 20 Mar 2017
63. Eiss NS, Wightman JP (1983) A fundamental approach to the sticking of insect residues to aircraft wings: semi-annual technical report. National Aeronautics and Space Administration, NASA CR 173063
64. Eiss NS, Wightman JP, Gilliam DR, Siochi EJ (1984) A fundamental approach to the sticking of insect residues to aircraft wings: annual technical report. National Aeronautics and Space Administration, NASA CR 173721
65. Eiss NS, Wightman JP, Gilliam DR, Siochi EJ (1985) A fundamental study of the sticking of insect residue to aircraft wings. National Aeronautics and Space Administration, NASA CR 176231
66. Siochi EJ, Eiss NS, Gilliam DR, Wightman JP (1987) A fundamental study of the sticking of insect residues to aircraft wings. *J Colloid Interface Sci* 115:346–356
67. Barnstorff K (2017) NASA tests green aviation technology on Boeing ecode demonstrator. <https://www.nasa.gov/aero/nasa-tests-green-aviation-technology-on-boeing-ecode-demonstrator.html>. Accessed 20 Mar 2017
68. Smith J, Lorenzi T, Wohl C, Penner R, Siochi E (2012) Influence of surface energy on insect residue adhesion. Paper presented at the 35th annual meeting of the Adhesion Society, New Orleans, 26–29 Feb 2012

69. Wohl CJ, Smith JG, Penner RK, Gardner JM, Connell JW, Siochi EJ (2013) Polyimide-based nanocomposite coatings for contamination mitigation of aircraft surfaces. Paper presented at the 36th annual meeting of the Adhesion Society, Daytona Beach, 3–6 Mar 2013
70. Wohl CJ, Smith JG, Gardner JM, Penner RK, Connell JW, Siochi EJ (2014) Novel epoxy particulate composites for mitigation of insect residue adhesion on wing leading edge surfaces. Paper presented at the 37th annual meeting of the Adhesion Society, San Diego, 23–26 Feb 2014
71. Shanahan MH, Wohl CJ, Smith JG Jr, Doss JR, Penner RK, Gardner JM, Connell JW, Siochi EJ (2015) Flight testing surfaces engineered for mitigating insect adhesion on a Falcon HU-25C. Paper presented at the 38th annual meeting of the Adhesion Society, Savannah, 20–25 Feb 2015
72. Wohl CJ, Doss JR, Shanahan MH, Smith JG Jr, Penner RK, Connell JW, Siochi EJ (2015) Influence of surface properties and impact conditions on adhesion of insect residues. Paper presented at the 38th annual meeting of the Adhesion Society, Savannah, 20–25 Feb 2015
73. Wohl CJ, Smith JG Jr, Palmieri FL, Shanahan MH, Penner RK, Connell JW, Siochi EJ (2017) Fruit fly impact dynamics on fluorinated epoxy composite surfaces. Paper presented at the 40th annual meeting of the Adhesion Society, St. Petersburg, FL, 26 Feb–1 Mar 2017
74. Bayer IS, Krishnan KG, Robinson R, Loth E, Berry DH, Farrell TE, Crouch JD (2016) Thermal alternating polymer nanocomposite (TAPNC) coating designed to prevent aerodynamic insect fouling. *Sci Rep* 6:38459. <https://doi.org/10.1038/srep38459>
75. AERodynamic Surfaces by advanced Multifunctional Coatings (AEROMUCO) (2017) [http://cordis.europa.eu/project/rcn/96952\\_en.html](http://cordis.europa.eu/project/rcn/96952_en.html). Accessed 20 Mar 2017
76. Young TM, Tobin EF, Kok M (2012) Laboratory testing of insect contamination for laminar flow applications using an insect-impact test facility. Paper presented at the 28th International Congress of the Aeronautical Sciences, Brisbane, 23–28 Sept 2012
77. Kok M, Tobin EF, Zikmund P, Raps D, Young TM (2014) Laboratory testing of insect contamination with application to laminar flow technologies, part 1: variables affecting insect impact dynamics. *Aerosp Sci Technol* 39:605–613
78. Kok M, Raps D, Young TM (2013) Effects of surface roughness and energy on insect residue adhesion to aircraft leading edge surfaces. Paper presented at the 36th annual meeting of the Adhesion Society, Daytona Beach, 3–6 Mar 2013
79. Kok M, Mertens T, Raps D, Young TM (2013) Influence of surface characteristics on insect residue adhesion to aircraft leading edge surfaces. *Prog Org Coat* 76:1567–1575
80. Berton B, Courty JC, Kok M, Tobin E, Young TM (2014) Evaluation of functional coatings for laminar flow applications on future business jets through ground and flight testing. AIAA 2014-2578 presented at the AIAA aviation, AIAA flight testing conference, Atlanta, 16–20 June 2014
81. Kok M, Young TM (2014) Evaluation of insect residue resistant coatings – correlation of a screening method with a conventional assessment technique. *Prog Org Coat* 77:1382–1390
82. Wortmann FX (1974) A method for avoiding insect roughness on aircraft (installation of highly elastic rubber coverings on leading edges), National Aeronautics and Space Administration, NASA TT-F 15454. (this was a translation of “Eine möglichkeit zur vermeidung der insect tenrauhigkeit an flugzeugen”, 1963). *Luftfahrttechnik Raumfahrttechnik* 9:272–274
83. Yi O, Eiss NS, Wightman JP (1988) Investigation of factors affecting the sticking of insects on aircraft wing surfaces, National Aeronautics and Space Administration, NASA CR 183041

# The Physics of Insect Impact and Residue Expansion



Christopher J. Wohl, Frank L. Palmieri, and John W. Connell

**Abstract** The phenomena of insect impacts on aircraft surfaces are complex; therefore, tailoring surface properties to minimize the adhesion of insect residues is particularly challenging. By using a first-level approximation model, where an insect impact can be approximated as a water droplet impact, information can be leveraged toward understanding insect residue accretion. However, an insect consists of an exoskeleton covering hemolymph, which is significantly more complex than water. Therefore, the energetic requirement for exoskeleton rupture will be briefly considered and the properties of the hemolymph will be discussed. Next, relevant phenomena from water droplet impact studies will be used to describe events that occur during an insect impact. A more detailed analysis of the particular water droplet impact phenomena needed to describe and model insect impact events will be reviewed. Based on this analysis, several conclusions can be drawn regarding the surface properties most likely to be beneficial for the prevention of insect residue adhesion. Among these are the requirements for moderate hydrophobicity and surface roughness, as well as recognition that the prevention of insect residue adhesion can be approached by targeting specific phases of the event itself.

**Keywords** Capillary pressure · Droplet impact · Hydrophobicity · Insect residue · Laminar flow · Surface roughness · Wetting phenomena

## Contents

1	Introduction .....	238
2	Insect Properties Relevant to Aircraft Impact Events .....	240
2.1	Exoskeleton Composition and Rupture .....	240
2.2	Hemolymph Properties .....	244

---

C. J. Wohl (✉), F. L. Palmieri, and J. W. Connell  
NASA Langley Research Center, Hampton, VA, USA  
e-mail: [c.j.wohl@nasa.gov](mailto:c.j.wohl@nasa.gov)

3	Insect Impact Events .....	246
3.1	Fruit Fly Impact on Smooth Surfaces .....	247
3.2	Insect Impact on Rough Surfaces: Random Topography .....	252
3.3	Insect Impact on Rough Surfaces: Patterned Topography .....	262
4	Water Droplet Impact on a Solid Surface .....	269
4.1	Low-Velocity Droplet Impact .....	269
4.2	High-Velocity Droplet Impact .....	280
5	Outlook .....	285
	References .....	286

## Abbreviations

$\alpha$	Half apex angle
$\delta_{\text{Max}}$	Maximum penetration depth
$\varepsilon$	Spreading factor
$\varepsilon_{\text{Break}}$	Strain at break
$\varepsilon_{\text{H}}$	Insect excrescence height
$\theta_{\text{A}}$	Contact angle, advancing
$\theta_{\text{CB}}$	Contact angle, Cassie-Baxter
$\theta_{\text{W}}$	Contact angle, Wenzel
$\theta_{\text{Y}}$	Contact angle, Young
$\mu$	Dynamic viscosity
$\rho$	Water droplet and insect hemolymph density
$\sigma$	Surface tension
$A$	Ablation constant
$A_{\text{C}}$	Capillary area
Al	Aluminum
AWCA	Advancing water contact angle
$C$	Chitin balloon circumference
$C_0$	Initial chitin balloon circumference
CAH	Contact angle hysteresis
CFRB	Critical falling height for rebound
$D$	Droplet diameter
$D_{\text{max}}$	Maximum droplet diameter
$\varepsilon$	Restitution factor
$E$	Laser pulse energy
$E_0$	Threshold pulse energy
$E_{\text{Break}}$	Energy at break
$E_{\text{kin}}$	Energy, kinetic
$E_{\text{s1}}$	Energy, droplet surface before impact
$E_{\text{s2}}$	Energy, droplet surface at maximum spreading diameter
$E_{\mu}$	Energy, viscous dissipation
$F$	Force

$H$	Thickness
$k$	Water hammer pressure coefficient
$K_I$	Toughness
$K_L$	Transition parameter from spreading to splashing
$K_{L,E}$	Empirical spreading/splashing transition parameter
$K_u$	Kurtosis
$L$	Pillar spacing
$L_C$	Capillary perimeter
$m$	Sphere mass/fruit fly mass
$Oh$	Ohnsorge number
$P$	Pressure
$P_0$	Pressure, initial
$P_C$	Pressure, capillary
$P_D$	Pressure, Bernoulli
$P_{WH}$	Pressure, water hammer
$r$	Cylinder radius
$R$	Roughness
$R_0$	Sphere radius
$R_a$	Roughness, arithmetic mean
$Re$	Reynolds number
$ROA$	Roll-off angle
$R_P$	Roughness parameter
$R_q$	Roughness, root mean square
$RWCA$	Receding water contact angle
$Sk$	Skewness
$T$	Time
$t_{coag}$	Time required for hemolymph coagulation
$th$	Chitin beam/sphere wall thickness
$V$	Velocity
$V_0$	Velocity, impact
$V_C$	Velocity, jetting threshold
$V_{CL}$	Velocity, contact line
$V_r$	Velocity, rebound
$V_{Rup}$	Velocity, rupture
$v_s$	Speed of sound
$We$	Weber number
$Z$	Ablation depth

## 1 Introduction

Insect residues present on airfoil surfaces can potentially change the nature of airflow over these surfaces [1–4]. When impact residues exceed a critical height, they can cause a premature transition from laminar to turbulent airflow. Although not a significant issue for current commercial aircraft (for example, laminar flow is utilized on Boeing 787-8/-9 nacelles, 787-9 vertical fins, and 737 Max winglets), architectures for next-generation commercial aircraft will utilize laminar flow over greater portions of the aircraft. Consequently, the prevention of debris accumulation on these surfaces will become extremely important, since premature transition to turbulent flow may significantly increase drag, translating to greater fuel burn rates. Thus, understanding how the processes involved in an insect impact event can be affected by surface and materials properties may contribute to improvements in vehicles designed with laminar flow technologies.

One important consideration regarding the prevention of insect residue adhesion is the timing and location of insect residue accretion on an aircraft in flight. As described by Smith et al. [5], the stage of a flight profile when insect impact events occur has been studied extensively. Insect impact events occur predominantly during the taxi/take-off and approach/landing portions of a flight profile, when the aircraft is operating at the lowest altitudes where the insect population is the greatest. Insect residues that have been accreting during the taxi or takeoff portion of the flight will likely persist on the surface throughout the flight profile. There is some evidence that natural erosion of the accreted residues can occur due to freeze/fracture events under the cold environmental conditions at cruise altitudes or upon flight through rain or moisture present in clouds. However, these processes are neither controllable nor reliable, so they are not viable mitigation strategies. Similarly, insect residues accreted during the approach or landing portions of the flight profile would need to be removed by ground crew. This is a practice that is unlikely to be adopted by industry due to prohibitive cost and time requirements.

Compared with the relatively concise understanding of when insect residues are accreted, there have not been extensive studies on airfoil location and orientation, and how the size of insect residue accretions changes these parameters [6]. Some early work by Coleman provides an excellent discussion of how these residues affect airflow properties, as well as what insect residue heights would likely cause a premature transition to turbulent airflow for different positions on an airfoil surface [1]. Fiore and Selig simulated the impact of insects, as well as that of solid particulates, on wind turbine blades to elucidate some of these relationships [7]. Simulated insects, treated as aerodynamic bodies with aerodynamic drag being the only associated force acting on them, were introduced upstream of the airfoil and the trajectory was calculated stepwise until an impact event occurred. To quantify the insect residue on the airfoil, the excrescence height,  $\varepsilon_H$ , was calculated according to an empirical quadratic equation developed by Bragg and Maresh [8] that depends on the insect's velocity perpendicular to the impact surface. Using this approach, the dependence of  $\varepsilon_H$  on the angle of attack (the angle between a reference line on an airfoil and the vector representing the relative motion of the airfoil) and span-wise

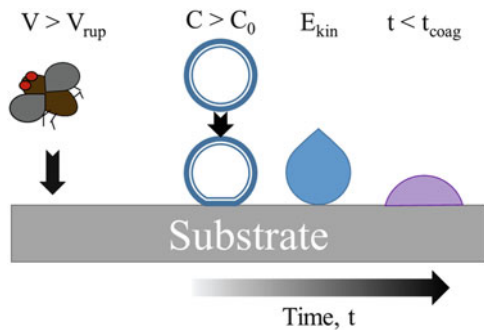


position,  $r$  (that is, the distance from the spar hub with  $R$  being the full blade length), was determined. The simulations indicated that the peak in insect residue was calculated to be at the stagnation point and that the maximum residue height was observed for conditions with the highest free stream velocity, i.e., closer to the blade tip. Interestingly,  $\epsilon_H$  was determined to be independent of the angle of attack. Based on the result that the critical height for disruption of laminar airflow is lowest at or near the stagnation point, the minimization, or prevention, of insect residue adhesion on aircraft designed for laminar flow is critical if laminar flow is to be maintained.

Also reviewed by Smith et al. [5], a myriad of active and passive mitigation approaches toward the prevention of insect residue accretion have been investigated. A majority of these reports were empirical studies that determined the effectiveness of a mitigation strategy. Furthermore, the characterization techniques utilized in these studies to differentiate a coating that performed well versus one that performed poorly can yield contradictory results. For example, evaluating coatings based on the amount of insect residue remaining after an impact event would necessarily lead to the coating with the least amount of residue being classified as the best performer. However, if the ability to remove the residues from the coating, the “cleanability,” was to be utilized to assess coating performance, it is possible that a different coating would perform better [9]. This approach to assessing the efficacy of a coating was further developed by Gruenke [10]. Both of these assessment techniques are based on the consideration of how the coating would perform on a commercial aircraft, and ultimately how this would affect the fuel efficiency of the vehicle. Defining a “best practice” to evaluate coatings for insect residue adhesion mitigation is cumbersome, i.e., no clear solution toward mitigation of insect residue adhesion has been identified. Thus, no clear metric by which to compare approaches has been developed. The purpose of this chapter is to consider the physics of an insect impact event, to identify the influence of surface properties on residue expansion, embedding, and adhesion. The reason that some surfaces exhibit reduced residue accretion that is tenaciously retained, while others demonstrate significant residue accretion that is relatively easy to remove may be better understood through an understanding of the physics and chemistry involved at the various stages of an insect impact event.

Herein, an insect impact will be described as a series of steps (Fig. 1). Each step will be considered based on a governing principle chosen either for practicality or based on

**Fig. 1** Insect impact modeled as a three-stage process: rupture of a chitin sphere, water droplet impact, and surface wetting. The governing principle for each stage is indicated above the representative image



impact conditions. For example, only insect impact velocities,  $V$ , above the rupture velocity,  $V_{\text{rup}}$ , will be considered. Discussion of exoskeleton rupture will be confined to consideration of a chitin balloon that ruptures due to an increase in circumference,  $C$ , upon impact. Based on impact conditions, kinetic energy,  $E_{\text{kin}}$ , will be the primary energetic contributor to the initial insect residue expansion. Finally, subsequent residue-surface interactions will be considered up to the time when coagulation,  $t_{\text{coag}}$ , changes the fluid properties of the residue, i.e., there is a significant increase in viscosity. This chapter is divided into sections dealing with the insect impact event itself, including exoskeleton rupture, hemolymph properties, and discussions on insect residue expansion on surfaces of increasing complexity. A review of water droplet impact studies with relevance to insect impact is also included. That discussion is organized according to increasing impact velocity. Finally, the outlook on coatings for the prevention of insect residue adhesion is provided.

## 2 Insect Properties Relevant to Aircraft Impact Events

Insects exhibit a truly exceptional biodiversity and thrive in every climate on Earth [11]. An array of these insects, with different physical characteristics, inhabit a portion of commercial aircraft operational spaces. Small winged insects are the most common and include fruit flies, syrphid flies, aphids, and mosquitoes, among other insect types [12]. Larger insects, such as honey bees, butterflies, moths, and wasps can also be encountered, albeit far less frequently. The composition of different species of insects varies considerably, and even the composition of a single species can vary depending on the time of year and life cycle of the insect.

Since insects are invertebrates, there is a distinct continuous boundary between the insect's exoskeleton and hemolymph (insect blood) which affects rupture and debris deposition after an impact event. This is in contrast to vertebrates, where the skeletal system is interwoven with the circulatory system. Therefore, the properties of these components of an insect's physiology, exoskeleton and hemolymph, can be considered separately. In the following sections, the composition and mechanical properties of the insect exoskeleton are described. This is important because the skeletal properties affect the insect rupture velocity and kinetic energy dissipation as a result of exoskeleton rupture. Additionally, the rheological and coagulative properties of the hemolymph are discussed. These properties, along with the surface properties, play a role in determining the likelihood of hemolymph droplet burst, the capillary pressure, and several dimensionless parameters used to describe droplet impact.

### 2.1 Exoskeleton Composition and Rupture

Insects can be roughly divided into those with a hard exoskeleton (beetles, wasps, praying mantis, grasshoppers, etc.) and those with a soft exoskeleton (mosquitoes, flies, gnats, etc.). The cuticle is the main part of an insect exoskeleton, providing the

insect with its shape, environmental protection, and means of locomotion [13]. The mechanical properties of the cuticle dictate the energetic requirements for rupture and can play a central role in the determination of whether an insect impact will result in the exposure of hemolymph. The cuticle is a composite material consisting of chitin nanofibers embedded in an organic matrix, and can range in thickness from approximately 1 to 200  $\mu\text{m}$  [13]. Chitin nanofibers are about 3 nm in diameter and 0.3  $\mu\text{m}$  long. The stiffness of an individual chitin nanofiber is likely to be in the order of 150 GPa (Fig. 2). Chitin crystals within an insect cuticle will orient to maximize

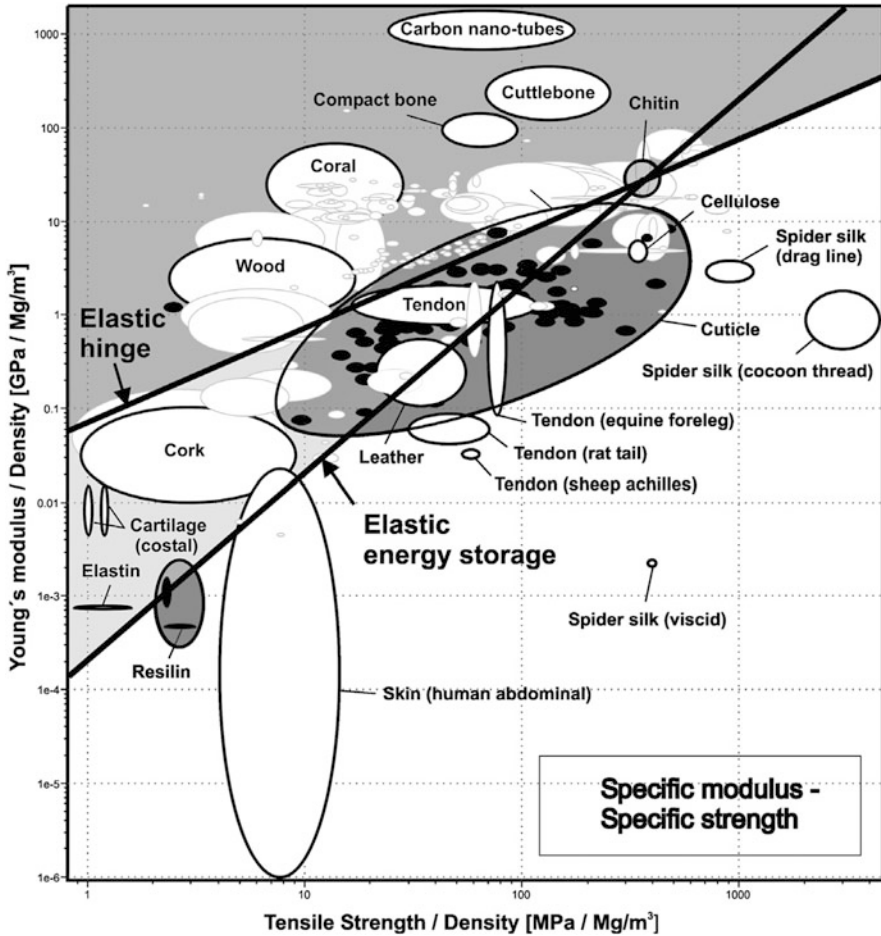


**Fig. 2** Mechanical properties of components of insect anatomy. The elastic hinge guideline demarcates materials (*below the line*) that would be of utility for enabling insect mobility as a result of failure occurring only after very large deformation. The elastic energy storage guideline identifies materials (*below the line*) that exhibit efficient energy storage as a means of conserving energy expended in locomotion. Both of these guidelines pass through chitin. Reproduced from Vincent and Wegst [13]

interaction with protein beta-sheets. Interaction strengths for these configurations have been estimated to be in the order of 30 MPa, or about half that measured for carbon fibers in a resin matrix. At the microstructural level, the mechanical properties of the cuticle are governed by the extent of the interactions between proteins and chitin. Softer cuticles have more hydration and less protein complexity, and are comprised of approximately equal-weight fractions of chitin and protein and 40–75% water. Stiff cuticles contain 15–30% chitin and only 12% water. Mechanical properties measured in tension have indicated that soft cuticles exhibit modulus values ranging from 1 kPa to 1 MPa (resilin) to 60 MPa in the abdomen of a *Rhodnius prolixus*, the assassin bug [14]. Stiffer cuticular components, such as crystalline chitin nanofiber domains, can exhibit modulus values as high as 10 to 20 GPa, which was measured parallel to the chitin orientation in the tibial flexor apodeme of a locust [15].

Crystalline chitin composite orientation and composition are used to maximize compliance and toughness for insect exoskeletons [13]. An inner compliant layer and an outer less compliant layer enable greater deformation before failure and increased elastic energy storage. This is the so-called sclerotized configuration and the utility of this configuration is understood using classic beam theory, where a beam will exhibit a tensile strain on the convex side and a compressive strain on the concave side when bent (Fig. 3). By changing the nature of the materials in a dual-layer beam configuration, the compression and tension experienced by the composite material are better accommodated.

Integration of the complexity of an insect exoskeleton into a model for exoskeleton rupture upon insect impact is beyond the scope of this chapter. However, an estimate for the energy required to rupture an insect exoskeleton was arrived at by assuming the exoskeleton to be comprised only of the most rigid component of the exoskeleton, chitin. This approach was anticipated to result in the greatest energetic requirement for exoskeleton rupture, though the inclusion of more flexible materials (e.g., resilin, etc.) was expected to reduce energetic requirements for exoskeleton rupture upon impact. Therefore, for investigating the rupture of an insect exoskeleton, the exoskeleton was modeled as a chitin sphere filled with an incompressible fluid to represent the hemolymph. Upon impact of the chitin sphere with an incompressible surface, the sphere deforms, as depicted in Fig. 4. Since the fluid within the sphere is incompressible, the volume of the deformed sphere remains constant, and

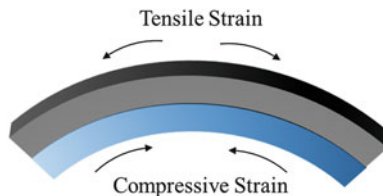


**Fig. 3** Bending of any structure results in compressive and tensile strain of the structure. Portions of insect exoskeleton are comprised of a dual-layered system, with properties tailored to address these strains and minimize inelastic deformation

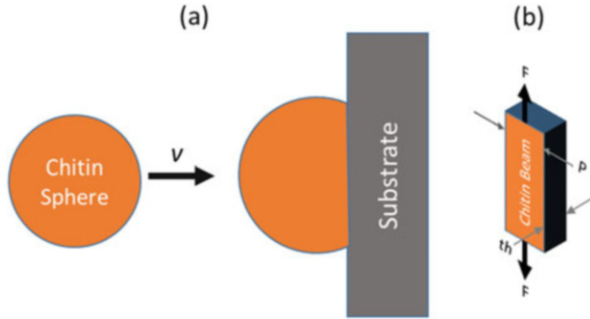


**Fig. 4** (a) Impact of an idealized chitin sphere with an incompressible substrate. (b) Three-dimensional (3D) free body diagram showing forces and dimensions on the wall of the chitin sphere during impact

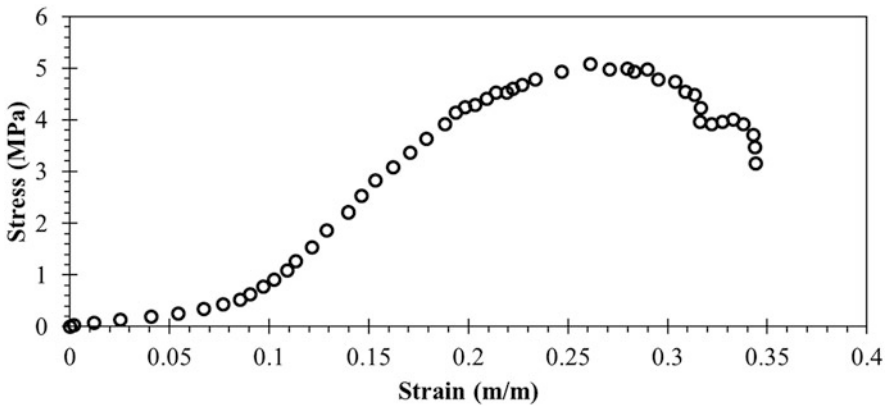


**Fig. 5** Digitized data from Fig. 3 of Ref. [14]. The experiments were performed at an extension rate of 0.18 mm/min. This curve was integrated numerically to obtain the energy to break (toughness), and the final data point was considered to be the strain at break

the surface area increases. During impact, the strain in the chitin shell results in a tensile force ( $F$ ) in the chitin. The thickness of the sphere wall is denoted as  $th$  and the circumference of the sphere at the point of break is denoted as  $C$ .

The total energy absorbed by the chitin film to break is the toughness ( $K_I$ ), which is given by the area under a stress/strain curve (Fig. 5). In this analysis, all elastic energy was assumed to be returned to the fluid inside the sphere upon rupture. The influence of this energy being transferred back to the fluid will be described below. A yield strain value of 0.2 was used to calculate the relative amounts of plastic and elastic energy required to break the chitin cuticle. This was based on tensile measurements performed on abdominal cuticle samples taken from the *Rhodnius prolixus* insect, the assassin bug [14]. The lost energy due to plastic deformation accounts for two-thirds of the toughness, while one-third of the energy was stored elastically during the strain to break.

**Table 1** Constants used for determination of exoskeleton rupture energetic requirements

Sphere radius, $R_0$	0.75 mm
Sphere mass, $m$	1.85 mg
Hemolymph density, $\rho$	1.045 g/cc
Rupture velocity, $V_{\text{Rup}}$	10.7 m/s
$\epsilon_{\text{Break}}$	0.344 m/m
$K_I$	990 kJ/m <sup>2</sup>

The energy required to rupture the sphere is given by Eq. (1), where  $E_{\text{Break}}$  is the energy required to split the sphere into two equal hemispheres and  $\epsilon_{\text{Break}}$  is the strain at break.

$$E_{\text{Break}} = K_I \text{th} C^2 \epsilon_{\text{Break}} \quad (1)$$

This equation can be evaluated to determine an approximate value for  $\text{th}$  if  $E_{\text{Break}}$  is substituted with the kinetic energy of the chitin sphere at the minimum rupture velocity less the elastic energy returned to the fluid. As an example, the thickness of a fruit fly exoskeleton can be estimated if values for an average fruit fly size, mass, and hemolymph density are used, as well as the experimentally determined fruit fly rupture velocity (Table 1) [1, 16]. Under these conditions and using Eq. (1), the fruit fly exoskeleton thickness was estimated to be 13.9  $\mu\text{m}$  and energetic net cost for exoskeleton rupture at rupture velocity was 69  $\mu\text{J}$ , with 35  $\mu\text{J}$  returning to the hemolymph which will be utilized for fluid impact and expansion processes. For an aircraft traveling at take-off velocity (70 m/s), this indicates that a negligible amount ( $\sim 1\%$ ) of the kinetic energy ( $1/2mV^2$ ) would be utilized for insect rupture. The contribution of the insect's velocity, i.e., the speed at which the insect is flying through the air, is not considered in this calculation. Thus, a majority of the energetic interactions occur between the hemolymph and the impacted surface.

## 2.2 Hemolymph Properties

Insect hemolymph is a complex aqueous mixture of proteins, small organic compounds, and electrolytes, among other components. Hemolymph has been determined to be a non-Newtonian fluid, i.e., the viscosity is shear-rate-dependent [17]. Both human blood and insect hemolymph are shear-thinning fluids, with the viscosity decreasing as the shear rate increases [17, 18]. Since hemolymph is a shear-thinning fluid, the spreading of the hemolymph on the surface after exoskeleton rupture will depend strongly on impact speed, the energy from which would translate into shear forces upon impact. Higher speed impact equals a higher shear rate, which causes more reduction in viscosity.

Autonomous coagulation-like reactions add to the complexity of hemolymph-surface interactions. Upon exposure to oxygen after an exoskeleton rupture event, cascade reactions are initiated within the hemolymph, resulting in the rapid formation of fibrillar structures in an attempt to hinder the loss of additional hemolymph and trigger wound healing (Fig. 6) [19]. For details of insect hemolymph clotting processes,

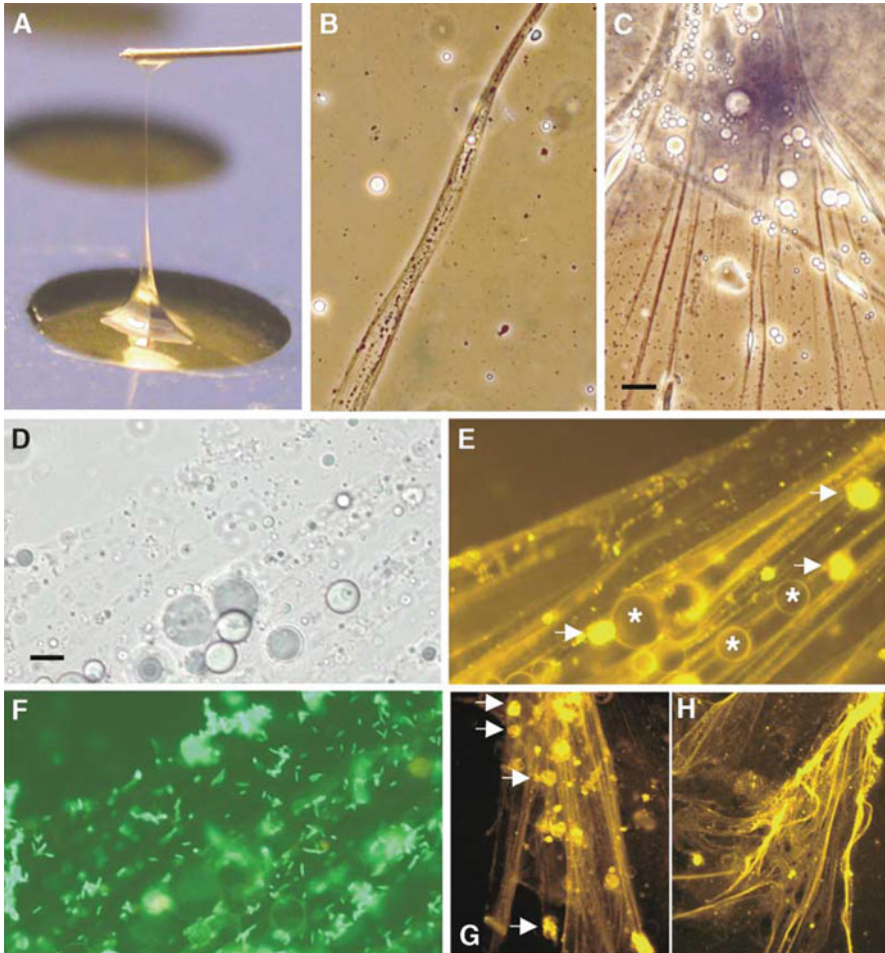


**Fig. 6** The *Drosophila* Hemolymph Clot Entraps Bacteria (a–c) *Drosophila* hemolymph clotting. (a) Hemolymph from eight wandering larvae was bled onto a well (4 mm diameter), and the increase in viscosity and formation of strands was demonstrated by drawing the clot out with a needle. (b and c) Phase-contrast views of the center of the resulting fiber (b) and the base (c). (d–f) Labeling of the *Drosophila* clot and entrapment of bacteria. Hemolymph was bled onto a drop containing GFP-labeled bacteria. (d) Nomarski exposure of the section. (e) The same section labeled with PNA visualized under UV light (the arrows indicate hemocytes, the asterisks fat body fragments). (f) GFP-labeled bacteria are visualized by green fluorescence. The figure shows results from using gram-negative bacteria, but similar results were obtained with gram-positive bacteria. (g) PNA-labeled clot preparation performed in the absence of bacteria (hemocytes indicated by arrows). (h) A preparation of the clot after lysis of hemocytes (with 0.5% Igepal, Sigma; note that the fibrous strands remain intact). The scale bars correspond to 20  $\mu\text{m}$

the reader is referred to recent reviews [20, 21]. The viscosity of the hemolymph rapidly changes from values similar to that of water to a near gel-state as a result of this rapidly generated fibril network. This coagulating fluid is very sticky and adheres to a large

variety of surfaces, including glass, plastic, and metal, entrapping various insect parts generated from the impact event. In this mix, melanization, a wound-healing response resulting in the formation of melanin, ultimately generates a hard mass that is difficult to detach. Although the authors are not aware of any kinetics studies of hemolymph coagulation, it is envisioned that coagulative processes are likely to play a role in the later stages of insect residue expansion, i.e., coagulation would inhibit rebound behavior after the hemolymph reached a maximum expansion, as described below.

### 3 Insect Impact Events

Focusing on the time immediately after insect exoskeleton rupture and before coagulation has dramatically altered the fluid properties of the hemolymph, the impact event can be approximated as a liquid droplet impacting a surface. Although this may seem like a simplistic approximation when considering the inherent complexity of an insect impact, a similar approximation was made for the analysis of bird-strike phenomena by reasoning that the yield stress of the solid material was greatly exceeded due to the rapid deceleration forces [22]. Similarly, high-velocity impacts of gels on solid surfaces have been demonstrated to be well represented as liquid droplet impacts [23]. This assumption enables the relatively thorough experimental and theoretical understanding of water droplet (or any incompressible fluid) impacts on solid surfaces to be utilized for exploring relevant interactions for insect impact events. Specific relationships developed from droplet impact studies are cited in this section as they relate to a relevant property of an insect impact event. A more in-depth review of the droplet literature follows, arranged by impact velocity. For a review of liquid droplet impacts refer to the works of Rein [24] and Yarin [25].

For the fruit fly impact velocities discussed here ( $\sim 70$  m/s), the dynamics associated with the initial contact and expansion of a hemolymph droplet impacting a surface will be inertia controlled. Hence, interactions between the fluid and surface will be overcome by the inertia-driven processes of residue expansion. (Note: the influence of airflow on the spreading of hemolymph was not considered here.) Inertia control can be verified by considering the physical properties of the hemolymph, and the magnitude of the Weber (We), Reynolds (Re), and Ohnesorge (Oh) numbers (Eqs. 2–4).

$$\text{Re} = \frac{\rho D V_0}{\mu} \quad (2)$$

$$\text{We} = \frac{\rho D V_0^2}{\sigma} \quad (3)$$

$$\text{Oh} = \frac{\text{We}^{1/2}}{\text{Re}} \quad (4)$$



**Table 2** Insect hemolymph properties and impact conditions

Hemolymph density, $\rho$	1.045 g/cc
Droplet diameter, $D_0$	1.5 mm
Dynamic viscosity, $\mu$	0.798 mPa s <sup>a</sup> [30]
Surface tension, $\sigma$	42 mN/m [31]
Impact velocity, $V$	70 m/s
Reynolds number, Re	132
Weber number, We	$1.75 \times 10^5$

<sup>a</sup>This value is for water at 30°C

Here  $\rho$  is the liquid density,  $D$  is the droplet diameter,  $V_0$  is the impact velocity,  $\mu$  is the liquid dynamic viscosity, and  $\sigma$  is the liquid surface tension. The Re number is the ratio of kinetic to viscous energies; while the We number is the ratio of kinetic to capillary energies. Thus, Re accounts for energy consumed as a result of viscous dissipation and We accounts for energy consumed as a result of surface tension. The Oh number is the ratio of the square root of We to Re and represents the ratio of viscous and capillary energies. If both the We and Re numbers are greater than 1, the initial impact and expansion dynamics will be inertia controlled [26, 27]. Using the insect hemolymph properties listed in Table 2 and an impact velocity of 70 m/s, these values were determined to be  $1.75 \times 10^5$  and 132, respectively, i.e., significantly greater than 1. For comparative purposes, an impact velocity can be calculated at which the lesser of the Re and We values is equal to 1. This was determined to be 0.55 m/s. As this is significantly lower than the fruit fly rupture velocity (10.7 m/s) [28], any impact resulting in exoskeleton fracture will also yield an initial residue expansion that is driven by kinetic energy. Similarly, Pasandideh-Fard et al. have indicated that capillary effects can be ignored for liquid expansion if  $We \gg Re^{0.5}$  [29].

### 3.1 Fruit Fly Impact on Smooth Surfaces

Processes that occur during an insect impact are extremely complex, as a result of the speed at which the impact occurs, the geometry of both the insect and the impact surface, and the non-equilibrium state of the hemolymph once it is exposed as a result of exoskeleton rupture. In order to understand the basic principles involved in insect impact and residue expansion, a few reasonable assumptions were utilized. For example, the orientation of the fruit fly immediately prior to impact was considered inconsequential for this analysis. There was some precedent for this consideration in the work of Kok et al., in which they determined that above approximately 60 m/s the orientation of the insect, a fruit fly in their work, did not significantly affect the magnitude of the residues that remained adhered to the impacted surface [32]. It was unclear what this threshold velocity would be for an insect with a hard exoskeleton, though it was assumed that it would be greater than that determined for a fruit fly. Likewise, although it was known that insect hemolymph is a non-Newtonian fluid [17], and that coagulation changes the fluid properties, the hemolymph was treated as a Newtonian fluid. Specifically, the application of relationships from the literature based on water droplet behavior requires

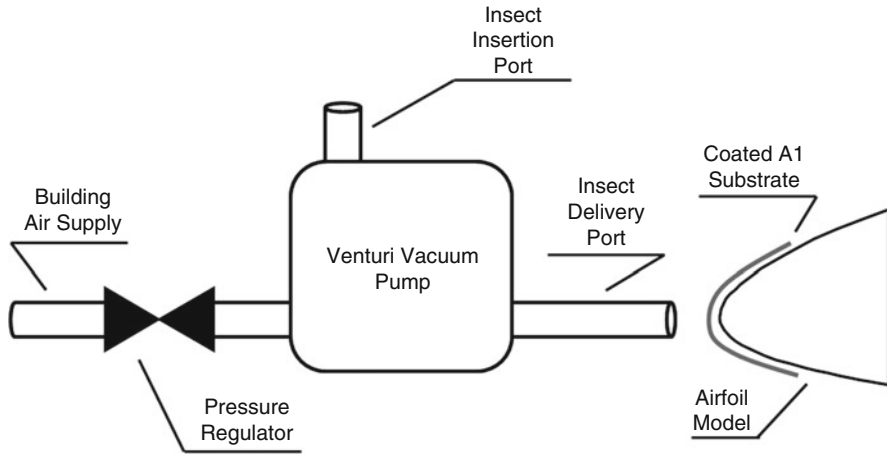


Fig. 7 Schematic of in-house pneumatic insect delivery device

the assumption that hemolymph behaves in a similar fashion. Finally, this analysis focused on work performed in our facility as a result of access to each detail of the tested surfaces and to the full gamut of material and surface characterization results collected. If this seems limiting, the general conclusions regarding the performance of evaluated surfaces arrived at were in agreement with published results from other facilities [28, 32, 33]. Additionally, reviewing the results of Gruenke [10], Gross et al. [34], and Kok et al. [35] provides further insight. Collectively, these assumptions were combined with the vast research on fluid droplet impact behavior and experimental results, to identify relevant correlations between droplet impact and insect impact behaviors.

An analysis of insect impact is simplest when considering impact on surfaces with relatively low roughness and only differences in chemical composition. To that end, aluminum (Al) surfaces (Al 2024T3) were chemically modified using aliphatic alkoxy silanes (Gelest, Morrisville, PA, USA) that were selected to provide significant differences in surface energies. These were hexyltrimethoxysilane (C6), (heptadecafluoro-1,1,2,2-tetrahydrodecyl)triethoxysilane (F17), and 2-[methoxy (polyethyleneoxy)-6-9-propyl]trimethoxysilane (hydrophilic, SiOH). Prior to the deposition of the coating, the surfaces were cleaned with ethanol and air-dried. Coatings were applied by spray deposition of 1–2 wt% aqueous ethanol solutions, after acid hydrolysis with glacial acetic acid under ambient conditions. Advancing water contact angle (AWCA) values were determined using a First Ten Angstroms (Portsmouth, Virginia, USA) contact angle goniometer (FTA-1000B). Although the hydrophilic coating contained a small amount of nanometer-scale silica particles, the roughness values measured with an optical profilometer were not dramatically influenced.

To evaluate the efficacy of these coatings regarding the reduction of insect residue adhesion, wingless fruit flies (*Drosophila melanogaster*, purchased from The Fruit Fly Shop, San Diego, CA, USA) were propelled toward the surface of interest using a custom-built pneumatic insect delivery device (Fig. 7). The details of this device can be found elsewhere [36]. A Venturi vacuum pump was modified to entrain an

insect in an airflow that was directed into a benchtop wind tunnel and toward the surface of interest. Two different surfaces were impacted through the course of the experiments described here: a cylinder ( $r = 38$  mm) and a leading edge of an airfoil shape. The airflow was adjusted such that a fruit fly traveled at approximately 70 m/s ( $\sim 160$  mph) upon exiting the delivery nozzle toward the surface. The wind tunnel was operating (approximately 20 m/s parallel to the primary jet direction of the airflow associated with insect propulsion) to simulate the airflow that would be passing over the test surface as a result of an aircraft in flight. Testing was conducted at ambient temperature (approximately 21°C) and at about 50 to 60% relative humidity. High-speed photography was obtained during impact events, using a Vision Research (Wayne, NJ, USA) Phantom 12 camera at a rate of 50,000 or 100,000 frames per second.

Once the surface was impacted with at least three fruit flies that had remained intact until impact, the insect residues were analyzed for the maximum residue height and total residue areal coverage, using an optical profilometer (Microprof 100; FRT of America, San Jose, CA, USA). It was experimentally determined that when the insects were propelled at velocities much greater than 70 m/s, they became fragmented prior to impact. This likely was the result of shear forces experienced by the insect as it was propelled through the delivery tubing. This mid-air fragmentation exposed hemolymph and would initiate coagulation prior to impact. As insects would not be present in a fragmented state under aircraft operational conditions, insects that were fragmented prior to impact in these studies were excluded from the analysis. Details regarding image capture and data processing can be found elsewhere [36]. Various roughness parameters for the coating were also determined by areal scans, using the optical profilometer at similar resolutions. High-resolution scanning electron micrographs were collected on a Hitachi S-5200 Field Emission high-resolution scanning electron microscope (HRSEM; Hitachi, Hillsboro, Oregon, USA).

Prior to reviewing the results collected from testing these surfaces, there are a few important considerations from the research on water droplet impact studies that are worth noting. These are presented in the order they would appear or become relevant during an insect impact. First, based on the impact velocity, jetting (the expulsion of material from the advancing solid-liquid contact front) should be expected. For all of the impact phenomena discussed here, we assumed that the droplet impact process was confined to the acoustic limit, i.e., the motion of material within the droplet (shockwave propagation) was restricted to no faster than the speed of sound ( $v_s$ ) in the liquid. If the insect hemolymph responds in a similar fashion to water in this regard, that velocity is 1,484 m/s. This restriction does not apply to the advancing contact line, which, at very short times (up to several tens of nanoseconds) after impact, will be traveling much faster than the speed of sound. The velocity of the advancing contact line decelerates rapidly, and jetting occurs when the advancing contact line velocity drops below the shockwave velocity. Supporting information and the governing time-resolved equation (Eq. 24) for the advancing contact line velocity is found in Sect. 4.2. Jetting should not be confused with fingering patterns observed upon water droplet impacts at lower velocities which arise due to advancing contact line instabilities [37].

Second, beyond anticipating jetting, the behavior of the remaining impacting liquid depends strongly upon the impact velocity. At relatively low velocities, droplet

rebound behavior was observed to depend on the nature of the impacted surface (surface chemical and topographical properties), enabling droplet rebound responses that varied from a strongly pinned droplet all the way to complete droplet rebound and detachment from the surface. These phenomena were considered extensively (in Sect. 4.1.1). One aspect of the anticipated behavior of an impacting liquid droplet that was particularly relevant to this discussion was whether droplet splashing (fracture), arising from high-impact velocities, occurs. For a given set of impact conditions based on  $Re$  and  $We$  numbers, an empirically determined relationship was identified to determine whether splashing or simply spreading would be observed. For the impact conditions discussed here, splashing would certainly be expected. Splashing may be exacerbated as a result of the onset of coagulation processes, which would likely inhibit the uniform expansion of fluid due to differences in viscoelastic response.

The final point to consider before discussing the results from this first set of coatings was that the initial expansion properties were predominantly governed by inertia effects. Thus, changes in surface chemistry are anticipated to result in relatively minor changes in remaining residue properties.

Based on the results listed in Table 3, any improvements in the performance of the chemically modified surfaces to minimize insect residue adhesion were nominal at best. This was particularly noteworthy as the AWCA values varied from 68 to 110°. This also reinforces the ideas that the initial residue expansion was inertia controlled (i.e., surface energy did not play a significant role) and that no appreciable hemolymph retraction (a process influenced by surface energy) occurred due to droplet fragmentation and potentially, coagulation. As the maximum AWCA value physically possible was determined to be approximately 120° [38], it was anticipated that a more hydrophobic surface would provide nominal improvements beyond those listed in Table 3.

High-speed photography captured impact events, and still frames from these videos provided further insight into the response of the surfaces listed in Table 3. Hemolymph jetting, resulting from the liquid contact line advance velocity slowing to the speed of sound, was readily observed in the images obtained immediately after contact. This indicated that the contact line advancing velocity had decreased to below the speed of sound within 20  $\mu s$ . This was supported by high-velocity water droplet impact studies (see Sect. 4.2). At approximately the same time after the initial impact, the general shape and degree of residue expansion appeared to depend on the AWCA (Fig. 8). Based on these images, it was observed that the surface with the greatest AWCA value

**Table 3** Water contact angle measurements and fruit fly impact results for silane-functionalized Al alloy surfaces

Coating	AWCA, °	Profilometry analysis	
		Insect height, $\mu m$	Insect area, $mm^2$
Aluminum	84	69	1.27
C6	108	69	1.16
OH	68	65	1.10
F <sub>17</sub>	110	66	0.71

AWCA Advancing water contact angle

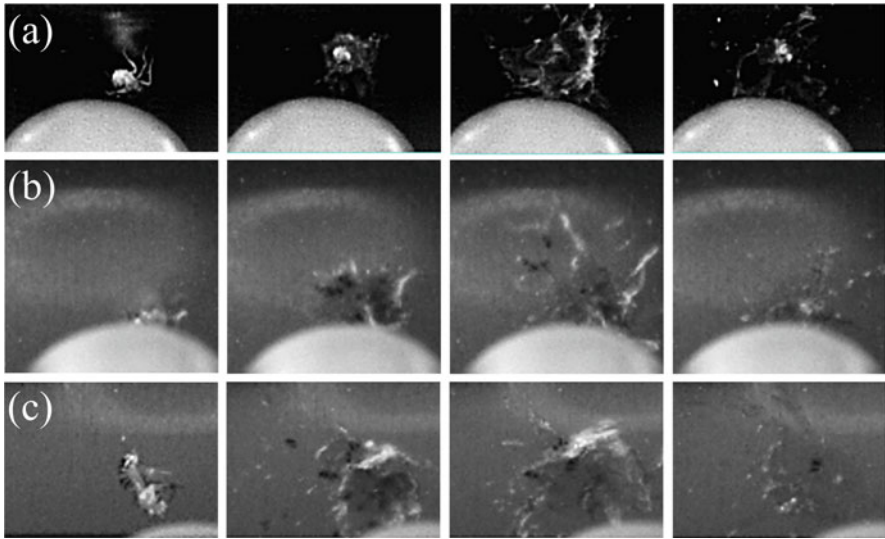


**Fig. 8** Series of still images from fruit fly impacts on (a) Al alloy, (b) OH-functionalized, and (c) F<sub>17</sub>-functionalized surfaces. The times relative to the initial contact progress *from left to right* as: 0  $\mu$ s, 40  $\mu$ s, 80  $\mu$ s, and 2 ms. The *light-colored object in the bottom of these images* is the nozzle (1-cm outer diameter) from the pneumatic insect delivery device

(F<sub>17</sub>) exhibited the fastest residue expansion, while the Al alloy's surface was the slowest. Although this apparent dissimilarity in residue expansion rate was observed, the ultimate degree of residue deposition was not greatly affected, as can be seen in the images captured 2 ms after fruit fly impact. In each case, extensive “wetting” of the surface by hemolymph was observed in a projection-like fashion radiating outward from the point of impact. Likewise, large hemolymph deposits and exoskeletal fragments were observed within the surface area wetted by the hemolymph.

Although these impacts occurred on a curved cylindrical surface, it can be observed that there was preferential expansion and deposition of residues moving toward the top of the images. This arose as a result of the impact occurring slightly above the mid-plane of the cylinder. As most impact events that occur in a commercial aircraft environment, as well as all of the impacts discussed in this work, do not occur on surfaces oriented normal to the impact, it is important to consider the forces acting on the insect residues. For an angled impact, the impact force can be separated into two vectors oriented tangential and normal to the surface, resulting in residue expansion and rebound, respectively (Fig. 9). A portion of a gravitational component was considered to act opposite to the horizontal impact force component, although the magnitude of this was likely to be negligible relative to the impact force. Reorienting this arrangement of forces shows that an insect impact event is the force-wise equivalent of a droplet impact on an inclined surface.

The behavior of water droplets impacting inclined surfaces has been studied extensively [39, 40]. Recently, Yeong et al. studied water droplet impact behavior

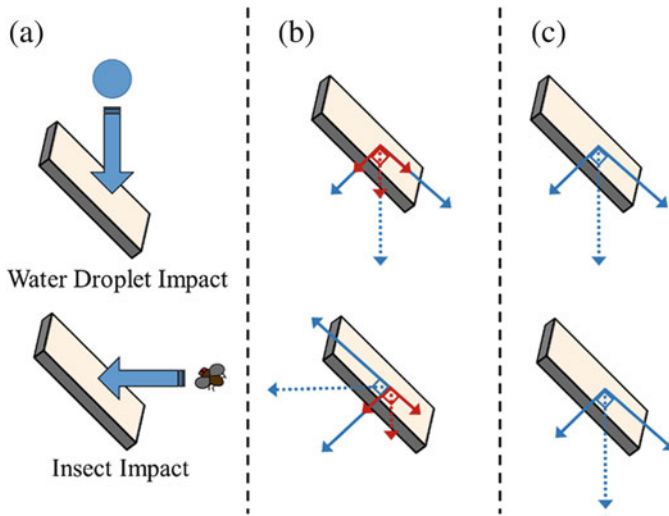


**Fig. 9** (a) Schematic for water droplet impact (*top*) and insect impact (*bottom*) on an inclined plate. (b) Force diagrams for the impact events, with the contributions from kinetic energy (*blue*) and gravity (*red*) separated into vectors parallel and normal to the impacted surface. (c) For high-velocity impacts, the gravitation contribution can be ignored. By rotating the insect impact force diagram  $180^\circ$  about the point of impact, the force diagrams become identical

on inclined superhydrophobic surfaces and concluded that the “bulge” of fluid on the leading edge (downhill side) of the droplet was diminished as the hydrophobicity of the surface increased [41]. Although the velocities utilized in their work were significantly lower than what would be expected for insect impact events on aircraft, this conclusion can be translated to an insect impact event to estimate the relative distribution of insect residues on an airfoil. Further implications regarding the expansion of hemolymph on an aircraft wing arise from consideration of this bulging behavior. As the hemolymph expands across an impacted surface away from the leading edge, this concentration on the downhill side projects debris further from the leading edge, where the critical height causing laminar flow to transition into turbulent flow is greater [42]. Thus, the motion of residues, especially those with tall features, to greater distances away from the leading edge could reduce the likelihood of these features changing the airflow properties.

### 3.2 *Insect Impact on Rough Surfaces: Random Topography*

Since there was no discernable difference in insect residue adhesion mitigation on chemically modified or topographically smooth and uniform surfaces, the next step was to consider surfaces with topographical features. A series of epoxy-based coatings were generated in which the surface chemistry was kept consistent between

coating formulations, while the topography was changed. This was achieved by the inclusion of a surface modifying agent that was thermodynamically drawn to the coating surface [43], with the inclusion of filler materials that provided topographical features in the as-prepared coating.

Details of these coatings have been published elsewhere [44]. Briefly, the epoxy resin was a combination of the diglycidyl ether of bisphenol A (DER 331™; The Dow Chemical Co., Midland, MI, USA), an aromatic diamine (Ethacure® 100; Albemarle, Charlotte, NC, USA), and an amine-terminated fluorinated aliphatic ether [45]. The aliphatic ether comprised approximately 1 wt% of the total resin content, enough to saturate the surface of the epoxy coating with fluorinated species, based on AWCA and X-ray photoelectron spectroscopic analyses [45]. Two filler materials [molybdenum disulfide ( $\text{MoS}_2$ ), <2- $\mu\text{m}$  diameter; and silica ( $\text{SiO}_2$ ), 7 nm, both from Sigma Aldrich, St. Louis, MO, USA] were incorporated into the formulations at the relative amounts indicated in Table 4. The topography was imparted by the filler content, and the resultant topographies appeared random. These formulations were spray-coated from a 1:1 methyl ethyl ketone: methyl amyl ketone solution onto Al alloy substrates (Al 1,100, 0.076 mm thickness) and cured at 100°C for 2 h, followed by curing at 170°C for 4 h. Representative HRSEM images for these coatings are shown below (Fig. 10). As can be seen, the presence of  $\text{SiO}_2$  resulted in topographical features with hierarchical roughness spanning both micrometer- and nanometer-length scales. The inclusion of  $\text{MoS}_2$  at low quantities resulted in nominal changes in surface topography according to HRSEM images; while at higher loadings, large polygonal structures were visible, arising from the platelet geometry of this material (data not shown). Likewise, hierarchical topographical features were observed on the surfaces of coatings with fumed silica, as a result of particulate agglomeration within the resin matrix. Surface roughness parameters (arithmetic mean,  $R_a$ , and root mean square,  $R_q$ ) were determined using the Microprof profilometer. For this series of epoxy composite coatings, increased filler content typically resulted in greater roughness. The unfilled epoxy exhibited a

**Table 4** Epoxy composite coating formulation details

Coating	Filler	Filler content, wt%	$R_a$ , $\mu\text{m}$	$R_q$ , $\mu\text{m}$
A	None	–	0.33	0.44
B	$\text{MoS}_2$	5	0.50	0.76
C	$\text{MoS}_2$	10	0.57	0.88
D	$\text{MoS}_2$	25	1.03	1.37
E	$\text{SiO}_2$	5	0.95	1.77
F	$\text{SiO}_2$	10	1.67	2.76
G	$\text{SiO}_2$	25	2.99	4.96
H	$\text{MoS}_2/\text{SiO}_2$	1.25/3.75	1.57	2.63
I	$\text{MoS}_2/\text{SiO}_2$	2.5/7.5	1.73	3.15
J	$\text{MoS}_2/\text{SiO}_2$	6.25/18.75	3.68	6.04

$R_a$  Roughness, arithmetic mean;  $R_q$  roughness, root mean square

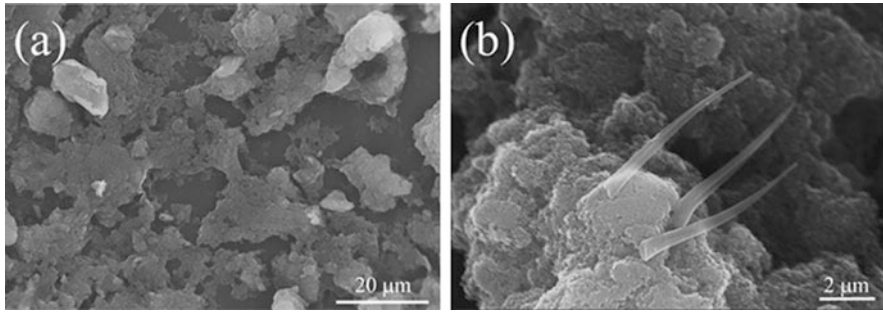


**Fig. 10** Micrometer-scale (a) and nanometer-scale (b) random topographies typically observed on epoxy composite surfaces with any amount of  $\text{SiO}_2$  present in the formulation. The spindle structures in (b) are exoskeleton debris from a fruit fly impact at a different location on this particular sample

**Table 5** Water contact angle measurements and fruit fly impact results on epoxy composite coatings

Coating	AWCA, °	RWCA, °	ROA, °	Insect height, $\mu\text{m}$	Insect area, $\text{mm}^2$
Al alloy	76.2	58.4	>60	$163 \pm 79$	$0.91 \pm 0.54$
A	105.3	86.2	>60	$203 \pm 73$	$0.68 \pm 0.30$
B	104.9	83.8	>60	$175 \pm 52$	$0.43 \pm 0.30$
C	105.1	86.6	>60	$210 \pm 70$	$0.44 \pm 0.40$
D	111.6	92.6	>60	$127 \pm 66$	$0.48 \pm 0.36$
E	120.2	98.5	>60	$87 \pm 77$	$0.07 \pm 0.08$
F	142.1	106.8	37	$69 \pm 33$	$0.07 \pm 0.04$
G	139.8	128.4	7	$104 \pm 44$	$0.09 \pm 0.06$
H	115.1	95.6	>60	$45 \pm 28$	$0.03 \pm 0.02$
I	143.2	110.6	>60	$66 \pm 44$	$0.06 \pm 0.05$
J	147.5	135.2	6	$145 \pm 64$	$0.22 \pm 0.10$

RWCA receding water contact angle, ROA roll-off angle

roughness similar to that of the Al alloy surface it was coated on ( $R_a$  and  $R_q$  for the Al alloy were measured to be  $0.33 \mu\text{m}$  and  $0.39 \mu\text{m}$ , respectively).

Water contact angle values determined on these surfaces spanned a broad range of hydrophobicity, and the difference between AWCA and receding water contact angle (RWCA) values also varied considerably between surfaces (Table 5). In general, greater filler content resulted in higher contact angle values and, in some cases, low roll-off angles (ROAs), features which would be anticipated for a chemically hydrophobic surface with the topographical features exhibited in Fig. 10. For fruit fly impact testing, these samples were wrapped around the airfoil geometry depicted schematically in Fig. 7, with the remainder of the impact experimental parameters consistent with those described previously. The results of these experiments are shown in Table 5.

Still images from impacts on three of the coatings listed in Table 5 (A, C, and G) demonstrated significant differences (Fig. 11). Jetting was again observed, based on



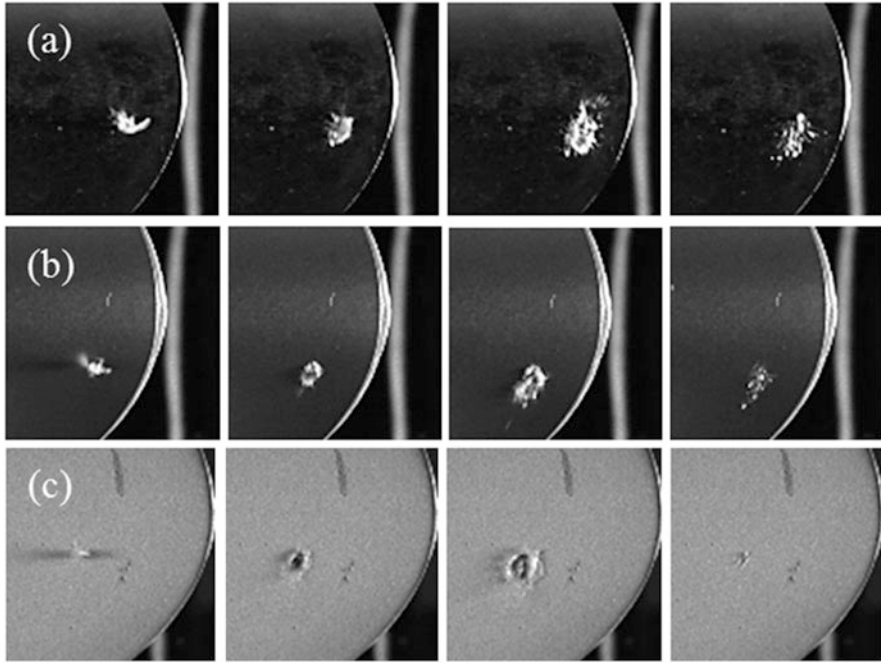


**Fig. 11** (a–c) Series of still images from fruit fly impacts on coatings described in Table 5. (a) Unfilled epoxy surface A, (b) epoxy composite surface C, and (c) epoxy composite surface G. The times relative to the initial contact progress *from left to right* as: 0  $\mu$ s, 40  $\mu$ s, 80  $\mu$ s, and 2 ms

impact velocity. Likewise, the degree of residue expansion along the surface was not consistent for these coatings with increased surface roughness. This resulted in more rapid expansion and an abrupt transition from a uniform hemolymph expansion ring to a disrupted expansion front, i.e., the degree of radial expansion was not consistent for different expansion angles. The difference was particularly noticeable when comparing the unfilled epoxy surface (A) to the epoxy composite surface (G). As a reminder, although the coating formulations differ regarding filler content, the surface chemistries should not differ much. The greatest differentiating factor between these surfaces should be roughness. At 40  $\mu$ s (second image in Fig. 11c), a clear contrast was seen within the ring of expanding residue for the impact on G. This can be correlated to “dewetting” of the hemolymph from the surface as the residues expanded. The results of the dewetting are clearly observed as a reduction in the deposited residues in the 2-ms image. In contrast, the impact on A does not indicate this differentiation at early impact times. In fact, after 80  $\mu$ s, the expanding hemolymph ring (corona) remained intact, and the entire area within the corona appeared to be relatively uniform in color. This was attributed to a continuous thin hemolymph film in that region. At 2 ms, this entire area can be seen to contain deposited residues. Although the images captured for a fruit fly impact on C indicate some degree of disruption within the expanding hemolymph corona, significantly greater residue amounts were observed after impact on this surface compared to

impact on G. A two-sample  $t$ -test of the difference in the areal coverage values for these two surfaces resulted in a  $p$ -value of 0.02. For the difference between two means to be considered statistically significant with 95% confidence, a  $p$ -value of 0.05 is required.

To quantify these observations, microscopy images were collected on a Zeiss (Oberkochen, Germany) LSM 5 Exciter confocal microscope outfitted with a camera to collect optical images of the entire surface region that contained insect residues. Within this region, the largest area of continuous insect residue was identified (Fig. 12a) and taken to be the initial expansion area. This initial expansion area did not include the additional hemolymph deposits arising from advancing contact line destabilization, as these deposits arose after the initial expansion had destabilized, and would be representative of a slightly later stage of the impact event. These deposits yielded the fingering patterns prevalent on many of the surfaces investigated here. The initial impact area, excluding the residues associated with the fingering pattern, calculated as an ellipse with the major and minor axes being the maximum length and width, was determined to correlate well ( $R^2 = 0.96$ ) with the inverse root mean square surface roughness ( $R_q$ , Fig. 12b). This can be observed empirically by comparing the perimeters of each initial area (Fig. 12c).

The initial impact area was particularly relevant for ascertaining the efficacy of a particular surface regarding insect residue adhesion, for several reasons. First, a

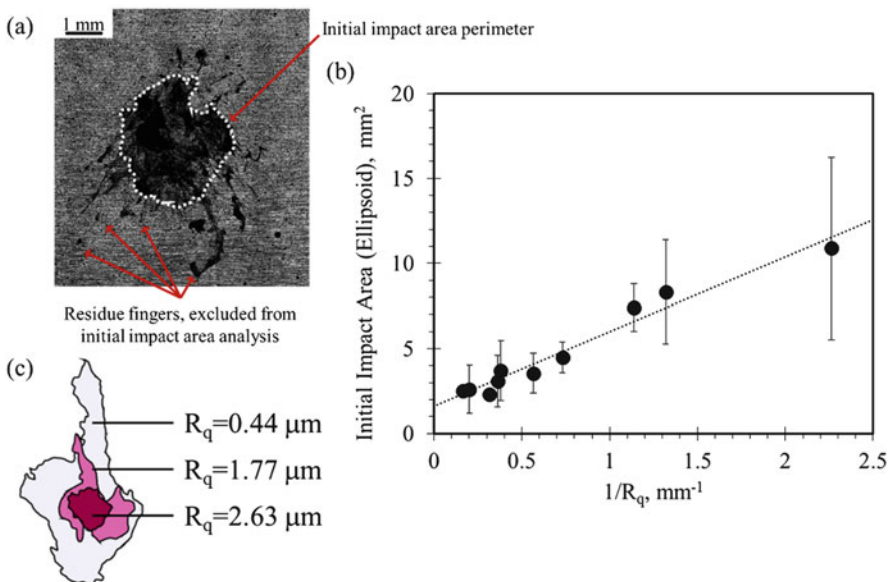


**Fig. 12** (a) The initial impact area perimeter, indicated as a *dashed line*, for remaining residues on a surface that has been impacted by a fruit fly. (b) The initial impact area was determined to be inversely related to the epoxy composite surface roughness. (c) Comparison of the initial impact area perimeters, calculated as ellipses from microscopy measurements, on surfaces with different roughness values

smaller initial impact area was indicative of a greater degree of residue being dislodged or possibly never having come into contact with the surface. This was due to the disrupted expansion residue direction of motion, which would be normal to the point of disruption, i.e., away from the surface. Second, a smaller initial impact area was indicative of a smaller volume of residue on the surface that could act as an adhesive for exoskeleton fragments. Exoskeleton fragments were often observed to be the tallest residue features. Thus, prevention of an adhesive (hemolymph) that would enable the retention of exoskeleton fragments at the site of impact is preferred. Surfaces that exhibited a smaller initial impact area were therefore considered to be more promising for the mitigation of airflow disruption, as a result of both a reduction in retained hemolymph in general, and a reduced propensity to enable the adhesion of exoskeleton fragments.

From Fig. 12b, the behavior of hemolymph impacting a smooth surface of this chemical composition can be predicted. As described in Sect. 4.1, the ratio of the maximum spreading diameter of a droplet to the initial droplet diameter, called the spreading efficiency, was related by Scheller and Bousfield to the  $Re$  and  $Oh$  numbers calculated for the droplet itself (Eq. 10) [27]. This relationship used to calculate a spreading efficiency was compared to the average size of a fruit fly (3–4 mm for body length and 1.5 mm for the body width). Using an  $R_q$  value of  $0.1 \mu\text{m}$  (reasonable for an extremely smooth surface; i.e., roughness would not significantly impede liquid spreading), the initial impact area was calculated to be  $42 \text{ mm}^2$  according to the linear fit line in Fig. 12c, resulting in an initial impact diameter of 7.3 mm for a perfectly symmetric expansion. Using  $Re$  and  $Oh$  numbers of 134 and 0.098 (Table 2), respectively, a required initial droplet size generating this initial impact diameter under these impact conditions was calculated to be approximately 3.5 mm, according to Eq. (10). This was slightly more than twice the size of a fruit fly body width and supports the hypothesis of hemolymph likely behaving as a shear-thinning fluid; thus, spreading immediately after impact was likely to occur with the liquid behavior characterized by a much lower viscosity than would be measured at an equilibrium state. Toivakka reported that a shear-thinning liquid would likely exhibit up to a 50% increase in spreading relative to a Newtonian fluid [26], in good agreement with the numbers calculated here.

Once deposited, the hemolymph in the initial impact area will initially exist as a thin continuous film like a water droplet at the time of maximum expansion. Instabilities can form in this thin film, especially over a rough surface, resulting in holes in the hemolymph film. As described more extensively in Sect. 4.2.1, the growth or collapse of these holes depends on the fluid receding contact angle. The greatest hole stability was observed on moderately hydrophobic surfaces [46]. A coating which promotes hole stability and growth in a hemolymph film would be expected to minimize the initial impact area and reduce exoskeleton debris adhesion. Using optical micrograph images, insect areal coverage patterns were analyzed for continuity of hemolymph coverage (Fig. 13). It was determined that surfaces with mid-range water contact angle (WCA) values, i.e., between  $110^\circ$  and  $150^\circ$ , demonstrated the greatest degree of discontinuity associated with hole formation and expansion shortly after the initial impact event.

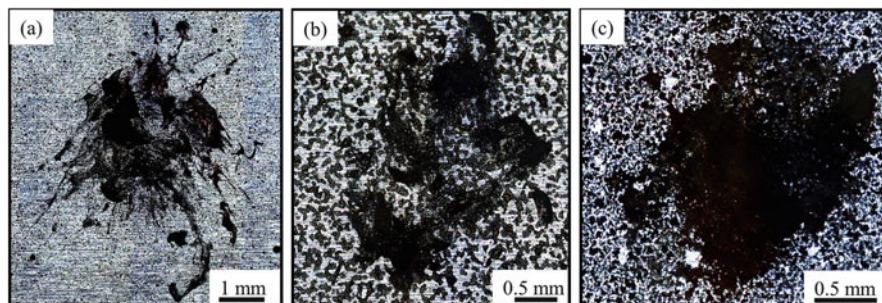


**Fig. 13** Mosaic microscopy images of (a) epoxy composite surface B, (b) epoxy composite surface H, and (c) epoxy composite surface J. Voids within the hemolymph expansion area can be seen as discontinuities (*light areas*) in the darkened regions

As can be seen in Table 5, the epoxy formulations exhibited a broad range of hydrophobicity. However, no clear linear trend could be developed between WCA values and the resultant insect residue properties. In the work by Dhiman and Chandra, where thin film hole formation and stability were discussed, a relationship between hole formation and a critical Re number calculated for a droplet impact and RWCA value was derived, showing that a minimum critical Re number was present at RWCA values consistent with moderate hydrophobicity [46]. The critical Re number was an indicator of how likely thin film hole stability and growth would be. Droplet impact events above the critical Re number would result in hole formation stability and growth, ultimately resulting in thin film collapse. For surfaces that were hydrophilic to negligibly hydrophobic (i.e., RWCA value close to  $90^\circ$ ) or for superhydrophobic surfaces, the critical Re number was larger than that for surfaces that exhibited moderate hydrophobicity (this is covered in greater detail in Sect. 4.2.1). By comparison with an insect impact event, it would be anticipated that a surface exhibiting hole stability and growth would be more likely to exhibit a reduction in insect residue retention after an insect impact occurred. To assess this relationship, the results of insect impacts on the epoxy surfaces described here (insect residue height and areal coverage in Table 5) were plotted with their RWCA values. Interestingly, the shape of this empirical relationship appears similar to the plot described by Dhiman and Chandra (Fig. 14) [46]. In fact, when the data in these plots were fitted to simple quadratic expressions, the minima were found to be in reasonable agreement with the minimum in the critical Re number relationship derived by Dhiman and Chandra (Table 6), further supporting the idea that hole stability in a thin hemolymph film may play a role in the amount and distribution of residues left behind after an insect impact event.

Another consideration is the fraction of the impacted surface that was actually wetted by the hemolymph. As a liquid droplet impacts a roughened hydrophobic surface, such as the epoxy surfaces discussed here, the liquid will ingress into the surface asperities, resulting in localized wetting. Depending on the properties of the surface (chemical composition and the shape, size, and density of roughness elements) and those of the impacting droplet (velocity, surface tension, viscosity), the liquid may (1) wet the surface entirely or (2) only partially wet the surface due to

**Fig. 14** Relationships between (a) normalized insect residue height and (b) areal coverage with receding water contact angle (RWCA) values measured on epoxy composite surfaces. These trends are compared to data reproduced from the work of Dhiman and Chandra [46] (c) for thin film stability as a function of RWCA value

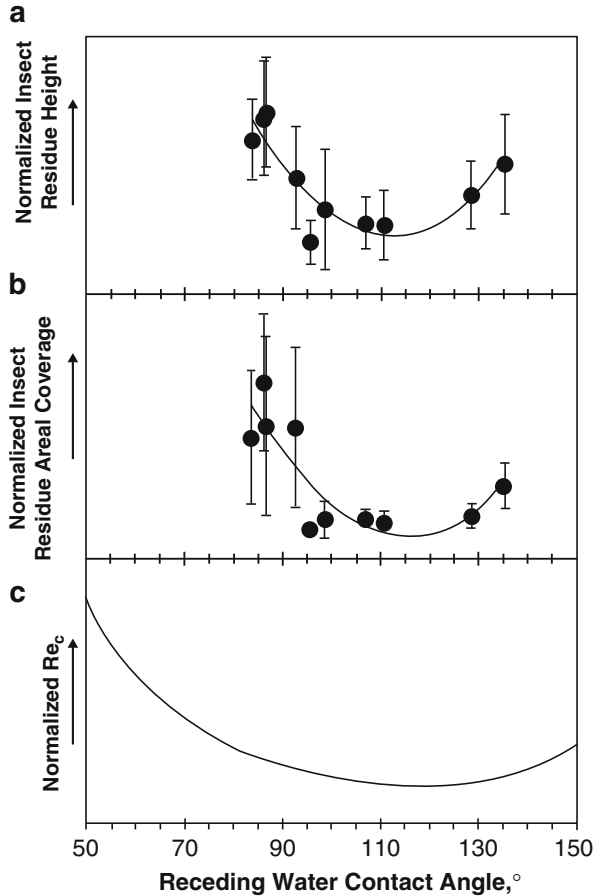


**Table 6** Comparison of minimal values from Fig. 14

Relationship	RWCA minimum value
Insect residue height	112°
Insect residue areal coverage	123°
Dhiman and Chandra [46]	118°

forces preventing full penetration of the liquid into the surface by entrapping air. This is discussed in more detail in Sect. 4.1.2. There are three forces involved when considering whether surface features (described here as pores) will be wetted; capillary pressure ( $P_C$ , arising from interfacial tension) that prevents wetting of the pores, Bernoulli pressure ( $P_D$ , an increase in pressure due to a decrease in fluid velocity), and water hammer pressure ( $P_{WH}$ , an increase in pressure due to momentum conservation) that will all work to wet the pores, either over the entire liquid coverage area, or at the immediate impact site. Pore wetting is prevented over the entire liquid coverage area when the value of  $P_C$  is greater than the sum of the  $P_D$  and  $P_{WH}$  values (see Eqs. 16–18 for their definitions). The hemolymph properties listed in Table 2, an impact velocity of 70 m/s and a Young’s AWCA value of 115° (this is

**Table 7** Calculated approximate pressure values for a fruit fly impact on surface G

$P_C$	20 MPa
$P_D$	25 kPa
$P_{WH}$	22 MPa

$P_C$  pressure, capillary;  $P_D$  pressure, Bernoulli;  $P_{WH}$  pressure, water hammer

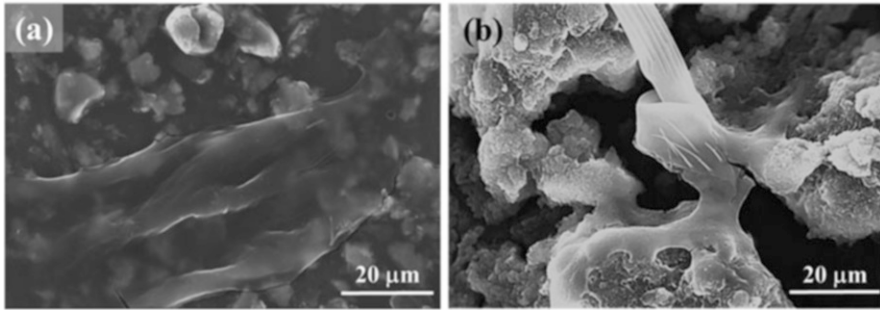


**Fig. 15** (a, b) High-resolution scanning electron microscope (HRSEM) images collected on epoxy composite surfaces B (a) and G (b) after fruit fly impact

the AWCA value for a smooth surface), were used to approximate the magnitude of these pressures (Table 7). To calculate a  $P_C$  value, the  $R_a$  value measured for surface G (3.0  $\mu\text{m}$ ) was used to generate a hypothetical axisymmetric surface with circular pore features. If the pore width and pitch (spacing from the start of one pore to the start of the next) are arbitrarily chosen as 10  $\mu\text{m}$  and 20  $\mu\text{m}$ , respectively, the pore depth would be calculated to be 6  $\mu\text{m}$ . This surface was chosen because the high relative  $R_a$  value would translate to a greater  $P_C$  value relative to the other surfaces. With these parameters, the  $P_C$  for a single pore was calculated to be 2.3 kPa. Using the initial droplet diameter, the number of pores in the initial contact area (note that this is different from the initial impact area, as there is no spreading considered at this point) was determined to be approximately 8,800; which correlated to a total  $P_C$  value of approximately 20 MPa. Thus, under these impact conditions ( $P_{WH} > P_C > P_D$ ), it would be anticipated that the hemolymph would wet the area of initial contact, but would not appreciably wet the total area of initial impact.

Although it is difficult to unequivocally determine what portion of an impacted surface was wetted at various stages of an impact event and if a surface that was previously wetted exhibited “dewetting” behavior at a later time, microscopy can help to elucidate the ultimate state of the residues. Shown in Fig. 15 are images captured of epoxy composite surfaces B (Fig. 15a) and G (Fig. 15b) after fruit fly impact. As shown, the hemolymph appears to have spread indiscriminately over the lower roughness surface (B,  $R_a = 0.50 \mu\text{m}$ ), while there was significant contact line curvature on the rougher surface (G,  $R_a = 3.00 \mu\text{m}$ ), which indicates unfavorable interactions between the hemolymph and the surface; i.e., the hemolymph retracted rather than expanded along the surface. In fact, on several of the surfaces with relatively high roughness values, bridging of hemolymph (as seen in Fig. 15b), was observed, indicating the poor wettability of hemolymph on these surfaces. This finding is in agreement with the

calculated higher  $P_C$  value, relative to  $P_D$ , which would prevent hemolymph from wetting as it spread beyond the initial contact area. This non-continuous wetting manifests as disruption of the contact line expansion during the expansion process, resulting in a reduction in retained insect residues, previously described in this sub-section.

A series of tests were conducted with fruit flies impacting samples mounted to a flat plate where images were collected at a rate of 100,000 frames/s. This was done to enable greater comparison of the early impact dynamics between these topographically rich surfaces and an Al alloy control (Fig. 16). The remaining conditions associated with the insect impact experiments were identical. The influence that the surface properties have on the insect impact events for each case can be considered in light of the related liquid droplet impact phenomena discussed in this section and Sect. 3.1. First, in the images captured immediately after impact (30  $\mu\text{s}$  for the Al alloy surface and 20  $\mu\text{s}$  for the epoxy composite surface), exoskeleton rupture had occurred and hemolymph jetting was clearly visible. At this time, the velocity of the advancing contact line had slowed to significantly less than the speed of sound. Only 20  $\mu\text{s}$  later, the initial impact area had already been generated (note that it was significantly smaller for the roughened epoxy composite surface) and holes in the resultant film were visible on the epoxy composite surface.

Also apparent at this interval was that a larger portion of the exoskeleton debris that had impacted at the initial impact area remained adhered to the Al alloy surface as a result of the hemolymph layer continuity. At significantly longer times ( $t = 1 \text{ ms}$ ), the implications from these interactions were evident. A large areal coverage of insect hemolymph was present on the Al alloy surface, and significant exoskeleton fragments remained adhered to the surface. In contrast, the hemolymph areal coverage was significantly reduced on the epoxy composite surface, and any remaining exoskeleton debris was relatively small. Presumably, larger exoskeleton

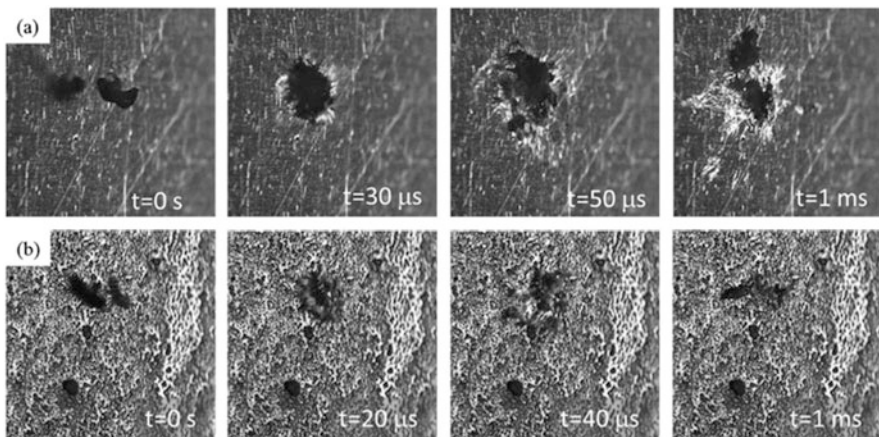


**Fig. 16** (a, b) Series of still frames collected from fruit fly impact (a) on an Al alloy surface and (b) on epoxy composite surface H. For scale reference, the average length of a fruit fly is 3 mm and both series of images were collected at the same distance

fragments that impacted the surface after the hemolymph expansion were either immediately or eventually dislodged from the surface due to the limited presence of hemolymph, resulting in insufficient adhesion.

### 3.3 *Insect Impact on Rough Surfaces: Patterned Topography*

At this point, it is evident that, for initial impact phenomena, surface roughness plays a critical role. In Sect. 3.2, the surface roughness was described according to magnitude only. In order to evaluate other properties of surface roughness; for example, whether a majority of the topographical features would be considered to be peaks above a reference plane or valleys below that plane, surfaces with controlled or patterned topographies need to be evaluated. To that end, a series of Al alloy (2024-T3) surfaces were laser ablation-patterned, using a frequency-tripled Nd:YAG laser (355 nm; PhotoMachining Inc.,) with a beam diameter of 25  $\mu\text{m}$ . Initial laser ablation characterization experiments were conducted to determine the relationship between pulse energy and ablation depth (data not shown). The resultant surfaces were characterized using confocal microscopy, and the determined ablation depth in Al alloy surfaces was scaled according to an established relationship (Eq. 5) [47]:

$$z = \frac{1}{a} \ln \frac{E}{E_o} \quad (5)$$

where  $z$  is the ablation depth in  $\mu\text{m}$ ,  $a$  is a constant dependent upon the substrate being ablated,  $E$  is the laser pulse energy, and  $E_o$  is the pulse energy at the ablation threshold. The ablation threshold energy,  $E_o$ , of the Al alloy substrate was determined to be approximately 10  $\mu\text{J/pulse}$ . Based on previous work, the pattern transcribed into the Al alloy surface was a cross-hatch pattern when a laser translation speed of 25.4  $\text{mm s}^{-1}$  was used [48]. The pulse energy varied from 45 to 90  $\mu\text{J pulse}^{-1}$  and the pattern line spacing varied from 12.7 to 101.6  $\mu\text{m}$ . Other variable laser ablation parameters are indicated in Table 8. All surfaces were laser ablation-patterned prior to chemical modification with F17, as described in Sect. 3.1.

The controlled topographically modified surfaces were characterized using contact angle goniometry and optical profilometry (Table 9). Most of the ablated surfaces were

**Table 8** Laser ablation parameters for topographical modification of Al alloy surfaces

Excitation wavelength	355 nm
Pulse duration	30 ns
Pulse energy	40 to 95 $\mu\text{J pulse}^{-1}$
Laser frequency	80 kHz
Scan speed	25.4 $\text{mm s}^{-1}$
Pattern	90° cross-hatch
Line spacing	12.7 to 101.6 $\mu\text{m}$
Number of ablation cycles	1



**Table 9** Surface characterization of laser ablation-patterned Al alloy surfaces

Coating	Pulse energy, $\mu\text{J}/\text{pulse}$	Line spacing, $\mu\text{m}$	Ablation depth, $\mu\text{m}$	Water contact angle, $^\circ$		Profilometry results		
				Ablated	Silanated	$R_{\text{av}}$ , $\mu\text{m}$	Skewness, Sk	Kurtosis, Ku
Control	–	–	–	84 <sup>a</sup>	–	0.31	–	–
Control and F17	–	–	–	–	110	–	–	–
LA-1	40	50.8	3.68	26	170	1.854	-0.714	2.96
LA-2	40	25.4	3.45	82	162	2.227	0.162	2.502
LA-3	40	12.7	–	5 <sup>b</sup>	165	0.595	0.287	3.046
LA-4	65	101.6	5.45	5	162	2.549	-1.36	4.457
LA-5	65	50.8	7.53	5	166	3.402	-0.648	2.686
LA-6	65	25.4	8.75	5	167	4.166	0.567	2.672
LA-7	65	12.7	–	5	165	1.197	0.456	3.74
LA-8	99	101.6	8.9	5	166	2.154	-1.3	4.3
LA-9	99	50.8	8.3	5	167	5.328	-0.406	2.279
LA-10	99	25.4	7.12	5	171	5.11	0.873	3.302
LA-11	99	12.7	–	5	164	3.459	0.691	4.339

<sup>a</sup>Control surfaces were not laser ablation (LA)-patterned

<sup>b</sup>Contact angles reported as 5 $^\circ$  were not able to be accurately measured due to rapid wetting of the surface where contact angles on these surfaces approached 0 $^\circ$

**Table 10** Results of fruit fly impact on laser ablation-patterned Al alloy surfaces

Coating	Profilometry results		Roughness parameter
	Insect height, $\mu\text{m}$	Insect area, $\text{mm}^2$	
Control	69	1.27	
Control and F17	66	0.71	
LA-1	60	0.26	0.380
LA-2	66.1	1.33	0.061
LA-3	62	0.45	0.490
LA-4	89.7	0.31	0.793
LA-5	97	1.43	0.171
LA-6	100.7	0.77	0.121
LA-7	71.5	0.45	0.475
LA-8	66.4	0.40	0.865
LA-9	63.9	0.50	0.058
LA-10	66.6	1.31	0.188
LA-11	66.9	0.28	0.289

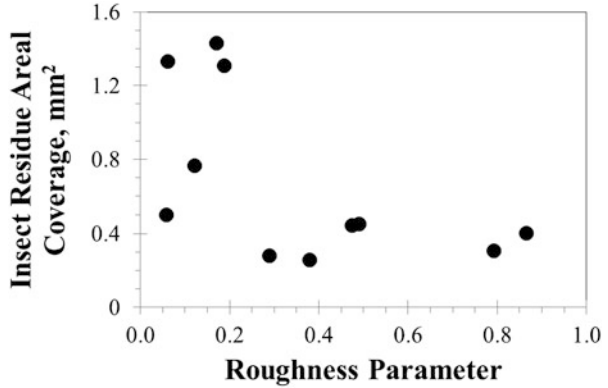
superhydrophilic and became superhydrophobic upon surface fluorination. Likewise, the roughness, skewness, and kurtosis varied considerably across this sample set, which was a good indicator that these surfaces would provide meaningful results with respect to the relationship between surface roughness and insect residue adhesion.

Each surface was then tested for insect residue adhesion performance, using the pneumatic insect delivery device described in Fig. 7 with the cylindrical impact surface. From the results shown in Table 10, the changes in surface topography as a result of changing laser ablation parameters were seen to influence the amount of insect residue that remained on the surface. Although not shown, no clear trend was observed when either the insect residue height or the areal coverage was compared to the WCA data, laser ablation power, or line spacing.  $R_a$  roughness also demonstrated only a moderate inverse correlation with insect residue areal coverage (i.e., typically, greater surface roughness resulted in lower insect residue adhesion).

Closer inspection of the nature of the surface topographies imparted by laser ablation did reveal that the surface energy had an unpredicted dependence on the surface morphology. In particular, both the kurtosis, a measure of how “spiky” a surface is, and the skewness, a measure of whether a surface exhibits a greater “peak” or “valley” nature relative to an average mid-plane, were determined to be inversely proportional to insect residue areal coverage (Fig. 17). Kurtosis (Ku) values  $<3$  indicated rounded features and values  $>3$  indicated sharp (spiky) features. Skewness (Sk) values  $<0$  indicated topographies that would be better described as a series of valleys and Sk values  $>0$  indicated topographies that would be better described as a series of peaks. The roughness parameter ( $R_p$ ) in Fig. 17 and Table 10 was calculated according to Eq. 6:

$$R_p = \frac{\text{Ku}|\text{Sk}|}{3R_q} \quad (6)$$

**Fig. 17** Dependence of insect residue areal coverage on a roughness parameter for fruit fly impacts on laser ablation-patterned chemically modified Al alloy surfaces



where  $R_q$  was included to normalize the numerator relative to the overall roughness of the surface, the 3 in the denominator was included to normalize the  $K_u$  values, and the absolute value of  $S_k$  was utilized to remove the differentiation between peak and valley natures; i.e., only the magnitude of planar deviation was considered. An increase in  $R_p$  ( $R_p > 0.2$ ) typically resulted in a decrease in insect residue areal coverage. There was not a strong correlation with insect residue height, providing further evidence that roughness plays a more significant role in the residue expansion process. This result indicated that a surface with frequent (high  $R_q$ ) perturbations that are either sharp (high  $K_u$ ), or are significantly removed from the reference plane (high absolute value of  $S_k$ ), or both, would be expected to exhibit poor performance; i.e., greater residue areal coverage. This surface would effectively be a “bed of nails” and would consequently exhibit significant adhesion with insect residues. The topography, which would already be wetted as a result of the large water hammer pressure ( $P_{WH}$ ), would inhibit rapid hemolymph expansion, resulting in hole destabilization and greater potential for the retention of exoskeletal debris. Similarly, a relatively smooth surface would yield a similar roughness parameter and exhibit significant insect residue adhesion due to a readily “wetted” surface. In contrast, a surface with less frequent perturbations (low  $R_q$ ) that deviated significantly from the reference plane, and exhibited some significance in aspect ratio, would be anticipated to exhibit improved performance, relative to the bed of nails just described. The reduction in areal coverage, as a result of an increasing  $R_p$  value, appeared to approach an asymptote potentially related to the surface wetting as a result of  $P_{WH}$  overcoming  $P_C$  in the immediate contact area.

HRSEM of the laser-ablated surface prior to insect impact was utilized to provide additional information on the surface topography (Fig. 18). As anticipated, the topographical feature height increased with increasing ablation power. However, the general shape of the pillars also changed. At 40-mJ pulse energies, the pillars appeared to have rounded features (Fig. 18a), while the pillars generated at 65 mJ appeared to be more angular, almost saw-tooth-like (Fig. 18b). At higher magnification levels, differences in the finer surface features were also apparent. A significantly lower amount of material was re-deposited onto the surface when it was exposed to 40-mJ pulses, resulting in large areas that appeared to be relatively smooth (Fig. 18c). At higher pulse energies though, a significant portion of the surface was covered with

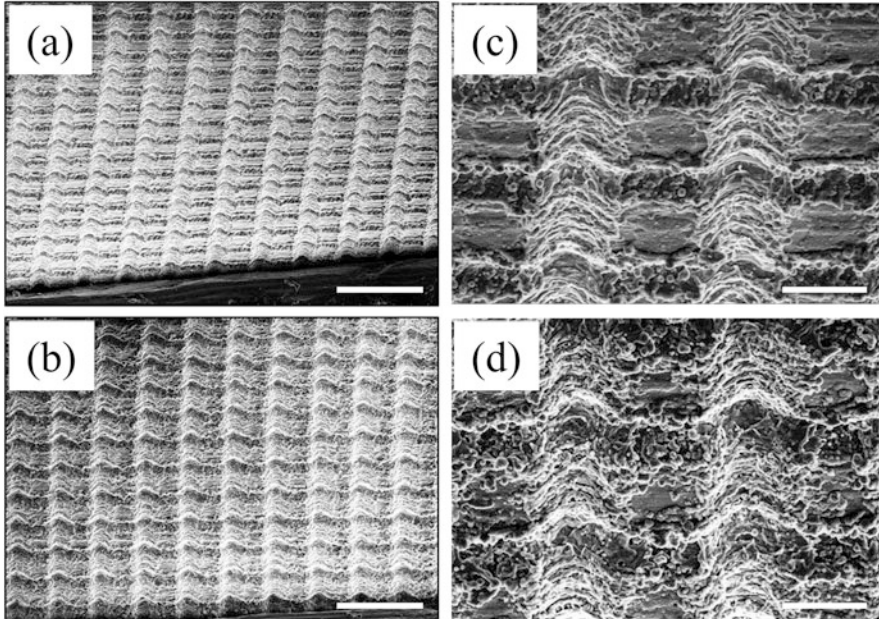


**Fig. 18** (a–d) Scanning electron microscope images of laser ablation (LA)-patterned surfaces: LA-1 (a and c) and LA-5 (b and d). The *scale bar* is 100  $\mu\text{m}$  for images (a) and (b) and 50  $\mu\text{m}$  for images (c) and (d)

micrometer-size deposits that were likely the result of photo-physical material ejection followed by deposition back onto the surface. With 65-mJ pulse energies, a significant portion of the surface deposits had sharper features (Fig. 18d).

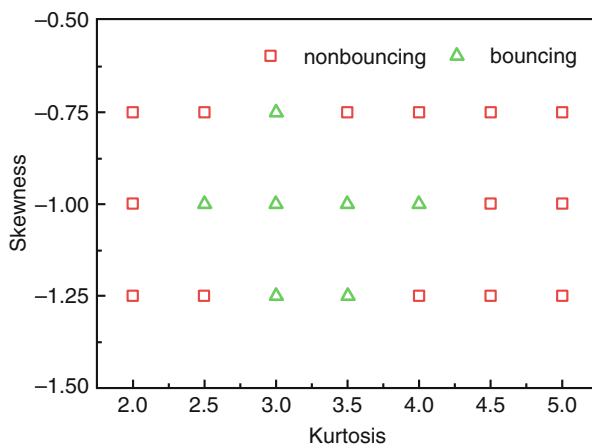
As previously mentioned (see introduction of Sect. 3), the initial stages of insect impact and residue expansion are inertia controlled. Therefore, as the fluid advances along the impacted surface, overcoming a distinct difference in surface height (i.e., a sharp asperity) is energetically unfavorable. This may lead to contact line pinning, hindering residue expansion, thereby stabilizing the thin film of hemolymph spreading across the surface. Likewise, destabilization of the advancing contact line, leading to splashing due to the conservation of momentum, and thereby leading to residue propagation along regions of the contact line (not influenced by contact line pinning) will also be important. Crooks and Boger investigated the influence that surface roughness has on droplet spreading and splashing for fluids with different fluid elasticity [49]. The measure of fluid elasticity is the viscoelastic response of a fluid where a non-Newtonian (Boger) fluid will behave as an elastic solid when stretched. In their work, a non-dimensional area of deformation was calculated by dividing the area of an ellipse containing all of the droplets by the initial droplet radius. The transition from spreading to splashing was observed as a discontinuity in the non-dimensional area of deformation plotted against impact velocity. Their work demonstrated that surface roughness does not affect spreading behavior, but rather changes the threshold velocity for splashing to occur with increasing surface

roughness, reducing the threshold velocity. Although all of the fruit fly impacts described in this work are expected to demonstrate splashing (see Sect. 3.1), the interactions between the expanding hemolymph and the surface remain important, as they will determine how soon after impact splashing will occur. The sooner that the onset of splashing occurs, the smaller is the initial area “wetted” by the insect residue. This interaction is likely to become increasingly complex as the topographical structures become more complex.

A further investigation of the influence that more complex surface roughness characterization parameters have on impacting droplet behavior was conducted by Yuan and Zhang [50]. In their work,  $Sk$  and  $Ku$  were evaluated, among other, more traditional, surface characterization parameters ( $R_a$  and WCA, etc.). The authors determined that, for a surface with a Young’s contact angle  $>90^\circ$ , at the outer bound of skewness (i.e., large peaks or large valleys), a water droplet’s retraction time would be lower than it would be on smoother surfaces. Variation of  $Ku$ , which was paired with  $Sk$ , influenced whether the droplet would adhere to the surface or bounce (Fig. 19). The authors attributed these observations to two energy consumption processes on surfaces: viscous dissipation and structure-induced dissipation due to energetic requirements to overcome pinning effects on sharp asperities. Rough surfaces with low  $Sk$  values do not have these rough asperities, and will exhibit rebound at lower impact velocities. The effects of  $Ku$ , paired with  $Sk$ , indicated that there was a balance between a surface exhibiting micrometer-scale roughness without nanometer-scale features (attributed to roughness-induced hydrophobicity being weak) versus too many peak-type asperities (attributed to pinning interactions resulting in more energy consumption). These results are consistent with what was observed for changes in insect residue areal coverage on the laser ablation-patterned surfaces.

The implications of these complexities, as they relate to insect residue adhesion, are significant, as can be seen in the still images captured for fruit fly impacts on LA-1 and LA-5 surfaces (Fig. 20). For LA-1, the relatively rounded features and moderate surface roughness resulted in an initial residue expansion that rapidly

**Fig. 19** Results of water droplet impact experiments on surfaces with different skewness ( $Sk$ ) and kurtosis ( $Ku$ ) values. Reprinted with permission from Yuan and Zhang [50]. Copyright 2017 American Chemical Society



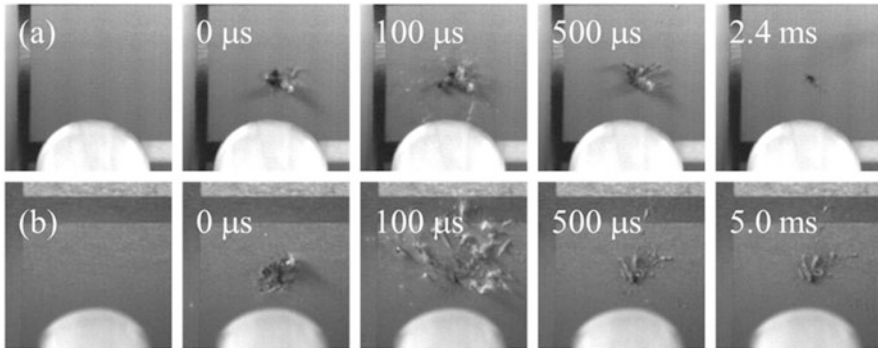


**Fig. 20** (a, b) Still frames taken from insect impact studies performed on laser-patterned chemically modified Al alloy surfaces (a) LA-1 and (b) LA-5

destabilized, due to preferential splashing mechanisms. As a result, at 100  $\mu\text{s}$ , the expanding hemolymph was observed to have translated significant distances away from the exoskeleton, which was ultimately dislodged from the surface, due to the lack of hemolymph to act as a binding material. As previously mentioned (see Sect. 3.2), the hemolymph that does deposit at the initial impact site is likely to be stabilized (i.e., any hole formation is likely to result in hole closure on these extremely superhydrophobic surfaces), and this can be seen in the image collected at 2.4 ms in Fig. 20. In this image, a small area directly at the point of impact can be readily observed because of discoloration associated with the deposited hemolymph.

Fruit fly impact on LA-5 exhibited dramatically different hemolymph spreading behavior relative to that on LA-1. Due to the nature of the surface asperities, as indicated by the lower  $R_a$  and greater  $Sk$  and  $Ku$  magnitudes, the hemolymph was pinned, resulting in further stabilization and therefore inhibited splashing; i.e., more spreading occurred prior to splashing on LA-5. This result can be readily observed by comparing the 100- $\mu\text{s}$  image with that collected from the LA-1 test. The presence and persistence of the hemolymph initial deposits enabled exoskeleton fragments to bond to the surface, resulting in greater retention of insect residues for a long time.

Vaikuntanathan and Sivakumar studied droplet impacts and wetting on controlled surface topographies, using grooved surfaces [51]. They observed wetting arising from  $P_C$  being overcome by  $P_{WH}$  but not by  $P_D$ . Similarly, asymmetric liquid expansion, which was related to contact line pinning, was observed on their surfaces. As their surfaces were patterned in a two-dimensional (2D) fashion, i.e., the topographies consisted of a series of parallel grooves, expansion perpendicular to the groove axis was impeded by contact line pinning. Expansion across the grooves required wetting a surface with greater roughness relative to a surface parallel to the groove axis. This behavior can be correlated to the hemolymph expansion and retention on the laser-patterned surfaces, described here as follows: upon initial impact, these surface topographies would be wetted to some degree as the initial kinetic energy is dissipated. Immediately in the contact area, the surface would be completely wetted due to the magnitude of  $P_{WH}$ . However, as the residue continued to expand, it would not fully wet

the surface and would be more susceptible to removal (due to advancing contact line instability and stable hole formation/expansion) by getting entrained in the airflow as it expands on the moderately rough surface (LA-1). With contact line pinning exhibited at greater roughness values, such as would be the case for LA-5, the hemolymph would be retained to a greater extent, due to increased retention at the point of pinning, which would act to destabilize hole formation (i.e., a thicker layer of insect residue would require more energy for hole formation). Other researchers have studied wetting behavior on surfaces with areas of disparate roughness values and have observed preferential expansion on areas with lower roughness [52, 53].

Collectively, the results of these analyses indicate that, in order to design a surface with intrinsic adhesion prevention properties, it is important to consider the portion of the insect impact and residue expansion process that should be targeted. If the purpose of the surface is to enhance “cleanability,” a relatively smooth surface should be considered. On such a surface, the degree of residue entrainment in fine surface asperities would be minimal, allowing easier access of cleaning solutions or mechanical agitators to the coagulated deposits (see Gruenke [10]). If the purpose of the surface is to minimize the expansion area of insect hemolymph, the nature of the roughness and capability of the surface to stabilize thin fluid film hole formation should be considered. For the prevention of significant residue expansion and the retention of air pockets in the initial impact area (i.e.,  $P_C > P_{WH}$ ), precise control of the surface topography is required. This would likely limit the plausibility of pursuing this approach on a large scale.

## 4 Water Droplet Impact on a Solid Surface

Section 3 applied the extensive results from experimental studies of water droplet impact to the various processes involved in insect impact and residue expansion. Here, these studies will be described in greater detail in order to provide a more complete picture of the research utilized to support the observations made during an insect impact event. Although not exhaustive, this review of droplet impact dynamics brings to light the broad range of behaviors associated with fluid-surface interactions, and correlates these behaviors with insect impact dynamics. The topics covered herein should be valuable for researchers working to advance the design and engineering of surfaces with intrinsic insect residue adhesion mitigating properties.

### 4.1 Low-Velocity Droplet Impact

For low-velocity droplet impact, the droplet will either deposit, partially rebound, fully rebound, or break up while receding on the surface (Fig. 21). Which of these outcomes occurs depends on the liquid surface tension, surface roughness, and surface energy. Other potential outcomes (shown in Fig. 21; prompt splash and corona splash) that require a high impact velocity will be discussed later (see Sect. 4.2).

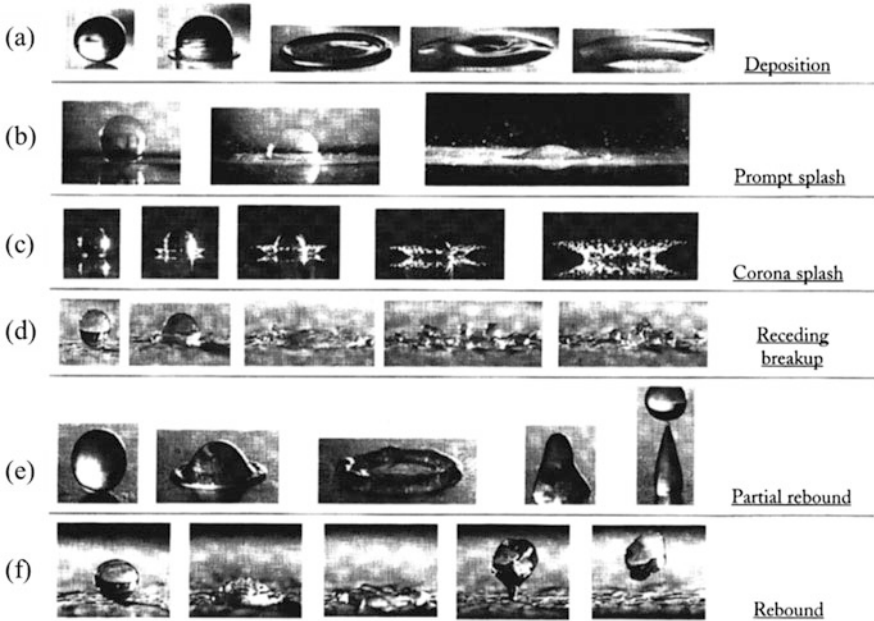


**Fig. 21** Potential outcomes from fluid droplet impacts. Reproduced from Rioboo et al. [54]

Droplet deposition is the simplest result of a droplet impact on a solid surface. Low impact velocities and high surface energies (i.e., low AWCA values) can both contribute to droplet deposition. Additionally, large values for contact angle hysteresis (CAH, the difference between the AWCA and the RWCA) can lead to droplet deposition. As the droplet (where  $D_0$  is the initial droplet diameter) initially contacts the surface, the kinetic energy will be dissipated as a result of deformation and expansion. Both of these phenomena will consume energy, based on viscous dissipation and interfacial interactions, respectively. The impacting droplet contact line will continue to advance until the sum of the kinetic energy ( $E_k$ ) and surface energy of the impacting droplet ( $E_{s1}$ ), which takes the liquid surface tension ( $\gamma_{LV}$ ) into account, is equal to the sum of the surface energy of the expanded droplet ( $E_{s2}$ ) [55] and the energy consumed due to viscous dissipation ( $E_\mu$ , Eq. 7).

$$E_k + E_{s1} = E_{s2} + E_\mu \quad (7)$$

$$E_k = \frac{\pi}{12} \rho D_0^3 V^2 \quad (8)$$

$$E_{s1} = \pi \gamma_{LV} D_0^2 \quad (9)$$

The nature of the expressions for  $E_{s2}$  and  $E_\mu$  will depend on both the shape adopted by the expanded droplet and on how complex the equations describing fluid motion within the impacting droplet are [37, 55, 56]. At this point, a maximum droplet diameter,  $D_{Max}$ , is reached, which is often used to define a spreading factor,  $\xi$



(Eq. 10). Scheller and Bousfield correlated this behavior to  $Re$  and  $Oh$  values based on the kinematics of the fluid droplet [27].

$$\xi = \frac{D_{Max}}{D_0} = 0.61 \times (Re^2 Oh)^{0.166} \quad (10)$$

Lee et al. studied the influence that surface tension, viscosity, wettability, and surface roughness had on the maximum spreading diameter [57]. They determined that fluids with lower surface tension (and similar viscosity to each other) would spread further and take longer to reach  $D_{Max}$ . Likewise, an increase in viscosity (and similar surface tension to each other) resulted in a faster dissipation of kinetic energy, which was observed as a reduced  $D_{Max}$ . Interestingly, when different liquids, with different surface tension and contact angle values, impacted substrates of similar roughness,  $D_{Max}$  was nearly identical. Water demonstrated an interesting transition behavior, with increasing velocity from behaving as a low spreading fluid (i.e., relatively high viscosity) to a high spreading fluid (i.e., relatively low surface tension).

#### 4.1.1 Droplet Retraction and Rebound

Once the droplet has expanded to  $D_{Max}$  the droplet will begin retracting until a stable conformation is achieved. The liquid tends toward a spherical conformation as a result of surface tension, which is impeded by interfacial and gravitational interactions. If the impact velocity was low and/or the surface energy is high, liquid retraction will likely be nominal and a stable conformation will be readily achieved. However, as the impact velocity increases or the surface energy of the substrate decreases, the liquid retraction processes necessary to obtain a stable confirmation will increase. The liquid velocity upon retraction will increase and, for most surfaces, a bulge will form in the center of the liquid droplet. The direction of liquid travel will change from along the surface to normal to the surface, which can result in partial or complete rebound of the liquid droplet. Fukai et al. developed a 2D model of the response of liquid droplets impacting solid surfaces that accounted for inertial, viscous, gravitational, and surface tension effects [58]. In addition, the Lagrangian approach was used, which enabled the droplet spreading to be modeled with a propagating ring structure, recoiling, and subsequent oscillation. Enhancements were made to account for differences in advancing and receding contact angle values (i.e., wetting behavior). This is important for the latter stages when the inertial effects no longer dominate behavior. Their simulations described a mass concentration as a concentric ring that travels to the drop periphery, followed by a reduction as the mass is redistributed upon the droplet expanding to the maximum radius (Fig. 22). Once this redistribution occurred, thinning at the droplet periphery caused the droplet to start retracting. On a non-wetting surface, with an AWCA of  $92^\circ$ , the outer ring was more pronounced, recoil was initiated more rapidly, and the upward bulk motion was stronger once the peripheral mass recombined with the central mass. Ultimately, it took longer for a droplet to attain equilibrium on a hydrophobic surface than on a wetted surface, due to more pronounced oscillations.

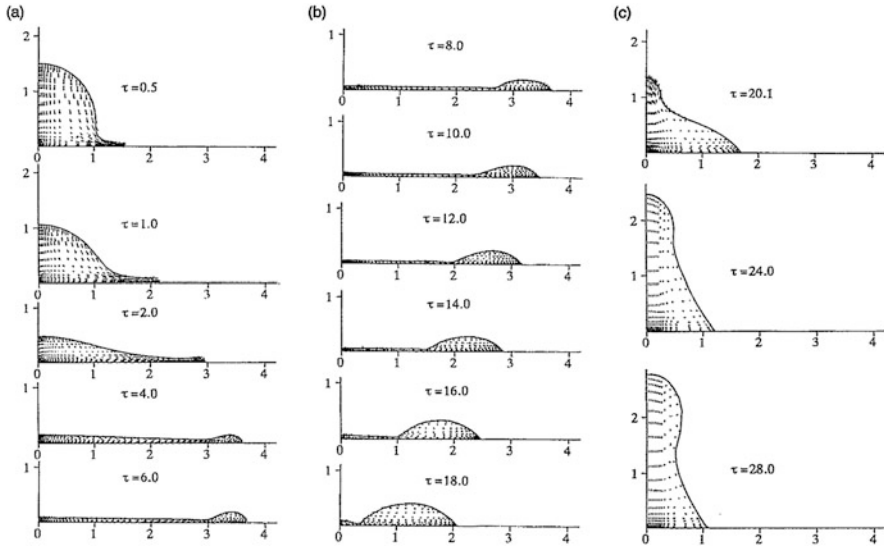


**Fig. 22** Snapshots from a model of droplet evolution upon impacting a hydrophobic surface. Reproduced from Fukai et al. [58]

Superhydrophobic surfaces have been intensely studied, with particular focus being given to conditions under which full droplet rebound was observed. Two conditions are often cited as requirements for a surface to be considered superhydrophobic; an AWCA value of  $150^\circ$  and an ROA of  $\leq 10^\circ$ . Wang et al. suggested a third criterion for a surface to be considered superhydrophobic, a restitution coefficient ( $\varepsilon$ ) of at least 0.8 [59]. The restitution coefficient is the ratio of the velocities of droplet rebound,  $V_R$ , and impact,  $V_0$  (Eq. 11).

$$\varepsilon = \frac{V_R}{V_0} \quad (11)$$

The restitution coefficient is dramatically affected by CAH, and the authors described this phenomenon as arising from at least six sources, classified into two different categories: thermodynamic and kinetic hysteresis. For thermodynamic hysteresis, there are two causes: surface roughness and surface heterogeneity. For kinetic hysteresis, there are four causes: surface orientation, surface deformation, liquid penetration, and surface mobility. The restitution coefficient is height-dependent, with an onset velocity described as the critical falling height for rebound (CFRB), defined as a height below which rebound would not be observed. As velocity increases, this factor would increase until a plateau would be reached beyond which a new (or increasingly favorable) relaxation pathway would appear as vigorous droplet motion and energy dissipation brought about by viscous interactions within the droplet.

### 4.1.2 Pressure Balance and Localized Wetting

As no surface can be rendered superhydrophobic without the introduction of topography (the maximum AWCA on a flat surface cannot exceed  $120^\circ$ ) [38], the degree that surface topographies are “wetted” by an incident fluid is an important topic. Consider first the quasi-static deposition of a water droplet on a topographically modified surface. Within the contact area, the Laplace pressure will act to wet the surface, while capillary pressure will act to prevent the advance of the three-phase contact line (Fig. 23).

The two possible wetting states, one with air pockets retained underneath the water droplet and the other with the entire contact area completely wetted, are referred to as Cassie-Baxter and Wenzel states, respectively (Eqs. 12 and 13) [61, 62]. Contact angle values associated with these wetting states (Cassie-Baxter and Wenzel), as well as the contact angle value measured on a smooth surface (the so-called Young’s contact angle), are indicated as  $\theta_{CB}$ ,  $\theta_W$ , and  $\theta_Y$ , respectively. Although the Cassie-Baxter state is considered to be a metastable state, the energetic requirements for transition to the Wenzel state can be significant enough to prevent transition to the fully wetted state (where the fraction of the surface that is not wetted in the Cassie-Baxter state is denoted as  $f$ ), even upon impact from significant heights [63, 64]. It is relatively straightforward to equate these two relations to determine a roughness,  $r$ , at which this transition would occur (Eq. 14). This principle has been utilized to design superhydrophobic surfaces [65–69].

$$\cos \theta_W = r \cos \theta_Y \quad (12)$$

$$\cos \theta_{CB} = rf \cos \theta_Y + (f - 1) \quad (13)$$

$$r = \frac{f - 1}{\cos \theta_Y (1 - f)} \quad (14)$$

The entire surface will be wetted (Wenzel state) if the Laplace pressure exceeds the capillary pressure; for a surface with topographies that are open, such as a pillar

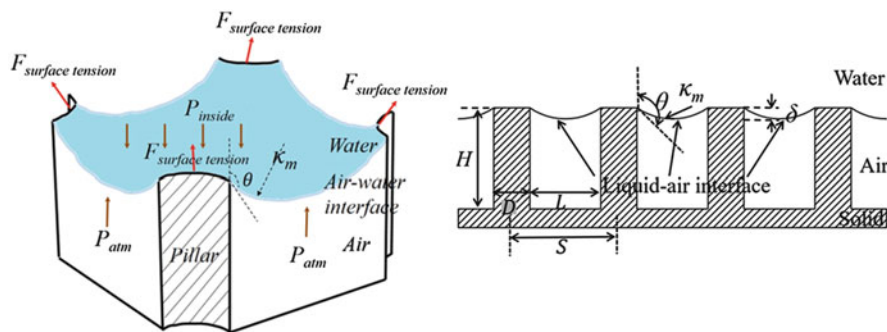


**Fig. 23** Two representations of the balance of forces involved in the retention of air pockets underneath a water droplet. Reprinted with permission from Wang et al. [60]. Copyright 2017 American Chemical Society

array, the capillary pressure is equal to atmospheric pressure. Recently, Wang et al. studied the transition from a Cassie-Baxter to a Wenzel state using a quartz crystal microbalance (QCM) [60]. In this work, a series of square pillar arrays, generated in poly(methylmethacrylate) (PMMA), were subsequently hydrophilized via exposure to oxygen plasma or hydrophobized through the absorption of a perfluorinated silane. A decrease in pillar height (pillar diameter and spacing were kept constant at 10 and 15  $\mu\text{m}$ , respectively) resulted in a transition from the Cassie-Baxter to the Wenzel state, which was observed as a decrease in the WCA (Fig. 24). Similar differences were observed in the frequency response of the QCM on which these surface studies were conducted.

Using these results, Wang et al. [60] calculated a maximum penetration depth,  $\delta_{\text{max}}$ , based on the pillar spacing,  $L$ , and AWCA ( $\theta_A$ ) on a flat surface (Eq. 15).

$$\delta_{\text{max}} = \frac{L(1 - \sin(\pi - \theta_A))}{2 \cos(\pi - \theta_A)} \quad (15)$$

For surfaces with topographical features with heights less than  $\delta_{\text{max}}$ , a water droplet placed on this surface will spontaneously transition to a Wenzel state. For surfaces with feature heights greater than  $\delta_{\text{max}}$ , additional energy, such as that provided by a falling or otherwise propelled droplet, may increase feature penetration depths beyond  $\delta_{\text{max}}$ . Nonomura et al. evaluated the influence that additional energy exhibited on pore wetting behavior by studying a water droplet placed over a pore in a polydimethylsiloxane (PDMS) substrate [70]. The entire assembly was dropped from a specific height, and the behavior of the water droplet was captured using high-speed photography (1,000 frames/s). As the pores were of comparable diameter to the initial droplet diameter, and were open to the atmosphere on the other side (i.e., the pore could

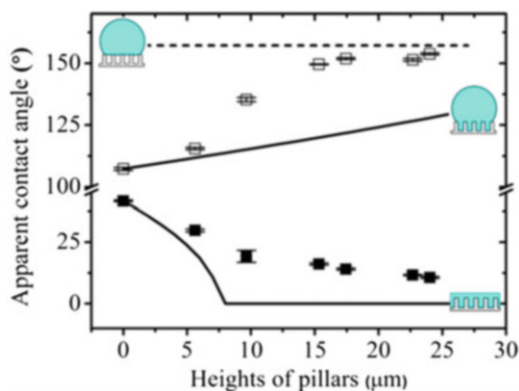


**Fig. 24** Water contact angles, measured on poly(methylmethacrylate (PMMA) surfaces, that were rendered hydrophilic (*closed squares*) or hydrophobic (*open squares*). The *solid lines* were calculated based on Wenzel wetting and the *dashed line* was calculated assuming a Cassie-Baxter wetting state. Reprinted with permission from Wang et al. [60]. Copyright 2017 American Chemical Society

be considered to be infinite in length when considering whether the bottom would be wetted upon impact), the results can be qualitatively related to the majority of impact studies included in this work. Nonomura et al. observed transitions in wetting behavior for water droplets provided with increasing energy; i.e., an increase in experiment drop height resulted in greater and irreversible droplet penetration.

One important observation from the Nonomura work was that the AWCA was maintained within the pore, even at significant penetration depths. This behavior is one reason that hydrophilic materials can be made superhydrophobic by the introduction of re-entrant structures [71, 72]. Once the droplet has advanced to  $\delta_{\max}$ , energetically, the only way to continue to increase the penetration depth would be to transition the pinned state from the top of the topographic feature to some distance along the wall of the feature side-; i.e., the surface would physically penetrate the droplet, if not the entire feature length to the substrate itself. This is referred to as feature impalement. Impalement can occur as a result of two different interactions; if the Bernoulli pressure ( $P_D$ ) is greater than the capillary pressure ( $P_C$ ) or if the water hammer pressure ( $P_{WH}$ ) is greater than  $P_C$ . The balance between the pressures, and the droplet impact outcomes, are shown in Fig. 25. If  $P_C$  is greater than the sum of  $P_D$  and  $P_{WH}$ , then complete dewetting, and likely rebound, will occur (result in upper right of Fig. 25). If  $P_C$  is greater than  $P_D$  but less than  $P_{WH}$ , wetting will only occur within the area of initial impact (result in lower right of Fig. 25). If  $P_C$  is less than  $P_D$ , which would necessitate it to be less than  $P_{WH}$ , wetting will occur over the entire surface (result not shown in Fig. 25).

An additional pressure, the gas-layer pressure, working to compress the fluid itself, may also play a role, but is not considered; rather, the compression of the air trapped underneath the droplet is considered [74]. The equations (Eqs. 16–18) for the three pressures to be considered here are:

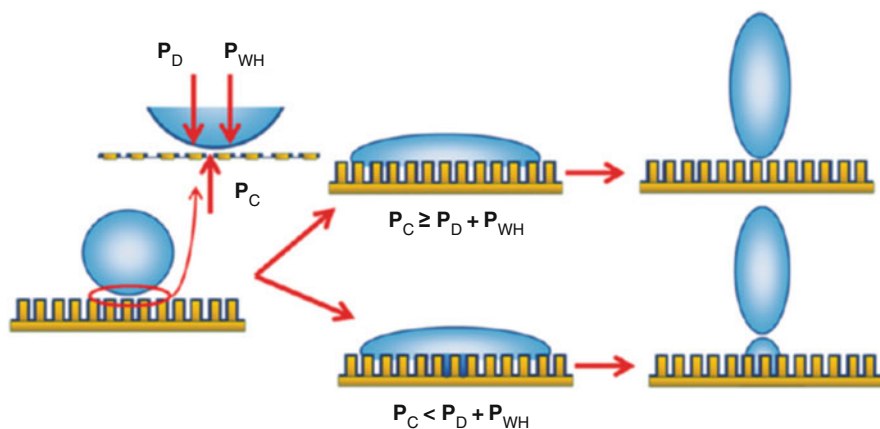


**Fig. 25** Comparison of force magnitudes for droplet impact on a textured surface. If capillary pressure exceeds the sum of the Bernoulli and water hammer pressures, complete rebound may occur (*upper case*). If this is not true, at least partial substrate wetting will take place (*lower case*). Reprinted with permission from Dash et al. [73]. Copyright 2017 American Chemical Society

$$P_C = -\gamma_{LV}(\cos \theta) \frac{L_C}{A_C} \quad (16)$$

$$P_D = \frac{\rho V^2}{2} \quad (17)$$

$$P_{WH} = k\rho cV \quad (18)$$

$L_C$  is the capillary perimeter and  $A_C$  is the capillary area. Malavasi et al. studied topography impalement for different fluids, and determined that the critical velocity for feature impalement increased with a decrease in topographic feature (pore) size and an increase in fluid surface tension [74]. In a similar study, Papadopoulos et al. studied the effects of surface feature impalement by studying the evaporation of water droplets [75]. Although this was a stationary experiment, the nature of the observed feature impalement was quite similar to what would be observed during a droplet impact event. As a result of a reduction in volume due to droplet evaporation, the Laplace pressure ( $P_L = 2\gamma/D_0$ ) increases until either the liquid underneath the contact area contacts the substrate (sagging; see Fig. 23 for an example of liquid sagging between topographical features) or the contact line de-pins from the pillar tops (impalement). A transition from sagging to impalement was observed with a reduction in pillar spacing, transitioning from sagging to impalement. This was the result of the curvature necessary to support substrate contact and pinning at the pillar top not being energetically favorable, due to the requirement for the contact line contact angle needing to exceed the advancing contact angle to maintain this state. Based on these results, given specific impact conditions (high impact velocity or low fluid surface tension), the superhydrophobic behavior of a surface would fail (i.e., a surface wetting state would transition from a Cassie-Baxter to a Wenzel state) regardless of surface topography and contact angle values.

Bartolo et al. performed both droplet impact and external pressure experiments to study droplet impalement [76]. In this work, Sylgard 184 (a silicone elastomer; Sigma Aldrich) surfaces were generated with triangular arrays of cylindrical posts. For droplet impact experiments, transition from deposition to bouncing to impalement was observed, arising from increased impact velocity (increased drop height). Transition velocity from deposition to bouncing was determined to be independent of cylindrical post height, while, up to 20  $\mu\text{m}$ , the transition velocity from bouncing to impalement was determined to depend on cylinder height. For experiments on surfaces with cylindrical post heights greater than 20  $\mu\text{m}$ , the transition velocity to impalement was independent of post height. In another series of experiments, a water droplet was placed on a Sylgard 184 surface decorated with cylindrical posts, and a fluorinated glass slide was pressed against the droplet. The pressure resulting in transition from a Cassie-Baxter to a Wenzel state was determined. Additionally, evaporation experiments, similar to those conducted by Papadopoulos et al. [75], were performed. Collectively, a critical impalement pressure, the pressure at which the investigated surfaces adopted a Wenzel wetting state, was determined and it was shown to follow a trend similar to that in the impact experiments (Fig. 26).

For surfaces with post heights  $<20\ \mu\text{m}$ , this pressure was dependent on post height. At greater post heights; the critical impalement pressure was constant. Thus, a topography-independent pressure was identified such that, at greater pressures, the resultant droplet would be impaled by the topography and the contact line would advance toward the substrate, i.e., the surface between the posts.

Based on impact experiments on flat surfaces, values assigned to the water hammer pressure coefficient,  $k$ , have varied from 0.2 to 1.0 for a rigid surface, with the primary differentiating factors being compliance or compressibility [77–80]. However, Dash et al. determined that this coefficient exhibited a dependence on capillary pressure [73]. In their work, water droplets were impacted on surfaces consisting of a square array of hollow pillars that exhibited sessile water droplet contact angle values ranging from  $153$  to  $157^\circ$ . Water droplets were impacted on these surfaces at increasing heights to determine a critical velocity (height) at which incomplete rebound of the droplet occurred. At this critical velocity, it was assumed that  $P_C$  was equal to the sum of  $P_D$  and  $P_{WH}$ . This relationship was utilized to determine an empirical  $k$  value (Eq. 19):

$$k = \frac{P_C - P_D}{\rho c V} \quad (19)$$

Based on their results, as well as the results from two other studies [81, 82], Dash et al. calculated a water hammer pressure coefficient that was significantly less than 0.2 and that exhibited a linear dependence on capillary pressure [73].

For combinations of surface properties and impact conditions where complete wetting can be prevented, full droplet rebound can be observed. These impact events

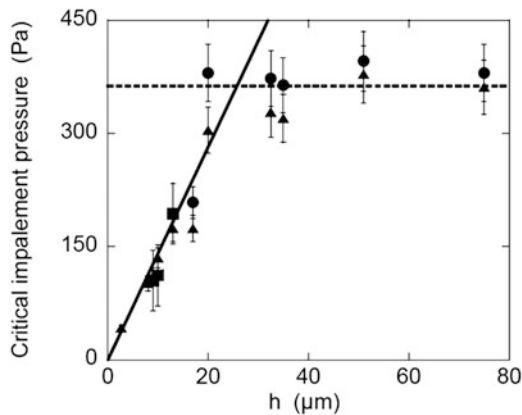


**Fig. 26** A compilation of the critical impalement pressure measured on pillar array surfaces of different heights,  $h$ . The circles were measured from evaporation experiments and the triangles were measured from impact experiments. The solid line is a linear fit for pillar heights  $<20\ \mu\text{m}$  and the dashed line is a constant value averaged for measurements made on surfaces with pillar heights  $>20\ \mu\text{m}$ . Reproduced from Bartolo et al. [76]

are described as the contact time, which is the amount of time the droplet is in contact with the surface from the moment of initial contact to the first full rebound resulting in complete detachment from the surface. For droplet impacts that exhibit symmetric rebound, return of the majority of the droplet mass to the center of the mass, followed by vertical displacement of the droplet, led to droplet contact time being reduced by minimizing the contact area between the droplet and the surface, i.e., increasing the fraction of the interaction area that represents entrapped air [83]. Asymmetric rebound, so-called pancake bouncing, has been demonstrated as an alternative approach to further reduce contact time [84]. Liu et al. studied this phenomenon on a series of topographically modified copper surfaces that were subsequently imparted with hierarchical topographies by immersion in a caustic solution, and rendered hydrophobic by functionalization with a perfluorinated silane [85]. The rebound behavior was demonstrated to depend on the surface topography, with asymmetric rebound observed to greater extents as the half apex angle,  $\alpha$ , increased for truncated pyramidal post arrays (Fig. 27). Liu et al. have determined that asymmetric rebound arises when droplet expansion/retraction timescales are similar for both lateral expansion and topography impingement (which must be fully reversible) based on changes in surface energy as the amount of “wetted” surface area changed. Shen et al. also studied surface topographical influence on droplet contact time, and generated macro-scale surface topographies with hierarchical micro- and nano-scale features that exhibited contact times approximately equal to the time required to achieve droplet expansion to  $D_{\max}$  [86]. Pancake rebound was also studied on elastic substrates by Weisensee et al., in which they determined that if the oscillatory response of the substrate occurred at a similar frequency to the liquid expansion and recoil events, there would be a transfer of vertical momentum from the substrate to the droplet, facilitating rebound in the droplet expanded state [87].

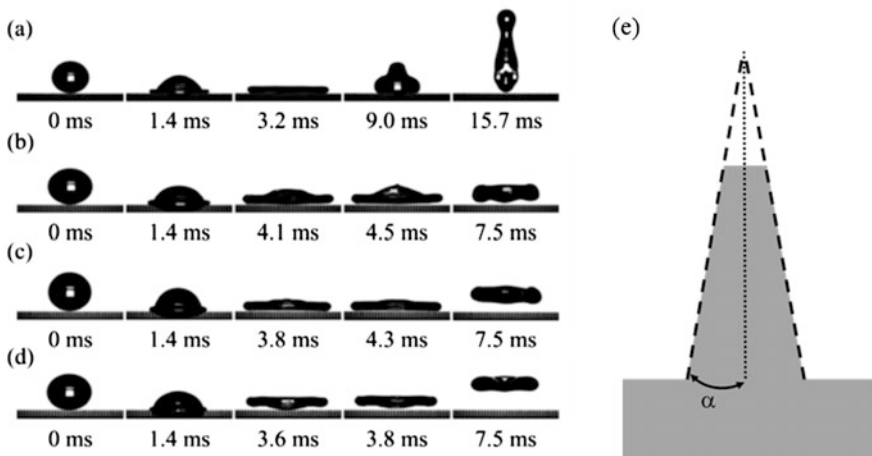


**Fig. 27** (a–e) Water droplet impacts on topographically modified copper surfaces with straight post arrays (a) and truncated pyramid arrays with a half-apex angle,  $\alpha$ , of (b) 1°, (c) 1.7°, and (d) 3.6°. (e) Schematic of a truncated pyramid with  $\alpha$  indicated. Reproduced from Liu et al. [85]



Surface-droplet interaction conditions often lead to the partial wetting of a surface in a manner rather different from a simple transition from a Cassie-Baxter to a Wenzel state. Instead, wetting can occur as a result of the immediate vicinity of the impact site experiencing significantly greater interaction forces prior to expansion of the droplet. Deng et al. described this as a two-phase interaction, with the first phase, the “contact phase,” comprising the exertion of the “water hammer pressure” [88]. This pressure arises from the compression of the liquid behind the shockwave envelope. The impact event then transitions from the contact stage to the “spreading stage,” where the shockwave propagation exceeds the contact line advance and the pressure drops from the water hammer pressure to the Bernoulli or dynamic pressure (the authors referred to this as the “wetting pressure”). These phenomena are further described in Sect. 4.2 on high-velocity impact. The authors observed a transition from complete pinning, to partial pinning, to complete rebound as a result of increasing the density of pillar topographies on a silicon wafer. This transition was attributed to a change in the pressure balance from allowing substrate wetting during both the contact and spreading stages, to allowing substrate wetting only during the contact phase, to not allowing wetting to occur during either stage of droplet impact as pillar density increased. Dash et al. investigated the structure-property relationship between surface topography and pressure balance as it related to substrate wetting on a series of square pillar arrays that were either solid or hollow [73]. The surfaces were generated using standard lithography techniques on a silicon wafer, followed by spin-coating the surface with a conformal Teflon<sup>®</sup> (Dupont, Wilmington, DE USA) AF1600 coating. One unique aspect of the hollow square pillar array surfaces is that there were regions that were open to exchange (the interstitial areas), as well as regions that were isolated from “communicating” with the surroundings (the hollow area within a single square pillar). The authors determined that the presence of the isolated regions increased the “robustness” of the surface with respect to retaining entrapped air, i.e., there was a persistent Cassie-Baxter wetting state throughout the initial impact and droplet rebound process. The threshold, critical velocity, for transition to partial wetting as a result of water hammer pressure was readily observed as the retention of a small microdroplet upon rebound of the water droplet. The difference between complete rebound and only partial rebound was found to be very sensitive to experimental conditions; a velocity variation of 2% resulted in different outcomes.

As the droplet impact velocity increases, the amount of kinetic energy translated into droplet spreading can be so great that droplet fracture, or break up, can occur. This is often referred to as splashing. Splashing can occur immediately upon impact (Fig. 21b) or upon liquid expansion (Fig. 21c). Immediate droplet splashing occurs when the droplet velocity is high enough to cause the formation of shockwaves. Cossali et al. studied droplet impact conditions and identified a parameter,  $K_L$ , that defined the transition from spreading to splashing (Eq. 20) [89]. Splashing occurred when  $K_L$  was calculated to be greater than an empirical relationship with surface roughness,  $K_{L,E}$  (Eq. 21). A non-dimensional surface roughness was calculated according to Eq. (22). Based on this relationship, the required energy for splashing is greatest for a smooth surface. It should be noted that, for a fruit fly impact on a smooth surface,  $K_L$  calculated according to Eq. (21) is 670, while the calculated

value of  $\text{Oh}^{-0.37}\text{We}$  was  $4.13 \times 10^5$ ; i.e., splashing should be anticipated for insect impact events that occur at or near take-off/landing speeds.

$$K_L = \text{Oh}^{-0.37}\text{We} \quad (20)$$

$$K_{L,E} = 49 + \frac{3.76}{R_{\text{ND}}^{0.63}} \quad (21)$$

$$R_{\text{ND}} = \frac{R_a}{2R_0} \quad (22)$$

## 4.2 High-Velocity Droplet Impact

As droplet velocity increases further, the processes involved with fluid expansion along the impacted surface change. The complexity of this process increases considerably at this point, and a review of this subject is outside the scope of this chapter. The reader is referred to the works of Lesser and Field and the references therein [78, 90]. A relevant phenomenon for this discussion is the observation of jetting (Fig. 28); which is referred to in Fig. 21b as prompt splash, not to be confused with fingering, which can occur as a result of corona instabilities (referred to in Fig. 21c as corona splash) [91]. Jetting arises from a shockwave that propagates in the solid surface normal direction. These jets travel at up to ten times the impact velocity [90], though their appearance is not instantaneous. Instead, this phenomenon occurs after the shockwave velocity, equal to the speed of sound ( $\sim 1,500$  m/s in water) if the acoustic limit is assumed, exceeds the contact line advancing velocity [23]. A threshold velocity,  $V_C$ , has been determined (Eq. 23), below which jetting would not occur [92]:

$$V_C = \left(\frac{2\sigma}{\rho D}\right)^{1/2} \quad (23)$$

Based on the impact velocities discussed in this chapter, and the relative size of the impacting objects, it is likely that nearly all impacts will result in the jetting of material away from the impact site. The jetting angle has been determined to not be parallel to the substrate, but rather to be at an angle that may be related to the material and surface properties of the impacted surface [23, 93]. Range and Feuillebois also determined that the nature of the surface roughness, likewise, played a role: square groove-decorated surfaces exhibited greater critical velocities than triangular groove-decorated surfaces [93].

As the contact line advances, the velocity diminishes rapidly. Haller described an equation to calculate the change in contact line velocity,  $v_{\text{CL}}$  (Eq. 24) [91]:

$$v_{\text{CL}} = \frac{[V(R_0 - Vt)]}{\sqrt{2R_0Vt - V^2t^2}} \quad (24)$$

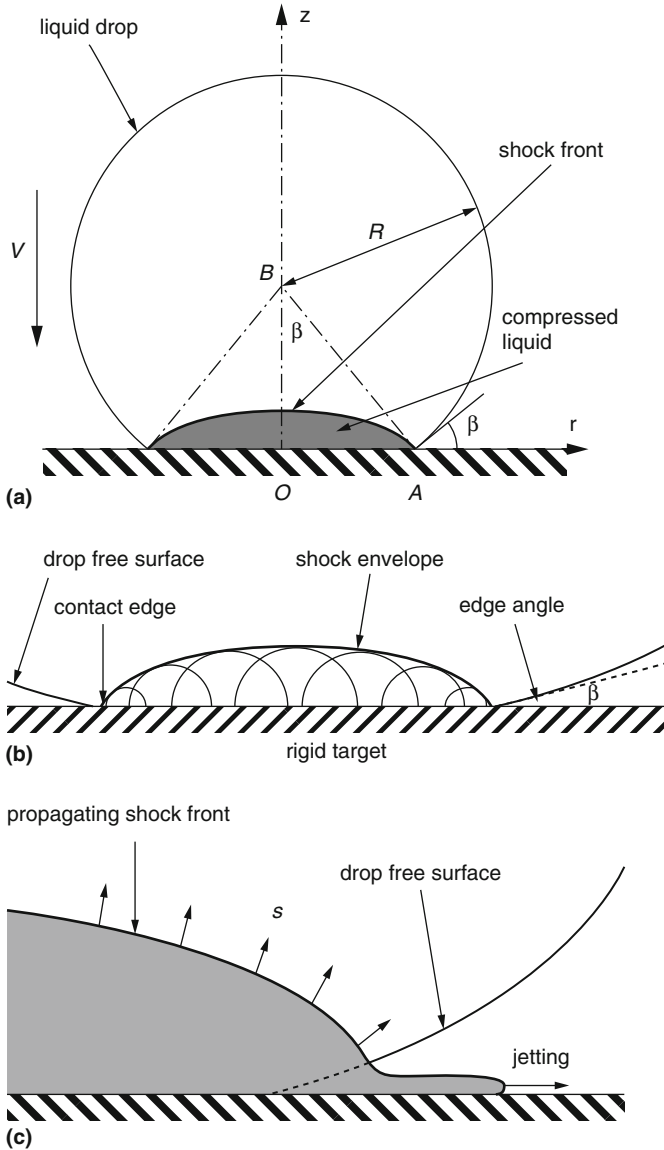


**Fig. 28** When a droplet impacts a surface at high velocity, a compressed liquid region is formed (a). A shockwave is generated and attached to the advancing contact line (b). Jetting will occur when the velocity of the advancing contact line falls below the speed of sound in the droplet (c). Reproduced from Haller et al. [91]

For a droplet the size of a fruit fly impacting a surface at approximately 70 m/s, the velocity 1 ns after impact of the contact line would be approximately 5,100 m/s. However, 10 ns after impact, this velocity would drop to approximately the speed of sound in water; i.e., jetting would be observed. Thus, none of the experiments

described previously in this chapter would have had the time resolution to observe the generation of these jets immediately after their formation. Toivakka simulated liquid droplet impacts and generated pressure profiles over the contact area [26]. They calculated the time that the maximum pressure was exerted on the surface to be a few microseconds after impact, and strain rates, as the value for the pressure wave that travelled from the impact site to the periphery of the contact area, could be as high as  $10^6 \text{ s}^{-1}$ . The delay in observation of the maximum pressure agrees well with the travel of the shockwave away from the surface, followed by relief waves that follow the path of the shockwave and result in a downward liquid jet [90]. The downward jet has more than enough force to damage the surface, and has been studied extensively [78, 94, 95]. This downward jetting could potentially influence the adhesion forces experienced between an insect and a surface, but consideration of change in substrate composition and morphology as a result of insect impact is beyond the scope of this chapter.

#### 4.2.1 Thin Film Stability After Droplet Impact

After jetting has transpired, a portion of the remaining liquid droplet may rebound. Typically, the periphery of the spreading droplet becomes thicker as the central portion of the droplet has turned into a thin liquid film. The stability of this thin film, i.e., the prevention of hole formation and eventual rupture, was determined to depend on its thickness. Dhiman and Chandra studied this phenomenon by dispensing 0.6-mm distilled water droplets that were impacted at 10–30 m/s by spinning a flywheel [46]. This resulted in  $Re$  numbers that ranged from 5,800 to 17,400. Impacts on a smooth glass substrate were stable up to 11,600  $Re$ ; on plexiglass (PMMA), which had a slightly higher AWCA ( $58$  vs  $80^\circ$ ), impacts were destabilized (Fig. 29). Impact on a wax surface ( $AWCA = 107^\circ$ ) was unstable at all impact speeds. On a superhydrophobic surface ( $AWCA = 160^\circ$ ), long fingers, which extended and eventually formed droplets, were first seen on the periphery, with a continuous film formed at the impact location. This suggested that hole formation was suppressed on the superhydrophobic surface. Thus, contact angle was one of the dominant factors in determining film thickness and stability, as was predicted through thermodynamic analysis [96]. The stability of the hole, i.e., whether it would tend to close or grow, was observed to be largely dependent on the size of the meniscus (Fig. 30). The area of the meniscus,  $S$ , will be large at very low and high WCA values. Thus, hole growth will be energetically unfavorable and the hole will close. At intermediate WCA values, the meniscus is smaller and it is more energetically favorable to support hole growth.

To solve for the boundary between film stability and instability, Dhiman and Chandra [46] set the free energy change ( $\Delta F$ ) to 0 and solved for the critical film thickness,  $h$ , for which a hole of radius,  $r$ , would result in an unstable film. They estimated the film thickness after impact according to the conservation of mass before and after impact. To do this, they had to estimate a maximum spreading value (Eq. 5), which they did using an energy balance model dependent on the

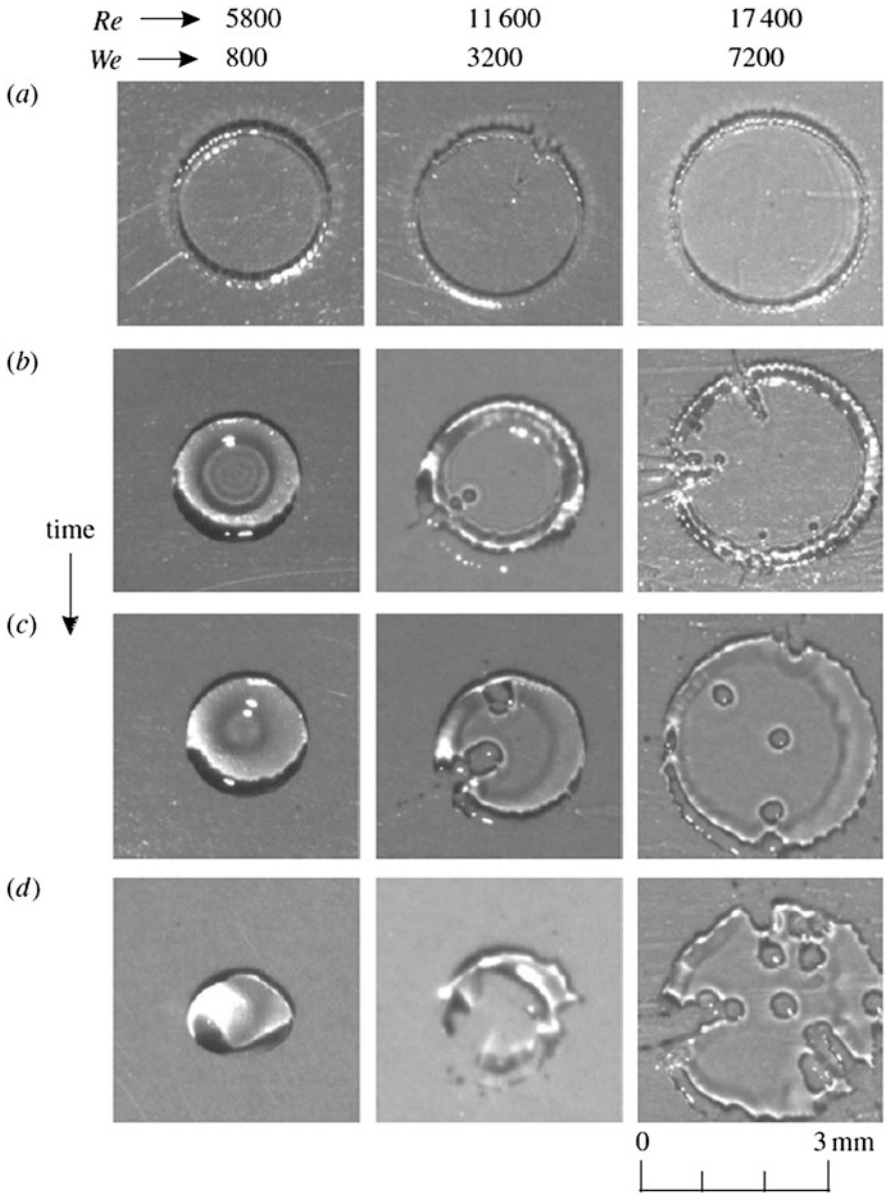
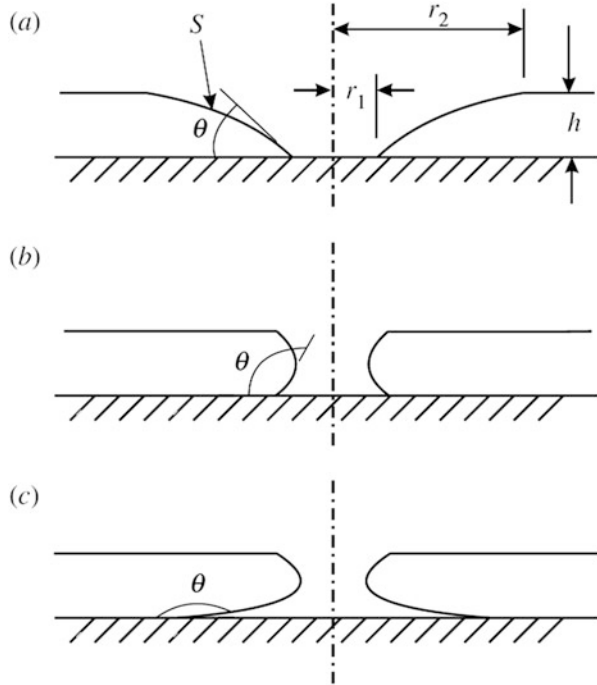


**Fig. 29** Water droplet impacts on a smooth plexiglass (PMMA) surface under different impact conditions. Reproduced from Dhiman and Chandra [46]

**Fig. 30 (a–c)**  
Representation of film stability as it relates to water contact angle. In (a) and (c), hole retention and growth is destabilized due to the low (a) or high (c) water contact angle value. However, at intermediate contact angles (b), hole generation and growth is stabilized and this feature can lead to further hole formation and ultimately thin liquid film break up. Reproduced from Dhiman and Chandra [46]



AWCA value. Based on these observations, Dhiman and Chandra developed a criterion for film rupture (Eq. 25):

$$\left(\frac{16}{3r_1^* \sin \theta_r}\right) \frac{1}{\sqrt{Re_c}} = 1 + \frac{(1 - \cos \theta_r)^2}{\sin^2 \theta_r} \left[ \cosh\left(\frac{16}{3r_1^* \sin \theta_r \sqrt{Re_c}}\right) - \sinh\left(\frac{16}{3r_1^* \sin \theta_r \sqrt{Re_c}}\right) \right] \quad (25)$$

Film rupture will occur if the droplet impact conditions exceed a critical Re number,  $Re_c$ . Based on this relationship, for film rupture to occur, hydrophilic and superhydrophobic surfaces will require greater impact velocities relative to surfaces with moderate hydrophobicity, consistent with the Dhiman and Chandra [46] experimental results. This relationship was utilized previously to correlate contaminant insect residue properties with surface properties (see Fig. 14).

This review of droplet impact dynamics brings to light the broad range of behaviors associated with fluid-surface interactions and correlates them with insect impact dynamics. The topics covered herein should be valuable for researchers working to advance the design and engineering of surfaces with intrinsic insect residue adhesion-mitigating properties.

## 5 Outlook

Significant progress has been made in identifying the surface properties that contribute to insect residue adhesion. One of these properties is surface topography. Several reports have indicated that the magnitude of the roughness ( $R_a$  or  $R_q$ ) affects insect residue adhesion; however, other methods to characterize surface topography, such as skewness and kurtosis, have largely been overlooked. Very recently, lateral correlation length was also identified as a contributor to insect residue adhesion [33]. This, as well as skewness, kurtosis, and potentially other roughness parameters, should be investigated more thoroughly. Methods to alter how forces are distributed through the expanding residues, such as pancake bouncing, have not received much attention and would likely improve the mitigation of insect residue adhesion. The other major contributor to insect residue adhesion is surface chemistry. Although the influence of surface chemistry is entwined with that of surface roughness, hydrophobicity as a result of a low surface energy material was determined to play a clear role, especially as it related to the de-pinning of the contact line from the tops of topographical features. Likewise, contact line destabilization, hole formation, and stabilization processes are modified by surface chemistry. Superhydrophobic surfaces, and to a lesser degree moderately hydrophobic surfaces, induced destabilization of the advancing hemolymph contact line, and reduced the wetted surface area. Surfaces of modest hydrophobicity were determined to exhibit the greatest hole stability, leading to reductions of the wetted area at later stages of residue expansion.

Based on the current state of research, the requirements for a surface to be insect residue adhesion-resistant are:

1. The coating must be at least hydrophobic to enable disruption of the expanding hemolymph thin film. This could be implemented as a continuous coating or as a co-continuous network of multiple components, one of which exhibits some degree of hydrophobicity (see Gross et al. [34]).
2. The nature of the topography beyond just the  $R_q$  height variation is important. Surfaces with modest variation around a mean are predicted to be more effective than surfaces with extreme skewness values (valley- or peak-dominated) or those with high kurtosis values.

It is likely that this list will be modified as research advances. The process within an insect impact event (i.e., contact line destabilization, hole formation, force distribution) or the results of hemolymph-surface interactions (i.e., minimization of residue accretion, cleanability, etc.) will be significant for determining the direction of coating development. The perfect solution, a coating with no insect residue remaining after an impact event, has yet to be identified.

## References

1. Coleman WS (1961) Roughness due to insects. In: Lachman GV (ed) *Boundary layer and flow control: its principles and applications*. Pergamon Press, Oxford, pp 682–747
2. Braslow AL, Maddalon DV (1993) Flight tests of three-dimensional surface roughness in the high-crossflow region of a swept wing with laminar-flow control. National Aeronautics and Space Administration, NASA TM 109035
3. Maresh JL, Bragg MB (1984) The role of airfoil geometry in minimizing the effect of insect contamination of laminar flow sections. In: AIAA 2nd applied aerodynamics conference, Seattle, WA, 21–23 Aug 1984
4. Lin JC, Whalen EA, Eppink JL, Siochi EJ, Alexander MG, Andino MY (2016) Innovative flow control concepts for drag reduction. In: 54th AIAA aerospace sciences meeting, San Diego, CA, 4–8 Jan 2016
5. Smith JG Jr, Robinson R, Loth E (2017) An overview of insect residue accretion and mitigation strategies on aerodynamic surfaces. In: Berry DH, Wohl CJ (eds) *Contamination mitigating polymeric coatings for extreme environments*. Springer, Berlin, Germany
6. Robison R, Loth E (2017) Critical height for boundary layer transition on airfoil leading edges. In: AIAA SciTech Forum, Grapevine, TX, 9–13 Jan 2017
7. Fiore G, Selig MS (2014) A simulation of operational damage for wind turbine blades. In: 32nd AIAA applied aerodynamics conference, Atlanta, GA, 16–20 June 2014
8. Bragg MB, Maresh JL (1986) A numerical method to predict the effect of insect contamination on airfoil drag. The Ohio State University Research Foundation, Aeronautical and Astronautical Engineering Report AARL 86-01
9. Patzelt GJ, Stenzel V, Geils J, Stake A (2016) Anti-icing and anticontamination properties of coatings induced by surface structure. *J Coat Technol Res* 13(4):589–596
10. Gruenke S (2017) Requirements, test strategies and evaluation of anti-contamination and easy-to-clean surfaces and new approaches for development. *Adv Polm Sci*. [https://doi.org/10.1007/12\\_2017\\_38](https://doi.org/10.1007/12_2017_38)
11. Gullan PJ, Cranston PS (2010) *The insect: an outline of entomology*. Wiley, Chichester, West Sussex, UK
12. Glick PA (1939) The distribution of insects, spiders, and mites in the air. United States Department of Agriculture. *Tech Bull* 673
13. Vincent JFV, Wegst UGK (2004) Design and mechanical properties of insect cuticle. *Arthropod Struct Dev* 33:187–199
14. Reynolds SE (1975) The mechanical properties of the abdominal cuticle of rhodnius larvae. *J Exp Biol* 62:69–80
15. Hepburn HR, Joffe I (1974) Locust solid cuticle—a time sequence of mechanical properties. *J Insect Physiol* 20:497–506
16. Wigglesworth VB (1984) *Insect physiology* 8th edn. Springer, New York
17. Lehane M (2012) *Biology of blood-sucking insects*. Springer Science and Business Media, New York
18. Sochi T (2014) Non-newtonian rheology in blood circulation. <https://arxiv.org/abs/1306.2067>. Accessed 5 Mar 2016
19. Scherfer C, Karlsson C, Loseva O, Bidla G, Goto A, Havemann J, Dushay M, Theopold U (2004) Isolation and characterization of hemolymph clotting factors in *Drosophila melanogaster* by a pullout method. *Curr Biol* 14:625–629
20. Dushay MS (2009) Insect hemolymph clotting. *Cell Mol Life Sci* 66:2643–2650
21. Theopold U, Li D, Fabbri M, Scherfer C, Schmidt O (2002) The coagulation of insect hemolymph. *Cell Mol Life Sci* 59:363–372
22. Ensan MN, Zimcik DG, Lahoubi M, Andrieu D (2008) Soft body impact simulation on composite structures. *Trans Can Soc Mech Eng* 32(2):283–296



23. Field JE, Dear JP, Ogren JE (1989) The effects of target compliance on liquid drop impact. *J Appl Phys* 65(2):533–540
24. Rein M (1993) Phenomena of liquid drop impact on solid and liquid surfaces. *Fluid Dyn Res* 12:61–93
25. Yarin AL (2006) Drop impact dynamics: splashing, spreading, receding, bouncing. *Annu Rev Fluid Mech* 38:159–192
26. Toivakka M (2003) Numerical investigation of droplet impact spreading in spray coating of paper. In: TAPPI advanced coating fundamentals symposium, Chicago, IL, USA, 11–15 May 2003
27. Scheller BL, Bousfield DW (1995) Newtonian drop impact with a solid surface. *AIChE J* 41(6):1357–1367
28. Kok M, Tobin EF, Zikmund P, Raps D, Young TM (2014) Laboratory testing of insect contamination with application to laminar flow technologies, part I: variables affecting insect impact dynamics. *Aerosp Sci Technol* 39:605–613
29. Pasandideh-Fard M, Qiao YM, Chandra S, Mostaghimi J (1996) Capillary effects during droplet impact on a solid surface. *Phys Fluids* 8(3):650–659
30. Rumble JR (ed) (2017) Handbook of chemistry and physics 98th edn. CRC Press, Boca Raton, FL
31. Wohl CJ, Smith JG Jr, Penner RK, Lorenzi TM, Lovell CS, Siochi EJ (2013) Evaluation of commercially available materials to mitigate insect residue adhesion on wing leading edge surfaces. *Prog Org Coat* 76:42–50
32. Young TM, Tobin EF, Kok M (2012) Laboratory testing of insect contamination for laminar flow applications using an insect-impact test facility. In: 28th International Congress of the Aeronautical Sciences, Brisbane, Australia, 23–28 Sept 2012
33. Krishnan KG, Milionis A, Loth E, Farrell TE, Crouch JD, Berry DH (2017) Influence of hydrophobic and superhydrophobic surfaces on reducing aerodynamic insect residues. *Appl Surf Sci* 392:723–731
34. Gross AF, Nowak AP, Sherman E, Ro C, Yang SS, Behroozi M, Rodriguez AR (2017) Insect abatement on lubricious, low adhesion polymer coatings measured with an insect impact testing system. *Adv Polm Sci*. [https://doi.org/10.1007/12\\_2017\\_35](https://doi.org/10.1007/12_2017_35)
35. Kok M, Tobin EF, Zikmund P, Raps D, Young TM (2017) Laboratory investigation into anti-contamination coatings for mitigating insect contamination with application to laminar flow technologies. *Adv Polm Sci*. [https://doi.org/10.1007/12\\_2017\\_31](https://doi.org/10.1007/12_2017_31)
36. Wohl CJ, Smith JG Jr, Penner RK, Gardner JM, Connell JW, Siochi EJ (2013) Polyimide-based particulate composite coatings for contamination mitigation of aircraft surfaces. In: 36th annual meeting of the Adhesion Society, Daytona Beach, FL, 3–6 Mar, 2013
37. Mundo C, Sommerfeld M, Tropea C (1995) Droplet-wall collisions: experimental studies of the deformation and breakup process. *Int J Multiphase Flow* 21(2):151–173
38. Nishino T, Meguro M, Nakamae K, Matsushita M, Ueda Y (1999) The lowest surface free energy based on  $-CF_3$  alignment. *Langmuir* 15:4321–4323
39. Sikalo S, Tropea C, Ganic E (2005) Impact of droplets onto inclined surfaces. *J Colloid Interface Sci* 286:661–669
40. Chiarot PR, Jones TB (2010) Grazing impact of continuous droplet streams with a superhydrophobic surface. *Exp Fluids* 49:1109–1119
41. Yeong YH, Burton J, Loth E (2014) Drop impact and rebound dynamics on an inclined superhydrophobic surface. *Langmuir* 30:12027–12038
42. Braslow AL, Knox EC (1958) Simplified method for determination of critical height of distributed roughness particles for boundary-layer transition at mach numbers from 0 to 5. National Advisory Committee for Aeronautics, Technical Note 4363
43. Lopez-Donaire ML, Santerre JP (2014) Surface modifying oligomers used to functionalize polymeric surfaces: consideration of blood contact applications. *J Appl Polym Sci* 131(14):40328

44. Wohl CJ, Smith JG Jr, Penner RK, Gardner JM, Connell JW, Siochi EJ (2014) Novel epoxy particulate composites for mitigation of insect residue adhesion on future aircraft surfaces. In: 37th annual meeting of the Adhesion Society, San Diego, CA, 23–26 Feb 2014
45. Wohl CJ, Cooper LL, Applin SI, Connell JW (2015) Synthesis and surface characterization of copoly(imide alkyl ether)s containing pendant fluoroalkyl groups. *J Appl Polym Sci* 132 (9):41538
46. Dhiman R, Chandra S (2010) Rupture of thin films formed during droplet impact. *Proc R Soc A* 466:1229–1245
47. Kreutz E, Frerichs H, Stricker J, Wesner D (1995) Processing of polymer surfaces by laser radiation. *Nucl Instrum Methods Phys Res, Sect B* 105:245–249
48. Wohl CJ, Belcher MA, Chen L, Connell JW (2010) Laser ablative patterning of copoly(imide siloxane)s generating superhydrophobic surfaces. *Langmuir* 26(13):11469–11478
49. Crooks R, Boger DV (2000) Influence of fluid elasticity on drops impacting on dry surfaces. *J Rheol* 44:973–996
50. Yuan W-Z, Zhang L-Z (2017) Lattice boltzmann simulation of droplets impacting on superhydrophobic surfaces with randomly distributed rough structures. *Langmuir* 33:820–829
51. Vaikuntanathan V, Sivakumar D (2016) Maximum spreading of liquid drops impacting on groove-textured surfaces: effect of surface texture. *Langmuir* 32:2399–2409
52. Zhang D, Chen F, Yang Q, Si J, Hou X (2011) Mutual wetting transition between isotropic and anisotropic on directional structures fabricated by femtosecond laser. *Soft Matter* 7:8337–8342
53. Zhang D, Chen F, Yang Q, Yong J, Bian H, Ou Y, Si J, Meng X, Hou X (2012) A simple way to achieve pattern-dependent tunable adhesion in superhydrophobic surfaces by a femtosecond laser. *ACS Appl Mater Interfaces* 4:4905–4912
54. Rioboo R, Tropea C, Marengo M (2001) Outcomes from a drop impact on solid surfaces. *Atomization Sprays* 11:155–165
55. Mao T, Kuhn DCS, Tran H (1997) Spread and rebound of liquid droplets upon impact on flat surfaces. *AIChE J* 43(9):2169–2179
56. Bennett T, Poulidakos D (1993) Splat-quench solidification: estimating the maximum spreading of a droplet impacting a solid surface. *J Mater Sci* 28:963–970
57. Lee JB, Derome D, Guyer R, Carmeliet J (2016) Modeling the maximum spreading of liquid droplets impacting wetting and nonwetting surfaces. *Langmuir* 32:1299–1308
58. Fukai J, Shiiba Y, Yamamoto T, Miyatake O, Poulidakos D, Megaridis CM, Zhao Z (1995) Wetting effects on the spreading of a liquid droplet colliding with a flat surface: experiment and modeling. *Phys Fluids* 7(2):236–247
59. Wang B-B, Zhao Y-P, Yu T (2011) Fabrication of novel superhydrophobic surfaces and droplet bouncing behavior-part 2: water droplet impact experiment on superhydrophobic surfaces constructed using ZnO nanoparticles. *J Adhes Sci Technol* 25:93–108
60. Wang P, Su J, Shen M, Ruths M, Sun H (2017) Detection of liquid penetration of a micropillar surface using the quartz crystal microbalance. *Langmuir* 33:638–644
61. Cassie A, Baxter S (1944) *Trans Faraday Soc* 40:546–551
62. Wenzel RN (1936) Resistance of solid surfaces to wetting by water. *Ind Eng Chem* 28:988–994
63. Wang ZL, Lopez C, Hirs A, Koratkar N (2007) Impact dynamics and rebound of water droplets on superhydrophobic carbon nanotube arrays. *Appl Phys Lett* 91:023105
64. Kim H, Lee C, Kim MH, Kim J (2012) Drop impact characteristics and structure effects of hydrophobic surfaces with micro- and/or nanoscaled structures. *Langmuir* 28:11250–11257
65. Fang G, Li W, Wang X, Qiao G (2008) Droplet motion on designed microtextured superhydrophobic surfaces with tunable wettability. *Langmuir* 24:11651–11660
66. Yabu H, Hirai Y, Kojima M, Shimomura M (2009) Simple fabrication of honeycomb- and pincushion-structured films containing thermoresponsive polymers and their surface wettability. *Chem Mater* 21(9):1787–1789
67. Hipp B, Kunery I, Durr M (2010) Systematic control of hydrophobic and superhydrophobic properties using double-rough structures based on mixtures of metal oxide nanoparticles. *Langmuir* 26(9):6557–6560

68. Yang J-T, Yang Z-H, Chen C-Y, Yao D-J (2008) Conversion of surface energy and manipulation of a single droplet across micropatterned surfaces. *Langmuir* 24(17):9889–9897
69. Yong J, Chen F, Yang Q, Zhang D, Dy G, Si J, Yun F, Hou X (2013) Femtosecond laser weaving superhydrophobic patterned PDMS surfaces with tunable adhesion. *J Phys Chem C* 117:24907–24912
70. Nonomura Y, Tanaka T, Mayama H (2016) Penetration behavior of a water droplet into a cylindrical hydrophobic pore. *Langmuir* 32:6328–6334
71. Tuteja A, Choi W, Ma M, Mabry JM, Mazzella SA, Rutledge GC, McKinley GH, Cohen RE (2007) Designing superoleophobic surfaces. *Science* 318:1618–1622
72. Luo BH, Shum PW, Zhou ZF, Li KY (2010) Surface geometrical model modification and contact angle prediction for the laser patterned steel surface. *Surf Coat Technol* 205:2597–2604
73. Dash S, Alt MT, Garimella SV (2012) Hybrid surface design for robust superhydrophobicity. *Langmuir* 28:9606–9615
74. Malavasi I, Veronesi F, Calderelli A, Zani M, Raimondo M, Marengo M (2016) Is a knowledge of surface topology and contact angles enough to define the drop impact outcome? *Langmuir* 32:6255–6262
75. Papadopoulos P, Mammen L, Deng X, Vollmer D, Butt H-J (2013) How superhydrophobicity breaks down. *Proc Natl Acad Sci U S A* 110(9):3254–3258
76. Bartolo D, Bouamrine F, Verneuil E, Buguin A, Silberzan P, Moulinet S (2006) Bouncing or sticky droplets: impalement transitions on superhydrophobic micropatterned surfaces. *Europhys Lett* 74(2):299–305
77. Engel OG (1955) Waterdrop collisions with solid surfaces. *J Res Natl Bur Stand* 54(5):281–198
78. Field JE (1999) Elsi conference: invited lecture – liquid impact: theory, experiment, applications. *Wear* 233–235:1–12
79. Lesser MB (1981) Analytical solutions of liquid-drop impact problems. *Proc R Soc Lond A* 377:289–308
80. Heymann FJ (1969) High speed impact between a liquid drop and a solid surface. *J Appl Phys* 40(13):5113–5122
81. Kwon HM, Paxson AT, Varanasi KK, Patankar NA (2011) Rapid deceleration-driven wetting transition during pendant drop deposition on superhydrophobic surfaces. *Phys Rev Lett* 106(3):036102
82. Wu J, Ma R, Wang ZK, Yao S (2011) Do droplets always move following the wettability gradient? *Appl Phys Lett* 98:204104
83. Bird JC, Dhiman R, Kwon H-M, Varanasi KK (2013) Reducing the contact time of a bouncing drop. *Nature* 503:385–388
84. Moevius L, Liu Y, Wang Z, Yeomans JM (2014) Pancake bouncing: simulations and theory and experimental verification. *Langmuir* 30:13021–13032
85. Liu Y, Whyman G, Bormashenko E, Hao C, Wang Z (2015) Controlling droplet bouncing using surfaces with gradient features. *Appl Phys Lett* 107:051604
86. Shen Y, Tao J, Tao H, Chen S, Pan L, Wang T (2015) Approaching the theoretical contact time of a bouncing droplet on the rational macrostructured superhydrophobic surfaces. *Appl Phys Lett* 107:111604
87. Weisensee PB, Tian J, Miljkovic N, King WP (2016) Water droplet impact on elastic superhydrophobic surfaces. *Sci Rep* 6:30328
88. Deng T, Varanasi KK, Hsu M, Bhate N, Keimel C, Stein J, Blohm M (2009) Nonwetting of impinging droplets on textured surfaces. *Appl Phys Lett* 94:133109
89. Cossali GE, Coghe A, Marengo M (1997) The impact of a single drop on a wetted solid surface. *Exp Fluids* 22:463–472
90. Lesser M (1995) Thirty years of liquid impact research: a tutorial review. *Wear* 186–187:28–34
91. Haller KK, Ventikos Y, Poulidakos D, Monkewitz P (2002) Computational study of high-speed liquid droplet impact. *J Appl Phys* 92:2821–2828
92. Rioboo R, Voue M, Vaillant A, De Coninck J (2008) Drop impact on porous superhydrophobic polymer surfaces. *Langmuir* 24:14074–14077

93. Range K, Feuillebois F (1998) Influence of surface roughness on liquid drop impact. *J Colloid Interface Sci* 203:16–30
94. Gohardani O (2011) Impact of erosion testing aspects on current and future flight conditions. *Prog Aerosp Sci* 47:280–303
95. Jilbert GH, Field JE (2000) Synergistic effects of rain and sand erosion. *Wear* 243:6–17
96. Sharma A, Ruckenstein E (1989) Dewetting of solids by the formation of holes in macroscopic liquid films. *J Colloid Interface Sci* 133(2):358–368

# Laboratory Investigation into Anti-contamination Coatings for Mitigating Insect Contamination with Application to Laminar Flow Technologies



**Mariana Kok, Edmond F. Tobin, Pavel Zikmund, Dominik Raps, and Trevor M. Young**

**Abstract** Insect contamination on aircraft leading edge surfaces can result in premature transition of the boundary layer, leading to an increase in skin friction drag and fuel consumption. An evaluation of candidate anti-contamination coatings was undertaken. Coatings were characterized before impact testing. Surface energy was quantified by dynamic contact angle analysis and surface roughness measured using a profilometer. Superhydrophobic coatings showed a reduction in contamination when compared to the higher surface energy specimens tested. The surface topography and chemistry, in particular the sliding angle of a coating, were found to have a significant influence on the effectiveness of a coating. Insect residue areas were theoretically predicted using high-speed liquid droplet theory and compared to experimentally obtained results. Tests with different insect species were conducted to investigate the effect of insect size and type on the effectiveness of the coatings and the evaluation procedure. Good correlations were obtained between the two test

---

M. Kok and T. M. Young (✉)

Department of Mechanical, Aeronautical and Biomedical Engineering, University of Limerick, Limerick, Ireland

e-mail: [trevor.young@ul.ie](mailto:trevor.young@ul.ie)

E. F. Tobin

Carlow Institute of Technology, Carlow, Ireland

P. Zikmund

Institute of Aerospace Engineering, Brno University of Technology, Brno, Czech Republic

D. Raps

Airbus Helicopters, Donauwörth, Germany

facilities used. The effect of substrate temperature on insect impact dynamics and adhesion was also evaluated.

**Keywords** Impact dynamics • Insect contamination • Insect impact

## Contents

1	Introduction .....	292
2	Experimental Materials and Methods .....	293
2.1	Insect Species .....	293
2.2	Materials .....	294
2.3	Coating Characterization .....	295
2.4	Insect Residue Analysis .....	295
2.5	Topography .....	295
2.6	Insect Impact Tests .....	296
3	Results and Discussion .....	296
3.1	Coating Characterization .....	296
3.2	Coating Evaluation .....	299
3.3	Variables Impacting the Effectiveness of Coatings .....	302
3.4	Insect Impact Dynamics and Residue Area Analysis .....	307
4	Conclusions .....	309
	References .....	310

## 1 Introduction

The use of coatings to mitigate insect contamination on aircraft surfaces has been an active area of research since the 1970s, with contributions from both the aerospace industry and research institutions [1–15]. The adherence of insect debris to laminar flow surfaces can induce localized boundary layer transition, resulting in an increase in skin friction drag and reduced fuel efficiency [16, 17]. Insect residue adhesion is influenced by a number of different factors, including (1) material type and surface characteristics, (2) aerodynamic factors (e.g., aircraft wing geometry and velocity), (3) entomological factors (e.g., insect species encountered and insect density), and (4) environmental factors (e.g., temperature, wind, and rain) [18].

The threat of insect contamination is highest at altitudes below 150 m, corresponding to taxiing, taking-off and landing, and low-level climbing and descent [9, 18, 19]. The insect population is highest during spring and summer, and the insect species encountered greatly depends on seasonal variations [20–23]. Experimentalists [18, 24, 25] obtained a representative insect population and established that the majority of the insects encountered at low altitudes were small and fragile, between 1 and 3 mm long. Of the insects sampled, 86% belonged to the order Diptera, to which *Drosophila melanogaster* belongs [22, 26, 27]. Coleman [18] suggested *Drosophila melanogaster* as a representative insect, and a number of experimentalists have thus opted to use it in insect contamination studies [3, 4, 7, 28–31]. It was previously shown that coating performance during laboratory tests did not always extrapolate to flight test data [1]. Tests conducted in a controlled

laboratory ensure the use of insects of the same species and of consistent size and mass; however, during flight tests the coatings are exposed to a wider range of the insect population (specific to the test zone). It is therefore not yet known whether different insect species influence the effectiveness of anti-contamination coatings.

In a previous study, we investigated the main influential factors affecting insect impact dynamics and adhesion to representative surfaces. Important factors affecting the insect rupture patterns, in particular the rupture velocity (i.e., the speed needed to fracture the exoskeleton), impact velocity, and impact angle, were evaluated [32]. In the current study, an evaluation of different anti-contamination coatings is presented based on laboratory testing conducted using two different insect impact test facilities (at the University of Limerick, Ireland, and at Airbus Group Innovations, Ottobrunn, Germany). To evaluate different chemical functionalities, a range of coatings were selected. Rough superhydrophobic coatings were chosen based on recent results presented by Kok et al. [2, 3, 33]. Sol-gel coatings were chosen based on their easy-to-clean and/or self-cleaning properties and their use in a range of industries [34, 35]. Sol-gel processing also allows for various microstructures to be achieved (e.g., porous, hybrid, organic-inorganic, amorphous, and crystalline microstructures [36, 37]). The desired properties can therefore be obtained by tailoring the material. Electropolished surfaces were chosen to test the behavior of smooth hydrophilic surfaces. To ensure a benchmark, two coatings currently used on commercial aircraft and certain military aircraft were selected. A number of different test methods have been used to evaluate the effectiveness of anti-contamination coatings [1–14, 18, 38, 39], and it is therefore beneficial to know whether data obtained by different facilities can be correlated. Consequently, the results obtained by the two insect impact test facilities used in this study are compared. To evaluate the influence of different insect species on the effectiveness of anti-contamination coatings, testing with different insect species is described. Challenges of testing with live insects are also identified. The effect of temperature on insect residue adhesion is examined.

## 2 Experimental Materials and Methods

### 2.1 Insect Species

Testing was conducted with three different species of insect, namely Wild-type (WT) *Drosophila melanogaster*, *Drosophila hydei*, and *Musca domestica* (also known as the common housefly). Insect mass values are shown in Table 1. Differences in the mass of *D. melanogaster* used during testing could be attributed to a difference in diet and growth environment [40, 41]. *D. hydei* and *M. domestica* were chosen to evaluate the effect of insect size.

**Table 1** Insect mass

Insect species (test facility)	Family	Order	Mass (mg) <sup>a</sup>	Size (mm) [Reference]
<i>D. melanogaster</i> (UL)	Drosophilidae	Diptera	0.81 ± 0.14	1.5 [42, 43]
<i>D. melanogaster</i> (AGI)	Drosophilidae	Diptera	1.19 ± 0.03	1.5 [42, 43]
<i>D. hydei</i>	Drosophilidae	Diptera	2.30 ± 0.06	3.0 [42, 43]
<i>M. domestica</i>	Muscidae	Diptera	11.8 ± 0.20	5–8 [44, 45]

<sup>a</sup>Mass values were averaged from a minimum of three replicates, obtained using an Explorer<sup>®</sup> Analytical Balance

**Table 2** Coating description

Specimen number	Description
Specimen 1	AA2024-T3 clad was pre-treated with a Cr(VI)-free anodizing process and then coated with a primer, a basecoat, and a conventional 3 K polyurethane clear coat. This coating is a standard polyurethane clear coat widely used on in-service commercial aircraft.
Specimen 2	A water-based, three-component, isocyanate-cured polyurethane topcoat used on specific military aircraft.
Specimen 3	A polyurethane-based superhydrophobic coating, a structured coating with first particles in the range of 50 µm and second particles (100 nm) that have a hydrophobic shell.
Specimen 4	A polyurethane-based superhydrophobic coating similar to Specimen 3 but formulated to achieve a higher abrasion resistance.
Specimen 5	A polyurethane-based superhydrophobic coating similar to Specimen 3 formulated to achieve a different microstructure.
Specimen 6	An epoxy-based structured superhydrophobic coating, with first particles in the range of 50 µm and second particles (100 nm) that have a hydrophobic shell.
Specimen 7	AA2024-T3 clad was sandblasted using a vacuum grit blasting process to achieve a high roughness value.
Specimen 8	Acrylic aircraft polish on a polyurethane clear coat.
Specimens 9	Sol-gel coatings based on a 4:1 silica/zirconia hybrid sol-gel. Sol-gel coatings were specifically formulated for this study by CREST (Dublin Institute of Technology, Dublin, Ireland).
Specimen 10	Sol-gel coating, similar to Specimen 9 based on a 4:1 silica/zirconia hybrid sol-gel.
Specimens 11	AA2024-T3 electropolished to obtain a highly smooth surface finish.
Specimen 12	Electropolished similar to Specimen 11, but with a lower surface energy.
Specimen 13	AA2024-T3 electropolished similar to Specimens 11 and 12.
Specimen 14	AA2024-T3 electropolished to achieve a highly smooth surface finish, with a similar surface energy as Specimen 11.
Specimen 15	Used as-received.

## 2.2 Materials

Aluminum alloy (AA2024-T3 clad) was used as a substrate material for all applied coatings. Coating descriptions can be found in Table 2.



### 2.3 Coating Characterization

Static contact angles, using polar and non-polar test liquid (droplet size 5  $\mu\text{L}$ ), Milli-Q deionized water, and diiodomethane (*ReagentPlus*<sup>®</sup> 99%, Sigma Aldrich), were measured using a digital optical contact angle meter (CAM 200, KSV Instruments Ltd., Helsinki). An average of at least 10 measurements ( $n = 10$ ) at different positions on the specimen were taken 5 s after deposition to avoid evaporation or absorption errors. The surface free energies of the specimens, and their respective polar ( $\gamma_s^p$ ) and dispersive ( $\gamma_s^d$ ) contributions, were calculated using the Owens–Wendt method. The sliding angle (SA), that is, the angle of surface inclination at which a droplet of certain weight begins to roll off, was measured by depositing a droplet of Milli-Q deionized water (5  $\mu\text{L}$ ) on each of the specimens. The coating was then tilted (using a movable stage) and sequential photographs of the droplet were taken every 10 ms using a computer-controlled camera until the droplet rolled off and the sliding angle was calculated. Arithmetic mean surface roughness (Ra) values were obtained using a Hommel Tester T1000 wave (ISO 4287/1 and DIN 4768 standards were followed). For both sliding angle and roughness measurements, averages of five measurements were taken on each specimen.

### 2.4 Insect Residue Analysis

Insect residue area measurement and height analysis were undertaken as described in Kok et al. [32]. Residue area and height values obtained were averaged from a minimum of 10 impacts ( $n = 10$ ).

### 2.5 Topography

The topography of the insect residues was examined using a Hitachi SU-70 field-emission scanning electron microscope (SEM). An ultra-thin layer of electrically conductive material (gold) was deposited on the specimens prior to imaging. Microscopic images were taken using a Zeiss Optical Microscope AXIO Imager A1 at magnifications ranging from  $\times 5$  to  $\times 20$ .

## 2.6 *Insect Impact Tests*

### 2.6.1 **Insect Impact Test Facilities**

Insect impact tests were conducted in two test facilities. The first was a custom-built facility called SPIrIT (Stationary samPLe Insect Impact Test) at the University of Limerick (Limerick, Ireland) and the second was iCORE (icing and COntamination REsearch Facility) at Airbus Group Innovations, formerly known as EADS Innovation Works (Ottobrunn, Germany). The SPIrIT facility comprised a compressed air cylinder, a solenoid-operated diaphragm valve, and a smooth-bore tube (barrel). When triggered, compressed air would accelerate the insect, supported by a foam sabot, down the tube to impact the target (which could be adjusted to provide normal or oblique impact angles) at speeds ranging from 10 to 100 m/s. iCORE is a small, reconfigurable wind tunnel (cross section  $0.15 \times 0.10$  m). An insect delivery device was designed to facilitate insects to be introduced into the airflow (upstream of the target) and to accelerate the insects to a speed that matched the airspeed in the test section (100 m/s). Test panels were mounted on a plate installed in the tunnel test section, such as to enable an oblique impact angle of  $30^\circ$  to be achieved. Further details of the test equipment and test procedures are provided by Kok et al. [2, 32].

### 2.6.2 **Effect of Temperature on Insect Adhesion Properties**

To investigate the effect of substrate temperature on the insect adhesion properties, candidate coatings were tested at elevated ( $70^\circ\text{C}$ ) temperatures. Two cartridge heaters were inserted into an aluminum block 0.012 m thick, 0.08 m wide, and 0.15 m long. Anti-contamination coatings were attached to the heated block and the surface temperature measured using a thermocouple attached to the surface (at the center of the block). The test temperature of the heated surface was  $70^\circ\text{C}$ , which was controlled to within  $\pm 2^\circ\text{C}$ . The ambient room temperature of  $18^\circ\text{C}$  was assumed to be constant during the experiment. The target area was illuminated using two Dedolight DLH 400D light sources. The impact dynamics were imaged using a high-speed camera (Photron Fastcam Photron<sup>®</sup> SA1.1) at 20,000 fps, which was aligned at an angle ( $\theta$ ) of  $30^\circ$  to the impact plate. Testing was conducted at impact velocities of approximately 100 m/s at normal impact angles ( $\alpha = 90^\circ$ ).

## 3 **Results and Discussion**

### 3.1 *Coating Characterization*

Surface characteristics of the coatings are shown in Table 3. Standard deviation values of the measured contact angle and roughness values were less than 10%.

**Table 3** Surface energy components, roughness, and sliding angle values of the respective coatings

Coating	$\gamma_s^p$ (mj/m <sup>2</sup> )	$\gamma_s^d$ (mj/m <sup>2</sup> )	$\gamma_s$ (mj/m <sup>2</sup> )	Ra ( $\mu$ m)	SA ( $^\circ$ )
Specimen 1	1.49	35.7	37.2	0.02	>180
Specimen 2	5.63	33.4	39.0	0.99	>180
Specimen 3	0.19	1.02	1.21	8.98	13
Specimen 4	0.04	0.09	0.13	23.08	11
Specimen 5	0.18	0.52	0.70	5.26	8
Specimen 6	0.00	2.04	2.04	4.91	19
Specimen 7	29.4	10.8	40.1	1.5	>180
Specimen 8	26.5	1.20	27.7	0.04	>180
Specimen 9	18.0	5.15	23.1	0.05	>180
Specimen 10	13.0	4.02	17.1	0.63	>180
Specimen 11	29.4	50.2	79.7	0.08	>180
Specimen 12	11.3	39.5	50.7	0.07	>180
Specimen 13	11.6	39.5	51.1	0.06	>180
Specimen 14	29.8	47.7	77.5	0.05	>180
Specimen 15	3.23	30.9	34.1	0.06	>180

The surface energy and roughness values obtained followed the expected trend. Superhydrophobic surfaces (Specimens 3–6) exhibited contact angle values higher than  $150^\circ$ , which led to extremely low surface energy values, with minimal polar and dispersive contributions. The rougher superhydrophobic surface (Specimen 4) exhibited a lower surface energy value when compared to the smoother superhydrophobic surfaces. This was expected, as the hydrophobicity of a surface can be increased by increasing the surface roughness (by increasing the surface area) [46–52]. Specimen 4 also had the lowest surface energy value of all coatings evaluated. Sol-gel coatings (Specimens 9 and 10) showed relatively low surface energy values with higher contributions from the polar functionalities. The electropolished surfaces (Specimens 11–14) displayed the highest surface energy values – this correlates with the change in wettability as a result of electropolishing. The surface polarities of the electropolished surfaces were high and ranged from 22.2% to 38.4% of their total surface energy. The as-received AA2024-T3 clad (Specimen 15), however, had a lower surface energy ( $34.1 \text{ mJ/m}^2$ ) than the polyurethane control surface (Specimen 1) and had a surface polarity contribution of only 9.5% to the total surface energy. The contact angle values for the sandblasted specimen (Specimen 7) showed greater time dependence than other coatings examined. A decrease in the contact angle values was seen with time; this influence of time on contact angle measurements, particularly on rough surfaces, is well known [53, 54].

The sliding angle is a dynamic measure of the hydrophobicity of a surface, so to obtain a surface with a low sliding angle, a sufficiently low surface energy and specific microstructure are needed [55–59]. The smooth anti-contamination coatings (Specimens 1, 2, and 8–15) do not have the inherent properties necessary to achieve a low sliding angle. This resulted in the water droplets adhering or

'pinning' to the surface, and the droplets did not slide off even when the surface was tilted upside down. The sliding angle values of Specimens 1 and 2 (polyurethane controls) and 7–15 are therefore only added for completeness. The superhydrophobic surfaces examined here (Specimens 3–6) consisted of both micro- (50  $\mu\text{m}$ ) and nano-sized (100 nm) particles, allowing for a hierarchical surface structure, with the nano-sized asperities protruding from the micro-sized features (Fig. 1a, b). Water droplets deposited onto these surfaces rolled off easily because

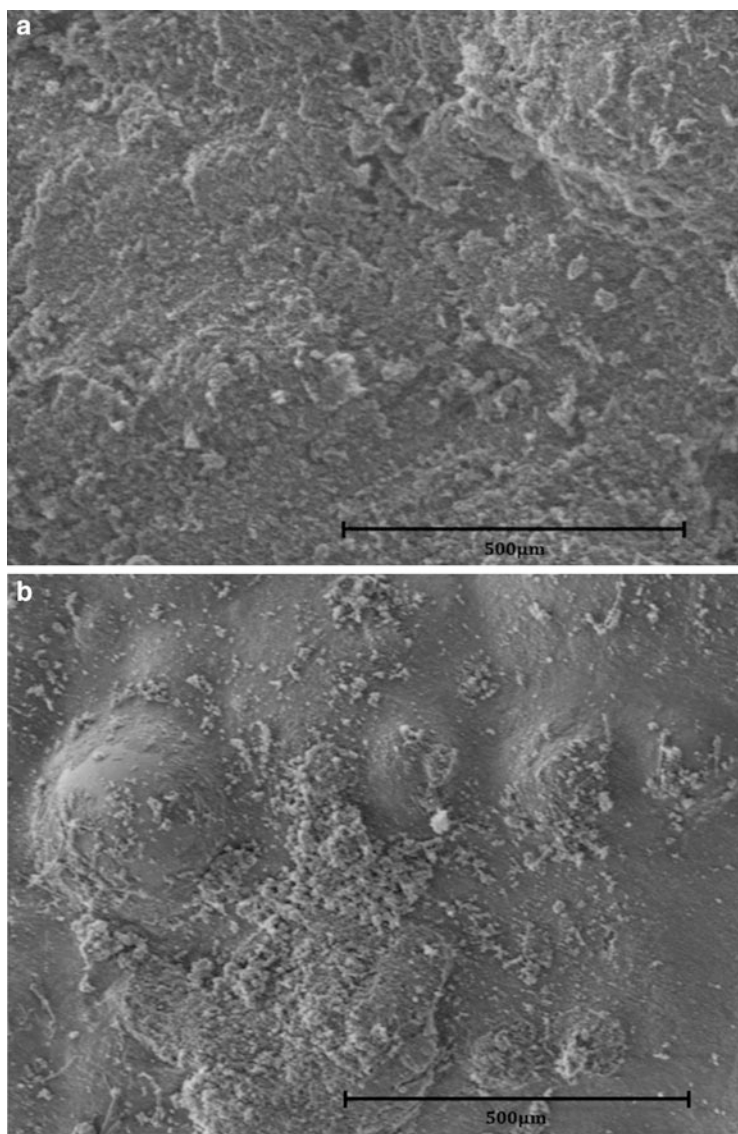


**Fig. 1** SEM micrographs of (a) Specimen 4 and (b) Specimen 5

of sliding angles  $<20^\circ$  – this is a characteristic of surfaces that exhibit a self-cleaning or ‘lotus’ effect.

### 3.2 Coating Evaluation

Coatings were tested using *D. melanogaster*, and coating performance was evaluated based on the measured residue impact area and height values (Figs. 2 and 3). As expected, the electropolished surfaces (Specimens 11 and 12) had the largest insect residue area values. Electropolished surfaces have high wettability and low roughness values, allowing the hemolymph to spread easily upon impact [2]. Sol-gel coatings (Specimens 9 and 10) did not show a reduction in contamination when compared to the reference coatings (Specimens 1 and 2), whereas Specimen 7, which had no inherent chemical functionality, showed a reduction in residue adhesion when compared to the reference coatings. Its effectiveness can be attributed to the rough topography of the surface; previous studies suggested that a rough surface can inhibit the hemolymph from spreading on the surface [2]. However, because of the relatively high surface energy ( $40.1 \text{ mJ/m}^2$ ) of the coating, it did not allow for a sufficient reduction in contamination. A combination of both chemistry (to obtain a low surface energy) and topography is therefore needed to reduce insect residue adhesion. This can clearly be seen from the rough

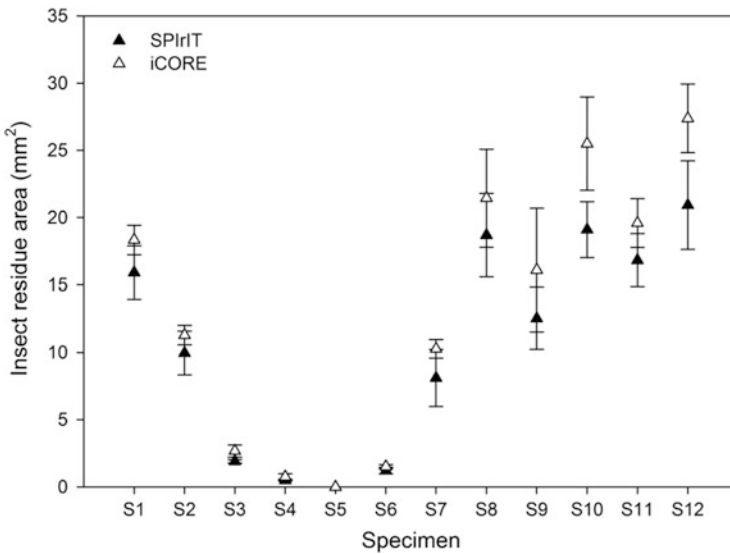


**Fig. 2** Insect residue area (mm<sup>2</sup>) against corresponding specimen. (Test facilities: iCORE and SPIrIT, insect type: *D. melanogaster*, impact angle: 30°, impact velocity: 100 m/s)

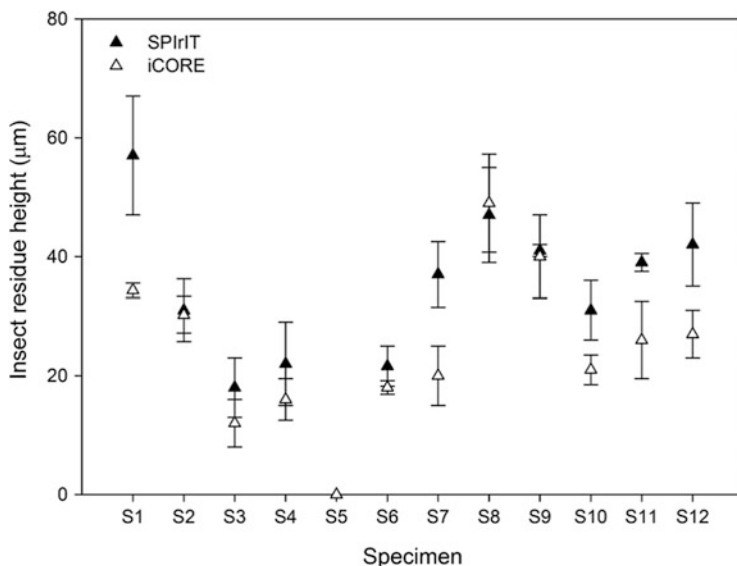


**Fig. 3** Insect residue height against corresponding specimen. (Test facilities: iCORE and SPIrIT, insect type: *D. melanogaster*, impact angle: 30°, impact velocity: 100 m/s)

superhydrophobic coatings (Specimens 3–6), which showed a substantial reduction in contamination. Specimen 5 consistently showed no insect residue adhering to the surface (in both test facilities). In most test cases, no residue was left on the surface after impact onto Specimen 4. The inconsistency in complete mitigation (for every consecutive test) can be explained by surface chemistry inhomogeneity, as hydrophilic spots may have been present on the superhydrophobic surface [46]. The environmental instability of superhydrophobic coatings can also be a reason for the discrepancy; most superhydrophobic coatings are not durable, are easily scratched off, and their properties deteriorate over time [60].

The effectiveness of the superhydrophobic coatings tested here is in contrast to results obtained by Siochi et al. [61], who found no significant reduction in contamination with tests conducted on superhydrophobic coatings. Similarly, Kok et al. [2] showed that smooth superhydrophobic coatings exhibited no reduction in contamination; however, when the micro-scale roughness value of the coating was increased, a substantial reduction in contamination was obtained. It is therefore postulated that differences in mitigation properties can be attributed to variations in the microstructure of the superhydrophobic coatings. Recent results published by Kok and Young [33] evaluating hierarchically structured superhydrophobic coatings showed a significant difference in the effectiveness of superhydrophobic coatings, highly dependent on the sliding angle value of the coating. It was found that only superhydrophobic coatings exhibiting a specific microstructure, allowing a low sliding angle, showed mitigation of insect residue adhesion. Superhydrophobic surfaces with higher sliding angle values showed higher insect residue area values.

Sliding angle values for the surfaces examined in [2, 61] are not known; however, it is postulated that the ineffectiveness could therefore be attributed to differences in the microstructure and sliding angle values of the coatings.

As mentioned in Sect. 3.1, a sufficiently low surface energy and specific microstructure are required for a surface to exhibit a low sliding angle. The smooth anti-contamination coatings (Specimens 1, 2, and 8–15) evaluated here do not have the inherent properties necessary to achieve a low sliding angle. The superhydrophobic coatings exhibited a hierarchical surface structure; this resulted in a low surface energy and also allowed for a low sliding angle value to be obtained. Superhydrophobic surfaces tested here had similar sliding angle values, shown to be effective by Kok and Young [33]. It is postulated that surfaces that exhibit a specific microstructure and low sliding angle (Specimen 5) allow the insect residue on the surface to adopt a Cassie–Baxter (composite) wetting state. The insect residue does not adhere to the surface but is easily swept off by the incoming airflow [33, 47, 62]. Because of the high impact pressure imparted on the surface at high impact speeds (100 m/s), the composite interface is easily destroyed, which results in a transition from the Cassie–Baxter to a Wenzel (homogeneous) wetting state [2, 4]. This was evident from Specimens 3, 4, and 6, which showed that insect residue adhered to the surface. The microstructure of Specimen 5 therefore allows a sufficient air cushion to be obtained between the insect residue and the surface, and a fully composite interface is formed (irrespective of the high-speed impact). A specific microstructure can therefore alter the dynamics of the insect impact and prevent the adhesion of insect residue to the surface. To mitigate insect residue adhesion effectively, the topographical features and surface chemistry (to allow a low surface energy) of a surface need to be optimized.

The residue area values for all coatings tested using iCORE were on average 20% higher than those obtained using SPiRiT, although the residue height values were lower. In Kok et al. [32], it was shown that the exposure to a constant airflow during the insect impact event results in more spreading of the hemolymph upon impact, leading to an increase in the residue area. Similarly, the excrescence height decreases because of the airflow, as more exoskeleton is swept away upon impact. It is also worth noting that, although *D. melanogaster* was used in all tests, insect masses were on average 30% higher for those used during testing in iCORE (Table 1). The inconsistency in insect mass was attributed to a difference in diet and growth environment [38, 40]. The insect mass, although having some influence on the measured values, was assumed not to be a major contributing factor to the difference in residue area and height values. In Kok et al. [32], it was shown that when variables such as the insect mass and influence of coating chemistry were eliminated, the airflow is the main contributing factor responsible for differences in residue area and height values. There was, however, one coating that was inconsistent with the average trend: Specimen 8 showed a slightly lower residue height value when tested using SPiRiT. The standard deviation band for the residue area and height values were high, and this inconsistency was thus attributed to experimental error and therefore omitted. The ranking based on insect residue area values of each anti-contamination coating tested remained the same, irrespective of the test facility used. Although the exposure to airflow during an insect impact event is a

key parameter responsible for different insect residue patterns, and is highly dependent on the test facility used, it should not affect the ranking of anti-contamination coatings. No direct correlation was obtained between the measured residue area and height values; this was consistent with recent observations by other experimentalists [2, 5].

### 3.3 Variables Impacting the Effectiveness of Coatings

#### 3.3.1 Different Insect Species

To determine whether insects of different sizes and species would have an effect on the testing procedure and the ranking (or effectiveness) of the anti-contamination coatings, tests were conducted using three different species of insect, namely *D. melanogaster* (0.81 mg), *D. hydei* (2.30 mg), and *M. domestica* (11.8 mg). Experiments conducted using *M. domestica* proved particularly difficult, as the insects were awkward to handle and were not easily sedated. This resulted in a significant scatter in the results with high standard deviations – the results obtained using *M. domestica* are therefore not presented here. Measured residue height and area values for *D. melanogaster* and *D. hydei* are given in Figs. 4 and 5. Insect residue area values for *D. hydei* were on average 50% larger than those obtained using *D. melanogaster*. This was as expected, as *D. hydei*'s average body length

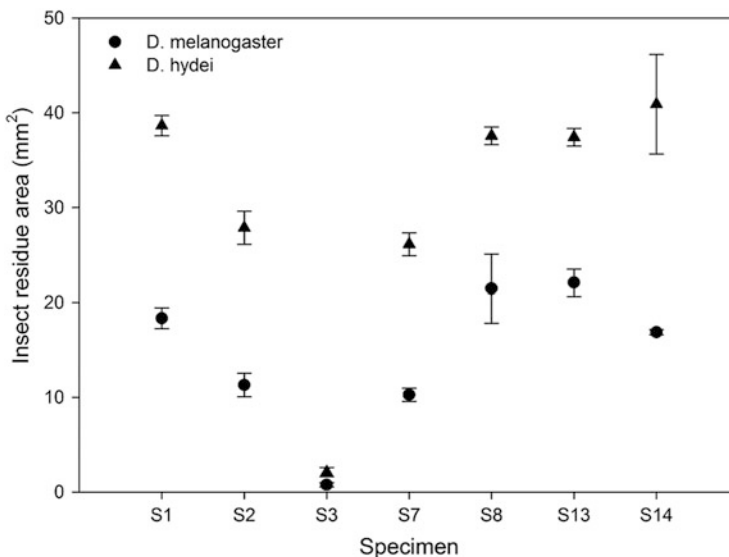


**Fig. 4** Insect residue area against specimen number. (Test facility: iCORE, impact angle: 30°, impact velocity: 100 m/s)



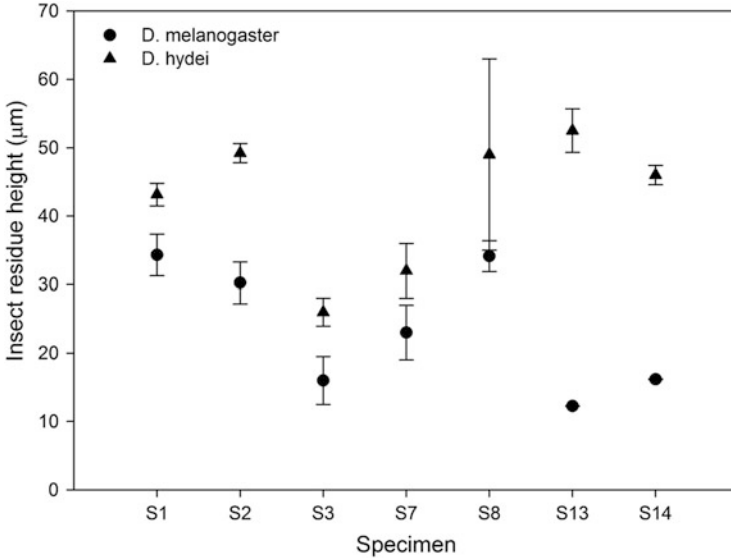


**Fig. 5** Insect residue height against specimen number. (Test facility: iCORE, impact angle: 30°, impact velocity: 100 m/s)

**Table 4** *D. melanogaster* and *D. hydei* comparison results

Coating ranking	Insect species	
	<i>D. melanogaster</i>	<i>D. hydei</i>
1	Specimen 3	Specimen 3
2	Specimen 7	Specimen 7
3	Specimen 2	Specimen 2
4	Specimen 14	Specimen 13
5	Specimen 1	Specimen 8
6	Specimen 8	Specimen 1
7	Specimen 13	Specimen 14

(approximately 3 mm) is twice that of *D. melanogaster* (approximately 1.5 mm) [63, 64]. There was significant scatter in the height values obtained with Specimen 8 when testing with *D. hydei*. Large discrepancies in values obtained with Specimen 8 were also evident in Sect. 3.2 – it was speculated that this could be because of an inconsistency in coating chemistry.

It was evident that there was a difference in the coating ranking (based on insect residue area values) depending on the insect species and size (Table 4). Specimen 3 showed the least contamination, with the smallest residue area irrespective of insect type. This was expected, as rough superhydrophobic surfaces showed good anti-contamination properties in previous studies [2]. Specimens 2, 3, and 7 ranked the same irrespective of insect species, although the ranking for the other coatings was different. On closer inspection, it was apparent that minor differences exist between the insect residue area values for these specimens. The measured insect

residue area values for Specimens 1, 8, 13, and 14 ranged from 16.9 to 22.1 mm<sup>2</sup> for *D. melanogaster* and from 37.4 to 41.0 mm<sup>2</sup> for *D. hydei*. The variances in the measured residue area values are small; and it is thus inconclusive as to whether the effectiveness of the anti-contamination properties of the coating is dependent on insect type.

Macroscopic images showed no visible difference between the residue patterns of *D. melanogaster* and *D. hydei* (Fig. 6a, b). Both images show hemolymph

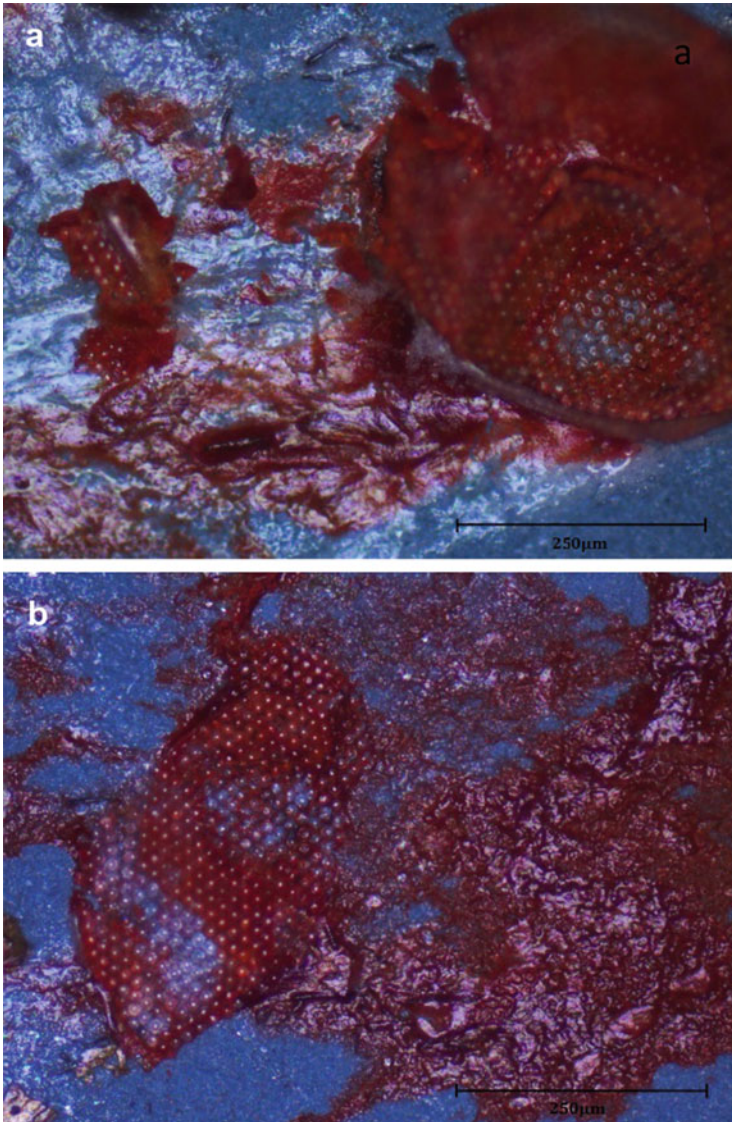


**Fig. 6** Macroscopic images of (a) *D. hydei* and (b) *D. melanogaster*. (Test facility: iCORE, specimen: 2, impact angle: 30°, impact velocity: 100 m/s)

adhered to the specimen and visible residue from the eyes (which can be identified as hexagonal packing [63]). Differences between *D. hydei* and *D. melanogaster* include insect size, life cycle (the life cycle of *D. hydei* is much longer than that of *D. melanogaster*), and breeding patterns. However, similarities in DNA and amino acids of *D. melanogaster* and *D. hydei* are well known [64, 65]. The authors have also conducted tests using different genetic mutations of *D. melanogaster*, for example, white-eyed and ebony (results are not presented here); however, no difference in residue patterns or adhesion properties were found. A controlled laboratory setting provides a method of recording the exact number of impacts (as the number of insects introduced into the delivery device is known) – this allows for an effective means to assess the anti-contamination properties of the coatings. Testing with different insect species would therefore give an overall result for the effectiveness of the coatings.

In order to test with different insect sizes, the sabot used in SPIrIT had to be modified to accommodate bigger insects. No other modifications of the insect delivery device or significant changes to the test procedure were necessary. The air pressure had to be increased to ensure that a consistent impact speed could be achieved. For the insertion into the insect delivery device, handling bigger insects (*D. hydei* and *M. domestica*) was easier, as the insects were not so fragile. An increase in the exposure time to CO<sub>2</sub> during the sedation process was necessary as the CO<sub>2</sub> wore off quicker depending on the mass of the insect; this confirmed the initial observations by Kok et al. [2]. This effect was particularly evident when sedating *M. domestica*, which have a body size significantly larger than that of *D. melanogaster* or *D. hydei*, as they needed a longer exposure time to CO<sub>2</sub>. The insect size had no significant impact on the insect trajectories, and high-speed video footage confirmed that the bigger insects did not break-up because of the high air pressure (Fig. 7). Caution was taken when handling the insects during the sedation and insertion process. Disintegration prior to impact or injury to the insect body would change the resultant residue area and height values and therefore skew the results (as discussed in Kok et al. [32]). Disintegration of the insect body could also

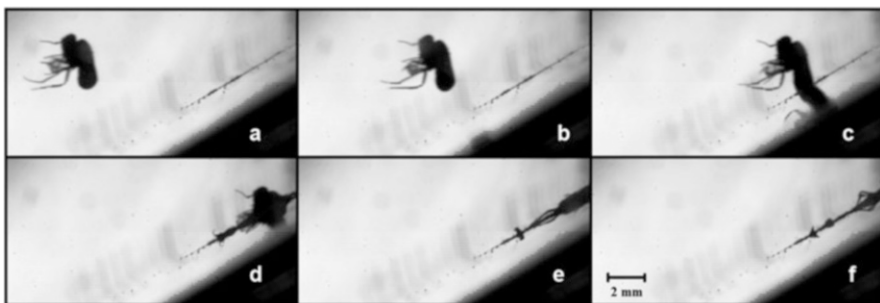


**Fig. 7** Image sequence of *D. hydei*. (Test facility: iCORE, Specimen: 13, impact angle: 30°, impact velocity: 100 m/s). (a, b) Insect approaching the test plate. (c, d) Insect impacting the surface. (e, f) Insect residue spreading on the surface, which is subsequently removed by the incoming airflow

change the adhesion mechanism of the hemolymph as the coagulation process would be affected [5, 9].

### 3.3.2 Effect of Temperature on Insect Adhesion Properties

During the ground segment of the flight phase (taxiing, boarding, ground handling), the aircraft wing skin temperature can reach up to 70°C during the summer months in certain regions and with aircraft operating in tropical or desert regions [66]. It has also been suggested by Spiro et al. [67] that heating insect impingement areas (such as the inlet cowl of an engine) to 180–500°C reduced insects adhering to the aircraft surface and/or removed debris already deposited. Conversely, Tegarden [68] found that heating a titanium substrate to 200–371°C did not show any reduction in contamination when compared to candidate anti-contamination coatings tested at normal temperatures. It was therefore of interest in the current study to determine whether substrate temperature has an effect on insect residue adhesion. As a qualitative comparison, high-speed video footage of insects impacting on heated (70°C) and unheated (20°C) surfaces were analyzed (Figs. 8 and 9). Two aspects of the effect of temperature were evaluated: (1) the evaporation of the hemolymph and other body fluids and (2) protein coagulation accelerated by high temperatures. No visible differences in the impact dynamics, spreading mechanism of the hemolymph, or the spreading rates for the higher surface temperature specimens (substrate temperature was 70°C) were found. Residue height and area measurement analyses were conducted; however, no differences were found in the values when compared to ambient temperature impacts (20°C substrate). Macroscopic images of the specimens showed no difference in the hemolymph drying behavior or discoloration of the specimens impacted at 70°C. This was as expected as Spiro et al. [67] first noted discoloration of insect debris at high temperatures of 260°C and significant charring when the temperature reached 400°C.



**Fig. 8** Image sequence of *D. melanogaster*. (Test facility: SPIrIT, specimen: 15, substrate temperature: 20°C, impact angle: 90°, impact velocity: 100 m/s). (a) Insects approaching the test plate. (b) Insects impacting the surface. (c) Insect residue spreading on the surface

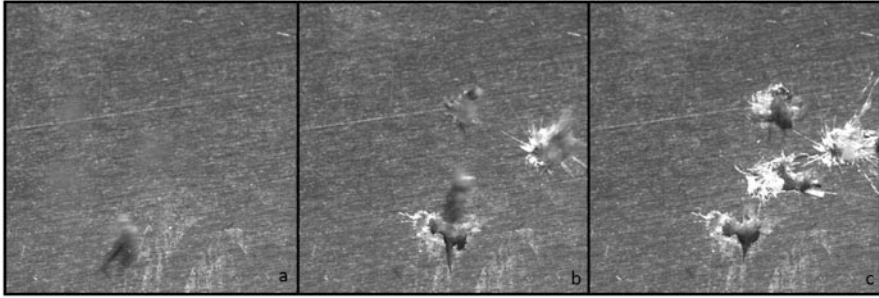


**Fig. 9** Image sequence of *D. melanogaster*. (Test facility: SPIrIT, specimen: 15, substrate temperature: 70°C, impact angle: 90°, impact velocity: 100 m/s). (a) Insects approaching the test plate. (b) Insects impacting the surface. (c) Insect residue spreading on the surface

### 3.4 Insect Impact Dynamics and Residue Area Analysis

The dynamics of an insect impact are influenced by a range of factors including the impact velocity, impact angle (normal or oblique), the shape and size of the insect, and properties of the surface (e.g., surface energy, roughness, and sliding angle). To predict the maximum spread of the hemolymph upon impact, a simple energy conservation equation was formulated. The sum of the kinetic and surface tension energies prior to impact are equated to the sum of the surface energy and losses caused by viscous dissipation (this model is normally used in high-speed liquid droplet impacts) [69–73]. Coatings tested in Sect. 3.2 were inclined at an angle of 30°; however, experimental and theoretical studies on droplet impact onto inclined surfaces are limited and, therefore, to simplify the problem, the standard equations are used [74–76]. To quantify the maximum spread of the hemolymph, non-dimensional parameters such as the Reynolds ( $Re$ ), Weber ( $We$ ), and Ohnesorge ( $Oh$ ) numbers (1–3) can be used [71–73]:

$$Re = \frac{\rho DV_0}{\mu} \tag{1}$$

$$We = \frac{\rho DV_0^2}{\sigma} \tag{2}$$

$$Oh = \frac{We^{1/2}}{Re} \tag{3}$$

where  $\rho$ ,  $\mu$ , and  $\sigma$  denote liquid density, viscosity, and surface tension, and  $D$  and  $V_0$  the droplet diameter and impact velocity, respectively. Because of reported difficulties in obtaining properties of hemolymph [2, 5], the surface tension and viscosity of water are assumed. Using an impact velocity  $V_0$  of 100 m/s and an idealized droplet diameter of 600  $\mu\text{m}$  (obtained by using the insect size and mass), the  $Re$ ,  $We$ , and  $Oh$  can be calculated as 62,700, 85,890, and 0.0046, respectively.

The large  $Re$  and  $We$  numbers indicate that the insect's kinetic energy is large enough to overcome both the surface tension and viscosity of the hemolymph, and spreading on the surface takes place. The kinetic energy is therefore more dominant in the impact process than the effects of surface tension and viscous forces [77]. This is consistent with observations by Kok and Young [33], who stated that because of the high impact velocity and short time frame within which the impact occurs ( $<1$  s), the viscosity (and/or an increase in viscosity produced by the biochemical change within the hemolymph upon impact) would not have an effect on the initial deposition but would only affect the strength of the adhesion to the surface. The method of deposition of the droplet onto the surface therefore has a significant effect on the contribution of the properties of the liquid on the spreading regime. When the drop is placed on the surface, the kinetic energy of the drop is small and the process of spreading is dominated by intermolecular forces of the liquid (e.g., surface tension, viscosity). It was shown by [76–79] that at low impact velocities ( $<20$  m/s), the viscosity significantly affects the spreading regime of liquid droplets, with low- viscosity fluids resulting in prompt splashing, whereas high-viscosity fluids result in delayed splashing. Similarly, Clanet et al. [80] and Bobinski et al. [81] defined an impact number ( $P$ ), which incorporates the influence of viscosity. They showed that when  $P < 1$ , the influence of viscosity was deemed negligible and the impact could be treated as inviscid (the impact number was only shown to be applicable at low-velocity impacts).

Using the values obtained from (1–3), the maximum spreading diameter can be calculated using (4) [5, 64]:

$$\frac{D_{\max}}{D} = 0.61 (\text{Re}^2 Oh)^{0.166} \quad (4)$$

$D_{\max}$  was calculated to be 5.86 mm and, assuming a constant area is covered, this equates to a circular residue area value of 27.0 mm<sup>2</sup>. This theoretically predicted value is in a similar range to the values obtained experimentally. The lowest residue area value obtained in Sect. 3.2 (neglecting the complete mitigation of Specimens 4 and 5) had a value of 1.2 mm<sup>2</sup> (Specimen 6), whereas the largest residue area obtained was 21.0 mm<sup>2</sup> (Specimen 12). Equation (4) is a function of the impact velocity and liquid properties and does not account for the influence of surface properties on the spreading of the hemolymph. It was shown that characteristics of the surface, such as surface energy, surface roughness, and sliding angle, have a significant effect on the spreading mechanism of the hemolymph and the resultant insect residue area (Sect. 3.2). Theoretical models incorporating properties of the surface, such as wettability (by advancing contact angle) and surface roughness, have been proposed by [71, 75, 82–86]. However, these models use a single parameter, either the surface roughness or the advancing angle, to predict the maximum spreading diameter and therefore simplify the dynamics of the spreading regime. The use of the advancing contact angle to predict the maximum spreading diameter was also confined to low impact velocities ( $<10$  m/s) [71, 75, 82–84]. To ascertain the influence of surface roughness on the spreading characteristics, a surface roughness parameter ( $S_r$ ) was established [85, 86]. However, this model

predicts that the surface with the highest  $Ra$  (corresponding to the highest  $S_T$ ) would have the greatest influence on the spreading and does not account for the influence of surface energy. As shown in Sect. 3.2, the spreading and adhesion of insect residue to a surface is highly dependent on the topography (microstructure) and chemistry (surface energy) of the surface. The surface found to be most effective in this study had topographical features at various length scales and allowed for a sufficiently large air cushion to be obtained between the insect residue and the surface, resulting in a Cassie–Baxter wetting state. The microstructure is therefore a critical parameter influencing the spreading and adhesion mechanisms. To predict effectively the maximum spreading diameter and/or the effectiveness of a coating, theoretical models need to include a range of surface parameters.

## 4 Conclusions

Candidate anti-contamination coatings evaluated showed a reduction in insect residue compared to the reference surfaces, with superhydrophobic coatings showing complete mitigation. The use of superhydrophobic coatings in aerospace applications are, however, limited because of the lack of durability of these coatings. Results indicated that both chemistry and topographical characteristics of the surface influence insect residue adhesion. Surfaces shown to be most effective in mitigating insect residue adhesion exhibited a low surface energy, high micro-scale roughness, and low sliding angle value.

Testing with different insect species showed an influence on the ranking (or effectiveness) of the anti-contamination coatings. Two insect impact test facilities, with different equipment, were compared and good correlations in the coating rankings were obtained. The coating rankings of all anti-contamination coatings were similar, irrespective of the test facility used. Coatings tested in iCORE did, however, show an increase in the resulting insect residue area and a decrease in the residue height value when compared to values obtained using SPIrIT. This was attributed to the constant airflow supplied during the insect impact event. The airflow resulted in more spreading of the hemolymph upon impact, increasing the residue area obtained. Similarly, the excrescence height decreased because of the airflow, as more exoskeleton is swept away upon impact. The exposure to airflow during an insect impact event is therefore a key parameter responsible for differences in insect residue patterns, which are highly dependent on the test facility used; however, this should not affect the ranking of the anti-contamination coatings tested. The influence of surface temperature on the insect impact dynamics and subsequent adhesion of insect debris were found to be negligible.

**Acknowledgements** This work is supported by the European Union through FP7 Framework project AEROMUCO (AERodynamic surfaces by advanced MULTifunctional COatings). The research leading to these results received funding from the MEYS under the National Sustainability Programme I (Project LO1202). The authors would like to acknowledge the following organizations for providing test materials for this study: CREST, Dublin Institute of Technology,

Dublin, Ireland; Airbus Group Innovations, Ottobrunn, Germany; and Dassault Aviation SA, Paris, France.

## References

1. Wohl CJ, Smith JG, Connell JW et al (2013) Engineered surfaces for mitigation of insect residue adhesion. In: Proceeding of the 51st AIAA aerospace sciences meeting, Grapeville, Dallas, Texas, 7–10 Jan 2013
2. Kok M, Mertens T, Raps D, Young TM (2013) Influence of surface characteristics on insect residue adhesion to aircraft leading edge surfaces. *Prog Org Coat* 76(11):1567–1575
3. Kok M, Raps D, Young TM (2013) Effects of surface roughness and energy on insect residue adhesion to aircraft leading edge surfaces. In: Proceeding of the 36th annual meeting of the adhesion society, Daytona Beach, USA, 3–6 Mar 2013
4. Wohl CJ, Smith JG, Penner RK et al (2013) Polyimide-based particulate-composite coatings for contamination mitigation of aircraft surfaces. In: Proceeding of the 36th annual meeting of the adhesion society, Daytona Beach, USA, 3–6 Mar 2013
5. Wohl CJ, Smith JG, Penner RK et al (2012) Evaluation of commercially available materials to mitigate insect residue adhesion on wing leading edge surfaces. *Prog Org Coat* 76:42–50
6. Wortmann FX (1974) A method for avoiding insect roughness on aircraft: installation of highly elastic rubber coverings on leading edges. NASA – TT-F15454, Apr 1974
7. Siochi EJ, Eiss NS, Gilliam DR, Wightman JP (1987) A fundamental study of insect residues to aircraft wings. *J Colloid Interface Sci* 115(2):346–356
8. Eiss NS Jr., Wightman JP, Gilliam DR, Siochi EJ (1984) A fundamental approach to the sticking of insect residues to aircraft wings. Annual Technical Report. NASA CR-173721, Apr 1984
9. Yi O, Eiss NS, Wightman JP (1988) Investigation of factors affecting the sticking of insects in aircraft wing surfaces. NASA CR-183041, Sep 1988
10. Lorenzi T, Wohl C, Penner R et al (2011) Insect residue contamination on wing leading edge surfaces: a materials investigation for mitigation. In: Proceeding of the 242nd American chemical society national meeting and exposition, Denver, USA, 28 Aug–1 Sept 2011
11. Smith J, Lorenzi T, Wohl C et al (2012) Influence of surface energy on insect residue adhesion. In: Proceeding of the 35th annual meeting of the adhesion society, New Orleans, USA, 26–29 Feb 2012
12. Young TM, Tobin EF, Kok M (2012) Laboratory testing of insect contamination for laminar flow applications using an insect-impact facility. In: Proceedings of the 28th international congress of the aeronautical sciences (ICAS), Brisbane, Australia, 23–28 Sept 2012
13. Grünke S (2012) Anti-contamination and easy-to-clean coatings for aerodynamic efficient surfaces. In: Proceeding of 19th international conference on surface treatments in the aeronautics and aerospace industries, Biarritz, France, 31 May – 1 June 2012
14. Kok M, Smith Jr JG, Wohl CJ et al (2015) Critical considerations in the mitigation of insect contamination on aircraft surfaces – a review. *Prog Aersp Sci* 75:1–14
15. AEROMUCO (AEROdynamic surfaces by advanced MULTifunctional COatings). [www.aeromuco.eu](http://www.aeromuco.eu), Accessed Oct 2014
16. Joslin RD (1998) Aircraft laminar flow control. *Annu Rev Fluid Mech* 30:1–29
17. Marsden DJ (1978) Wind tunnel tests of a slotted flapped wing section. *Can Aeronaut Space J* 24:83–91
18. Coleman WS (1961) Roughness due to insects. In: Lachmann GV (ed) *Boundary layer and flow control*, vol II. Pergammon Press, Oxford, pp 682–747



19. Croom CC, Holmes BJ (1985) Flight evaluation of an insect contamination protection system for laminar flow wings. In: SAE, general aviation aircraft meeting and exposition, Wichita, US, 1985 Apr. 16–19, pp. 4.486–4.495 (Report No.: SAE Paper 850860)
20. Lowman MD (1982) Seasonal variation in insect abundance among three Australian rain forests, with particular reference to phytophagous types. *Aust J Ecol* 7:353–361
21. Pedigo LP, Rice ME (2006) *Entomology and pest management*, 5th edn. Pearson Prentice Hall, Columbus
22. Freeman JA (1946) The distribution of spiders and mites up to 300ft. in the air. *Anim Ecol* 15(1):69–74
23. Johnson CG (1969) *Migration and dispersal of insects by flight*. Methuen, London
24. Hardy AC, Milne PS (1939) Studies in the distribution of insects by aerial currents. *J Anim Ecol* 7:199–229
25. Johnson CG, Penman HL (1951) Relationship of aphid density to altitude. *Nature* 168:337–338
26. Carpenter FM, Burnham L (1985) The geological record of insects. *Annu Rev Earth Planet Sci* 13:297–314
27. Pennycuik CJ (1972) *Animal flight*. Edward Arnold, London
28. Lachmann GV (1960) Aspects of insect contamination in relation to laminar flow aircraft. A.R. C Technical Report 484, London
29. Wortmann FX (1984) A possibility of avoiding surface roughness due to insects. NASA TM 77419
30. O'Donoghue D (2001) The investigation of the potential of fluorosurfactants and proteolytic and enzyme in water organic C-solvent systems for aircraft wing contamination alleviation. MSc thesis, University of Limerick, Ireland
31. O'Donoghue D, Young T, Pembroke JT, O'Dwyer T (2002) An investigation of surfactant and enzyme formulations for the alleviation of insect contamination on hybrid laminar flow control (HLFC) surfaces. *Aerosp Sci Technol* 6(1):19–29
32. Kok M, Tobin EF, Zikmund P et al (2014) Laboratory testing of insect contamination with application to laminar flow technologies, part I: variables affecting insect impact dynamics. *Aerosp Sci Technol* 39:605–613
33. Kok M, Young TM (2014) The evaluation of hierarchical structured superhydrophobic coatings for the alleviation of insect residue to aircraft laminar surfaces. *Appl Surf Sci* 314:1053–1062
34. Balamurugan A, Balossier G, Laurent-Maquin D et al (2008) An in vitro biological and antibacterial study on a sol–gel derived silver-incorporated bioglass system. *Dent Mater* 24(10):1343–1351
35. Jaiswal S, McHale P, Duffy B (2012) Preparation and rapid analysis of antibacterial silver, copper and zinc doped sol–gel surfaces. *Colloids Surf B: Biointerfaces* 94:170–176
36. Sakka S (2013) *Handbook of advanced ceramics: materials, applications, processing, and properties*, 2nd edn. Elsevier, Amsterdam, pp 883–910
37. Tan SN, Wang W, Ge L (2011) *Comprehensive biomaterials: Vol. 3: methods of analysis*. In: Ducheyne P (ed) *Comprehensive biomaterials*. Elsevier, Amsterdam
38. Peterson JB, Fisher DF (1978) Flight investigation of insect contamination and its alleviation. In: *Proceeding in the CTOL transport technology conference*, Langley Research Center, Hampton, Virginia, NASA CP 2036, Feb–Mar 1978, pp 357–363
39. Krishnan KG, Milionis A, Loth E et al (2017) Influence of hydrophobic and superhydrophobic surfaces on reducing aerodynamic insect residues. *Appl Surf Sci* 393:723–731
40. De Jong G, Bochdanovits Z (2003) Latitudinal clines in *Drosophila melanogaster*: body size, allozyme frequencies, inversion frequencies, and the insulin-signalling pathway. *J Gene* 82(3):207–223
41. De Moed GH, De Jong G, Scharloo W (1997) Environmental effects on body size variation in *Drosophila melanogaster* and its cellular basis. *Genet Res* 70:35–43
42. Patterson J, Wagner R, Wharton L (1943) *The drosophilidae of the southwest*. The University of Texas Press, Austin, p 327

43. Stamps JA, Yang LH, Morales VM, Boundy-Mills KL (2012) *Drosophila* regulate yeast density and increase yeast community similarity in a natural substrate. *PLoS One* 7(7):e42238
44. Larrain P, Salas C (2008) House fly (*Musca domestica* L.) (Diptera: Muscidae) development in different types of manure. *Chil J Agric Res* 68(2):192–197
45. Amino K (1985) Breeding of the housefly, *Musca domestica* (Diptera; Muscidae) in fresh dung of cattle fed on pasture grass. *J App Entomol Zool* 20:143–150
46. Nosonovsky M, Bhushan B (2007) Hierarchical roughness optimization for biomimetic superhydrophobic surfaces. *Ultramicroscopy* 107:969–979
47. Bhushan B, Jung YC (2007) Wetting study of patterned surfaces for superhydrophobicity. *Ultramicroscopy* 107:1033–1041
48. Shibuichi S, Onda T, Satoh N, Tsujii K (1996) Super water-repellent surfaces resulting from fractal surfaces. *J Phys Chem* 100:19512–19517
49. Yost FG, Michael JR, Eisenmann ET (1995) Extensive wetting due to roughness. *Acta Metall Mater* 45:299–305
50. Semal S, Blake TD, Geskin V et al (1999) Influence of surface roughness on wetting dynamics. *Langmuir* 15:8765–8770
51. Erbil HY, Demirel AL, Avci Y, Mert O (2003) Transformation of a simple plastic into a superhydrophobic surface. *Science* 299:1377–1380
52. Burton Z, Bhushan B (2005) Hydrophobicity, adhesion and friction properties with nano-patterned roughness and scale dependence. *Nano Lett* 5:1607–1613
53. Muster TH, Prestidge CA (2002) Application of time-dependent sessile drop contact angles on compacts to characterise the surface energetics of sulfathiazole crystals. *Int J Pharm* 234:43–54
54. Wang X, Chen Z, Shen Z (2005) Dynamic behavior of polymer surface and the time dependence of contact angle. *Sci China Ser B Chem* 48(6):553–559
55. Feng L, Zhang Y, Xi J et al (2008) Petal effect: a superhydrophobic state with high adhesive force. *Langmuir* 24:4114–4119
56. Choo S, Choi HJ, Lee H (2014) Replication of rose-petal surface structure using UV-nano imprint lithography. *Mater Lett* 121:170–173
57. Xi J, Jiang L (2008) Biomimic superhydrophobic surfaces with high adhesive forces. *Ind Eng Chem Res* 47:6354–6357
58. Karaman M, Cabuka N, Özyurt D, Köysüren Ö (2012) Self-supporting superhydrophobic thin polymer sheets that mimic the nature's petal effect. *Appl Surf Sci* 259:542–546
59. Olin PH, Lindstrom SB, Pettersson T, Wagberg L (2013) Water drop friction on superhydrophobic surfaces. *Langmuir* 29:9079–9089
60. Mahadik SA, Fernando PD, Hegade ND et al (2013) Durability and restoring of superhydrophobic properties in silica-based coatings. *J Colloid Interface Sci* 405:262–268
61. Siochi EJ, Smith JG, Wohl CJ et al (2013) Engineered surfaces for mitigation of insect residue adhesion. In: *Proceeding of SAMPE*, Long Beach, CA, 6–9 May, 2013
62. Nosonovsky M, Bhushan B (2009) Superhydrophobic surfaces and emerging applications: non-adhesion, energy, green engineering. *Curr Opin Colloid Interface Sci* 14:270–280
63. Stumm-Tegethoff BFA, Dicke AW (1974) Surface structure of the compound eye of various *Drosophila* species and eye mutants of *Drosophila melanogaster*. *Theor Appl Genet* 44:262–265
64. Michiels F, Falkenburg D, Müller AM et al (1987) Testis-specific  $\beta 2$  tubulins are identical in *Drosophila melanogaster* and *D. hydei* but differ from the ubiquitous  $\beta 1$  tubulin. *Chromosoma* 95(6):387–395
65. Miedema K, Harhangi H, Mentzel S et al (1994) Sequence conservation between both species has been demonstrated to show functionality relevant regions of a gene interspecific sequence comparison of the muscle-myosin heavy-chain genes from *Drosophila hydei* and *Drosophila melanogaster*. *J Mol Evol* 39:357–368

66. Deckstein D, Traufetter G (2013) Weight loss for superjumbos: the A380 and the aviation engineering dilemma. <http://www.spiegel.de/international/business/airbus-struggles-to-handle-A380-engineering-dilemma-a-822391.html> [Last Accessed 26 Aug 2013]
67. Spiro CL, Fric TF, Leon RM (1997) General electric company. Aircraft anti-insect system. US Patent 5683062
68. Tegarden FW (1996) Hybrid laminar flow nacelles – a test for the future. General electric company, Cincinnati, Ohio, USA – Royal Aeronautical Society, London, pp 1–11
69. Yarin AL (2006) Drop impact dynamics: splashing, spreading, receding, bouncing. *Annu Rev Fluid Mech* 38:159–192
70. Chen JH (2005) Characteristics of drop impact on elastic and compliant surfaces. *J Mar Sci Technol* 12(2):151–161
71. Aziz SD, Chandra S (2000) Impact, recoil and splashing of molten metal droplets. *Int J Heat Mass Tran* 43:2841–2857
72. Wang B, Zhao Y, Yu T (2011) Fabrication of novel superhydrophobic surfaces and droplet bouncing behaviour – part 2: water droplet impact experiment on superhydrophobic surfaces constructed using ZnO nanoparticles. *J Adhes Sci Technol* 25:93–108
73. Rein M (1993) Phenomena of liquid drop impact on solid and liquid surfaces. *Fluid Dyn Res* 12:61–93
74. Šikalo Š, Tropea C, Ganić EN (2005) Impact of droplets onto inclined surfaces. *J Colloid Interface Sci* 286:661–669
75. Cui J, Chen X, Wang F et al (2009) Study of liquid droplets impact on dry inclined surface. *Asia Pac J Chem Eng* 4(5):643–648
76. Liang G, Guo Y, Yang Y et al (2013) Spreading and splashing during a single drop impact on an inclined surface. *Acta Mech* 224:2993–3004
77. Jin L, Yang C, Leong KC (2012) Dynamic behaviour of liquid droplet impacting on heated surfaces. *Adv Multiphase Flow Heat Transf* 4:28–39
78. Toivakka M (2003) Numerical investigation of droplet impact spreading in spray coating of paper. TAPPI 8th advanced coating fundamentals symposium. TAPPI Press, Atlanta
79. German G, Bertola V (2009) Impact of shear-thinning and yield-stress drops on solid substrates. *J Phys Condens Matter* 21(37):375111
80. Clanet C, Beguin C, Richard D, Quere D (2004) Maximal deformation of an impacting drop. *J Fluid Mech* 517:199–208
81. Bobinski T, Sobieraj G, Gumowski K et al (2014) Droplet impact in icing conditions – the influence of ambient air humidity. *Arch Mech* 66(2):127–142
82. Zang D, Wang X, Geng X et al (2013) Impact dynamics of droplets with silica nanoparticles and polymers additives. *Soft Matter* 9:394–400
83. Ukiwe C, Mansouri A, Kwok DY (2005) The dynamics of impacting water droplets on alkane-thiol self-assembled monolayers with co-adsorbed CH<sub>3</sub> and CO<sub>2</sub>H terminal groups. *J Colloid Interface Sci* 285:760–768
84. Pasandideh-Fard M, Qiao YM, Chandra S, Mostaghimi J (1996) Capillary effects during droplet impact on a solid surface. *Phys Fluids* 8(3):650–659
85. Mundo C, Tropea C, Sommerfeld M (1997) Numerical and experimental investigation of spray characteristics in the vicinity of a rigid wall. *Exp Thermal Fluid Sci* 15:228–237
86. Mundo C, Sommerfeld M, Tropea C (1995) Droplet-wall collisions: experimental studies of the deformation and breakup process. *Int J Multiphase Flow* 21:151–173

# Insect Abatement on Lubricious, Low Adhesion Polymer Coatings Measured with an Insect Impact Testing System



Adam F. Gross, Andrew P. Nowak, Elena Sherman, Christopher Ro, Sophia S. Yang, Maryam Behroozi, and April R. Rodriguez

**Abstract** Insect debris disrupts laminar flow, obstructs operator vision, and degrades vehicle aesthetics. To protect vehicle surfaces, anti-contamination coatings have been under development for 70 years, but no known homogeneous coating both adequately reduces debris and survives on vehicle surfaces. Coatings with synergistic combinations of physical properties and materials, however, may enable improved anti-fouling and maintain long-term durability. Transparent, spray-on coatings were developed that contain a combination of fluorinated and hygroscopic chemistries in which the fluorinated component reduces wetting of insect debris while the hygroscopic component produces a lubricating layer of absorbed water that interferes with debris adhesion. Debris area after insect impact was approximately twice as low on these coatings as compared to homogeneous control materials. Furthermore, the sensitivity of debris accumulation to hygroscopic content, and thus lubricity, was measured. At least 13 wt% hygroscopic content in the developed coatings was required for decreased debris accumulation compared to a pure fluorinated surface. Lastly, resistance to common vehicle fluids and scribe-tape adhesion was measured on fluorinated-hygroscopic coatings as initial demonstrations of durability.

**Keywords** Anti-insect coatings • Anti-soiling coatings • Fluorinated-hygroscopic polymers • Nanostructured polymers

---

A. F. Gross (✉), A. P. Nowak, E. Sherman, C. Ro, S. S. Yang, M. Behroozi, and A. R. Rodriguez  
HRL Laboratories, LLC, Malibu, CA, USA  
e-mail: [afgross@hrl.com](mailto:afgross@hrl.com)

## Contents

1	Introduction .....	316
2	Experimental Materials and Methods .....	318
3	Results and Discussion .....	321
3.1	Coating Structure .....	321
3.2	Statistical Analyses of Insect Debris Areal Data .....	324
3.3	Comparison to Previous Results .....	326
3.4	Importance of Lubrication on Insect Debris Prevention .....	327
3.5	Initial Durability Testing .....	328
4	Conclusions .....	329
	References .....	330

## 1 Introduction

Insect impact residue affects vehicle fuel economy, aesthetics, and operator vision. On aircraft, insect residue interferes with airflow over a laminar flow surface, thereby increasing drag and fuel consumption [1]. On automobiles, the light dispersion of headlights, operator vision through the windshield, and consumer aesthetic appeal are degraded by insect remains. Many passive and active solutions to reduce insect debris on vehicles have been proposed, yet weight, power, or durability limitations have inhibited their adoption [2]. Active systems such as mechanical scrapers or shields [3, 4] as well as sacrificial continually released liquid layers [5] have been tested on aircraft. The best performing liquid layer-emitting systems add a large size and weight penalty, and the complexity of scrapers and shields has prevented their use [3, 5]. In contrast, passive solutions such as anti-contamination coatings are attractive because of their low mass and scalability. However, no passive coatings are in use today because of durability challenges [2].

Most approaches for passive, insect debris-preventive coatings cannot achieve both debris prevention and high durability, which are preconditions for use on a vehicle. Superhydrophobic coatings are best at reducing insect debris in laboratory testing, but their limited durability because of fragile asperities and high solid filling fractions are barriers to adoption [6–9]. Similarly, temporary protective coatings that erode during flight reduce contamination but require time-consuming application before each or every few flights [10]. Higher durability materials such as hydrophobic coatings [11] had no debris reduction effect, whereas fluorinated coatings reduced debris from fruit flies but not from crickets in laboratory testing [7, 11] and were not effective in flight testing [12]. A recent approach combined low-residue and high-durability materials by creating superhydrophobic layers of hydrophobic silica thermally fused between layers of fluorinated thermoplastic [13]. This material reduced insect debris similar to a pure superhydrophobic surface and survived 15 cycles of linear Taber abrasion because of the thermoplastic layers. Large-scale adoption of this material is inhibited by the layered composite requiring

a thermal treatment between each applied layer and because these coatings were not tested for resistance to common equipment and maintenance fluids used on aircraft.

Toward the goal of obtaining both long-term durability and insect debris reduction, cross-linked, scalable, spray-on polymer coatings were made that exhibit both debris-reducing lubrication and adhesion-preventing fluorination. Lubricating segments are introduced because shedding liquid layers were previously shown to reduce insect debris [5, 10]. Moreover, the hygroscopic lubricating component extracts additional water from the environment during rain, frosting, or high humidity to replenish surface lubrication. In addition, a surface with a low surface energy was created by introducing fluorinated segments into the polymer backbone to counteract the amount of debris that accumulated on hydrophilic surfaces [7], which would be created by a static lubricated surface. Both segments are structured in a block copolymer geometry for control over the length-scale and density of hygroscopic and fluorinated discrete domains on the coating surface and cross-linked to maintain domain structure and improve durability. Testing insect debris accumulation against this combination of fluorinated and hygroscopic materials in a structured polymer shows whether multiple properties expressed in one coating are more effective than single property materials such as Teflon<sup>®</sup>.

Although the idea of a lubricated coating is not common in work to prevent insect debris, it is well-established in the anti-icing literature. For example, purely hydrophilic films [14–17] create a liquid water layer on a surface to inhibit ice adhesion. Additionally, trapping non-aqueous fluids on surfaces significantly reduces adhesion to ice on the surface [18–21]. These approaches cannot be used directly for insect debris prevention because insect debris accumulation is greatest on hydrophilic surfaces [7] created by aqueous films and because there is no way to replace lost non-aqueous fluid. The coatings described in this chapter avoid both issues by collecting aqueous lubrication from the environment onto a hydrophobic surface.

Developing a passive insect abatement coating for vehicles requires practical and predictive test methods that measure soiling under conditions similar to the coating service environment. Flight and on-vehicle automotive testing provide the most authoritative data, although the cost and lead times are significant. Thus, relevant pre-screening methods are beneficial. Wind tunnels that impact crickets and fruit flies against coated surfaces have been developed that mimic an impact at flight or automotive speeds [6, 7]. An alternative approach is to measure wetting and sliding angles of droplets of hemolymph, or insect blood, on surfaces [8]. Finally, a wet abrasion approach was developed which measures the amount of debris removed after abrasion cycles [22]. All approaches come to similar conclusions about the ranking of surfaces [3–5, 22] and thus we prioritized speed of testing and developed an insect impact tester in which the insect type, impact speed, and angle of impact are highly adjustable. This chapter presents the insect impact device, coating structure, trends in debris reduction with coating composition, and a comparison to known materials to demonstrate significantly reduced insect accumulation compared to homogenous control surfaces.

## 2 Experimental Materials and Methods

A fluorinated-hygroscopic copolymer network was synthesized and subsequently tested for insect impact debris reduction. The polymer network was prepared through addition of a hygroscopic and fluorinated alcohol terminated block copolymer precursor combined with a diisocyanate to produce a prepolymer mixture. The prepolymer was prepared by mixing diisocyanate and the alcohol terminated precursor at 100°C for 2 h under nitrogen gas. The viscous mixture was dispersed in solvent, a polyol curative was added, and this mixture was applied with a low volume, low pressure spray gun (Ampro A6034) to a thickness of approximately 100  $\mu\text{m}$  on sample coupons. The coated coupons were baked for 2 h at 60°C to cure the coating fully.

Sample coupons were made from 5  $\times$  5 cm, 0.5 mm thick 6061-T6 Al coupons (McMaster Carr), primed 6061-T6 Al coupons, or Mylar sheets (McMaster Carr). The primed coupons were prepared by spraying 3M AC-131 adhesion promoter on the coupons, allowing them to dry for at least 1 h, and then spraying a 25–50  $\mu\text{m}$  thick coating of PPG CA7502 primer and allowing it to dry for at least 12 h before subsequent coating with fluorinated-hygroscopic copolymers.

Three coatings with variations in fluorinated and hygroscopic content were developed to measure how composition affects insect residue accumulation. The coatings were named FH-XX where FH denotes fluorinated-hygroscopic and XX is the weight percent of hygroscopic material. The composition, water equilibrium contact angles, and arithmetic average of the roughness ( $R_a$ ) are shown in Table 1. The contact angle was measured five times on each sample with 20- $\mu\text{L}$  drops of deionized water using a Rame-Hart Nrl Ca Contact Angle Goniometer.  $R_a$  measurements were obtained using atomic force microscopy and are described below. All errors in Table 1 are one standard deviation.

Control samples were made from (1) bare 6061-T6 Al, (2) 6061-T6 Al coated with a Covestro waterborne clear coat which consisted of primarily Bayhydur XP 2547 (polyisocyanate) and Bayhydrol A 2542 (polyol), and (3) adhesive backed 1.5 mm thick Teflon. The adhesive-backed Teflon was purchased from McMaster Carr and adhered onto 6061-T6 Al sheets prior to insect impact testing.

Water uptake was measured by first spraying and curing a FH-16 coating on Mylar and then peeling the coating off the substrate. The free-standing film was weighed on a Mettler AE200 balance, exposed to 90% RH for 6 h, and weighed

**Table 1** Fluorinated-hydrophobic coating composition and wetting data

Coating name	Wt% hygroscopic oligomers	Wt% fluorinated oligomers	Wt% urethane linkages	Water equilibrium contact angle	$R_a$ (nm)
FH-16	16	43	41	103 $\pm$ 2°	0.4 $\pm$ 0.1
FH-13	13	34	53	101 $\pm$ 3°	Not measured
FH-8	8	41	51	101 $\pm$ 2°	0.4 $\pm$ .0.1

again after exposure. The humidity was controlled in an enclosed chamber attached to a Sable Systems International DG-4 Humidity and Dewpoint Controller.

Insect impact testing was performed with a custom-built pneumatic system designed to discharge small insects toward an inclined substrate and control the angle and speed of impacts. This type of system was first suggested in 1979 [23] and uses compressed air to propel an insect through a hollow tube and onto a coated test panel. The design described here improved on the suggested air gun approach by including optical gates to measure insect velocity and adding an additional chamber before the barrel to control the air pressure onset rate. A schematic of the system and labels on major components are shown in Fig. 1. The insect impact device was driven by 140-psi compressed air that first passed through an air regulator, which controls pressure and thus the bug impact velocity. The air was released by a solenoid valve after the regulator which, when open, acted as a trigger for insect acceleration and subsequent impact. Once the solenoid valve was opened, high pressure air flowed through the tubing assembly into a small air storage tank, and exited via the outlet into a tube containing an insect. The air storage tank was critical to allow more gradual acceleration of the insect as sudden acceleration resulted in insects exploding within the barrel rather than on the substrate. As air flowed through the exit tube, the insect was caught in the airstream, exited the acceleration tube, passed through two infrared photo-gates that measured the insect's velocity as it exited the tubing, and impacted the substrate. The substrate was set at a fixed distance from the outlet and could be angled from perpendicular to nearly parallel to the flight path on a mechanical stage. Impact velocities of 25–60 m/s were regularly achieved. Minimal variation in impact location was observed over multiple impacts with all debris contained within a 2.5 cm radius area.

Although any insect with one dimension smaller than 6 mm can be used, young crickets were selected because of (1) larger insects causing the greatest reduction in automotive operator vision and (2) ease of handling and availability. Larger insects such as crickets compared to the usually tested small fruit flies create increased debris areas at the cost of greater scatter in the data [24]. It was hoped that the larger debris area from crickets would outweigh the detrimental scatter effect and provide greater demarcation between samples. Young, live crickets were purchased from

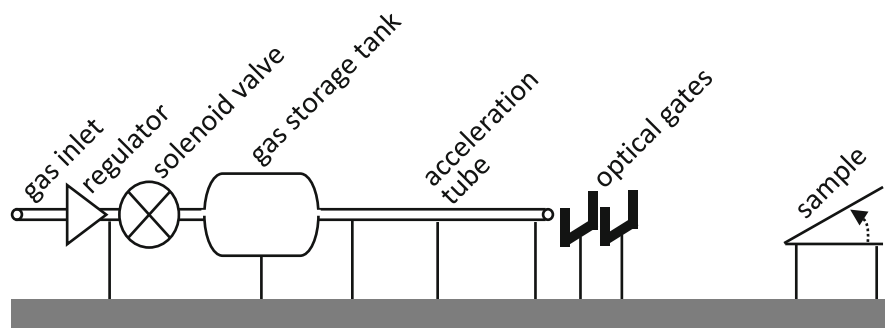


**Fig. 1** Insect impact system



local pet stores. These crickets must be live in order to preserve their water content and best simulate rupture found in the natural environment upon impacting a surface. Before testing, crickets were rendered unconscious by flooding their container with humidified  $N_2$  gas for 5 min. Longer exposures resulted in dehydrated crickets that bounced off surfaces. Furthermore, all cricket preparation and impact testing were performed at 45–55% relative humidity to remove variations from environmental dehydration on insect debris area. Crickets were impacted at the same angle and loaded in the same geometry in every experiment as previous work has shown that impact angle and insect geometry upon impact both affect rupture and debris patterns [25].

To perform an impact test, a substrate was mounted, an insect was inserted through the outlet of the acceleration tube, and the solenoid valve was opened for 2 s to create an impact. The degree of soiling was quantified by measuring the area of insect debris via optical imaging. High contrast was required to perform the image analysis and was achieved by staining the insect debris with an alcohol-based ninhydrin solution (1–5 wt%) to produce a deep purple color from the organic matter. An optical image was collected with the coating and camera in a preset geometry. An imaging routine written in MATLAB then calculated the debris area over a known area of coating by counting the number of pixels above a minimum color threshold. Insect debris area was compared to control surfaces consisting of bare aluminum plates, polyurethane clear coat, and Teflon sheets. All impacts reported were at  $60^\circ$  from normal incidence.

Atomic force microscopy (AFM) imaging was performed by Advanced Surface Microscopy (Indianapolis, IN) on FH-16 and FH-8 samples. The surfaces of 1 mm thick polymer films were imaged in both amplitude and phase modes using Tapping Mode™ on a Dimension 3100 large sample AFM (Bruker). Roughness was calculated from the amplitude (height) scans and all values were the average of eight areas measured on the coating. FH-13 was not measured.

Statistical analysis of data was performed with Microsoft Excel. ANOVA analysis was performed using Single Factor ANOVA in the Data Analysis toolbox. The ANOVA analyses also provided the means and variances used in Tables 2 and 5. The Kruskal–Wallis test was performed using a spreadsheet available at <http://www.biostathandbook.com/kruskalwallis.xls>.

Adhesion and pencil hardness were tested on surfaces after fluid exposures as initial measurements of coating durability. Fluid exposure was performed by submerging half of coated coupons in a fluid at  $22^\circ C$  for 1–30 days, cross hatch adhesion was performed by following ASTM D3359.B, and pencil hardness testing was performed by following ASTM D3363. More specifically for wet adhesion testing, FH-16 was applied on Al panels, cured, soaked in deionized water for 14 days, wiped with cheesecloth, and tested for wet adhesion following ASTM D3359.B. For fluid and cleaner resistance, FH-16 was applied on primed 6061-T6 Al panes, cured, and exposed to Turbo oil 2389 aircraft engine oil, Skydrol LD-4 aviation hydraulic fluid, SAE AMS 1424 Type I deicing fluid, jet reference fuel B, Simple Green, 409 degreaser, Optikleen windshield washer fluid, and Windex for

**Table 2** Statistics for the data in Fig. 4

Sample	Number of points	Mean residue (mm <sup>2</sup> debris area/mg insect)	Variance
FH-16 coating	46	0.71	0.64
FH-16 coating $\leq 36$ m/s	23	0.27	0.11
FH-16 coating $> 36$ m/s	23	1.15	0.79
6061-T6 Al	82	2.28	4.01
6061-T6 Al $\leq 36$ m/s	25	1.40	1.61
6061-T6 Al $> 36$ m/s	57	2.66	4.61
Clear coat	19	1.61	3.31
Clear coat $\leq 36$ m/s	11	0.46	0.12
Clear coat $> 36$ m/s	8	3.18	3.43
Teflon	16	1.64	2.45
Teflon $\leq 36$ m/s	8	0.61	0.47
Teflon $> 36$ m/s	8	2.67	2.36

14–30 days at 21°C. Upon removal from the fluid, the coating was wiped with cheesecloth and pencil hardness was measured following ASTM D3363.

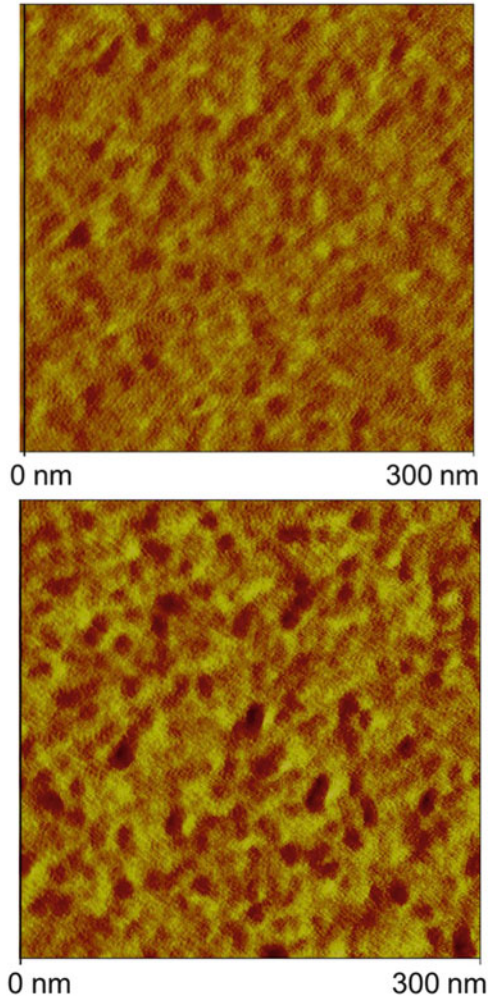
### 3 Results and Discussion

#### 3.1 Coating Structure

Tough and transparent coatings resulted from spraying the fluorinated-hygroscopic copolymer formulations on Mylar and aluminum substrates. To determine whether both fluorinated and hygroscopic domains are expressed on the surface, the FH-16 coating was investigated with phase contrast AFM imaging as shown in Fig. 2 (top). Both fluorinated (yellow) and hygroscopic (red) domains are observed at the surface. The domain sizes are  $\sim 10$  nm which explains the transparency of these coatings. The AFM image from the FH-8 also shows  $\sim 10$ -nm domains (Fig. 2, bottom), and thus the structure is independent of fluorinated and hygroscopic levels and instead driven by the copolymer precursor structure. The key difference between the images is that less hygroscopic material (red color) is present in FH-8 compared to FH-16, which matches the differences in hygroscopic composition between these coatings.

Both fluorinated and hygroscopic phases affect the interactions between these coatings and water. In the FH-16 coating, the fluorinated domain's influence on wetting is demonstrated by the  $103 \pm 2^\circ$  contact angle, which is very similar to Teflon<sup>®</sup> (Table 1). The influence of the hygroscopic materials is shown by the coating absorbing 2 wt% water after 6 h in 90% RH, which demonstrates that the hygroscopic domains are also exposed at the surface. Although this coating is hygroscopic, water absorption is very slow and no changes in droplet dimensions

**Fig. 2** Phase contrast images of FH-16 (*top*) and FH-8 (*bottom*) coatings showing ~10-nm fluorinated (yellow) and hygroscopic (red) domains at the surface. The numbers at the bottom of each image show the length of coating surface imaged



on the surface are observed over 30 min. These results show that both fluorinated and hygroscopic properties coexist instead of one property completely dominating, which would be expected if one material phase segregated preferentially to the surface.

Insect debris accumulation on surfaces was measured by impacting small (<6 mm diameter) crickets against various coatings at velocities between 25 and 62 m/s. Velocities of 26–36 m/s (56–81 mph) represent automotive freeway speeds and faster 37–62 m/s (82–139 mph) velocities represent aircraft speeds during the acceleration phase of takeoff. Images of a control aluminum alloy 6061-T6 test panel and the same aluminum panel coated with the fluorinated-hygroscopic FH-16 coating are shown in Fig. 3 after 41 m/s impacts with crickets and subsequent staining. Debris on the fluorinated-hygroscopic copolymer covers less area and is

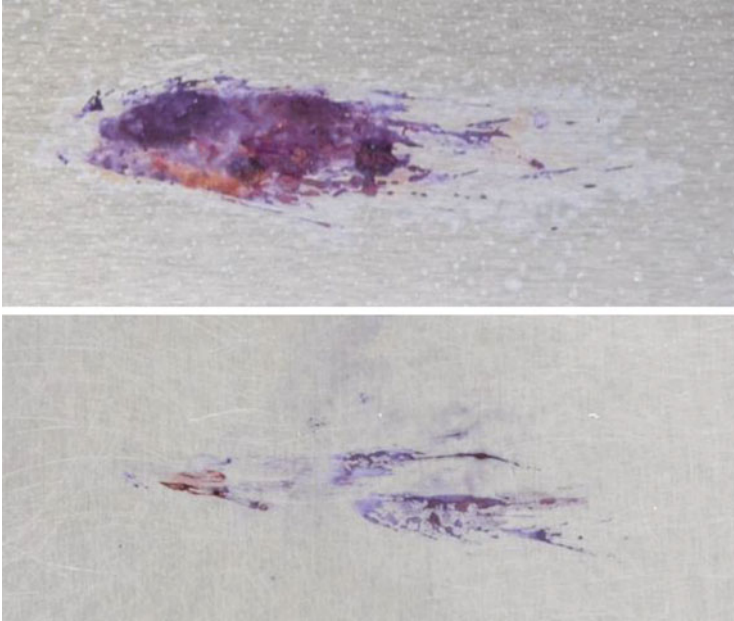


**Fig. 3** Optical images of ninhydrin-stained insect debris on a 6061-T6 Al control panel (*top*) and an FH-16-coated panel (*bottom*). The debris area is greater and more contiguous on the 6061-T6 Al panel

not contiguous in comparison to the continuous debris field on the 6061-T6 Al control panel.

Reduced insect debris accumulation is observed on FH-16-coated panels compared to 6061-T6 Al control panels, polyurethane clear coat control panels, and Teflon control panels in Fig. 4. All insect areal data are normalized to the insect mass and linear fits were performed with an intercept of zero as guides to the eye. The mean and variance of all data sets are shown in Table 2 for all velocities and for data collected at  $\leq 36$  and  $>36$  m/s. These ranges segment the data by automobile freeway vs aircraft takeoff speeds to investigate whether an impact velocity dependence observed by other authors [25] is present in this data.

The FH-16 coating shows approximately two times lower average debris levels and lower variances than the control coatings across all velocity ranges (Table 2). The data have significant scatter, which is not surprising because other researchers found that scatter increased with insect size and crickets are much larger than the usually tested fruit flies [24]. Because of the scatter in the data, these differences must be validated with additional statistical analyses.

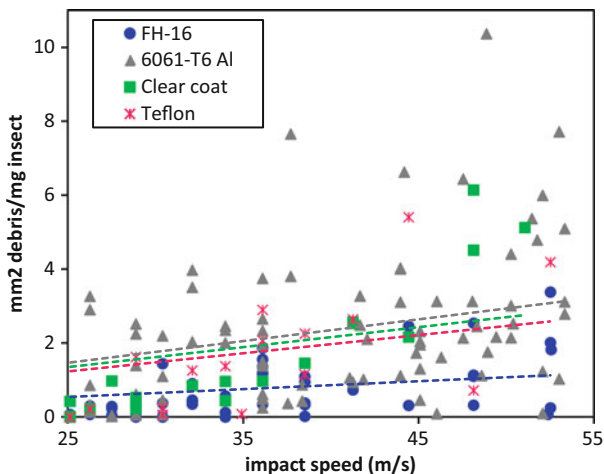


**Fig. 4** Insect impact areal residue shown for the FH-16 coating and three control surfaces. The *dotted lines* are intended as guides to the eye. The FH-16 coating has <50% the debris area of the three control surfaces

### 3.2 Statistical Analyses of Insect Debris Areal Data

Statistical analysis can establish whether data sets are distinct as long as the assumptions behind a chosen statistical test agree with the data. To choose the correct test, the user must determine (1) whether the sets being compared have the same number of data points, (2) whether the variances between the data sets are equal, and (3) whether the individual data sets have a Gaussian (normal) distribution [26]. The data in Table 2 have unequal numbers of data points in each group, have unequal variances, and have non-Gaussian distributions (Fig. 5). The Kruskal–Wallis test is designed to determine whether data sets are indeed statistically distinct for this situation [26, 27]. Similar to the ANOVA analysis, the Kruskal–Wallis provides a  $p$  value, which is the probability that the difference measured between the two compared data sets would be equal or larger if the data sets were the same [28, 29]. Smaller values of  $p$  increase confidence that the groups are in fact distinguishable and a hypothesis of similarity (or null hypothesis) between data sets should be rejected. A commonly accepted threshold for significance is  $p \leq 0.05$ , which is also referred to as the 95% confidence level [30].

When performing multiple comparisons between samples in a set of data, the error rate for the set of data increases because of the greater chance of one incorrect result amongst multiple comparisons [31]. The probability of an error is magnified based on the formula  $1 - (1 - p)^n$ , where  $p$  is the  $p$  value used for pairwise comparisons and  $n$  is the number of comparisons [31]. There are three comparisons between FH-16 and the controls in Fig. 4, and thus there is a  $1 - (1 - 0.05)^3 = 0.1426$  or a 14% chance of a false positive in all of the comparisons if the  $p$  value for individual comparisons is set to 0.05. However, if the individual

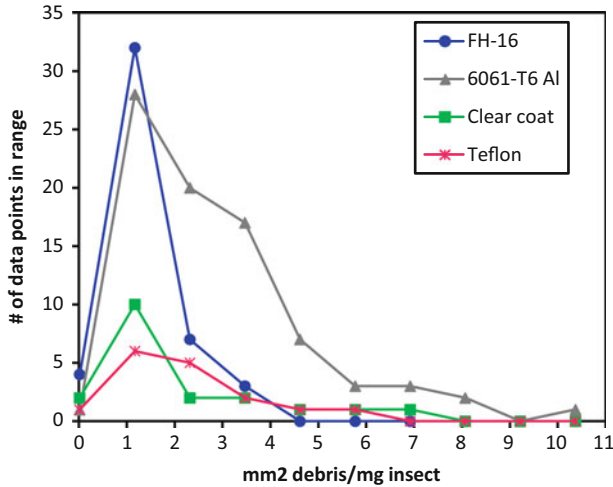


Fig. 5 Histogram of data from Fig. 4 showing non-Gaussian distributions

$p$  values are adjusted to produce an overall data set  $p$  value of 0.05, smaller individual  $p$  values are required for the pairwise comparisons equal to  $p = 1 - (1 - \alpha)^{1/n}$  where  $\alpha$  is the  $p$  value for the full set of comparisons and  $n$  is the number of comparisons [31]. Thus, a 95% confidence level between FH-16 and the controls in Fig. 4 was achieved for  $p = 1 - (1 - 0.05)^{1/3} = 0.017$ .

The Kruskal–Wallis test was used to compare insect debris on the FH-16 coating vs the controls and showed statistically significant differences (95% confidence level) for FH-16 vs Al at all speeds and for FH-16 vs Teflon and clear coat controls at >36 m/s. The pairwise  $p$  values for all comparisons between FH-16 and the controls are shown in Table 3 and statistically significant results ( $p \leq 0.017$ ) are shown in bold text. The approximately two times increase in areal debris between the controls and FH-16 is statistically significant for FH-16 vs Al at all speeds and is statistically significant for FH-16 vs clear coat and Teflon at >36 m/s.

To demonstrate the sensitivity of statistical analysis to assumptions contained in a test, ANOVA analysis was performed on the data in Fig. 4 [26]. ANOVA analysis assumes unequal numbers of data points, equal variances amongst data sets, and Gaussian data distribution. The latter two conditions are false for the data in Fig. 4.

Table 3 Kruskal–Wallis analysis of the FH-16 coating insect areal residue compared to control surfaces

	FH-16 vs 6061-T6 Al alloy	FH-16 vs polyurethane clear coat	FH-16 vs Teflon sheet
Data segmentation			
Data collected across all velocities	$p = \mathbf{1.1E-7}$	$p = 3.9E-2$	$p = 3.6E-2$
Data collected at $\leq 36$ m/s	$p = \mathbf{1.4E-3}$	$p = 8.0E-2$	$p = 4.6E-1$
Data collected at $> 36$ m/s	$p = \mathbf{6.6E-4}$	$p = \mathbf{2.9E-3}$	$p = \mathbf{7.7E-3}$

**Table 4** ANOVA analysis of the FH-16 coating insect areal residue compared to control surfaces

Data segmentation	FH-16 vs 6061-T6 Al alloy	FH-16 vs polyurethane clear coat	FH-16 vs Teflon sheet
Data collected across all velocities	$p = \mathbf{1.3E-6}$	$p = \mathbf{7.1E-3}$	$p = \mathbf{3.3E-3}$
Data collected at $\leq 36$ m/s	$p = \mathbf{1.5E-4}$	$p = 1.4E-1$	$p = 1.3E-1$
Data collected at $> 36$ m/s	$p = \mathbf{1.6E-3}$	$p = \mathbf{2.6E-4}$	$p = \mathbf{1.8E-3}$

The results of ANOVA analysis are shown in Table 4. The data should be compared to a  $p$  value of 0.017 to adjust for the family-wise error rate at the 95% confidence level and statistically significant results are shown in bold text.

ANOVA analysis found statistically distinct data sets when comparing FH-16 vs clear coat or Teflon across all impact velocities in comparison to the Kruskal–Wallis test that found these samples were not statistically significant until speeds at  $> 36$  m/s. All other comparisons in Tables 3 and 4 reached identical conclusions. The Kruskal–Wallis test is more trustworthy because (1) all assumptions are met, unlike ANOVA, (2) its results are more conservative, and (3) finding a lack of statistically significant data at lower velocities matches other researchers who empirically determined a minimum impact speed of  $> 30$  m/s to reduce scatter in their data [32]. Thus the differences in insect debris area between the controls and FH-16 are statistically distinct at the 95% confidence level at all impact speeds for Al and at  $> 36$  m/s for clear coat and Teflon controls.

### 3.3 Comparison to Previous Results

The  $\sim 50\%$  debris areal reductions in Fig. 4 between FH-16 and control surfaces compares well with previous data on cricket impacts on single property coatings. Wohl et al. measured the area and height of cricket impact residue on commercially available surfaces and coatings and saw no areal reduction on any of the surfaces vs Al plates [6]. The tested surfaces ranged from fluorinated to hydrophilic materials and did not have the phase separated regions of different polarities that are in the materials tested here. Thus fluorinated or hydrophilic properties alone are not sufficient to reduce debris. However, observing a debris areal reduction for FH-16 vs single property surfaces such as Teflon demonstrates the value of combining multiple properties (low adhesion and lubricity) with controlled phase separation in one coating to boost performance. The debris reduction observed in Table 2 does not equal the up to 100% debris reduction observed when fruit flies are impacted against a superhydrophobic surface [7]. In all reports using superhydrophobic surfaces, data were only presented from fruit flies and it is not known whether superhydrophobic surfaces would achieve such significant debris reductions against larger crickets with comparatively greater volumes of internal liquid and higher impact momentums than fruit flies.

### 3.4 Importance of Lubrication on Insect Debris Prevention

We hypothesized that the debris reduction observed on the fluorinated-hygroscopic copolymer is caused by the presence of an absorbed water layer created by the hygroscopic material. To verify this premise, two additional coatings were formulated with decreasing amounts of hygroscopic material (Table 1) and tested against cricket impacts. Higher velocities were used for these experiments compared to Fig. 4 in order to be more relevant to aircraft takeoff speeds and to be at speeds where statistically significant differences in residue were observed between all samples. The insect residue areal data in Fig. 6 with statistical analysis in Table 5 show the expected trend of decreasing insect debris with greater hygroscopic/lubricating material in a multi-property coating.

The importance of hygroscopic content for debris reduction is reinforced by neither fluorinated content nor hardness explaining trends with soiling in Table 5. The amount of fluorination in the coatings is reduced from FH-16 (43 wt%) to FH-8 (41 wt%) to FH-13 (34 wt%). However, soiling follows the trend FH-16 < FH-13 < FH-8, and thus there is no correlation between fluorinated content and debris reduction. Additionally, all three coatings have equivalent contact angles (Table 1), which further indicates that the differences in fluorinated content are not altering wetting that could, in turn, affect soiling. Besides fluorinated content, the hardness

**Fig. 6** Insect impact areal residue for the FH-8, FH-13, and FH-16 coatings as well as 6061-T6 Al. The residue area appears to decrease with increasing hygroscopic content in the coatings. The lines are a guide to the eye

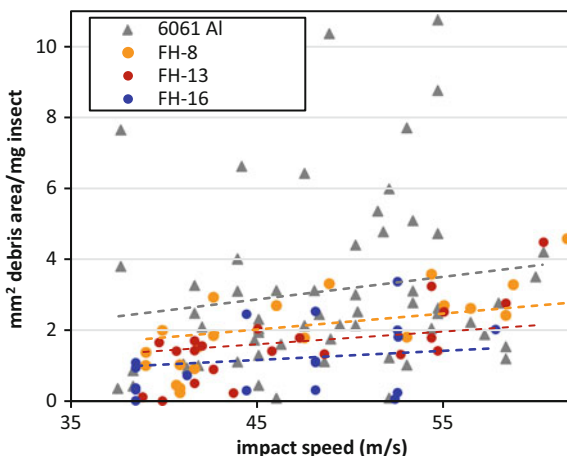


**Table 5** Statistics for the data in Fig. 6

Sample	Number of points	Mean residue (mm <sup>2</sup> debris area/mg insect)	Variance
FH-16 coating	18	1.16	0.98
FH-13 coating	21	1.61	1.10
FH-8 coating	21	2.03	1.35
6061-T6 Al	60	3.09	5.73



**Table 6** Statistical analysis of the data in Fig. 6

Coatings with residue data distinct at the 95% confidence level ( $p$ value)	Coating with non-distinct residue data ( $p$ value)
FH-16 vs 6061-T6 Al ( $p = 1.6E-4$ )	FH-16 vs FH-8 ( $p = 2.4E-2$ )
	FH-16 vs FH-13 ( $p = 2.1E-1$ )
FH-13 vs 6061-T6 Al ( $p = 5.1E-3$ )	FH-13 vs FH-8 ( $p = 1.7E-1$ )
	FH-8 vs 6061-T6 Al ( $p = 1.1E-1$ )

of the coatings could affect soiling by changing surface deformation during insect impact and rupture. The coating hardness derives from the amount of hydrogen bonded urethane linkages and the data in Fig. 6 do not correlate with these levels either; FH-16 and FH-8 have similar amounts of urethane content and very different debris levels. All three FH coatings have no measureable differences in pencil hardness (measured as HB) which also confirms that hardness does not affect debris accumulation. Because a trend with hygroscopic material is observed, but no trend with fluorination or hardness levels are seen, we conclude that the insect debris reduction is driven by lubrication but enabled by the presence of both hygroscopic and low-adhesion materials.

Kruskal–Wallis analysis was performed on the data in Fig. 6 and showed that differences between the FH-13 and FH-16 coatings and 6061-T6 Al were statistically significant, but that differences between fluorinated-hygroscopic coatings with different hygroscopic content were not statistically significant. The scatter in the insect areal debris data is likely preventing statistical significance between the fluorinated-hygroscopic coatings. The pairwise  $p$  values are shown for all comparisons in Table 6. Because there are six pairwise comparisons between the four data sets, the  $p$  value required for the 95% confidence interval for all comparisons is  $1 - (1 - 0.05)^{1/6} = 0.0085$ .

Observing a statistically significant trend in debris reduction between coatings with larger levels of lubrication and single property surfaces (FH-16 vs Teflon in Table 3; FH-13 and FH-16 vs 6061-T6 Al in Table 6) indicates that lubrication when combined with fluorinated materials provides reduced soiling after insect impacts. This is further reinforced by losing statistical significance as hygroscopic content is reduced (FH-8 vs 6061-T6 Al in Table 6). We believe that greater debris reduction can be obtained from increasing hygroscopic levels, if the hydrophobic character of the coating is maintained, and we are currently pursuing this investigation.

### 3.5 Initial Durability Testing

A coating must stay adhered to an underlying surface over its lifetime and protect that surface from corrosion. A common test for durability on a surface is to expose a coating to common vehicle fluids and cleaners and measure changes in hardness

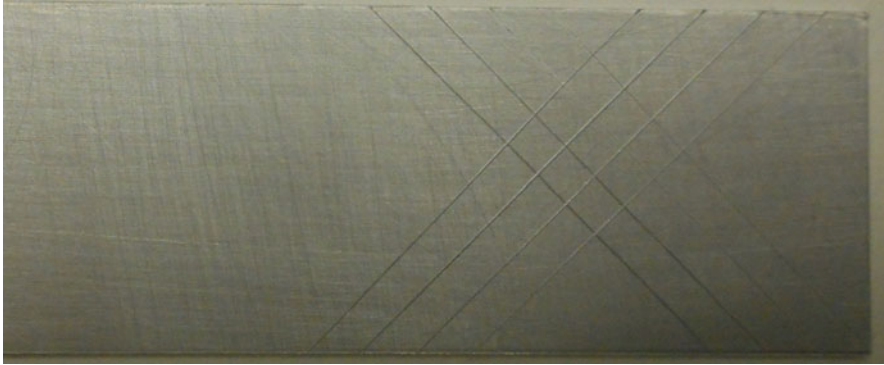


**Fig. 7** FH-16 has an ASTM D3359.B wet adhesion 5B rating after being submerged in deionized water for 14 days

and adhesion. FH-16 was tested for wet adhesion following a 14-day soak in deionized water using ASTM D3359.B. None of the coating delaminated as shown in Fig. 7 and the adhesion was rated 5B (0% debonded). For fluid exposure testing, FH-16 was coated on primed 6061-T6 Al panels and the pencil hardness was measured before and after 14 days of room temperature fluid exposure to Turbo oil 2389 aircraft engine oil, Skydrol LD-4 aviation hydraulic fluid, SAE AMS 1424 Type I deicing fluid, jet reference fuel B, Simple Green, 409 degreaser, Optikleen windshield washer fluid, and Windex. In all cases the HB pencil hardness was unchanged before and after exposure. Aviation hydraulic fluid is especially damaging to coatings [33] and the exposure was extended to 30 days as a more decisive test. Again, a pencil hardness of HB was measured. Thus common vehicle fluids are not expected to degrade coating integrity. Environmental exposure testing, which measures whether the coating survives on a vehicle surface after ultraviolet (UV) exposure and temperature cycling, is to be reported in future work.

## 4 Conclusions

A fluorinated-hygroscopic copolymer coating that expresses both low adhesion and lubricating properties accumulated approximately half the areal debris compared to three control surfaces after cricket impacts at velocities greater than 36 m/s. A reduction in this insect debris only occurred when both hygroscopic and fluorinated materials were present in significant amounts; statistically significant differences in debris area on the fluorinated-hygroscopic coating vs 6061-T6 Al disappeared when the hygroscopic content was reduced below 13%. Fluorinated-hygroscopic copolymer coatings did not debond in a wet adhesion scribe test after a 14-day water soak and did not lose pencil hardness after 14 days in common automotive and aerospace fluids and cleaners. Future work can focus on increasing the hygroscopic material

level to reduce insect debris further, test the ease of removal of insect debris from the coating surface, and perform UV exposure durability testing.

**Acknowledgements** The authors thank HRL Laboratories, LLC for funding and thank Souren Soukiazian for technical assistance.

## References

1. Coleman WS (1959) The characteristics of roughness from insects as observed for two-dimensional incompressible flow past airfoils. *J Aerosp Sci* 26:264–280
2. Kok M, Smith JG et al (2015) Critical considerations in the mitigation of insect residue contamination on aircraft surfaces – a review. *Prog Aerosp Sci* 75:1–14
3. Lachman GV (1960) Aspects of insect contamination in relation to laminar flow aircraft. A.R.C. Technical Report, C.P. No. 484
4. Humphreys BE, Horstmann KH (2000) Flight testing of a HLF wing with suction, ice-protection and anti-contamination systems. In: Proceedings of the CEAS/drag net European drag reduction conference, vol 76, pp 39–57
5. Coleman WS (1952) Wind tunnel experiments on the prevention of insect contamination by means of soluble films and by liquids discharged over the surface. Report to the boundary layer control committee, B.L.C.C. Note 39, M.O.S., London
6. Wohl CJ, Smith JG et al (2013) Evaluation of commercially available materials to mitigate insect residue adhesion on wing leading edge surfaces. *Prog Org Coat* 76:42–50
7. Kok M, Mertens T et al (2013) Influence of surface characteristics on insect residue adhesion to aircraft leading edge surfaces. *Prog Org Coat* 76:1567–1575
8. Milionis A, Krishnan KG et al (2015) Hemolymph drop impact outcomes on surfaces with varying wettability. *Appl Surf Sci* 345:36–43
9. Bocquet L, Lauga E (2011) A smooth future? *Nat Mater* 10:334–337
10. Pearce WE (1983) Evaluation of laminar flow control systems concepts for subsonic commercial transport aircraft. NASA-CR-159251
11. Lorenzi TM, Wohl CJ, et al. (2011) Insect residue contamination on wing leading edge surfaces: a materials investigation for mitigation. In: Proceedings of 242nd American Chemical Society national meeting and exposition, Denver, CO
12. Fisher DF, Peterson JB (1978) Flight experience on the need and use of inflight leading edge washing for a laminar flow airfoil, AIAA aircraft systems and technology meeting, Los Angeles
13. Bayer IS, Krishnan KG et al (2016) Thermal alternating polymer nanocomposite (TAPNC) coating designed to prevent aerodynamic insect fouling. *Sci Rep* 6:38459
14. Chernyy S, Jäm M et al (2014) Superhydrophilic polyelectrolyte brush layers with imparted anti-icing properties: effect of counter ions. *ACS Appl Mater Interfaces* 6:6487–6496
15. Dou R, Chen J et al (2014) Anti-icing coating with an aqueous lubricating layer. *ACS Appl Mater Interfaces* 6:6998–7003
16. Lee H, Alcaraz ML et al (2013) Zwitter-wettability and antifogging coatings with frost-resisting capabilities. *ACS Nano* 7:2172–2185
17. Chen J, Dou R et al (2013) Robust prototypical anti-icing coatings with a self-lubricating liquid water layer between ice and substrate. *ACS Appl Mater Interfaces* 5:4026–4030
18. Wong T-S, Kang SH et al (2015) Bioinspired self-repairing slippery surfaces with pressure-stable omniphobicity. *Nature* 477:443–447
19. Tesler AB, Kim P et al (2015) Extremely durable biofouling-resistant metallic surfaces based on electrodeposited nanoporous tungstite films on steel. *Nat Commun* 6:8649

20. Zhu L, Xue J et al (2013) Ice-phobic coatings based on silicon-oil-infused polydimethylsiloxane. *ACS Appl Mater Interfaces* 5:4053–4062
21. Golovin K, Kobaku SPR et al (2016) Designing durable icephobic surfaces. *Sci Adv* 2:e1501496
22. Kok M, Young TM (2014) Evaluation of insect residue resistant coatings – correlation of a screening method with a conventional assessment technique. *Prog Org Coat* 77:1382–1390
23. Carmichael BH (1979) Summary of past experience in natural laminar flow and experimental program for resilient leading edge. NASA CR-152276
24. Kok M, Tobin EF, et al. (2017) Laboratory investigation into anti-contamination coatings for mitigating insect contamination with application to laminar flow technologies. *Adv Polym Sci*. [https://doi.org/10.1007/12\\_2017\\_31](https://doi.org/10.1007/12_2017_31)
25. Kok M, Tobin EF et al (2014) Laboratory testing of insect contamination with application to laminar flow technologies, part I: variables affecting insect impact dynamics. *Aerosp Sci Technol* 39:605–613
26. McDonald JH (2014) *Handbook of biological statistics*, 3rd edn. Sparky House Publishing, Baltimore, pp 126–139, 157–164
27. Kruskal WH, Wallis WA (1952) Use of ranks in one-criterion variance analysis. *J Am Stat Assoc* 47:583–621
28. Dorey F (2010) In brief: the P value: what is it and what does it tell you? *Clin Orthop Relat Res* 468:2297–2298
29. McKillup S (2012) *Statistics explained: an introductory guide for life scientists*, 2nd edn. Cambridge University Press, New York, p 57
30. Cowles M, Davis C (1982) On the origins of the 0.05 level of statistical significance. *Am Psychol* 37:553–558
31. <http://www.real-statistics.com/one-way-analysis-of-variance-anova/experiment-wise-error-rate/>. Accessed 25 August 2017
32. Tegarden FW (1996) Hybrid laminar flow nacelles - a test for the future. Engine-airframe integration conference. Royal Aeronautical Society, Bristol, pp 11.1–11.11
33. Skydrol. <https://en.wikipedia.org/wiki/Skydrol>. Accessed 25 August 2017

# Requirements, Test Strategies, and Evaluation of Anti-Contamination and Easy-to-Clean Surfaces, and New Approaches for Development



Silke Gruenke

**Abstract** The use of novel insect mitigating surfaces on leading edges of aircraft is one method to assist in preserving natural laminar conditions on selected areas such as wings or vertical stabilizers. Development of such surfaces is extremely challenging because of stringent requirements on resistance to aircraft fluids and to environmental conditions such as ultraviolet radiation, rain, and sand erosion.

For assessment of insect-mitigating properties of surfaces, new laboratory methods were developed that are suitable for comparing insect contamination behavior and cleanability of surfaces. When testing surfaces while considering the influence of topography and chemistry using these methods, it was observed that superhydrophobic surfaces with a particular topography are essential to reduce contamination significantly. For these surfaces, the roughest surfaces produced the lowest contamination. This observation confirms results recently published by other authors. However, the current study shows that roughness is a disadvantage for cleanability. Easy cleanability after contamination with flies or insect hemolymph-containing liquid was only observed for smooth, hydrophobic surfaces.

**Keywords** Anti-contamination • Easy-to-clean • Insect adhesion • Insect mitigation

---

S. Gruenke (✉)  
Airbus Operations GmbH, Bremen, Germany  
e-mail: [silke.gruenke@airbus.com](mailto:silke.gruenke@airbus.com)

## Contents

1	Introduction .....	334
2	Requirements on Insect-Mitigated Surfaces .....	335
3	Development of Test Methods .....	336
3.1	Test Strategies .....	336
3.2	Contamination Behavior .....	338
3.3	Bonding Strength and Removability .....	338
4	Experimental .....	339
5	Results .....	342
5.1	Contamination Tests .....	342
5.2	Manual Wiping Test with Insect Homogenate .....	343
5.3	Automatic Cleaning by Washability Tester .....	344
5.4	Results of Irrigation Tests .....	346
5.5	Flight Tests .....	346
5.6	Durability Tests .....	347
6	Conclusions .....	348
	References .....	350

## 1 Introduction

Reducing the drag on an aircraft by enabling natural laminar flow (NLF) is one method to increase fuel efficiency. An important constraint for realizing NLF is surface quality and smoothness. Tiny air flow disturbances at the surface can cause an early transition from laminar to turbulent flow. Even at the leading edges of aircraft parts, insects impacting and bonding to the surface may act as boundary layer disturbances that lead to a loss of laminarity.

The most obvious solution to the problem is to develop an anti-contamination surface where insect residues would not adhere or at least be significantly reduced. Additionally, surfaces demonstrating low adhesion strength to debris should be self-cleaning during flight through the action of the airstream itself, and by impacting rain.

Surfaces with easy-to-clean properties enable easier removal of contaminants because the contaminant is less bonded to the surface. This behavior is achieved by smooth hydrophobic surfaces, which are characterized by a water contact angle  $>90^\circ$  and low surface energies. A low surface energy surface reduces the spreading of the sticky liquid (hemolymph) from a ruptured insect and minimizes adhesion of the insect debris, including hemolymph [1, 2].

Superhydrophobic surfaces with a water contact angle around  $150^\circ$  are obtained by combining a defined texturing of the surface with a hydrophobic chemical treatment. According to the latest findings, such surfaces demonstrate a significantly reduced amount of contamination [3–6]. In the framework of AEROMUCO, nanostructured, superhydrophobic titanium surfaces showed promising properties for anti-icing and insect mitigation [3].

In this chapter, requirements on insect mitigating surfaces are given and strategies for testing these properties are presented. Additionally, results of insect adhesion and cleanability tests of several selected surfaces are described.

## 2 Requirements on Insect-Mitigated Surfaces

Requirements for a novel insect-mitigating coating are a large reduction in the amount of adhering debris from the insect impact and a large improvement in self-cleanability in comparison to current aircraft surfaces. Further aerodynamic requirements for achieving NLF conditions are the avoidance of significant backward-facing steps at the end of the coating and a low surface roughness ( $R_a < 0.2 \mu\text{m}$ ), which must not be exceeded after several years of operation.

A durable surface must be resistant to all kinds of operating fluids (e.g., cleaning agents, phosphate ester-based hydraulic fluid, kerosene). In addition, the surface functionality must cope with temperature variations ranging from  $-60$  to  $80^\circ\text{C}$  and ultraviolet (UV) radiation. Furthermore, the coating must be compatible with lightning protection and de-icing systems. However, as most of the surfaces to be kept clean are located at the leading edges, resistance to rain and sand erosion is the main challenge.

From in-service experience of the flying fleet, the property of erosion resistance is difficult to achieve with organic polymer coatings. Today's standard external polyurethane (PUR)-based coatings have limited resistance to heavy rain and ice crystal and sand erosion that occurs on the tips of leading edges, and they have to be repaired or reapplied after definite intervals. Durable protection of leading edges over the lifetime of aircraft is only achieved by metallic leading edges (e.g., aluminum sheets or stainless steel foils).

However, the occurrence of insect impact is not limited to the tip of the leading edge. Impacts also disturb airflow behind this area, which should be avoided to achieve NLF conditions. Thus, an option is to apply insect-mitigating coatings with less erosion resistance to the area directly behind the erosion-prone leading edge tip.

As the same area prone to insects is also affected by ice accretion, ice-phobic properties are also desirable for insect adhesion-mitigating surface. There are some similarities between behavior of surfaces regarding insect adhesion and ice adhesion, but also some differences caused by the complexity of ice formation conditions [6].

Of course, for any development of a new coating, relevant Health, Safety, and Environment regulations have to be considered, such as A1091 – Airbus Requirements for the Management of Hazardous Substances – and Regulation (EC) No 1907/2006 of the European Parliament and of the Council of 18 December 2006 concerning the registration, evaluation, authorization, and restriction of Chemicals (REACH).

## 3 Development of Test Methods

### 3.1 Test Strategies

Prerequisite for a systematic and successful material development is the availability of suitable test methods. As there were no available standards for insect mitigating surfaces, new test methods had to be developed. For a first screening of surfaces, simple insect adhesion and cleanability tests for a relative comparison of surfaces are sufficient. In the next step, quantitative methods simulating environmental conditions and allowing the prediction of behavior of surfaces during operation need to be developed. Flight tests over short periods are then necessary for verification of functionality under real conditions and for correlation with laboratory test results. Flight tests over longer periods should be performed for proving durability of functionality. At this time, any potential impact of operational procedures such as aircraft cleaning and de-icing should also be observed.

The steps of development of test methods can be correlated with phases of material development. In aerospace industry, development processes are assessed by the Technology Readiness Level (TRL), which were originally defined by NASA [7]. The generic TRL Readiness Assessment Criteria were applied to the development process of a functional coating and formulated in the following way:

- TRL 1–2: Technology concept – Product and supplier review and screening test for comparison of candidates
- TRL 3: Proof of concept – Demonstrating functionality of coating including standard paint properties and durability under laboratory conditions
- TRL 4: Validation in laboratory environment – Quantitative testing of functionality, simulation of environmental conditions, for example, by wind tunnel
- TRL 5–6: Validation of coating and demonstration in a relevant environment – Tests under realistic operational conditions or flight tests
- TRL 7–8: Development completed and coating system qualified through test and demonstration – Qualification of material and related application process
- TRL 9: Actual coating system “flight proven” through successful mission operation – Entry into service

The first step of development of new methods is to identify relevant environmental parameters. Figure 1 illustrates in which phases of flight insects impact the surface, what happens with the debris during flight, and how it is removed.

Insects impact the leading edge during the first phase of flight, that is, during start, take-off, and initial climb of aircraft. They are also accumulated during landing and taxiing and adversely affect the aerodynamic performance of subsequent flights unless they are removed when the plane is on the ground. When an insect impacts the aircraft, the insect cuticle (chitin skeleton) ruptures, the insect



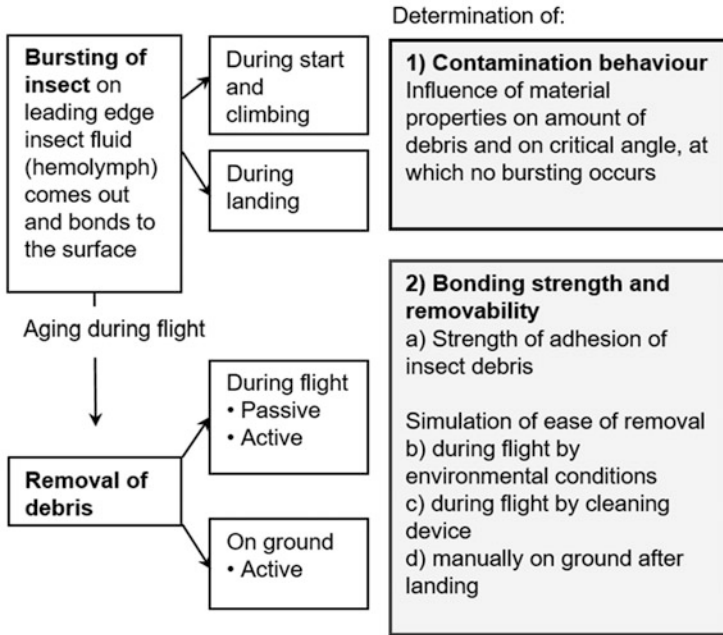


**Fig. 1** Impact, bonding and removal of insects and deduced objectives of test procedures

fluid (the hemolymph) comes out, and it can bond tightly to the surface. This extreme adhesion is a result of the insect’s own body proteins. During rupture of the insect body, the proteins contact oxygen in the air, the enzyme phenoloxidase is activated, and it catalyzes reactions leading to coagulation and strong bonding of the hemolymph [8]. The insect body also contains lipids, which enhance the adhesion. Once bonded, the insect residues on the leading edge are exposed to intense environmental conditions: airstream, rain and sand erosion, varying temperatures, and UV radiation. In the case of weak bonding, the insect debris might be removed by these environmental conditions (passive removal or self-cleaning effect). For strongly-bonded residues an active cleaning method for removal is necessary. If NLF conditions are to be ensured during cruising, a cleaning device has to be implemented into the leading edge design. Cleaning on ground would only have an effect for subsequent flights.

To conclude, differentiation must be made between the contamination after insect impact and the removal of insect debris. Both effects do not necessarily correlate for a particular surface and they have to be investigated separately. The amount of residues bonding to the surface is determined by spreading of the hemolymph and wetting of the surface. The strength of adhesion, that is, the ease of removability of the residues, is determined by chemical and/or physical bonding between the insect components and the surface.

### **3.2 Contamination Behavior**

The amount of residues (height, area, and volume) can be determined by special microscopic methods such as those utilized on a digital microscope, laser scanning confocal microscope, or 3D microscope. It might be obvious to measure the height of insect debris as a key parameter, as the height of residues remaining on the aircraft part is a relevant parameter for aerodynamics. However, Kok et al. and Lin et al. found no clear influence of the coating topography or surface chemistry on residue height of fruit flies debris, although areal coverage and volume of residues seemed to be more relevant for laboratory tests [5, 8]. This observation is probably because the height of residues depends on whether only hemolymph adheres or whether the exoskeleton also bonds to the surfaces [9].

Under laboratory conditions, insect impact can be simulated by a simple “insect-gun.” Here, a single insect is accelerated to speed relevant to aircraft by means of pressurized air [1, 6, 10]. Alternatively, in a wind tunnel, insects can impact surfaces under simulated airstream conditions [6]. Car tests and flight tests are used to collect insects under real conditions [10].

Relevant parameters for the insect impact are speed and angle of impact [6]. Evaluation of impacts after a car test showed the following observation. If an insect impacts the surface at 90°, parts of the exoskeleton often bond to the surface, leading to residues with a large height. Lower angles allow rolling-off of parts of the exoskeleton and often lead to a wider asymmetric spreading of the hemolymph liquid [2]. Of course, the type and size of insect species have a strong influence on how an insect impacts the surface. Insects also vary in body structure, hardness of chitin skeleton, amount of body liquids, and biochemical composition of body liquids. According to our own observations during several test series with flies, even the age and feeding of the insect has an influence on the contamination behavior as the content of the digestive tract, the condition of ovaries, and the ratio between fatty components and hemolymph liquid also influence the resulting amount of residues.

### **3.3 Bonding Strength and Removability**

For testing adhesion strength of films on surfaces, conventional paint adhesion test methods can be used, such as the tape test or a modified scratch test described in [6]. A more practical approach to assess insect removability would be to select the relevant cleaning procedure and to simulate this in the laboratory.

Self-cleaning during flight by environmental conditions can be simulated in a climate chamber, where the removal of debris by irrigation of contaminated samples under varying airstream and rain conditions can be studied. For in-flight cleaning, a system solution has to be designed which features a movable tool. A

washability tester can be used to simulate such a cleaning device under laboratory conditions. Cleaning on the ground can be simulated by manual wiping tests.

The objective for all cleaning test methods is to determine any correlation between cleaning properties and surface properties such as roughness, surface energy, and contact angle of water. Prerequisite is a reproducible and realistic contamination of test samples. Collecting insects during a test flight or test car drive is very elaborate and not feasible for serial test programs. Furthermore, conditions are not reproducible because of the different insect species and angles and velocities of impact. However, shooting of live or numbed insects also has some disadvantages. In our own test series we observed that, because of the coincidental splattering pattern and the different adhesion of the insect components (skeleton, hemolymph, tissues), the reproducibility of cleaning results was limited. Another aspect is that the breeding of flies in the laboratory and application via a bug gun is relatively cumbersome. Thus, for preparation of reproducible contaminations with reasonable effort, a substitute fluid with similar adhesion properties to insect hemolymph would be beneficial. However, because of complex bonding reactions taking place at the moment of insect rupture, it is not a simple task to simulate the adhesion properties of insects [10].

In our own tests, first attempts with hen's egg mixtures and bovine serum albumin showed different adhesion behavior compared to insect residues. Using Schneider's insect medium, a commercially available synthetic product containing many of the constituents of insect hemolymph, brittle properties were observed after applying it to a surface, which made it difficult to determine the adhesion strength. Comparable observations were made by Kok, who tested similar potential substitute fluids by means of a wet abrasion scrub tester [3]. As an outcome of our testing, stabilized homogenates of insect larvae and adult insects seem the most appropriate. As homogenates of different species behave slightly differently on certain surfaces, two different homogenates made of flies (*Musca domestica*) and manduca larvae (*Manduca sexta*) were used. The homogenates can be easily applied as a thin film on surfaces. A simple manual wiping test was determined to be a fast and effective method for comparing the cleanability of surfaces and to investigate the influence of aging on the cleanability [2].

## 4 Experimental

### – Shooting of insects

By means of a pressurized air-gun, flesh (meat) flies (*Sarcophagidae*), 10–15 mm long, were propelled individually toward the surface of interest at a speed of around 100 m/s obtained by 8 bar air pressure. The spatial orientation of the fly during shooting could not be influenced, that is, it was coincidental if an insect impacted the surface head-on, backward, or laterally. Rupture of the fly by the impact was assured through video monitoring (high speed camera) [6].

Impacts for one test series were performed all in the same day to ensure that the meat flies were in the same condition.

– Determination of debris area

The contaminated area of a surface after fly impact was determined by means of a structured-light 3D scanner VHX-2000 E (Keyence).

– Contamination with insect homogenate for manual wiping tests

By means of a mask, a small amount of insect homogenate was applied to the surface to be tested. On hydrophobic surfaces 20  $\mu\text{L}$  were applied on a square of 1  $\text{cm}^2$  by means of an Eppendorf pipette. After drying, a thin film was obtained. On superhydrophobic surfaces it was not possible to obtain a thin film. The hemolymph contracted because of the low wettability of surfaces. Therefore, droplets of 100  $\mu\text{L}$  were applied in a silicon mask with round holes.

– Wiping test

After drying for 1 day at room temperature ( $\sim 22^\circ\text{C}$ ), the removability of the homogenate was tested by dry wiping. The wiping was performed manually by means of a fabric.

– Cleaning trials by means of abrasion and washability tester Elcometer 1720

Cleaning trials with different cleaning materials (brush, cleaning pad, sponge, crockmeter tool) in dry and wet conditions were performed (Fig. 2). Weights were added to the scrub head to increase the surface pressure and intensify the cleaning efficiency. The objective was to clean surfaces with a minimum number of cycles

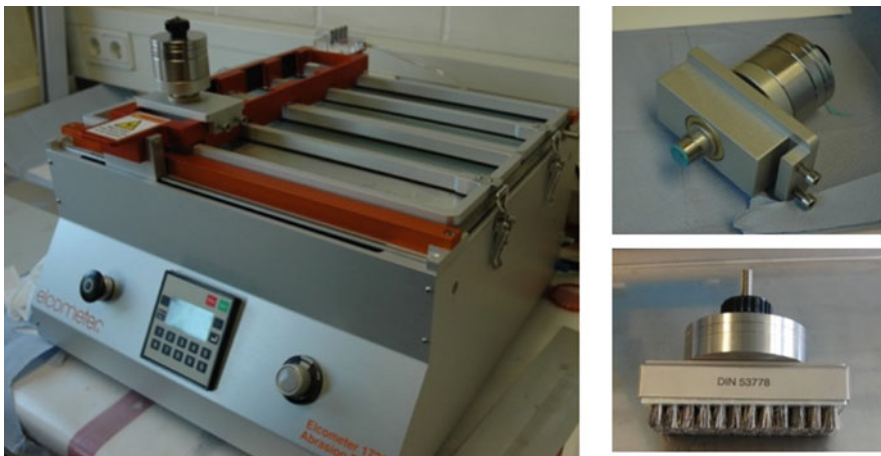


**Fig. 2** Washability tester (left); crockmeter tool according ASTM F 1319 with weights (right top); brush with weight (right bottom)

**Table 1** Parameter for irrigation tests in a climate chamber

Phase 1	Break	Phase 2
Wind = 15 m/s		Wind = 45 m/s
Rain duration = 180 s	60 s	Rain duration = to be determined (max. 240 s)

with the overall goal of removing the debris after two passes. Initial conditions for achieving this aim were approximated based on previous experiments.

– Irrigation tests in a climate chamber

For development of this test method, contaminated samples were irrigated by means of a nozzle under varying air flow. In the chamber, the samples were first treated for 180 s with rain and air flow 15 m/s (= phase 1). After a 60-s interruption to refill the water tank, samples were treated with rain and air flow of 45 m/s (= phase 2). Table 1 summarizes the applied parameters. The test time duration was determined by when all debris was removed from surfaces, the longest time observed being 240 s. The monitoring of the sample was accomplished by means of a webcam. By applying these conditions it was possible to distinguish the cleanability of different surfaces.

– Roughness measurements

Roughness was determined by means of a portable stylus profilometer MarSurf M300 (Mahr).

– Contact angle and surface energy

Contact angle and surface energy were determined by means of a DSA100 (Krüss) with an applied drop size of 3  $\mu\text{L}$ .

– QUV fluorescent light test based on DIN EN ISO 16474-3 [11]

Test conditions were equal to Method C: Type 2 UVB-313 lamps, Cycle 4 (4 h UV at  $(60 \pm 2)^\circ\text{C}$ , 4 h condensed water  $(50 \pm 2)^\circ\text{C}$ ). Test duration was 1,000 h in accordance with AMS3095A [12]. To get information about the aging during this period, samples were also investigated after 200 and 400 or 500 h.

– Coating candidates

Hydrophobic and superhydrophobic candidate coatings were selected (see Table 2).

TiO<sub>2</sub> nanotube surfaces with a defined micro and nano topography were prepared by applying an anodic bath procedure [13]. Some samples were additionally roughened by media blasting before anodizing to investigate the influence of macro-roughness. The superhydrophilic TiO<sub>2</sub> surfaces were post-treated with a thin hydrophobic coating to obtain superhydrophobic properties.

**Table 2** Coating candidates

Designation	Description	Roughness $R_a$ [ $\mu\text{m}$ ]	Contact angle [ $^\circ$ ]
Steel (reference)	CrNi-steel 1.4544.9	0.2	93
External standard topcoat (reference)	Standard PUR-based coat used for external aircraft surfaces	0.02	75
Modified clear coat	Smooth hydrophobic PUR-based clear coat	0.02	107
Sol-gel	2K-Polysiloxane-epoxy coat	0.06	104
DLC	Diamond-like carbon, anti-adhesive hard coating, a-C:H:Si	0.12	86
TiO <sub>2</sub> + functionalized Silane	Ti anodized and post-treated with fluoroalkyl functionalized silanes	0.3	150
TiO <sub>2</sub> + MVD	Ti anodized and post-treated with MVD coating	0.3	152
TiO <sub>2</sub> blasted + MVD	Ti blasted, anodized and post-treated with MVD coating	1.2	151
Structured PUR coat	Superhydrophobic polymer coat based on PUR with a defined texture	2.3	149

## 5 Results

### 5.1 Contamination Tests

The amount of contamination after shooting meat flies by means of the pressurized “air-gun” onto several surfaces at an angle of less than  $45^\circ$  was determined according to Sect. 3.1. Visually, the steel substrate demonstrated the largest contamination, whereas the superhydrophobic candidates, the TiO<sub>2</sub> nanotube surfaces, and the rough polymeric coat showed the lowest contamination. Furthermore, the TiO<sub>2</sub> nanotube surface further modified with MVD (molecular vapor deposition) showed a slightly lower contamination than the same non-modified surface. The rough PUR coating was almost free of debris. Figure 3 shows the areas of debris determined in relation to the roughness of surfaces.

The comparison of the average height of meat fly residues gave no hint of a correlation to surface properties, which confirms the observations of Kok [8]. The coincidental orientation and impingement of the insects on the test surfaces by the applied method resulted in very high standard deviations for the height of residues because of the coincidental adherence of parts of exoskeleton, legs, or wings. Therefore, potential differences between different surfaces could not be determined using residue height. However, the assessment of the area of contamination reduces the effect of any upright adherent parts.

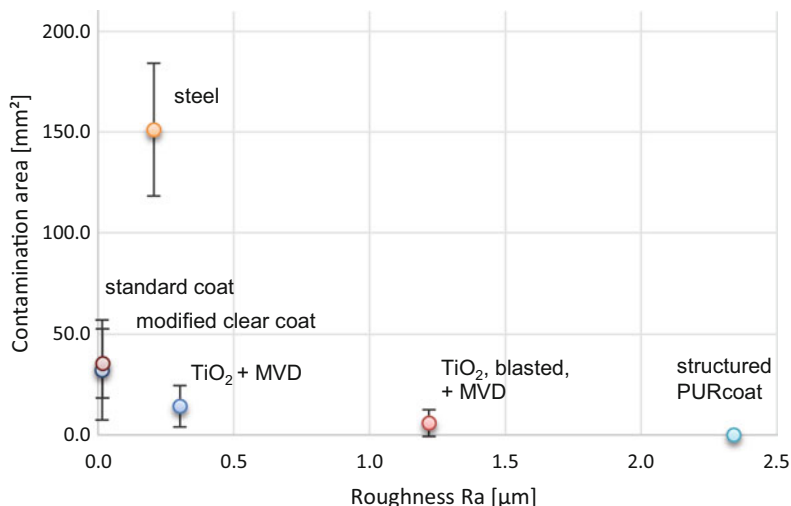


Fig. 3 Relation between contamination area and roughness of surfaces

## 5.2 Manual Wiping Test with Insect Homogenate

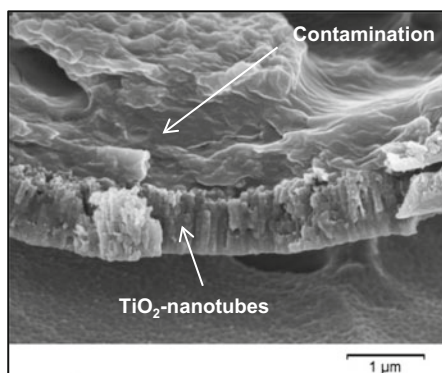
Results of the manual wiping test are summarized in Table 3. The insect homogenate could only be easily removed from smooth hydrophobic surfaces. Steel, the coated  $\text{TiO}_2$  surfaces, and the rough organic polymer surface were not cleanable by dry wiping. The SEM photograph of a contaminated  $\text{TiO}_2$ -nanotube surface in Fig. 4 shows that the hemolymph of the insect seeped into the intermediate spaces of the nanostructure, which resulted in the observed strong bonding.

Table 3 Results of manual wiping tests after contamination with insect homogenate

Samples	Roughness $R_a$ [ $\mu\text{m}$ ]	Contact angle [ $^\circ$ ]	Insect extract	
			Fly ( <i>Musca domestica</i> ) larvae	Manduca larvae
Steel	0.2	93	–	–
External standard coat	0.02	75	+	–
Modified clear coat	0.02	107	++	+
Sol-gel	0.06	104	++	+
DLC	0.12	86	++	o
$\text{TiO}_2$ + functionalized silane	0.3	150	–	–
$\text{TiO}_2$ + MVD	0.3	152	–	–
$\text{TiO}_2$ blasted + MVD	1.2	151	–	–
Superhydrophobic structured PUR coat	2.3	149	–	–

Assessment: ++ very easy cleanable, + cleanable with several wipes applying light to moderate pressure, o cleanable with several wipes applying high pressure, – not cleanable by dry wiping

**Fig. 4** SEM picture of  $\text{TiO}_2$  nanotube surfaces contaminated with fly debris



### 5.3 Automatic Cleaning by Washability Tester

#### 5.3.1 Tests with Crockmeter Tool

Tests with flat samples impacted with flesh flies showed that a dry cleaning procedure with a brush or sponge cannot guarantee a 100% removal of debris after a few passes. Even surfaces that demonstrated easy-to-clean properties in Sect. 5.2 showed persistence of some slight residues. Wetting with small water droplets significantly improved the cleaning result.

A high surface pressure was found necessary to achieve a good cleaning result within a few passes. When cleaning with a sponge or a brush there was often the risk of slipping over the contaminant. The best result was obtained with the crockmeter tool (stainless steel cylindrical rod, test felt, textile fixing ring) with additional weight because of this method having the highest weight/surface ratio in comparison to the other tools such as brush or cleaning pads. A moderate cleaning speed was more efficient than a fast cleaning speed, probably because of the longer soaking time of the debris.

When investigating the influence of aging of fly debris, it was interesting to observe that directly after impact flies were easier to remove from steel than from the standard external topcoat, although the opposite was found for dried debris (see Table 4). Figure 5 shows the cleaning result of a steel panel contaminated with fresh debris as an example.

**Table 4** Amount of cleaning cycles for complete cleaning of surfaces as a function of age after insect impact event (test parameters: additional 200-g weight, two drops of 30- $\mu\text{L}$  water, 10 cycles/min)

Surface	Age of debris	Amount of cycles
Steel	5 min	2–3
	7 days	6–7
Standard PUR coat	5 min	5–6
	7 days	2
Modified clear coat	7 days	2



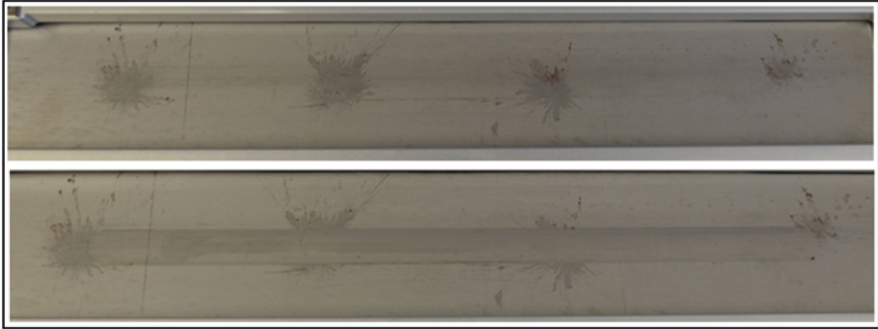


**Fig. 5** Steel panel with debris from four flesh fly impacts, before cleaning (top); after wet cleaning with washability tester and crockmeter tool (bottom). Test parameters: additional 200-g weight, two drops of 30- $\mu$ L water, 10 cycles/min

### 5.3.2 Tests with Nylon Thread

When thinking about the design of an in-flight-cleaning device, a wet procedure would require the transport of liquid cleaning solution on board. The additional weight would impede the objective to save jet fuel. Therefore, a new test set-up was designed, inspired by a cleaning approach utilized on gliders, where a tightened nylon thread is moved over the wing leading edge and cuts the contaminant from the surface. Thus, the crockmeter tool was replaced by a tool equipped with a nylon thread. Flat samples were replaced by curved samples.

In comparison to the tests in Sect. 5.3.1 using the washability tester under dry conditions, much better cleaning results were observed. Figure 6 shows the cleaning results of some candidate surfaces. Observations are summarized in Table 5. The best result was obtained for the modified hydrophobic clear coat, where parts of the skeleton were completely removed and only a few hemolymph residues remained. On steel, some parts of the exoskeleton remained.

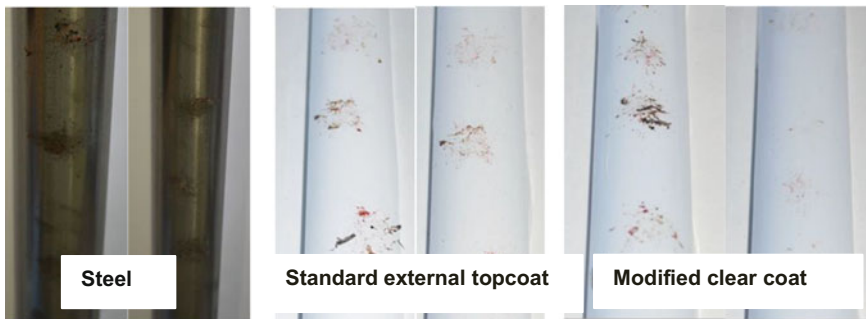


**Fig. 6** Profile samples with aged meat flies debris before (left) and after (right) one dry cleaning cycle with wire

**Table 5** Residues of fresh and aged (dried) meat flies after one pass of cleaning

Surface	Fresh debris	Dried debris
Steel	No skeleton	Parts of skeleton
	Spread liquid (hemolymph and red spots)	Parts of hemolymph (harder to clean than fresh debris)
Standard coat	Small parts of skeleton	No skeleton
	Parts of hemolymph	Residues of hemolymph (aged meat flies slightly easier to remove than fresh ones)
Modified clear coat	No skeleton	No skeleton
	Less hemolymph than on standard coat and steel	Only a few hemolymph residues, less than on standard coat and steel

**Table 6** Assessment after irrigation tests in climate chamber

Aging condition of debris (meat fly)	Ranking of candidates related to time needed for complete cleaning
3 days at room temperature	Sol gel > hydrophobic clear coat > DLC > steel foil
2 h at $-40^{\circ}\text{C}$	Sol gel > hydrophobic clear coat/DLC > steel foil
2 h at $60^{\circ}\text{C}$	DLC > hydrophobic clear coat > sol gel > steel foil
2-day cycle (2 h $-40^{\circ}\text{C}$ /2 h $60^{\circ}\text{C}$ )	DLC > hydrophobic clear coat > sol gel > steel foil

## 5.4 Results of Irrigation Tests

Applying the sequence of irrigation testing summarized in Table 1, a complete cleaning was obtained after 60–240 s in phase 2 of irrigation for all coating candidates. Table 6 shows the ranking of candidates. Depending on the aging procedure of the fly debris, the ranking of the easy-to-clean coating candidates differed slightly. However, in each case the steel substrate required the longest irrigation time for complete removal of meat fly debris.

## 5.5 Flight Tests

The hydrophobic surfaces, DLC, modified clear coat, and sol-gel coating, were tested in a flight test on a Dornier Do 228. Results published in [2] are summarized in Table 7. Four flights were performed with four samples on each wing per flight. Steel was used as the reference. Sample size was 25 cm width and 33 cm length around chord (i.e., 16.5 cm on upper and lower wing from tip of leading edge).

The assessment showed that the number of insect strikes  $>50\ \mu\text{m}$  in height on the upper wing was not significantly reduced. However, large deviations between the four flights led to high statistical errors in the results, so slight advantages of a

**Table 7** Amount of insects relative to steel above or below a specified height (mean value in bold, standard deviation in italic)<sup>a</sup>

Surface	All insects	<30 $\mu\text{m}$	>30 $\mu\text{m}$	>50 $\mu\text{m}$	>100 $\mu\text{m}$
Steel	<b>1.0</b>	<b>1.0</b>	<b>1.0</b>	<b>1.0</b>	<b>1.0</b>
DLC	<b>0.6</b> $\pm$ 0.2	<b>0.2</b> $\pm$ 0.2	<b>1.1</b> $\pm$ 0.4	<b>1.1</b> $\pm$ 0.5	<b>1.3</b> $\pm$ 0.4
Modified clear coat	<b>0.7</b> $\pm$ 0.3	<b>0.5</b> $\pm$ 0.2	<b>1.0</b> $\pm$ 0.4	<b>1.0</b> $\pm$ 0.4	<b>1.0</b> $\pm$ 0.4
Sol-gel	<b>0.9</b> $\pm$ 0.2	<b>0.4</b> $\pm$ 0.1	<b>1.3</b> $\pm$ 0.3	<b>1.4</b> $\pm$ 0.3	<b>1.4</b> $\pm$ 0.3

<sup>a</sup>Calculation:

– Average of insects on steel surface was set as 1.0 for each wing side and each flight

candidate coating may not be discernible. Only the occurrence of small debris (<30  $\mu\text{m}$  in height) seemed to be reduced by DLC and the modified clear coat. Another interesting result was the observation that, after flying for 10 min through rain, almost all debris was removed on all surfaces, which demonstrated the natural (self-)cleaning during flight.

## 5.6 Durability Tests

The surface energy of hydrophobic coatings was determined at the initial condition and after immersion in room temperature water for 336 h, after immersion in room temperature aviation hydraulic fluid (Type V, phosphate ester based) for 720 h, and during exposure in the 1,000-h QUV test described in Sect. 2 after 200 and 400 or 500 h (after 500 h the test was stopped because of early failure of samples). In parallel, cleanability by means of the manual wiping test was determined to investigate whether easy-to-clean properties and surface energy correlate. Results are summarized in Table 8.

For all coating candidates, a loss of functionality occurred when the surface energy significantly increased during aging. The modified clear coat showed the best durability against fluids, but the easy-to-clean effect was completely lost between 200 and 500 h of QUV (313 nm) exposure, and 1,000 h are required for passing the AMS3095A test [12]. Both the DLC and the sol-gel candidate demonstrated insufficient resistance to fluids and to QUV.

The durability tests of coated  $\text{TiO}_2$ -nanotube surfaces showed a high resistance to water and the aggressive hydraulic fluid, but also a high sensitivity to the QUV test. After 200 h QUV the water contact angles decreased significantly. After 400 h QUV the surface appearance of all  $\text{TiO}_2$  samples had changed. The superhydrophobicity had converted to superhydrophilic behavior and water contact angle was not measurable any more. The superhydrophobic PUR coating demonstrated a reverse behavior – a higher UV resistance but a low chemical resistance to hydraulic fluid. The latter excludes the superhydrophobic PUR coating from application on aircraft. Measured water contact angles are summarized in Table 9.

**Table 8** Surface energy [mN/m] and cleanability of hydrophobic candidates at initial condition and after applying different aging procedures (cleanability was determined by manual wiping test with fly larvae homogenate)

Coating	Initial condition	Water immersion – 336 h	Hydraulic fluid immersion – 720 h	Exposure to QUV 313 nm
	Surface energy/ cleanability	Surface energy/ cleanability	Surface energy/ cleanability	Surface energy/ cleanability
Modified clear coat	20.1/++	26.2/++	24.2/++	200 h: 35.2/o 500 h: 40.7/–
DLC	33.7/++	42.2/–	38.3/+	200 h: 43.8/– 500 h: 43.8/–
Sol-gel	22.6/++	39.6/–	44.6/–	200 h: <sup>a</sup> /+ 500 h: <sup>a</sup> /–

Assessment: ++ very easy cleanable, + cleanable with several wipes applying light to moderate pressure, o cleanable with several wipes applying moderate pressure, – not cleanable by dry wiping

<sup>a</sup>Surface energy not determined

**Table 9** Water contact angles of superhydrophobic coatings at initial condition and after aging

Coating	Initial condition	Water 336 h	Hydraulic fluid 720 h	QUV 313 nm
TiO <sub>2</sub> + functionalized silane	150°	148°	144°	200 h: 118° 400 h: n.a.
TiO <sub>2</sub> + MVD	151°	144°	147°	200 h: 112° 400 h: n.a.
TiO <sub>2</sub> blasted + MVD	151°	145°	146°	200 h: 128° 400 h: n.a.
Superhydrophobic PUR coat	149°	147°	95°	200 h: <sup>a</sup> 400 h: 145°

<sup>a</sup>Value not determined

## 6 Conclusions

Several test methods were developed to evaluate the benefit of insect-mitigating surfaces. The contamination behavior and the strength of adhesion on surfaces do not inevitably correlate, and both properties have to be investigated separately. The amount of residues remaining on the surface after insect impact was assessed by shooting insects on surfaces and measuring the surface area by means of microscopic techniques. The strength of adhesion was assessed by determining the removability of debris. Different cleaning scenarios led to several approaches for test development.

By applying the newly developed methods and testing some selected hydrophobic and superhydrophobic coating candidates, the following observations were made:

- Superhydrophobic rough TiO<sub>2</sub> surface and the rough superhydrophobic PUR coating demonstrated very low contamination after impact of meat flies, which was significantly lower than on hydrophobic smooth coatings. The areal coverage of debris after insect impact is strongly determined by the topography and surface roughness of the surface, whereas surface chemistry has a lower influence. This finding confirms that made in the AEROMUCO (AEROdynamic surfaces by advanced MULTifunctional COatings) [4, 8] program. The final conclusion of the ERA (Environmentally Responsible Aviation) Program was also that a modification of the surface topography is needed for an effective reduction of insect residues [5, 14, 15].
- TiO<sub>2</sub> nanotube surfaces post-treated with a thin hydrophobic layer are the most promising candidates for reducing insect impact. TiO<sub>2</sub> surfaces offer high erosion resistance, which would suggest their applicability on leading edges. However, it is still challenging to find a thin coating (<1–2 μm) which preserves the nanotubes structure and sustains erosion and QUV resistance at the same time.
- In a flight test, briefly described above, only hydrophobic coatings were tested, with the result that they showed no significant difference between each other or when compared to the steel reference control in contamination tests. It is hypothesized that superhydrophobic surfaces, demonstrating a significantly lower contamination in laboratory-based testing, would be beneficial in flight tests. Lin and Whalen reported a reduction of 41% in the number of visible bug hits for a candidate coating with a surface topography modified with nanoparticles after performing 15 flight tests [5].
- Structuring of the surface improves adhesion of contaminants and impedes cleanability. Results of dry manual cleaning tests with insect homogenate showed that roughness of the superhydrophobic candidates is a disadvantage for cleaning. Yi et al. previously demonstrated that surface roughness can increase mechanical adhesion of residues, as the excrement of the insects essentially gets stuck in the grooves of the surface [1].
- Modified organic clear coats with water contact angles around 100° and with a smoothness of  $R_a$  equal to 0.02 μm were evaluated as the most mature candidates for the concept of easy-to-clean coatings. They show an improved cleanability compared to standard surfaces, but demonstrate no significant reduction in the amount of residues staying on the surface. They demonstrated a high chemical resistance, but the resistance to QUV (UVB radiation) has to be improved. Potential application areas for such easy-to-clean coatings are directly behind the top of the leading edge, which is also prone to insect impact but requires less erosion resistance.
- To date, current available test methods allow a relative ranking of coatings. Requirements for passing or not passing a test cannot be defined yet because of missing correlation to flight tests. Several authors have also noted the difficulty in finding a relationship between laboratory wind tunnel tests and flight tests [14, 16]. It has also been the experience of these authors that a series of flight tests are necessary for statistically assured data because of the very random

occurrence of type and amount of insects and insect swarms which depends on specific weather conditions.

- Reviewing the results presented in this chapter and the results of other recently publications, it seems that the search for functional surfaces which fully prevent the bonding of insects and ensure a *clean* surface is still a challenge. It is even more challenging to ensure that the functionality of such a surface does not degrade significantly during operation of an aircraft.
- If no durable insect mitigating surfaces can be found, system solutions for the protection of NLF leading edges against insect impact such as the Krueger flap [3, 15] or a cleaning device have to be developed as an alternative solution.

**Acknowledgements** Part of the research work leading to the results published in this chapter has been co-funded by the European Commission “Seventh Research Framework Programme” (FP7/2007-2013) for the Clean Sky Joint Technology Initiative under Grant Agreement no CSJU-GAM-SFWA-2008-001. Further development work was funded by BMWi under LUFO V-1 LDAinOp no 20A1103A.

We acknowledge the Fraunhofer Institute in Bremen, IFAM, for performing several tests as a partner in JTI-SFWA and LUFO LDAinOp. Furthermore, we acknowledge DLR Braunschweig for performing the flight test and Airbus Group Innovation for providing TiO<sub>2</sub> samples.

## References

1. Yi O et al (1988) A fundamental approach to the sticking of insect residues to aircraft wings. Virginia Tech Center for adhesive and sealant science. CAS/CHEM 188:29–88
2. Gruenke S (2012) Anti-contamination and easy-to-clean coatings for aerodynamic efficient surfaces. In: Proceedings of 19th international conference on surface treatments in the aeronautics and aerospace industries, Biarritz, France, 31 May–1 June 2012
3. Kok M, Young TM (2014) Evaluation of insect residue resistant coatings – correlation of a screening method with a conventional assessment technique. Prog Org Coat 77:1382–1390
4. Kok M, Young TM (2014) The evaluation of hierarchical structured superhydrophobic coatings for the alleviation of insect residue to aircraft laminar flow surfaces. Appl Surf Sci 314:1053–1062
5. Lin JC, Whalen EA et al (2016) Innovative flow control concepts for drag reduction. In: Proceeding of the 54th AIAA aerospace sciences meeting, San Diego, USA, 4–8 Jan 2016: AIAA 2016-0864
6. Patzelt G et al (2016) Anti-icing and anticontamination properties of coatings induced by surface structure. J Coat Technol Res 13(4):589–596
7. Mankins JC (1995) Technology readiness levels: a white paper. NASA, Office of Space Access and Technology, Advanced Concepts Office. 6 April 1995
8. Kok M et al (2013) Influence of surface characteristics on insect residue adhesion to aircraft leading edge surfaces. Prog Org Coat 76:1567–1575
9. Krishnan KG et al (2017) Influence of hydrophobic and superhydrophobic surfaces on reducing aerodynamic insect residues. Appl Surf Sci 392:723–731
10. Kok M et al (2015) Critical considerations in the mitigation of insect residue contamination on aircraft surfaces – a review. Prog Aerosp Sci 75:1–14
11. DIN EN ISO 16474-3 (2013) Paints and varnishes – methods of exposure to laboratory light sources, part 3: fluorescent UV lamps, European Committee for Standardization, Brussels

12. AMS3095A (2004) Paint: high gloss for airline exterior system. SAE International, Warrendale, PA. 1 Dec 2004
13. Wermuth L et al (2015) Superhydrophobic surfaces based on self-organized TiO<sub>2</sub>-nanotubes. *Prog Org Coat* 87:242–249
14. Siochi E et al (2013) Engineered surfaces for mitigation of insect residue adhesion. In: Paper presented at the SAMPE 2013, Long Beach, CA, USA, 6–9 May 2013
15. Wohl C et al (2013) Evaluation of commercially available materials to mitigate insect residue adhesion on wing leading edge surfaces. *Prog Org Coat* 76:42–50
16. Shanahan M, Wohl C et al (2015) Flight testing surfaces engineered for mitigating insect residues adhesion on a Falcon HU-25C. In: Abstracts of the 38th meeting of the adhesion society, Savannah, Georgia, USA, 21–25 February 2015

**Part IV**  
**Biofouling-Mitigation Coatings**



# Candy and Poisons: Fouling Management with Pharmacophore Coatings



**Daniel Rittschof**

**Abstract** This chapter provides a context and perspective to consider novel materials for use in fouling management. Fouling and biofouling are defined and the rationale for existing fouling management is provided. Fouling management in even benign environments is difficult because commercial approaches use broad-spectrum stable biocides with non-target effects on humans, environmental health, and food safety. These historic approaches target death as the only biological endpoint. If novel approaches are to be implemented, biological alternatives to broad-spectrum long-lived biocides must be discovered, designed, and fitted within existing business models, infrastructures, and regulatory frameworks. The title, “Candy and Poisons”, highlights the two major issues for sustainable fouling management. Potent, short-lived toxins and pharmacophores, protected in coatings and chemically and biologically destroyed, are eaten as is candy within hours to days after release. Fouling on roofs as an example of an extreme environment and speculation about the use of conserved biological pathways in fouling management are discussed. Major concerns for all fouling management approaches are humans, environmental health, and food safety. With novel approaches, health and food safety should be addressed at the beginning of the technology development. The most difficult hurdle that a new technology faces is the regulatory framework. Present regulatory structures repress new technology and are slowly reducing options for the highly toxic management approaches. Policy changes that support novel technologies and close loopholes for long-lived toxins are needed to stimulate environmentally appropriate solutions.

**Keywords** Biofouling • Conserved pathways • Extreme environments • Fouling management • Novel materials

---

D. Rittschof (✉)  
Duke University Marine Laboratory, Beaufort, NC, USA  
e-mail: [Ritt@duke.edu](mailto:Ritt@duke.edu)

## Contents

1	Overview .....	356
2	Fouling and Biofouling .....	356
3	Fouling Management .....	357
4	Fouling of Polymers in Extreme Environments .....	358
5	Macro-Fouling and Micro-Fouling Concepts That Could Drive Future Fouling Management Research .....	359
6	Candy and Poisons .....	360
7	Polymers and Controlled Release .....	361
8	Environmental Concerns .....	362
9	Application Concerns .....	363
10	Conclusion .....	363
	References .....	363

## 1 Overview

This chapter is intended to provide context for anyone interested in developing polymers for novel fouling management strategies. Included is a perspective on molecular and biological fouling, existing fouling management strategies, the multi-functionality required of fouling management polymer systems, and the major hurdles that must be overcome to enter the fouling management market. The goal is to provide perspective on the key physical, biological, business, and regulatory aspects that should be considered in developing novel fouling management materials. Insight is provided into several approaches with potential. This chapter is not an exhaustive review, but can be used to gain access to the primary and secondary literature in the field.

## 2 Fouling and Biofouling

Fouling is the deposition of unwanted material, inorganic or organic, on manmade surfaces. Sorption of organic molecules to polymer surfaces is a form of fouling, as are ionic bonding and plating of materials onto surfaces. Biofouling is the deposition and growth of living organisms on manmade surfaces. Fouling and biofouling fundamentally change the properties of surfaces and can compromise performance in perceptual, structural, physical, chemical, and biological ways. Compromised performance is the driving force for development of fouling management strategies.

The complexity of fouling is best described in aqueous marine systems [1–3]. Compared to the other major biological fluid, air, the high viscosity of water has consequences for bacteria and filter-feeding organisms. Instead of expending energy to pump water, attachment to surfaces provides the energetic advantage of passive movement of water to obtain nutrients and eliminate wastes. Fouling is in three general categories: molecules, microbes, and macro-organisms. In most instances, for example on ship hulls in ports, the three categories of fouling are

largely independent and the relative abundance of potential molecular, microbial, and macro-invertebrate colonizers determines the nature of the fouling on a surface [4]. Macro-invertebrates are known to respond to peptide pheromones [5–7]. Additionally, larvae respond to shear, rugosity, a variety of chemicals, and surface energy [8–11]. Many larvae respond to secondary compounds [12, 13] and bacterial films [14, 15].

In harbors, preconditioning of a surface by microbes, a kind of succession, is required for subsequent fouling by a macro-fouling worm [16, 17]. Depending on the macro-fouler species and the age and composition of the film [18, 19], microbial films can promote [20], inhibit [21], or have no effect [22] on settlement of the larvae of the same macro-fouler. Most, but not all, fouling organisms in harbors settle in the absence of a specific larval inducer. In temperate and tropical harbors, seasonal fouling (summer vs winter and monsoon vs inter-monsoon) is more obvious than successional fouling. In many ports around the world, the biofouling community includes the same cosmopolitan species that are introduced from fouled hulls or with ballast water released from ships [23]. These cosmopolitan fouling species are opportunists such as barnacles, bryozoans, hydroids, and tube worms with short larval intervals and rapid growth to maturity [24, 25].

After immersion of a surface, properties of the surface such as surface energy have a strong influence on initial deposition of molecular films [26], bacterial films [27], and colonization by macro-foulers [11, 28]. However, in a matter of days, surfaces move toward a common surface energy [26], and biofouling communities become very similar in any particular habitat. However, what happens in one habitat does not reflect what might happen in another [24]. Similarly, in a single habitat, the timing of when free surface becomes available can impact the nature of the mature fouling community. This is especially true in subtidal communities [29].

### 3 Fouling Management

Modern commercial fouling management using polymer systems was developed for ship hulls because performance and fuel costs are directly tied to hull fouling. Molecular fouling is an unsolved, and currently un-addressed, challenge. As micro-fouling is decoupled from macro-fouling, both must be managed. In marine environments, some level of micro-fouling occurs on all, even very toxic, surfaces. Macro-fouling, with its dramatic effects on performance, corrosion, and fuel costs, is the target of commercial ship hull fouling management solutions.

Although business models are, of necessity, proprietary in a competitive market, one can speculate on basic components of coatings company business models. Fouling management coatings are part of complex coating systems, which are physically tough, have anticorrosive properties, release toxins at predictable rates based upon polymer thickness, and can usually be repaired if damaged. Present commercial management solutions are based on broad-spectrum long-lived inorganic (copper ions in some form) and long-lived organic herbicides, pesticides, and

fungicides. Many polymer systems employ highly toxic organotin as catalysts. Although organotins are banned by the IMO as antifoulants, organotins can be and are used as catalysts in coatings. However, the damaging effects of all long-lived broad-spectrum biocides on environments and non-target species are resulting in government regulations that increasingly restrict the use of long-lived biocides and provide incentives for more environmentally benign alternatives, usually in the form of short-lived biocides such as Sea-nine 211 [30] and the pyrithiones [31]. Foul-release (easy clean) surfaces are in the mix of emerging commercial products with the most promising new systems combining toxic and foul-release properties.

As the very newest of coatings gain market share, it is likely that they are regulated if they threaten food security and ecosystem stability, as was the case for tributyltin hydrolyzing coatings. These new coatings contain much less organotin and are a major advance over the historic organotin coatings, which resulted in measurable levels of organotins in the global shipping lanes and extensive environmental damage. Because the large fouling management coatings companies have business models based upon broad-spectrum biocides, they are continuously looking for compatible and registered biocides for their existing coatings systems.

## 4 Fouling of Polymers in Extreme Environments

Biofouling occurs in most environments where water wets surfaces. Probably the best studied extreme environments are pipes and heat exchangers. In heat exchangers and pipes, micro-fouling is the target because it decreases performance and causes corrosion. It is striking that microbial corrosion, generally at welds and imperfections in pipes, occurs even in heated oil pipelines and eventually compromises the structural integrity of the pipe [32].

Roofs are extreme environments [33]. They experience ultraviolet exposure, fluctuating temperatures including freezing and thawing, extreme changes in moisture, and pH fluctuations, and they provide unusual biological challenges. Roofs foul with inorganic, organic, and living material. There is pressure to manage fouling on roofs because fouling is unsightly, corrosive, and compromises the integrity and engineered functions of the roof. Fouling on asphalt roofing shingles is routinely managed by the addition of copper granules during shingle production. The granules leach copper ions when exposed to moisture. Releasing copper ions from granules eventually fails in effectiveness when consortia of organisms, which usually include nitrogen-fixing cyanobacteria *Gloeocapsa* spp., develop resistance to copper ions [34].

Some kinds of fouling occur on all roofs, independent of their composition. Physical fouling by particulates, aerosols, and propagules is guaranteed. Delivery of additional compounds and propagules by leaves as well as birds and their feces sets the stage for biofouling. Biofouling can be from organisms that physically occupy

surfaces and from organisms that actively degrade and consume the surface. Two general statements that can be made about roof biofouling are that the communities that develop are adapted to the extreme environment and that the communities degrade the performance that the engineers designed and planned for the product, usually in a great variety of ways. Thus, the pressure for fouling management is for solutions that extend the functional life and appearance of the product.

As with most fouling management, the general approach to roof fouling is some form of killing and removal of the fouling. This can range from simple physical approaches such as pressure washing to washing with toxic mixtures to incorporation of biocides in the roofing product. Because of the very large surface areas of roofs and their direct proximity to people, pets, and water sheds, a major consideration for responsible businesses is literally the down-stream impacts of fouling management on human and environmental health. One simply needs to consider children playing in biocide-laden puddles and animals and humans drinking biocide-laden water and eating biocide laden fish and vegetables to appreciate the magnitude of the responsibility and the challenge as some biocides, for example organotins, produce toxicity to humans and animals at such low concentrations [35] that acceptable levels in drinking water are actually below detectable levels by current analytical techniques.

## **5 Macro-Fouling and Micro-Fouling Concepts That Could Drive Future Fouling Management Research**

In contrast to the use of long-lived broad-spectrum biocides to manage fouling, one could use disruption of evolutionarily conserved pathways with short-lived biomagnified pharmacophores to manage macro-fouling. For example, most macro-foulers have a life cycle that includes a dispersal stage, usually a planktonic propagule that culminates in a settlement stage. The settlement stage of macro-foulers goes through a process called metamorphosis in which they change from the larval dispersal form to a juvenile form that resembles the adult. Metamorphosis is highly conserved and similar in transduction, even in distantly related animals such as oysters and barnacles. For example, in oysters and barnacles, the peptide pheromones for gregarious settlement and metamorphosis are similar enough that one synthetic mimic triggers metamorphosis in both kinds of larvae [7].

As noted above, there are many triggers for macro-fouler metamorphosis. However, although not studied extensively, the pathways that transduce those triggers may be highly conserved. In biological systems, survival of an individual may be possible if one alters the beginning of a complex pathway but may not be possible if one alters the pathway somewhere in the internal transduction process. Thus, it is likely, for example, that interference in the transduction pathway that directs metamorphosis could be used to prevent settlement of oysters and barnacles [36, 37]. It is encouraging that there are likely a finite and relatively small number

of these conserved pathways. Once identified, these pathways could be the target of more environmentally benign approaches.

As basic science advances our understanding of organisms and communities and their evolution, new opportunities for management arise. At the microbial level, this can be as simple as using a compound such as *N*-acetyl-L-cysteine, which disrupts bacterial adhesion and production of extracellular polysaccharides [10]. One more complex consideration is that consortia, complex interactive assemblages of microorganisms, could be considered as a different way to organize a functional metazoan. Thus, microorganisms in one instance function as individuals and in other instances, when conditions permit, function as a large and very complex interdependent organism. In fouling management, individual microbes are easy to manage whereas the metazoan equivalent, a complex interdependent consortium, develops emergent properties such as resistance to biocides. One unstudied option for management of consortia would be a two-step process with step one being disrupting the communication that enables the metazoan-like consortium and step 2 managing key individuals in the disrupted consortium. It is possible that a biomimetic approach that uses components of the innate immune response found in all metazoans [38, 39] could be used to manage micro-fouling.

A Singapore-based research group began testing these concepts at the beginning of this century [40]. The group used human pharmaceuticals with known mechanisms of action in humans and other vertebrates to test the hypothesis that these molecules would interrupt the transduction cascades in marine macro-fouling larvae and in microbes [40–47].

## 6 Candy and Poisons

In the future, if novel approaches to fouling management are to become a reality, society would benefit from close collaboration between engineers, polymer chemists, and biologists. This collaboration has been attempted for decades, but it is not obvious how to include new concepts into the existing regulatory framework and business models. Once broad-spectrum death is no longer the definitive endpoint of fouling management, it is important to understand the biological basis of new fouling challenges and their consequences [23]. The theory of sustainable approaches is simple in concept. The approach used should have minimal environmental, food safety, and human health impacts, even when the novel technology gains a large market share. One needs to consider how this might be accomplished.

In considering bioactive molecules, there are molecules that impact transduction events such as induction of metamorphosis or coordination of microbial consortia. The molecules that mediate these pathways are minute in concentration and their response is biologically amplified. These bioactive molecules are active in microgram per milliliter or lower concentrations and susceptible to simple chemical and biological degradation once released into the environment. The ideal active ingredient would survive release from the polymer for the time it took to diffuse out of

the approximately 500- $\mu\text{m}$  non-slip layer over a coating [48–50]. At that point, the molecule would be either impacting a fouling organism or susceptible to chemical and biological degradation. Although the biologically consumable molecule would essentially kill propagules on or near the surface, it would become candy for some portion of microbes. Very biologically potent biodegradable molecules would be best because they could do their intended job of fouling management of a surface without impacting species away from the surface or adding too many nutrients to the environment.

This idea is the basis of a patent family [46, 47]. In that family, a pharmaceutical, Immodium™, a drug in pill form taken by mouth, an antidiarrheal, was found to impact bacteria and disrupt transduction of metamorphosis when presented in microgram per milliliter concentrations. The chemically refractory and poorly biodegradable drug was de-engineered to a skeleton bioactive pharmacophore. The pharmacophore was simplified to maximize biodegradability. Then the degradable pharmacophore was re-engineered to enable delivery in a polymer coating.

It is frustrating that polymer coatings, especially carbon-based products such as polymers, can be candy to organisms and that biology can degrade the appearance and performance of a product. Even polydimethyl siloxane-based coatings support microbes, and the action of the microbes generates novel molecules such as silico-steroid conjugates with unknown biological activity and degradation pathways [51]. Many new building materials such as composite lumber and roof sheeting materials support microbes that degrade the appearance and performance of the material. A major, continuing challenge is the production of engineered building materials that remain durable although environmentally safe.

## 7 Polymers and Controlled Release

Synthetic polymers provide a variety of mechanisms for delivery of active compounds. However, a very important issue is the release of biologically active molecules, which must be registered if they are not incorporated covalently into a larger polymer. One needs to look closely at the regulations governing the kinds of molecules that can be added to polymers. Because it is rules and regulations that provide the limits for how additives are delivered; these define business limits but do not address the biological consequences of gaining market share. This phenomenon is well illustrated with the general banning of organotin as fouling management tools [30].

One simple mechanism for delivery of active molecules takes advantage of the free space in a polymer matrix. One can load that space with compounds that slowly migrate to the surface where they are active until they diffuse away. Loading can be either before or after polymerization. If the chemistry of the additive is impacted by polymerization, then the loading can be after polymerization. Post-loading changes the physical properties of the polymer. Evaluations of many foul-release coatings in the 1990s showed that the coatings industry has used this approach for decades.

Classic versions are polydimethyl siloxane (PDMS) polymers loaded with silicone oils and silicone detergents. Interestingly, a common catalyst dibutyltin dilaurate used to polymerize PDMS coatings added at 250  $\mu\text{g/g}$  of coating confers antifouling properties on coatings for at least a few months [52]. There are several new coatings on the market that have vastly improved physical characteristics and that combine foul-release and antifouling approaches. How these coatings work is proprietary.

A second management mechanism is to link additives covalently to surfaces or encapsulate them so they are inert particles. This idea is attractive because it reduces the impact of the additives on coating cure, provides an easy way to modify formulations, and exactly fits the purchase-and-mix business model of coatings companies. Linking or encapsulation enables carefully controlled delivery based on the chemistry of the environment of submersion. The environment of immersion is a well understood complicating variable that is routinely addressed by global suppliers whose reputation depends on effective regional and trans-oceanic products.

A third mechanism is to incorporate active ingredients into the polymer backbone of the film. This mechanism was the basis of the most recently banned antifouling coatings based upon organotin. The active compound tributyltin was included, not because it was toxic but because it resulted in a hard, smooth coating that self-polished. The coating was magic for a very long time because it was so toxic the microscopic propagules it killed died and rotted well before they were observed in fouling assessments. Organotin was reported to repel organisms, when in fact it was not detected by propagules and killed newly settled organisms by entering their mitochondrial membranes and destroying energy production. Organotins would be a very attractive approach *if only* organotins were not also biologically active at levels about 2,000 times lower than the acute toxic dose and if the organotins did not build up in the environment as the antifouling coatings gained market share. Organotins are probably the best modern example of the major shortcomings of the mix-and-kill business model that uses long-lived broad-spectrum biocides.

## 8 Environmental Concerns

As with everything else in our rapidly changing technological society, laws and regulations routinely lag behind technological advances. Although not mandated by law, it is becoming obvious that sustainable businesses must perform due diligence to ensure that their products are safe. This means that the question of potential human health, environmental health, and food safety impacts must be asked and answered early on in product development.



## 9 Application Concerns

Biologically, there is one major concern with using biologically active molecules to manage fouling. It is likely that the active ingredients interact with human physiology. These concerns are the same as safety concerns around the use of volatile organic compounds and broad-spectrum toxins, but different in that exact effects are not known.

## 10 Conclusion

Fouling management is essential in our modern society. Population growth and globalization increasingly stress all biological systems and threaten human health, environmental health, and food safety. Novel environmentally benign approaches to fouling management would benefit society. This benefit could be based on increased transdisciplinary research that prioritized and was funded to develop benign approaches. It will be interesting to see which cultures maximize these concepts in the future.

**Acknowledgement** This work was partially supported by the grants from the US Office of Naval Research. Although the ideas are mine, I would not have had them without the many collaborators who shaped my thinking through our working relationships and the enjoyment of attempting to figure out how the world works. Thanks to the editors and reviewers, who greatly improved this chapter. Finally, thank you to J. Miller who solved my reference issues and did so much more.

## References

1. Costlow JD, Tipper RC (eds) (1984) Marine biodeterioration: an interdisciplinary study. Naval Institute Press, Annapolis
2. Hellio C, Yebra DM, Sitton R (eds) (2010) Advances in antifouling coatings and technologies. Woodhead Publishing, Cambridge
3. Dürr S, Thomason J (eds) (2010) Biofouling. Wiley-Blackwell, New York
4. Clare AS, Rittschof D, Gerhart DJ, Maki JS (1992) Molecular approaches to non-toxic antifouling. *Invertebr Reprod Dev* 22(1–3):67–76
5. Burke RD (1984) Pheromonal control of metamorphosis in the pacific sand dollar, *Dendraster Eccentricus*. *Science* 225:442–443
6. Burke RD (1986) Pheromones and the gregarious settlement of marine invertebrate larvae. *Bull Mar Sci* 39:323–332
7. Rittschof D, Cohen J (2004) Crustacean peptide and peptide-like pheromones and kairomones. *Peptides* 25(9):1503–1516
8. Crisp DJ (1965) Surface chemistry, a factor in the settlement of marine invertebrate larvae. In: *Proceedings of the 5th marine biological symposium: Botanica Gothoburgensia*, vol 3. pp 51–65

9. Crisp DJ (1974) Factors affecting the settlement of marine invertebrate larvae. In: Grant PT, Mackie M (eds) Chemoreception in marine invertebrate larvae. Academic Press, New York, pp 177–266
10. Oloffson A-C, Hermansson M, Elwing H (2003) N-Acetyl-L-cystine affects growth, extracellular polysaccharide production, and bacterial biofilm formation on solid surfaces. *Appl Environ Microbiol* 69:4814–4822
11. Roberts D, Rittschof D, Holm ER, Schmidt AR (1991) Factors influencing initial larval settlement: temporal, spatial, and surface molecular components. *J Exp Mar Biol Ecol* 150:203–211
12. Pawlik JR (1992) Chemical ecology of the settlement of benthic marine invertebrates. *Oceanogr Mar Biol Annu Rev* 30:273–335
13. Rittschof D (2001) Natural product antifoulants and coatings development. In: McClintock J, Baker P (eds) Marine chemical ecology. CRC Press, New York, pp 543–557
14. Hadfield MG, Paul VJ (2001) Natural chemical cues for settlement and metamorphosis of marine invertebrate larvae. In: McLintock JB, Baker BJ (eds) Marine chemical ecology chap. 13. CRC Press, New York, pp 431–461
15. Hadfield M (2011) Biofilms and marine invertebrate larvae: what bacteria produce that larvae use to choose settlement sites. *Annu Rev Mar Sci* 3:453–470
16. Unabia CRC, Hadfield MG (1999) Role of bacteria in larval settlement and metamorphosis of the polychaete *Hydroides elegans*. *Mar Biol* 133:55–64
17. Huang Y, Callahan S, Hadfield MG (2012) Recruitment in the sea: bacterial genes required for inducing larval settlement in a polychaete worm. *Sci Rep* 2:228
18. Dobretsov S, Qian P-Y (2006) Facilitation and inhibition of larval attachment of the bryozoan *Bugula neritina* in association with mono-species and multi-species biofilms. *J Exp Mar Biol Ecol* 333:263–274
19. Khandeparker L, Anil AC, Raghukumar S (2006) Relevance of biofilm bacteria in modulating the larval metamorphosis of *Balanus amphitrite*. *FEMS Microbiol Ecol* 58:425–438
20. Qian P-Y, Vengatesen T, Lau SCK, Cheung SCK (2003) Relationship between bacterial community profile in biofilm and attachment of the acorn barnacle *Balanus amphitrite*. *Aquat Microb Ecol* 33:225–237
21. Lau SC, Thiyagarajan V, Cheung SC, Qian P-Y (2005) Roles of bacterial community composition in biofilms as a mediator for larval settlement of three marine invertebrates. *Aquat Microb Ecol* 38:41–51
22. Maki JS, Rittschof D, Costlow JD, Mitchell R (1988) Inhibition of attachment of larval barnacles, *Balanus amphitrite*, by bacterial surface films. *Mar Biol* 97:199–206
23. Rittschof D (2008) Ships as habitats: biofouling -- a problem that requires global solutions. *Cosmos* 4(1):71–81
24. Vasishtha N, Sundberg DC, Rittschof D (1995) Evaluation of release rates and control of biofouling using monolithic coatings containing an isothiazolone. *Biofouling* 9:1–16
25. Rittschof D (2000) Natural product antifoulants: one perspective on the challenges related to coatings development. *Biofouling* 32:193–205
26. Meyer AE, Baier RE, King RW (1988) Initial fouling of nontoxic coatings in fresh, brackish and sea water. *Can J Chem Eng* 66:55–62
27. Baier RE (1984) Initial events in microbial film formation. In: Costlow JD, Tapper RC (eds) Marine biodeterioration: an interdisciplinary study. Naval Institute Press, Annapolis, pp 57–62
28. Holm ER, Cannon G, Roberts D, Schmidt AR, Sutherland JP, Rittschof D (1997) The influence of initial surface chemistry on the development of the fouling community at Beaufort, North Carolina. *J Exp Mar Biol Ecol* 215:189–203
29. Sutherland JP (1984) The structure and stability of marine macrofouling communities. In: Costlow JD, Tapper RC (eds) Marine biodeterioration: an interdisciplinary study. Naval Institute Press, Annapolis, pp 202–206
30. Jacobson AH, Willingham GL (2000) Sea-nine antifoulant: an environmentally acceptable alternative to organotin antifoulants. *Sci Total Environ* 258(1):103–110

31. Romano JA, Rittschof D, McClellan-Green PD, Holm ER (2010) Variation in toxicity of copper pyrrhione among populations and families of the barnacle, *Balanus amphitrite*. *Biofouling* 26(3):341–347
32. Kerns J, Little B (eds) (1994) Microbial induced corrosion testing. ASTM Publication Code Number (PCN) 04-012320-27
33. Berdahl P, Akbari A, Levinson R, Miller WA (2008) Weathering of roofing materials. *Constr Build Mater* 22:423–433
34. Manns L (1995) Metal binding capacity of the exopolymer excreted by the common blue green algae, *Gloeocapsa*. Masters dissertation, Duke University
35. Environmental Protection Agency (2003) Ambient aquatic life water quality criteria for tributyltin (TBT)-Final. EPA 822-R03-031, p 129
36. Dahlstrom M, Martensson L, Jonsson PR, Arnebrant T, Elwig H (2000) Surface active adrenoreceptor compounds prevent settlement of cyprid larvae of *Balanus improvisus*. *Biofouling* 16:191–203. <https://doi.org/10.1080/08927010009378444>
37. Gohad NV, Aldred N, Orihuela B, Clare AS, Rittschof D, Mount AS (2012) Observations on the settlement and cementation of barnacle (*Balanus amphitrite*) cyprids larvae after artificial exposure to noradrenaline and the locations of adrenergic receptors in the organism. *J Exp Mar Biol Ecol* 416:153–161
38. Essock-Burns TA, Wepprich A, Thompson A, Rittschof D (2016) Enzymes manage biofilms on crab surfaces aiding in feeding and antifouling. *J Exp Mar Biol Ecol* 479:106–113
39. Essock-Burns T (2015) Exploring the interface between macroorganisms and microorganisms: biochemical, ecological and evolutionary concepts. Dissertation, Duke University
40. Rittschof D, Lai CH, Kok LM, Teo SL-M (2003) Pharmaceuticals as antifoulants: concept and principle. *Biofouling* 19(Suppl. S):207–212
41. Choong AMF, Teo SL-M, Leow JL, Koh HL, Ho PCL (2006) A preliminary ecotoxicity study of pharmaceuticals in the marine environment. *J Toxicol Environ Health A* 69(21):1959–1970
42. Rittschof D (2009) Novel antifouling coatings: a multiconceptual approach. In: Flemming H-C, Murthy PS, Venkatesan R, Cooksey KE (eds) *Marine and industrial biofouling*. Springer, Berlin Heidelberg, pp 179–188
43. Choong AMF, Maki JS, Ikhwan JTB, Chen C-L, Rittschof D, Teo SL-M (2010) Pharmaceuticals as antifoulants: inhibition of growth and effects on adhesion of marine bacteria. In: Chan J, Wong S (eds) *Biofouling types, impact and anti-fouling*. Nova Science Publishers, New York, pp 221–246
44. Chai CLL, Teo SL-M, Jameson FKM, Lee SSC, Likhitsup A, Chen C-L, Rittschof D (2014) Loperamide-based compounds as additives for biofouling management. *Int Biodeterior Biodegrad* 89:82–87
45. Rittschof D, Chai C, Teo SL-M, Maki JS (2015) Fouling and its next generation management: a perspective. *J Agric Mar Sci* 19(1):16–23
46. Chai CLL, Burkett BA, Teo SL-M, Rittschof D, Lee SSC, Dickinson GH, Hong H (2015) Antifouling compounds and use thereof. US Patent 9,169,223, 27 Oct 2015
47. Chai CLL, Burkett BA, Teo SL-M, Rittschof D, Lee SSC, Dickinson GH, Hong H (2015) Antifouling compounds and use thereof. US Patent Appl Pub US2016/0009926 A1, 14 Jan 2016
48. Rittschof D (2008) Novel antifouling coatings: a multiconceptual approach. In: Flemming HC, Murthy PS, Venkatesan R, Cooksey KE (eds) *Marine and industrial biofouling*. Springer, New York, pp 179–187
49. Rittschof D (2010) Future trends in antifouling research. In: Hellio C, Yebra DM, Sitton R (eds) *Advances in antifouling coatings and technologies*. Woodhead Publishing, Cambridge, pp 725–748
50. Rittschof D (2010) Research on practical environmentally benign antifouling coatings. In: Dürr S, Thomason J (eds) *Biofouling*. Wiley-Blackwell, New York, pp 396–409

51. Rittschof D, Orihuela B, Harder T, Stafslie S, Chisholm B, Dickinson GH (2011) Compounds from silicones alter enzyme activity in curing barnacle glue and model enzymes. *PLoS One* 6 (2):e16487
52. Rittschof D, Holm ER (1997) Antifouling and foul-release: a primer. In: Fingerman M, Nagabhushanam R, Thompson M-F (eds) *Recent advances in marine biotechnology*, vol. 1, endocrinology and reproduction. Science Publishers, Enfield, pp 497–512

# Unique Silicone-Epoxy Coatings for Both Fouling- and Drag-Resistance in Abrasive Environments



Robert Baier, Mark Ricotta, Vincent Andolina, Faraaz Siraj,  
Robert Forsberg, and Anne Meyer

**Abstract** Multiple years of international trials in both oceanic and freshwater sites have led to successful easy-release coatings based on the methyl-silicone polymers now widely employed as substitutes for tributyltin- and copper-based ship bottom paints. These have been found to be too soft for harsh conditions, especially during abrasion, but do serve for useful periods in commercial and military circumstances where abrasion is not frequent. This chapter reviews abrasion-related research of the past 20 years that identifies a novel version of silicone-based coatings with a retained easy-release value of Critical Surface Tension (CST) of about 26 mN/m, compounded with a tough epoxy component that allows the two-component coating to survive and function well in extremely abrasive circumstances. This coating has been applied to a power plant’s large intake grate (“rack”) subject to debris impact and intense zebra mussel fouling, an airfoil blade coating showing significantly lower drag than competitive paints, a turbine encasement seal layer remaining functional in zebra mussel-infested waters, and an easy-release surface for flash-frozen ice, simultaneously also resisting damage by transit through ice floes. The coating is formulated using polymeric methyl-silicone granules that are dispersed within an oil-in-water multiple emulsion in an epoxy base that maintains excellent substratum adhesion while allowing the methyl-silicone-based matter to dominate and be continuously refreshed via minimum wear at the environmental interface.

**Keywords** Abrasion-resistant • Drag reduction • Fouling release • Ice release • Non-toxic coating • Silicone

## Contents

1	Introduction .....	368
2	Materials .....	369
3	Methods .....	370
4	Results .....	371
5	Discussion and Conclusion .....	375
	References .....	376

## 1 Introduction

Although prior work has led to the commercial and military acceptance of methyl silicone-based, non-toxic, and easy-release coatings [1, 2] to minimize biofouling concerns of the world's shipping and power industries, the best of these have been found to be too susceptible to abrasion for routine service in ice fields, dusty or turbid conditions, water-intake grates ("trash racks"), and turbine encasement seals, among other harsh environments. At the same time as improving the wear-resistant qualities of these coatings, one must maintain or improve the drag-reduction properties [3, 4]. The former coatings, when applied to racks that were subsequently physically scraped with steel rakes and scoured with water-lances to release accumulated zebra mussel (*Dreissena* sp.) debris and ice frazil, required only 5 psi water-lance pressure to clean the coatings completely. The underlying mechanical trash raking-induced damage to the methyl silicone-based coating was easily seen. In contrast, requiring only 50 psi water-lance pressure, a specific meld of silicone and epoxy ingredients produced a hardy paint that released all debris without visual (or measured surface property) damage to the coating. Conversely, similarly challenged field-exposed trash racks fabricated from carbon-loaded high-density polyethylene required over 2,000 psi water-lance pressure to remove most of their debris, always leaving behind the zebra mussel byssus threads attached by the still retained adhesive byssus discs. Mussel byssus threads, terminated in adhesive discs, are the proteinaceous "beards" seen protruding from the shells of mussels in both seawater and fresh water. The best of the easy-release methyl silicone-based coatings required only 5 psi for complete biofouling removal, byssus discs, and all other deposits, but these coatings were also the most readily damaged by abrasion and released from their substrata.

The intermediate 50 psi fouling-release-strength coating, not as biofouling-resistant as a pure polydimethylsiloxane (PDMS) coating, was chosen for testing of its drag reduction properties in both stagnation point flow and as an airfoil coating in a large towing tank [3, 4], and for its ease of shedding of flash-frozen ice droplets [5] in comparison with numerous comparative materials. Table 1 and [1, 2] identify the comparative test materials. Only the coating that is the subject of this chapter was demonstrably able to resist concrete, zebra mussel, and hard rubber reciprocating-seal-induced wear on cyclically operating turbine enclosures at a major power plant [6].

**Table 1** Summary of materials used in testing

Material abbreviation (as used in Fig. 4)	Description
Glass control	Glass microscope slide (detergent-washed)
RFGDT glass	Radiofrequency glow-discharge treatment (RFGDT) cleaned glass, water-wettable
PM4545-76 blade	Wearlon formulation 76 coating on helicopter blade
RFGDT rough glass	Glass microscope slide, sandblasted with 50- $\mu$ m silica and washed before RFGDT
Rough glass	Glass microscope slide, sandblasted with 50- $\mu$ m silica and washed
ODS	Octadecylsilane-coated glass
DMS	Dimethylsilane-coated glass
F-150 naval primer	Epoxy primer paint (Navy formulation F-150) on glass
PM2020-98	Wearlon formulation 98 on glass
PDMS (BACK)	PDMS reference standard from National Institutes of Health; smooth side
PDMS blade	PDMS coating on helicopter blade
3-HEPT glass	Fluorosilane-coated glass
PM4545-76	Wearlon formulation 76 on glass
F1-M	Wearlon formulation F1-M on glass
PDMS (FRONT)	PDMS reference standard from National Institutes of Health; rough side
DC3140	Dow Corning formulation 3140 methylsilicone on smooth glass
PVS	Kerr Corporation polyvinylsiloxane on smooth glass
3-HEPT rough glass	Fluorosilane coating on sandblasted glass
F1-M blade	Wearlon formulation F1-M on helicopter blade
PM2020-98 blade	Wearlon formulation 2020.98 on helicopter blade
PVS rough	Kerr Corporation polyvinylsiloxane replica of sandblasted glass

Stagnation point flow, towing tank, and/or ice adhesion experiments

Here we describe the characterization of the selected coating by both compositional and surface characterization criteria.

## 2 Materials

Originally introduced in response to the zebra mussel invasion of the Great Lakes in the early 1980s [2], numerous compositions of epoxy and silicone were developed into water-based emulsions for application to critical lake infrastructures and to transiting ships to provide easy release of the encrusting mussels. The compositions are described in a compilation of early reports of the zebra mussel appearance and consequences [7]. They basically encompass mixtures of epoxy and silicone ingredients in what are called “inverse emulsions” to produce strongly adhesive coatings with otherwise exposed, and renewable, waxy surfaces. During a Sea Grant’s first

**Table 2** Characteristics of Wearlon PM2020.98

---

<i>General composition:</i> water-borne, epoxy-based dual emulsion; indicative elements: Si, O
<i>Attributes:</i> low surface energy; low friction; abrasion resistance; chemical/water/weather/corrosion resistance; excellent adhesion to metallic substrata

---

government-industry-university cooperative program [8], the particular composition called Wearlon 2020.98 was selected through intensive testing from a larger group of non-toxic compositions.

According to its manufacturer (John Smith, Plastic Maritime Corporation, PO Box 2131, Wilton, NY 12831, private communication):

The Wearlon chemistry is based on taking two incompatible products—silicone and epoxy—that, when emulsified, become compatible. With the addition of a curing agent, an exothermic reaction occurs resulting in the breakdown of the emulsion, the release of water, and the formation of a silicone-epoxy block copolymer. A different mole% of silicone to epoxy results in a variety of products. The higher the silicone content to epoxy, the softer the coating becomes. The curing agents, catalysts, surfactants, and wetting agents, are the company's proprietary information.

Table 2 summarizes the characteristics of the best-performing coating in this series, designated Wearlon 2020.98. Testing was carried out with coated aluminum, steel, and concrete surfaces with deposits of Wearlon 2020.98 of 75–100  $\mu\text{m}$  dry film thickness.

### 3 Methods

Coatings of the various supplied and numerous comparative materials were all characterized by a combination of physico-chemical methods and performance tests. Specific chemical compositions were characterized by Multiple Attenuated Internal Reflection InfraRed Spectroscopy (MAIR-IR) [9], and the measured CSTs and calculated surface energies of the coatings were derived from contact angle measurements with a series of highly purified test fluids by methods now widely used in fouling-release paint testing [10]. Details of the contact angle liquids utilized, their molecular features and reactivities, and the interpretive methodology are found therein. Scanning electron photomicroscopy and light microscopy produced the illustrative images necessary to observe each specimen's surface heterogeneity. Energy-dispersive X-ray analysis provided spot-by-spot identification of the elemental abundances in each visualized region. The specific instrumentation utilized is named in the prior references [9, 10].

For stagnation point drag testing, specific laboratory devices were constructed and operated as described earlier [1, 3]. For airfoil drag testing, helicopter rotor blades were individually surface-prepared and tested (both before and after coating application) in a large water towing tank [4].



For friction and wear studies, coated steel coupons were mounted into laboratory devices originally developed for long-term testing of dental (toothbrush, resin, tooth) wear, both by rotating units and linear reciprocating units employing hard rubber (turbine chamber seal) partners [6]. The rotating unit was also utilized to test the ice-shard wear resistance of the various coatings after frozen water-droplet push-off testing had revealed the 2020.98 composition to be the easiest release for flash-frozen ice [5]. Laboratory trials with rime ice impaction on rapidly rotating rods in a hot-water-condensing freezer chest had previously indicated qualitatively that the 2020.98 coating would be a good candidate for easy ice release, but that lab study was not continued.

### 4 Results

Figure 1 illustrates the near-surface internal distributions of the silicone-based and epoxy-based ingredients of the dried 2020.98 composition, illustrating a dual emulsion [7] spheroidal separation of the silicone-dominated ingredient from the continuous-phase epoxy-rich component responsible for excellent substratum adhesion with no required primer coats. Figure 2 shows the MAIR-IR spectrum of the methylsilicone-dominated surface zone of the self-cured water-borne final 2020.98 formulation. Figure 3 is a plot of the contact angle data (cosines) against the liquid/

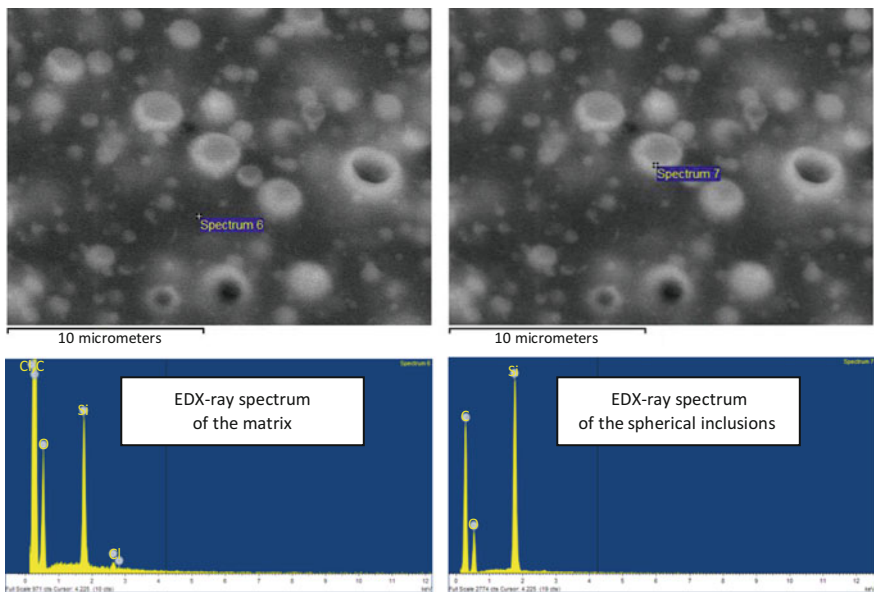


**Fig. 1** Characterization of formulation 2020.98 coating by backscattering scanning electron microscopy and energy-dispersive X-ray analysis. Circular particulate inclusions have higher silicon content than the bulk phase

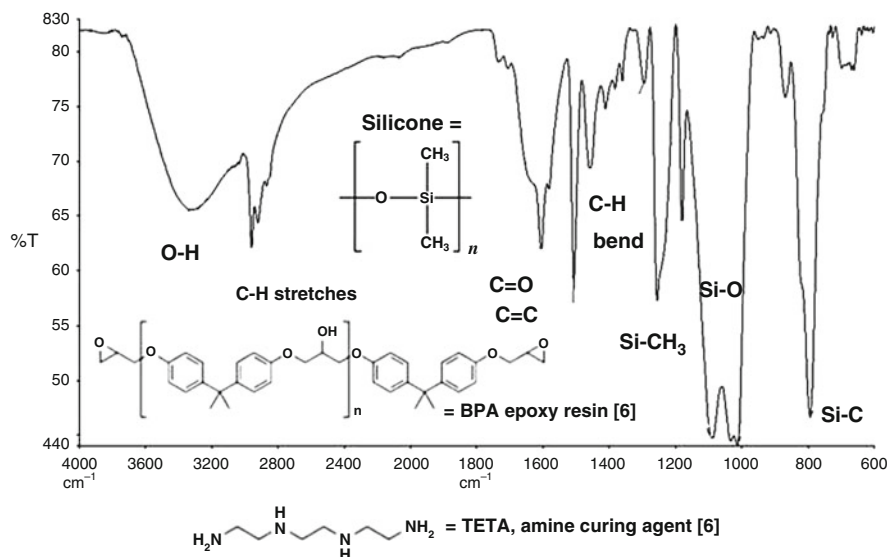


**Fig. 2** MAIR-IR spectrum of the surface zone of Formulation 2020.98. Absorption band positions indicate dominance by methylsilicone components, as confirmed by Critical Surface Tension data (see Fig. 3)

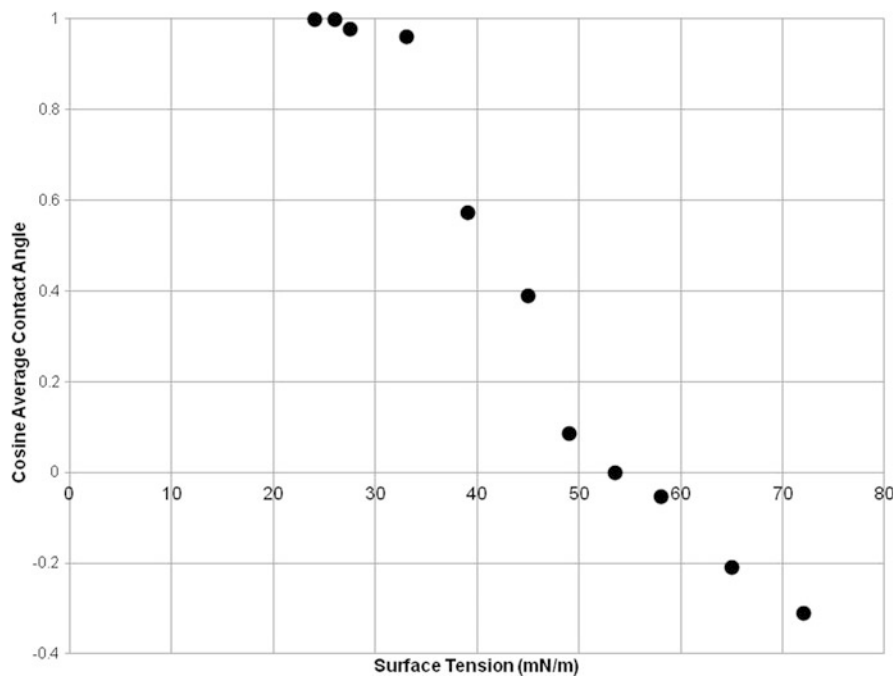


**Fig. 3** Contact angle data plot (Zisman plot) for Formulation 2020.98. CST = 26 mN/m

vapor surface tensions of pure diagnostic liquids, leading to an extrapolated intercept at the zero contact angle value ( $\cos = 1$ ) of 26 mN/m, called the CST by the originator of this surface characterization method [11]. CST values between 20 and 30 mN/m have historically been associated with the easiest shedding of attaching biological debris at low shear stresses [12]. In the case of the 2020.98 formulation, vigorous wear against hard rubber and other articulated substances actually “polished” the formulation to an improved, lower-energy surface state by attacking the softer silicone-rich granules and smearing their low-energy contents over the easy-release interface.

From stagnation point chamber studies, the 2020.98 formulation coatings showed the second best results in terms of minimizing flow drag of water moving from its stagnation point at 90° from contact with the test surface at a constant water pressure of 27 psi (second only to a soft polyvinylsiloxane replica of roughened glass) in stagnation point chamber tests of 21 different materials (Fig. 4). In the water tunnel-based coated-airfoil trials, the 2020.98 formulation on airfoil rotor blades showed as much as a 5% drag reduction over the values for the clean, smooth, uncoated helicopter rotor blades [3]. This exceptional effectiveness was attributed to the presence of a microscopic roughness of about 20 μm for the blade-applied 2020.98 surface coating trapping water-released air bubbles in the hydrophobic micro-topographic valleys so that the actual shear took place through a water-air boundary layer of lower viscosity than wholly liquid water [4].

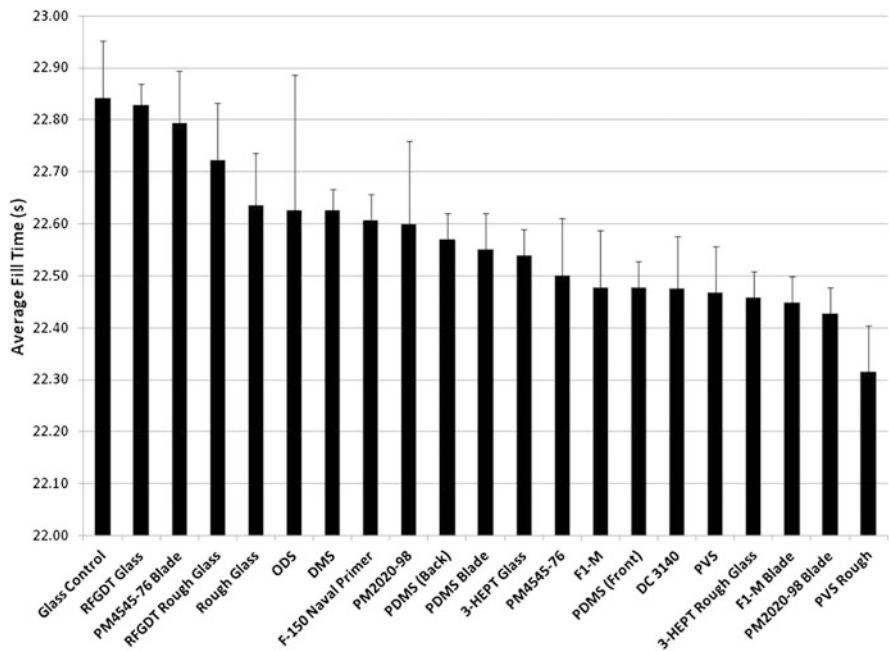


**Fig. 4** Plot of average fill times in stagnation point flow cell. See Table 1 for descriptions of materials specified on X-axis

Regarding ice adhesion studies, quantitation of attachment strength was obtained by placing droplets of water (10–20  $\mu\text{L}$  in volume), where the water contact angles had been measured in advance, onto the surfaces of well-characterized reference materials in contact with a liquid nitrogen bath, producing an average temperature approaching  $-20^\circ\text{C}$ . After measuring their diameters, the frozen droplets were pushed off the surfaces in accordance with a published ASTM test method [5, 13], assuring that the pusher was flush with the substratum surface so that no peeling force was experienced. Characteristics of the test materials are summarized in Table 3. Again, the 2020.98 formulation gave the easiest-release values. The concurrent observation that the push-off strength was slightly lower than that for isolated PDMS was again attributed to the micro-roughness of the 2020.98 coating trapping gas at the droplet base.

Anticipating use of these coatings in newly opening Arctic shipping lanes, coated steel coupons were rotated at 60 revolutions per minute through ice cubes piled at the air/water interface of the same device used earlier for wear testing. When the 2020.98 coating was compared with numerous methyl silicone coating formulations mentioned earlier in this chapter [2], the paint damage was the least for 2020.98 at conditions corresponding to icy-water passages of many miles. Preliminary Lake Erie winter-icing exposures were evaluated in preparation for actual Arctic field trials.

**Table 3** Surface characteristics of materials used in ice adhesion experiments

Material	CST (mN/m)	Polar component of surface free energy (mN/m)	Dispersion component of surface free energy (mN/m)	Ice adhesion (Shear strength) in laboratory experiments (psi)
Polytetrafluoroethylene <sup>a</sup>	18	1	19	7
PDMS <sup>b</sup>	22	3	20	27
PM2020-98 (Wearlon) <sup>b</sup>	26	5	26	9
Low density polyethylene	30	2	29	26
Polystyrene (bacterial grade)	30	4	30	25
Fused silica	31	49	32	34
Glass control <sup>b</sup>	33	24	26	40
Pyrolytic carbon	37	10	35	45
Titanium (commercially pure)	37	51	32	50
Calcium hydroxyapatite	39	55	39	78
Stainless steel (316L)	40	45	38	137
Mica	41	65	38	55

<sup>a</sup>Similar to 3-HEPT in Table 1 and Fig. 4

<sup>b</sup>Also in Table 1 and Fig. 4

## 5 Discussion and Conclusion

It is important to consider the wide scope of the opportunities presented by these tougher-than-normal coatings. For example, an insect mitigating coating would reduce laminar flow drag. One of the conclusions of recent articles is that roughness is needed in addition to low surface energy [14]. The 2020.98 coating on drag-reducing blades is a good match of these characteristics. (2) As another example, during the testing of foul-release coatings at Pearl Harbor, Hawaii, small-boat operators ferrying tourists from shore to the USS Arizona Memorial asked for a more hardy paint that could be not only fouling-free but also sufficiently strong to survive the frequent impacts of these boats with the shoreline docking facilities. Many related options for selection of abrasion-survivable paints are available. Toward that goal, the following are the key surface qualities determined for the 2020.98 composition that has performed best in the studies described, as determined by both the Zisman technique and the theoretical surface energy component method of Kaelble [11, 15]: CST = 26 mN/m; dispersive component of the total surface free energy = 22.8 mN/m; polar component of the total surface free energy = 5.2 mN/m; calculated composite total surface free energy = 28.0 mN/m. The observed water contact angle against this paint's surface is hydrophobic, at 103°. The commercial name (Wearlon) connotes that this is a tough coating with a high methyl silicone content.

The results briefly noted here describe a “compromise” coating of silicone admixed with epoxy that is not as intrinsically “easy-release” for biomass as the pure silicone coatings alone, but is sufficiently wear-resistant (while renewing its surface features continuously) to serve in high-abrasion settings.

In such circumstances, the abrasive qualities of the impacting environment actually provide mechanical forces that assist in the removal of the otherwise deposited biomass. The simultaneous shedding of ice, concomitant with resistance to ice impact and frictional damage, suggests these hardy easy-(but not easiest)-release coatings should find their most rapid commercial adoption for service in the opening Arctic environment. A concern is that ships that acquire adverse biofouling layers in warmer waters may carry these foulants into cold water regions, with possibly negative environmental consequences. To meet the present abrasion challenge, however, current sufficiently abrasion-resistant ship hull paints are among the most fouling-prone and retentive coatings known and, as such, could be rapidly replaced by the less fouling-retentive low-drag, coatings described here.

**Acknowledgments** Aspects of the work reported here were developed with support from the Office of Naval Research, Grant N00014-89-J-3101 and Sea Grant/NOAA Projects R/EMS-2 and E/IF-1. We thank Mr. John Smith of Plastic Maritime Co. for supplies of the paint ingredients, and Mr. Lucas Latini for supply of the helicopter rotor blades and towing tank fixtures. Dr. Claes Lundgren provided access to the Project THEMIS towing tank at University at Buffalo, and supervised those tests.

## References

1. Baier RE, Meyer AE, Forsberg RL (1997) Certification of properties of nontoxic fouling-release coatings exposed to abrasion and long-term immersion. *Nav Res Rev* XLIX(4):60–65
2. Wells AW, Meyer AE, Matousek JA, Baier RE, Neuhauser EF (1997) Nontoxic foul-release coatings for zebra mussel control. In: *Waterpower '97: proceedings of the international conference on hydropower*, vol 1. American Society of Civil Engineers, pp 451–460
3. Baier RE, Meyer AE, Forsberg RL, Ricotta MS (1997) Intrinsic drag reduction of biofouling-resistant coatings. In: *Proceedings, emerging nonmetallic materials for the marine environment. US-pacific Rim workshop*, U.S. Office of Naval Research, Honolulu, HI, pp 1–36 to 1–40
4. Ricotta MS (1998) Investigation of possible mechanisms for inherent drag reduction by biofouling-release coatings. MS Thesis, State University of New York at Buffalo. (expanded conclusions in Baier RE, Ricotta MS, Meyer AE, Forsberg RL, Latini LJ, Pendergast DR (2002) Drag reduction by easy release of surface-attached foulants). In: *Proceedings 25th annual meeting of The Adhesion Society*, pp 352–355
5. Siraj FM, Baier RE (2016) Water droplet contact-adhesion of ice on reference materials. In: *Proceedings of the 39th annual meeting of The Adhesion Society*, San Antonio, Texas, 21–24 Feb 2016
6. Andolina VL (2012) Evaluation of a hydrophobic 'easy-release' silicone-epoxy coating for maintaining underwater sealing of a sliding steel/neoprene/steel interface subject to biofouling. MS Thesis, State University of New York at Buffalo
7. Garti N, Smith J (1995) New non-stick epoxy-silicone water-based coatings, part I: physical and surface properties. In: *Proceedings of the fifth international zebra mussel and other aquatic nuisance organisms conference*, Toronto, Canada, pp 151–169
8. Hogan JN (1996) Sea Grant scholars: Sea Grant helps educate future decision makers. *Coastlines*, New York Sea Grant Institute 26(1):32–33
9. Baier RE, Loeb GI (1971) Multiple parameters characterizing interfacial films of a protein analogue, polymethylglutamate. In: Craver CD (ed) *Polymer characterization: interdisciplinary approaches*. Plenum Press, New York, pp 79–96
10. Meyer A, Baier R, Wood CD, Stein J, Truby K, Holm E, Montemarano J, Kavanagh J, Nedved B, Smith C, Swain G, Weibe D (2006) Contact angle anomalies indicate that surface-active eluates from silicone coatings inhibit the adhesive mechanisms of fouling organisms. *Biofouling* 22:411–423
11. Zisman WA (1964) Relation of the equilibrium contact angle to liquid and solid constitution. Contact angle, wettability, and adhesion. *Advances in Chemistry Series*, vol 43. American Chemical Society, Washington, pp 1–51
12. Baier RE (2006) Surface behaviour of biomaterials: The *theta surface* for biocompatibility. *J Mater Sci Mater Med* 17:1057–1062
13. ASTM D5618-94 (1994) Standard test method for measurement of barnacle adhesion strength in shear. *Am Stand Test Mat*, paint, tests for formulated products and applied coatings, vol 06.01
14. Kok M, Mertens T, Raps D, Young TM (2013) Influence of surface characteristics on insect residue adhesion to aircraft leading edge surfaces. *Prog Org Coat* 76:1567–1575
15. Kaelble DH (1970) Dispersion-polar surface tension properties of organic solids. *J Adhes* 2:66–81

# Index

## A

Abrasion-resistant, vi, 3, 13, 375  
Adhesion, 2, 21, 54, 100, 125, 146, 168, 189, 222, 238, 292, 317, 360, 369  
Aerospace, v, 2–14, 28, 32, 90, 99, 101, 104, 105, 112–114, 119, 125, 129, 168–182, 292, 309, 329, 336  
Aerospace coatings, v, 170, 172, 175  
Anti-contamination, vi, 2, 3, 165, 291–310, 316, 333–350  
Antifogging, v, 186–212  
Anti-icing, v, 2, 5, 21, 43, 53–92, 124–126, 130, 159, 168, 179, 317, 334  
Atmospheric icing, 123–140

## B

Bioadhesion, 21–43  
Biofouling, v, vi, 3, 13, 14, 21, 23, 28, 41, 43, 356–359, 368, 375  
Biofouling-mitigation coatings, v, vi, 13  
Biomimetics, v, 3, 186, 360

## C

Capillary pressure, 29, 115, 119, 240, 259, 273–275, 277  
Coating durability, v, 167–181, 191, 209, 309, 316, 320, 347  
Coatings, 2, 25, 54, 100, 125, 146, 168, 186, 221, 239, 292, 316, 335, 357, 368

Conserved pathways, 359, 360  
Contamination-mitigating coatings, v, 3–9

## D

Drag reduction, 9, 13, 21, 221, 228, 368, 373  
Drop freezing time, 58, 59, 74, 86, 91  
Droplet impacts, 10, 84, 101, 102, 112, 114, 115, 117, 119, 170, 239, 240, 246, 248–252, 258, 261, 267–270, 275, 276, 278–284, 307  
Durability, v, vi, 3, 9, 12, 13, 54, 60, 67, 68, 90, 105, 140, 146, 148, 152, 161, 162, 165, 168–182, 191, 209, 211, 309, 316, 320, 328–329, 336, 347  
Durable, vi, 2, 9, 105, 106, 125, 169, 170, 180, 196, 197, 206, 211, 219, 300, 335, 350, 361

## E

Easy-to-clean, 293, 333–350  
Extreme environments, 3, 24, 25, 32, 43, 358, 359

## F

Fluorinated-hygroscopic polymers, 317, 318, 321, 327, 329  
Fouling management, 355–363  
Fouling release, 13, 368, 370

Frost-resisting, v, 186–211  
 Frost-resisting coatings, 187, 202–205, 209  
 Functional coating, 209, 306, 336

## H

Hydrophilicity, 57, 189, 194, 195, 199, 202, 204, 207, 209, 211  
 Hydrophobicity, 126, 168, 175, 189, 195, 199, 201, 202, 204, 211, 252, 254, 258, 267, 285, 297

## I

Ice, 2, 21, 54, 100, 124, 146, 168, 186, 317, 335, 368  
 Ice accretion, 4, 5, 9, 13, 53–57, 59–61, 64–66, 73, 74, 77, 86–92, 100–104, 108, 113, 118, 119, 135, 154, 168, 174, 179, 182, 335  
 Ice accumulation, 6, 90, 120, 124, 126, 132, 135, 137–139  
 Ice adhesion, 4, 41, 54, 101, 124, 146, 168, 369  
 Ice adhesion test, 5, 64–66, 74, 79, 87, 106, 107, 112, 128, 132, 146, 148, 154–158, 164, 170, 174–176, 178–181  
 Ice formation test, 147–154, 164  
 Ice-mitigating coatings, v, 3–9  
 Icephobic, 41, 43, 54, 55, 59, 60, 62, 63, 73, 76, 80, 86, 91, 124–140, 145–165  
 Icephobic coatings, 86, 125, 132, 135–140, 146, 147, 149, 158, 159, 161  
 Ice release, 108, 114, 168–182, 371  
 Icing wind tunnel, 4, 56, 99–119, 132, 158–161  
 Impact dynamics, 261, 269, 284, 293, 296, 306–309  
 Insect, 2, 21, 55, 219, 238, 292, 316, 334, 375  
 Insect adhesion, 42, 296, 306, 335, 336  
 Insect contamination, vi, 9, 291–310  
 Insect impact, vi, 10–12, 25, 223, 235–285, 293, 296, 301, 305, 307, 309, 315–350  
 Insect-mitigating coatings, 9–13, 335, 375  
 Insect mitigation, v, vi, 2, 14, 41, 334  
 Insect residue, 2, 9–11, 14, 21, 28, 218–229, 236–285, 292, 293, 295, 299–303, 305–309, 316, 318, 327, 334, 337, 339, 349

## L

Laminar flow (LF), 9, 10, 218, 219, 221–229, 238, 239, 252, 292–309, 316, 334, 375  
 Layer-by-layer assembly, 206

Liquid-impregnated surfaces (LIS), 55, 56, 62, 70, 80

## M

Marine coatings, v, 1–14  
 Mitigation, v, vi, 2–5, 8, 9, 12–14, 41, 100, 103, 217–229, 238, 239, 252, 257, 285, 300, 308, 309, 334

## N

Non-toxic coating, 368  
 Novel materials, v, 10

## P

Physiology, 222, 240

## S

Semi-interpenetrating polymer network (SIPN), 202–205, 208, 209  
 Silicone, vi, 4, 13, 14, 60, 62, 64, 65, 68, 69, 73, 74, 76–80, 86, 88, 91, 133, 134, 147, 168, 169, 227, 276, 362, 368–375  
 Slippery liquid-infused porous surfaces (SLIPS), 43, 55, 56, 62, 66, 70, 147  
 Superhydrophobic coating, 4, 66, 75, 76, 83–86, 99–119, 125, 132, 159, 160, 168, 186, 211, 293, 294, 300, 301, 309, 316, 341, 348, 349  
 Surface characterization, 146, 148, 161–164, 248, 263, 267, 369, 373  
 Surface morphology, 32–37, 39, 42, 186, 264  
 Surface roughness, 10, 27, 28, 32, 38–42, 61, 77, 89, 99, 106, 107, 114, 138, 153, 161, 164, 186, 188, 189, 195, 228, 253, 255, 256, 262, 264, 266, 267, 269, 272, 279, 280, 285, 297, 298, 335, 349  
 Surface topography, 23, 36, 40, 41, 43, 114, 160, 253, 264, 265, 269, 276, 278, 279, 285, 349

## W

Wetting phenomena, 279